

UNIVERSIDAD DE OVIEDO

Department of Electrical, Electronics, Computers and  
Systems Engineering

**PhD Thesis**

**Control strategies for enhanced dynamic  
response in hybrid AC/DC microgrids  
considering energy storage integration**

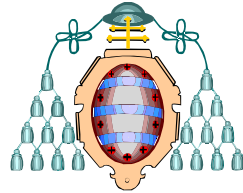
by

Ángel Navarro Rodríguez

PhD Program in Energy and Process Control  
Electrical Energy Conversion and Power Systems Research Line

June 2019





UNIVERSIDAD DE OVIEDO

Department of Electrical, Electronics, Computers and  
Systems Engineering

PhD Thesis

**Control strategies for enhanced dynamic  
response in hybrid AC/DC microgrids  
considering energy storage integration**

by

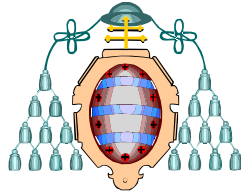
Ángel Navarro Rodríguez

**Dissertation submitted in fulfillment of the requirements for the degree of  
Doctor of Philosophy in the Energy and Process Control PhD program of  
the University of Oviedo with International Mention**

Thesis supervisor: Pablo García Fernández. Professor at Department of Electrical,  
Electronics, Computers, and Systems Engineering, University of Oviedo

June 2019





UNIVERSIDAD DE OVIEDO

Departamento de Ingeniería Eléctrica, Electrónica de  
Computadores y Sistemas

**Tesis Doctoral**

**Estrategias de control para una respuesta  
dinámica mejorada en microrredes híbridas  
AC/DC considerando la integración de  
almacenamiento de energía**

Ángel Navarro Rodríguez

**Tesis presentada en cumplimiento de los requisitos para la obtención del  
grado de Doctor en el programa de Doctorado en Energía y Control de  
Procesos de la Universidad de Oviedo con Mención Internacional**

Director de tesis: Pablo García Fernández. Profesor Titular del Departamento de  
Ingeniería Eléctrica, Electrónica, de Computadores y Sistemas de la Universidad de  
Oviedo

June 2019



*To my mother and sister,  
in memory of my father...*



# Acknowledgements

First of all, I want to express my most sincere gratitude to my supervisor, The Professor Pablo García Fernandez, for giving me a vote of confidence, for his guidance, for his patience, for his dedication, for all the knowledge he has transmitted me, for recognizing all my efforts and for constantly feeding my motivation. Thank you for understanding and for withstanding me during my difficult times and also for celebrating every achievement.

I would like to thank all the personnel in Laboratory for Electrical Energy Management Unified Research (LEMUR) research group, for offering me the opportunity to work and coexist with them. Thank you to all the professors in the group for the good moments and advice, and thanks to all of them that have allowed me to collaborate in their research, Jorge García, Jose Manuel Cano, Cristian Blanco. I have to express my special gratitude to Professor Cano, for lending me a hand when I had to storage all my belongings before traveling to Nottingham for my PhD international stay. I can not forget all my student colleges and lab mates, that have become more than coworkers and have given me so many good times, thanks to Ramy, Irene, Sarah, Miguel Huerta, Geber, Andrés, María, Miguel, Bassam and all those that I have forgotten to mention, missing the ones that have moved away for continuing their professional careers (thanks Gabriel for becoming, and still be, a friend during the time we shared in the lab). My special thank to Carlos, for also becoming a friend and count on me for every plan and concert and driving me in all those long road trips.

I also thank to all the people that I met during my stay in Nottingham, expressing my gratitude to the Department of Electrical and Electronic Engineering with Power Electronics, Machines and Control (PEMC) research group at the University of Nottingham in the United Kingdom. I am infinitely grateful to Professor Mark Sumner for his advice and making my stay very comfortable, letting me to use the facilities in his group laboratory. Thank you also to my lab mates, specially to the post-doc staff, Richard, Seksak and Chris, for their advice and help. I would not forget either my flat mates, that made my stay a wonderful time.

I express gratitude to the Electrical Engineering Department at the University of Oviedo, for introducing me in the research and teaching carrier. I have to express my gratitude to the Spanish Government, Innovation Development and Research

Office-MEC, as this work has been partially supported under research grant ENE2013-44245-R (Project “Microholo”) and ENE2016-77919 (Project ”Conciliator”), and to the European Union through ERFD Structural Funds (FEDER). I also have to acknowledge the government of Principality of Asturias in Spain and the Foundation for the Promotion in Asturias of Applied Scientific Research and Technology (FICYT), for their support and founding through the Severo Ochoa research grant BP14-135.

I want to thank also my friends and relatives, that have make me feel their support even being very far away from Asturias. My special thank to my ex-partner, that although finally last year our lives have taken separated paths, has accompanied me during most of this process, supporting me and sharing my best but also my worst moments. Thank you also to the musicians crew in Avilés, Iker, Sara, Paco and Javi, for letting me play music with them a little time every weak. Beside all this people, I am very joyful to have met María, that have been a light in my darkness during my hardest times, and although have appeared at the very end of this process, she has offered me the best of supports for finishing this thesis even been hundreds of kilometers away. Thanks for all her long calls, for her advice and help and specially for the shared moments that have been all wonderful and I hope they keep growing.

Finally, I am infinitely grateful to my familiy, Angel, Candi and Ana. I am extremely grateful to my parents for the effort and dedication they have given me, as well as their comprehension of my decisions and acts, allowing me to follow the paths I have chosen along my life. I will never forget the opportunities they have enabled for me, and I will always take into account that my academic progress would not have been possible without their support, help, love and care. Thanks to my mother, for being an example of stronghold, comprehension self-improvement and love. Thanks to my intelligent sister, for still being my little sister although both of us are near the adulthood, and thanks for still withstanding my nonsense and jokes after all this years. Thanks to my father, for his dedication, hard work and love given to his family during all his life, without failing us a single day, and thank him for being proud of me till his last day. I want to dedicate this thesis to him, that although has not lived enough to see this adventure finished, he has supported me during all this PhD years and at the end has given me the strength for finishing the writing of this thesis.

# Resumen (Spanish)

El creciente interés por minimizar la dependencia de combustibles fósiles en el sector eléctrico ha desencadenado la búsqueda de alternativas de generación basadas en energías renovables. Este objetivo ha llevado a la definición del concepto de microrred, que se ha presentado principalmente en tres topologías durante los últimos años: microrredes AC, DC e híbridas AC/DC. Sin embargo, la alta penetración de convertidores electrónicos de potencia, generación renovable, y cargas electrónicas, implican nuevos retos en este tipo de redes, que pueden comprometer su fiabilidad y robustez.

Esta tesis se centra en el control dinámico de microrredes híbridas AC/DC mediante el diseño de nuevas estrategias para una mejor respuesta dinámica. Las propuestas de este trabajo incluyen soluciones para el control de convertidores conectados a la red, el control primario de microrredes híbridas AC/DC con alta penetración de convertidores electrónicos de potencia y cargas de potencia constantes, la compensación de la falta de inercia que caracteriza a este tipo de redes, y el desarrollo de herramientas para abordar el retardo y la latencia en la estimación de la frecuencia y fase de red, así como la estimación de la impedancia de línea.

La presente investigación incluye varias contribuciones y propuestas en los campos de control de convertidores conectados a red y microrredes híbridas AC/DC: 1) Un esquema de control de corriente basado en observador para convertidores trifásicos conectados a la red mediante un filtro LCL, diseñado para evitar el uso de sensores de corriente en el lado de red. 2) Un método online de estimación de la impedancia de red utilizando inyección de pulsos, con una carga computacional moderada y una distorsión armónica total reducida en comparación con otras alternativas, siendo válido para diferentes aplicaciones en el campo de las microrredes (detección de islanding, localización de fallas, control adaptativo...). 3) Análisis del control dinámico de tensión de convertidores AC y DC bajo una alta presencia de cargas de potencia constante. Se analizan los efectos adversos causados por dichas cargas en los controles de tensión convencionales que utilizan reguladores proporcionales-integrales, lo que pone de manifiesto los beneficios de una nueva alternativa de control de tensión basado en control cuadrático, no utilizada antes en aplicaciones AC. 4) Un compensador de potencia activo para microrredes trifásicas AC, basado en un sistema de almacenamiento de energía, adecuado para mejorar la respuesta transitoria de la frecuencia y magnitud de la tensión de red, proporcionando una inercia virtual o una capacitancia virtual

respectivamente. Se ha diseñado un compensador de transitorios de frecuencia utilizando un observador de Luenberger, capaz de funcionar sólo durante los transitorios y superar el problema del retraso en la estimación de la frecuencia. La solución permite reducir el retardo de fase del compensador, mejorando la compensación de transitorios en comparación con los métodos existentes. 5) Un método predictivo de estimación y aislamiento de la secuencia principal y armónicos de red basado en la transformada de Goertzel, que mejora la dinámica de la estimación de magnitud y fase en redes distorsionadas. El estimador puede ser empleado para diferentes aplicaciones de AC (sincronización, control fundamental, compensación armónica...) El método propuesto es capaz de estimar la fase, las secuencias positiva y negativa y las componentes armónicas con una respuesta dinámica mejorada en comparación con otras alternativas de última generación. 6) Un esquema de control descentralizado para la regulación de redes de continua utilizando generadores virtuales DC combinados con un control droop P/V. El método propuesto permite ajustar la contribución de cada unidad a la inercia global y al reparto de potencia en estado estacionario, extendiendo el concepto de generador síncrono virtual a redes DC. 7) Definición de dos estrategias de control primario diferentes para una microrred híbrida AC/DC con sistemas de almacenamiento de energía integrados, compuesta por un bus DC y varias subredes AC trifásicas. La primera alternativa se basa en el uso de una topología de control maestro-esclavo tanto en el lado de DC como en las subredes AC. La segunda, está basada en el uso de generadores virtuales DC y generadores virtuales sincrónicos. 8) Dos alternativas de control dinámico mejorado para microrredes híbridas de AC/DC, que exploran el reparto de potencia activa de forma cooperativa entre las subredes DC y AC. El primero se basa en un algoritmo de distribución de potencia adaptable y el segundo en un novedoso esquema de generador virtual híbrido AC/DC. Ambas soluciones tienen como objetivo reducir la dependencia de la red eléctrica principal y mejorar la respuesta en bus DC en condiciones de baja inercia.

Las estrategias de control propuestas han sido verificadas mediante simulaciones y pruebas experimentales. La validación práctica del trabajo realizado se ha llevado a cabo en una microrred híbrida AC/DC de laboratorio desarrollada en las instalaciones del grupo LEMUR en la Universidad de Oviedo, España, y en la microrred de laboratorio del grupo PEMC en la Universidad de Nottingham, Reino Unido.

# Abstract

The ultimate goal of minimizing the fossil fuels dependency in the electrical sector, has triggered the search for alternatives to conventional generation systems based on renewable distributed generation. Those necessities have led to the definition of the microgrid concept, that has been presented in three main topologies during the last years: AC, DC and hybrid AC/DC microgrids. However, the penetration of power electronic converters, renewable energies, reduced size generators, and tightly regulated loads, involve new challenges in this kind of grids, that can compromise their reliability and robustness.

This thesis is focused on the dynamic control of hybrid AC/DC microgrids by promoting new strategies for an improved dynamic response. The proposals in this work includes solutions for the control of grid-tied converters, the primary control of hybrid AC/DC microgrids with high penetration of power electronic converters and constant power loads, paying special attention to the role of interlinking converters, the compensation for the lack of inertia that characterize this kind of grids, and provide tools to address the delay and latency in frequency/phase estimation and the estimation of grid impedance, useful for its application in the converter/primary control, active power compensation, protections or power quality.

The research includes several contributions and proposals in the fields of grid-tied converter control and hybrid AC/DC microgrids: 1) An observer-based current control for LCL in grid-tied 3-phase converters is designed for avoiding the grid-side current sensors. 2) An online grid impedance estimation method is developed based on pulsed signal injection. The method presents a reduced computational burden and total harmonic distortion when compared to other alternatives, being valid for different applications in the field of microgrids (islanding detection, fault location, adaptive control...) 3) The dynamic voltage control of 3-phase AC and DC converters is extensively analyzed under a high penetration of constant power loads. Their adverse effects in conventional feedback voltage control based on proportional-integral regulators is analyzed, evincing the benefits of a novel alternative quadratic-based voltage control, not used before in AC applications. 4) An active power compensator in 3-phase AC microgrids based on an energy storage system, suitable for improving the transient response for the frequency and voltage magnitude by providing virtual inertia or virtual capacitance respectively. An enhanced Luenberger observer-based frequency drift compensator is

devised, able to operate continuously or only during transients and overcome the issue of frequency estimation delay. The solution allows a reduction of the compensator phase lag, improving the initial transient compensation when compared with previous proposed methods. 5) A predictive sequence estimation method based on the sliding Goertzel transformation, that improves the dynamics of frequency and phase estimation under highly distorted grid conditions. The estimator can be employed for different AC applications (synchronization, fundamental control, harmonic compensation...) The proposed method is able to estimate the grid phase, the positive and negative sequences and the harmonics components with an improved dynamic response when compared to state-of-the-art alternatives. 6) A decentralized control scheme is presented for the regulation of DC grids based on DC virtual generators combined with DC P/V droop control. The proposed method allows to adjust the contribution of each unit to the overall inertia and to the steady state power sharing, extending the virtual synchronous generator concept to DC applications. 7) Two different primary control strategies are defined for a hybrid AC/DC microgrid with integrated energy storage systems, composed by a DC bus and several 3-phase AC subgrids, one based on voltage-controlled grid-forming master-slave in both DC and AC sides, and the other based on DC virtual generators and virtual synchronous generators. 8) Two enhanced dynamic control alternative for hybrid AC/DC microgrids, exploring the cooperative active power sharing between the DC and the AC subgrids. The first one is based on an adaptive power sharing algorithm and the second on a novel hybrid AC/DC virtual generator scheme. Both solutions aim for a reduction in the dependence from the utility grid and improve the response in the DC subgrid under low inertia conditions.

The proposed control strategies have been verified both by simulation and by experimental tests. Practical validation of the conducted work has been carried out in a hybrid AC/DC lab microgrid developed in the facilities of the LEMUR group in the University of Oviedo, Spain, and in the facilities belonging to the PEMC group in The University of Nottingham, UK.

# Nomenclature

$\mathbf{v}$	Voltage complex vector.
$\mathbf{i}$	Current complex vector.
$\mathbf{x}_s$	Arbitrary complex vector.
$\omega_e$	Fundamental angular frequency.
$\omega_r$	Rotor angular velocity.
$h$	Harmonic order.
$v_i$	Inverter output voltage.
$v_g$	PCC grid voltage.
$v_c$	Capacitor LC / LCL voltage.
$i_i$	Inverter-side current.
$i_g$	Grid-side current.
$x_{dq}$	Voltage/current in synchronous reference frame.
$x_{\alpha\beta}$	Voltage/current in the $\alpha\beta$ stationary reference frame.
$P_i$	Inverter side shared active power.
$P_g$	Grid side shared active power.
$P_{NGHC_k}$	Active power shared by a nanogrid head converter.
$P_{mains}$	Active power shared by the utility grid.
$P_{bess}$	Active power shared by the central battery energy storage.
$P_{fc}$	Active power shared by the frequency compensators.
$P_{vc}$	Active power shared by the voltage compensators.
$B_j^k$	AC j nodes within the nanogrid k.
$Z_{L_j}^k$	Line impedance between nodes in the nanogrid k.
$L_1$	Inverter side LCL filter inductance
$R_1$	Inverter side LCL filter ESR
$L_2$	Grid side LCL filter inductance
$R_2$	Grid side LCL ESR
$Z_L$	Grid line impedance
$i_{dc}$	Current flow in a DC bus.
$i_{C_{dc}}$	DC capacitor current.
$\mathbf{x}$	State vector in the state space representation.
$\mathbf{u}$	Input vector in the state space representation.
$\mathbf{y}$	Output vector in the state space representation.

<b>A</b>	State matrix in the state space representation.
<b>B</b>	Input matrix in the state space representation.
<b>C</b>	Output matrix in the state space representation.
<b>D</b>	Feed-forward matrix in the state space representation.
<b>Z</b>	Impedance matrix.
<b>L</b>	Inductance matrix.
<b>R</b>	Resistance matrix.
<b>X</b>	Variables vector in the RLS implementation.
<b>W</b>	Coefficients vector in the RLS implementation.
<b>W</b>	Coefficients vector in the RLS implementation.
<b>P</b>	Covariance matrix in the RLS implementation.
<b>g</b>	Adaptation gain in the RLS implementation.

# Acronyms

<b>MG</b>	Microgrid.
<b>NG</b>	Nanogrid.
<b>PG</b>	Picogrid.
<b>MGHC</b>	Microgrid head converter.
<b>NGHC</b>	Nanogrid head converter.
<b>MGTC</b>	Microgrid transformation center.
<b>PCC</b>	Point of common coupling.
<b>DPG</b>	Distributed power generation.
<b>DG</b>	Distributed generator.
<b>DER</b>	Distributed energy resource.
<b>RES</b>	Renewable energy source.
<b>MPPT</b>	Maximum power point tracking.
<b>RDG</b>	Renewable distributed generator.
<b>NRDG</b>	Non-renewable distributed generator.
<b>ESS</b>	Energy storage system.
<b>ES</b>	Energy storage.
<b>BESS</b>	Battery energy storage system.
<b>DESS</b>	Distributed energy storage system.
<b>SMES</b>	Superconducting magnetic energy storage.
<b>SoC</b>	State of charge.
<b>PEC</b>	Power electronic converter.
<b>IGBT</b>	Insulated-gate bipolar transistor.
<b>APF</b>	Active power filter.
<b>AFE</b>	Active front end.
<b>PWM</b>	Pulse width modulation.
<b>SST</b>	Solid state transformer.
<b>VSI</b>	Voltage source inverter.
<b>VSC</b>	Voltage source converter.
<b>CSI</b>	Current source inverter.
<b>STATCOM</b>	Static synchronous compensator.
<b>D – STATCOM</b>	Distributed static synchronous compensator.
<b>VI</b>	Virtual inertia.

<b>VC</b>	Virtual capacitance.
<b>VSG</b>	Virtual synchronous generator.
<b>VSM</b>	Virtual synchronous machine.
<b>PMSG</b>	Permanent magnet synchronous generator.
<b>PMSM</b>	Permanent magnet synchronous machine.
<b>SG</b>	Synchronous generator.
<b>AVR</b>	Automatic voltage regulator.
<b>bemf</b>	Back electromotive force.
<b>TFDC</b>	Transient frequency drift compensator.
<b>RoCoF</b>	Rate of change of frequency.
<b>CPL</b>	Constant power load.
<b>CIL</b>	Constant impedance load.
<b>CCL</b>	Constant current load.
<b>P</b>	Proportional (controller).
<b>PI</b>	Proportional integral (controller).
<b>PD</b>	Proportional derivative (controller).
<b>PID</b>	Proportional integral derivative (controller).
<b>PR</b>	Proportional resonant (controller).
<b>PDF</b>	Pseudo-derivative feedback (controller).
<b>DVC</b>	Direct voltage controller.
<b>QVC</b>	Quadratic voltage controller.
<b>THD</b>	Total harmonic distortion.
<b>FLL</b>	Frequency locked loop.
<b>PLL</b>	Phase locked loop.
<b>SRF</b>	Synchronous reference frame.
<b>PFS</b>	Pre filter stage.
<b>AC</b>	Alternating current.
<b>DC</b>	Direct current.
<b>LPF</b>	Low pass filter.
<b>DSOGI</b>	Dual second order generalized Integrator.
<b>SGT</b>	Sliding Goertzel transform.
<b>PSI</b>	Pulsed signal injection.
<b>HFSI</b>	High frequency signal injection.
<b>LFSI</b>	Low frequency signal injection.
<b>BSSI</b>	Binary sequence signal injection.
<b>LTI</b>	Linear and time invariant (system).
<b>DCL</b>	Digital communication link.
<b>RLS</b>	Recursive least square.
<b>MRAS</b>	Model reference adaptive system.
<b>DSP</b>	Digital signal processor.
<b>FFT</b>	Fast Fourier transform.
<b>BW</b>	Bandwidth.
<b>IEEE</b>	Institute of electrical and electronics engineers.

# Contents

Acknowledgements . . . . .	VII
Resumen (Spanish) . . . . .	IX
Abstract . . . . .	XI
Nomenclature . . . . .	XIII
Acronyms . . . . .	XV
<b>1 Introduction</b> . . . . .	<b>1</b>
1.1 Background and motivation . . . . .	1
1.2 Thesis objectives . . . . .	5
1.3 Thesis contributions . . . . .	6
1.4 Thesis publications . . . . .	7
1.4.1 Peer-reviewed journal papers . . . . .	7
1.4.2 Peer-reviewed conference papers . . . . .	8
1.4.3 Peer-reviewed journal papers in review process . . . . .	10
1.5 Thesis outline . . . . .	11
<b>2 Literature review and state of the art</b> . . . . .	<b>13</b>
2.1 Introduction . . . . .	13
2.2 The microgrid paradigm: definition, architectures, components and challenges . . . . .	13
2.2.1 The microgrid concept . . . . .	14
2.2.2 The microgrid architecture . . . . .	14
2.2.3 Distributed generation and energy storage . . . . .	20
2.2.4 Load characteristics in MGs . . . . .	22
2.2.5 Power electronic converters for low voltage MGs applications . . . . .	23

2.2.6	Standards, recommendations and grid codes . . . . .	27
2.3	Microgrid and grid-tied DERs control . . . . .	28
2.3.1	Background on coordinated control methods in microgrids . . . . .	29
2.3.2	Hierarchical control in AC microgrids . . . . .	30
2.3.3	Primary local control of PECs-interfaced DERs in AC microgrids . . . . .	31
2.3.4	The virtual synchronous generator concept . . . . .	33
2.3.5	Control aspects in DC microgrids . . . . .	35
2.3.6	Control aspects in hybrid AC/DC microgrids . . . . .	37
2.3.7	AC and DC PI-based grid-forming converters . . . . .	40
2.4	Dynamic active power compensation for quality improvement in AC and DC MGs . . . . .	42
2.4.1	Energy storage systems for AC and DC active power compensation . . . . .	44
2.4.2	Transient frequency compensation and virtual inertia . . . . .	45
2.4.3	Transient DC voltage magnitude compensation and virtual capacitance . . . . .	49
2.4.4	Transient AC voltage magnitude compensation in V/P regulated and fixed frequency systems . . . . .	50
2.5	Estimation methods in MGs applications . . . . .	51
2.5.1	Estimation methods for LCL filter control . . . . .	51
2.5.2	Impedance estimation . . . . .	52
2.5.3	Grid phase, frequency and sequence estimators . . . . .	54
2.6	Summary and research opportunities . . . . .	55
<b>3</b>	<b>Microgrid description, dynamic modelling, and grid-tied converters control</b>	<b>63</b>
3.1	Introduction . . . . .	63
3.2	Description of the hybrid AC/DC microgrid . . . . .	64
3.2.1	Microgrid topology . . . . .	64
3.2.2	Solid state transformer . . . . .	66
3.2.3	LVDC bus modelling . . . . .	68
3.2.4	Nanogrid head converters . . . . .	69
3.3	Dynamic modelling of grid-tied 3-phase AC VSIs . . . . .	70
3.4	Current control in grid-tied VSIs interfaced by L, LC and LCL filters . . . . .	72
3.5	The Luenberger observer . . . . .	74

---

3.5.1	Luenberger observer model . . . . .	75
3.5.2	Observer tuning . . . . .	77
3.5.3	Control system application . . . . .	78
3.6	Observer-based LCL filter current control for grid-tied 3-phase VSIs . .	79
3.6.1	Grid-side current observer model . . . . .	80
3.6.2	Analytical linear model of the current observer . . . . .	80
3.6.3	Observer compensator tuning . . . . .	83
3.6.4	Analytical response of the grid-side current observer . . . . .	84
3.6.5	Simulation results . . . . .	87
3.6.6	Grid-side current observer digital implementation . . . . .	88
3.6.7	Experimental results . . . . .	89
3.7	Grid impedance estimation in 3-phase systems based on pulsed signal injection . . . . .	91
3.7.1	Pulsed signal injection . . . . .	91
3.7.2	RLS algorithm implementation . . . . .	95
3.7.3	Simulation results . . . . .	101
3.7.4	Experimental results . . . . .	102
3.8	Voltage control in 3-phase AC and DC grid-forming converters . . . . .	106
3.8.1	Problem definition and system modelling . . . . .	107
3.8.2	Voltage control design alternatives: DVC vs QVC . . . . .	109
3.8.3	Closed-loop disturbance rejection: analytical models and analysis	113
3.8.4	Effect of the capacitor in the system response . . . . .	122
3.8.5	Virtual capacitance for enhanced disturbance rejection . . . . .	123
3.8.6	Effect of the nominal operating point and the controller bandwidth	124
3.8.7	Grid-forming system design: an application example . . . . .	127
3.8.8	The quadratic voltage control applied to AC grid-forming units .	128
3.8.9	Experimental results . . . . .	131
3.9	Conclusions . . . . .	134

---

<b>4</b>	<b>Enhanced dynamic active power support and synchronization in weak AC microgrids</b>	<b>137</b>
4.1	Introduction . . . . .	137
4.2	Dynamic active power compensation for enhanced transient response in AC microgrids . . . . .	138
4.2.1	The 3-phase dynamic active power compensator . . . . .	139
4.2.2	Voltage magnitude compensation . . . . .	140
4.2.3	Frequency compensation . . . . .	142
4.3	Observer-based transient frequency drift compensation in weak AC microgrids . . . . .	143
4.3.1	Frequency drift problem and system modelling . . . . .	143
4.3.2	Feedback-based transient frequency compensator . . . . .	146
4.3.3	Observer-based transient frequency compensator . . . . .	154
4.3.4	Experimental results . . . . .	157
4.4	Predictive sequence estimator for control of grid-tied converters under highly distorted conditions . . . . .	165
4.4.1	The Goertzel algorithm . . . . .	166
4.4.2	The predictive sliding Goertzel-based sequence estimator . . . . .	168
4.4.3	Offline system evaluation . . . . .	177
4.4.4	Online system evaluation . . . . .	183
4.5	Conclusions . . . . .	188
<b>5</b>	<b>Cooperative primary control in hybrid AC/DC microgrids</b>	<b>191</b>
5.1	Introduction . . . . .	191
5.2	Primary control implementation in a hybrid AC/DC microgrid with multiple AC subgrids . . . . .	192
5.2.1	QVC-based microgrid control proposal . . . . .	195
5.2.2	VG-based microgrid control proposal . . . . .	197
5.3	Improved cooperative active power control discussion . . . . .	203
5.4	Hybrid microgrid control based on adaptive dynamic power sharing . . . . .	205
5.4.1	The DC bus voltage control scheme . . . . .	206
5.4.2	Adaptive NGs power sharing algorithm . . . . .	207
5.4.3	The AC nanogrids cooperative voltage control scheme . . . . .	209
5.4.4	Simulation and experimental results . . . . .	213

5.4.5	Disturbance to output frequency response . . . . .	220
5.5	Hybrid AC/DC microgrid control based on hybrid AC/DC virtual generators . . . . .	222
5.5.1	The proposed hybrid AC/DC virtual generator . . . . .	222
5.5.2	Simulation results . . . . .	225
5.6	Conclusions . . . . .	229
<b>6</b>	<b>Conclusions and future work</b>	<b>231</b>
6.1	Conclusiones (Spanish) . . . . .	231
6.2	Conclusions . . . . .	235
6.3	Future work . . . . .	239
	<b>Bibliography</b>	<b>268</b>
<b>A</b>	<b>Simulation and experimental implementation</b>	<b>271</b>
A.1	Clarke-Park transform . . . . .	273
A.2	Digital control implementation . . . . .	275
A.3	Simulation and experimental setup: evaluation of the observer-based LCL filter control . . . . .	276
A.4	Simulation and experimental setup: evaluation of the grid impedance estimation method based on pulsed signal injection . . . . .	277
A.5	Simulation and experimental setup: analysis of DVC and QVC . . . . .	278
A.6	Simulation and experimental setup: evaluation of the observer-based transient frequency compensation . . . . .	279
A.7	Simulation and experimental setup: evaluation of the predictive sequence estimator . . . . .	281
A.8	Simulation setup: LVDC control based on droop control and DCVGs . . . . .	283
A.9	Simulation and experimental setup: evaluation of the <i>basic</i> and <i>cooperative</i> QVC-based MG control . . . . .	284
A.10	Simulation setup: evaluation of the <i>basic</i> and <i>cooperative</i> VG-based MG control . . . . .	285
	<b>Appendix</b>	<b>271</b>
<b>B</b>	<b>Algorithms pseudo-code and diagrams</b>	<b>287</b>
B.1	Transient detection algorithm . . . . .	289
B.2	Sliding Goertzel transform algorithm . . . . .	290

---

<b>C</b>	<b>Journal publications</b>	<b>291</b>
C.1	Observer-based Transient Frequency Drift Compensation in AC MGs . . .	293
C.2	Adaptive Active Power Sharing Techniques in a Hybrid DC/AC MG . . .	307
C.3	Observer-Based PSI for Grid Impedance Estimation . . . . .	322
C.4	Predictive Frequency-Based Sequence Estimator . . . . .	337
<b>D</b>	<b>Conference publications</b>	<b>351</b>
D.1	LFSI for grid impedance estimation in three phase systems . . . . .	353
D.2	Transient Frequency Drift Compensation on Weak MGs . . . . .	364
D.3	Voltage control for grid forming converters in DC and AC MGs . . . . .	375
D.4	Adaptive Active Power Sharing Techniques in a Hybrid DC/AC MG . . .	388
D.5	Predictive frequency-based sequence estimator . . . . .	398
D.6	Cooperative Control in a Hybrid DC/AC MG based on HVG . . . . .	409

# Chapter 1

## Introduction

### 1.1 Background and motivation

The increasing concern about environmental issues as the green house effect, the imminent lack of fossil fuels and the environmental risks and social concerns associated to nuclear power plants (waste, radioactivity...), led to the rise of new sustainable alternatives for energy generation. During the last decades of the 20th century, several technologies based on renewable energy harvesting were developed and started to be integrated in the conventional electricity system mainly at distribution levels, giving rise to the concept of distributed generation (DG). This trend could potentially have a negative impact in the conventional grid robustness, due to the unpredictability and intermittent nature of this new generation concept. Moreover, this variable participation of renewable DGs (RDGs), decoupled from the load profile, created the necessity for energy storage systems (ESSs) with relatively fast dynamic response, not only to take full advantage of the renewable resources, but to provide an effective solution for ancillary services and power quality. Since then, the research on renewable energies, ESSs and the fast development of semiconductor technologies together with the new social needs and lifestyle have created the need for modifying and adapting the electricity systems as they stand today.

The conventional grid concept is based on a centralized generation in large scale power plants, which primary resources are fossil fuels (coal, natural gas, petroleum...), nuclear energy or hydropower, that fed a set of loads (clients) distributed along the territory covered by the electrical system. The generation is adapted to the load demand, being the stationary participation of each power plant dependent on its controllability, or dynamics, and ruled by a grid operator. In addition, those conventional power stations are interconnected by means of large synchronous generators that provide the system with a high inertial energy, supporting the mismatches between generation and load during transients. Thus, characteristics as robustness, reliability and stability are

inherent to the conventional electrical system. However, the centralized scheme often implies the necessity of long transmission lines and associated transformation centers to transport and distribute the energy until reaching the final consumer.

In order to reduce emissions, integrate renewable sources and reduce power losses, the use of DGs has become increasingly popular. Moreover, with the new society needs and thanks to the technology development during the last years, the term DG is not only linked to medium size renewable plants but also to small size renewable generation and non-renewable solutions as diesel generators. In addition, the affordability of small size DGs, and ESSs, enables the client to become an active entity and participate not only drawing but also delivering power into the grid, giving rise to concepts as micro-generation, self-consumption or nearly zero-energy buildings (nZEB).

Nevertheless, the integration of a large number of DGs in the distribution network becomes a challenge for the conventional electrical grid, as it is not conceived for supporting a decentralized operation, presenting issues related to stability, power quality and economical dispatch, compromising its reliability. In order to reduce the impact of DGs penetration in the grid, the foreseen solution consists in grouping together a set of electrical devices in clusters composed of renewable and non-renewable DGs (NRDGs), ESSs and loads, defined as microgrid (MG). This solution not only allows to integrate the DGs and promote the local consumption (reducing losses), but also the disconnection (*islanded* mode) from the main grid. It is also a solution to provide power supply in remote locations, isolated areas (due to geographical location or natural disasters), large vehicles (ships, aircraft...), islands and critical areas where the grid connection is not reliable. The conceptual comparison between the traditional system and the microgrid paradigm is represented in Fig. 1.1.

Unlike conventional grids, characterized by a massive inertia, a low resistance to reactance impedance ratio ( $R/X$ ) and a robust behavior against contingencies, MGs are usually dominated by low inertia generators that present a high output impedance. This, in combination with the high  $R/X$  ratio of the distribution lines, the integration of several distributed intermittent renewable generation sources (RES), and the existence of electronic dynamic loads of a significant power compared to the system rated power, can cause an important quality degradation in the power grid. All these characteristics turns MGs into weak-grids, susceptible to power quality issues, transient instability and contingencies due to active power changes.

Since MGs are weak electrical networks, they are affected by several factors that influence the power quality. Unpredictable pulsating generation and, in some cases unbalanced (single-phase microgeneration) can lead to generation/consumption power mismatches and unbalanced voltages and currents. The lower rigidity and inertia affects the dynamics and stability of both the AC parameters (frequency and voltage magnitude) as well as DC parameters (bus voltage value). The presence of tight regulated, unbalanced or non-linear loads can create significant transients, voltage distortion, stability issues, unbalances and introduce low frequency harmonics in the MG buses. This situation is significantly worsened when the MG is operated in *islanded* mode, as imbalances between generation and local consumption affect the stability of

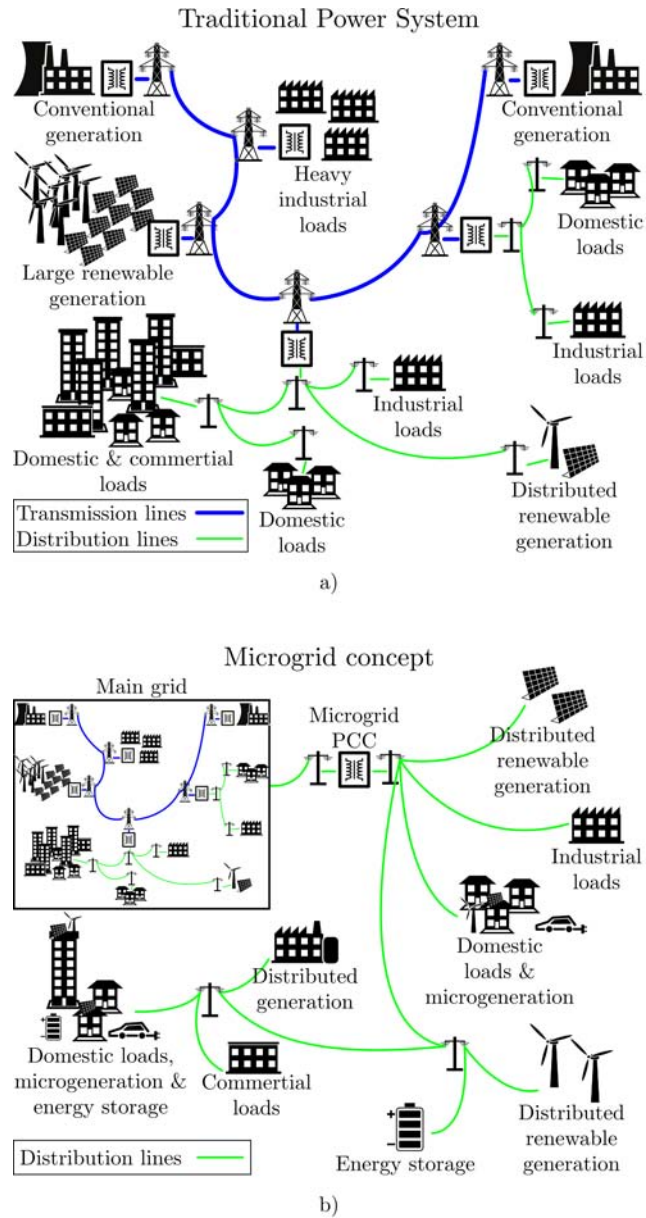


**Figure 1.1:** Microgrid concept. a) Traditional power system. b) Microgrid.

the grid.

In addition, although the increasing penetration of power electronic converters (PECs) contributes to a better controllability of the system and the integration of renewable energy sources, also adds complexity to the system control. The semiconductors development has allowed the evolution of two main lines of technology in the matter concerned. The microelectronics provides with faster, smaller, cheaper and more powerful microprocessors as well as better data storage systems, which allow to implement more complex processes. This, in conjunction with the fast development of communication technologies, enable the implementation of more sophisticated control systems, giving rise to concepts like Smart Grid. On the other hand, the field of power electronics offers switching devices (IGBTs, SiC MOSFETs...) that allow for higher switching frequencies and dynamics, better controllability, reduced size and lower losses, enabling the development of new PECs topologies, extending their applications within the electrical system. The versatility and the ease of PECs for decoupling the dynamics and electrical characteristics of the primary energy source/load (voltage waveform, voltage and current levels ...), are turning them into the preferred option for the interconnection of DGs, ESS, and loads with the electrical grids. However, they also present some problems: 1) decoupling the primary energy source involves also decoupling its inertia; 2) the fast dynamics allowed by PECs may affect the robustness of the system; 3) the conventional protections may lose effectiveness due to the fast switching capability of PECs; 4) the system operation is affected by the need of current and voltage measurement as well as synchronization in AC systems; 5) PECs reduce the system efficiency as power conversion stages always entail power losses.

Although nowadays most of MGs are AC, the increasing presence of DC DGs and loads (or AC DGs and loads with an AC/DC/AC conversion stage), that require additional stages of PECs for its integration in the AC buses, has contributed to the rise of DC MGs. However, considering the maturity of the AC system as well as the fact that many of the actual loads and generation systems are AC, has pushed the proposal of hybrid AC/DC MGs.

Despite their advantages, the weakness and stability problems associated to MGs have demanded a significant research interest since their appearance, specially in the fields of MG control and power quality improvement. Furthermore, with the appearance of hybrid AC/DC MGs, where distributed energy resources (DERs) and loads may share power in both AC and DC buses, new MG issues arise concerning the stability, voltage regulation and quality maintenance in both DC and AC grids. This thesis attempts to contribute in the field of MGs focusing on the development of solutions for improving the dynamic voltage and frequency control in AC, DC and hybrid AC/DC microgrids, providing estimation and converter control strategies for MG applications in order to improve the grid reliability.

## 1.2 Thesis objectives

This thesis will analyze and propose new control strategies and solutions for an improved dynamic response and converter control in hybrid AC/DC microgrids dominated by power electronic converters. The study will emphasize the improvement of the transient response in the active power by using energy storage systems.

The particular needs of hybrid AC/DC microgrids, and the quality and reliability issues derived from the high penetration of PECs, tightly regulated loads and low inertia, lead to the necessity for developing new solutions that ensure their robustness and reliability.

The study will consider the control of grid-tied converters, including the estimation of parameters and variables for improved control strategies, the coordinated operation among the different converters for the dynamic control of voltage and frequency in the DC and AC sides of microgrids, the dynamic interaction between the DC and AC subgrids, and the role of energy storage systems integrated in the system. In order to tackle this topics, the following objectives have been defined:

1. State of the art in control systems of AC/DC microgrids. This objective will offer an overview on the field of microgrids, covering the following aspects in search for the identification of opportunities and technology gaps:
  - Microgrid architectures and types, defining the typical elements that populate them and the challenges with respect to traditional grids.
  - Microgrid control strategies, focusing on the grid-tied devices control and their role in the primary control layer of AC, DC and hybrid AC/DC MGs.
  - The integration of energy storage systems as a solution for the lack of inertia and improved dynamic response in microgrids.
  - Estimation methods for the improvement of converter control, focusing on impedance, sequence and frequency estimation and synchronization.
2. Analysis and development of current and voltage control techniques for grid-tied PECs. This objective involves the modelling of the system plant considered for the control design in both DC and AC applications, the proposal of new solutions for the current control of L, LC and LCL filters based on the use of observers and estimation methods, and the study of tightly regulated electronic loads effect in the DC and AC voltage control, analyzing the use of alternatives to the conventional feedback PI-based control as the quadratic control.
3. Development of new dynamic control architectures for DC voltage and AC voltage magnitude and frequency control in hybrid AC/DC microgrids. The design will be mainly focus on the primary control layer of a hierarchical control applied to a hybrid AC/DC microgrid. The proposed control schemes should consider the control of the AC/DC interlinking converters, the role of DERs in the microgrid,

the participation of ESSs, and the operation during *grid-connected* and *islanded* modes. An special attention will be given to the dynamic active power sharing between the DC and AC sides of the microgrid, pursuing for a cooperative operation between the different subgrids.

4. Development, analysis and integration of solutions for dynamic active power compensation pursuing to improve the lack of inertia in 3-phase weak AC systems. The use of ESSs enables a dispatchable bidirectional active power sharing with the microgrid, being suitable candidates for transient and stationary participation.
5. Estimation of parameters and variables in weak and distorted microgrids. The proper estimation of variables and parameters can improve the operation of the converters and the microgrid. The estimation of grid variables, by means of estimators or observers, will be considered for the reduction in the number of sensors (current measurements) and the estimation of variables that cannot be measured directly (phase, frequency, voltage and current sequences, disturbances...) In addition, the estimation of grid impedance will be investigated as a tool for future applications in MGs.
6. Simulation and experimental validation. A final objective of the research is to evaluate the performance of the proposed methods under a controlled environment. For that, the proposed strategies will be tested through simulations in MATLAB<sup>®</sup> and MATLAB/Simulink<sup>®</sup>, and validated in different experimental setups within the laboratory of the LEMUR group at the University of Oviedo, Spain, and in the facilities of the PEMC group at The University of Nottingham, United Kingdom.

### 1.3 Thesis contributions

The specific contributions of this thesis, derived from the established objectives, are listed below:

1. A novel hybrid AC/DC microgrid architecture with multiple AC subgrids and interlinking converters has been explored, based on the microgrid proposed in [1]. The role of the different elements that integrate it has been studied and an experimental full scale prototype has been developed and tested [2-4].
2. An LCL filter control has been proposed based on a Luenberger-based observer that allows to avoid the use of the grid-side current sensor and indicate potential changes in the grid impedance [5,6].
3. The stability limits, performance and design of DC and AC grid-forming converters have been deeply analyzed, pursuing the proper selection of the control scheme and filter parameters. Special attention has been paid to tightly regulated

electronic loads, proposing the use of a quadratic-based control for both the DC and the AC voltage control [7].

4. Two alternatives for the active power sharing between DC and AC buses in a hybrid MG have been proposed when the interlinking converter has the role of grid-forming, one based on quadratic voltage control and another based on virtual generators, including a VSG-based for DC microgrids regulation [2–4]. In addition, an improved cooperative power sharing strategy has been proposed for both control alternatives, pursuing to reduce the dependence in the utility grid and promote the collaboration between the AC and DC subgrids.
5. A grid impedance estimation method, able to operate under unbalances, is proposed based on pulsed signal injection for the excitation of the grid, triggered by an LCL observer internal signal, and recursive least square for the system parameters estimation [5,6].
6. The use of virtual capacitance and active power voltage compensator has been proposed for voltage compensation in AC grids ruled by a P/V (active power/voltage magnitude) relation [3,7].
7. In order to cover two of the main handicaps in transient frequency compensation and virtual inertia, an enhance observer-based transient frequency compensator has been proposed to reduce the effect produced by the delay and bandwidth of the frequency estimator and a transient detector has been designed to avoid the unwanted participation during steady state [8,9].
8. To overcome the phase delays introduced by filtering stages and increase the immunity in distorted grids, a predictive sequence estimator has been proposed based on a sliding Goertzel transform, able to estimate the fundamental and harmonic components of grid voltages and currents [10,11].

## 1.4 Thesis publications

The work described in this thesis has resulted in the following journal and conference publications.

### 1.4.1 Peer-reviewed journal papers

- JP1** Á. Navarro-Rodríguez, P. García, R. Georgious, J. García and S. Saeed, "Observer-Based Transient Frequency Drift Compensation in AC Microgrids," in *IEEE Transactions on Smart Grid*, vol. 10, no. 2, pp. 2015-2025, March 2019. doi: 10.1109/TSG.2017.2786085.

- JP2** Á. Navarro-Rodríguez, P. García, R. Georgious and J. García, "Adaptive Active Power Sharing Techniques for DC and AC Voltage Control in a Hybrid DC/AC Microgrid," in *IEEE Transactions on Industry Applications*, vol. 55, no. 2, pp. 1106-1116, March-April 2019. doi: 10.1109/TIA.2018.2873543
- JP3** P. García, M. Sumner, Á. Navarro-Rodríguez, J. M. Guerrero and J. García, "Observer-Based Pulsed Signal Injection for Grid Impedance Estimation in Three-Phase Systems," in *IEEE Transactions on Industrial Electronics*, vol. 65, no. 10, pp. 7888-7899, Oct. 2018. doi: 10.1109/TIE.2018.2801784.
- JP4** C. B. Charro, P. García-Fernandez, Á. Navarro-Rodríguez and M. Sumner, "Predictive Frequency-Based Sequence Estimator for Control of Grid-Tied Converters Under Highly Distorted Conditions," in *IEEE Transactions on Industry Applications*, vol. 54, no. 5, pp. 5306-5317, Sept.-Oct. 2018. doi: 10.1109/TIA.2018.2846552.
- JP5** P. García, S. Saeed, Á. Navarro-Rodríguez, J. Garcia and H. Schneider, "Switching Frequency Optimization for a Solid State Transformer With Energy Storage Capabilities," in *IEEE Transactions on Industry Applications*, vol. 54, no. 6, pp. 6223-6233, Nov.-Dec. 2018. doi: 10.1109/TIA.2018.2860561.
- JP6** R. Georgious, J. García, Á. Navarro-Rodríguez and P. García, "A Study on the Control Design of Nonisolated Converter Configurations for Hybrid Energy Storage Systems," in *IEEE Transactions on Industry Applications*, vol. 54, no. 5, pp. 4660-4671, Sept.-Oct. 2018. doi: 10.1109/TIA.2018.2838086.
- JP7** J. M. Cano, Á. Navarro-Rodríguez, A. Suárez and P. García, "Variable Switching Frequency Control of Distributed Resources for Improved System Efficiency," in *IEEE Transactions on Industry Applications*, vol. 54, no. 5, pp. 4612-4620, Sept.-Oct. 2018. doi: 10.1109/TIA.2018.2836365.
- JP8** Georgious Ramy, García Jorge, García Pablo and Navarro-Rodríguez Ángel. (2018). A Comparison of Non-Isolated High-Gain Three-Port Converters for Hybrid Energy Storage Systems. *Energies*. doi: 11.658.10.3390/en11030658.
- JP9** A. Suárez González, P. García, A. Navarro Rodríguez, G. Villa and J. M. Cano, "Sensorless Unbalance Modelling and Estimation as an Ancillary Service for LV 4-Wire/3-Phase Power Converters," in *IEEE Transactions on Industry Applications*, Early Access, May 2019. doi: 10.1109/TIA.2019.2918046

#### 1.4.2 Peer-reviewed conference papers

- CP1** P. García, J. M. Guerrero, J. García, Á. Navarro-Rodríguez and M. Sumner, "Low frequency signal injection for grid impedance estimation in three phase systems," 2014 IEEE Energy Conversion Congress and Exposition (ECCE), Pittsburgh, PA, 2014, pp. 1542-1549.

- CP2** A. Navarro-Rodriguez, P. Garcia, R. Georgious and J. Garcia, "A communication-less solution for transient frequency drift compensation on weak microgrids using a D-statcom with an energy storage system," 2015 IEEE Energy Conversion Congress and Exposition (ECCE), Montreal, QC, 2015, pp. 6904-6911.
- CP3** Z. Wang, A. Castellazzi, S. Saeed, Á. Navarro-Rodríguez and P. Garcia, "Impact of SiC technology in a three-port active bridge converter for energy storage integrated solid state transformer applications," 2016 IEEE 4th Workshop on Wide Bandgap Power Devices and Applications (WiPDA), Fayetteville, AR, 2016, pp. 84-89.
- CP4** P. García, S. Saeed, Á. Navarro-Rodríguez, J. Garcia and H. Schneider, "Switching frequency optimization for a solid state transformer with energy storage capabilities," 2016 IEEE Energy Conversion Congress and Exposition (ECCE), Milwaukee, WI, 2016, pp. 1-8.
- CP5** J. M. Cano, A. Suárez, Á. Navarro-Rodríguez and P. García, "Improved efficiency of local EPS through variable switching frequency control of distributed resources," 2016 IEEE Energy Conversion Congress and Exposition (ECCE), Milwaukee, WI, 2016, pp. 1-7.
- CP6** J. Garcia, R. Georgious, P. Garcia and A. Navarro-Rodriguez, "Non-isolated high-gain three-port converter for hybrid storage systems," 2016 IEEE Energy Conversion Congress and Exposition (ECCE), Milwaukee, WI, 2016, pp. 1-8.
- CP7** R. Georgious, J. García, Á. Navarro-Rodríguez and P. García, "A study on the control loop design of non-isolated configurations for hybrid storage systems," 2016 IEEE Energy Conversion Congress and Exposition (ECCE), Milwaukee, WI, 2016, pp. 1-6.
- CP8** C. Blanco, P. García, Á. Navarro-Rodríguez and M. Sumner, "Predictive frequency-based sequence estimator for control of grid-tied converters under highly distorted conditions," 2017 IEEE Energy Conversion Congress and Exposition (ECCE), Cincinnati, OH, 2017, pp. 2940-2947.
- CP9** A. Suárez-González, P. García, Á. Navarro-Rodríguez, G. Villa and J. M. Cano, "Sensorless unbalance correction as an ancillary service for LV 4-wire/3-phase power converters," 2017 IEEE Energy Conversion Congress and Exposition (ECCE), Cincinnati, OH, 2017, pp. 4799-4805.
- CP10** A. Navarro-Rodríguez, P. García, J. M. Cano and M. Sumner, "Limits, stability and disturbance rejection analysis of voltage control loop strategies for grid forming converters in DC and AC microgrids with high penetration of constant power loads", 2017 19th European Conference on Power Electronics and Applications (EPE'17 ECCE Europe), Warsaw, 2017, pp. P.1-P.10.

- CP11** A. Navarro-Rodríguez, P. García, R. Georgious and J. García, "Adaptive active power sharing techniques for DC and AC voltage control in a hybrid DC/AC microgrid," 2017 IEEE Energy Conversion Congress and Exposition (ECCE), Cincinnati, OH, 2017, pp. 30-36.
- CP12** P. García, Á. Navarro-Rodríguez, S. Saeed and J. García, "SoC Estimation in Li-ion Batteries Exploiting High-Frequency Model Properties," 2018 IEEE Energy Conversion Congress and Exposition (ECCE), Portland, OR, 2018, pp. 1103-1110.
- CP13** Á. Navarro-Rodríguez, P. García, C. Blanco, R. Georgious and J. García, "Co-operative Control in a Hybrid DC/AC Microgrid based on Hybrid DC/AC Virtual Generators," 2018 IEEE Energy Conversion Congress and Exposition (ECCE), Portland, OR, 2018, pp. 1156-1163.
- CP14** A. Suárez, C. Blanco, P. García, Á. Navarro-Rodríguez, J. Manuel and C. Rodríguez, "Online Impedance Estimation in AC Grids Considering Parallel-Connected Converters," 2018 IEEE Energy Conversion Congress and Exposition (ECCE), Portland, OR, 2018, pp. 5912-5919.

### 1.4.3 Peer-reviewed journal papers in review process

- JPR1** Á. Navarro-Rodríguez, P. García, J. M. Cano and M. Sumner, "Dynamic Analysis and Design of Grid Forming Converters with PI-based Voltage Control in DC and AC Microgrids," In review process for the IEEE Transactions on Power Electronics. Submission due date: August 9<sup>th</sup>, 2019.

## 1.5 Thesis outline

The main body of this thesis document is organized in six chapters and an appendix according to the following outline:

- **Chapter 1** has introduced the thesis topic, defining the objectives and contributions of this research.
- **Chapter 2** presents a review of the existing literature on the relevant topics involved in the present thesis in order to support the contributions described in the following chapters. The concepts, technologies, methods, devices and tools related to the primary and dynamic control of voltage magnitude and frequency in low voltage DC, AC and hybrid microgrids are discussed.
- **Chapter 3** introduces the hybrid AC/DC microgrid studied in this thesis and models the grid-tied converters in the AC subgrids, defining the inner and outer control loops of VSI control. The chapter presents an observer-based current controller for LCL filters, an impedance estimation method based on pulsed signal injection, and the analysis of AC and DC grid-forming voltage control topology considering the challenges imposed by constant power loads.
- **Chapter 4** establishes the basics of an ESS-based active power compensator for frequency or voltage compensation. It proposes an enhanced transient frequency drift compensator based on a Luenberger observer that allows to overcome the problems derived from the delay and bandwidth of frequency estimators and the unwanted participation during steady state. It also includes a grid sequence estimator based on the sliding Goertzel transform that allows to extract the phase and magnitude of the fundamental and harmonic components of the grid voltages and currents.
- **Chapter 5** defines two different primary control strategies for the AC/DC microgrid under study and proposes two different techniques for the cooperative power sharing control between the DC and AC buses of the hybrid AC/DC microgrid under study. The strategies pursue for the reduction of the dependency in the utility grid and the stress in a central BESS, ensuring the operation under low inertia in the DC subgrid and promoting the collaboration of the different AC subgrids in the microgrid.
- **Chapter 6** states the conclusions, summarizing the results achieved during the development of the thesis, and presents suggestions for future research opportunities in the line of this study.
- The **Appendix** contains the relevant information regarding the simulation and experimental implementations, the pseudo-code for the algorithms developed in the thesis and the journal and conference publications strictly related to the contents in the thesis document.



## Chapter 2

# Literature review and state of the art

### 2.1 Introduction

This chapter presents a review of the existing literature on the relevant topics involved in the present thesis in order to support the contributions described in the following chapters. The concepts, technologies, methods, devices and tools related to the primary and dynamic control of voltage magnitude and frequency in low voltage DC, AC and hybrid microgrids are discussed. The state of the art has been addressed through the following points: 1) Definition, characteristics, components and classification of types and topologies of microgrids; 2) Dynamic control techniques and primary control in microgrids considering the participation of the different grid elements (distributed generation, renewable energy sources and energy storage systems); 3) Power Quality improvement in DC and AC microgrids using active power for voltage magnitude and frequency compensation; 4) Tools and techniques for the estimation of grid frequency/phase and impedance in microgrid applications.

### 2.2 The microgrid paradigm: definition, architectures, components and challenges

The concept of microgrid is becoming more and more popular, and since its first definition [12], it has merited the attention of researchers, companies and regulatory entities, making the concept to evolve and become a feasible option. This section briefly describes the MG characteristics covering its definition, architectures and components.

### 2.2.1 The microgrid concept

The paradigm of microgrid was originally proposed as a flexible solution for the integration of distributed generation into the conventional power grid in order to avoid the negative impact presented by a high penetration of small decentralized resources. The integration of several independent small DGs directly into the traditional network, based on centralized operation, can degrade the system performance compromising the stability, the power quality and the economic dispatch. To overcome this effect, a microgrid is defined as a cluster of DGs, ESSs and customers loads, interconnected through low voltage lines, operated as an autonomous system, seen by the grid as a single entity [12]. Fig. 2.1 shows the conceptual representation of a MG including the common elements that compose this type of systems. While the MG duty is to reduce the impact of DGs and loads on the utility grid, the customers requirements (power quality, reliability, efficiency ...) should be ensured within the MG. In addition, issues and contingencies that take place in the utility grid should present a reduced or null effect within the MG. Furthermore, a MG can not only operate connected to the grid (*grid-connected* mode) but also disconnected from the grid as an electrical and economical independent isolated system (*islanded* mode) [12–15]. This independence makes MGs a proper solution for increasing the accessibility in areas with null or poor access to electricity and promote a more sustainable, efficient and responsible electricity usage based on local generation.

The decoupling from the main power grid allows to define characteristics of the MG as the type of signal (DC or AC), voltage levels, frequency and number of phases independently of the transmission or distribution system to which the MG is connected. Thus, the MGs can have different designs depending on the application, according to the local generation technology and the integrated loads, in order to achieve the most appropriate solution in terms of efficiency, controllability and cost.

Due to factors as scale, generation technologies, load and line properties, customer necessities and electrical characteristics (voltage levels, frequency of operation, type of grid...), the rules of operation, architecture and control of the traditional power systems can not be applied directly to MGs [12]. Likewise, MGs present particular quality issues and requirements that lead to the necessity for specific technologies, control architecture, network architecture, standards and benchmarks different from the ones applied in the conventional power system.

### 2.2.2 The microgrid architecture

Considering the network model, two main projects regarding the overall definition of structure, operation and regulation of microgrids can be highlighted: the American model, defined by the Consortium for Electric Reliability Technology Solutions (CERTS) [16, 17], and the European model, defined in the projects MICROGRID and MORE MICROGRID projects [17, 18]. While the first one considers both power and heat services, the European model only takes into account the power distribution.

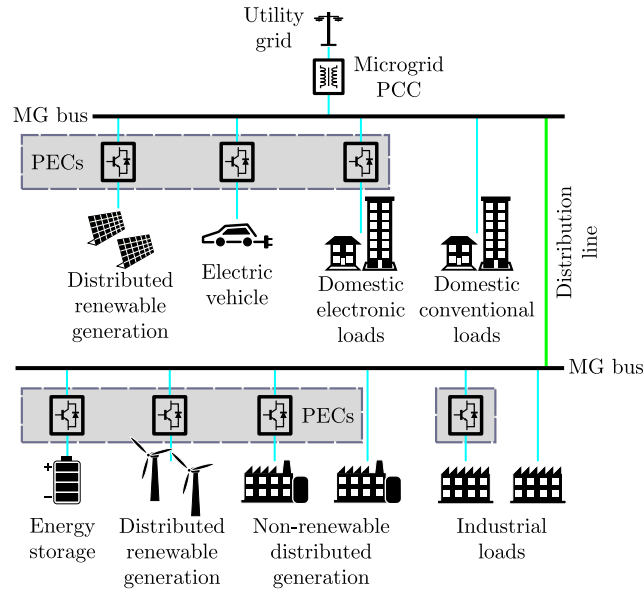


**Figure 2.1:** Conceptual microgrid representation.

Although the original definition of microgrid is lax and flexible about the dimensions, the covered area, as well as the size and number of DERs and loads, the evolution of microgrid concept has led to new subcategories of grids, differentiating between the terms microgrid (MG), Nanogrid (NG) and Picogrid (PG) [17]. Those concepts refer to the coverage of the system being usually related to applications in neighborhoods, buildings and households respectively.

A more technical and widely used classification is the one based on the type of signal for the interconnection between the microgrid elements. Thus, three main types of microgrid architectures are considered: AC, DC and hybrid AC/DC microgrids [19–22]. As in any other AC system, AC microgrids can also be subdivided depending on the number of phases: single phase, 3-phases or 3-phases/4-wires (3-phase with neutral line); and the system frequency: line frequency (50/60 hertz) or high frequency (suitable for size and weight reduction of MG devices) [23].

### 2.2.2.1 The AC microgrid architecture

The typical AC microgrid architecture is shown in Fig. 2.2 [22, 24–26]. It consists in one AC bus (or several AC buses connected through short distance lines) that interconnects the different DERs and loads. The main grid is connected directly to the AC bus of the microgrid by means of a circuit breaker that allows the disconnection for *islanded* operation. A transformer can be present to provide galvanic isolation and step down the voltage when the AC MG is located at the medium voltage distribution

system. Apart from the basic architecture, several topologies have been proposed based on previous AC power systems. In [24] a review of the most relevant architectures in the literature is presented.

### 2.2.2.2 The DC microgrid architecture

DC MGs enable the possibility to reduce the conversion stages in DC DERs and loads. Among the DC architectures, the most typical and extended configuration is the unipolar single-bus DC MG. An example is shown in Fig. 2.3, consisting in a two-poles DC bus that interconnects DERs and loads, coupled to an AC grid through an AC/DC interface that can be implemented by means of different power conversion stages providing or not galvanic isolation: An AC/DC converter without isolation, an AC/DC converter connected to AC via an AC/AC transformer or one of those with an additional DC/DC non-isolated (bidirectional boost converter) or isolated (SST) stage, are the most common configurations [22, 25–28]. Nonetheless, the increasing interest in DC MGs has led to the definition and proposal of numerous topologies and configurations. [27] classifies the DC MGs depending in the number of poles/wires, in unipolar (2-wires) and bipolar (3-wires), while [28] differentiates between single-bus and multi-bus with several buses connected through DC lines. Regarding the grid structure, in [27–29] the configurations are classified in radial, ring, mesh, zonal and multi-terminal DC MGs.

### 2.2.2.3 AC vs DC microgrids

The integration in the grid of new concepts of generation, energy storage and electronic loads has relaunched the debate about the benefits and drawbacks of DC against AC grids [20, 30, 31].

The literature exposes certain advantages of DC MGs over AC MGs: 1) A significant drawback of AC MGs are the need for synchronization and the power quality issues related to phase and frequency [25]. Unlike in DC MGs, where just the measured voltage magnitude is necessary for synchronization, in AC MGs the synchronization depends on an estimation of the voltage phase derived from the measured phase voltages. In addition, while in DC MGs only the voltage magnitude has to be controlled, AC MGs require frequency and voltage magnitude regulation, that includes reactive power, harmonics and unbalances management, adding control complexity to the system. 2) More conversion steps are generally necessary in AC MGs [30]. Some studies stand that nearly 30% of the generated AC power is connected to the grid through a PEC with an inherent efficiency reduction [32]. Considering that most of DERs and electronic loads are converted to DC power at some stage (back to back AC/DC/AC scheme) or are originally DC, DC MGs facilitates the connection of those, by eliminating one DC/AC power conversion, increasing the efficiency, reducing costs and power quality issues [25, 26].

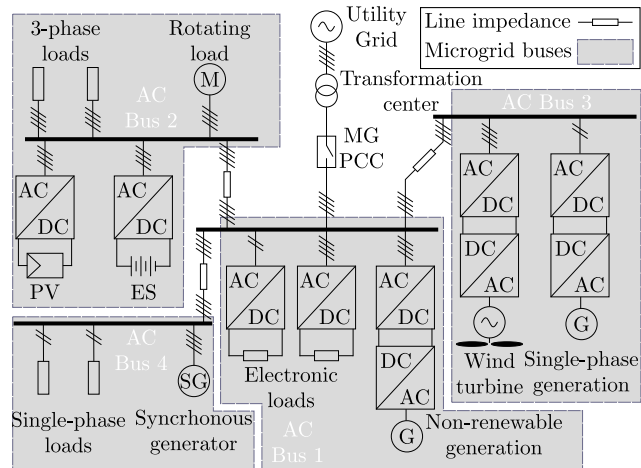


**Figure 2.2:** A typical AC microgrid architecture.

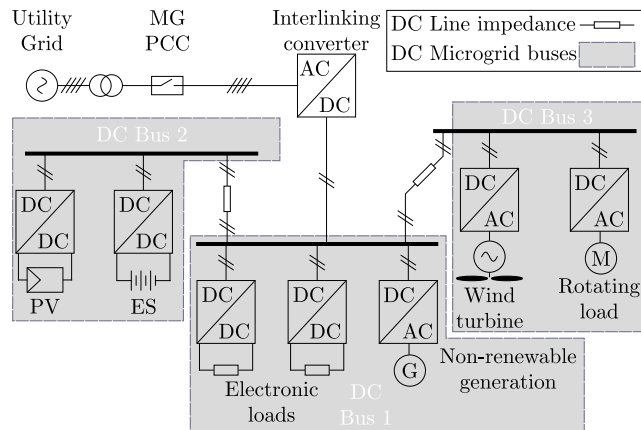


**Figure 2.3:** A typical DC microgrid architecture.

However, DC MGs also present some drawbacks: 1) The power distribution is limited to short line lengths due to resonances. 2) Most of actual loads require AC power, so DC MGs might not be enough for maintaining compatibility. 3) The voltage transformation in DC requires PECs, as opposed to AC power transformers, presenting lower efficiency and reliability. 4) The integration of conventional AC generators requires an AC/DC conversion [22].

An exhaustive compilation of merits and demerits of AC and DC MGs as well as the common power conversions required in MGs is presented in [25]. Considering that both AC and DC MGs require multiple DC/AC and AC/DC conversions for the integration of loads and DERs, the concept of hybrid AC/DC MG has been presented as a solution for maintaining the advantages of both, reducing the conversion stages while keeping compatibility with existing technology [33].

#### 2.2.2.4 Hybrid AC/DC microgrid architecture

An example of the conceptual Hybrid AC/DC MG is represented in Fig. 2.4. It basically results from the joint of an AC MG and a DC MG, connected through an interlinking AC/DC bidirectional converter [22, 25].

Several topologies for hybrid MGs have been proposed during the last years, classified by the interconnection with the mains and the connection between the DC and the AC networks.

An in-depth review and classification of isolated and partially isolated topologies is given in [34]. Two main groups are differentiated:

- The coupled AC, where the AC bus is connected to the mains through a transformer and the DC bus can be connected through an AC/DC converter to the AC before (partially isolated) or after (completely isolated) the AC transformer.
- The decoupled AC, where the MG is decoupled from the mains by means of an AC/DC/AC conversion that provides a point of connection for the AC bus and the DC bus. Three configurations are considered:
  - In the two-stage completely isolated, the mains are connected through an AC/DC isolated converter (for example an AC/DC merged to a DC/DC SST) that provides a point of connection for the DC bus, while the AC bus is connected to the DC bus through a DC/AC converter.
  - In the two-stage partially isolated, the mains are connected through an AC/DC non-isolated converter that provides a point of connection for the DC bus, while the AC bus is connected to the DC bus through an isolated DC/AC conversion.
  - In the three-stage partially isolated, the mains are connected through an AC/DC non-isolated converter plus a DC/DC isolated converter that provides a point of connection for a the DC bus, while the AC bus is connected

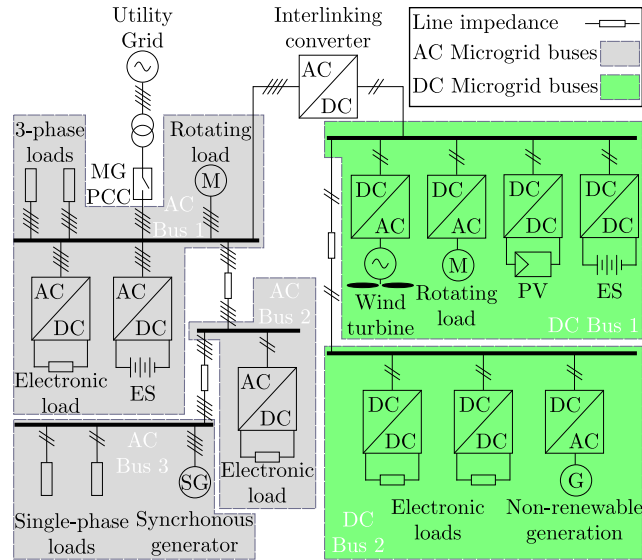


**Figure 2.4:** A typical hybrid AC/DC microgrid architecture.

to the DC bus through a non-isolated DC/AC converter. This configuration permits an additional non-isolated DC bus coupled after the first stage between the AC/DC non-isolated converter and the DC/DC isolated converter.

Another review in typical found hybrid MG topologies is given in [35], which classifies them in conventional hybrid, hybrid multi-microgrid with multiple AC grids, hybrid multi-microgrid with multiple DC grids, and SST based hybrid MG (three-stage). When talking strictly about the DC and AC subgrids interconnection, [35] differentiates between two main topologies for the interlinking converters: 1) the single-stage, consisting of a DC/AC VSI, and 2) the two-stage, based on a DC/DC/AC topology (DC/DC converter coupled to a DC/AC VSI), that presents a higher degree of freedom for controllability and allows the connection of an ESS in the DC-link.

Despite the variety of configurations that the hybrid AC/DC MG permits, most of the examples in the literature are based on a direct connection with the mains in the AC grid and an interlinking converter between the DC and AC buses (coupled AC), being susceptible to contingencies in the mains [33,36–38]. An alternative MG topology is proposed in [1], based on the two-stage completely isolated concept, that integrates multiple AC nanogrids with multiple interlinking converters. This configuration, shown in Fig. 2.5, allows to reduce the impact of distributed generation in the utility grid and the sensitivity of the MG to contingencies in the AC mains, apart from adding controllability and flexibility to each AC NG.

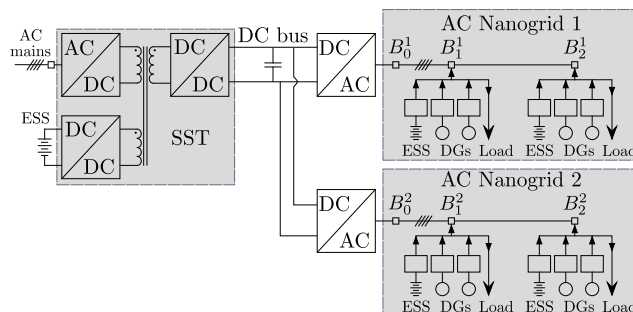


Figure 2.5: Architecture of the microgrid proposed in [1].

### 2.2.3 Distributed generation and energy storage

Distributed energy resources (DERs) supply power to the MG and provide ancillary services. DERs found in microgrids and distribution systems differ significantly from conventional power generation, presenting different issues that affect the microgrid operating principles. Independently of the primary energy resource, the following common characteristics can be considered [12, 15]:

- Although in some cases it can reach a few MW, the rated power of DERs is usually small, in the range of 1's-1000's of kW as opposed to the MW-GW levels in conventional generation.
- DERs have to be interconnected with the low voltage feeders in the MG. In many cases DERs present a DC output, voltage levels or frequencies different from the one on the MG lines. Moreover, some of the technologies, mainly RESs, need for power electronics to operate. Thus, in most of the cases, DERs will be interfaced with the MG through power electronic converters (PECs) either to operate efficiently or adapt their output.
- In conventional power systems, energy stored as generators' inertia provide the initial energy balance during disturbances. The low rated power, the integration of DERs through PECs, the penetration of RESs and the usually slow response of prime movers in micro-generators, make DERs inertia-less which can lead to a lack of inertia in the MG, specially during *islanded* mode.
- Although the communication between DERs may be used to enhance the system performance or improve the power sharing in a distributed system, it results impractical for the real time control. Thus, the dynamic control of each DER and its associated PECs should be based on the local information, i.e. in the DER's point of common coupling (PCC).

Several reviews on existing technology for DERs are found in the literature [15, 19, 23, 32, 39–42]. Among them, it is worth to highlight the review given in [32],

that includes the description of most common DER technologies, their advantages and drawbacks, their applications, common ratings and the usual power topologies used for interfacing with the MG.

DERs can be classified in three groups: Non-Renewable Distributed Generators (NRDGs), Renewable Distributed Generators (RDGs) and ESSs. [12, 15, 32]. A brief overview on each group is given hereunder.

### 2.2.3.1 Non-Renewable Distributed Generators

Non-renewable distributed generators are based on the combustion of fossil fuels and are used as dispatchable generation. The most extended NRDG alternatives are diesel and spark ignition reciprocating internal combustion engines, gas turbines combined heat and power (CHP) units and micro-turbines driven by bio-gas, propane or natural gas [15, 19, 32]. As in conventional generation, these technologies are based on electromechanical energy conversion through electric generators. Depending on the characteristics of those generators, they can be directly connected to the grid by means of a line frequency synchronous/induction generators with (AVR) and speed governor [39] or through PECs in case of high frequency generators or DC MGs [32].

### 2.2.3.2 Renewable Distributed Generators

Renewable distributed resources group technologies as wind, photovoltaic, biomass, small hydro power, geothermal, ocean energy and solar thermal [32]. With the exception of hydro power, that in some cases can provide hydro storage, the power generation of this resources is intermittent. With the absence of mains grid during *islanded* mode, these kind of DERs are insufficient to ensure the continuity and reliability of the supply within a MG being necessary their coexistence with dispatchable sources and ESS. RDGs normally require a PEC interface to interconnect with the grid, decoupling the primary energy source, and are operated in maximum power point tracking mode (MPPT) whenever is possible, in order to obtain the maximum efficiency [32, 39].

### 2.2.3.3 Energy Storage Systems (ESSs)

Energy storage systems (ESSs) appear as a solution to increase the usage and efficiency of RESs, balancing the generation and consumption profiles, reducing the dependency on non-renewable dispatchable generation [43]. In addition, some ES technologies, as supercapacitors, flywheels or Li-ion batteries, present fast dynamics that might be suitable for compensating the lack of inertia in MGs [12]. Thus, ESS may participate in the system regulation improving the power imbalance, power quality, reliability and stability of the MG [19, 43]. Several reviews can be found in the literature that gathers the description, classification, comparison and usage of the existing ES technologies in relation with the electrical grid [19, 43–46]. According to those reviews, the most extended technologies in MG applications can be classified as electrochemical

systems (batteries, flow batteries), electrical systems (capacitors, supercapacitors and superconducting magnetic energy storage (SMES)) mechanical energy storage systems (flywheel, pumped hydro and compresses air storage...), chemical (hydrogen), thermal (sensible and latent heat storage) and thermochemical (solar hydrogen). In the scope of this thesis, the considered ESSs will be based on Li-ion batteries, capacitors and supercapacitors due to its popular acceptance in MG applications and the high power density that they present [44]. In addition, the use of Li-ion batteries is also justified by the emerging concept of *Second Life Batteries* consisting in the second usage of batteries discarded for their use in electrical vehicles, integrating them in ESSs for the improvement of power quality in micro-grids [47, 48].

### 2.2.4 Load characteristics in MGs

Microgrids are conceived to feed any kind of load present in the conventional grid, from industrial and professional equipment to domestic appliances and transportation. The development of electronics and power semiconductor together with the current society needs have lead to the rise of more and more sophisticated electric loads, which require power electronic converters (PECs) to operate and connect to the grid [32]. Loads in MGs can be classified as follows depending on their characteristics: 1) Depending on the supply, loads can be DC or AC. Due to the conventional AC distribution system, DC loads or AC regulable loads are commonly interfaced with the grid through one or more stages of PECs. 2) In the case of AC loads, those can be divided in single-phase (phase-neutral or phase-phase), or three-phase, that normally present a balanced behavior. 3) According to the interface, loads can be directly connected (passive loads and grid-connected electric motors) or PEC interfaced (industrial drives). 4) Depending on the interaction with the grid and their dynamic behaviour, loads are classified in three types: Constant Impedance Loads (CILs), Constant Power Loads (CPLs) and Constant Current Loads (CCLs).

In this thesis, the last classification will be mainly considered. The simplified behavior of the different types of loads is illustrated in Fig. 2.6. Power electronics adds controllability to sensitive loads that needs a tight power regulation, allowing to decouple the effect of the grid (voltage or frequency variations). However, as an unwanted effect, they compromise the stability in low inertia MGs.

While Constant Current Loads (CCL) are rarely found, more and more electrical appliances and industrial equipment behave as CPLs, presenting a tight control of load power. A high presence of tightly regulated CPLs contribute negatively to the low inertia, in contrast to the self-regulating effect given by Constant Impedance Loads (CILs). The challenges imposed by CPLs and their non-linearity and stability issues have been a major concern in the literature [49–54]. In order to determine the stability boundaries and characterize systems with CPLs, one of the most extended solutions consists in approximating the CPL behaviour to a negative impedance [51, 52, 55, 56]. However, this method is subject to a determined equilibrium point and, in some systems, impedance introduces also some non-linearities [7]. Regarding the existing so-

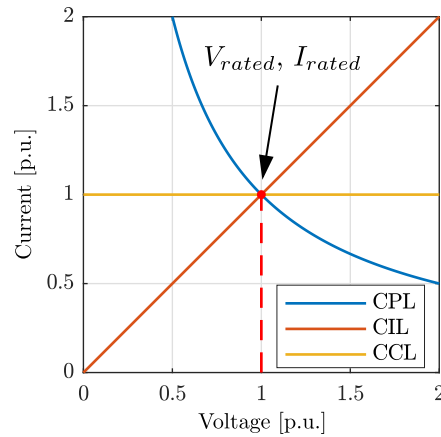


**Figure 2.6:** Voltage-Current curves of the different types of loads in MGs.

lutions to mitigate the effect of CPLs, a review on hardware solutions (increasing capacitance or resistive loads) and control strategies (linear and boundary controllers) is given in [32].

### 2.2.5 Power electronic converters for low voltage MGs applications

The previous sections evidence the important role of PECs in power systems, especially in distribution networks and MGs. They are present in DGs, ESSs, loads and power quality solutions for power conversion and grid interfacing. This section briefly introduces the AC/DC and DC/DC power converter topologies involved in the research objectives identified in this thesis.

#### 2.2.5.1 DC/AC voltage source inverter (VSI) for 3-phase MGs applications

DC/AC converters are used in DERs and loads to interface with AC grids whenever the primary power source or load cannot be connected directly to the grid. Then, they are necessary when the primary power source/load is DC or with AC power sources/loads that require an intermediate AC/DC DC/AC conversion stage. Among the DC/AC converter topologies, one of the most adopted in low voltage MGs or distribution systems is the 2-level 3-phase Voltage Source Inverter (VSI) due to its reduced number of switching devices and ease of control [57–59]. Regarding the Power Electronic Devices (PEDs), the Insulated Gate Bipolar Transistor (IGBT) is the most adopted choice in low/medium voltage and medium power, with ratings in the order of 6kV and hundreds of amperes [60]. Although other options are gaining importance

in grid applications, as SiC MOSFET transistors that reduce the converter losses, in this thesis the IGBT will be the prevalent switching device due to its robustness and maturity.

### Two level 3-phase IGBT Inverter alternatives

The basic 3-phase VSI (Fig. 2.7a) consist of 3 legs (one per phase) with 2 series-connected IGBT per leg and a DC link. This topology lacks the neutral connection, therefore does not allow to control the zero-sequence current. It permits phase voltages up to  $\frac{1}{2}v_{dc}$  and  $\frac{1}{\sqrt{3}}v_{dc}$ , using Sinusoidal Pulse Width Modulation (SPWM) and Space Vector Modulation (SVM) (or third harmonic injection PWM (THIPWM)) respectively for generating the gate signals that drives the switches [61].

The split DC link topology, shown in Fig. 2.7b), adds a passive neutral connection in the midpoint of the DC link without the need for extra switches. However, it present some limitations: 1) the maximum phase voltage is limited to  $\frac{1}{2}v_{dc}$ , so higher voltage is necessary in the DC link; 2) due to the direct neutral connection, the capacitors carry high currents and low order harmonics; 3) the zero-sequence current flows directly through the DC link, leading to oscillations in the DC link and imbalances in the capacitors that become critical under phase current unbalances [62–65].

The 3-phase 4-leg inverter (3P4L), depicted in Fig. 2.7c), presents an additional active leg to control the neutral current, giving an additional degree of freedom for zero-sequence control without affecting the DC link, avoiding the issues of the split DC link topology. This topology requires smaller capacitance and allow to increase the maximum phase-neutral voltage to  $\frac{1}{\sqrt{3}}v_{dc}$  by applying tridimensional space vector modulation (3D-SVM) [64, 66, 67], or third harmonic injection in the neutral leg [65]. In some cases this topology is combined with the previous one to reduce drastically the EMI, common-mode currents and injected ground current on the neutral conductor [68].

### VSI filter alternatives

VSI require a passive filter for the connection to the grid in order to reduce the harmonic distortion introduced by the modulation and to enable the current and voltage control at the converter point of connection. The most utilized filter topologies are the L, LC and LCL filters, represented for one phase in Fig. 2.8 [69–71]. L filters are a simple solution that allows to control the output current of the VSI. In order to improve the filtering capability, higher order LC and LCL filters can be employed instead. These configurations also add the possibility to control the capacitor voltage and the grid-side current respectively. However, the increase filter order could lead to resonances between the reactive elements that needs to be managed either by the control system or by modifications in the hardware [72–74]. The superior filtering performance achieved by the LCL filter presents important drawbacks in the design of the converter current controller due to the resonance created by the capacitor and the inductances [71]. Several alternatives have been proposed in the literature for overcoming this challenge which can be classified into passive and active damping techniques.

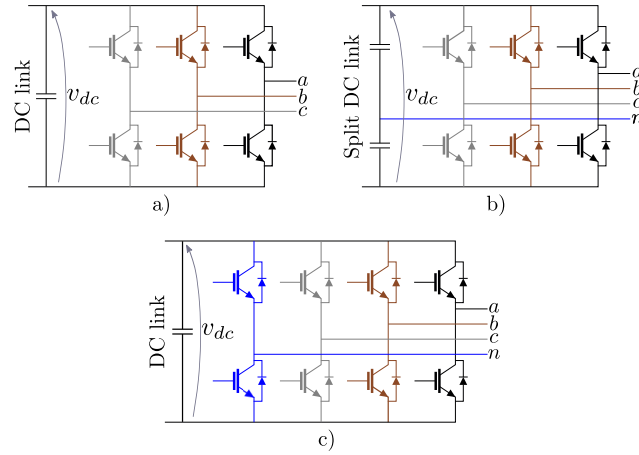


**Figure 2.7:** 2 level 3-phase VSI alternatives. a) 3-phase VSI. b) 3-phase 4-wire split capacitor with passive neutral VSI. c) 3-phase 4-legs VSI with active neutral (3P4L).

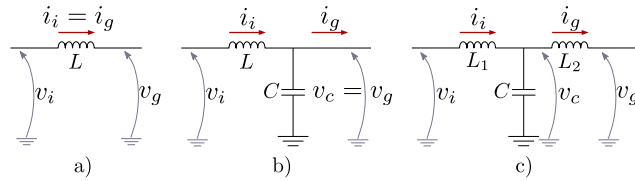


**Figure 2.8:** AC filter alternatives. a) L filter. b) LC filter. c) LCL filter.

On the one hand, passive damping techniques require the use of additional passive elements, such as series or parallel resistances which increase the system losses [71]. On the other, active damping methods often need for additional current and voltage sensors or estimation methods able to substitute such sensors, increasing either the system cost or the control complexity [75–81]. Thus, in any case the selection of the converter filter stage becomes a trade-off between filtering performance, cost, efficiency and control complexity.

### 2.2.5.2 DC/DC power electronic converters (PES) for energy storage and DC DERs integration

DC DGs, ESs and loads usually require a DC/DC conversion whether they are integrated in DC or AC networks as an interface with a DC grid or a DC link. The main purposes are to adapt the DC voltage levels and/or add controllability. Among the solutions, two main groups can be distinguished, the non-isolated and the isolated DC/DC converters. Although, many DC/DC topologies have been defined, the bidirectional DC/DC synchronous boost converter has become a very extended non-isolated

solution in MGs, distribution networks and transportation applications [82, 83]. With regard to isolated converters, the dual active bridge (DAB) and derived topologies is gaining popularity for interfacing multiple energy sources, loads and ESSs [84].

### Single phase bidirectional synchronous boost converter

The DC/DC bidirectional synchronous boost converter topology is shown in 2.9. This topology provides a simple solution for bidirectional applications consisting of a DC link, a 2 switches branch and a boost inductor. The control of this topology is usually based on the regulation of the current through the inductor by controlling the average voltage at the middle point of the two switches ( $v_i$ ) [82].

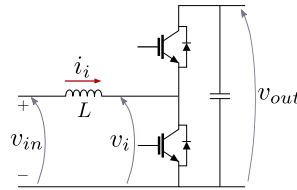


Figure 2.9: DC/DC bidirectional synchronous boost converter.

### Interleaved bidirectional synchronous boost converter

The interleaved bidirectional synchronous boost converter is an improved version of the previous topology. This alternative allows to reduce the output current ripple produced by the switching of PEDs through interleaving the PWM carriers that drive each of the converter legs [83, 85, 86]. In addition, it allows to reduce the size of the inductors as the switching frequency component is inherently attenuated. Among the options, 2-phase, 3-phase and 4-phase interleaved topologies can be found. As the additional phases increase the cost and complexity of the converter (additional switches, inductors, sensors...), the interleaved DC/DC bidirectional synchronous boost converter, shown in Fig. 2.10, offers a good trade-off [83].

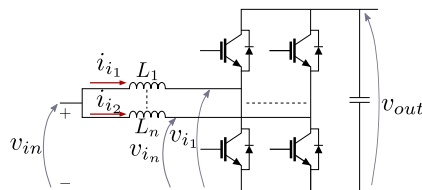
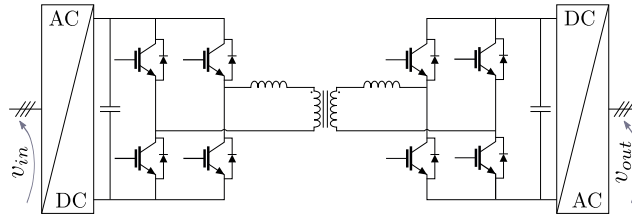


Figure 2.10: Multi-phase interleaved DC/DC bidirectional synchronous boost converter.

### Solid state transformer (SST)

The solid state transformer (SST), appears as an alternative to the low frequency

AC transformers conventionally used for achieving galvanic isolation. By using AC/DC converters, a high frequency AC transformer and a dual active bridge (DAB) power converter, the SST leads to a significant volume and weight reduction compared with conventional power transformers [84]. In addition to the galvanic isolation, the SST allows to control dynamically the power flow between ports and modify the transformation ratio between them by controlling the phase shift between active bridges. Fig. 2.11 illustrates the typical topology of a 2 port SST (2P-SST), based on a dual active bridge (DAB) with a high frequency transformer in the AC side of the converter. Several conversions stages take place: 1) an inverter converts the AC to DC; 2) the DC is converted to high frequency square waveform AC; 3) the high frequency transformer provides galvanic isolation and transforms the voltage between the AC terminals of the active bridges; 4) the AC voltage at the secondary port of the transformer is converted back to DC; 5) finally the DC voltage is converted back to AC.



**Figure 2.11:** Two port solid state transformer (2P-SST) based on Dual Active Bridge (DAB).

As a solution for integrating multiple devices maintaining the galvanic isolation between them, multiport solutions consisting of multiport high frequency transformers and multiport active bridge have been proposed [87–89]. One of the solutions is the three port solid state transformer based on a triple active bridge shown in Fig. 2.12.

Despite the advantages of SST, its design still presents room for improvements. The efficiency and volume reduction by using SiC PEDs are ones of the most important concerns in SST topologies [90–92]. PEDs technology and the switching frequency appear to be the key issues in the path to the improvement [93, 94].

### 2.2.6 Standards, recommendations and grid codes

The increasing interest in MGs as a feasible alternative power system has generated a necessity for normalization. This has led national and international standardizing institutions to the definition of standards and recommendations for the design, control, protections, quality, contingencies management, as well as interconnection and interaction of DERs in MGs [15, 23, 32, 95, 96]. As can be discerned from previous sections, MGs can be considered as a particular case of distribution networks. Thus, apart from the specific standards defined for MGs [97–101], the codes relative to the interconnection of DERs [102–109] and power quality [110–112] in distribution networks also apply in this type of grids.

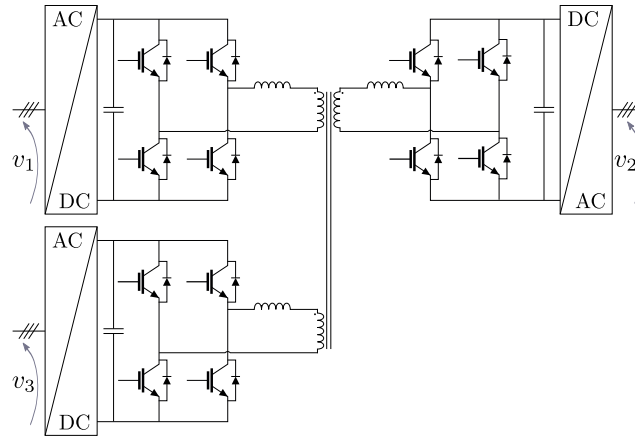


**Figure 2.12:** Three port solid state transformer (3P-SST) based on Triple Active Bridge (TAB).

It is worth to point out the case of DC MG. Although some of the standards and guidelines applies to both AC and DC [100], or specifically to DC MGs [98], unlike in AC MGs, the standarization in DC MGs still implies a barrier for its proliferation. With the aim of compiling the specific standards under development regarding this technology, [28] and [29] present detailed reviews on the standards and organizations working towards the normalization of DC MGs.

### 2.3 Microgrid and grid-tied DERs control

Since the microgrid appearance several studies and proposals have focused the attention on the control structure of the MG and the control of the DERs, pursuing a proper, effective and efficient interaction between the different grid components. Although most of the solutions where originally developed for AC MGs, they can be applied to DC MGs under certain modifications. Several control schemes (central controller, master-slave, droop-based control, hybrid approaches...) are found in the literature to ensure the voltage/frequency control and power sharing in AC distribution networks [37,113–115], and DC grids [55,116]. This section gives a general overview on coordinated and local control, and also discusses the most relevant particular methods used in AC, DC and hybrid AC/DC MGs.

### 2.3.1 Background on coordinated control methods in microgrids

Several control classifications have been proposed in the literature for coordinated control in MGs. The authors in [117] and [118] differentiate between 2 main structures involving the complete operation of the MG: 1) the *decentralized or distributed control*, where each of the units are mainly controlled based on local variables, usually based on active power-frequency (P/f) and reactive power-voltage (Q/V) droop control of DERs [119,120]. This alternative lacks of a central controller, although it contemplates the use of low-bandwidth communications between the DERS and the central central monitoring system; and 2) the *hierarchical control* [121], based on the hierarchy used in conventional large power systems or industrial processes, that usually divides the control of the MG in 3 layers (primary, secondary and tertiary) to accomplish the different control task from the dynamic control and stability to the economical dispatch.

In [55], a classification based on the communication between the different elements is presented. Three categories are distinguish: 1) the *decentralized control*, where there are no digital communication links (DCLs) and the only communication channel are the power lines (voltage, frequency, current...); 2) the *centralized control*, based on the communication via DCLs between the distributed units and a central controller, that allows both direct communication with the units or through a hierarchical structure; and 3) the *distributed control*, where there is digital communication between the distributed units and the coordinated control is implemented locally in each unit.

The authors in [122] remark the importance of the transient behavior requirements of a MG, classifying the MG control in 3 types depending on how they achieve the transients. 1) The *physical prime mover* consists in a *master-slave* configuration where a central relatively large unit (ESS, PEC connected DG or synchronous generator (SG)) handles the transient power flows and sets voltage magnitude and frequency to balance steady-state real and reactive power flows, when the mains are disconnected or decoupled. Despite the ease of this option, it relies on the central generator, presenting problems of resizing, cost of the main generator, and reliability under contingencies. 2) The *virtual prime mover* is based on a *centralized control* where a central control unit controls several DERs using fast communication links, creating a virtual source that dominates and controls the dynamics of the MG. This allows to solve some of the problems of the *physical prime mover* and improve the sharing of transient power between smaller units, however it relies in communication links with its associated problems (need for back-up in case of failure, communication links cost, bandwidth and limitation of communication channels). 3) The *distributed control*, that, as explained before, is based on the local control of the generation units, contemplating the use of slow communications for steady state control. This configuration allows to operate in both *islanded* and *grid-connected* modes.

An interesting classification is given in [123], where the control of the MG is divided in load sharing strategies and energy management. While the load sharing strategies can belong to the primary control of a hierarchical scheme, the energy management

would match with the upper control layers and can be centralized or decentralized. Among the load sharing strategies, two main groups are highlighted: 1) in the *active load sharing methods*, that includes master-slave and current limitation control, a DER unit acts as a master, regulating the system voltage and frequency, while the rest of DERs are operated as grid followers or slaves; 2) the *droop control* is achieved by implementing in the DERs control the P/f and Q/V droop characteristics of synchronous generators.

In most of the cases, the existing control structures are oriented to an autonomous operation of the MG whether it is operated in *islanded mode* or connected to the mains through an interlinking converter, as in DC MGs, that decouples the MG from the utility grid voltage. However, when the mains are connected directly to the MG, the control can be simplified. During *grid-connected* mode the operation is usually governed by a grid following behavior of the DG units that follow the active/reactive power or current references given by the MG operator [25, 124], or are operated in MPPT basis in the case of renewable DERs [125]. In this mode, the standard IEEE 1547-2003 is commonly applied [121].

A complete review and compendium of the existing control strategies for the implementation of the different levels in a *hierarchical control* is given in [126]. The study is oriented to AC/DC MGs and the described classification results useful for both AC, DC or hybrid MGs.

### 2.3.2 Hierarchical control in AC microgrids

As it is drawn by the literature, the *hierarchical control* is the most accepted and extended approach for the implementation of modern MGs [97, 121, 126]. This control structure divides the different control tasks in several layers. Typically 3 layers are defined based on the coverage of the control: primary control (local), secondary (microgrid or microgrid bus) and tertiary (global). In [121] an additional level is contemplated in charge of the local low level control of DERs and PECs. The main functions of each level are briefly described below [121, 126]:

- *Inner control loops* (Level 0): This control is performed at the device level and comprises the inner current and voltage control loops of the PECs as well as the phase synchronization with the point of connection. In some cases it is included within the primary control layer [126].
- *Primary control* (Level 1): This layer defines the local control for dynamic power sharing and interaction of the DGs and ESSs units with the MG, adjusting the outer local control loops (frequency and voltage references, active and reactive power commands...) for generating internal current/voltage references. This level has to provide an optimal power management of the resources (maximum power point tracking) as well as voltage and frequency stability and low level protections.

- *Secondary control* (Level 2): It ensures the operation within the limits of the defined levels for electrical variables and restores the steady state voltage and frequency in case of deviations. It is also in charge of black start management and resynchronization with the mains to transit from *islanded* to *grid connected* mode.
- *Tertiary control* (Level 3): This level performs the power system management. It controls the active and reactive power flow between the MG and the utility grid during *grid connected* mode, pursues the optimization of costs and efficiency by changing the DERs participation, is in charge of the coordination between MGs and manage the islanding, reconnection and actuation after contingencies in either the utility grid or the MG as faults or critical stability issues.

Among these four levels, the control tasks in inner control loops and primary control are the focus of this thesis.

### 2.3.3 Primary local control of PECs-interfaced DERs in AC microgrids

Methods based on master-slave control [37, 127, 128] and droop control [55] appears as the preferred strategies for primary level load sharing control in MGs [123]. For the implementation of those methods, the local converter control has been categorized in the literature in three or two main types depending on their function and application: grid-forming, grid-feeding/following and grid-supporting (divided in current-source-based grid-supporting and voltage-source-based grid-supporting) [123, 129] or simply grid-forming (considering also the grid-supporting options in this group) and grid-feeding/following [125, 126]. The simplified representation of the different converter control for AC applications is shown in Fig. 2.13, where the inner control loop usually consists in a proportional-integral (PI) based current control in dq synchronous reference frame or a proportional-resonant (PR) in stationary reference frame [129, 130].

The operation basics of each control type are summarized below [129]:

- *Grid-forming converters* (Fig. 2.13a): grid-forming converters operate as a low-output impedance source setting the voltage amplitude  $V$  and frequency  $\omega$  of the grid. They usually consist of a VSI with an LC filter controlled through a closed-loop voltage control (synchronous or stationary reference frame) which follows certain voltage amplitude  $V^*$  and frequency  $\omega^*$  references. In master-slave based control schemes, these converters form the grid, assuming the instantaneous power mismatches, while the grid-feeding converters follow them using the formed voltage as a reference. This converters are mainly thought to operate in *islanded* systems as the parallel operation with other grid-forming converters or synchronous generators present some challenges like the need for a precise

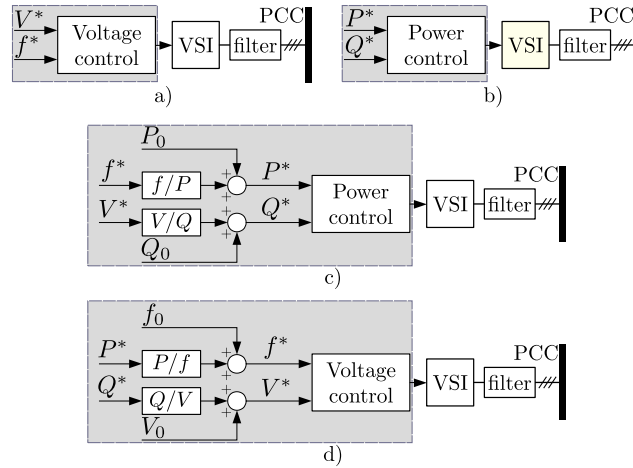


**Figure 2.13:** Conceptual representation of grid-tied converters in MGs. a) grid-forming, b) grid-feeding/following, c) current-source-based grid-supporting, d) voltage-source-based grid-supporting [129].

synchronization between units or the dependence of the power sharing in the converter output impedance.

- *Grid-feeding converters* (Fig. 2.13b): grid-forming converters operate as current sources, delivering power to a regulated grid. Unlike grid-forming, this converters cannot operate autonomously and requires a proper synchronization to realize an accurate current control. They usually implements an active and reactive power control (PQ control) in a VSI with an L or LCL filter, but do not contribute to voltage regulation. The power references in this kind of converters are usually given by a grid operator or by a higher level controller as a MPPT controller.
- *Grid-supporting converters* (Fig. 2.13c) and 2.13d): grid-supporting converters are conceived to participate in the grid voltage amplitude and frequency regulation by adjusting the active and reactive power shared with the grid according to an outer control loop that uses local variables information. They can behave as a voltage source or as a current source depending on the outer control loop that is usually based on droop control [119]. The current-source-based grid-supporting is based on an external frequency-active power ( $f/P$ ) and voltage-reactive power ( $V/Q$ ) droop outer control, that generates active and reactive power references for the internal control loop. In some cases, the active power can not be freely regulated, as in renewable DGs operated in MPPT mode, and the converter just provides reactive power support [123]. The voltage-source-based grid-supporting is based on an external active power-frequency ( $P/f$ ) and reactive power-voltage ( $Q/V$ ) droop outer control, that generates the frequency and voltage magnitude references for an internal grid-forming based controller, emulating a simplified

synchronous generator behavior. While the first approach operates as a grid follower, the second approach allows the operation in both *grid connected* or *islanded* MGs, and permits the parallel operation between converters of the same type without communication lines by using droop control and virtual output impedance.

Following the previous discussion, it is necessary to point out that, unlike in conventional systems with large transmission and distribution lines, the low voltage lines in MGs are mainly resistive. Thus, the voltage amplitude depends mainly in active power, while the frequency is related with the reactive power, giving rise to an alternative control of grid-supporting converters based on  $(P/V)$  and  $(Q/f)$  droops [129].

Some authors simplify the presented classification embodying the grid-supporting as a subgroup of the grid-forming or grid-feeding converters [125, 126]. In [125] the authors distinguish between *Non-interactive* and *interactive* control methods:

- The *Non-interactive grid-following* control pursues the power export with or without MPPT.
- The *interactive grid-following* control functions are the power dispatch and the active and reactive power support.
- The *Non-interactive grid-forming* control regulates the voltage magnitude and frequency of the MG.
- The *interactive grid-forming* control operates in droop control mode for load sharing.

Apart from the methods discussed in this section, some others exist in the literature. A hierarchical classification of converters control methods for primary control is given in [126].

Among the methods that have not been yet discussed, it is worth to highlight the virtual-impedance-based control as an additional feature of converter control for providing active power stabilization, and ancillary services for power quality improvement in MGs [131]. The virtual impedance concept is becoming more and more popular as a method for a number of applications: power flow control, fault and disturbance ride-through, harmonic and unbalance compensation and stability robustness [132]. This method is usually integrated as an external loop for droop-based control and becomes an important component within an increasingly popular control scheme known as virtual synchronous generator [123].

### 2.3.4 The virtual synchronous generator concept

The high penetration of DGs and RES interfaced by PECs with reduced or no inertia present and adverse effect on the MG dynamic performance and stability. Thus, facing

the impact of low inertia and low damping has become one of the main challenges in MGs. Although droop control is based on the simplified characteristic of synchronous generators (SGs) [123], this method only consider the stationary coupling between  $P/f$  (active power and rotating speed) and  $Q/V$  (automatic voltage regulator (AVR)), obviating the inertial energy of the SG. The lack of inertia in droop control may lead to rapid changes in grid frequency, meaning large values of rate of change of frequency  $df/dt$  (RoCoF) that can lead to protection tripping and stability issues [133]. In addition, fast frequency changes can affect the synchronization of grid-tied devices, leading to inaccurate operation or malfunctioning [134, 135].

In order to address this problem, the solution relies on fortifying the system by including additional inertia. During the recent years a relatively novel approach for modifying the inertia in MGs is becoming popular, consisting in the emulation of synchronous generators (SGs) through PECs leading to the concepts of Virtual Synchronous Generator (VSG) (also called synchronverter or virtual synchronous machine (VSM)) and virtual inertia (VI) [136–140]. The integration of VSGs in the MGs allows to imitate the behavior of conventional grids dominated by synchronous generators (SG), regulating voltage magnitude and frequency, providing the MG with an additional inertia that softens the frequency and magnitude rate of change during active power transients [133]. Appart from stand-alone operation (grid-forming), the VSG scheme can also be combined with  $Q/V$  and  $P/f$  droops in order to manage the steady state power sharing in the MG [141]. In fact, the literature reveals that an equivalent behaviour of droop control to VSG can be achieved by using low pass and lead-lag filters in the droop control scheme [133, 142]. With the correct control method and droop control, VSGs permits to avoid the use of frequency or phase detectors for synchronization when operated in paralleland with other VSGs or SGs in a MG. Thus, VSGs can be applied for master-slave or load-sharing solution between parallel units in both steady-state and transients, similarly to traditional SMs dominated grids, and can be applied in both *grid-connected* and *islanded* MGs. Additionally, the stability and dynamic active power balance in a low inertia MG not dominated by VSGs can be improved by adding additional VI as an ancilliary service using DGs or ESSs (following converters that can provide support during transients) increasing the grid inertia and damping, adding flexibility to the system [8, 9, 143–145].

Among the control schemes for VSGs, two main groups can be distinguish: 1) the open-loop-based schemes, where the frequency and voltage magnitude referenced are directly applied to the VSI PWM control, acting the VSI passive filter as the SVG output impedance (Fig. 2.14) [133]; and 2) the closed-loop-based schemes, that includes an inner current control loop that controls the current through the VSI filter and implements an external voltage control loop by means of virtual impedance [133] (Fig. 2.15), or an external power control loop that generates current references [144, 146].

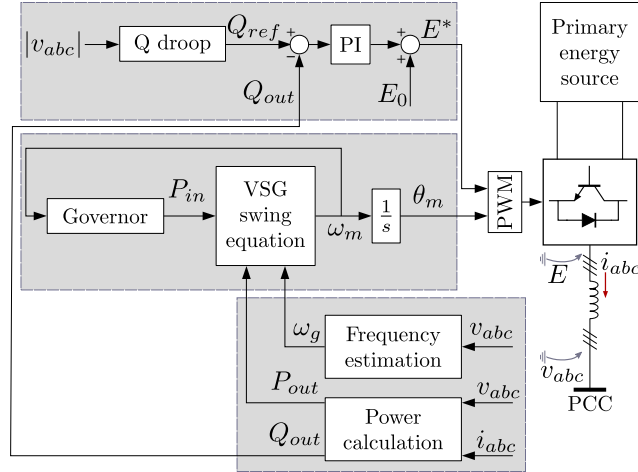


**Figure 2.14:** Simplified diagram of an open loop virtual synchronous generator control [133].

### 2.3.5 Control aspects in DC microgrids

DC microgrids eliminates many of the control issues found in AC systems (the need for synchronization of DERs, harmonics and unbalances that affect such a synchronization, etc.), simplifying the control methods locally (converter level) and globally (power system level). In addition, several concepts and control structures can be adapted from the basics of control in AC MGs reviewed previously. Although several DC MG control structures have been proposed [147–149], as in AC MGs, the most appealing solution is the hierarchical control [121]. In this case, the hierarchical control in DC MGs appears as a simplified adaptation of the AC structure [121, 148]:

- *Inner control loop* (Level 0): the inner control loop usually consist of a closed-loop current control.
- *Primary control* (Level 1): it defines the local control for dynamic power sharing and interaction between the DGs and ESSs, but in this case just the voltage magnitude should be regulated by controlling the active power sharing, usually using a master-slave or droop-based strategy.
- *Secondary control* (Level 2): it ensures the operation within the limits of the defined levels for electrical variables and restores the steady state voltage magnitude in case of deviations.
- *Tertiary control* (Level 3): This level is in charge of the energy management in the DC MG and regulates the active power exchange with an external DC supply, as a DC distribution system, or an AC/DC converter coupled to the AC utility grid or another AC MG.

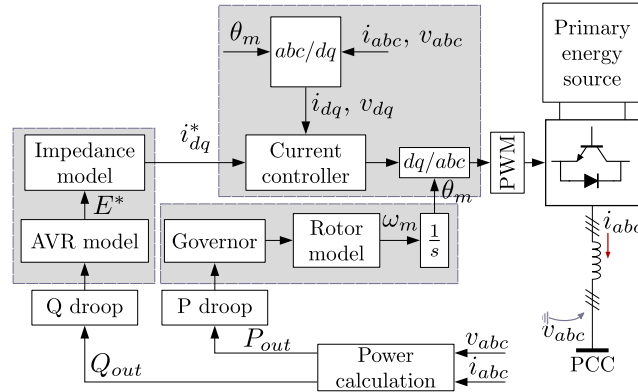


**Figure 2.15:** Simplified diagram of a closed-loop virtual synchronous generator control [133].

Focusing on the primary local control, two main strategies stand out for paralleled operation of converters in DC MGs: the active load sharing (or master-slave based) and the droop-based control [147, 149–151]:

- *Active load sharing:* these methods present a tight voltage regulation and can be divided in two types [150]. 1) The master-slave control is similar to that of AC MGs, a master converter (grid-forming) regulates the bus voltage absorbing the dynamic power mismatches while the rest of units are operated in current control mode (grid-feeding). Some variations have been also proposed as the multiple slack [116], where more than one converter participate in the voltage regulation. 2) The centralized control consist in a central controller that performs an outer control loop for voltage regulation and sends the resulting current reference to several DG or ESS units that share it equally or differently depending on their characteristics and function within the MG (transient support, stationary support or both). However this method is highly dependent on fast communication links and usually is only suitable for close neighboring DERs [152].
- *Droop control:* Compared to AC MGs, in DC droop only the relation between current (or power [153]) and voltage has to be considered. Two main droop control strategies can be found in DC MGs, the current-fed or I/V droop and the voltage-fed or V/I [154–156]. The two alternatives are shown in Fig. 2.16, where the feedback voltage in the current-fed method can be the local voltage (point of connection of the DER) or the global voltage (DC bus voltage after the line impedance, requiring fast communication links) [156]. Both techniques are compared in [155], where their dynamic response performance is analyzed, showing the I-V droop faster dynamics.

As in AC MGs, DC MGs are usually characterized by a low inertia as they are mainly dominated by PECs interfaced units. As in AC control, the droop solution

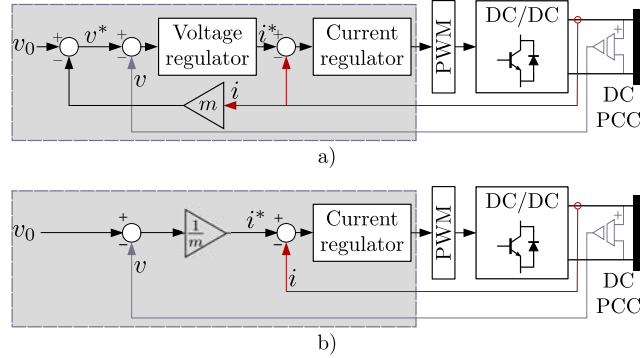


**Figure 2.16:** Simplified control diagrams of droop control for DC microgrids. a) V/I droop (voltage-fed strategy), b) I/V droop (current-fed strategy) [155].

is mainly conceived to provide power sharing in equilibrium conditions and lacks of an inertial behavior to change between equilibrium points. In master-slave DC MGs, the dynamic robustness mainly depends on the master unit, however, the master control usually presents bandwidth limitations, relying the dynamics on the output capacitance. Unlike in AC grids dominated by synchronous generators VSGs or droop control, the inertia of the grid is determined by the equivalent capacitance in the DC buses. Thus, an equivalence can be established between inertia and capacitance. As in AC grids, such an equivalent capacitance can be either real or added virtually through PECs control techniques [2–4, 7, 157, 158]. A control based on virtual inertia is presented in [157], where a virtual-inertia based on a low pass filter is implemented in a MPPT regulated slave RES within a master-slave DC MG for providing support to a master ESS. On the other hand, in [158] a droop based DC MG implements a virtual capacitance as an additional feature of the I/V droop control, smoothing the transient response under load changes. These concepts can be exploited to improve the dynamic stiffness of the grid [7] and establish a transient power sharing scheme for different sources depending on their characteristics as the rated power, bandwidth or dispatchability [4].

### 2.3.6 Control aspects in hybrid AC/DC microgrids

The control concepts in AC MGs and DC MGs can be combined to operate hybrid MGs, being the main control concern the power sharing between AC and DC buses, relying it on the interlinking converter control [126]. Although some solutions have been proposed for this matter, this field still present several opportunities for improvement [35, 126]. A recent research reviews the most common functionalities implemented in interlinking converters [35]:

- *Active power control:* This strategy requires to control the active power flow be-

tween regulated DC and AC buses through an interlinking converter. The active power reference has to be updated continuously. One of the adopted solutions for ensuring this power sharing consist of a combination of DC and AC droop controllers, establishing a relationship between the power reference, the AC frequency and the DC voltage. Thus, the error of the normalized frequency and DC voltage fed a PI regulator that generates the power reference for the interlinking converter. However, this strategy lead to active power flow even for low difference in loading condition of the AC and DC grids. Apart from a droop-based strategy, the active power reference can also be provided by an upper layer controller, for example to balance the power flow of the ESSs depending on the state of charge [159].

- *Reactive power control:* Apart from the active power control, the interlinking converter can contribute to reactive power by acting as a static compensator (STATCOM).
- *AC/DC bus voltage control:* The interlinking converter can be operated as a DC grid-forming, regulating the DC bus voltage or as an AC grid-forming, regulating voltage magnitude and frequency in the AC bus. Although some proposals are found in the literature for achieving simultaneous AC and DC voltage regulation relying on droop control, upper control layers and fast communication links [160, 161], operating grid-forming functionalities in both sides is a challenging task. This is especially the case in single-stage interlinking converters where the DC port is directly couple to the AC port without an intermediate energy storage stage, presenting a reduced degree of freedom.
- *Parallel interlinking converter control:* Multiple interlinking converters can be connected in parallel to increase the power exchange capabilities between DC and AC grids. However, this can involved an unequal power sharing between the interlinking converters and lead to undesired circulating currents.

Regarding the primary control of a hybrid MG, five alternatives are described in [159], where the interlinking converter adopts different modes of operation:

1. *Single grid-forming unit in the AC MG:* In this configuration, an AC grid-forming unit regulates the voltage magnitude and frequency while the rest of units are operated in grid-feeding mode. The interlinking converter operates as a DC grid-forming, regulating the voltage in the DC network. Thus, the control of the AC grid-forming and the interlinking converter can be decoupled, behaving the interlinking converter as a generation or consumption unit for the AC network.
2. *Single grid-forming unit in the DC MG:* A DC unit behaves as a grid-forming in the DC network while the interlinking converter regulates the voltage magnitude and frequency in the AC network, acting as an AC grid-forming. In this case, the interlinking converter is seen as a generation/consumption unit by the DC network.

3. *Multiple grid-forming units in the AC MG:* Several grid-supporting units (voltage-source-based) regulate the voltage magnitude and frequency in the AC network by using a sharing mechanism as droop control. In this case, the interlinking converter can act as a grid-forming for the DC network as in the single AC grid-forming case.
4. *Multiple grid-forming units in the DC MG:* In this case, several sources regulate the DC grid, (for example using V/I droop control), while the interlinking converter can operate as AC grid-forming.
5. *Multiple grid-forming units in both AC and DC MGs:* In this configuration grid-forming units are present in both AC and DC buses of the MG. Depending on the necessities of the MG, the interlinking converter can be used for different purposes:
  - Voltage and frequency deviation balancing, modifying the power flow between MGs (power through the interlinking converter) depending on the AC frequency and the DC voltage as describe previously for the Active power control mode of interlinking converters.
  - Energy storage state of charge (SoC) balancing, adjusting the power flow in the interlinking converter for improving the use of ESS located in the AC and DC networks.
  - Transient power variation support. By reacting to sharp power mismatches in both DC and AC buses, changing the transient power flow between DC and AC, the interlinking converter can improve the stability and disturbance rejection in both buses.

Among the examples in the literature, most of the hybrid MGs present one DC network and one AC network, interfaced by an interlinking converter that performs an active power control [33, 36–38]. Conversely, the topology in [1] is based on DC/AC 3-phase 2-level single-stage interlinking converters operated as AC grid-forming units. As highlighted in [162], the interlinking converters have two roles to fulfill, they behave as sources to one network and appear as loads to the other. The tight regulation in the grid-forming interlinking converters, allows for decoupling the AC from the DC bus dynamics, thus, the AC networks behave as constant power loads (CPLs) for the DC network. Counter-intuitive, this might become an issue if the DC network present a low inertia, for instance during *islanded* mode or under low DC equivalent capacitance. The solution to avoid critical dynamic and stability issues can rely on making the interlinking converters participate also on the regulation of the DC bus, or adapt their dynamic behavior based on the DC voltage. Although active power control techniques described before permit to balance the power of both AC and DC sides when grid-forming are present in both networks, the dynamic power sharing between DC and AC buses in a hybrid MG when the interlinking converters are operated in grid-forming mode, is not yet exploited. Moreover, the use of the typical grid-forming control scheme

in PECs dominated grids leads to a relation of active power and voltage magnitude (P/V) instead of frequency, being the active power control based on DC voltage and frequency not applicable. In [49], an study on cascaded converters stability is carried out, presenting an analogous problem. A power balancing mechanism between AC and DC using a  $V_g/V_{dc}$  droop is also proposed in [128, 163, 164] for increasing the usage of DC link capacitor in DGs interfaced by PECs. However, the first method is related to a pure DC MG while the second is implemented in AC/DC/AC grid tied converters operated in droop-based grid feeding, lacking of solutions for interlinking converters in hybrid AC/DC MGs.

It results clear that the development of hybrid MGs relies on the interlinking converters operation and topology. Some opportunities for the evolution of interlinking converters are underlined in [35]:

- Looking for solutions for an effective three port interlinking converter to interface the AC bus, DC bus and the utility grid. The authors in [35] suggest that solutions can be based on SST.
- The sizing of interlinking converters can be designed taking into account some factors as the critical loads, generation and the available energy storage in the AC and DC grids.
- New strategies for interlinking converters should be investigated to enhance the dynamic response of the hybrid MGs. The authors in [35] suggest the development of solutions based on virtual synchronous generators (VSGs). An appealing approach on this line, that can serve as inspiration for hybrid MGs applications, is presented in [165], where a virtual synchronous machine is proposed as an interface between a DC grid and a AC distribution grid. However, it only considers the connection to the AC grid behaving as a grid-feeding or supporting device.

### 2.3.7 AC and DC PI-based grid-forming converters

Considering the high presence of electronic loads, DERs interfaced by PECs and the significant penetration of renewable generation ruled under maximum power point tracking, grid control based on master-slave can simplify the MG design and operation [55, 116, 166]. In both cases, AC or DC, this approach requires a grid-forming converter controlling the voltage magnitude in DC MGs and voltage amplitude and frequency in AC MGs, usually using a feedback control based on proportional integral (PI) regulators [37, 127, 128]. Unlike in conventional grids, the low natural inertia of MGs makes them prone to suffer contingencies during active power transients. Thus, in the case of master-slave configuration, the grid-forming has to compensate the lack of inertia with a stiff control and a proper disturbance rejection ability.

The high presence of tightly regulated constant power loads (CPLs) contribute negatively to the low inertia and pose a challenge for grid-forming controller, affecting its

dynamic control, leading to large voltage oscillations or voltage collapse [167]. The dynamic and stability issues related to the non-linearity that CPLs introduce in voltage control schemes based on voltage feedback and PI regulators, have been already addressed in the literature [49–54, 116]. Hardware (increasing capacitance or resistive loads) and control solutions (linear and boundary controllers) have been proposed to reduce the effect of CPLs [32]. Nonetheless, the dynamics, stability limitations and selection of both the passive elements (passive filters, capacitance, ratio between CPL and conventional resistive loads...) and the controller parameters for a grid-forming control under CPL have been poorly discussed.

Seeking for ease, grid-forming voltage control in both AC and DC systems have been commonly implemented using PI regulators considering a capacitor as the system plant. The conventional implementation is based on the linear relationship between the voltage and the current at the capacitor and consist of a PI voltage feedback regulator that generates a current reference for the inner control loops of the converter, using an approach based on synchronous reference frame for the case of AC systems [129]. Hereinafter this method will be referred as direct voltage control (DVC). Despite its apparent simplicity, achieving good dynamic behavior is not straightforward, as already reported in the literature [168]. This is due to the non-linear behavior of the voltage reaction to both CPL and CIL disturbances, compared with the linear response that it present for the reference tracking.

An alternative feedback control strategy have been proposed in the literature referred as fast-acting DC-link voltage controller or energy based controller, that here in after will be referred as quadratic voltage control (QVC) [168–171]. This controller uses the capacitor energy storage capability as an approach to linearize the relation between the voltage and the power at the DC-link capacitor using a quadratic voltage feedback instead of a linear voltage feedback. This controller has been traditionally applied in back to back converters (DC/DC/AC and AC/DC/AC) for the voltage control of the DC-link [172–175]. Nonetheless, its application can be generalized to any cascaded-based voltage control such as grid-forming converters in both DC and AC MGs. However, those techniques have not been further exploited for those applications and few examples are found on the analysis of the dynamic performance and tuning [153, 168, 176].

In [153] the quadratic approach is combined with a droop control in a DC microgrid. However, the performance under presence of CPLs is not evaluated, the tuning of the PI parameters is not deeply discussed. In [176] the quadratic control is applied in the interlinking converter of a hybrid MG operated as a DC grid-forming. Nonetheless, the study is not focus on the operation and benefits of this controller and, as in the previous study, its dynamic behavior and stability analysis under CPLs, as well as the discussion on the selection of the capacitance and the regulator parameters, are not provided.

Considering all above, although the quadratic approach (QVC) has been applied for DC regulation applications in DC MGs, to the author's knowledge, no records of this alternative are found for AC applications.

Regarding the dynamic stiffness of grid-forming converters, either DVC or QVC based, in some cases the PI regulator might not be enough to ensure proper disturbance rejection and transient voltage quality, especially under CPLs. The literature has revealed that the effects of CPLs can be attenuated by increasing the system capacitance or the resistive loads and reducing the CPLs or the system inductance [167]. This can reduce the voltage transient oscillations as well as increase the stability margins. However, unlike the controller parameters, the modification of the system hardware is restricted. Alternatively, the dynamic performance can be enhanced through control methods as linear PD or boundary controllers [167], or by load decoupling, using measurements, observers or estimators [177, 178]. Methods adapted from virtual inertia concept may also result in an appealing simple solution [7, 158].

## 2.4 Dynamic active power compensation for quality improvement in AC and DC MGs

The weakness and stability issues associated to microgrids have been considered since their appearance, receiving special attention the solutions focused on the suppression of grid contingencies [179–181]. The problems pertaining to power quality have become a special concern, being even more critical than in conventional power systems given the lack of inertia, the significant presence of non-linear loads and the high penetration of PECs. Studies for different types of quality problems have been carried out with the aim of mitigating unbalances, harmonics and frequency and voltage variations, pursuing for the power quality improvement in AC microgrids [182–186]. The problems usually considered in AC MGs include frequency/voltage deviation, power factor, voltage sags/swells, fluctuations, flicker, harmonics, DC injection and voltage/current imbalances [97]. The IEEE Std 1159<sup>TM</sup>-2009, [110], compiles and defines the different phenomena affecting the power quality in power systems. Among the power quality phenomena, this thesis will take into account those related to voltage and frequency variations, focusing specially on transients and short duration events. The relevant phenomena related to voltage magnitude and frequency variations are briefly described below [110, 187, 188]:

- *Transients*: It is described as an undesired and momentary variation in the power system. This event involves variations in the power systems and appear during transitions from one operating condition to another. It can be classified into two categories:
  - *Impulsive*: It is a sudden, non-power frequency (non-fundamental frequency) change from the nominal condition the voltage, current, or both from the nominal condition, that is unidirectional in polarity. It is usually characterized by its rise and decay times, and the typical duration goes from ns to few ms. This phenomenon can excite the resonance frequency in the grid.

- *Oscillatory*: It is a sudden, non-power frequency (non-fundamental frequency) change in the steady-state condition of voltage, current or both, that includes both positive and negative polarity values, changing rapidly between them. It is described by its magnitude, duration and spectral content (predominantly frequency). The natural frequency usually goes from less than 5 kHz to 5 MHz, the duration goes from  $\mu\text{s}$  to tens of ms depending on the natural frequency and the voltage magnitude can go from 0 to 8 pu.
- *Short duration voltage variations*: These are voltage variation lasting between 0.5 cycles of the fundamental period to 1 minute, that can be originated by significant changes in load, starting of large motors and faults.
  - *Interruption*: It occurs when the supply voltage or load current decreases to less than 0.1 pu for less than 1min. Depending on their duration they can be momentary (0.5 cycles-3s) or temporary (3s-1min).
  - *Sag (dip)*: It is a decrease to between 0.1 and 0.9 pu in rms voltage or current at the nominal frequency. Depending on their duration they can be instantaneous (0.5 cycles-30 cycles), momentary (30 cycles-3s) or temporary (3s-1min)
  - *Swell*: It is an increase in rms voltage above 1.1 pu. The typical values can rise from 1.1 pu up to 1.8 pu. Depending on their duration they can be instantaneous (0.5 cycles-30 cycles), momentary (30 cycles-3s) or temporary (3s-1min)
- *Voltage fluctuations*: Also known as *flicker*, consist of systematic variations of the voltage envelope ( $< 25\text{Hz}$ ), or a series of random variations in the nominal voltage, between 0.9 pu to 1.1 pu. It causes visible fluctuations in the lighting intensity. It can be created by loads with significant cyclic variations in consumption, or loads that exhibit continuous and rapid variations.
- *Power frequency variations*: They consist in the deviation of the system fundamental frequency from its nominal value. This definition applies to any frequency variation although the typical duration and frequency deviation are  $< 10\text{s}$  and  $\pm 0.1\text{ Hz}$  respectively. In conventional distribution systems, the frequency variations are mainly due to unbalances between load and generation and are magnified under low inertia conditions. The frequency shift and its duration depends on the load characteristics and the response of the system to load changes. Weak power systems can have frequency variations due to low inertia, tuning issues of the control systems or large load changes.

Although this definitions might have been conceived initially for AC power systems, as defended in [189], the IEC Std 61000, [188], and the IEEE Std 1159<sup>TM</sup>-2009, [110], make no distinction between AC and DC power quality. Thus, the phenomena given above can be adapted to DC power quality (excepting the *power frequency variations*).

An example of particular DC power quality definitions based on those standards appears in the european standard ETSI 300 132-3-1, [190], where the classification of voltage quality phenomena are simplified to voltage variations, voltage dips, voltage interruptions and voltage surges.

Up to this point, a general description on the power quality phenomena has been given. However, the levels of operation in microgrids and distribution systems depends on national and international regulations and grid codes that dictate or recommend the ride through requirements and operation of the interconnected DERs under abnormal conditions [102,108,109,191–193]. The IEEE Std 1547<sup>TM</sup>-2018 defines the actuation of DERs in power systems (*grid-connected* and *islanded*) under contingencies related to voltage and frequency levels, establishing the maximum and minimum acceptable values, the clearing times, the rate of change of frequency (RoCoF) and the voltage/frequency ride-through for abnormal operating performance [102]. Apart from worsening the voltage quality, compromising the stability and reliability of the system, the operation under abnormal conditions can eventually lead to the disconnection of DERs meaning a load shedding or a black out if the abnormal operation is not cleared in time. In low inertia MGs, this restrictions become critical, as the RoCoF as well as the transient and short time duration voltage and frequency variations can trip the system protections.

Those magnitude and frequency variations in AC MGs, as well as the voltage variations in DC MGs, are related partially or totally to active power (connection/disconnection of loads, disconnection of generators, faults...). Taking this fact into consideration, a suitable solution relies on the participation of DERs not only in the primary control but also providing ancillary services. However, unlike reactive power support, the DGs might not be able to modify their active power reference rapidly enough due to slow dynamics of the prime mover or MPPT control in the case of RESs. Thus, ESS appears as a proper solution for both long term support and ancillary services that involve fast active power exchange.

### 2.4.1 Energy storage systems for AC and DC active power compensation

Although some phenomena, as waveform distortion (as harmonics), imbalance or power factor correction, are usually mitigated through solutions based on reactive power control (active power filter (APF), static synchronous compensator (STATCOM)...), the issues derived from the low inertia and high resistive lines in MGs usually require solutions capable of sharing active power statically and dynamically. Thus, problems as mismatches in the active power flow, transient and dynamic stability or voltage and frequency oscillations can be effectively addressed through active power control [194]. An extended solution for integrating energy storage for active power sharing in 3-phase AC networks consists of coupling an ESS to the DC link of a STATCOM, referred in the literature as STATCOM with ESS (D-STATCOM with ESS in the case of distribution) or simply ESS [195,196]. The ESSs for dynamic applications are usually based on batteries, supercapacitors, flywheels or superconductors

(SMES) [197–204]. The first two consist in DC sources that can be interfaced by a bidirectional DC/DC converter (isolated or not [32]) or directly connected to the DC link, while in the other cases, an AC/DC VSI will acts as interface (Fig. 2.17).

The power topology can vary depending on the application and the energy storage technology. Concerning the grid side inverter, different topologies has been proposed [194], being the two level 3-phase VSI the preferred one in low and medium voltage applications due to its simplicity, effectiveness and cost.

Fig. 2.18 shows an example of the typical topology of an IGBT D-STATCOM with DC ESS. The control degree of freedom is incremented with respect to the STATCOM, being possible to enable the active power control by means of the grid-tied VSI (mode 1) or the DC/DC converter (mode 2), while the other converter regulates the DC link voltage (DC/DC converter in mode 1 and VSI in mode 2).

Regarding the applications of such a topology, it is already being used in transmission lines as improvement for Flexible AC Transmission Systems(FACTS) in order to enhance the power flow capabilities in the grid [195, 199, 201, 205, 206], and recently, it has been introduced in distribution networks [203], acting as energy storage and as a solution for integration of intermittent renewable energy power plants, mainly related to the wind power generation being associated to a wind turbine or wind farm [197, 200, 204, 207–210]. It is also being introduced in micro-grids for power quality improvement, active power compensation and primary frequency control [143, 185, 195, 198, 211, 212]

In DC MGs the voltage quality is directly related to active power. Thus, as in AC systems, ESSs can contribute to the improvement of stability and quality providing ancillary services in DC grids. The interfacing of ESS with DC networks results similar to the interfacing with intermediate DC-links in AC applications. Although several topologies have been proposed for energy storage integration [32, 213–215], four main groups for interconnection can be distinguished as shown in Fig. 2.19. For DC energy storage technologies as batteries or supercapacitors, the interface can be made by means of non-isolated DC/DC bidirectional converters, [32, 213, 214, 216–218], isolated DC/DC converters as SST, [32, 213–215, 219], and in some cases it is possible to connect the DC energy storage directly to a DC bus [220]. In the case of AC energy storage, as flywheels, the connection can be made by means of an AC/DC inverter [32, 215]. Apart from the typical interface options, some alternatives have been proposed for hybrid energy storage integration that allow to interface several storage devices in a single topology that can be isolated [213] or non-isolated [221, 222].

## 2.4.2 Transient frequency compensation and virtual inertia

As mention in previous sections, in AC systems dominated by synchronous generators, by VSIs operated in droop control or by virtual synchronous generators, there is a predominant dependency between frequency and active power. In low inertia systems, including MGs, this dependency becomes critical during transient

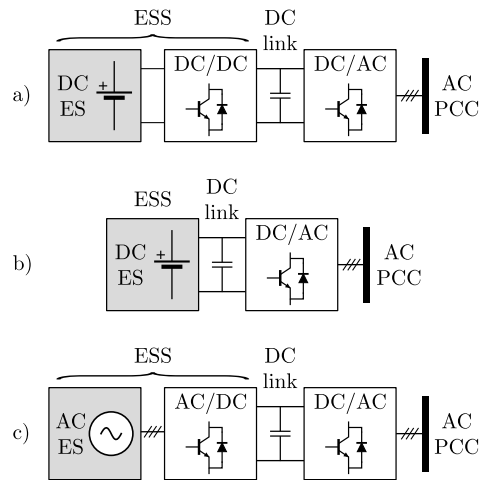


**Figure 2.17:** Integration of energy storage systems (ESSs) in AC networks. a) Integration of a DC ES using a DC/DC converter. b) Integration of a DC ES through direct connection to the DC link. c) Integration of an AC ES using a back to back AC/DC/AC topology.

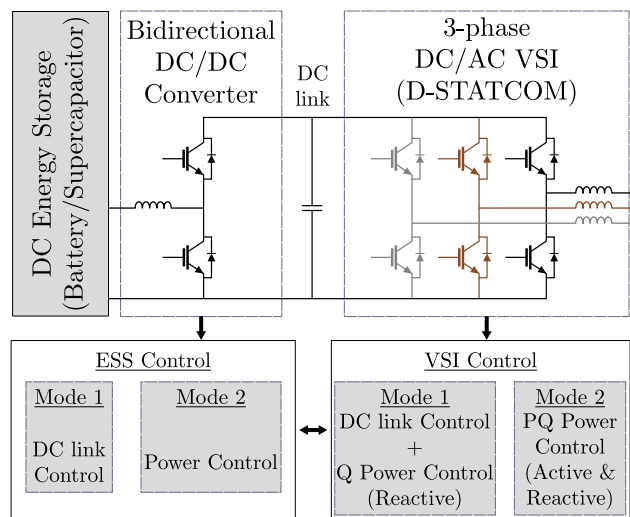


**Figure 2.18:** Typical configuration of a D-STATCOM with ESS for integration of DC energy storage in a 3-phase AC grid.

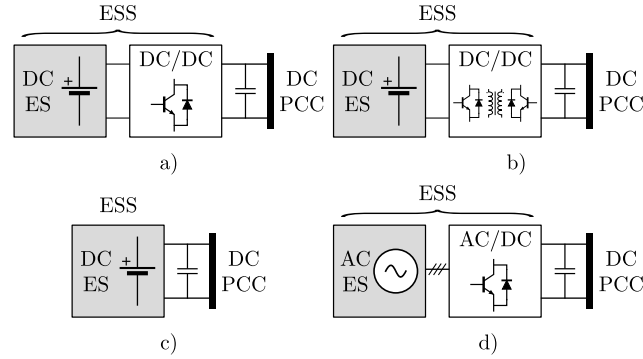


**Figure 2.19:** Integration of energy storage systems (ESSs) in DC networks. a) Integration of a DC ES using a non-isolated DC/DC converter. b) Integration of a DC ES using an isolated DC/DC converter. c) Integration of a DC ES through direct connection to the DC network. d) Integration of an AC ES using an AC/DC converter.

operation, as active power mismatches between load and generation can lead to significant transient frequency variations and instability. Thus, the stability, the frequency profile, and the dynamic active power balance in the grid can be improved by means of ESSs, increasing the grid inertia and damping, adding flexibility to the system [8, 9, 136, 138, 142, 143, 143–146, 185, 186, 212, 223, 224].

In order to accomplish the compensation, two main tendencies are found in the literature, solutions requiring fast communication with a generation plant [143, 185, 212], and autonomous communication-less solutions that do not require for communication links to operate, being the most popular solution of this type the concept of virtual inertia (VI) [9, 136, 138, 142, 145, 146, 223, 224].

While the solutions relying in communication links may result unpractical when it comes to increasing the inertia or damping of an existing system (for example if the information of the system variables and the access to the generators control is restricted), the solutions of virtual inertia and virtual damping have gain popularity during the last years. Improving the inertia and damping of the system can be considered as an ancillary service to improve the power quality while the frequency regulation during steady state is considered part of the primary and secondary controls. Generally, virtual synchronous generators (VSG) can provide both transient and steady state support, thanks to the combination of virtual inertia and droop control, participating in the primary regulation of both voltage magnitude and frequency [133]. However, if the transient compensation is provided as an ancillary service through ESSs, some of the functions of the VSG, such as the participation during steady state, might be disabled. Thus, a transient frequency compensator may consist of a particular case of VSG with reduced or null steady state active power participation and with or without reactive power compensation as an additional ancillary service.

The transient active power compensation in the matter of concern is usually

achieved through a closed-loop control scheme that relies on the system frequency as a feedback [144, 185]. The compensator should be designed for improving the transient disturbance rejection of the system. However, as it should only compensate during transients, some conventional closed-loop controllers as the proportional integral (PI) regulator can not be considered as a solution. For disturbance rejection oriented control, the possible alternatives may go from proportional (P) or proportional derivative (PD) regulators, including feedback differentiation [225–227], to disturbance input decoupling (DID) methods based on both, grid electrical variables measurement, as the current of critical loads, and grid parameters estimation through disturbance observers [228–231]. The PD regulators appears as a reliable and simple option, being the basic structure of virtual inertia (PD with feedback differentiation instead of error differentiation). However, the derivative action have to be used with caution as it can compromise the reliability and stability under noisy inputs. The second option, although adds complexity to the control, can provide an enhance performance as observers may allow not only to estimate electrical variables in the grid reducing the need for sensors but also enables to estimate variables that are not directly measurable [232]. Other alternatives have been proposed, as the solution provided in [144] consisting of an adaptive virtual inertia control.

Although solutions based on proportional regulators or virtual inertia have been widely adopted and improved in the literature [139, 144, 185, 233], they still exhibit common limitations [134]. Although the available energy and maximum power capabilities are critical in the selection of the power supply or energy storage technology, two main handicaps can be highlighted that affect to the design of a frequency compensator and need to be further addressed:

1. The undesired participation during steady state due to steady state frequency compensation.
2. The low bandwidth and delay of the grid frequency estimators.

In grids where the frequency is linked to the active power flow, the stationary value of grid frequency may deviates from its nominal value due to steady state errors in the frequency regulation or the droop characteristics of synchronous generators and droop controlled DGs. If the compensation scheme is based on feedback control, with the nominal frequency as the input reference, a steady state power sharing is expected when using P regulators, [185, 186], or virtual inertia combined with virtual damping, [144, 146, 234], due to the error seen by the proportional regulators. This stationary power sharing can be unexpected, or not considered by the system operator, and may entail an inadequate usage of the energy storage device subduing it to unnecessary charging/discharging cycles, which can be critical when using low energy density devices as supercapacitors or flywheels. A solution to this issue may consist in isolating the transients from the stationary operation, i.e., decoupling the stationary frequency value. A method to achive this porpuse is given in [234], where an open-loop estimator is proposed for estimating the grid frequency in steady state based on the

model of droop control in the microgrid. Thus, the estimated stationary frequency can be used to modify the frequency reference in the compensator control. However, open-loop estimators lose robustness as the parameters in the system varies, and a precise knowledge of droop coefficients of the grid connected devices would be necessary.

It is well known that the delay and low bandwidth acquisition in the feedback channel of a closed-loop control system may cause a reduction in the stability margins of the system, limiting the maximum regulator gains and consequently the overall system bandwidth, worsening the disturbance rejection capabilities [235]. This is an issue directly applicable to frequency compensation. Unlike voltages and currents, that can be measured with high bandwidth sensors, the frequency is usually estimated through phase locked loops (PLLs) or frequency locked loops (FLLs) that usually present a significantly low bandwidth, especially under distorted conditions [236–238]. In addition to the stability and gains limitations, this fact complicates the compensation of fast frequency variations produced by the combination of sudden step changes in the active power flow and the low inertia of a system, as fast transient variations of frequency might not be seen in the estimated grid frequency. The stability issues due to PLL bandwidth and delay in systems with parallel power converters that require precise grid synchronization have been already discussed in the literature [239, 240]. In addition, the effects of the frequency feedback delay in frequency estimators used for frequency control have been highlighted in the literature, having relatively recent researchs worried about this topic [134, 135]. In [135], the frequency is estimated through a PLL and used as the input of a droop controller for a grid-tied converter. The study considers the PLL bandwidth modifications due to voltage magnitude deviations and evaluates the effects of PLL time constant in the stability of the droop-based system. A more explicit review on the frequency estimator bandwidth role in virtual inertia is given in [134]. The authors analyze the stability limits imposed by the estimator bandwidth for different PLL/FLL approaches through small signal frequency stability, and expose the relation between the estimator bandwidth with the virtual inertia maximum gains. The research shows the dependency of the potential support that a device can provide through virtual inertia and the PLL bandwidth, establishing the basics of a method to determine the maximum VI gains that ensure system stability. However, up to the author’s knowledge, solutions to this specific challenge are not found in the literature for microgrids applications.

### 2.4.3 Transient DC voltage magnitude compensation and virtual capacitance

Analogous to the frequency transients in AC grids dominated by synchronous generators, droop control or VSGs, in DC networks the voltage transients are linked to changes in the active power. Unlike for grid frequency, the voltage can be measured with high bandwidth sensors, avoiding the issues of feedback delay presented in frequency compensation. In this case, saving some exceptions as directly connected ESS [220], all DERs are interfaced by power converters making the DC system a to-

tally PECs dominated grid where none real inertia is provided by generators, being the system inertia and damping dependent on the system equivalent capacitance and resistance respectively. As discussed in Section 2.3.5 the inertia and damping can be either real or virtual, considering an analogy between virtual inertia and virtual capacitance [157, 158, 241, 242].

Although some solutions exist in the literature that can contribute to the improvement of DC voltage dynamics [116, 157, 158, 219, 221, 222, 241], the specific function of transient compensation as an ancillary service in DC microgrids has not been as much studied as in AC applications. In [116] the authors proposed an ESS solution for DC voltage profile smoothing in a DC microgrid. During *grid-connected*, the ESS actuates as a transient compensator based on a proportional regulator, using a high pass filter to avoid the participation during steady state. In [243] a virtual capacitance based on pseudo derivative feedback is proposed for improving the transient response in a grid-forming DC/DC converter control that present an interesting inspiration for its possible adaptation to ancillary services. An example of virtual inertia for transient improvement in DC grids is seen in [219]. In some cases the compensation is performed using multiport centralized converters with hybrid energy storage, realizing power peak saving by means of a centralized voltage controller or the feed-forward of load current, using in both cases a power sharing control based on filters with different cut-off frequencies [221, 222]. All these examples can settle the basics of DC voltage compensation during transients for power quality improvement.

#### 2.4.4 Transient AC voltage magnitude compensation in V/P regulated and fixed frequency systems

The voltage magnitude control in AC grids has been traditionally related to reactive power due to the mainly inductive component of power lines and output impedance of generators. Fast dynamic solutions based on power electronics as STATCOM and unified power flow controller (UPFC) were widely accepted as alternatives to traditional devices (on-load tap changing transformers (OLTCs), thyristor switched capacitors (TSCs), thyristor controlled reactors (TCRs), static var compensators (SVCs)...), being able to provide both transient and stationary support.

In [244], an enhanced STATCOM control is presented for dynamic voltage compensation and improvement of voltage transients in inductive networks based on an adaptive control and a grid impedance estimator. However, as highlighted in that research, when the line resistance becomes significant, as is the case of distribution networks and microgrids, the relation between voltage magnitude and active power is magnified, being more effective to realize the voltage compensation by means of active power injection when the ratio between line inductance and resistance ( $X/R$ ) is below unity.

In addition, if the network is dominated by PECs, decoupling the rotating velocity of generators from the grid frequency, the relation between active/reactive power and

voltage magnitude/frequency will depend also in the control scheme of the microgrid. If the regulation is based on  $P/V$  and  $Q/f$  droops [129], in a master-slave scheme regulated by a fixed frequency grid-forming converter [1,166], or in microgrids regulated by  $V/I$  droop with fixed frequency [114], a direct relation will be established between active power and voltage magnitude.

In those cases, the active power variations will affect mainly the voltage magnitude being the grid inertia dependent on the grid equivalent capacitance as in the case of DC networks. Thus, the same principles as in DC microgrids may be applied for voltage magnitude compensation in AC grids complying with the characteristics defined in this section. However, to the best of the author's knowledge, the transient voltage magnitude compensation through active power remains as an unexplored technique, and although the concept of virtual capacitor has been used in AC applications for other matters as DC injection reduction [245,246], reactive power sharing improvement [247], or filtering harmonics [248], it has not been employed for transient active power sharing in order to improve voltage magnitude profile.

## 2.5 Estimation methods in MGs applications

The estimation of variables and parameters in grid applications appears as a powerful tool for improving the system performance and power quality, as well as reducing costs by reducing the number of sensors. In some cases the estimation of variables becomes an imperative need, as is the case of phase estimation for synchronization with the AC grid, or frequency estimation for frequency regulation and MG operation based on  $f/P$  droop control. Although not as critical as phase synchronization, the value of the grid line impedance is a worthwhile parameter for several applications that enables improvements in the grid quality and grid-tied converters operation. However, in some cases the impedance value is unknown and may varies with time and use, or suddenly changes due to contingencies. Thus, the impedance estimation becomes a field of interest for reactive power compensation, islanding detection, control of grid-tied VSIs and fault location among others.

This section discusses variable estimation strategies for the reduction of sensors in the control of LCL filters, impedance estimation methods for MGs and distribution network applications and techniques for phase and frequency estimation.

### 2.5.1 Estimation methods for LCL filter control

In order to accurately design the current controller in grid-tied converters, it is critical to consider the dynamic model of its filter stage (L, LC, LCL) and the available sensors. If LCL filters are used, several options arise for the placement of the voltage and current sensors [75,249]. In the case of AC voltage control at the output of the converter, or current control in the inverter side inductance, it is common to measure the voltage at the filter capacitor and currents in the inverter side. However, this

makes the grid side current dynamics dependent on the grid side impedance [250]. For a precise control of the grid side current, the grid impedance and the grid voltage can be decoupled by placing the voltage sensor in the point of common coupling (PCC), i.e., after the LCL filter. However, if active damping is used, apart from the grid side current measurement, this configuration will require either the measurement or the estimation of the capacitor voltage/current to effectively damp the current controller response, involving the use of additional sensors [251]. Lately, some researchers have addressed active damping implementation methods avoiding the use of extra elements [75–81]. The methods in that group could be split in those requiring to estimate the capacitor current or the inductance voltage and those that rely on digital filtering of the control signal. The first approach requires the use of time derivatives which are normally noisy or require the use of complicated control algorithms. The second alternative places a notch filter at the current controller output, in order not to react at the LCL resonance frequency [76]. However, the bandwidth of the current controller must be often decreased. An appealing alternative for the reduction of the number of sensors and robustness against parameter variation may rely on closed-loop observer based techniques, as the proposed in [252], where an LCL control is proposed based on a direct discrete-time domain observer.

### 2.5.2 Impedance estimation

Knowing the dynamic model and parameters of grid impedance and passive filters, allows to design a proper and accurate control as well as properly management of contingencies. As the impedance may vary dynamically, affecting to the system performance, the impedance estimation becomes an interesting tool for different grid applications (converter control, islanding detection, fault location...) [244, 253–256]. The methods for the identification of the grid impedance can be classified into those requiring the use of dedicated devices and those that can be implemented without any additional hardware. Methods in the first group are often able to estimate the impedance over a wide frequency range using signal injection and frequency based techniques [257, 258]. Regarding the second group, impedance estimation could be implemented using two different approaches: 1) model-based techniques and, 2) signal-injection based techniques. Model-based techniques use the transfer function between the voltage and the current for parameter estimation. In [259], the use of the LCL filter resonance is proposed in order to perform the estimation. As pointed out by the authors, the main issue of this technique is the existence of two resonance frequencies when reactive power passive compensation is added at the PCC. Recently, the identification of the equivalent grid inductance and resistance using closed-loop transient response has been proposed [260]. The method looks appealing and it is well supported with experimental validation, but it does not include the operation under unbalanced grid conditions and does not show the response to sudden changes on the grid impedance, which is critical for islanding detection. In [261], the use of the existing grid harmonics is proposed for the impedance estimation at different frequencies using a Kalman filter. However, only simulation results are provided. A similar approach

is proposed in [262]. The estimated model coefficients are on-line updated using an adaptive linear neuron (ADALINE) algorithm. The results are experimentally confirmed. However, all the electrical variables (grid current and voltages) need to be measured and operation under unbalanced conditions is not demonstrated. In [253], grid inductance is estimated using two consecutive samples of the grid current within a switching period. The estimation method is based on the discrete-time model at the grid frequency and, as recognized by the authors, the method is only valid for the inductive component. Moreover, the operation is only demonstrated for two different inductance values and unbalanced conditions are not considered.

Signal-injection based methods use an additional excitation in order to track the system response [263–269]. For the excitation signal, several approaches have been proposed: 1) Pulsed Signal Injection (PSI) [257, 269–271]; 2) High Frequency Signal Injection (HFSI) at constant high frequency [265, 266, 272–274]; 3) current regulator reaction [266]; 4) Low Frequency Signal Injection (LFSI) [264, 275, 276]; 5) Binary Sequence Signal Injection (BSSI) [267, 277, 278].

Regarding the PSI methods, the results presented in [257] are obtained in the absence of fundamental excitation and the pulses are injected period-to-period. The results in [270] are only focused on a pure inductive three phase balanced impedance. The method proposed in [269] is based on parameter identification using the pulse response and an adaptive model approach. The authors claim the method is able to estimate the grid admittance even with the presence of other power converters connected to the grid. However, the activation of the pulse injection is not fully described and the results are only tested under real-time emulation provided by an OPAL-RT simulator. The method shown in [271] uses a current-pulse injection with the peak of the sinusoidal trajectory of 2 p.u. Furthermore, the signal processing is based on the discrete Fourier transform (DFT), increasing the computational burden and the memory requirements.

HFSI methods and current regulator reaction present some issues: 1) The selection of the high frequency requires the consideration of the possible reaction of any active power filter (APF) connected to the same PCC, compensating the high frequency voltage/current harmonics; 2) the estimated impedance is not the transient impedance, which determines the grid current response to the voltage changes imposed by the power converter, which is the one needed for current controller tuning.

LFSI methods can be separated into those adding an additional excitation signal, similar to HFSI methods, and those using the changes in the commands delivered by the power converter. Using the first approach, a current/voltage excitation signal of a given frequency, often an inter-harmonic, is injected into the grid. The grid voltage/current response at that frequency is analysed and the impedance at the injection frequency is obtained, often using frequency based methods. In [264, 275] a 75Hz current signal is used. The same comments as mentioned before for the HFSI methods apply: the disturbance signal is continuously injected and the impedance is only estimated at the injection frequency. Additionally, due to the low-frequency signal injection, the reaction of the current regulators can compensate for the disturbance signal, thus reducing the effectiveness of the method. A solution given by the authors is to inject the excitation

signal as a current reference, but then the bandwidth of the current controller can compromise the accuracy of the estimation. The second class of methods, require modifying the converter fundamental command. In [276], the  $P$  and  $Q$  commands are altered and both the inductive and resistive part of the impedance are estimated. The main drawback of this method is the coupling between the induced changes in the fundamental command used for the estimation from those due to the regular operation of the converter. The results are only verified by simulation and there is no discussion of the estimation under unbalanced conditions.

BSSI methods are based on the injection of a pulse-train whose response is processed using frequency-based methods. They allow the grid impedance to be identified over a wide-range of frequencies. However, compared to PSI methods, they require a longer processing time because of the time required to inject the test signal and the calculations needed for the identification in the frequency domain. Moreover, most of the proposed methods are only validated for the estimation of the inductance term under balanced grid conditions.

### 2.5.3 Grid phase, frequency and sequence estimators

To perform an accurate control of the current fundamental component in grid-tied converters, the estimation of the magnitude, frequency and phase of the grid voltage fundamental component is required. Furthermore, if harmonic content is present in the grid voltage or current, the estimation of frequency, phase, and magnitude for these additional harmonics is a desirable feature. This, combined with suitable synchronization methods, has been the focus of much research over recent years. In this regard, the grid voltage may be polluted with harmonic components (due to the use of non-linear loads) or unbalanced conditions (due to single-phase loads) and, therefore, the grid magnitude and frequency may vary between values defined in the grid codes as load conditions change. Phase jumps may also occur and also grid voltage measurements may be incorrect, especially with respect to the dc components, due to the used voltage sensors [279]. All these effects can be augmented in weak systems as MGs, due to the low inertia and high R/L line ratios.

The VSI control is required to be fast and accurate under all of these polluted conditions, being the synchronization technique a key feature of the grid-tied inverters control. Moreover, in applications that directly depends on the estimated frequency as closed-loop frequency compensation through virtual inertia (VI), droop control or virtual synchronous generators (VSG), the performance and stability margins of the system relies on the accuracy and bandwidth of the frequency estimation [134, 135].

The existing synchronization techniques can be divided into two types: open-loop [280], [281] and closed-loop [238, 282–286]. Open-loop methods estimate the PCC voltage magnitude, frequency, and phase without any feedback, whereas closed-loop methods are based on locking the frequency (frequency-locked-loop (FLL) [238]) or phase (phase-locked-loop (PLL) [236, 237, 283]). Closed-loop techniques are preferred

as they tend to have better performance. However, most techniques are challenged by grid disturbances (mainly harmonics of the fundamental component), which can affect parameter estimation. One possible solution is to reduce the closed-loop controller bandwidth. However, this is at the price of a degradation in transient response, which is not an acceptable solution in most applications. Alternatively, a filtering stage can be implemented, being prefilter and filter in the loop techniques the most acceptable solutions [284].

A prefilter stage feeds the closed-loop method with a filtered version of the grid voltage that contains only the fundamental component. DSOGI-FLL [238], MCCF-PLL [285], DSOGI-PLL [282], or CCCF-PLL [286] are examples of prefilter stage methods. Filter in the loop techniques [284], [287] remove the unwanted effects of harmonics and unbalances within the closed-loop. In both cases, filters can be implemented by using second-order generalized integrators [238], [282], notch filters [284], complex-coefficient filters [285], [286], lead compensator [287], or moving average filters [288].

When using filtering stages, some aspects must be carefully considered: filters introduce phase delays that must be estimated and compensated in real time [289], transient response is impaired [279], filters need to adapt their central frequency during frequency deviations [285], and magnitude and phase jumps affect the estimation of frequency, magnitude, and phase [284]. In order to deal with these drawbacks, the use of frequency-based techniques as the Goertzel transform (GT) becomes an appealing alternative for real-time components estimation [290, 291, 291].

## 2.6 Summary and research opportunities

This chapter has reviewed the existing technology and literature regarding the implementation of modern AC, DC and hybrid AC/DC microgrids. Apart from establishing a framework for microgrid design and operation, the review has revealed several limitations and weaknesses, leading to opportunities of improvement in several fields attaining microgrids.

Within the main challenges, the literature highlights the lack of inertia, the penetration of renewable energies, the high presence of PECs, the dynamic issues given by constant power loads, the interaction between DC and AC buses in AC/DC microgrids, the accurate control of converters, and the problems derived from frequency and phase estimation. The following opportunities serve as motivation for this research:

1. The hybrid AC/DC microgrid has been accepted as a suitable grid solution for the integration of DC and AC generation, energy storage and loads in a single system, reducing the power conversion stages. However, the hybrid concept is not as mature as AC microgrids, offering a wide range for improvement of infrastructure and control design. Although several grid architectures have been proposed in the literature, the combinations for integrating DC and AC subgrids have not been

totally exploited. Despite the variety of configurations, most of the examples are based on a direct connection with the mains in the AC grid, having few examples of other hybrid microgrid structures that could potentially improve the quality within the MG and simplify the control by decoupling the contingencies and quality problems of the utility grid, as the two-stage completely isolated hybrid MG. Under this scenario, not only the microgrid topology should be defined but also the role and control of the devices that integrate it, adapting the existing methods and developing new techniques that suits a particular architecture.

2. The high penetration of renewable energies, interfacing power electronic converters and tightly regulated electronic loads, along with the trend to reduce the dependence on the utility grid and the fossil fuels, as well as integrating DC and AC devices in a single hybrid system, is changing the characteristics, requirements and operation basics of microgrids compared to conventional transmission and distribution systems. In addition, the reduced voltage levels, the high R/X ratio of lines, due to their short length, and the reduced overall system inertia, turn microgrids into weak systems prone to suffer contingencies derived from an inadequate dynamic active power sharing and interaction of the grid devices. All this factors establish a new scenario and conditions for the regulation of microgrids, differing from the basics of conventional power systems, being necessary the development and analysis of proper primary control techniques.
  - (a) As in AC MGs, DC MGs are also characterized by a low inertia as they are mainly dominated by PECs interfaced units. As in AC control, the droop solution is mainly conceived to provide power sharing in equilibrium conditions and lacks of an inertial behavior to change between equilibrium points. In master-slave DC MGs, the dynamic robustness mainly depends on the master unit, however, the master control usually presents bandwidth limitations, relying the dynamics on the output capacitance. Unlike in AC grids dominated by synchronous generators, the inertia of the grid is determined by the equivalent capacitance in the DC buses. Thus, an equivalence can be established between inertia and capacitance. As in AC grids, such an equivalent capacitance can be either real or added virtually through PECs control techniques, giving rise to concepts as DC virtual inertia and virtual capacitance that can be applicable either to master-slave control or droop control in DC as done in AC grids by means of VSGs. These concepts can be exploited to improve the dynamic stiffness of the grid and establish a transient power sharing scheme for different sources depending on their characteristics as the rated power, bandwidth or dispatchability.
  - (b) Grid-forming units appears as one of the effective and simple solutions for maintaining the regulation of both DC and AC networks when operated in standalone mode under a significant lack of dispatchable generation in systems dominated by RESs. The grid-forming converter, that can be supplied by an ESS, an utility grid or any other bidirectional supply, assumes

the role of master in a master-slave based control architecture. The typical control of these converters consists of a cascaded feedback PI voltage control in synchronous reference frame, establishing a fixed grid frequency reference. Despite its apparent simplicity, achieving good dynamic behavior is not straightforward and the dynamics can be worsened with the penetration of constant power loads that affects negatively to this control approach and can compromise the stability and disturbance rejection capability of the system. Some concerns arise from the literature review on this topic:

- i. The conventional PI-based voltage control using the voltage as a feedback (DVC) may present problems under the presence of CPLs and CILs. An alternative originated for DC-link voltage control based on quadratic voltage feedback, QVC, appears as an appealing solution for improving the voltage control in DC and AC microgrids.
  - ii. The dynamics, stability limitations and selection of both the passive elements (passive filters, capacitance, ratio between CPL and conventional resistive loads...) and the controller parameters for a grid-forming control under CPL have been poorly discussed. This includes both DC and AC applications and any of the control methods DVC or QVC.
  - iii. In some cases, the PI regulator might not be enough to ensure proper disturbance rejection and transient voltage quality, especially under CPLs. The literature has revealed that the effects of CPLs can be attenuated by increasing the system capacitance or the resistive loads and reducing the CPLs or the system inductance. However, unlike the controller parameters, the modification of the hardware of the system is restricted. Alternatively, the dynamic performance can be enhanced through control methods as linear PD or boundary controllers or by load decoupling. In addition, methods adapted from the virtual inertia concept, as the virtual capacitance, may result in an appealing simple solution in both AC and DC applications.
- (c) It results clear that the development of hybrid MGs relies on the interlinking converters operation and topology. The main control concern in hybrid AC/DC MGs is the power sharing between AC and DC buses, depending on the control of the interlinking converters. Active power control techniques have been proposed that permit to balance the power of both AC and DC sides when grid-forming are present in both networks, however, the dynamic power sharing between DC and AC buses in a hybrid MG when the interlinking converter is operated in grid-forming mode, is not yet exploited. Thus, some opportunities emerge for the enhancement of dynamic response of hybrid MGs through the control of interlinking converters:
- i. The use of the typical AC grid-forming control scheme in PECs dominated grids leads to a relation between active power and voltage magnitude (P/V) instead of frequency, being the active power control based on DC voltage and frequency droop not applicable. Thus, the adjust-

- ment of dynamic power sharing of the interlinking converter might be done based on the instantaneous magnitude of AC and DC voltages or any other technique that allow to adapt its dynamic robustness in order to soften the effect that sudden power changes in the AC subgrid produce in the DC subgrid.
- ii. The literature identifies the study of interlinking converters solutions based on VSGs as a research opportunity. Thus, the use of an interlinking converter based on VSG for forming the AC grid instead of a conventional grid-forming with fixed frequency might be also an appealing alternative considering the increasing popularity of VSG concept, and its possibility to be implemented in a grid with synchronous generators or other VSGs.
  - iii. When the interlinking converter operates as a grid-forming for the AC subgrid, the DC subgrids events are decoupled and the devices in the AC side become blind to the possible issues and contingencies in the DC side. This establishes a limitation, imposed by the control strategy, in the bidirectional dynamic active power flow between DC and AC subgrids, as some of the DGs or ESSs that provide ancillary services in the AC side could provide also indirect support for the DC side of the MG. Thus, finding techniques for improving the active power sharing between DC and AC MGs while keeping the grid-forming role of the interlinking converter, becomes an attractive solution compatible with the two previous statements.
3. The lack of inertia and damping is one of the main causes of stability and quality issues in MGs, being the responsible of significant frequency and voltage transients. Depending on the type of grid and the need to compensate either frequency or voltage, two different scenarios can be identified:
    - (a) In AC grids dominated by low inertia synchronous generators, low inertia VSGs or  $P/f$ - $Q/V$  conventional droop control, the improvement of inertia and damping of the grid as an ancillary service can be achieved by means of frequency compensation. One of the most popular techniques to perform the compensation relies on implementing a virtual damping and virtual inertia by means of an ESSs. Such a solution consist in emulating the active power to frequency transfer function of a synchronous generator. However, the implementation of this method relies on the estimation of grid frequency and the knowledge of the actual frequency reference (frequency at the equilibrium operating point), presenting some limitations that need to be further addressed:
      - i. In grids where the frequency is linked to the active power flow, the stationary value of grid frequency may deviates from its nominal value due to steady state errors in the frequency regulation or the droop characteristics of synchronous generators or droop controlled DGs. If

the compensation scheme is based on feedback control, with the nominal frequency as the input reference, an undesired steady state error in the power sharing can appear if the reference frequency is not updated to the actual stationary frequency. This may lead to an undesired participation of the compensator during steady state. This stationary power sharing can be unexpected, or not considered by the system operator, and may entail an inadequate usage of the energy storage device subduing it to unnecessary charging/discharging cycles. A solution to this issue may consist in isolating the transients from the stationary operation, i.e., decoupling the stationary frequency value.

- ii. The delay and low bandwidth acquisition in the feedback channel of a closed-loop control system may cause a reduction in the stability margins of the system. This is an issue directly applicable to frequency compensation. Unlike voltages and currents, that can be measured with high bandwidth sensors, the frequency is usually estimated through PLLs or FLLs that usually present a significant delay or low bandwidth. In addition to the stability and gains limitations, this fact complicates the compensation of fast frequency variations. Although this matter has been recognized in the literature as an important concern, the solutions to this challenge are barely found for microgrids applications.
- (b) The voltage magnitude control in AC grids has been traditionally related to reactive power due to the mainly inductive component of power lines and output impedance of generators. However, when the line resistance becomes significant and the grid is operated under  $P/V-Q/f$  droop control or regulated by a fixed frequency grid-forming converter, the voltage compensation by means of active power injection becomes more effective. In those cases, the active power variations will affect mainly the voltage magnitude being the grid inertia dependent on the grid equivalent capacitance as in the case of DC networks. Although the voltage compensation through active power has not been as explored as the frequency compensation, adapting the techniques used in DC microgrids might be an interesting approach.
4. The estimation of variables and parameters in grid applications can be a powerful tool for improving the system performance and enhance the grid-tied converters control. Three main topics have been approached in the literature review:
- (a) The proper estimation of magnitude, frequency and phase of the grid fundamental component, and the harmonics in some applications, is a requirement to perform an accurate synchronization and control of grid-tied power converters. Furthermore, the accuracy and stability issues due to synchronization and frequency estimation bandwidth and delay in systems with parallel power converters and applications that directly depends on the estimated frequency, are a major concern in the literature. The estimation becomes even more challenging in weak systems like MGs, where phase jumps, unbalances, harmonics and magnitude/frequency significant variations are prone

to happen, distorting the voltage and current. To reduce the effect of distortion in the variable estimation, several solutions have been proposed based on prefilter and filter in the loop techniques. However, the filtering stages may introduce phase delays or impaired transient response, need to adapt the fundamental frequency during frequency deviations and the magnitude, phase and frequency jumps affect the estimation. In order to deal with these drawbacks, the use of frequency domain techniques as the sliding Goertzel transformation appears as an interesting and novel approach for the implementation of an estimator for fundamental and harmonic components of the grid.

- (b) In order to control LCL filters it becomes necessary to damp the resonance produced by the interaction of the filter elements. This can be achieved either by passive or active techniques. For the second case, it is necessary the measurement or estimation of the capacitor voltage or current, involving the use of additional sensors or estimation techniques. Among the last group, the use of closed-loop observers appears as an appealing solution for the reduction of the number of sensors, providing robustness under parameters variation.
- (c) The value of the grid line impedance is a worthwhile parameter for several applications that enables to improve the grid-tied converters operation, the grid quality and the management during contingencies. However, in some cases the impedance value is unknown or may varies with time, use, or contingencies. Thus the impedance estimation becomes a powerful tool for ensuring the knowledge of the grid impedance value. Among the solutions for impedance estimation found in the literature, the methods based on PSI appears as a proper approach with short time signal injection, enabling a fast estimation and providing information about the transient impedance. However, some challenges have still to be overcome in these methods:
  - The grid impedance estimation techniques found in the literature for 3-phase systems only consider balanced grid conditions, leaving unexplored the estimation under unbalanced grid impedance.
  - The injected pulse distorts the grid voltage. Thus, the amplitude and duration of the injection should be minimized in order to reduce the total harmonic distortion (THD). In addition, some techniques require to inject several pulses contributing to the distortion for several cycles. A triggering mechanism could reduce the number of injected pulses, activating the injection only under an evidence of change in the impedance.
  - The identification of low grid impedance value compared to the converter filter impedance value still present a challenge.
  - Some of the methods involve a high computational burden and memory requirements due to signal processing based on frequency domain.

According to the opportunities identified in the literature regarding AC, DC and

hybrid AC/DC microgrids, this thesis proposes solutions in the following directions:

1. A novel hybrid AC/DC microgrid architecture, based on the decoupled AC two-stage isolated concept, has been explored, based on the microgrid proposed in [1]. The role of the different elements that integrate it has been studied and an experimental full scale prototype has been developed and tested [2–4].
2. Regarding the primary control in the new scenario established by modern AC, DC and hybrid microgrids, three issues has been tackled: a) a sharing mechanism that considers the transient performance based on VSG has been studied for DC microgrids regulation [4]; b) the stability limits, performance and design of DC and AC grid-forming converters has been deeply analyzed, pursuing the proper selection of control scheme and filter parameters considering the different types of loads in MGs [7]; c) two alternatives for the active power sharing between DC and AC buses in a hybrid MG have been proposed when the interlinking converter has the role of grid-forming [2–4].
3. In order to cover two of the main handicaps in transient frequency compensation and virtual inertia, an enhance observer-based transient frequency compensator has been proposed to reduce the effect produced by the delay and bandwidth of the frequency estimator and a transient detector has been design to avoid the unwanted participation during steady state [8,9]. In addition, the use of virtual capacitance and active power voltage compensator have been proposed for voltage compensation in AC grids ruled by a P/V relation [3,7].
4. In the field of parameters and variables estimation, three solutions are proposed for different applications: a) to overcome the phase delays introduced by filtering stages and increase the immunity in distorted grids, a predictive sequence estimator have been proposed based on a sliding Goertzel transform, able to estimate the fundamental and harmonic components of grid voltages and currents [10,11]; b) an LCL filter control based on a Luenberger-based observer that allows to avoid the use of the grid-side current sensor [5,6] and indicate potencial changes in the grid impedance; c) a grid impedance estimation method, able to operate under unbalances, is proposed based on pulsed signal injection for the excitation of the grid, trigger by an LCL observer internal signal, and recursive least square for the system parameters estimation [5,6].



## Chapter 3

# Microgrid description, dynamic modelling, and grid-tied converters control

### 3.1 Introduction

As exposed in the the previous chapter, microgrids constitute a suitable alternative for the implementation of the power systems of the future pursuing for the sustainability, efficiency and accessibility of electrical energy. Among the options, the combination of DC and AC accessible buses in a single hybrid microgrid appears as an appealing solution for reducing the power conversion stages while maintaining compatibility with the existing technology. A large portion of the thesis will focus on the study of the architecture, converter control and primary control in an experimental microgrid developed for research purposes in the amenities of the *Laboratory for Electrical Energy Management Unified Research* (LEMUR) group in the University of Oviedo. This chapter presents the microgrid under study, introducing its architecture, and focus on the modelling and dynamic control of grid-tied converters used in low voltage microgrid applications. The main contributions in this chapter mainly concerns the current and voltage converters control, and are summarized as follows: 1) Development of an observer-based current controller for grid-tied converters interfaced by an LCL filter. 2) A grid impedance estimation method based on pulsed signal injection with reduced distortion and moderate computational burden, suitable for adaptive control and anomalies detection. 3) Analysis and design of AC and DC grid-forming voltage control narrowing the operating margins, dynamic response and stability conditions under the presence of different type of loads, highlighting the challenges imposed by constant power loads (CPLs).

## 3.2 Description of the hybrid AC/DC microgrid

The microgrid modelled in this section will establish the context of the proposed methods, and will be used for the simulation and experimental validation of part of the results presented in the thesis.

### 3.2.1 Microgrid topology

The hybrid AC/DC microgrid under study is based on the topology presented in [1]. The simplified MG diagram is shown in Fig. 3.1. It consists in a two-stage completely isolated topology with multiple AC nanogrids ( $n$  denotes the total number of nanogrids) that allows to decouple the DC and AC buses from the utility grid (mains) through a microgrid head converter (MGHC). This configuration enables a seamless integration with the already existing infrastructure. All the power converters shown in Fig. 3.1, including the MGHC, TAB and NGHCs, remains within the transformation center owned by the distribution company. This minimizes the impact of the new technology over the distribution network, while keeping intact the advantages of microgrid based distribution systems: 1) reduced impact of the distributed generation in the mains, 2) reduced sensitivity of the microgrid to contingencies in the utility grid and 3) providing galvanic isolation through a multiport solid state transformer.

The MG is composed by a microgrid transformation center (MGTC), a low voltage DC bus (LVDC bus) and multiple 3-phase 4-wires AC nanogrids interfaced by single stage 3-phase 4-wires DC/AC interlinking converters with the LVDC bus, identified hereinafter as nanogrid head converters (NGHCs). The MGTC includes an interface with the utility grid, a central BESS, a 3 port solid state transformer (3P-SST) and the NGHCs. The 3P-SST is formed by an AC/DC 3-phase VSI that plays the role of microgrid head converter (MGHC), coupling the utility grid with the microgrid, a central BESS and a triple active bridge (TAB). The main purpose of the 3P-SST is to interface the utility grid, the central BESS and the LVDC bus, providing galvanic isolation between those three elements.

Concerning the AC nanogrids, they present the common elements of AC distribution grids as DGs, RES, distributed energy storage systems (dESS) and any kind of loads (conventional/electronic, balanced/single-phase, linear/non-linear...). In each NG, some or all of those elements can be spread over two buses ( $B_1^k$  and  $B_2^k$  where  $k$  is the NG identifier), representing buildings, while the NGHC bus ( $B_0^k$ ) is considered an slack bus where just the NGHC is connected. The buses are interconnected between them through 4-wires distribution lines characterized by a high  $R/L$  impedance ratio ( $Z_{L1}^k$  and  $Z_{L2}^k$ ).

In addition to the loads located in the nanogrids, the possibility to integrate DC loads connected to the LVDC bus is also envisaged in the described topology.

According to the described topology, a power flow map can be defined for the microgrid. Fig. 3.2 shows a simplified scheme of the power sharing within the microgrid

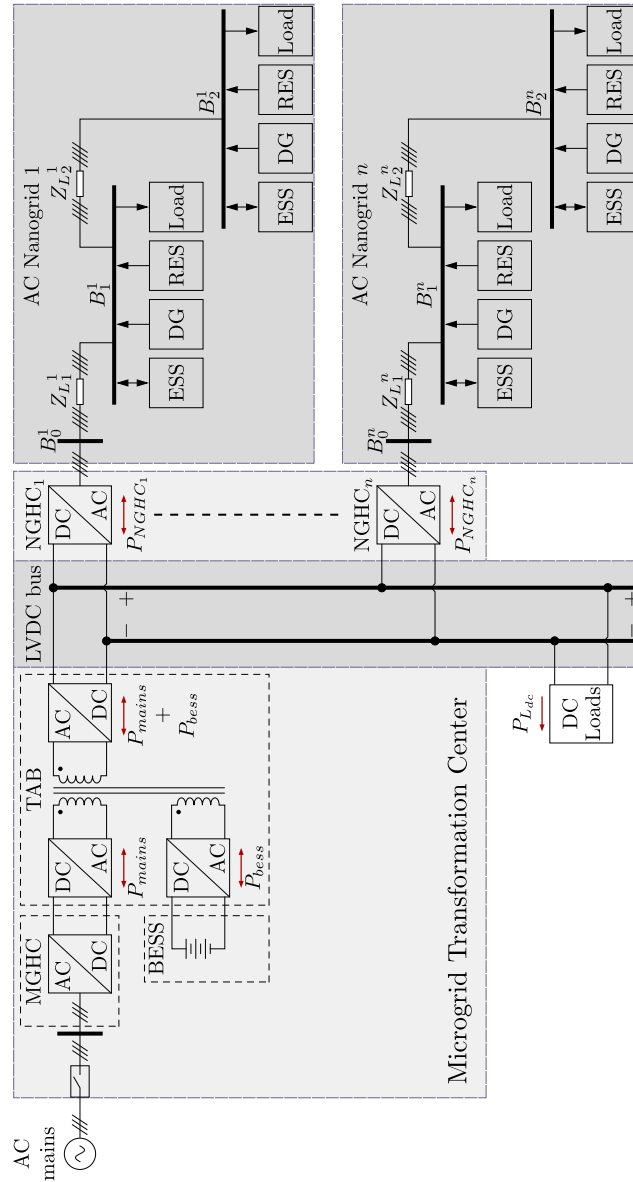
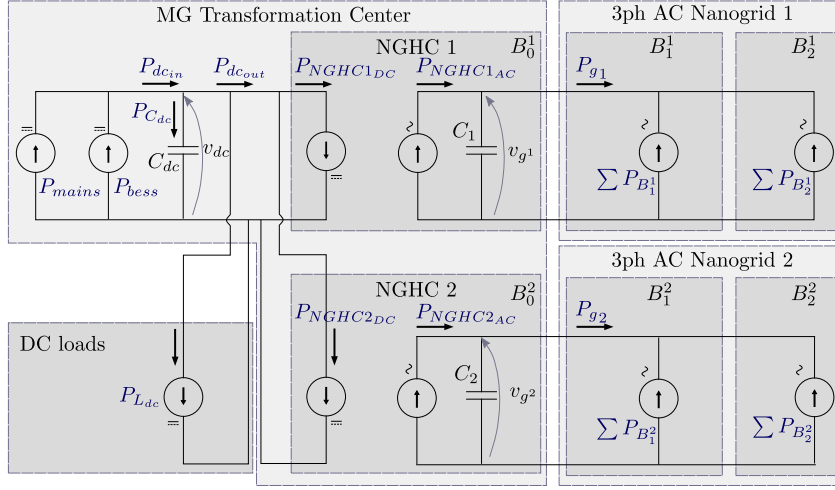


Figure 3.1: Topology of the Hybrid DC/AC Microgrid under study.

for an example that considers two nanogrids.  $\sum P_{B_j}^k$  ( $k$  denotes the NG, while  $j$  the node) is the total power share between DGs, dESS and active power loads within a bus in one nanogrid (3.1),  $P_{mains}$  is the power shared by the utility grid,  $P_{bess}$  the power shared by the central BESS,  $P_{L_{dc}}$  the power drawn by the loads connected to the LVDC bus,  $P_{NGHC_1}$  and  $P_{NGHC_2}$  the power drawn by the NGHCs,  $v_{dc}$  the voltage in the LVDC bus and  $C_{dc}$  the total equivalent capacitance of the LVDC bus.

$$\sum P_{B_j}^k = \sum (P_{DG_j^k} + P_{dESS_j^k} - P_{L_j^k}) \quad (3.1)$$



**Figure 3.2:** Simplified power sharing scheme within the Hybrid AC/DC MG.

### 3.2.2 Solid state transformer

The internal structure of the 3-port solid state transformer is shown in Fig. 3.3. In the system under study, the main aim of the SST is to provide galvanic isolation between the mains, the central BESS and the LVDC bus, while controlling dynamically the power flow between them. In order to achieve that, both the control of the MGHC and the TAB that integrate the 3P-SST are performed in a central controller that permits a centralized control of the central BESS and the MGHC.

Although this part of the system plays an important role in the microgrid operation, it is worth to point out that the low level internal current and phase control loops of the SST as well as the reactive power exchange with the utility grid are out of the scope of this thesis, focusing on the outer control loops that generates the active power or current references for the SST power flow. Some assumptions are established regarding this issue:

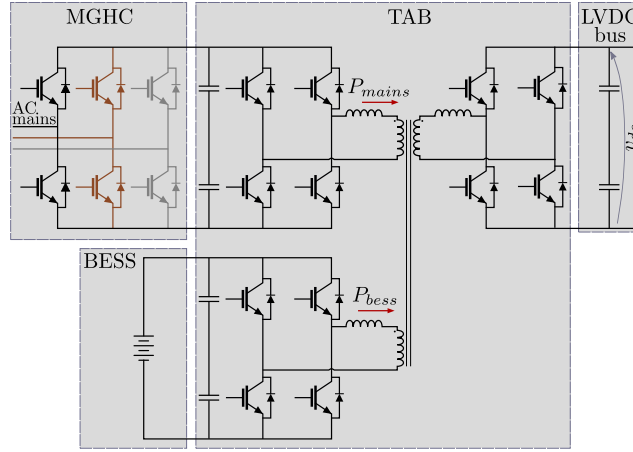


**Figure 3.3:** 3-port solid state transformer internal structure.

- The 3P-SST will be considered a black box that receives active power commands for the MGHC and the central BESS, sharing the resulting power with the LVDC bus (Fig. 3.4). The internal power control loops are approximated to low pass filters, assuming a bandwidth high enough to respect the cascaded control premises (at least ten times higher than the outer control loops).

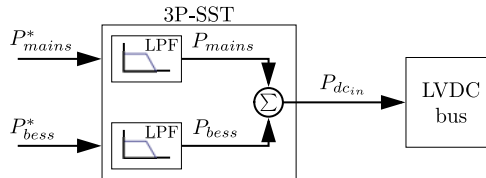


**Figure 3.4:** 3-port solid state transformer: simplification of the internal control loops.

- For simplification reasons, in the laboratory validation used in this thesis, the SST can be replaced by the simplified configuration shown in Fig. 3.5, where the DC output of the MGHC is connected directly to the LVDC bus, while the central BESS is interfaced with the LVDC bus by an interleaved DC/DC bidirectional converter. As the outer control loops that will be proposed in this thesis are agnostic to the inner control loops, they could be applied without distinction to the 3P-SST or to this alternative non-isolated topology.

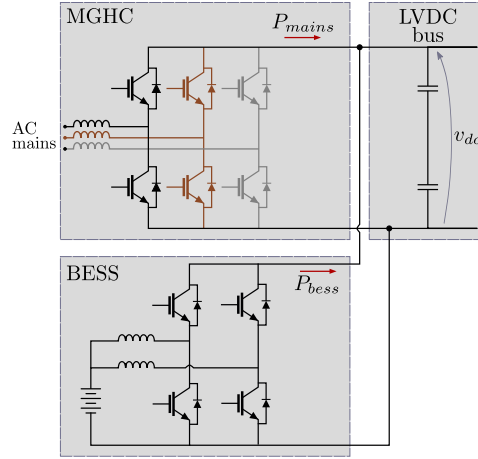


**Figure 3.5:** Alternative connection of the MGHC and the central BESS.

### 3.2.3 LVDC bus modelling

The simplified power flow diagram of the LVDC bus is represented in Fig. 3.6. Following this diagram and the power flow scheme previously seen in Fig. 3.2, the LVDC bus can be modelled as an equivalent DC capacitance with a input power resulting from the sum of the mains and central BESS power, and an output power that represents the NGs and the DC loads power consumption. Although the power flow is bidirectional, this will be the convention established for this research, identifying the sum of mains and BESS as the system input action and the output power as a system disturbance.

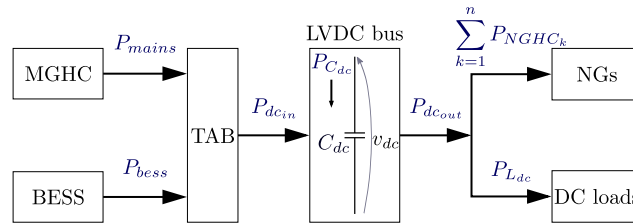


**Figure 3.6:** Simplified representation of the power flow in the LVDC bus.

Thus, the dynamic model of the LVDC bus is given by the expression in (3.2), where  $C_{dc}$  is the LVDC bus equivalent capacitor (the total capacitance of the bus),  $P_{dc_{in}}(t)$  is the power shared by the SST (the mains and the central BESS) (3.3),  $P_{dc_{out}}(t)$  is the power drawn by the NGHCs and the DC loads (3.4), while the  $P_{C_{dc}}(t)$  is the power flowing into the capacitor, associated to the transient power mismatches between  $P_{dc_{in}}(t)$  and  $P_{dc_{out}}(t)$ .

$$\frac{d}{dt}v_{dc}(t) = \frac{1}{C_{dc}v_{dc}(t)} \left( \underbrace{P_{dcin}(t) - P_{dcout}(t)}_{P_{C_{dc}}(t)} \right) \quad (3.2)$$

$$P_{dcin}(t) = P_{mains}(t) + P_{bess}(t) \quad (3.3)$$

$$P_{dcout}(t) = P_{L_{dc}}(t) + \sum_{k=1}^n P_{NGHC_k}(t) \quad (3.4)$$

### 3.2.4 Nanogrid head converters

The nanogrid head converters are responsible for interlinking the LVDC bus with the 3-phase 4-wires nanogrids, being their main aim the regulation of voltage magnitude and frequency in the nanogrids, acting as grid-forming units. Their topology consist of a 3-phase 2-level IGBT VSI with 4 active legs and a 3-phase LC filter that couples them to their respective nanogrid slack bus ( $B_0^k$ ). Fig. 3.7 shows the NGHC integration in the microgrid through the simplified power scheme for one of the NGHCs, including the most important elements participating on the power sharing.

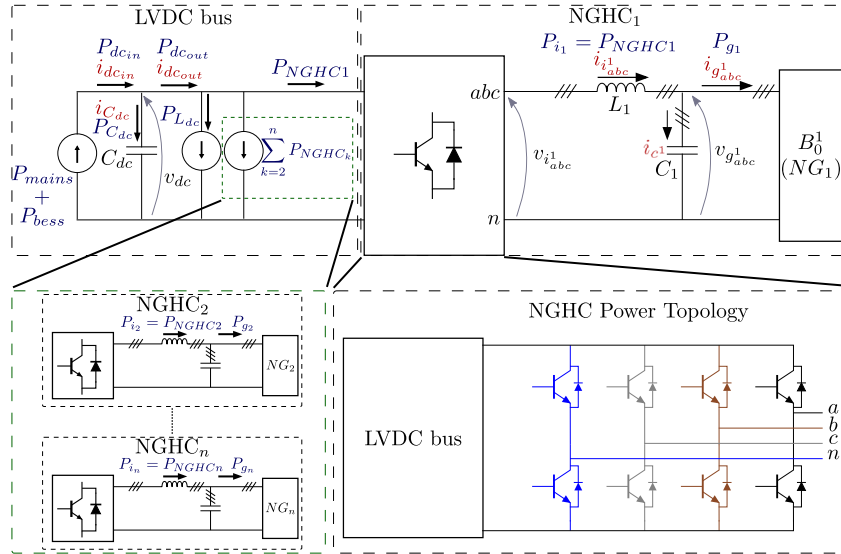


**Figure 3.7:** NGHC topology and simplified equivalent power scheme for one of the NGHCs.

The NGHC system is defined by the following variables and parameters:  $v_{ik}$  is the phase to neutral voltage at the converter terminals before the LC filter,  $i_{ik}$  is the current through the inductor of the NGHCs LC filter,  $v_{gk}$  is the NG phase voltage at

node  $B_0^k$ ,  $i_{gk}$  is the aggregated current drawn by the NG devices in the buses  $B_1^k$  and  $B_2^k$  (loads, DGs, dESS...),  $\omega_e^k$  is the nanogrid frequency,  $L_k$  is the LC filter inductance,  $R_k$  is the parasitic resistance of the LC filter inductance and  $C_k$  is the capacitance of the LC filter. The superindex  $k$  is the NG identifier.

Before defining the control scheme of the overall microgrid and the role of the interlinking converters and transformation center, the thesis will analyze and propose control strategies and tools for the grid connected devices. Given the expected presence of PECs in the MG under study and in MGs in general, the following sections will mainly focus on the modelling of grid-tied converters and line impedance, taking especial attention to 3-phase AC VSIs current control and DC and 3-phase AC voltage control.

### 3.3 Dynamic modelling of grid-tied 3-phase AC VSIs

Apart from the NGHCs, most of the devices connected to the AC nanogrids will be coupled by means of a 3-phase grid-tied voltage source inverter (electronic loads, energy storage and distributed generation). Those interface converters are commonly connected through an L, LC or LCL filter and their control can be bounded to the control of the filter output current or voltage. One of the most adopted methodologies for VSI control consists in simplifying the modelling of a 3-phase system to an arbitrary reference frame (usually  $dq0$  synchronous reference frame or  $\alpha\beta0$  stationary reference frame). Although the AC nanogrids present a 4 leg configuration, being subject to non-null zero sequence component, in the context of this thesis the system will be modelled as a balanced system without homopolar component, simplifying the filter model to a 2-phase arbitrary reference frame. This section provides a generalized modelling for grid-tied 3-phase VSIs useful for the design of the NGHCs and grid-connected devices control.

The unipolar diagram of a 3-phase grid-tied VSI is shown in Fig. 3.8. Although the general representation considers an LCL filter for coupling the converter to the network, L and LC filters are considered particular cases of LCL with  $L_2 = 0/C = 0$  and  $L_2 = 0$  respectively.

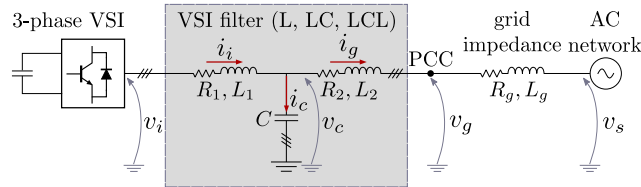


**Figure 3.8:** Simplified diagram of a grid-tied VSI.

The compact state space representation of an L, LC and LCL filter in an arbitrary reference frame can be expressed by (3.5), (3.6). The matrices **A**, **B** and **I** are defined

for L, LC and LCL filters in (3.7)-(3.9). The state and input vectors  $\mathbf{x}$  and  $\mathbf{u}$  are also different for each case, being defined as (3.10) and (3.11) for L, LC and LCL filters, corresponding to the current and voltages in Fig. 3.8. Each component at the state and input vectors is a complex variable that can be split into the real,  $x_x$ , and the imaginary,  $x_y$ , parts. Equations (3.5) and (3.6) could be particularized for the stationary  $(\alpha, \beta)$  or to the synchronous  $(d, q)$  reference frames by making  $\omega_e = 0$  or  $\omega_e = \omega_{grid}$  (grid frequency) respectively. The corresponding block diagram using complex vector notation for each case is shown in Fig. 3.9.

$$\frac{d}{dt}\mathbf{x}_x(t) = \mathbf{A} \cdot \mathbf{x}_x(t) + \omega_e \mathbf{I} \cdot \mathbf{x}_y(t) + \mathbf{B} \cdot \mathbf{u}_x(t) \quad (3.5)$$

$$\frac{d}{dt}\mathbf{x}_y(t) = \mathbf{A} \cdot \mathbf{x}_y(t) - \omega_e \mathbf{I} \cdot \mathbf{x}_x(t) + \mathbf{B} \cdot \mathbf{u}_y(t) \quad (3.6)$$

$$\mathbf{A}_L = \left[ -\frac{R_1}{L_1} \right] \quad \mathbf{A}_{LC} = \begin{bmatrix} -\frac{R_1}{L_1} & -\frac{1}{L_1} \\ -\frac{1}{C} & 0 \end{bmatrix} \quad \mathbf{A}_{LCL} = \begin{bmatrix} -\frac{R_1}{L_1} & -\frac{1}{L_1} & 0 \\ -\frac{1}{C} & 0 & -\frac{1}{C} \\ 0 & \frac{1}{L_2} & -\frac{R_2}{L_2} \end{bmatrix} \quad (3.7)$$

$$\mathbf{B}_L = \begin{bmatrix} \frac{1}{L_1} & 0 \\ 0 & -\frac{1}{L_1} \end{bmatrix} \quad \mathbf{B}_{LC} = \begin{bmatrix} \frac{1}{L_1} & 0 \\ 0 & -\frac{1}{C} \end{bmatrix} \quad \mathbf{B}_{LCL} = \begin{bmatrix} \frac{1}{L_1} & 0 \\ 0 & 0 \\ 0 & -\frac{1}{L_2} \end{bmatrix} \quad (3.8)$$

$$\mathbf{I}_L = [1] \quad \mathbf{I}_{LC} = \begin{bmatrix} 1 & 0 \\ 0 & 1 \end{bmatrix} \quad \mathbf{I}_{LCL} = \begin{bmatrix} 1 & 0 & 0 \\ 0 & 1 & 0 \\ 0 & 0 & 1 \end{bmatrix} \quad (3.9)$$

$$\mathbf{x}_L = [\mathbf{i}_i] \quad \mathbf{x}_{LC} = [\mathbf{i}_i, \mathbf{v}_g]^T \quad \mathbf{x}_{LCL} = [\mathbf{i}_i, \mathbf{v}_c, \mathbf{i}_g]^T \quad (3.10)$$

$$\mathbf{u}_L = [\mathbf{v}_i, \mathbf{v}_g]^T \quad \mathbf{u}_{LC} = [\mathbf{v}_i, \mathbf{i}_g]^T \quad \mathbf{u}_{LCL} = [\mathbf{v}_i, \mathbf{v}_g]^T \quad (3.11)$$

Depending on the application, the dynamic control objective of the grid-tied VSI will be the output current or the output voltage. The output current in L and LCL filters is a state variable, thus, they are usually used in current control mode. On the other hand, the output voltage in LC filters is a state variable, being commonly used for voltage control in the capacitor. One of the simplest solutions for this second case is to apply current-voltage cascaded scheme, tackling the current control through the L filter (inner control loop) and the voltage control at the C filter (outer control loop, slower than the inner control) separately, decoupling the two systems. Nonetheless, in some applications where the capacitor is small enough, the inner current of LC filters ( $i_i$ ) is controlled, ignoring the effect of the capacitor.

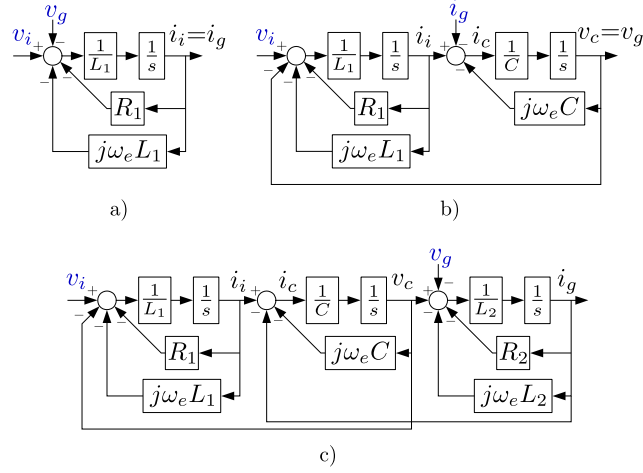


**Figure 3.9:** Filter block diagram in complex-vector form. a) L filter; b) LC filter; c) LCL filter.

### 3.4 Current control in grid-tied VSIs interfaced by L, LC and LCL filters

The inner current control loop of VSIs interfaced by an L, LC and LCL filters, usually consist of a  $dq$  synchronous reference frame feedback controller that follows a given current reference. The  $abc$  to  $dq$  transformation is detailed in Appendix A.1.

The typical inner loop control scheme for L and LC filters, adopted in this thesis for the NGHCs and other grid-tied devices, is represented in Fig. 3.10.  $\theta_e$  is the grid voltage phase used for synchronization,  $i_{i_d}^*$  and  $i_{i_q}^*$  are the inductor current references in the  $dq$  reference frame,  $v_{i_d}^*$  and  $v_{i_q}^*$  are the voltage reference at the converter terminals in  $dq$  reference frame, and  $v_{i_a}^*$ ,  $v_{i_b}^*$ ,  $v_{i_c}^*$  are the reference signals used for the generation of the VSI gate signal through PWM or SVPWM.

The controller  $C_i$  consist in a PI regulator defined by the time domain function in (3.12), where  $e(t)$  is the input error,  $u(t)$  is the output control action, and  $k_{p_i}$  and  $T_{i_i}$  are the proportional gain and the integral time constant respectively. The implementation of the controllers in this thesis will be achieved digitally (see Appendix A.2), however, it is worth to point out that the discretization delay is not considered in the research, assuming a sampling fast enough compared to the system dynamics.

$$u(t) = k_{p_i}e(t) + k_{p_i} \frac{1}{T_{i_i}} \int e(t)dt \quad (3.12)$$

In the case of LCL filters, the typical control scheme is similar to the one shown previously with two main modifications: 1) the output current is used in the feed-

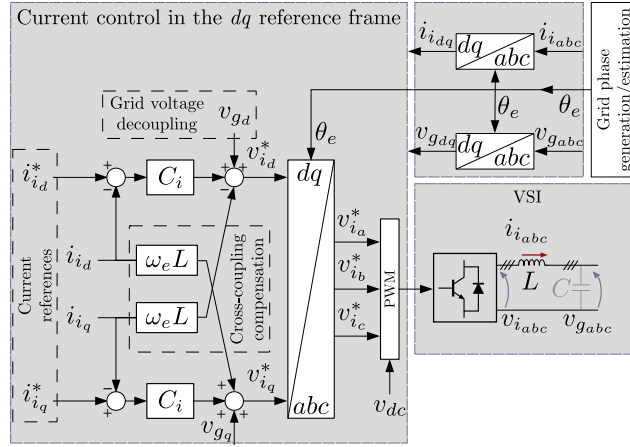


**Figure 3.10:** VSI inner current control topology implemented in the  $dq$  synchronous reference frame. The control topology can be applied to the inductor current control in L and LC filters.

back regulator instead of the converter side current, and 2) a damping technique is applied in the hardware or as a virtual active damping in the control scheme to avoid resonances [71, 75–81]. As passive damping requires a physical resistance and implies additional losses, the active damping has become a popular strategy. Fig. 3.11 shows the simplified output current control scheme of a VSI with an LCL filter using active damping, where  $k_a$  is the damping gain corresponding to a virtual series capacitor resistance

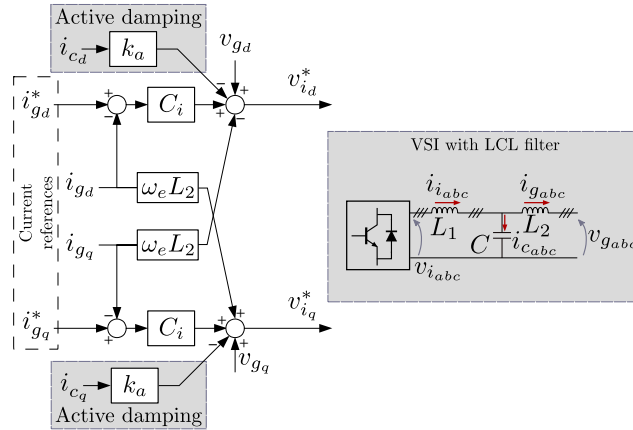


**Figure 3.11:** Output current control scheme for a VSI interfaced by an LCL filter using active damping.

Despite the apparent subtle changes, the modified control system needs the capaci-

tor current  $i_c$  and the output current  $i_g$ . Although the  $i_i$  sensor can be substituted by the  $i_g$  sensor, the need for  $i_c$  inherently involves the use of additional sensors or any other alternative able to provide an estimation of the currents in the LCL filter. The alternatives can rely on: 1) measuring  $i_g$  and  $i_c$ ; 2) measuring  $i_g$  and  $i_i$ , and obtain  $i_c$  as  $i_i - i_g$ ; 3) use estimation alternatives to avoid the use of additional sensors.

Among the options, this thesis proposes as a first contribution, the use of a Luenberger observer for the estimation of the capacitor current and the grid-side current. This will allow to eliminate one of the current sensors normally used when active damping techniques are applied.

### 3.5 The Luenberger observer

The Luenberger observer appears as a reliable and robust technique for the estimation of state variables in control systems [232]. Fig. 3.12 shows the conceptual representation of an observer-based control system compared with the standard control system configuration. Apart from the estimation of the output before sensors and the

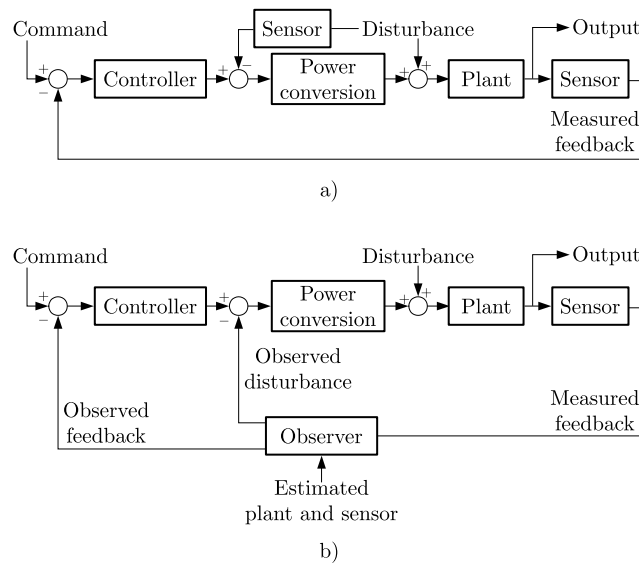


**Figure 3.12:** Luenberger observer in a control system. a) standard control system, b) observer-based control system.

system disturbance, Luenberger observer permits to observe any state in the system plant, In addition, its known robustness against changes in the system plant parameters makes it a proper tool for a number of applications: 1) augment the accuracy of sensors, avoiding noise and compensating the sensor transfer function, 2) reduce the phase lag inherent in the sensors, 3) estimate state variables, including non-measurable

variables, 4) reduce the number of sensors, 5) observe disturbance signals to increase the disturbance rejection of the control system.

This section explores the basics of the Luenberger observer using a characterization in the Laplace domain based on the approach used in [232].

### 3.5.1 Luenberger observer model

The typical model of the Luenberger observer is shown in Fig. 3.13 and is composed by the following elements:

- $U^*(s)$ : Reference of the plant excitation signal (usually the power converter output).
- $G_{PEC}(s)$ : Power converter output.
- $U(s)$ : Plant excitation signal (usually the power converter output).
- $D(s)$ : Disturbance input.
- $G_p(s)$ : Plant model.
- $X(s)$ : State variable (aim of control).
- $G_s(s)$ : Sensor model.
- $Y(s)$ : Sensor output.
- $C_o(s)$ : Observer closed-loop compensator.
- $\hat{D}(s)$ : Observed disturbance.
- $\hat{G}_p(s)$ : Plant estimated model.
- $\hat{X}(s)$ : Observed state variable (aim of control).
- $\hat{G}_s(s)$ : Sensor estimated model.
- $\hat{Y}(s)$ : Estimated sensor output.

However, this model is particularized for the observation of the state previous to the sensor transfer function. For the characterization in this thesis, the observable output is generalized to an unmeasured arbitrary state considered as the controlled variable. In addition, for simplification purposes, the power conversion transfer function block ( $G_{PEC}$ ) is eliminated, being possible to consider it as part of the system plant. The resulting model is represented in Fig. 3.14, where  $G_p$  and  $G_s$  have been replaced by  $G_{p_1}$  and  $G_{p_2}$ , being the complete system plant defined by  $G_{p_t}(s) = G_{p_1}(s)G_{p_2}(s)$ .

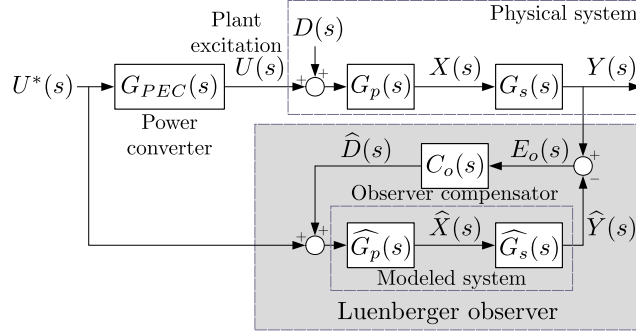


Figure 3.13: Typical form of the Luenberger observer.

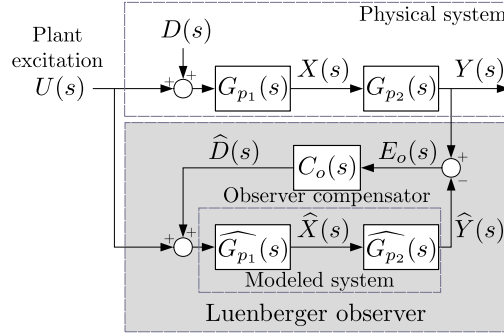


Figure 3.14: Generalized Luenberger observer model.

The model is defined by the transfer functions (3.13)-(3.17). The expressions (3.13)-(3.15) define the relation between the actual and observed states considering the observer in open loop, i.e. breaking the link of plant excitation  $U(s)$  with the observer model. It is noticed that they present a low pass filter form. In the case of (3.13),  $\hat{Y}(s)$  is strictly the filtered version of  $Y(s)$ , while in the other two cases,  $\hat{X}$  and  $\hat{D}$  this happens if the estimated plant transfer functions match the real system plant.

$$\frac{\hat{Y}(s)}{Y(s)} = \frac{\widehat{G}_{p_1}(s)\widehat{G}_{p_2}(s)C_o(s)}{1 + \widehat{G}_{p_1}(s)\widehat{G}_{p_2}(s)C_o(s)} \quad (3.13)$$

$$\frac{\hat{X}(s)}{X(s)} = \frac{\widehat{G}_{p_1}(s)G_{p_2}(s)C_o(s)}{1 + \widehat{G}_{p_1}(s)\widehat{G}_{p_2}(s)C_o(s)} \quad (3.14)$$

$$\frac{\hat{D}(s)}{D(s)} = \frac{G_{p_1}(s)G_{p_2}(s)C_o(s)}{1 + \widehat{G}_{p_1}(s)\widehat{G}_{p_2}(s)C_o(s)} \quad (3.15)$$

However, once the observer is feed with the same input  $U(s)$  as the physical model, considering no disturbance, the expressions (3.16) and (3.17) are obtained. It is worth noting that under a perfectly accurate estimated model the observed states become equal to the physical states, independently of the observer regulator  $C_o$ .

$$\frac{\widehat{X}(s)}{X(s)} = \frac{\widehat{G}_{p_1}(s)}{G_{p_1}(s)} \frac{1 + C_o(s)G_{p_1}(s)G_{p_2}(s)}{1 + C_o(s)\widehat{G}_{p_1}(s)\widehat{G}_{p_2}(s)} \quad (3.16)$$

$$\frac{\widehat{Y}(s)}{Y(s)} = \frac{\widehat{G}_{p_1}(s)\widehat{G}_{p_2}(s)}{G_{p_1}(s)G_{p_2}(s)} \frac{1 + C_o(s)G_{p_1}(s)G_{p_2}(s)}{1 + C_o(s)\widehat{G}_{p_1}(s)\widehat{G}_{p_2}(s)} \quad (3.17)$$

Nonetheless, in most of the cases it is not possible to exactly replicate the physical plant, due to its complexity (non linearity, high order systems...), in the observer model, usually being the last one a simplified version of the actual plant. In addition, the plant parameters might varies due to several causes as temperature, contingencies or aging. To maintain the reliability of the observer, the observer compensator  $C_o$  not only estimates the system disturbance but also compensates for errors in the estimated plant and variations in the physical plant.

$$\frac{\widehat{D}(s)}{U(s)} = \frac{C_o(s) \left( G_{p_1}(s)G_{p_2}(s) - \widehat{G}_{p_1}(s)\widehat{G}_{p_2}(s) \right)}{1 + C_o(s)\widehat{G}_{p_1}(s)\widehat{G}_{p_2}(s)} \quad (3.18)$$

Thus, the transfer function  $\frac{\widehat{D}(s)}{U(s)}$  in (3.18), obtained for  $D(s) = 0$ , shows how the output of  $C_o$  becomes 0 if the estimated plant is equal to the physical one. Otherwise, the observer regulator will react to any error between physical and estimated models.

### 3.5.2 Observer tuning

The selection of the observer compensator ( $C_o$ ) structure and gains is reduced to the tuning of the observer model as represented in 3.15, without considering any other part of the system. Thus, the observer is tuned as a conventional closed-loop control system. The main premises of  $C_o$  are to ensure stability, offer a proper reference tracking with zero steady state error and provide with the maximum bandwidth to the closed-loop function  $\frac{\widehat{Y}(s)}{Y(s)}$ . It is worth to point out, that the observer regulator will be effective for closed-loop control as soon as its bandwidth is high enough when compared with the control system bandwidth. Depending on the application, the topology used for the implementation of  $C_o$  may consist in PI, PID, PR or any other closed-loop control structure, as soon as the stated premises are ensured.

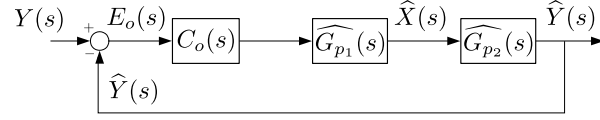


**Figure 3.15:** Luenberger observer represented in the traditional control format for tuning purposes.

### 3.5.3 Control system application

The Luenberger observer can be integrated in the control system for two main tasks: 1) performed a closed-loop control using an observed state as a feedback to avoid the use of sensors or improve the measured signals, 2) use the observed disturbance to perform a disturbance decoupling and improve the system disturbance rejection.

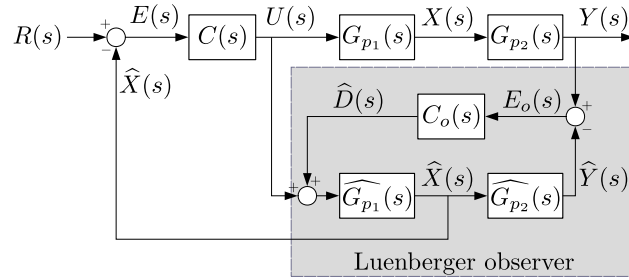


**Figure 3.16:** Feedback control based on Luenberger observer.

Fig. 3.16 shows the diagram of a feedback control based on observed state feedback, where  $R(s)$  is the reference input to the system and  $C(s)$  is the closed-loop regulator of the control system. The system is defined by the expressions (3.19)-(3.21). The reference to observed feedback state is given by (3.19), presenting a low pass filter structure that depends on the  $C$  regulator and in the observer transfer function  $G_{\frac{\hat{x}}{U}}(s)$  defined by (3.20). The output to reference transfer function is given in (3.21), where  $G_{\frac{X}{U}}(s) = G_{p1}$ . As  $G_{\frac{X}{U}}(s)$  and  $G_{\frac{\hat{x}}{U}}(s)$  should present a similar response within the observer bandwidth, the transfer function  $\frac{X(s)}{R(s)}$  also behaves as a low pass filter if the observer regulator is much faster than the control system regulator.

$$\frac{\hat{X}(s)}{R(s)} = \frac{G_{\frac{\hat{x}}{U}}(s)C(s)}{1 + G_{\frac{\hat{x}}{U}}(s)C(s)} \quad (3.19)$$

$$G_{\frac{\hat{x}}{U}}(s) = \frac{\hat{X}(s)}{U(s)} = \widehat{G}_{p1}(s) \frac{1 + C_o(s)G_{p1}(s)G_{p2}(s)}{1 + C_o(s)\widehat{G}_{p1}(s)\widehat{G}_{p2}(s)} \quad (3.20)$$

$$\frac{X(s)}{R(s)} = \frac{G_{p1}(s)C(s)}{1 + G_{\widehat{X}}(s)C(s)} = \frac{G_{\frac{X}{\widehat{X}}}(s)C(s)}{1 + G_{\widehat{X}}(s)C(s)} \quad (3.21)$$

The observer application for disturbance decoupling is shown in Fig. 3.17. In this case  $\frac{\widehat{D}(s)}{D(s)}$  is modified as (3.22) and the disturbance to output transfer function is shown in (3.23). The expression reveals a reduced reaction to disturbance (ideally 0 in steady state) within the bandwidth of the low pass filter system  $\frac{\widehat{D}(s)}{D(s)}$ .

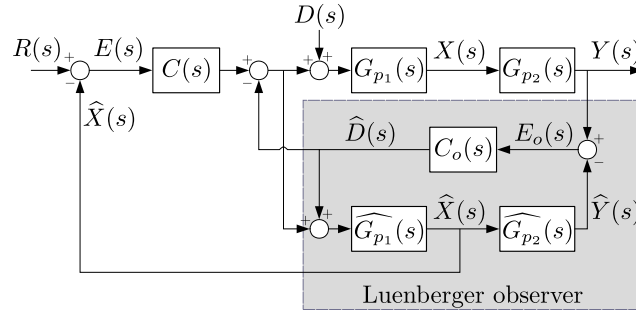


**Figure 3.17:** Disturbance decoupling using the observed disturbance.

$$\frac{\widehat{D}(s)}{D(s)} = \frac{G_{p1}(s)G_{p2}(s)C_o(s)}{1 + G_{p1}(s)G_{p2}(s)C_o(s)} \quad (3.22)$$

$$\frac{X(s)}{D(s)} = G_{p1}(s) - G_{p1}(s) \frac{G_{p1}(s)G_{p2}(s)C_o(s)}{1 + G_{p1}(s)G_{p2}(s)C_o(s)} \quad (3.23)$$

Within the scope of this thesis, the Luenberger observer will be applied in two of the contributions: 1) a grid-side current control for VSIs interfaced by an LCL filter, for reducing the number of sensors (Section 3.6) and 2) a transient frequency drift compensator, for the reduction of frequency estimation phase lag (Section 4.3).

### 3.6 Observer-based LCL filter current control for grid-tied 3-phase VSIs

The superior filtering performance of the LCL structure when compared to the L or LC alternatives has also important shortcomings in the design of the current controller [71]. Current control using an LCL filter is a challenging task due to the resonance created by the capacitor and the inductances and often an attenuation damping is needed, consisting the most common techniques in passive and active damping. As

commented before in Section 3.4, the second case usually requires the measurement or estimation of the capacitor current, being necessary additional sensors when compared to L or LC filters. An example of the system response for an LCL filter current control is shown in Fig. 3.18, comparing a control based on active damping, using the measured output current  $i_g$  as a feedback, and a current control based only on the use of the  $i_i$  current, neglecting the capacitor effect in the controller, being clear the benefits of the first case. This section proposes an alternative to eliminate the need for the grid-side current sensor of an LCL filter by using a Luenberger observer.

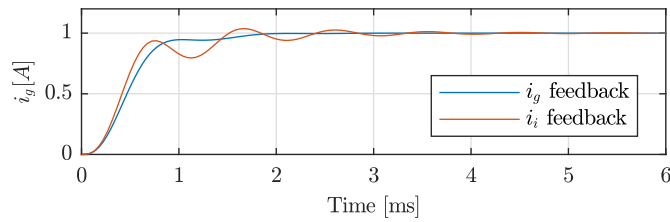


**Figure 3.18:** Step response of the transfer function  $\frac{I_g}{I_g^*}$  under two cases: 1) using active damping and the measured grid-side current as feedback (blue), 2) using the converter-side current as feedback, without active damping and neglecting the capacitor in the control system.

### 3.6.1 Grid-side current observer model

The observer is similar to the one developed in [252], where direct discrete-time domain design is used instead. The simplicity of the design in the continuous-time domain and the small difference in the performance for the parameters used in this research makes this an appealing solution. It is also related with [292], but the more convenient converter side current is used instead of the grid side one. This proposal eliminates the need for measuring the grid-side current and will estimate it using only sensors in two points: 1) converter-side current ( $i_i$ ), and 2) voltage at the PCC ( $v_g$ ). The observer-based current control block diagram in complex compact form is shown in Fig 3.19, where the system plant is the one defined for LCL filter in Section 3.3.

### 3.6.2 Analytical linear model of the current observer

In order to characterized the proposed controller, the observer and physical plants as well as the overall control system will be modelled in the Laplace domain using linear transfer functions, following the basics explained in Section 3.5. To do so, the modelling will assume to simplifications: 1) A perfect decoupling of the cross-coupling terms is assumed by use of feed-forward decoupling terms, and 2) the system is assumed to be symmetrical, so an equivalent single-axis model is used. The simplified representation of the LCL observer is shown in Fig. 3.20, where the variables seen in Section 3.5



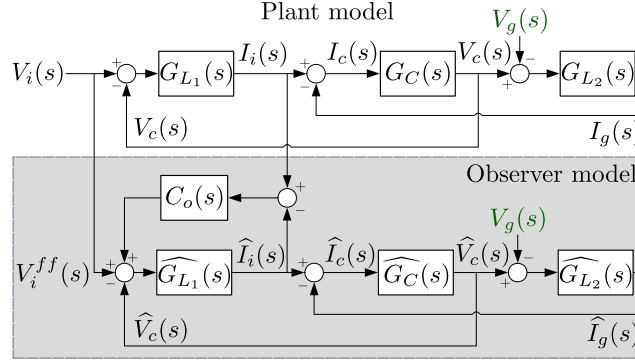


**Figure 3.20:** LCL system plant model and observer model in the Laplace domain.

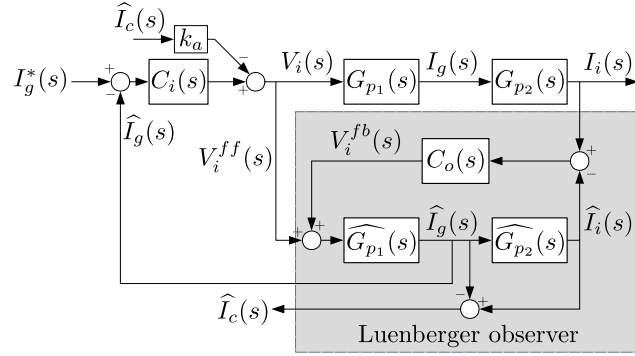


**Figure 3.21:** LCL observer-based current control represented in the conventional observer format.

$$G_{p_t}(s) = G_{p_1}(s)G_{p_2}(s) = \frac{I_i(s)}{V_i(s)} = \frac{G_{L1}(s) + G_{L1}(s)G_C(s)G_{L2}(s)}{1 + G_C(s)G_{L1}(s) + G_C(s)G_{L2}(s)} \quad (3.30)$$

$$G_{\frac{\hat{x}}{U}}(s) = \frac{\hat{I}_g(s)}{V^{ff}(s)} = \widehat{G}_{p_1}(s) \frac{1 + C_o(s)G_{p_t}(s)}{1 + C_o(s)\widehat{G}_{p_t}(s)} \quad (3.31)$$

From those expressions, the closed-loop transfer functions could be obtained using the ones derived in Section 3.5. However, the use of the active damping modifies the standard expressions, being necessary the particularization for the case of concern. The observed to physical output transfer function is given by (3.32). The reference tracking is defined by the transfer functions (3.33) and (3.34). As shown, both of them become similar as soon as  $G_{\frac{\hat{x}}{U}}(s) = G_{\frac{\hat{x}}{U}}(s)$ , avoiding in that case the use of  $I_g(s)$  measurement for the control.

$$\frac{\widehat{I}_g(s)}{I_g(s)} = \frac{\widehat{G}_{p_1}(s) 1 + C_o(s)G_{p_1}(s)G_{p_2}(s)}{\widehat{G}_{p_1}(s) 1 + C_o(s)\widehat{G}_{p_1}(s)\widehat{G}_{p_2}(s)} \quad (3.32)$$

$$\frac{\widehat{I}_g(s)}{I_g^*(s)} = \frac{G_{\frac{\widehat{x}}{v}}(s)C_i(s)}{1 + G_{\frac{\widehat{x}}{v}}(s)C_i(s) + k_a G_{\frac{\widehat{x}}{v}}(s) \left( \widehat{G}_{p_2}(s) - 1 \right)} \quad (3.33)$$

$$\frac{I_g(s)}{I_g^*(s)} = \frac{G_{\frac{x}{v}}(s)C_i(s)}{1 + G_{\frac{\widehat{x}}{v}}(s)C_i(s) + k_a G_{\frac{\widehat{x}}{v}}(s) \left( \widehat{G}_{p_2}(s) - 1 \right)} \quad (3.34)$$

This expressions will serve to analyze the response and robustness of the proposed method.

### 3.6.3 Observer compensator tuning

The system considered for the observer tuning is expressed by (3.35). Proportional-integral (PI) or proportional-resonant (PR) controllers can be selected depending on the implementation being at the synchronous or the stationary reference frame respectively. In this study, a synchronous reference frame has been selected, being  $C_o$  a PI defined by (3.36). The regulator  $C_o$  is tuned using zero-pole cancellation considering the two systems  $G_{L_1}$  and  $G_{L_2}$  to be connected in series, neglecting the capacitor current effect up to the observer bandwidth (3.37).

$$\frac{\widehat{I}_i(s)}{I_i(s)} = \frac{\widehat{G}_{p_i}(s)C_o(s)}{1 + \widehat{G}_{p_t}(s)C_o(s)} \quad (3.35)$$

$$C_o(s) = k_{p_o} \left( 1 + \frac{1}{T_{i_o}} \frac{1}{s} \right) \quad (3.36)$$

$$k_{p_o} = 2\pi f_{BW} (L_1 + L_2) \quad T_{i_o} = \frac{L_1 + L_2}{R_1 + R_2} \quad (3.37)$$

Neglecting the capacitor effect in the observer tuning may lead to resonances in its response. However, as the current control loop bandwidth is assumed to be far below the resonance frequency of the observer, it will have a reduced effect in the grid-side current control. In any case, the observer response can be damped using either active damping in parallel with  $C_o$  or modifying the capacitor plant model by adding a parallel connected resistance  $\widehat{R}_C$  as shown in Fig. 3.22, affecting to the observer plant in such a case.

Fig. 3.23 shows the open and closed-loop frequency responses of the observer for the system described in Appendix A.3, evaluated for different damping resistances. As the resonance frequency appears near 1kHz and the grid current control will be set with a 3 times lower bandwidth, in this thesis no damping has been used within the observer model.

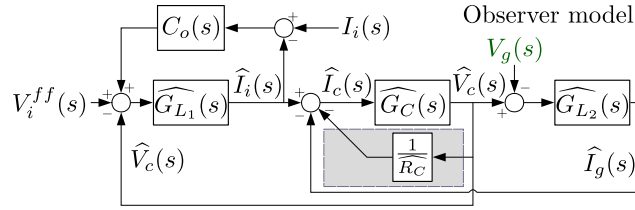


**Figure 3.22:** Inclusion of a parasitic parallel resistance in the observer plant for observer response damping at high frequencies.

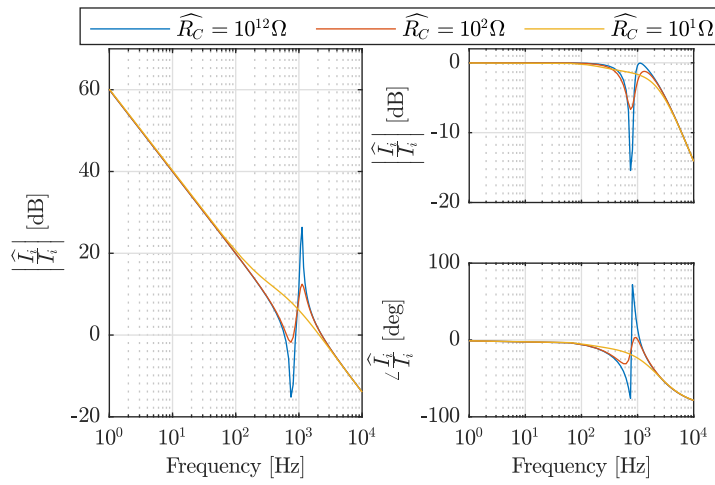


**Figure 3.23:** Bode diagram of the  $\hat{I}_i/I_i$  transfer function in open loop (left) and closed-loop (right) configuration to evaluate the observer response under the given  $C_o$  for different damping resistor values.

### 3.6.4 Analytical response of the grid-side current observer

Before performing a simulation in a 3-phase application, the proposed control scheme has been tested analytically using the transfer functions in Section 3.6.2. The analysis has been performed using the parameters in Appendix A.3 later used for the simulations and the experimental demonstration.

Fig. 3.24 shows the closed-loop response of the grid-side current control system, including the actual current and the estimated one. For demonstrating the robustness of the observer against changes in the system plant, the response has been evaluated for three different grid-side inductances, the nominal  $L_2$  and a variation of  $\pm 60\%$  over the nominal, demonstrating a stable response in any of the cases. Although the estimated responses (dashed lines) present deviations from the actual response (solid lines) at high frequencies, a flat and similar response is obtained within the minimum bandwidth of

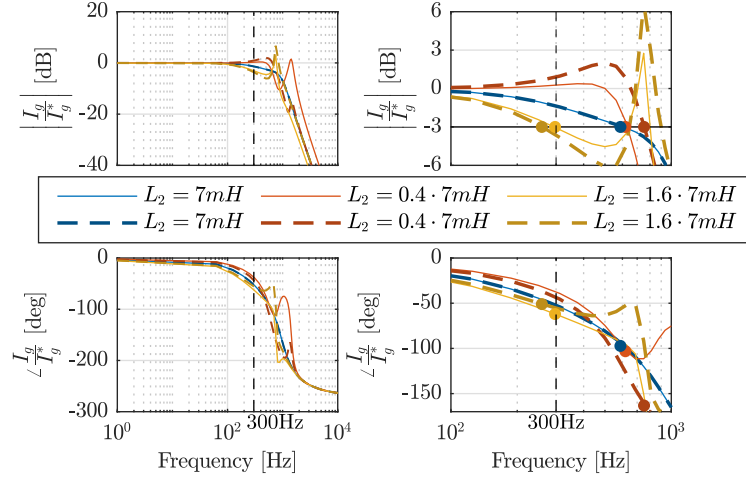


**Figure 3.24:** Frequency response of the observer-based LCL output current control. The response is shown for 3 different values of the grid-side inductances  $L_2$ , without updating  $C_i$  gains nor  $\widehat{L}_2$ . Solid lines:  $\frac{I_g}{I_g^*}$ ; dashed lines:  $\widehat{\frac{I_g}{I_g^*}}$ . Zoomed view of the response shown on the right.

300Hz used for tuning the current controller  $C_i$ , being the response clearly immune to parameters variation until around 400Hz. It is worth noting how the bandwidth (marked with dots) in some of the cases is even higher than the used in the zero-pole cancellation tuning due to the effect of the capacitor, which has not been considered in the selection of  $C_i$  gains in this case.

To highlight the accuracy of the current estimation within the controller bandwidth, Fig. 3.25 shows the frequency response of the transfer function  $\widehat{\frac{I_g}{I_g^*}}$  for different grid-side inductances. The parameters variation affects mainly at high frequencies, while a reduced effect is seen below the current control bandwidth. Thus, in the system under study, the effect of parameters variation will be seen only during sudden transients in the current reference.

The time domain response of the system is analyzed in Fig. 3.26 under an step change in the current command  $i_g^*$ , where the top plot shows the response of the proposed observer-based control system, while the bottom corresponds to a sensor-based control system with an ideal  $i_g$  sensor. As expected, the effect of parameters appears during transients, and the differences between the two cases are visible. However, the responses are similar with the original plant, and even under significant changes in the parameters, the observer-based system is stable and presents a comparable settling time with the sensor-based control, being the difference in the system damping. As a possible improvement of this issue, an adaptive damping  $k_a$  depending on the parameters variation could be considered in future developments.

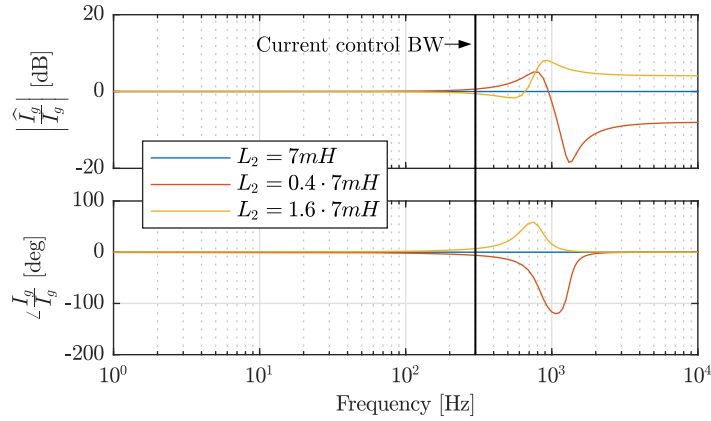


**Figure 3.25:** Frequency response of the estimated output current  $\widehat{\frac{I_g}{I_g}}$ .

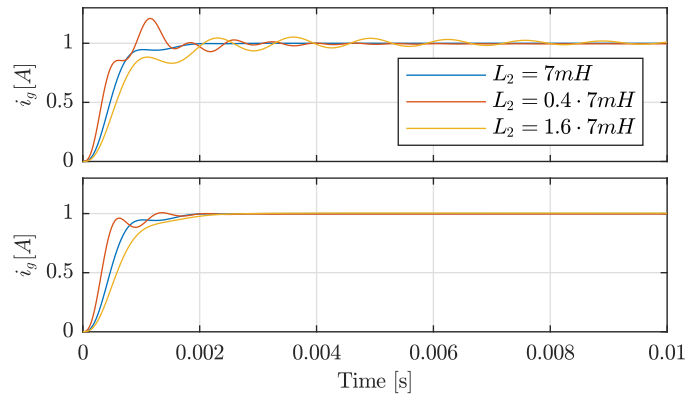


**Figure 3.26:** Response of the grid-side current under an step change of the current reference for 3 different values of  $L_2$ . Top, proposed observer-based LCL current control, and bottom, measured-based LCL current control.

The operation under parameters variation is possible thanks to the observer compensator. To finish with the analytical discussion, the effect of errors between the estimated plant and the physical plant at the output of the compensator is evaluated. The magnitude of the Bode diagram for the excitation input to observer regulator output transfer function  $\frac{V_i^{fb}}{V_i^{ff}}$  is represented in Fig. 3.27 for different values of  $L_2$ , showing how the compensator output increases in all frequencies as the plant deviates from the original plant ( $L_2 = 7\text{mH}$ ), becoming a clear indicator of parameters change.

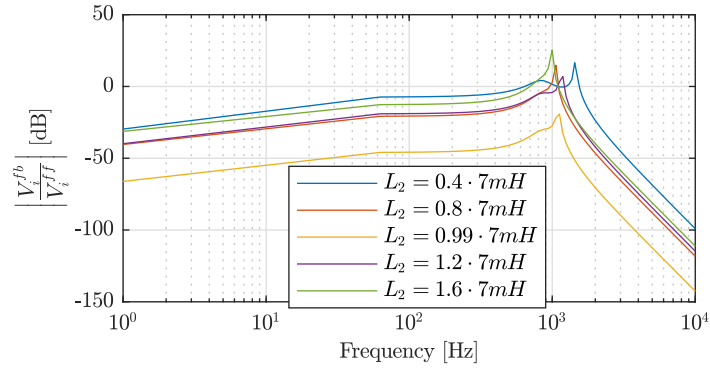


**Figure 3.27:** Effect of differences between the observer plant and the physical plant in the observer compensator  $C_o$  output. Magnitude frequency response of the transfer function  $\frac{V_i^{fb}}{V_i^{ff}}$ .

### 3.6.5 Simulation results

The observer-based control model has been tested through simulations in a 3-phase grid-tied converter using the setup described in Appendix A.3. The observer-based control performance has been implemented in the  $dq$  synchronous reference frame and its performance for different current commands and variations in the plant parameters is shown in Fig. 3.28. The results show a good match with the analytical responses seen previously, and present a correct tracking of the commanded current reference in any of the cases, being the estimated response similar to the measured one presenting a similar settling time and overshoot. It is worth to point out, that although the errors between the actual plant and the estimated plant have a perceptible effect on the responses, they do not affect the reference tracking and do not lead to significant differences in the dynamic response, apart from the increased overshoot with the reduction of grid-side impedance.

It has been shown in the analytical discussion how the observer regulator output signal,  $v_i^{fb}$ , reacts to changes in the physical plant, trying to compensate the mismatches between real and estimated plants. Thus, that signal can be used to detect changes in parameters as the grid-side impedance. Fig. 3.29 shows the simulation results when a sudden reduction of 50% in the grid-side impedance occurs at 0.08s. Although the variation affects to both components, a significant effect is perceived in the  $q$ -axis of  $v_i^{fb}$  due to the dominant inductive component in the grid-side impedance. Two cases have been simulated, one applying a sensor delay (right) and another using an ideal sensor (left). Two main conclusions are obtained from this figure:

- As commented before, the current and voltage sensor effects are not considered in the modelling of the observer, thus, they represent a modification of the physical

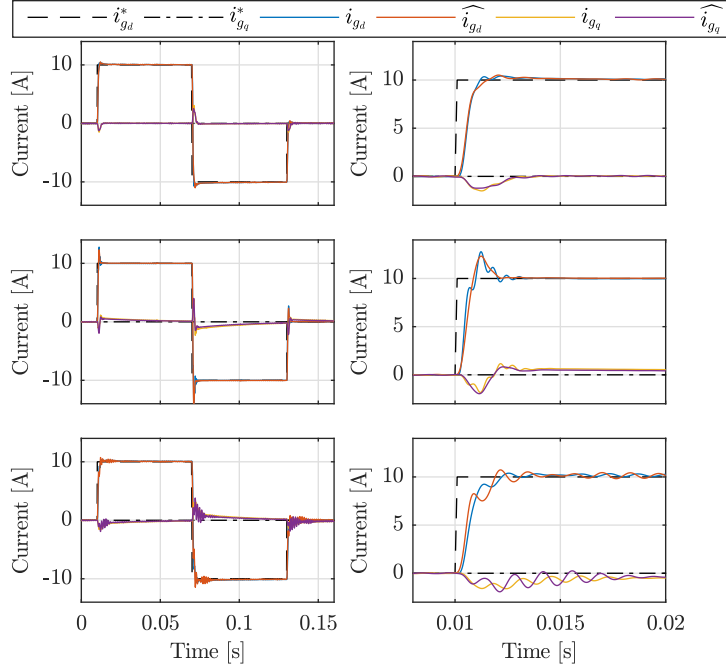


**Figure 3.28:** Simulation results for the observer-based control transient response. The results show the performance for three different values of  $L_2$ . Top,  $L_2 = 7\text{mH}$  (nominal), middle,  $L_2 = 0.4 \cdot 7\text{mH}$  ( $-60\%$ ), and bottom,  $L_2 = 1.6 \cdot 7\text{mH}$  ( $+60\%$ ). The right column shows a zoom view of the transient step response.

plant with respect to the observer plant. The results show how the observer regulator  $C_o$  compensate the delay without the need for including it in the modelling. Due to the dominant reactive impedance of the LCL filter, this effect is mainly present in the  $q$ -axis. In the case of ideal sensor, the estimated and physical plant are similar till the instant  $0.08\text{s}$ , and, as expected,  $v_i^{fb}$  is 0.

- The variation of  $v_i^{fb}$  ( $q$ -axis) due to a grid impedance change is noticeable, reaching around  $10\text{V}$ . This effect will be exploited as a marker of grid impedance changes as later shown in Section 3.7.

### 3.6.6 Grid-side current observer digital implementation

For the digital implementation, the Luenberger observer and the current controller designs must be translated to the discrete-time domain. Several options exist for the discretization. Considering that the method should be suitable for an adaptive implementation, the use of complicated matrices' operations must be reduced. As a

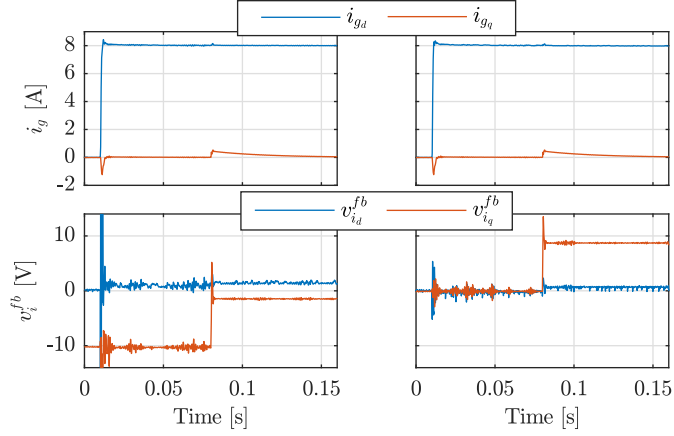


**Figure 3.29:** Simulation results for the observer compensator output. Reaction of  $C_o$  under changes in the physical plant. The results considering a sensor delay ( $v_g$  and  $i_i$ ) of  $100\mu$ s (left), and ideal sensor with zero phase-lag (right) are shown.

compromise between the accuracy and the computational burden, Tustin method is selected. The resulting expressions are shown in (3.38), (3.39), where  $[k]$  and  $[k - 1]$  correspond to the present and previous samples and  $T_s$  is the sample time.

$$\begin{aligned} \mathbf{x}_x[k] &= \mathbf{K}_{ix} \cdot \left( \mathbf{K}_{ax} \cdot \mathbf{x}_x[k - 1] + \frac{T_s}{2} \mathbf{B}_x (\mathbf{u}_x[k] + \mathbf{u}_x[k - 1]) \right) \\ &\quad + \frac{T_s}{2} \omega_e \mathbf{I} (\mathbf{x}_y[k] + \mathbf{x}_y[k - 1]) \end{aligned} \quad (3.38)$$

$$\begin{aligned} \mathbf{x}_y[k] &= \mathbf{K}_{iy} \cdot \left( \mathbf{K}_{ay} \cdot \mathbf{x}_y[k - 1] + \frac{T_s}{2} \mathbf{B}_y (\mathbf{u}_y[k] + \mathbf{u}_y[k - 1]) \right) \\ &\quad - \frac{T_s}{2} \omega_e \mathbf{I} (\mathbf{x}_x[k] + \mathbf{x}_x[k - 1]) \end{aligned} \quad (3.39)$$

where  $\mathbf{K}_{ax}$ ,  $\mathbf{K}_{ay}$ ,  $\mathbf{K}_{ix}$ ,  $\mathbf{K}_{iy}$  being the values of  $\mathbf{K}_a = \mathbf{I} + \frac{T_s}{2} \mathbf{A}$  and  $\mathbf{K}_i = (\mathbf{I} - \frac{T_s}{2} \mathbf{A})^{-1}$  for either the  $x$  or  $y$  axes. The observer controller ( $C_o$ ) is also discretized using Tustin approximation.

### 3.6.7 Experimental results

The observer-based control proposed in this section has been implemented experimentally using the experimental setup described in Appendix A.3. The observer performance, at the synchronous reference frame, is shown at Fig. 3.30 when the estimated LCL filter parameters match the real ones. Two experiments have been performed: 1) implementation of current control using the proposed observer-based control scheme, and 2) implementation of the control using a grid-side current sensor for applying a

sensor-based control approach. The figure compares the response of those two cases. As shown, the grid current is correctly tracked and the dynamic performance matches the results obtained in simulations. In addition, the result of the observer-based technique is comparable to the one obtained with the sensor-based control, verifying the proposed technique as an alternative to the control using grid-side sensors.

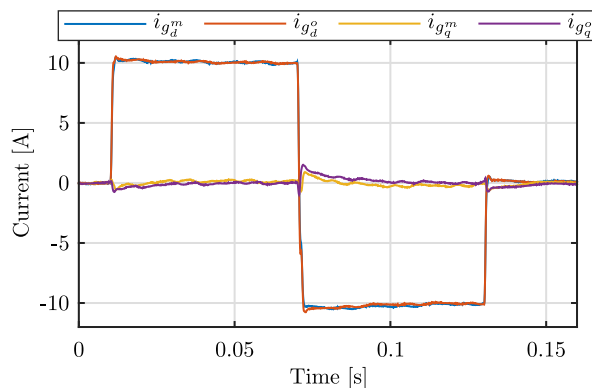


**Figure 3.30:** Experimental results for the grid-current observer transient response. The results show a comparison of the observer-based control with respect to the sensor-based using an additional grid-side current sensor. Superscript  $m$  is for the sensor-based control, whereas  $o$  is for the observer-based control.

In addition to the reduction in the number of sensors, it has been shown in simulations that the observer regulator output signal,  $v_i^{fb}$ , reacts to changes in the grid-side impedance. Fig. 3.31 shows the experimental results when a sudden reduction of 50% in the grid-side impedance occurs at 0.08s for three different current levels. As it can be seen, even if the changes in the fundamental command affect the observer signal, the variation due to the grid impedance change is for the shown cases more than 100% larger.

Although it has been demonstrated that the observer-based current controller presents an appropriate robustness against significant changes in the plant parameters, it is clear that the dynamic response is worsen with respect to a precise estimation of the plant. Thus, updating the observer plant and the controller  $C_i$  gains after a change in the physical plant, would improve the behavior, returning to the original condition  $\widehat{G}_{pt} \approx G_{pt}$ . In addition, taking advantage of the  $C_o$  output, the reaction of the observer can be used for detecting changes in the plant. The following section proposes an impedance estimation active method suitable for a number of grid applications including the estimation of the grid-side inductance and resistance in LCL filters, where the variation of  $v_i^{fb}$  can be used for triggering a pulse injection mechanism, thus avoiding the injection of a continuous disturbance into the grid.

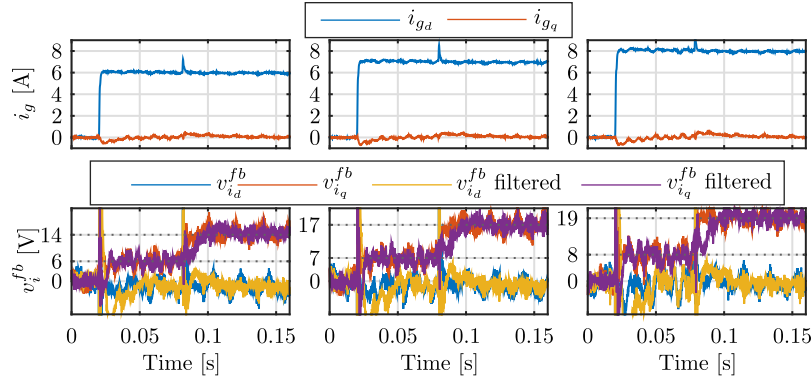


**Figure 3.31:** Experimental results for the transient detection. Top row: fundamental grid currents components at the synchronous reference frame for three different current references, 6, 7 and 8 Amps. Bottom row: observer regulator output components at the synchronous reference frame. Yellow and magenta traces show the filtered  $d$  and  $q$  components signals with a  $2^{nd}$  order Butterworth filter tuned with a cut-off frequency of 75Hz.

### 3.7 Grid impedance estimation in 3-phase systems based on pulsed signal injection

This section proposed a versatile impedance estimation method based on pulsed signal injection. The injection is triggered only when necessary i.e., when a significant change in the impedance is detected, and perform the impedance estimation with a reduce computational cost based on an RLS-based algorithm. For determining the change in the impedance, it has been seen in Section 3.6 that the observer compensator output result an appealing trigger. The method is a suitable tool for a range of applications as islanding and fault detection in microgrids, and adaptive control to improve the dynamic participation of converters in other applications for power quality and secondary control. Although the method will be design for 3-phase AC systems in this thesis, it could be potentially applied to DC applications. The strategy presented in this section focuses on the estimation of the grid impedance  $Z_g$  assuming it consists in a resistive and inductive components ( $R_g$  and  $L_g$ ) in series configuration as shown in Fig. 3.32. The excitation and estimation of such a system is performed by a current controlled grid-tied VSI by using the estimated or measured grid-side current  $i_g$  and the PCC voltage  $v_g$ .

#### 3.7.1 Pulsed signal injection

There are different PSI alternatives related with the injection parameters which can be adjusted. As shown in Fig. 3.33, the signal is centered at the zero crossing of the phase to neutral voltages. Zero crossing is detected by the PLL also used for

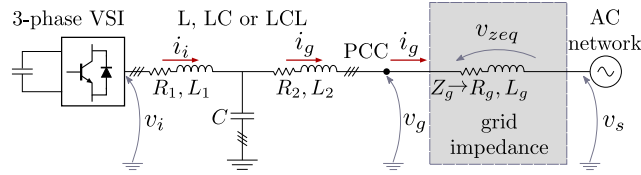


**Figure 3.32:** Simplified diagram of a grid-tied VSI connected to an AC network through a significant line impedance.

grid synchronization. This instant has been selected in order to minimize the voltage distortion, as it will be discussed later.

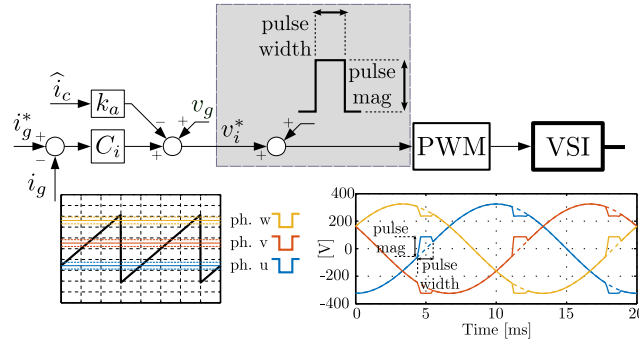


**Figure 3.33:** PSI implementation. The pulse injection is synchronized and centered with respect to the grid voltage zero crossing. On the phase representation (*ph.u, v, w*), dashed lines show the starting and end of each phase pulse and solid ones the zero crossing of the respective phase.

Three different pulse injection alternatives are investigated. Two of them are implemented in the *abc* reference frame, while the third one is in the *dq* reference frame. The pulses are injected by modifying the duty cycle provided by the current controller. During the pulse injection, the fundamental voltage command is disabled for the case of *abc* injection (see Fig. 3.33) whereas is added to the injected pulse in the *dq* reference frame implementation. As seen in Fig. 3.33, both the pulse width and the magnitude can be changed. Obviously, larger pulses will help in the estimation procedure, but will also increase the resulting current THD. The values in Appendix A.4 have been used. Resulting waveforms for the inverter commands and the applied voltages are shown in Fig. 3.34. The corresponding currents in the synchronous reference frame are depicted in Fig. 3.35. The three alternatives are described following:

1. **Method#1:** Pulse width is set to the desired value and the magnitude is set to zero. Under these conditions, the fundamental voltage command is clamped to zero during the pulse injection time. In the *dq* reference frame, even if the

pulse is mostly applied at the  $q$ -axis, both components are modified. The pulses exhibit a triangular shape at the  $q$ -axis and the resulting current has a sinusoidal waveform.

2. **Method#2:** Fundamental command is held at the corresponding value at the beginning of the pulse injection and when the phase crosses the zero is changed to the symmetrical value with respect to zero. In the  $dq$  reference frame,  $d$ -axis component is also affected, although in a less noticeable way than for Method#1. The pulses at the  $q$ -axis are also transformed to a triangular shape, but the resulting current has a triangular waveform of opposite phase when compared to previous method.
3. **Method#3:** Pulses are directly injected at the  $q$ -,  $d$ -, or both axes by adding the pulses to the fundamental command delivered by the current controller. When compared to the pulse injection in the  $dq$  reference frame for both Method#1 and Method#2, the resulting excitation is stepwise in the  $abc$  reference frame but has triangular form in the  $dq$  reference frame. Even if the RLS algorithm is to be implemented in the  $\alpha\beta$  reference frame, in order to allow the identification to work under unbalanced conditions it has been tested that the results are improved when square pulses are applied in the  $dq$  reference frame.

It must be remarked that all the pulse injection strategies share the fact that the applied distortion to the voltage command is symmetrical with respect to the zero crossing, thus resulting in a zero average voltage error. Selecting one method or the other is based on the sensitivity of the current response and on the implementation burden. In this thesis, Method#3 is considered, with the injection kept at the  $q$ -axis.

Experimental results of the system operating in closed-loop using the observer estimated grid current with a 500 Hz bandwidth are shown in Fig. 3.36. The results show that, even if the current controller reaction is affecting the pulses injection, they are clearly visible on the grid voltage and thus could potentially be used for the RLS estimation. It is also remarkable the close matching compared to the simulated results shown in Fig. 3.35. At this point, it is needed to comment on the additional THD distortion induced by the pulse injection. As it has been explained, pulse injection is disabled until a change in the impedance is detected by the observer. Whenever this happens, three pulses are injected (one at the zero crossing of each of the phases). The expected result is that the THD distortion is notably reduced with respect to existing techniques. In order to corroborate that, first a suitable procedure for the THD definition for pulsating signal has been carried out. As provided by the IEC61000-4-7 standard, ten fundamental periods of the voltage and current signals for 50Hz of nominal frequency are analyzed. Considering the pulsating and discontinuous nature of the proposed injection mechanism, the THD is calculated in time domain using (3.40).

$$THD[\%] = \frac{\sqrt{\sum_{t=0}^{t=200ms} \mathbf{x}_{\alpha\beta}^{si}{}^2}}{\sqrt{\sum_{t=0}^{t=200ms} \mathbf{x}_{\alpha\beta}{}^2}} \cdot 100 \quad (3.40)$$

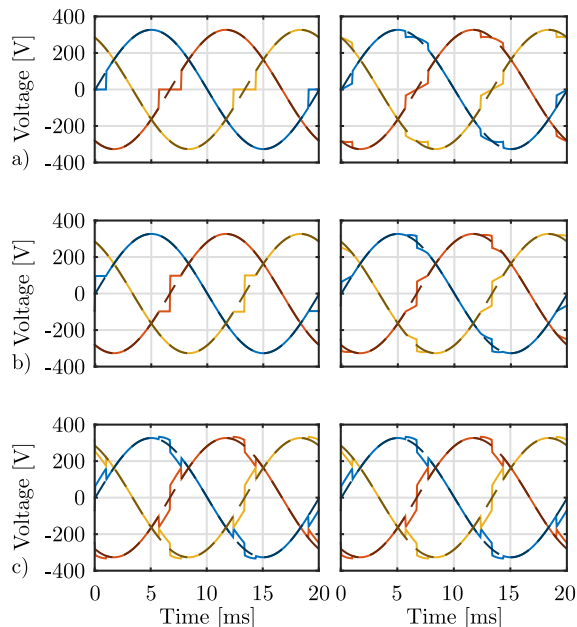


**Figure 3.34:** PSI waveforms for the three proposed methods in the  $abc$  reference frame. a) Method#1, b) Method#2 and c) Method#3. Left column shows the generated phase voltage command and right column the phase to neutral voltages. Dashed lines show the variables if the pulse injection is disabled.

where  $\mathbf{x}_{\alpha\beta}^{si}$  is the isolated injection voltage signal or the corresponding current response in the  $\alpha\beta$  reference frame and  $\mathbf{x}_{\alpha\beta}$  the overall voltage/current signal. The calculation of the THD is restricted to 200ms that corresponds to 10 fundamental cycles at 50Hz. The THD calculations are done for selected references proposed by other authors as commented in Chapter 2 during the state of the art discussion. The comparison is established for different implementations corresponding to all the alternative methods for impedance estimation, i.e: LFSI, HFSI, PSI and BSSI. The calculations are carried out using the same simulation models, with same grid conditions and using the signal injection parameters as indicated by the authors. Results for the comparison are summarized in Fig. 3.37. As it can be seen, the proposed method has the lowest THD for the grid voltage, both for the 2ms and the 1ms cases. Considering the grid current THD, the proposed observer-based method is the second best for the 2ms case, just after the HFSI method, and the best one for the case of 1ms. It is also worth noting that the comparison conditions represent the worst case scenario for our proposal. The calculated THD value assumes 3 pulses will be injected each 10 cycles, meaning that the observer is reacting to a change in the impedance each 10 cycles. However, the most important advantage of the observer-based method is the fact that the pulse injection is discontinuous, making the THD to be improved when the grid impedance

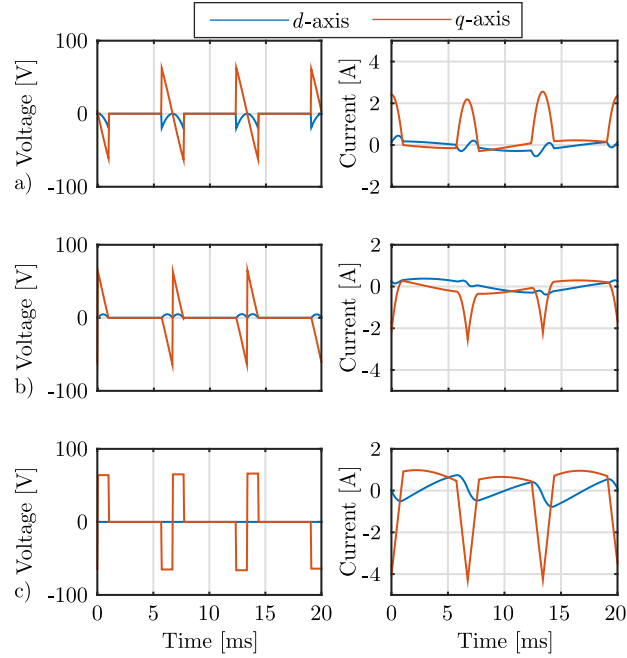


**Figure 3.35:** PSI waveforms for the three proposed methods in the  $dq$  reference frame. a) Method#1, b) Method#2 and c) Method#3. Fundamental component is removed in order to zoom on the injected pulsed components. Left column is for the  $v_{dq}$  voltages and right for the  $i_{dq}$  current.  $d$ -axis and  $q$ -axis are represented in blue and red respectively.

is kept stable. Fig. 3.38 shows an interesting comparison between the observer-based injection and the HFSI method. There, the THD results for the 2ms case are calculated as a function of the percentage of cycles in which the injection is applied. As it can be seen, the break-even point at which the proposed method improves the HFSI injection occurs when the ratio is lower than 4%. This condition is met after 40 grid cycles (0.8s).

### 3.7.2 RLS algorithm implementation

Measurement of the the grid impedance in real time requires an online estimation procedure. The existing literature approaches, as discussed before, rely on the injection of a voltage/current signal and measuring the resulting current/voltage [265, 274]; the use of the closed-loop current response for implementing a model reference adaptive system (MRAS) strategy [260]; or the use of observers or estimators [273]. In this study, the estimation of the system parameters is carried out by using an RLS approach [270, 293]. For that purpose, the differential voltage equation for the equivalent grid impedance in the stationary reference frame is discretized using Tustin method. The

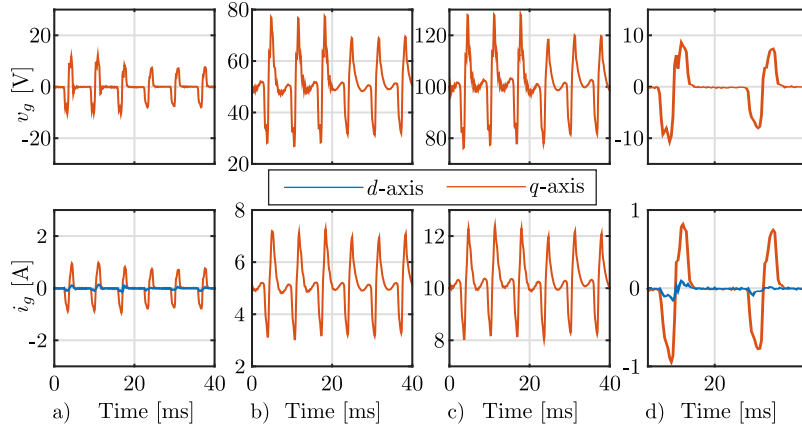


**Figure 3.36:** Experimental results using Method#3. System is operated in closed-loop with a bandwidth of 300Hz using the observed grid current. Top row shows the  $q$ -axis component of the grid voltage, whereas bottom row is for the observed grid current components in the synchronous reference frame. Different levels of  $q$ -axis current commanded: a) 0A, b) 5A, c) 10A, d) zoom for 0A condition. The  $d$ -axis components lead out of the scale in b) and c). At  $t = 20$ ms, the 2.4mH inductance series connected at the output of the LCL filter is changed to 0.6mH.

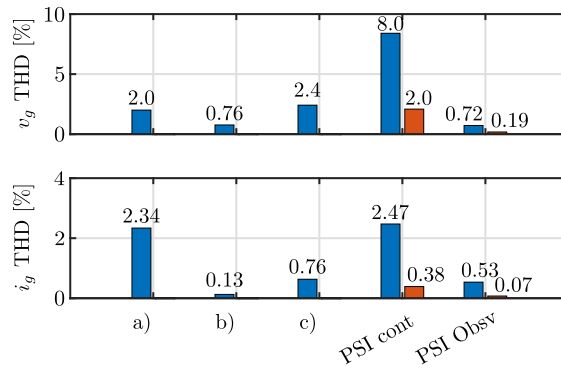


**Figure 3.37:** THD comparison for the different impedance estimation methods analyzed in this thesis with existing methods in the literature. Both the grid voltage,  $v_g$  and the grid current,  $i_g$  are shown. a) results in [264], b) results in [265,266] and c) results in [267,278]. PSI cont. and PSI Obsv. are the continuous and observer-based pulse injection for two different pulses duration (blue for 2ms and red for 1ms).

stationary reference frame is selected for the estimation in order to enable the system to work under unbalanced grid impedance conditions.

In a stationary reference frame aligned with the spatial angle orientation of the impedance, each individual term contributing to the equivalent grid impedance as seen

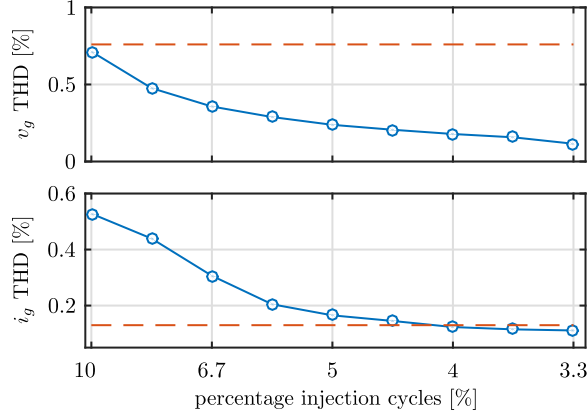


**Figure 3.38:** THD comparison for the PSI observer-based method (blue) and the HFSI method (dashed red) as a function of the percentage of cycles in which the injection is applied. Top, voltage at the PCC. Bottom, grid current.

by the converter, i.e. cable impedance and loads, can be represented in matrix form by (3.41).

$$\mathbf{Z}_{\alpha\beta i} = \mathbf{R}_{\alpha\beta i} + \mathbf{j}\omega_e \mathbf{L}_{\alpha\beta i} = \begin{bmatrix} Z_{\alpha\alpha i} & Z_{\alpha\beta i} \\ Z_{\alpha\beta i} & Z_{\beta\beta i} \end{bmatrix} \quad (3.41)$$

In (3.41), the  $i$  subscript is related to each individual impedance seen from the PCC. When the impedance is balanced,  $Z_{\alpha\alpha i}$  equals  $Z_{\beta\beta i}$ . Non diagonal terms ( $Z_{\alpha\beta i}$ ) represent the cross coupling between phases. Rotating the impedance matrix to a common  $\alpha\beta$  reference frame and considering  $n$  impedance elements, leads to (3.42).

$$\mathbf{z}_{\alpha\beta} = \sum_{i=1}^n \left( \Sigma Z_i \begin{bmatrix} 1 & 0 \\ 0 & 1 \end{bmatrix} + \Delta Z_i \begin{bmatrix} \cos \theta_e^i & \sin \theta_e^i \\ \sin \theta_e^i & -\cos \theta_e^i \end{bmatrix} + Z_{\alpha\beta i} \begin{bmatrix} -\sin \theta_e^i & \cos \theta_e^i \\ \cos \theta_e^i & \sin \theta_e^i \end{bmatrix} \right) \quad (3.42)$$

where  $\Sigma Z_i = \frac{Z_{\alpha\alpha i} + Z_{\beta\beta i}}{2}$ ,  $\Delta Z_i = \frac{Z_{\alpha\alpha i} - Z_{\beta\beta i}}{2}$ , and  $\theta_e^i$  is the spatial angular phase of the unbalance impedance. For example, for single-phase loads at phases  $u$ ,  $v$ ,  $w$ ,  $\theta_e^i$  equals  $0$ ,  $2\pi/3$  or  $4\pi/3$  respectively. In the case the system is balanced, only the matrix terms depending on  $\Sigma Z_i$  will remain. The relationship with the phase impedances can be obtained by using the definitions:  $\Sigma Z_i = \frac{za_i + zb_i + zc_i}{3}$  and  $\Delta Z_i = \frac{za_i + a \cdot zb_i + a^2 \cdot zc_i}{3}$ , where  $a = e^{j2\pi/3}$ .

By considering the overall grid impedance dominated by the resistance and inductance terms, (3.42) can be expressed as (3.43).

$$\begin{aligned}
\mathbf{Z}_{\alpha\beta} = & \sum_{i=1}^n \left( (\Sigma R_i + \mathbf{j}\omega_e \Sigma L_i) \begin{bmatrix} 1 & 0 \\ 0 & 1 \end{bmatrix} + \right. \\
& (\Delta R_i + \mathbf{j}\omega_e \Delta L_i) \begin{bmatrix} \cos \theta_e^i & \sin \theta_e^i \\ \sin \theta_e^i & -\cos \theta_e^i \end{bmatrix} + \\
& \left. (R_{\alpha\beta i} + \mathbf{j}\omega_e L_{\alpha\beta i}) \begin{bmatrix} -\sin \theta_e^i & \cos \theta_e^i \\ \cos \theta_e^i & \sin \theta_e^i \end{bmatrix} \right) \quad (3.43)
\end{aligned}$$

where,  $\Sigma R_i = \frac{R_{\alpha\alpha i} + R_{\beta\beta i}}{2}$ ,  $\Sigma L_i = \frac{L_{\alpha\alpha i} + L_{\beta\beta i}}{2}$ ,  $\Delta R_i = \frac{R_{\alpha\alpha i} - R_{\beta\beta i}}{2}$ ,  $\Delta L_i = \frac{L_{\alpha\alpha i} - L_{\beta\beta i}}{2}$ . From here, the voltage equation given by (3.44) can be obtained,

$$\mathbf{v}_{zeq\alpha\beta} = \mathbf{v}_{g\alpha\beta} - \mathbf{v}_{s\alpha\beta} = \mathbf{R}_{\alpha\beta} \mathbf{i}_{g\alpha\beta} + \mathbf{L}_{\alpha\beta} \frac{d\mathbf{i}_{g\alpha\beta}}{dt} \quad (3.44)$$

where  $\mathbf{v}_{zeq\alpha\beta}$  is the voltage drop vector across the overall equivalent impedance,  $\mathbf{v}_{g\alpha\beta}$  and  $\mathbf{v}_{s\alpha\beta}$  are the PCC voltage and the grid voltage vectors (see Fig. 3.32), and  $\mathbf{i}_{g\alpha\beta}$  is the grid current vector.  $\mathbf{L}_{\alpha\beta}$  and  $\mathbf{R}_{\alpha\beta}$  are, respectively, the sum of the inductance and resistance matrices for the different grid impedances as expressed in (3.43).

In the proposed estimation method, it is assumed that the  $\mathbf{L}_{\alpha\beta}$  is constant at the different harmonic frequencies, being the grid impedance the only variable affected by frequency according to (3.41) [294]. This has been experimentally validated by injecting harmonic components in the grid and measuring the corresponding harmonic impedance by calculating the Fast Fourier Transform (FFT) of the voltages and grid currents at the different frequencies. The results are shown in Fig. 3.39. As it is clearly shown, the inductance term remains almost constant around  $L = 0.5\text{mH}$ , whereas the impedance is clearly increasing with frequency due to the inductive behavior of the grid at that frequencies. At this research, none of the following effects are considered regarding the inductance variation: 1) inductance variation with saturation due to the fundamental command when the converter fundamental current is decoupled from load variations, 2) variations due to parasitic effects such as skin, proximity, and parasitic capacitance effects and, 3) equivalent impedance in distribution grids dominated by active elements (power converters).

From (3.44), the discrete approximation for the grid current  $\alpha\beta$  components using Tustin method with a sampling period  $T_s$  can be expressed according to (3.45), (3.46).

$$\begin{aligned}
i_{g\alpha}[k] = & a_1^\alpha \cdot i_{g\alpha}[k-1] + a_2^\alpha \cdot i_{g\beta}[k] + a_3^\alpha \cdot i_{g\beta}[k-1] \\
& + b_0^\alpha (v_{\alpha}[k] + v_{\alpha}[k-1]) \quad (3.45)
\end{aligned}$$

$$\begin{aligned}
i_{g\beta}[k] = & a_1^\beta \cdot i_{g\beta}[k-1] + a_2^\beta \cdot i_{g\alpha}[k] + a_3^\beta \cdot i_{g\alpha}[k-1] \\
& + b_0^\beta (v_{\beta}[k] + v_{\beta}[k-1]) \quad (3.46)
\end{aligned}$$

where  $a_1^\alpha$ ,  $a_2^\alpha$ ,  $a_3^\alpha$ ,  $b_0^\alpha$ ,  $a_1^\beta$ ,  $a_2^\beta$ ,  $a_3^\beta$ ,  $b_0^\beta$  are defined in (3.47)-(3.49), while  $v_\alpha, v_\beta$  represent the components of the difference between the PCC and the grid voltages.

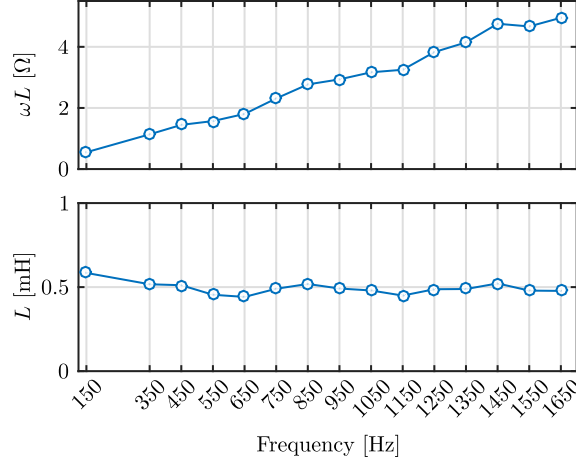


**Figure 3.39:** Experimental results. Measurement of the harmonic impedance of the grid by injecting a distorted converter voltage. Voltages and currents at the PCC are measured and registered and the data is calculated in frequency domain. Sample rate is set to 1Ms/s and spectral resolution is set to 1Hz.

$$a_1^\alpha = \frac{\frac{2}{T_s} L_{\alpha\alpha} - R_{\alpha\alpha}}{\frac{2}{T_s} L_{\alpha\alpha} + R_{\alpha\alpha}} \quad a_2^\alpha = -\frac{\frac{2}{T_s} L_{\alpha\beta} + R_{\alpha\beta}}{\frac{2}{T_s} L_{\alpha\alpha} + R_{\alpha\alpha}} \quad a_3^\alpha = \frac{\frac{2}{T_s} L_{\alpha\beta} + R_{\alpha\beta}}{\frac{2}{T_s} L_{\alpha\alpha} + R_{\alpha\alpha}} \quad (3.47)$$

$$a_1^\beta = \frac{\frac{2}{T_s} L_{\beta\beta} - R_{\beta\beta}}{\frac{2}{T_s} L_{\beta\beta} + R_{\beta\beta}} \quad a_2^\beta = -\frac{\frac{2}{T_s} L_{\alpha\beta} + R_{\alpha\beta}}{\frac{2}{T_s} L_{\beta\beta} + R_{\beta\beta}} \quad a_3^\beta = \frac{\frac{2}{T_s} L_{\alpha\beta} - R_{\alpha\beta}}{\frac{2}{T_s} L_{\beta\beta} + R_{\beta\beta}} \quad (3.48)$$

$$b_0^\alpha = \frac{1}{\frac{2}{T_s} L_{\alpha\alpha} + R_{\alpha\alpha}} \quad b_0^\beta = \frac{1}{\frac{2}{T_s} L_{\beta\beta} + R_{\beta\beta}} \quad (3.49)$$

From (3.45), (3.46) the values for the resistance and inductance terms can be obtained as (3.51).

$$R_{xx} = \frac{1 - a_1^x}{2b_0^x} \quad L_{xx} = \frac{T_s}{4} \frac{1 + a_1^x}{b_0^x} \quad (3.50)$$

$$R_{xy} = -\frac{a_2^x + a_3^x}{2b_0^x} \quad L_{xy} = \frac{T_s}{4} \frac{a_3^x - a_2^x}{b_0^x} \quad (3.51)$$

where  $x, y$  could be either  $\alpha$  or  $\beta$ .

The RLS algorithm will allow to estimate the resistances and inductances in (3.51) by determining the values of the coefficients  $a_i^x$  and  $b_j^x$ . The error driving the RLS update is obtained as the difference between the observed grid current,  $i_{g_x}[k]$ , as calculated by the observer, and the one estimated by the RLS algorithm,  $\widehat{i_{g_x}}[k]$ . Decoupling

of the unknown grid voltage,  $\mathbf{v}_{s\alpha\beta}$ , is achieved by only considering the current induced by the pulse injection. This is done by subtracting the fundamental current reference from the overall current. It is then assumed that the grid voltage is stiff enough to neglect any effect on it due to the injected pulses and thus it could be removed from the equation.

The least squares problem is formulated in recursive form using the equations (3.52)-(3.55), following the steps indicated in Fig. 3.40. The system equations are represented by defining the variables and coefficients vectors,  $\mathbf{X}^x[k]$ ,  $\mathbf{W}^x[k]$ , as (3.56) and (3.57) respectively, where superscript  $x$  could be either  $\alpha$  or  $\beta$ . The estimated RLS current,  $\hat{i}_g^x[k]$ , is determined by the product  $\mathbf{W}^x[k-1] \cdot \mathbf{X}^x[k]$  in (3.52). All the variables names are referred to those shown in Fig. 3.8.

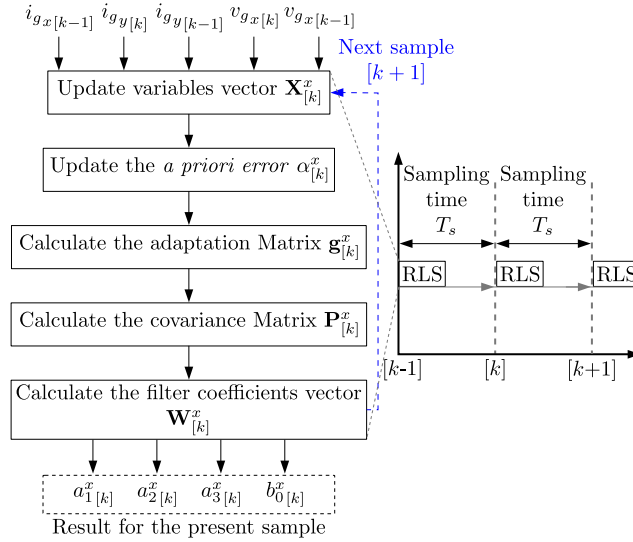


**Figure 3.40:** Steps of the recursive least square algorithm.

$$\alpha[k]^x = i_{g_x}[k] - \mathbf{W}^x[k-1] \cdot \mathbf{X}^x[k] \quad (3.52)$$

$$\mathbf{g}^x[k] = \mathbf{P}^x[k-1] \cdot \mathbf{X}^x[k] \cdot \left[ \lambda + \mathbf{X}^x[k]^T \cdot \mathbf{P}^x[k-1] \cdot \mathbf{X}^x[k] \right]^{-1} \quad (3.53)$$

$$\mathbf{P}^x[k] = \lambda^{-1} \cdot \mathbf{P}^x[k-1] - \mathbf{g}^x[k] \cdot \mathbf{X}^x[k]^T \lambda^{-1} \cdot \mathbf{P}^x[k-1] \quad (3.54)$$

$$\mathbf{W}^x[k] = \mathbf{W}^x[k-1] + (\alpha^x[k] \cdot \mathbf{g}^x[k])^T \quad (3.55)$$

$$\mathbf{X}^x[k] = \left[ i_{g_x}[k-1], i_{g_y}[k], i_{g_y}[k-1], v_{g_x}[k], v_{g_x}[k-1] \right]^T \quad (3.56)$$

$$\mathbf{W}^x[k] = [a_1^x[k], a_2^x[k], a_3^x[k], b_0^x[k], b_0^x[k]] \quad (3.57)$$

where  $\mathbf{P}_{(5 \times 5)}$  is the covariance matrix and it is initialized to  $\mathbf{P} = 0.01 \cdot \mathbf{I}_{(5 \times 5)}$ ;  $\mathbf{g}_{(5 \times 1)}$  is the adaptation gain, and  $\lambda = [0, 1]$  is the forgetting factor, which need to be selected as a tradeoff of the expected estimation bandwidth and the signal to noise ratio. Values between 0.95 and 1 are often selected. In this case, the values shown in Appendix A.4 have been used. After the injection of a new pulse, the estimation of the  $\mathbf{W}$  components for both the  $\alpha$  and the  $\beta$  components is updated and a new estimation for  $\mathbf{R}_{\alpha\beta}$  and  $\mathbf{L}_{\alpha\beta}$  is obtained using (3.51).

Regarding the computational burden of the proposed approach, the number of needed floating operations have been determined by using a Matlab based tool. A total of 632 floating operations (multiplications and additions) are needed. Considering the number of cycles for each floating point operation based on a TMS320F28335 controller with a 150Mhz clock, it leads to a computational time lower than  $20\mu s$ . Thus, it is considered that the implementation is feasible and fast enough on medium performance digital signal controllers.

### 3.7.3 Simulation results

In order to illustrate the performance of the method under different balanced and unbalanced conditions, the simulation shown in Fig. 3.41 has been carried out. Different RL impedances have been connected in series between the output of the converter and the grid. Additionally, a balanced resistive load has been connected in parallel to the converter output. Every 0.1s, a transient is generated, changing the equivalent grid impedance as stated in Table 3.1.

Table 3.1: Sequence of phase resistance and inductance values.

	0s	0.1s	0.2s	0.3s	0.4s	0.5s	0.6s	0.7s
$R_a$ [ $\Omega$ ]	10.55	10.7	10.5	10.7	10.55	10.7	10.55	10.55
$R_b$ [ $\Omega$ ]	10.5	10.6	10.4	10.6	10.5	10.5	10.5	10.5
$R_c$ [ $\Omega$ ]	10.4	10.55	10.35	10.55	10.4	10.4	10.4	7.85
$L_a$ [mH]	2.5	3.0	0.5	3.0	2.5	3.5	2.5	2.5
$L_b$ [mH]	2.5	3.0	0.5	3.0	2.5	2.5	2.5	2.5
$L_c$ [mH]	2.5	3.0	0.5	3.0	2.5	3.5	2.5	2.5

At  $t = 0.5s$ , an unbalance on the series impedance in phase- $a$  is induced. At  $t = 0.7s$ , phase- $a$  resistive load is reduced by 25%. Fast convergence and detection of asymmetries in the  $\alpha$  and  $\beta$  components are shown. Phase voltages at the PCC and estimated grid-side currents during the load transient are shown in Fig. 3.42. As clearly shown, the injection of the  $q$ -axis pulses is reflected at the PCC phase voltages and, consequently, at the estimated grid-side currents.

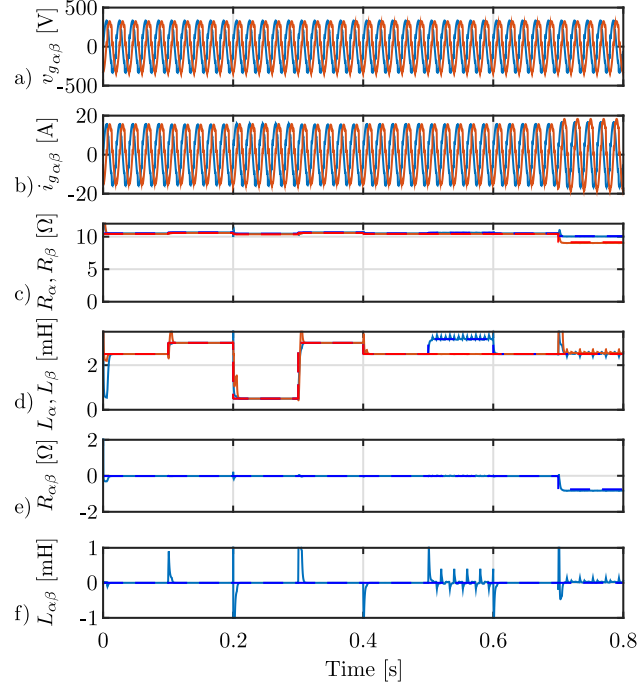


**Figure 3.41:** Simulation results. Transient response. From top to bottom: a)  $v_{g_\alpha}$  (blue),  $v_{g_\beta}$  (red). b)  $i_{g_\alpha}$  (blue),  $i_{g_\beta}$  (red). c), d)  $R_{\alpha\alpha}, R_{\beta\beta}$ . and  $L_{\alpha\alpha}, L_{\beta\beta}$  components for the matrices at the  $\alpha\beta$  reference frame. e) and f), the corresponding out-diagonal  $R_{\alpha\beta}$  and  $L_{\alpha\beta}$ . Every 0.1s a new condition is evaluated by varying the equivalent phase resistances and inductances using the sequence in Table 3.1.

### 3.7.4 Experimental results

The experimental results have been obtained under the setup described in Appendix A.4. In order to check the accuracy of the method under a controlled environment, initial results have been obtained by disconnecting the grid and interfacing the converter to a balanced resistive load while varying the series impedance.

Results for the estimated parameters during several transient conditions are shown in Fig. 3.43. As it can be seen, the estimated parameters are in close agreement with the actual impedance values. The unbalance condition is introduced between  $t = 5s$  and  $t = 15s$  by varying the series impedance at phase  $a$ , which is reflected into different values for the diagonal terms in the  $\mathbf{Z}_{\alpha\beta}$  matrix, as predicted by the theoretical analysis. The value for the connected parallel resistive load is also accurately determined, being the small variations on the resistance terms due to the changes of the associated inductance series resistances. The injected pulses in the  $\alpha\beta$  reference frame as well as the real and estimated currents are shown in Fig. 3.44. A good match

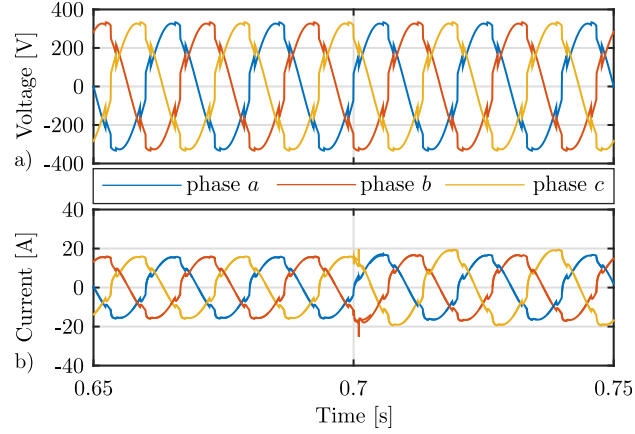


**Figure 3.42:** Simulation results. Transient response. a) phase voltages at the PCC ( $v_g$ ), b) grid current ( $i_g$ ). The waveforms correspond to the same conditions explained in Fig. 3.41. At  $t = 0.7s$  the load transient causes an unbalanced condition.

between both signals can be observed.

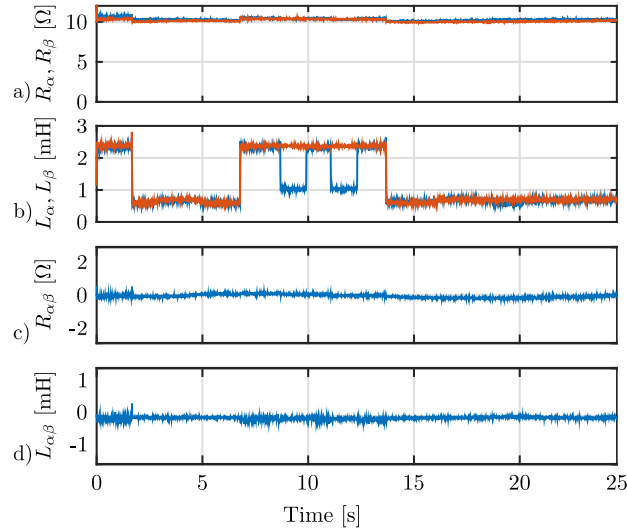


**Figure 3.43:** Experimental results. Transient response of the RLS algorithm. From bottom to top: a), b) the diagonal terms for the  $R_{\alpha\alpha}, R_{\beta\beta}$  and  $L_{\alpha\alpha}, L_{\beta\beta}$  matrices at the  $\alpha\beta$  reference frame are shown. c), d) the corresponding out-diagonal  $R_{\alpha\beta}$  and  $L_{\alpha\beta}$ . A change is introduced into the series impedance connected to phase  $a$  from 2.5mH to 0.5mH ([0.4167, 0.0833]p.u) The small variations on the resistance terms correspond to the resistive changes due to the connection/disconnection of the inductances.

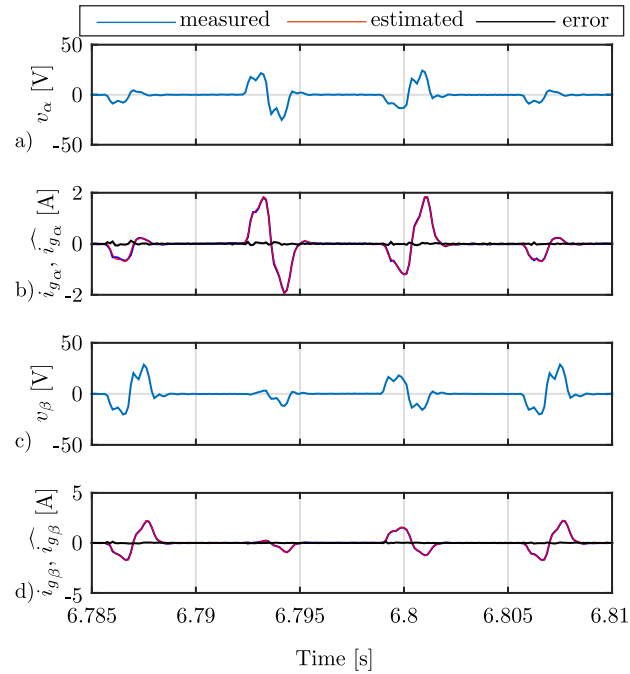


**Figure 3.44:** Experimental results. Transient response of the RLS algorithm. a) and c) show a zoom on the injected pulses, whereas b) and d) show the corresponding grid-side current response. In b) and c) the measured and estimated current components are depicted in blue and red. Estimation error is depicted in black.

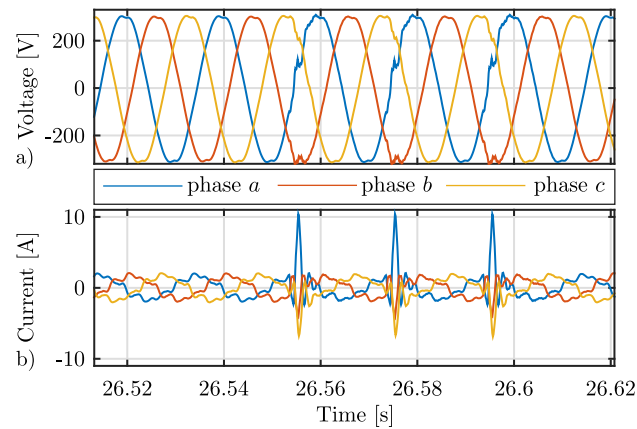


**Figure 3.45:** Experimental results. Injection of the pulses when the power converter is connected to the grid. a) Grid voltages and b) grid currents. The converter was operated with a fundamental current command  $i_q = 2.5\text{A}$ .

Finally, experimental results with a grid-tied converter have been obtained. The method is tested with two different levels of reactive current,  $i_q = [0, 2.5]\text{A}$ . The commanded value of the fundamental current has been kept at low level compared to the converter rated current (30A) in order to analyze the performance of the current control when the pulses are injected. The grid voltages in Fig. 3.45 show a noticeable harmonic content, which will allow to demonstrate the operation of the method under distorted grid conditions. In Fig. 3.45, the grid voltages at the instant the three pulses are injected following a change in the impedance are shown. The effect of the pulse injection over the grid voltage is clearly visible, as well as the effect in the grid-side current.

Before the RLS estimation, the grid voltage and the fundamental current are online decoupled. For the case of the voltage, the average value of the  $v_d$  and  $v_q$  components is subtracted. Being the pulse magnitude centered at zero, it does not affect the average value and thus the contribution of the grid can be easily removed. The resulting signal is rotated back to the stationary reference frame to be used in the estimation procedure. For the current signal, the current reference is subtracted from the overall current. Fig. 3.46 shows the estimation of the grid impedance during two different transients. The impedance values are filtered with a 5Hz low pass filter to remove the high frequency noise affecting the  $a_i$  and  $b_j$  values. As shown, the convergence of the method is considerably fast, arriving to the final value just after the injection of the last pulse.

To sum up, this section has presented a versatile online grid impedance method supported with results. Three pulse injection methods have been considered, resulting the  $q$ -axis the most appealing in this application, triggered by an observer compensator signal that allows to reduce the THD. The method is able to estimate the resistive and inductive components of balanced and unbalanced 3-phase grid-impedance in real time, using an RLS-based algorithm applied to an  $\alpha\beta$  model of the system.

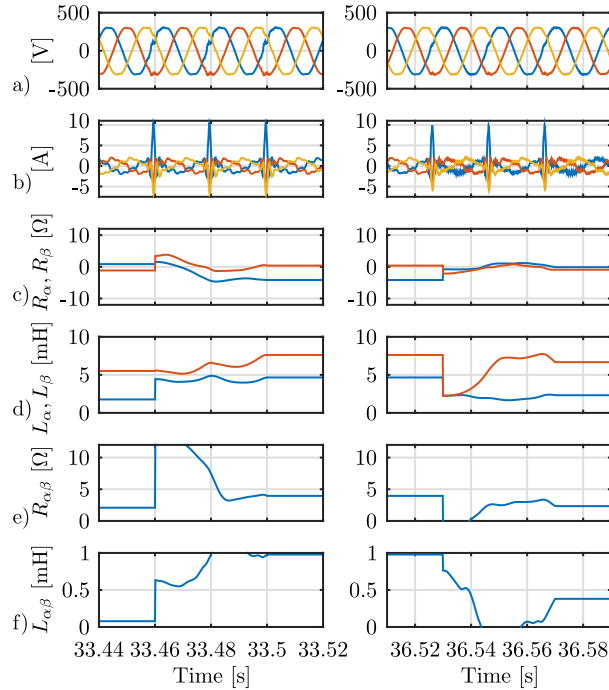


**Figure 3.46:** Experimental results. RLS results with the converter interfaced to the grid. From top to bottom: a) grid voltages. b) grid currents. c)  $R_\alpha$ ,  $R_\beta$ . d)  $L_\alpha$ ,  $L_\beta$ . e)  $R_{\alpha\beta}$ . f)  $L_{\alpha\beta}$ . The converter is current controlled with a reference  $i_q^* = 2.5\text{A}$ .

### 3.8 Voltage control in 3-phase AC and DC grid-forming converters

As an initial premise, the voltage regulation in both the LVDC bus and the AC nanogrids will be achieved by means of master-slave strategies based on grid-forming units. Although such a configuration appears as an effective and simple solution, the apparent simplicity of grid-forming voltage control in AC or DC might be shadowed by the difficulty to properly select the system and control parameters to achieve a good dynamic and stable behavior, specially under high penetration of constant power loads. Under this concern, an analysis of grid-forming voltage control strategies seems to be well-suited before applying it to the microgrid control. In both cases, the voltage regulation is considered part of the primary control and will be performed by external voltage control loops that generate either power or current references. In the case of the LVDC bus, the output generated by the voltage regulation loop will be sent to the SST as power references for the MGHC and the BESS. In the case of the AC nanogrids, the outer control loops will generate current reference used as inputs in the inner current control scheme seen in the previous section. Some alternative feedback

control topologies have been proposed based on the capacitor energy storage capability as an approach to linearize the relation between the voltage and the power at the DC-link [168–171]. However, those techniques have not been further exploited for grid-forming converter applications, existing few examples in the literature focused on the analysis of the dynamic performance [168].

This section analyzes the dynamic behavior of the voltage control loop used in grid-forming VSIs integrated in AC and DC MGs, maintaining a general focus agnostic to the application. Both the conventional voltage feedback control, referred as direct voltage control (DVC) hereinafter, and the control based on squared voltage, referred as quadratic voltage control (QVC), will be addressed, considering CPLs as the main disturbance. Taking advantage of the cascaded control premises, the inner control loop dynamics will be neglected. Thus, the analysis becomes valid for different applications such as AC slack, DC slack or DC-link control. An analytical study on the conventional voltage control schemes is performed based on system linearization and validated through simulations and experimentally. In addition, the use of virtual capacitance (VC) is introduced as a tool for disturbance rejection enhancement as well as to experimentally forecast the effect of resizing the capacitance in existing systems. This part of the study will deal with operation limits, the system stability and the disturbance rejection of the voltage control, leading not only to the proper selection of the control scheme and control parameters, but also to the sizing of the passive elements of the converter.

### 3.8.1 Problem definition and system modelling

In most of the MG applications requiring a voltage regulation, the system plant to be controlled consists of a capacitor whose voltage derivative is proportional to its current as seen in Sections 3.2.3 and 3.2.4. The following discussion assumes the system is modelled in the synchronous reference frame.

The control in this kind of applications is usually performed by a closed-loop cascaded controller consisting of an inner current/power control loop and an outer voltage control loop. Assuming the inner current/power control loop is fast enough, its dynamics can be neglected. Thus, as shown in Fig. 3.47, the voltage control can be assumed as a voltage regulator, which input is the error,  $e$ , between the voltage reference,  $v^*$ , and the measured voltage,  $\tilde{v}$ , while the control action is the current,  $i$ , entering the

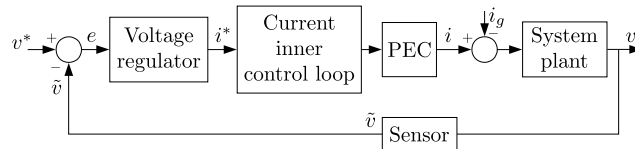


**Figure 3.47:** Simplified diagram of the control and system plant for the generic grid-forming unit.

system plant. Considering the existence of load disturbances, the system plant can be defined by (3.58), where  $C$  is the system plant total capacitance,  $v(t)$  is the capacitor voltage,  $i(t)$  is the control action of the voltage control loop, and  $i_g(t)$  is the load disturbance.

$$\frac{dv(t)}{dt} = \frac{1}{C} (i(t) - i_g(t)) \quad (3.58)$$

Nevertheless, constant current loads (CCLs) are not the only kind of loads found in power systems. More and more electrical appliances and industrial equipment behaves as CPLs, characterized by a tight control of load power, or as conventional constant impedance loads (CILs), presenting both of them a non-linear relation between power, voltage and current. Thus, the system in (3.58) must be reformulated as the non-linear system in (3.59), where  $i_L$ ,  $P_L$  and  $g_L$  are the current, power and conductance disturbances associated to CCLs, CPLs, and CILs respectively.

$$\frac{dv(t)}{dt} = \frac{1}{C} \left( i(t) - \underbrace{\left( i_L(t) + \frac{P_L(t)}{v(t)} + g_L(t)v(t) \right)}_{i_g(t)} \right) \quad (3.59)$$

Some assumptions are established regarding this expression: 1) Only pure resistive CIL are considered modelled as conductances,  $g(t)$  in (3.59); 2) Generation is considered by negative signs in  $P_L$  and  $i_L$ ; 3) The line impedance is neglected as the system load seen by the grid-forming is considered as an aggregated current source  $i_g$ .

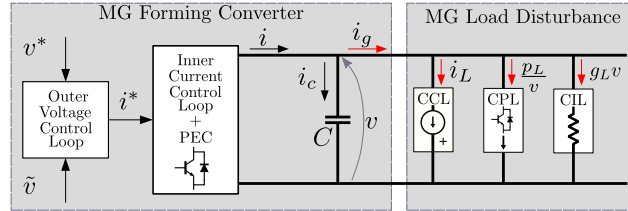


**Figure 3.48:** Simplified single line representation of the grid-forming converter and load disturbance in a DC or AC MG.

Fig. 3.48 shows the single phase representation of the defined non-linear system. The behavior of the different loads existing in a MG are illustrated in Fig. 3.49, where  $I_n$  and  $V_n$  indicate the load nominal current and voltage and  $I_{max}$  and  $V_{max}$  are the load maximum point of operation. The non-linearities due to CPL and CIL will affect the voltage regulation design and performance. Moreover, unlike CILs, it is well known that CPLs are prone to compromise the system stability. In the literature, several attempts have been carried out for obtaining a linear approximation by defining a negative impedance [51, 52, 55, 56]. In this section, the effect of the different types of load are approached by the linearization of the close loop system.

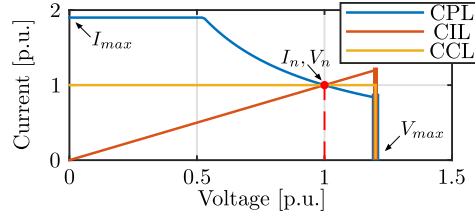


**Figure 3.49:** Voltage-Current curves of the different types of loads in MGs.

### 3.8.2 Voltage control design alternatives: DVC vs QVC

The voltage controller models will be analyzed using linearized models. Two control schemes, shown in Fig. 3.50, are considered for the implementation of the outer voltage control loop in a grid-forming unit, the direct voltage control (DVC) and the quadratic voltage control (QVC).

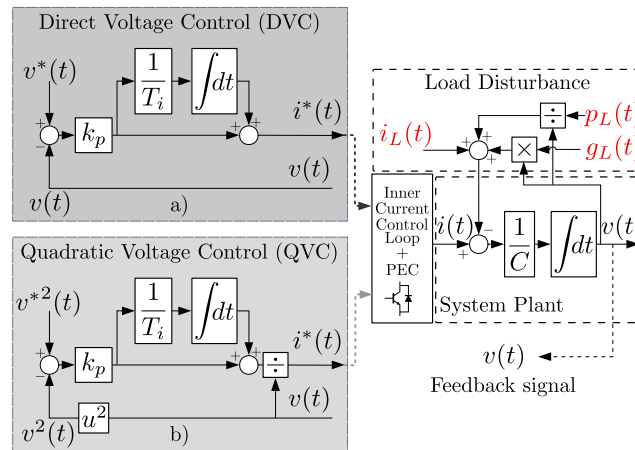


**Figure 3.50:** Voltage control schemes for the different types of loads in MGs. a) DVC; b) QVC.

#### 3.8.2.1 The direct voltage controller (DVC)

The DVC control scheme is shown in Fig. 3.50a). A PI regulator in the standard form has been selected for the analysis, defined by (3.60), where  $i^*$  is the control action,  $v^*$  the voltage reference,  $v$  the actual voltage, and  $k_p$  and  $T_i$  are the PI proportional gain and integral time constant respectively. The effect of the sensors is neglected, considering  $\tilde{v} = v$ . This controller is based on the linear relationship between the voltage and the current at the system plant capacitor.

$$i^*(t) = k_p(v^*(t) - v(t)) + k_p \frac{1}{T_i} \int (v^*(t) - v(t)) dt \quad (3.60)$$

Assuming an ideal inner current control loop ( $i^*(t) = i(t)$ ), the voltage closed-loop system when using DVC is defined by (3.61), and its extended differential equation is expressed as (3.62). Those expressions will be used as the starting point for the dynamic analysis of the DVC-based voltage control.

$$\begin{aligned} \frac{dv(t)}{dt} C &= k_p(v^*(t) - v(t)) + k_p \frac{1}{T_i} \int ((v^*(t) - v(t)) dt) \\ &\quad - i_L(t) - \frac{P_L(t)}{v(t)} - g_L(t)v(t) \end{aligned} \quad (3.61)$$

$$\begin{aligned} \frac{d^2v(t)}{dt^2} C v^2(t) + \frac{dv(t)}{dt} [v^2(t)k_p - P_L(t) + v^2(t)g_L(t)] + \frac{di_L(t)}{dt} v^2(t) + \\ \frac{dP_L(t)}{dt} v(t) + \frac{dg_L(t)}{dt} v^3(t) + v^2(t) \left[ k_p \frac{1}{T_i} v(t) - k_p \frac{1}{T_i} v^*(t) \right] = 0 \end{aligned} \quad (3.62)$$

Despite its apparent simplicity, achieving good dynamic behavior is not straightforward, as already reported in the literature [168]. This is due to the non-linear behavior of the voltage reaction to both CPLs and CILs disturbances as evidenced in (3.62). Nonetheless, if the disturbances are left apart, its reference tracking response is linear, defined by the Laplace domain transfer function (3.63).

$$\frac{V(s)}{V^*(s)} = \frac{k_p s + k_p \frac{1}{T_i}}{s^2 C + s k_p + \frac{1}{T_i} k_p} \quad (3.63)$$

### 3.8.2.2 The quadratic voltage controller (QVC)

An alternative to the DVC has been proposed in the literature referred as fast-acting DC-link voltage controller and energy based controller, in the context of applications for the DC-link control of DC/DC/AC and AC/DC/AC converters [168–171]. As a contribution of this thesis, its generalization to any cascaded-based voltage control, such as grid-forming converters in both DC and AC MGs applications is proposed. The control scheme is shown in Fig. 3.50b) and the regulator differential equation is given by (3.64). The closed-loop system using QVC is defined by (3.65) and its extended differential equation (3.66). As in the case of DVC, those expressions will be used as the starting point for the dynamic analysis of the QVC-based voltage control.

$$i^*(t) = \frac{k_p(v^{*2}(t) - v^2(t)) + k_p \frac{1}{T_i} \int (v^{*2}(t) - v^2(t)) dt}{v(t)} \quad (3.64)$$

$$\begin{aligned} \frac{dv(t)}{dt} C &= \frac{k_p(v^{*2}(t) - v^2(t)) + k_p \frac{1}{T_i} \int ((v^{*2}(t) - v(t)) dt)}{v(t)} \\ &\quad - i_L(t) - \frac{P_L(t)}{v(t)} - g_L(t)v(t) \end{aligned} \quad (3.65)$$

$$\begin{aligned} \frac{d^2v(t)}{dt^2} C v(t) + \frac{dv(t)}{dt} \left[ \frac{dv(t)}{dt} C + 2v(t)k_p + i_L(t) + 2v(t)g_L(t) \right] + \\ \frac{di_L(t)}{dt} v(t) + \frac{dP_L(t)}{dt} + \frac{dg_L(t)}{dt} v^2(t) + k_p \frac{1}{T_i} v^2(t) - k_p \frac{1}{T_i} v^{*2}(t) = 0 \end{aligned} \quad (3.66)$$

The control is based on the linear relation between the power flowing into the capacitor,  $p_c(t)$ , and the instantaneous voltage squared,  $v^2(t)$ , as stated in (3.67). In [168, 170], its design is realized by exploiting the relation between voltage variations and the energy stored in the capacitor,  $W_c$ . However, the tuning method used in those papers is oriented to the regulation of the DC-link of an active front end (AFE) exposed to the steady state disturbances produced by AC grid unbalances. In this thesis the dynamic behavior of QVC will be study instead.

$$v(t) \frac{dv(t)}{dt} = \frac{1}{C} p_c(t) \Rightarrow \frac{dv^2(t)}{dt} = \frac{2}{C} p_c(t) \quad (3.67)$$

One of the main advantages of QVC, concerning the disturbance rejection and stability analysis, is that the relation between  $v^2(t)$  and  $P_L(t)$  becomes linear, unlike in the case of DVC. This fact facilitates the delimitation of the stable region. However, the controlled variable is still  $v(t)$  and, considering other kind of disturbances that may be present in the grid, as CIL, the system performance should be evaluated according to the  $v(t)$  dynamics. For that reason, the system linearization becomes necessary in order to perform a proper dynamic analysis.

Leaving the disturbances aside, unlike in the DVC, in the QVC the relation between  $v$  and  $v^*$  is non-linear, (3.64). The system defined in (3.66) has been linearized using Taylor series. The linear approximation of the reference tracking transfer function is obtained as in (3.68), where  $V_0^*$  and  $V_0$  are the voltage reference and the actual voltage at the equilibrium point, respectively. Assuming  $V_0 \approx V_0^*$ , the transfer function is approximated by (3.69).

$$\frac{V(s)}{V^*(s)} \approx \frac{s2k_p V_0^* + 2k_p \frac{1}{T_i} V_0^*}{s^2 C V_0 + s2k_p V_0 + 2k_p \frac{1}{T_i} V_0} \quad (3.68)$$

$$\frac{V(s)}{V^*(s)} \approx \frac{s2k_p + 2k_p \frac{1}{T_i}}{s^2 C + s2k_p + 2k_p \frac{1}{T_i}} \quad (3.69)$$

### 3.8.2.3 Establishing an analytical tuning methodology

Before starting with the dynamic analysis of the presented controllers, an analytical tuning methodology will be proposed in order to establish a parametric design of the regulator gains. This will allow a proper comparison between the DVC and QVC, as well as a generalized dynamic analysis independent of the numeric value of regulator gains. Among the controllers tuning techniques available for linear systems, an analytical approach has been selected, aimed at simplifying the selection of PI regulator parameters [116]. The close loop system can be simplified as a second order system with natural frequency  $\omega_n$  and damping factor  $\zeta$ . Equations (3.63) and (3.69), can be expressed as (3.70), and assuming linearity, the system poles,  $\omega_n$  and  $\zeta$ , will be the same for disturbance rejection transfer functions. Thus, the PI regulator gains for DVC and QVC are tuned according to (3.71) and (3.72) respectively, leading to a similar response in both DVC and QVC. Fig. 3.51 shows an example of the reference tracking response, comparing the two methods when using  $\omega_n = 2\pi 50$  and  $\zeta = 0.7$  in both of them.

$$\frac{V(s)}{V^*(s)} = \frac{2\zeta\omega_n s + \omega_n^2}{s^2 + 2\zeta\omega_n s + \omega_n^2} \quad (3.70)$$

$$\text{DVC} \longrightarrow \quad k_p = 2\zeta\omega_n C \quad T_i = \frac{2\zeta}{\omega_n} \quad (3.71)$$

$$\text{QVC} \longrightarrow \quad k_p = \zeta\omega_n C \quad T_i = \frac{2\zeta}{\omega_n} \quad (3.72)$$

According to cascaded control theory, the bandwidth of the inner loop is assumed to be at least one decade higher than the outer loop. Thus,  $\omega_n$  can be selected so that complies with this requirement, while the damping factor,  $\zeta$ , can be selected as a trade-off between the overshoot and the settling time.

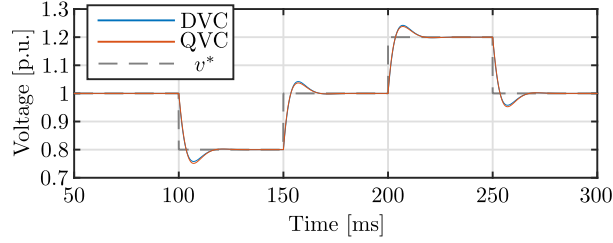


**Figure 3.51:** Non-linear simulated reference tracking response. Comparison between DVC and QVC when using  $\omega_n = 2\pi 50$  and  $\zeta = 0.7$  in both methods.

### 3.8.3 Closed-loop disturbance rejection: analytical models and analysis

Apart from being able to perform reference tracking, the main requirement of a grid-forming converter is to provide a stiff voltage control under disturbances. As seen previously, the QVC presents a natural non-linear response for any case, while the DVC is linear if only CCLs are taken into account. However, it is worth noting that the disturbance rejection of the system when using DVC becomes non-linear once CPLs or CILs are considered.

In order to analyze the system behavior under load disturbances, the disturbance rejection transfer functions (load disturbance to output voltage transfer functions) under different type of loads has been obtained by Taylor series linearization (TSL). The linearized transfer functions  $\frac{\Delta V(s)}{\Delta P_L(s)}$ ,  $\frac{\Delta V(s)}{\Delta I_L(s)}$  and  $\frac{\Delta V(s)}{\Delta G_L(s)}$  in the Laplace domain are shown respectively in eqs. (3.73) to (3.75) for the DVC, and in eqs. (3.76) to (3.78) for the QVC. It is necessary to point out that an operation close to the equilibrium point is assumed, considering equal the voltage reference and the voltage at the equilibrium point ( $V_0 = V_0^*$ ).

$$\left. \begin{aligned} \frac{\Delta V(s)}{\Delta P_L(s)} &\approx -\frac{sV_0}{s^2V_0^2C + s(k_pV_0^2 - P_{L0} + G_{L0}V_0^2) + \frac{1}{T_i}k_pV_0^2} & (3.73) \\ \frac{\Delta V(s)}{\Delta I_L(s)} &\approx -\frac{sV_0^2}{s^2V_0^2C + s(k_pV_0^2 - P_{L0} + G_{L0}V_0^2) + \frac{1}{T_i}k_pV_0^2} & (3.74) \\ \frac{\Delta V(s)}{\Delta G_L(s)} &\approx -\frac{sV_0^3}{s^2V_0^2C + s(k_pV_0^2 - P_{L0} + G_{L0}V_0^2) + \frac{1}{T_i}k_pV_0^2} & (3.75) \end{aligned} \right\} \text{DVC}$$

$$\left. \begin{aligned} \frac{\Delta V(s)}{\Delta P_L(s)} &\approx -\frac{s}{s^2 V_0 C + s(2k_p V_0 + I_{L0} + 2G_{L0} V_0) + 2\frac{1}{T_i} k_p V_0} & (3.76) \\ \frac{\Delta V(s)}{\Delta I_L(s)} &\approx -\frac{s V_0}{s^2 V_0 C + s(2k_p V_0 + I_{L0} + 2G_{L0} V_0) + 2\frac{1}{T_i} k_p V_0} & (3.77) \\ \frac{\Delta V(s)}{\Delta G_L(s)} &\approx -\frac{s V_0^2}{s^2 V_0 C + s(2k_p V_0 + I_{L0} + 2G_{L0} V_0) + 2\frac{1}{T_i} k_p V_0} & (3.78) \end{aligned} \right\} \text{QVC}$$

In these equations, the equilibrium point is defined by (3.79) for the DVC and by (3.80) for the QVC.  $V_0$  is the steady state voltage at the equilibrium point.  $P_{L0}$ ,  $G_{L0}$  and  $I_{L0}$  are the load level at the equilibrium point in terms of power associated to CPLs, conductance given by CILs and current drawn by CCLs at the equilibrium point. This evince a clear dependence of the dynamic response on the load level at the equilibrium point, affecting the steady state consumption and generation to the system dynamic performance, that can lead to an unexpected behavior.

$$\text{DVC} \rightarrow x_0 = [V_0, P_{L0}, G_{L0}] \quad (3.79)$$

$$\text{QVC} \rightarrow x_0 = [V_0, I_{L0}, G_{L0}] \quad (3.80)$$

As electronic constant power loads represent the most critical type of loads at the present time, although the three types of disturbances will be considered, an especial attention will be given to the CPL disturbance rejection transfer functions. Thus, the following analysis will mainly focus on the expressions in (3.73) and (3.76).

### 3.8.3.1 Normalization and verification of the CPL disturbance rejection transfer function

In order to validate the obtained linearized expressions, it is necessary to compare them with their non-linear response. However, before doing so, a normalization process is suggested that will enable a generalized analysis of the disturbance rejection transfer functions.

Using the expressions for the analytical tuning (3.71) and (3.72) in the expressions (3.73) and (3.76), the disturbance rejection transfer functions of DVC and QVC under

CPL disturbance can be expressed as a function of  $\omega_n$  and  $\zeta$  instead of  $k_p$  and  $T_i$ . After some operations and applying this substitution, the transfer functions (3.81) and (3.82) are obtained for DVC and QVC respectively, leading to similar expressions.

$$\frac{\Delta V(s)}{\Delta P_L(s)} \approx -\frac{1}{V_0 C} \frac{s}{s^2 + s(2\omega_n \zeta - \frac{P_{L0}}{V_0^2 C} + \frac{G_{L0}}{C}) + \omega_n^2} \quad (3.81)$$

$$\frac{\Delta V(s)}{\Delta P_L(s)} \approx -\frac{1}{V_0 C} \frac{s}{s^2 + s(2\omega_n \zeta + \frac{I_{L0}}{V_0 C} + \frac{2G_{L0}}{C}) + \omega_n^2} \quad (3.82)$$

By defining factors for representing the terms related to the load level at the equilibrium point, a general expression valid for both DVC and QVC is achieved, formulated as (3.83).

$$\frac{\Delta V(s)}{\Delta P_L(s)} \approx -K \frac{s}{s^2 + s(2\omega_n \zeta + \alpha_0 + \beta_0) + \omega_n^2} \quad (3.83)$$

Where the close loop gain can be defined as  $K = \frac{1}{V_0 C}$ , while  $\alpha_0$  and  $\beta_0$  are normalized factors that represents the effect of the load level, being defined by the expressions in Table 3.2 for the two different controllers. From (3.83), it is expected an identical response in absolute value for systems with different  $V_n$  or  $C$  as far as the product  $V_0 C$  remains constant.

Table 3.2: Definition of  $\alpha_0$  and  $\beta_0$

	$\alpha_0$	$\beta_0$
DVC	$\frac{-P_{L0}}{V_0^2 C}$	$\frac{G_{L0}}{C}$
QVC	$\frac{I_{L0}}{V_0 C}$	$\frac{2G_{L0}}{C}$

Furthermore, (3.83) can be normalized to per-unit (p.u.) by substituting the variable  $K$  by defining  $K_{pu}$  as (3.84), where  $V_n$  and  $P_n$  are the converter nominal voltage and power respectively, leading to the full normalized expression in (3.85), where  $\Delta V_{pu} = \frac{\Delta V}{V_n}$  and  $\Delta P_{Lpu} = \frac{\Delta P_L}{P_n}$ .

$$K_{pu} = \frac{P_n}{V_n} \frac{1}{V_0 C} \rightarrow V_n = V_0 \rightarrow K_{pu} = \frac{P_n}{V_0^2 C} \quad (3.84)$$

$$\frac{\Delta V_{pu}(s)}{\Delta P_{Lpu}(s)} \approx -K_{pu} \frac{s}{s^2 + s(2\omega_n\zeta + \alpha_0 + \beta_0) + \omega_n^2} \quad (3.85)$$

From (3.85), it is expected an identical response in p.u. for systems with different  $V_n$  or  $C$  as far as the term  $V_0^2 C$  remains constant.

In order to verify the linearized model, the response of  $\frac{\Delta V(s)}{\Delta P_L(s)}$  and  $\frac{\Delta V_{pu}(s)}{\Delta P_{Lpu}(s)}$  are compared in Figs. 3.52 and 3.53 with the simulation of the non-linear system obtained in Matlab/Simulink<sup>®</sup>, for DVC and QVC respectively. The results have been obtained for 2 scenarios, that serve as an example, with different  $V_n$  and  $C$ , maintaining the term  $V_0^2 C$  constant. The relevant parameters are listed in Table A.3 of Appendix A.5.

The error between the linear approximation and the simulation response is reduced near the equilibrium point, confirming the validity of the linear models as an analytical approach for system dynamic analysis. However, in the case of DVC, when the load level  $P_{L0}$  is not considered, the linear model considerably deviates from the actual response as the system deviates from the equilibrium point. In the figures, it is also clear how the p.u. response remains the same for the two scenarios, validating the equations (3.83) and (3.85).

### 3.8.3.2 Normalization of the CCL and CIL disturbance rejection transfer function

Following the procedure used with the  $\frac{\Delta V(s)}{\Delta P_L(s)}$  transfer function, the CCL and CIL disturbance rejection transfer function  $\frac{\Delta V(s)}{\Delta I_L(s)}$  and  $\frac{\Delta V(s)}{\Delta G_L(s)}$  can be also normalized. Although the main focus is to analyzed the system under constant power disturbances, here the disturbance transfer functions for CCL and CIL will be normalized for future uses.

Again, the disturbance rejection transfer functions (3.74) (3.75), (3.77) and (3.78) can be formulated as a function of  $\omega_n$  and  $\zeta$  instead of  $k_p$  and  $T_i$  by using (3.71) and (3.72). The resulting expressions are (3.86) and (3.87) for DVC, and (3.88) and (3.89) for QVC.

$$\text{DVC} \left\{ \begin{array}{l} \frac{\Delta V(s)}{\Delta I_L(s)} \approx -\frac{1}{C} \frac{s}{s^2 + s(2\omega_n\zeta - \frac{P_{L0}}{V_0^2 C} + \frac{G_{L0}}{C}) + \omega_n^2} \quad (3.86) \\ \frac{\Delta V(s)}{\Delta G_L(s)} \approx -\frac{V_0}{C} \frac{s}{s^2 + s(2\omega_n\zeta - \frac{P_{L0}}{V_0^2 C} + \frac{G_{L0}}{C}) + \omega_n^2} \quad (3.87) \end{array} \right.$$

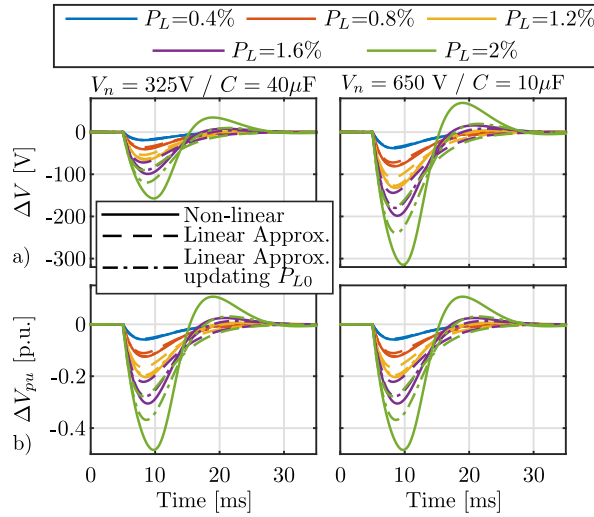


**Figure 3.52:** DVC: Non-linear simulated response compared with the linear approximation of  $\frac{\Delta V(s)}{\Delta P_L(s)}$  under increasing active power steps. a) Absolute value voltage deviation. b) p.u. voltage deviation.

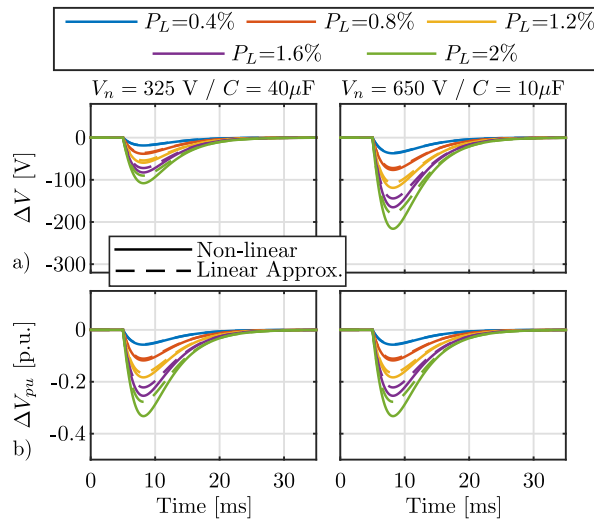


**Figure 3.53:** QVC: Non-linear simulated response compared with the linear approximation of  $\frac{\Delta V(s)}{\Delta P_L(s)}$  under increasing active power steps. a) Absolute value voltage deviation. b) p.u. voltage deviation.

$$\text{QVC} \left\{ \begin{array}{l} \frac{\Delta V(s)}{\Delta I_L(s)} \approx -\frac{1}{C} \frac{s}{s^2 + s(2\omega_n\zeta + \frac{I_{L0}}{V_0 C} + \frac{2G_{L0}}{C}) + \omega_n^2} \quad (3.88) \\ \frac{\Delta V(s)}{\Delta G_L(s)} \approx -\frac{V_0}{C} \frac{s}{s^2 + s(2\omega_n\zeta + \frac{I_{L0}}{V_0 C} + \frac{2G_{L0}}{C}) + \omega_n^2} \quad (3.89) \end{array} \right.$$

As done previously, by defining factors for representing the terms related to the load level at the equilibrium point and the close loop gain, the generalized expressions (3.90) and (3.91) for  $\frac{\Delta V(s)}{\Delta I_L(s)}$  and  $\frac{\Delta V(s)}{\Delta G_L(s)}$  are obtained valid for both DVC and QVC. The close loop gains  $K_I$  and  $K_G$  are defined as (3.92) and (3.93) respectively. The factors  $\alpha_0$  and  $\beta_0$  are the same as the ones obtained for the CPLs transfer function defined in Table 3.2.

$$\frac{\Delta V(s)}{\Delta I_L(s)} \approx -K_I \frac{s}{s^2 + s(2\omega_n\zeta + \alpha_0 + \beta_0) + \omega_n^2} \quad (3.90)$$

$$\frac{\Delta V(s)}{\Delta G_L(s)} \approx -K_G \frac{s}{s^2 + s(2\omega_n\zeta + \alpha_0 + \beta_0) + \omega_n^2} \quad (3.91)$$

$$K_I = \frac{1}{C} \quad (3.92)$$

$$K_G = \frac{V_0}{C} \quad (3.93)$$

The obtained expressions can be further normalized to p.u. by defining  $K_{I_{pu}}$  and  $K_{G_{pu}}$  as (3.94) and (3.95), where  $V_n$  is the nominal voltage and  $I_n$  is the converter nominal current.  $G_n$  is the nominal conductance load supported by the grid-forming converter defined as  $G_n = \frac{P_n}{V_n^2}$ . The full normalized expressions are defined in (3.96) and (3.97), where  $\Delta V_{pu} = \frac{\Delta V}{V_n}$ ,  $\Delta P_{Lpu} = \frac{\Delta I_L}{I_n}$  and  $\Delta G_{Lpu} = \frac{\Delta G_L}{P_n}$ .

$$K_{I_{pu}} = \frac{I_n}{V_n} \frac{1}{C} \rightarrow V_n = V_0 \rightarrow K_{I_{pu}} = \frac{I_n}{V_0 C} \quad (3.94)$$

$$K_{G_{pu}} = \frac{G_n}{V_n} \frac{V_0}{C} \rightarrow V_n = V_0 \rightarrow K_{I_{pu}} = \frac{G_n}{C} \quad (3.95)$$

$$\frac{\Delta V_{pu}(s)}{\Delta I_{Lpu}(s)} \approx -K_{I_{pu}} \frac{s}{s^2 + s(2\omega_n\zeta + \alpha_0 + \beta_0) + \omega_n^2} \quad (3.96)$$

$$\frac{\Delta V_{pu}(s)}{\Delta G_{Lpu}(s)} \approx -K_{G_{pu}} \frac{s}{s^2 + s(2\omega_n\zeta + \alpha_0 + \beta_0) + \omega_n^2} \quad (3.97)$$

### 3.8.3.3 Effect of the load levels in the system stability

One of the main properties of the system dynamic response exposed by the linearized models is its dependency on the load at the point of operation, i.e. at the steady state. Thus the system response is not only non-linear but also depends on the load level. To analyze the effect of the load level at the equilibrium point, the system root-contour for  $P_{L0}$  and  $G_{L0}$  when using DVC ((3.98) and (3.99)), and the system root-contour for  $I_{L0}$  and  $G_{L0}$  when using QVC ((3.100) and (3.101)), have been obtained for studying the stability limitations imposed by the load level.

$$\begin{aligned} \text{DVC root contour } P_{L0} &\rightarrow 1 + P_{L0}G(s)H(s) \approx \\ &1 + P_{L0} \frac{s}{s^2V_0^2C + s(2\omega_n\zeta CV_0^2 + G_{L0}V_0^2) + \omega_n^2 CV_0^2} \end{aligned} \quad (3.98)$$

$$\begin{aligned} \text{DVC root contour } G_{L0} &\rightarrow 1 + G_{L0}G(s)H(s) \approx \\ &1 + G_{L0} \frac{V_0^2 s}{s^2V_0^2C + s(2\omega_n\zeta CV_0^2 - P_{L0}) + \omega_n^2 CV_0^2} \end{aligned} \quad (3.99)$$

$$\begin{aligned} \text{QVC root contour } I_{L0} &\rightarrow 1 + I_{L0}G(s)H(s) \approx \\ &1 + I_{L0} \frac{s}{s^2V_0C + s(2\omega_n\zeta CV_0 + 2G_{L0}V_0) + \omega_n^2 CV_0} \end{aligned} \quad (3.100)$$

$$\begin{aligned} \text{QVC root contour } G_{L0} &\rightarrow 1 + G_{L0}G(s)H(s) \approx \\ &1 + G_{L0} \frac{2V_0s}{s^2V_0C + s(2\omega_n\zeta CV_0 + I_{L0}) + \omega_n^2 CV_0} \end{aligned} \quad (3.101)$$

The system response is affected by  $P_{L0}$  and  $G_{L0}$  in the case of DVC, and  $I_{L0}$  and  $G_{L0}$  for the case of QVC. Moreover, in addition to the dynamic performance, load dependent poles may lead to system instability. An especial concern rises for the DVC case, as the minus sign in the  $P_{L0}$  term might compromise the stability at some point of operation.

At this point, it is worth to point out that in the QVC approach,  $P_{L0}$  term does not affect the system performance, and does not contribute to the system instability. This fact arises as one of the main advantages of this method over the widely used DVC, and to the author knowledge it has not been reported before in the literature. Nonetheless, a dependency on CCLs appears in the QVC expression, represented by the load level  $I_{L0}$ . Although positive load currents,  $I_{L0} \geq 0$ , does not present stability problems, a potential issue appears when  $I_{L0} < 0$ , i.e. when constant current generation (CCG) is considered.

$G_{L0}$  appears in both methods and has a positive impact in the system damping for both DVC and QVC. However, if  $G_{L0} < 0$ , i.e., when some equipment in the grid behaves as a negative resistor, like a generator operating in voltage/current droop mode, the system response can be worsen until instability.

In order to establish a general methodology for determining the stability limits of DVC and QVC, the root contour expressions presented before, can be generalized into a single equation by using the terms  $\alpha_0$  and  $\beta_0$  defined previously in Table 3.2. The resulting expression is (3.102).

$$1 + (\alpha_0 + \beta_0)G(s)H(s) \approx 1 + (\alpha_0 + \beta_0) \frac{s}{s^2 + s2\omega_n\zeta + \omega_n^2} \quad (3.102)$$

This expression leads to the theoretical stability condition in (3.103), being the system stable whereas the condition is met.

$$\alpha_0 + \beta_0 \geq -2\omega_n\zeta \quad (3.103)$$

Fig. 3.54 shows the system root-contour for the  $(\alpha_0 + \beta_0)$  term and the Bode diagram of the closed-loop disturbance rejection  $\frac{\Delta V}{\Delta P_L}$  (3.83) with  $K = 1$  and  $\omega_n = 2\pi 50 \text{ rad/s}$ .

The figure clearly shows how the system damping is increased as  $\alpha_0 + \beta_0$  increases, while it tends to instability as  $\alpha_0 + \beta_0$  decreases, reaching the expected stability limit. In the case of using DVC,  $\alpha_0$  will present negative sign under CPL (i.e. if  $P_{L0}$  is positive). As commented before, in case  $\beta_0$  is not high enough to cancel the effect of  $\alpha_0$ , the system poles will move to the right as  $P_{L0}$  increases. An example of the stability limits for the scenario 1 defined in Table A.3 is summarized in Table 3.3.

For the same system, the time domain responses of DVC and QVC for a 2% CPL step (1kW) are shown in Fig. 3.55 for different load levels. It is clear how the system

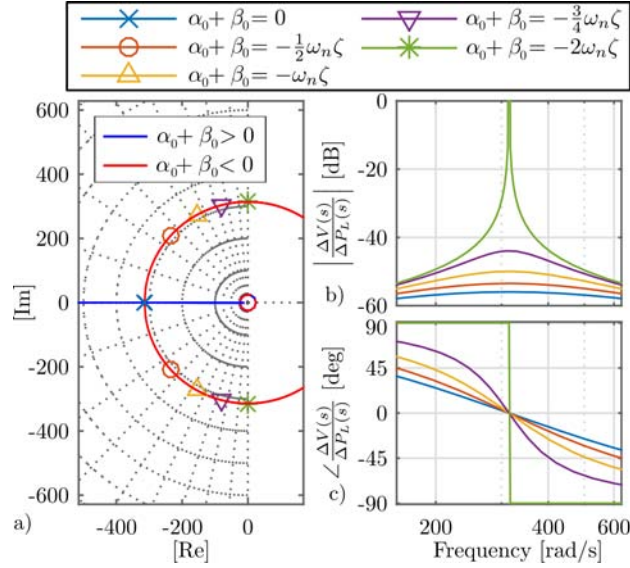


**Figure 3.54:** System response depending on the load level terms  $\alpha_0$  and  $\beta_0$ . a) System root-contour for the gain  $(\alpha_0 + \beta_0)$  valid for DVC and QVC. b) and c) Bode diagram of the closed-loop disturbance rejection transfer functions for different values of  $\alpha_0 + \beta_0$ .

Table 3.3: Example of stability limits for the system defined in Table A.3

	Load Level Stability Limits		
	$P_{L0}$ (if $G_{L0} = 0$ )	$I_{L0}$ (if $G_{L0} = 0$ )	$G_{L0}$ (if $P_{L0} = 0$ or $I_{L0} = 0$ )
DVC	2.66 kW	$\pm\infty$	$-25\text{m}\Omega^{-1}$
QVC	$\pm\infty$	-8.175 A	$-12.5\text{m}\Omega^{-1}$

tends to oscillate as the conditions in Table 3.3 are approached. Conversely, when the load levels move away from the stability limit, the system damping is improved.

The effect of  $P_{L0}$  in the time domain response is illustrated in Fig. 3.56, where the behaviour of DVC and QVC methods are compared under CPL increasing steps. As expected, unlike in the QVC, for the same load step, the response in the DVC method is altered for the worse at higher load levels.

### 3.8.3.4 Voltage collapse phenomena

The voltage level also represents a potential cause of instability as it deviates from the equilibrium point. The voltage collapse for both controllers is represented in Fig. 3.57 for a CPL disturbance, obtained by a non-linear simulation in Matlab/Simulink®.

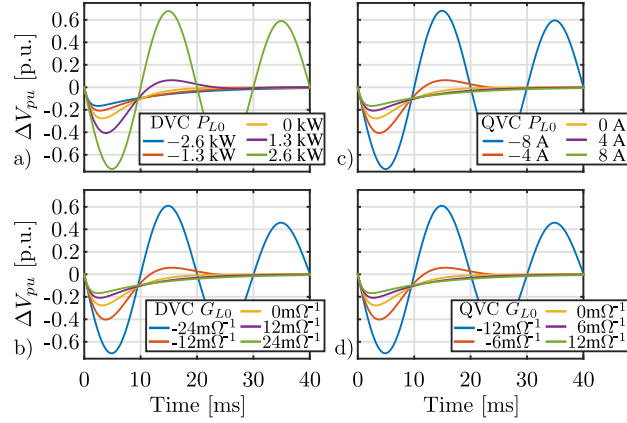


**Figure 3.55:** Step response under a CPL step disturbance of 2%(1kW). a) Influence of  $P_{L0}$  in DVC; b) Influence of  $I_{L0}$  in QVC; c) Influence of  $G_{L0}$  in DVC; d) Influence of  $G_{L0}$  in QVC.

As it is shown, the QVC is not only independent of the CPL load level at the equilibrium point,  $P_{L0}$ , but also withstands higher CPL step disturbances before it collapses. This demonstrates that the QVC can withstand higher CPL variations than the DVC method under the same conditions, as shown in Fig. 3.57a) and 3.57b), which is a clear advantage of the former controller. Fig. 3.57c) represents the dynamic equivalent version of the stationary  $V/P$  curve in power systems.

### 3.8.4 Effect of the capacitor in the system response

The capacitor and controller bandwidth take an important role in the system behavior. While the bandwidth is limited by the inner control loop, the size of the capacitor depends on the application. In DC voltage control applications, such as those found in DC-links, the capacitor is usually sized according to the expected oscillations caused by stationary power fluctuations, which in some cases leads to oversizing [170,295]. Regarding AC grid connected converters, the capacitor is often determined by the filtering requirements of switching frequency harmonics, leading usually to small capacitor values.

It is obvious that increasing the capacitor size while maintaining  $\omega_n$  and  $\zeta$ , will lead to an improved disturbance rejection without compromising the system stability. Fig. 3.58 shows the dynamic stiffness in the frequency domain and the time domain 1kW step response of the disturbance rejection transfer function  $\frac{\Delta V(s)}{\Delta P_L(s)}$  for different capacitor values using DVC and QVC. It is worth noting that the QVC and DVC performance is the same if  $P_{L0} = 0W$ .

As expected, the disturbance rejection is improved as the capacitor increases. The size of the capacitor has a direct influence on the maximum disturbance the system

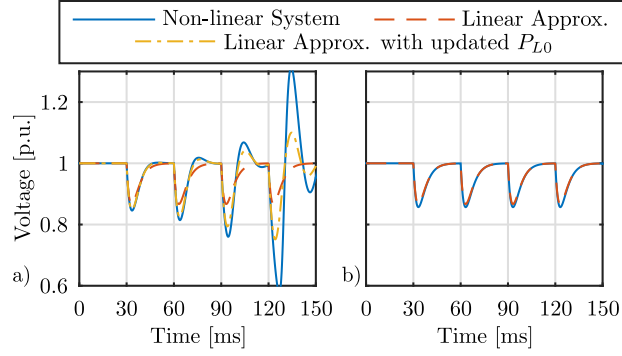


**Figure 3.56:** Voltage response under increasing CPL step disturbance. Load is increased by steps of 480W (9.6%) every 30ms. Dashed lines show the linear approximations. a) DVC. b) QVC. Results using the data in Table A.3.

can withstand, presenting the QVC a better performance over the DVC, specially noticeable under low capacitance.

### 3.8.5 Virtual capacitance for enhanced disturbance rejection

Unlike the controller parameters, the modification of the hardware of the system is more restricted. Other techniques for voltage control disturbance rejection enhancement have been proposed in the past, mainly based on load decoupling through measurements, observers or estimators [177]. A simpler alternative is presented in Fig. 3.59, where  $D(t) = C_v \frac{d}{dt}$ . Using a pseudo-derivative feedback control, it is possible to add a virtual capacitance  $C_v$  which ideally will be added to the passive capacitance  $C$ , increasing the total equivalent system plant capacitance, improving the disturbance rejection. In the case of applying this improvement, the DVC and QVC regulators would be reformulated as (3.104) and (3.105) respectively.

$$i^*(t) = k_p(v^*(t) - v(t)) + k_p \frac{1}{T_i} \int (v^*(t) - v(t)) dt - C_v \frac{dv(t)}{dt} \quad (3.104)$$

$$i^*(t) = \frac{k_p(v^*(t)^2 - v(t)^2) + k_p \frac{1}{T_i} \int (v^*(t)^2 - v(t)^2) dt}{v(t)} - C_v \frac{dv(t)}{dt} \quad (3.105)$$

Assuming an ideal derivative and ideal sensors, the transfer functions for DVC and QVC, as well as the PI parameters, can be modified by substituting the parameter  $C$  by  $C + C_v$ , without affecting the analysis performed up to this point in this section. It is worth noting that the virtual capacitance does not only allow to improve the dynamic stiffness but can also be used to emulate low capacitance systems by applying

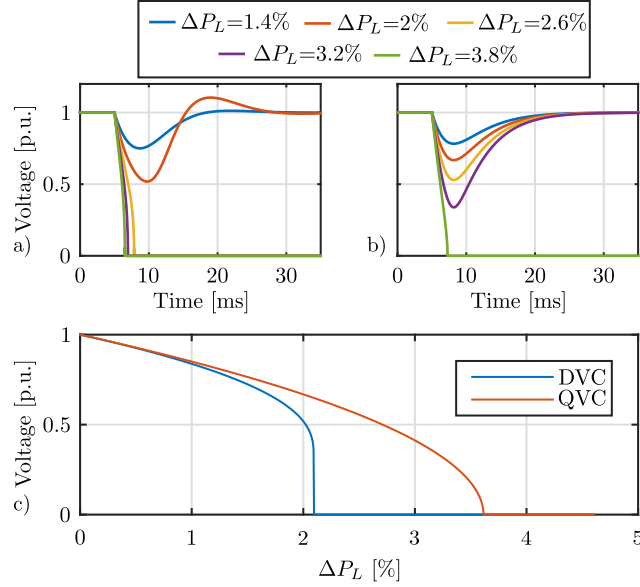


**Figure 3.57:** Voltage collapse for the DVC and QVC methods under CPL steps. a) DVC performance for an initial  $P_{L0} = 0$ ; b) QVC performance; c) DVC and QVC maximum voltage deviation as a function of the CPL step shown in percentage. Results using the data in Table A.3.

a negative value, i.e.  $C_v < 0$ . In addition, the virtual capacitance can be included in the grid-forming unit or added through a different converter as an ancillary service.

### 3.8.6 Effect of the nominal operating point and the controller bandwidth

Besides the stability limits, one of the most important characteristics considered for the design and analysis of the grid-forming control is the maximum voltage deviation under CPL steps. In this section, an analytical expression that allows to determine that deviation is proposed. The parameter  $K_{pu}$  was defined as (3.84) in order to normalize the effect of the capacitance, the nominal voltage and the nominal active power in the system response. This normalization makes this study applicable to any scenario. If we define a new damping factor  $\zeta'$  as (3.106), the analytical linearized response becomes a function of three factors:  $K_{pu}$ ,  $\omega_n$  and  $\zeta'$ . Moreover, the stability condition will be now dependent on  $\zeta'$ , being the system stable as far as  $\zeta' \geq 0$ .

$$\zeta' = \zeta + \frac{\alpha_0 + \beta_0}{2\omega_n} \quad (3.106)$$

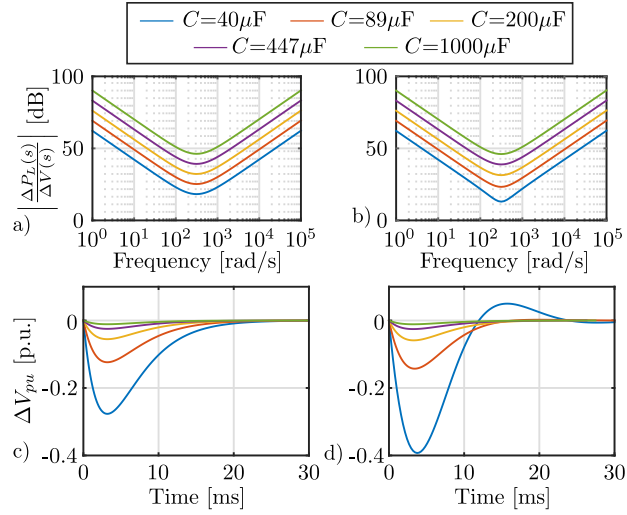


**Figure 3.58:** Evaluation of the capacitor size effect in the disturbance rejection capabilities. a) QVC dynamic stiffness,  $\frac{\Delta P_L(s)}{\Delta V(s)}$ , for different capacitor values (equal to DVC if  $P_{L0} = 0\text{W}$ ); b) DVC dynamic stiffness when  $P_{L0} = 1.2\text{k}$ ; c) QVC step response of the transfer function  $\frac{\Delta V(s)}{\Delta P_L(s)}$  (equal to DVC if  $P_{L0} = 0\text{W}$ ); d) DVC step response of the transfer function  $\frac{\Delta V(s)}{\Delta P_L(s)}$  for  $P_{L0} = 1.2\text{kW}$ .

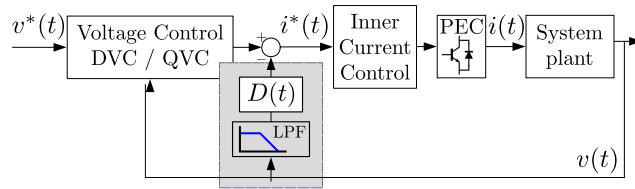


**Figure 3.59:** Modified voltage control scheme using pseudo-derivative feedback structure and  $C_v$ .

Thus, the maximum voltage deviation  $\Delta V_{max}^{pu}$  can be obtained analytically with the expression in (3.107), where  $t_m$  is the time instant of the maximum voltage deviation defined by (3.108).

$$\frac{\Delta V_{pu}^{max}}{\Delta P_{Lpu}} = \begin{cases} \frac{K_{pu} e^{(-t_m \omega_n \zeta')} \sin(t_m \omega_n \sqrt{1 - \zeta'^2})}{\omega_n \sqrt{1 - \zeta'^2}} & \text{if } 0 \leq \zeta' < 1 \\ K_{pu} t_m \frac{e^{-t_m \omega_n}}{\omega_n} & \text{if } \zeta' = 1 \\ \frac{K_{pu} e^{(-t_m \omega_n \zeta')} \sinh(t_m \omega_n \sqrt{\zeta'^2 - 1})}{\omega_n \sqrt{\zeta'^2 - 1}} & \text{if } \zeta' > 1 \end{cases} \quad (3.107)$$

$$t_m = \begin{cases} \tan^{-1} \left( \frac{2\zeta' \sqrt{1 - \zeta'^2}}{2\zeta'^2 - 1} \right) \frac{1}{2\omega_n \sqrt{1 - \zeta'^2}} & \text{if } 0 \leq \zeta' < 1 \\ \frac{1}{\omega_n} & \text{if } \zeta' = 1 \\ \frac{\log \left( \frac{1}{\zeta' - \sqrt{\zeta'^2 - 1}} \right)}{\omega_n \sqrt{\zeta'^2 - 1}} & \text{if } \zeta' > 1 \end{cases} \quad (3.108)$$

Although these expressions can be useful for the system design, it is worth noting, that they will become less accurate as the operating point moves away from the equilibrium point considered in the linearization process. It is also worth to point out that these expressions are valid for CIL and CCL disturbance substituting  $\frac{\Delta V_{pu}^{max}}{\Delta P_{Lpu}}$  by  $\frac{\Delta V_{pu}^{max}}{\Delta G_{Lpu}}$  or  $\frac{\Delta V_{pu}^{max}}{\Delta I_{Lpu}}$ , and  $K_{pu}$  by  $K_{G_{pu}}$  or  $K_{I_{pu}}$  respectively.

To evaluate the effect of  $K_{pu}$  and  $\omega_n$  considering the non-linearities, a non-linear simulation has been conducted as an example, considering  $\zeta = 1$  and  $P_{L0} = I_{L0} = G_{L0} = 0$  in the equilibrium point, having  $\zeta' = \zeta$ . Fig. 3.60 shows the maximum voltage deviation under a CPL step as a function of  $K_{pu}$ , and the power step disturbance,  $\Delta P_{Lpu}$ . The results are shown for DCV and QVC for two different bandwidths,  $\omega_n$ .  $\Delta V_{pu} = 1$  represents the system voltage collapse or instability. It is worth to point out that the QVC extends the region of operation, allowing a better disturbance rejection and avoiding voltage collapse with higher  $K_{pu}$  values compared with the DVC method. The solid black line represents the analytical results for a  $\Delta V_{pu} = 0.5pu$  obtained through the expression (3.107), being in close agreement with the non-linear simulation results.

The voltage control bandwidth plays also an important role in the maximum voltage deviation. As an example of its effect, Fig. 3.61 shows the maximum supported CPL

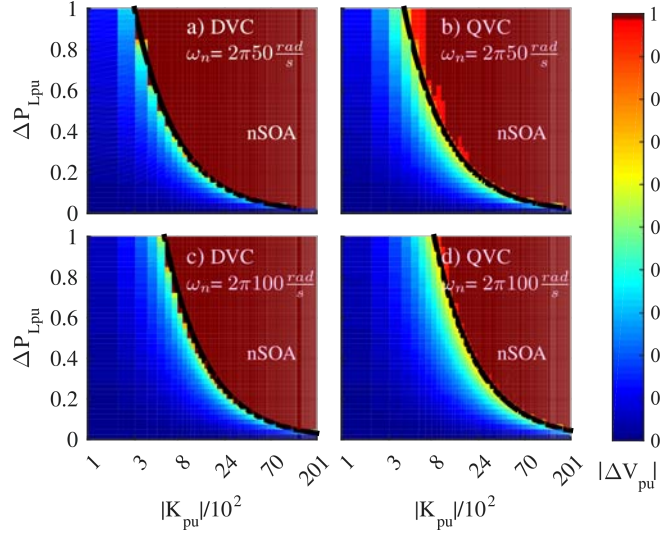


**Figure 3.60:** Maximum voltage deviation depending on the CPL step disturbance and the  $K_{pu}$  value. Simulation results. a) DVC,  $\omega_n=2\pi 50\text{rad/s}$ ; b) QVC,  $\omega_n=2\pi 50\text{rad/s}$ ; c) DVC,  $\omega_n=2\pi 100\text{rad/s}$ ; d) QVC,  $\omega_n=2\pi 100\text{rad/s}$ . Dark red is considered as the non-Safe Operating Area (nSOA).

step,  $\Delta P_{Lpu}$ , as a function of  $K_{pu}$ , and the controller bandwidth,  $\omega_n$ , for a maximum voltage deviation of  $\Delta V_{pu} = 0.65\text{pu}$ .  $\Delta P_{Lpu} = 1$  indicates that the system can withstand a CPL step of a power equal to the nominal, presenting again the QVC an extended operation when compared with the DVC.

### 3.8.7 Grid-forming system design: an application example

The expressions derived in the previous subsections can result as an useful and easy tool for the design and selection of the system parameters as well as its characterization. Both the analytical expressions and the simulation of the non-linear system, allows to select the value of  $K_{pu}$  or  $\omega_n$  to comply with a determined dynamic response, keeping the stability, under CPL steps. It also offers the possibility for predicting the system behavior. When looking for the system design, as  $K_{pu}$  depends on 3 parameters, its selection allows to determine the value of one parameter fixing the other 2. Thus, as an example, given a  $\omega_n$ , a determined nominal voltage,  $V_n$  and active power,  $P_n$ , the size of the capacitor,  $C$ , can be obtained for a desired response. Table 3.4 shows an example of design to select the capacitance given the system parameters ( $\omega_n$ ,  $\zeta$ ,  $V_n$ ,  $P_n$ ) and the maximum voltage deviation ( $\Delta V_{pu}^{max}$ ) for a determined maximum CPL step ( $\Delta P_{Lpu}^{max}$ ) when QVC is applied. The results are obtained using the expression in (3.107) and (3.108): 1) first,  $K_{pu}$  is cleared from (3.107), 2) second,  $C$  is cleared from

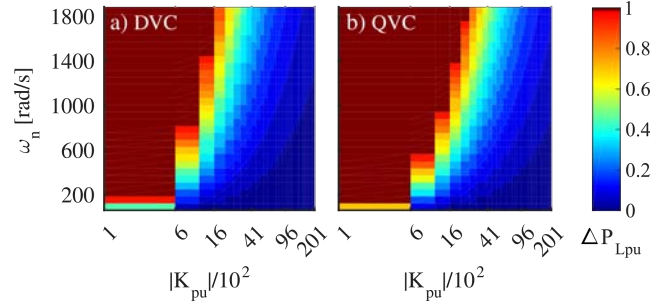


**Figure 3.61:** Maximum CPL step disturbance for a maximum voltage deviation of 0.65pu, depending on the  $K_{pu}$  value and the voltage control bandwidth,  $\omega_n$ , for  $\zeta = 1$  and  $\alpha_0 + \beta_0 = 0$ . a) DVC; b) QVC.

the  $K_{pu}$  expression (3.84).

Table 3.4: Example of system design using the proposed methodology

Design constrains and system parameters					
$\Delta P_{Lpu}^{max}$	$\Delta V_{max}^{pu}$	$\omega_n [\frac{rad}{s}]$	$\zeta$	$V_n [V]$	$P_n [kW]$
0.1	0.4	$2\pi 50$	1	325	50
Result					
$K_{pu} [s^{-1}]$			$C [\mu F]$		
<b>3416</b>			<b>138</b>		

Although  $\omega_n$  can be selected if the  $K_{pu}$  is fixed, the bandwidth, as commented before, will be usually determined by the characteristics of the inner control loop. On the other hand,  $\zeta$  can be selected depending on the expected  $\alpha_0$  and  $\beta_0$ , which are in turn dependent on the load rated value and type. As said before, an ideal current control loop has been considered for the design procedure. However, it is worth to point out that in case of LC or LCL filters, a resonance may appear at low frequencies if the current control loop bandwidth is not high enough. Although it is out of the scope of this thesis, considering the stability limitation imposed by that resonance will be a must for the future development.

### 3.8.8 The quadratic voltage control applied to AC grid-forming units

The direct voltage control have been widely applied in AC grid-forming converters control, mainly using the  $dq$  synchronous reference frame approach shown in Fig. 3.62 [129]. However, in the case of quadratic voltage control, there is no records of its used in 3-phase AC applications. In order to compared those two methods, and exploit the





functions (3.73)-(3.78) are also valid for each of the  $dq$  axis substituting  $P_{L0}$  by  $\frac{2}{3}P_{L0}$  and  $\Delta P_L$  by  $\frac{2}{3}\Delta P_L$ .

Considering all the above, a voltage control in the  $dq$  reference frame is proposed based on QVC and fixed frequency generation. The complete cascaded control scheme for a 3-phase AC grid-forming converter is shown in Fig. 3.63.

### 3.8.9 Experimental results

The control models presented in this section have been tested and validated experimentally under 2 different scenarios, covering the application of voltage control in both DC and AC grids, comparing the performance of DVC and QVC. The experimental results have been obtained through the experimental setup described in Appendix A.5.

#### 3.8.9.1 Experimental demonstration in a DC application

Fig. 3.64 illustrates the simplified scheme of the DC experimental setup. For the DC voltage control, a D-Statcom with a battery energy storage system (BESS) has been used (PM15F42C).

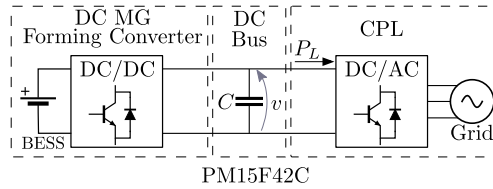


**Figure 3.64:** Experimental setup: DC application.

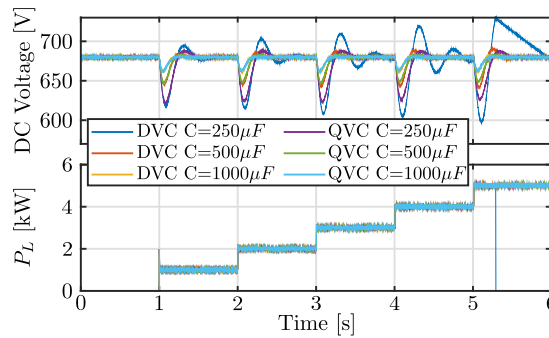


**Figure 3.65:** DC setup experimental results. DC grid-forming converter performance for different capacitor values. DVC and QVC are compared under multistep  $P_L$ .

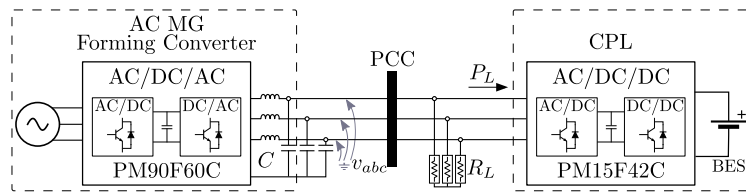
The DC bus voltage is controlled by a DC/DC forming converter (DC grid-forming unit) fed by a battery, while a DC/AC 3-phase grid tied converter operates as a DC CPL.

Fig. 3.65 shows the response of both DVC and QVC under increasing CPL steps for several capacitor values in the DC MG setup.

Due to the experimental setup limitations, the capacitor have been resized using virtual capacitance (Fig. 3.59 and eqs. (3.104) and (3.104)), being the physical capacitor value  $1000 \mu F$ . In order to better illustrate the performance comparison, the voltage regulator bandwidth  $\omega_n$  has been set to 6Hz. As shown, the results match the expected performance from the analytical analysis, being the response of the DVC worsen as the CPL level increases, presenting the QVC a better response, especially under low capacitor values.

### 3.8.9.2 Experimental demonstration in an AC application

Fig. 3.66 illustrates the simplified scheme of the AC experimental setup. In order to test the AC voltage control, the PM90F60C 3-ph converter has been used as the AC grid-forming converter while the D-Statcom with BESS (PM15F42C) plays the role of an AC CPL. An additional  $56 \Omega$  resistive load,  $R_L$ , has been included in the MG ( $G_{L0} = \frac{1}{56}$ ). The AC control has been implemented in the  $dq$  synchronous reference frame applying the DVC and QVC as in Figs. 3.62 and 3.62. Fig. 3.67 shows the



**Figure 3.66:** Experimental setup. AC application.

performance comparison between DVC and QVC in the AC 3-ph MG with an increasing CPL.

The instantaneous voltage magnitude is represented (the frequency is constant in the considered system). As expected from simulations, the DVC dependency on the load level makes its response to be worsen with increased CPL level ( $P_{L0}$ ). It is worth noting that the local resistive load provides an improved damping, allowing to move the stability limit from  $P_{L0} \simeq 2.66$  kW (see Table 3.3) to  $P_{L0} \simeq 5.5$  kW.

To demonstrate the use of virtual capacitance applied to the AC setup, the performance under different virtual capacitance values is shown in Fig. 3.68 comparing the step response of DVC and QVC. The improved response of the QVC with respect to the DVC should be highlighted, specially when low capacitance values are used.

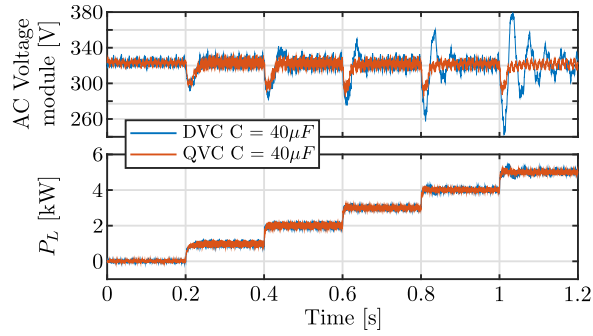


**Figure 3.67:** AC setup experimental results. DVC and QVC compared under multistep  $P_L$ .

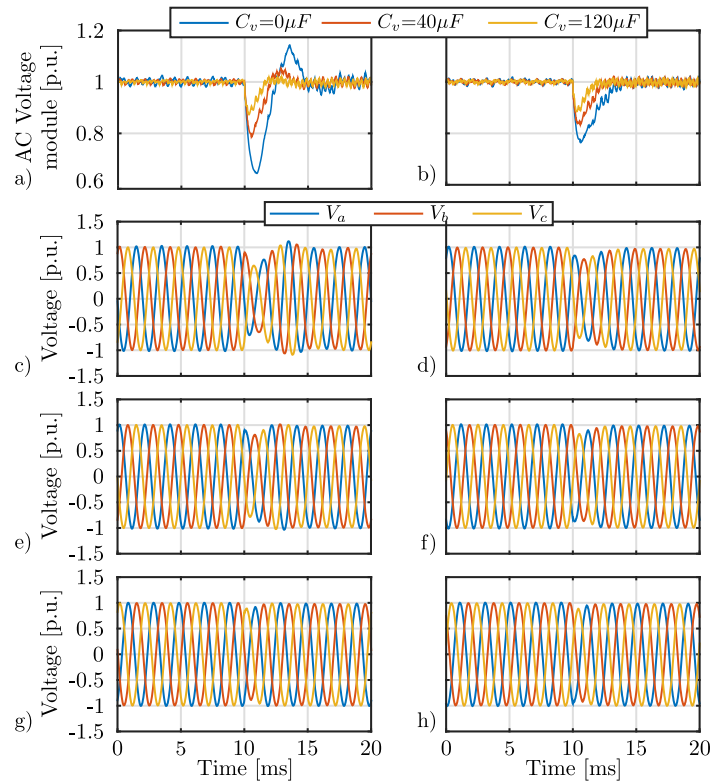


**Figure 3.68:** AC setup experimental results. DVC and QVC responses using different values of virtual capacitance. Step of  $P_L = 2.5$  kW at  $t = 0.1$  s. a) DVC voltage module; b) QVC voltage module; c), e) and g) DVC phase voltages for  $C_v = 0\mu F$ ,  $C_v = 40\mu F$  and  $C_v = 120\mu F$ ; d), f) and h) QVC phase voltages for  $C_v = 0\mu F$ ,  $C_v = 40\mu F$  and  $C_v = 120\mu F$ .

### 3.8.9.3 Response matching: analytical vs experimental results

In order to demonstrate the viability of the response prediction proposed in the Section 3.8.6, the experimental data in Figs. 3.65 and 3.67 have been compared with the expected response obtained analytically with the expressions (3.107) and (3.108). The results are shown in Fig. 3.69, exhibiting a close match between the experiments and the predicted maximum  $\Delta V_{pu}$ , demonstrating the potential capability of the derived analytical expressions for the prediction of the system performance and the design of the system.

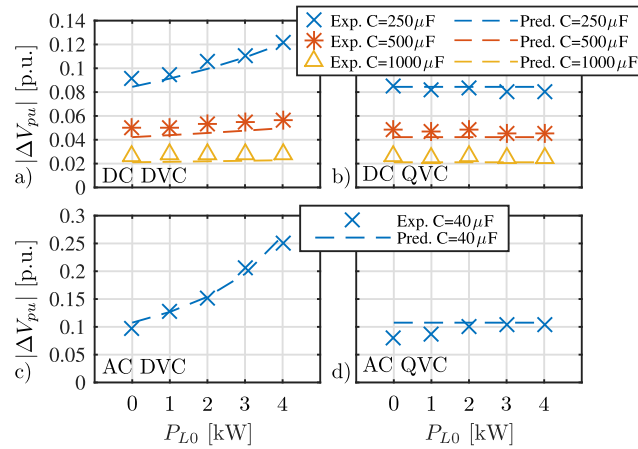


**Figure 3.69:** Comparison between the experimental results and the analytical prediction of  $\Delta V_{pu}$  for different values of  $P_{L0}$ . Dashed lines represent the predicted response. a) DC setup using DVC; b) DC setup using QVC; c) AC setup using DVC; d) AC setup using QVC.

Thus, apart from an in deep dynamic analysis and comparison of the DVC and QVC alternatives for grid-forming converters, this section may settle the basics for the future development of a simple voltage control design and analysis tool.

## 3.9 Conclusions

This chapter has presented the hybrid AC/DC microgrid under study, has modelled the main elements that composed it and the common grid-tied converters present in microgrids, proposing control strategies for converter current and voltage control improvement. The following points have been covered:

- The hybrid microgrid under study have been introduced, as well as the elements that composed this particular microgrid.

- The L, LC and LCL filters used in grid-tied AC VSIs have been modelled, considered as the control plant for current and voltage regulation. The current control loop for L, LC and LCL filters have been defined.
- The basics of the Luenberger observer have been discussed, evincing its capability to reduce the number of sensors and improving the sensor response in control systems.
- A novel LCL filter current controller has been proposed based on a Luenberger observer that allows to reduce the number of current sensors, eliminating the need for measuring the grid-side output current. Although the strategy has been evaluated in the  $dq$  reference frame, the presented design permits its implementation in an arbitrary reference frame. The method not only provides a high robustness against parameter variations but also appears as an appealing tool for detecting significant changes in the grid-side impedance.
- An on-line impedance estimation method has been proposed based on pulsed signal injection and a recursive least squares algorithm. Apart from presenting a moderate computational burden, the proposed method can be triggered from the disturbance signal coming from the Luenberger observer of the observer-based LCL grid current controller. This avoids the continuous injection of pulses, improving the THD compared to other approaches. Among the methods for the signal injection the  $q$ -axis injection in the synchronous reference frame has been finally selected for an increased sensitivity. The online RLS algorithm is implemented in the  $\alpha\beta$  reference frame to estimate balanced and unbalanced impedance. The estimation method has been verified through simulation and experimental results.
- The voltage control of grid-forming converters has been extensively analyzed considering the presence of different types of loads, with a special focus on CPLs. Two PI-based control methods, DVC and QVC, have been compared outlining their benefits and drawbacks, presenting the QVC an enhanced dynamic behavior under CPL disturbances. The ideas presented during the theoretical discussion allows for building a methodology for the voltage control loop design, including the selection of the capacitor value considering the dynamic performance. As demonstrated, the proposed analysis methodology can be applied to converter having different rated values, becoming a potential design tool. The methodology leaves up to the designer the selection of parameters which are application dependent such as the load level in the equilibrium point, the stability margins and the maximum voltage deviation under CPL disturbances. Additionally, the use of the virtual capacitance as a simple tool for response enhancement, and as a tool to experimentally forecast the effect of resizing the capacitance in existing systems, has been introduced. The presented ideas has been validated through simulations and experimental results.



## Chapter 4

# Enhanced dynamic active power support and synchronization in weak AC microgrids

### 4.1 Introduction

As revealed during the literature review in Chapter 2, microgrids are by definition weak systems with low inertia, that are prone to suffer critical grid quality and reliability problems under contingencies. Among the identified issues and research opportunities, this chapter focuses on the lack of inertia and the need for frequency and phase estimation, and synchronization in weak and distorted AC microgrids: 1) The lack of inertia leads to high transients variations in voltage and frequency and compromise the reliability and stability of grid. This can be mitigated by applying active power compensation by means of virtual inertia and virtual capacitance. 2) Although in microgrids with a P/V relation, the low inertia issue can be tackled by feedback-based voltage compensation, in grids with a P/f relation the frequency compensation presents a challenging handicap: the feedback frequency has to be estimated, requiring a reduced bandwidth in the controllers due to the estimation delay associated to existing frequency estimators. 3) Harmonics, unbalances, frequency and phase variations can corrupt and distort the voltage and currents in the grid. This may drive to the malfunction of grid-tied devices and a corrupted synchronization.

This chapter proposes solutions for tackling the highlighted issues: 1) An ESS-based dynamic power compensator is presented for the compensation of voltage and frequency in AC networks. 2) An observer-based frequency compensator is proposed. The per-

formance achieved by existing feedback control has been improved by the development of a transient observer, formed by a transient detection method that effectively decouples the grid reference frequency from the compensator inputs, and a Luenberger-based observer that provides a nearly-zero lag frequency estimation, allowing to increase the phase margin in the frequency controller. 3) A predictive sequence estimator is proposed based on the sliding Goertzel transform, able to estimate the phase and magnitude of positive, negative and harmonic components with faster response than existing methods.

## 4.2 Dynamic active power compensation for enhanced transient response in AC microgrids

In conventional grids the active power mismatches are absorbed by the high inertia and damping of generators. In addition, the rated power of generators is usually much higher than the expected maximum active power step disturbance. However, AC MGs dominated by PECs or low power SGs are characterized by a low inertia and damping. In those cases, the grid inertia depends on the control scheme of the grid-tied devices, the low inertia and damping of the small SGs or the capacitors connected to the microgrid lines (mainly the capacitors in the LC filters of grid-tied converters). Different scenarios are distinguished depending on the relation of the power with the voltage magnitude and frequency:

- In microgrids with high R/X ratio and regulated under a fixed-frequency scheme or P/V-Q/f droop, the active power will be linked to the voltage magnitude. In this case the synchronous generators can not be directly coupled to the microgrid buses, and the inertia and damping will depend on the capacitance in the grid, the self-regulating effect given by resistive loads (as the voltage is proportional to their active power consumption) and the control of the grid-tied converters.
- In microgrids regulated under a non-fixed frequency approach as conventional droop control, directly coupled SGs or VSGs, the active power will be linked to the grid frequency as in conventional grids. In such a case, the inertia and damping of the system is given by the SGs, the self-regulating effect given by the directly coupled rotating loads (motors) and the control of grid-tied converters.

In any of the cases, the use of PECs as interface of DGs, DERs and ESSs with the grid, involves a decoupling from the inertial characteristics of the generation and energy storage, being the exploitation of the inertial sources (generators inertia, DC-link capacitors, energy storage devices...) dependent on the PEC control.

The hybrid AC/DC microgrid used as background in this study, described in the previous chapter in Section 3.2, presents a multi-subgrid topology, where several AC nanogrids are connected to an LVDC bus. In addition to the high penetration of PECs

and CPLs in the microgrid, as this configuration decouple the utility grid and the NGs, each nanogrid will behave similar to an isolated AC system, being considered weak electrical grids, and a low inertia will be expected in them. Moreover, under contingencies (faults, overloads...), some of the nodes in the nanogrid may be physically disconnected from the rest of the microgrid, becoming the problem of low inertia even more critical.

A solution to increase the NGs inertia and damping, may consist in including the dynamic active power compensation as an ancillary service in any of the DGs, RESs or dESSs present in the nanogrids. The primary energy source in DGs might present a slow response and the RESs should be operated under MPPT control, thus, their main source to provide a fast dynamic power compensation is the energy stored in the DC-link capacitors of their intermediate stages, with a limited energy storage capability. However, ESSs appears as massive energy supplies with fast availability, being a more appropriate alternative.

This section will establish the basics of a 3-phase AC dynamic active power compensator (DAPC) valid for its integration in any of the buses of the AC nanogrids. The inner control loop of the compensator will received current or power references. Depending on the application, the device can compensate the voltage magnitude or the grid frequency by modifying the external control loop without modifying the inner control:

- If the compensator is integrated in a system where the active power is linked to the voltage magnitude, a voltage compensation control will be used using voltage damping and virtual capacitance.
- If the compensator is integrated in a system where the active power is linked to the grid frequency, a frequency compensation control will be used using frequency damping and virtual inertia.

The application of the techniques and models presented in this section will be seen later in this chapter (Section 4.3) and also in Chapter 5.

### 4.2.1 The 3-phase dynamic active power compensator

The dynamic active power compensator is shown in Fig. 4.1, and is based on the D-STATCOM with ESS concept [195, 196]. It consist of a grid-tied 3-phase VSI and an energy storage system. The ESS will be in charge of controlling the DC-link voltage while the VSI control will consist of an inner current control loop and an external control loop that can be designed for either voltage magnitude or grid frequency compensation. It is worth noting that the design of the compensator will be agnostic respect to the ESS, including its power stage and storage technology.

Fig. 4.2 shows in detail the power topology proposed for the grid-tied DC/AC converter, the position of the current and voltage sensors and the inner current control

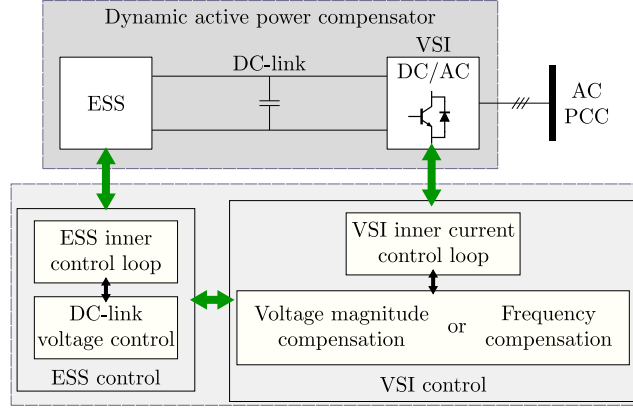


**Figure 4.1:** Conceptual scheme of the dynamic active power compensator valid for voltage magnitude and frequency compensation.

loop implemented in the  $dq$  synchronous reference frame. Neglecting the effect of the  $q$ -axis component in the instantaneous active power (4.1), and the effect of  $d$ -axis component in the instantaneous reactive power (4.2),  $i_{i_d}$  and  $i_{i_q}$  will be linked to the active and reactive power respectively.

$$P(t) = \frac{3}{2} (v_{g_d}(t)i_{i_d}(t) + v_{g_q}(t)i_{i_q}(t)) \rightarrow P(t) = \frac{3}{2} v_{g_d}(t)i_{i_d}(t) \quad (4.1)$$

$$Q(t) = \frac{3}{2} (v_{g_q}(t)i_{i_d}(t) - v_{g_d}(t)i_{i_q}(t)) \rightarrow Q(t) = -\frac{3}{2} v_{g_d}(t)i_{i_q}(t) \quad (4.2)$$

Thus, the inner control loop will receive the  $d$ -axis current reference  $i_{i_d}^*$  from the voltage magnitude or frequency external control loop, while the  $i_{i_q}^*$  generation is out of the scope of this thesis and will be assumed as  $i_{i_q}^* = 0$  so that the compensator present a unity power factor. In addition to  $i_{i_d}^*$ , an steady state  $d$ -axis current reference  $i_{i_d}^{*ss}$  can be considered to command the steady state power sharing of the device and control the charging and discharging of the battery. This function remains out of the scope of the thesis, assuming  $i_{i_d}^{*ss} = 0$ .

#### 4.2.2 Voltage magnitude compensation

The voltage magnitude compensation can be addressed using the principles of virtual capacitance seen in Section 3.8.5. The proposed generic control topology for the voltage compensator is shown in Fig. 4.3, and defined by the equation (4.3) in the time domain, where  $v_{g_d}$  is the  $d$ -axis grid voltage at the PCC and  $v_{g_d}^*$  is equivalent to the nominal peak voltage magnitude. A virtual capacitance ( $C_{vc} \frac{d}{dt}$ ) increases the grid

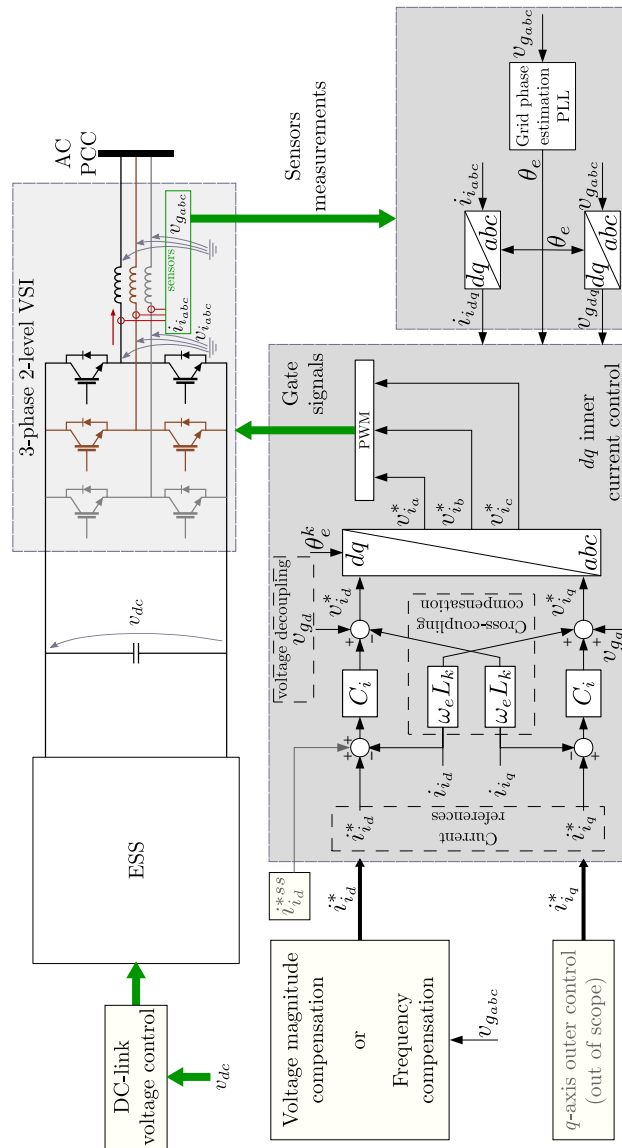


Figure 4.2: Detail view of the dynamic active power compensator topology and control.

equivalent capacitance, enhancing the initial transient voltage response under active power step disturbances. It is worth noting that a low pass filter is needed in the practical implementation of the derivative term in order to avoid problems generated by noise in the feedback signal. A P quadratic regulator ( $K_{vc}$ ) improves the grid voltage damping. Both parts of the controller (damping and virtual capacitance) can be implemented independently or combined.

$$i_{i_d}^*(t) = \underbrace{\frac{K_{vc} \cdot (v_{g_d}^*(t)^2 - v_{g_d}(t)^2)}{v_{g_d}(t)}}_{\text{damping factor}} - \underbrace{C_{vc} \cdot \frac{d}{dt} v_{g_d}(t)}_{\text{virtual capacitance}} \quad (4.3)$$

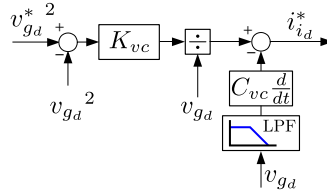


Figure 4.3: Voltage magnitude compensation outer control.

### 4.2.3 Frequency compensation

The frequency compensator will be based on the concept of virtual inertia and virtual damping used in synchronverters. The controller is shown in Fig. 4.4 and defined by the swing equation (4.4) in the time domain, where  $K_{fc}$  is the damping coefficient,  $J_{fc}$  the virtual inertia gain, and  $v_{g_d}$  is the  $d$ -axis grid voltage at the point of connection.

$$i_{i_d}^*(t) = \left( \underbrace{K_{fc} \cdot (w_e^*(t) - w_e(t))}_{\text{damping factor}} - \underbrace{J_{fc} \cdot \frac{dw_e(t)}{dt}}_{\text{virtual Inertia}} \right) \frac{w_e(t)}{\frac{3}{2}v_{g_d}(t)} \quad (4.4)$$

The frequency  $w_e$  has to be estimated using the voltage at the point of common coupling. Unlike in the voltage compensator, the feedback frequency cannot be directly measured and has to be estimated by using PLLs or FLLs. As well as in the virtual capacitance, a low pass filter is needed in the practical implementation of the derivative term. Both parts of the controller (damping and virtual inertia) can be implemented independently or combined as required.

The active power compensator presented in this section is able to compensate voltage or frequency depending on the relation between active power, voltage magnitude and frequency in low inertia AC systems. This solution will serve as the base for Section 4.3 and will be applied to the hybrid MG in Chapter 5.

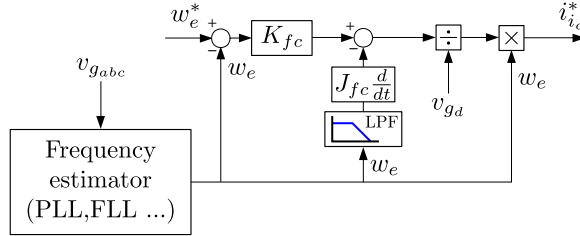


Figure 4.4: Frequency compensation outer control.

### 4.3 Observer-based transient frequency drift compensation in weak AC microgrids

Unlike in voltage compensation, the feedback control signal, i.e., the grid frequency, can not be measured directly and has to be estimated through methods like PLLs and FLLs that introduce a significant delay in the feedback loop. This section will extend the discussion of the transient frequency drift created by sudden active power changes in weak systems, proposing an observer-based frequency compensator that attempts to solve the limitations introduced by the phase lag of frequency estimators.

#### 4.3.1 Frequency drift problem and system modelling

Deviations on power grid nominal parameters can lead to non-optimal operation or malfunction of grid connected elements. Moreover, the violation of regulations could trigger the system protections, compromising the grid power quality and stability. As a reference, the default IEEE regulation for distributed resources is summarized in Table 4.1, where  $f_e$  and  $f_n$  are the instantaneous grid frequency and the nominal grid frequency respectively.

Table 4.1: Default clearing times under abnormal frequency operation based on IEEE Std 1547a-2014 [103].

Frequency [Hz]	Clearing Time [s]
$f_e < f_n - 3$	0.16
$f_e < f_n - 0.5$	2
$f_e > f_n + 0.5$	2
$f_e > f_n + 2$	0.16

##### 4.3.1.1 The transient frequency deviation problematic in low inertia MGs

MGs and distribution networks are often governed by low inertia synchronous generators, being the grid active power related to their rotating speed. In weak grids,

the connection and disconnection of the different grid elements, as power generators and loads, may cause variations on the voltage magnitude and grid frequency. This problem is illustrated in Fig. 4.6, where the load power disturbance and the induced frequency drift is shown. This issue can be mitigated by using a solution capable of injecting power to the grid with a much faster dynamic response than the grid generators, thus compensating the power mismatch.

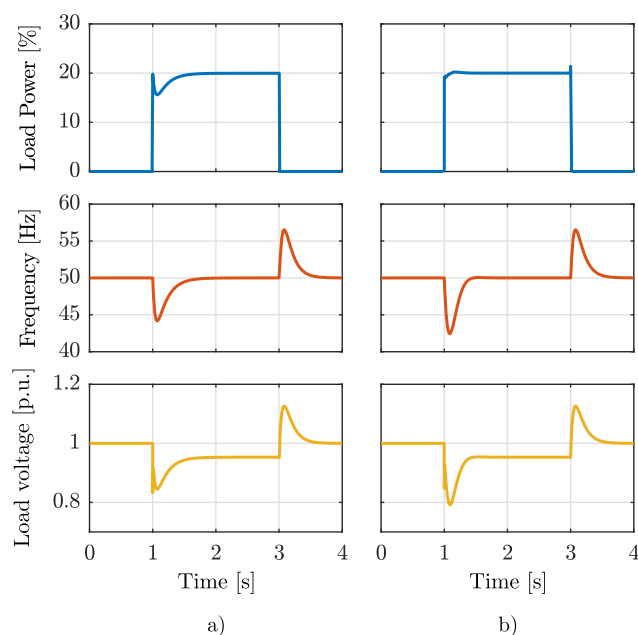


**Figure 4.5:** Illustration of the low inertia and frequency drift issue in weak microgrids. a) Response under constant impedance load (CIL). b) Response under constant power load (CPL).

#### 4.3.1.2 Simplified case of study: islanded AC 3-phase MG

Fig. 4.6 shows the proposed transient frequency drift compensator (TFDC) integrated in an experimental isolated AC system. The MG consists in a single node isolated 3-phase MG, governed by a distributed synchronous generator, feeding both passive and active loads. Such a generator operates in slack mode when the MG is disconnected from the utility grid, and presents a high output impedance ( $R_g, L_g$ ) and low mechanical inertia. The synchronous generator is implemented by a permanent magnet synchronous generator (PMSG) mechanically coupled to a permanent magnet synchronous motor (PMSM), acting as a speed governor. In order to make the setup to be as close as possible to a generic MG, both passive load, consisting of 3-phase resistors, and tightly regulated dynamic loads operated in Constant Power Load (CPL)

mode, are present in the MG. CPL are emulated by a grid tied AC/DC IGBT inverter coupled to a DC/DC converter that feeds a DC load.

The proposed frequency compensator is based on the dynamic active power compensator described in Section 4.2. The power topology will consist in a D-STATCOM with ESS, form by a 3-phase IGBT inverter coupled through a DC link to an interleaved DC/DC synchronous boost IGBT converter connected to an energy storage device. While the inner current control loop remains as in previous section, the frequency control scheme in Fig. 4.4 will be improved in this section.

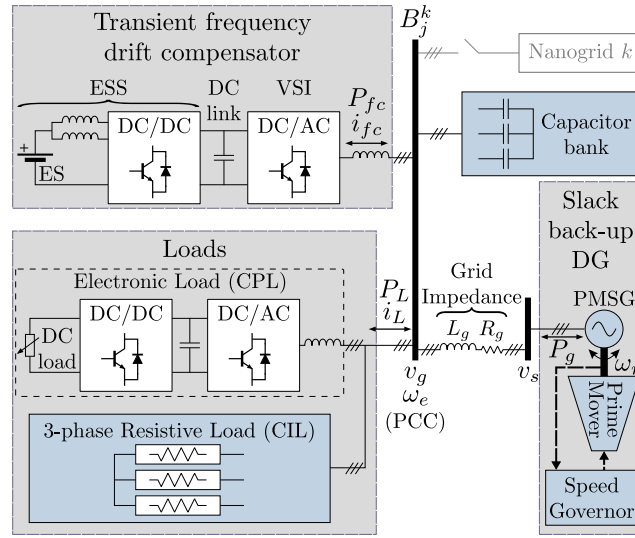


**Figure 4.6:** Integration of the frequency compensator under study in an isolated AC nanogrid arbitrary bus  $B_j^k$  governed by a distributed synchronous generator operating in slack mode.

#### 4.3.1.3 Generator model

For high-performance frequency compensation, the system dynamics must be deeply analyzed. Moreover, the system dynamic modelling becomes mandatory when using observer-based techniques. Fig. 4.7 shows the equivalent system of a synchronous generator coupled to a speed governor, where  $\omega_r$  is the rotor mechanical speed,  $C_g$  the governor controller,  $\tau_g$  the governor injected torque,  $J$  and  $b$  the generator inertia and friction coefficients,  $K_e$  and  $K_t$  the generator back electromotive force (bemf) and torque constant and  $p$  the number of pole pairs. The electrical load is represented by the parameters  $R_T$  and  $L_T$ ,  $i_L$  is the load current and  $T_L$  is the equivalent load torque.  $R_g$  and  $L_g$  represent the grid impedance, in this case, the generator stator impedance.

The generator mechanical system is coupled to its electrical counterpart, thus any change or disturbance in the electrical grid will be reflected in its mechanical system.

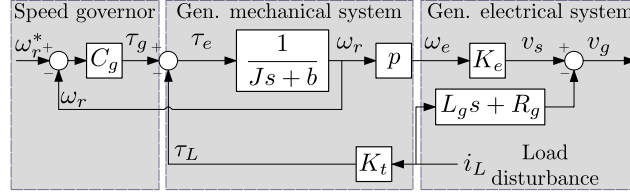


**Figure 4.7:** Equivalent block diagram of a PM synchronous generator supplying constant-impedance type loads.

When an electrical load demanding active power is suddenly connected to the grid, it will generate an equivalent load torque proportional to the load current at the generator's shaft. This torque will be seen as a disturbance by the governor, causing a speed variation which depends on the mechanical inertia and the governor control system. Considering the control system of the governor as a PI regulator in the ideal form (4.5), and neglecting the dynamic effect of the generator electrical subsystem, the disturbance transfer function  $D_g$  is given by (4.6).

$$C_g(s) = k_p \left( 1 + \frac{1}{sT_i} \right) \quad (4.5)$$

$$D_g(s) = -\frac{\omega_r(s)}{T_L(s)} = \frac{G_{gen}(s)}{1 + C_g(s)G_{gen}(s)} = \frac{\frac{1}{J}s}{s^2 + \frac{k_p + b}{J}s + \frac{k_p}{T_i J}} \quad (4.6)$$

For future use and analysis in this study,  $D_g(s)$  is reformulated by a general 2<sup>nd</sup> order expression (4.7).

$$D_g(s) = \frac{k_g \omega_{ng}^2 s}{s^2 + 2\xi_g \omega_{ng} s + \omega_{ng}^2} \quad (4.7)$$

If the governor is considered as an ideal PI regulator, the parameters are equivalent to  $k_g = \frac{T_i}{k_p}$ ,  $\omega_{ng} = \sqrt{\frac{k_p}{T_i J}}$  and  $\xi_{ng} = \frac{b + k_p}{2J\omega_{ng}}$ .

It is worth noting that not only the frequency but also the generator voltage is proportional to the mechanical speed through the bmf constant. Therefore, the compensation could positively affect both the active and reactive power sharing.

### 4.3.2 Feedback-based transient frequency compensator

The basic idea of the dynamic frequency drift compensation consists in maintaining the active power balance between the grid elements during transients. In the case under study, the transient active power mismatch between the generation and consumption in the grid will depend on the grid equivalent inertia determined by the synchronous

generators. For that reason, one of the first ideas that emerged consisted in introducing a VI by using an ESS that emulates the behavior of a synchronous generator, known in the literature as virtual synchronous machine [144]. The controller is defined by the pseudo-derivative feedback regulator (PDF), [225], given by (4.8).

$$i_{fc}^*(t) \cdot K_t = \tau_{fc}^*(t) = K_{fc} \cdot \left( w_e^*(t) - w_e(t) \right) - J_{fc} \cdot \frac{d}{dt} w_e(t) \quad (4.8)$$

Where  $\tau_{fc}^*$  is the equivalent torque generated reference ( $T_{fc}$  in the frequency domain),  $i_{fc}^*$  the current reference associated to active power ( $I_{fc}$  in the frequency domain), i.e., the  $d$ -axis current reference  $i_{id}^*$  in the case of concern,  $K_t$  is a constant that relates torque and current,  $K_{fc}$  the damping coefficient,  $J_{fc}$  the virtual inertia gain,  $w_e$  the instantaneous grid frequency and  $w_e^*$  the grid frequency reference. The conditions and constraints of the proposed solution are the following: 1) there is not communication between the proposed solution and any other system at the grid; 2) only the currents and voltages at the PCC are available; 3) the control relies on the the estimated grid frequency; 4) the method is focused on improving the transient frequency drift, limiting the power exchange between the proposed system and the grid; 5) the grid frequency command in the MG ( $w_e^*$ ) is unknown; 6) the possibility of binding the proposed solution to a significant load in the grid, gaining access to the load current, is also considered.

Under these constraints, the main problems to be tackled are summarized as:

- The frequency has to be estimated from electrical variables. The effects of measurement noise and delays as well as grid distortion over the used frequency estimation techniques must be considered.
- The transient state has to be detected in order to avoid active power injection during the steady-state. The frequency value in the steady-state must be decoupled.
- The use of derivative terms may compromise the reliability under noisy conditions.

#### 4.3.2.1 Proposed control system

The proposed system control scheme is shown in Fig. 4.8. Besides the internal current control loops, five blocks can be identified forming the compensator control:

1. Grid synchronization and frequency estimation: It provides the estimated grid angle ( $\hat{\theta}_e$ ) and the estimated grid frequency ( $\omega_{em}$ ). It is based on PLL, DSOGI-FLL techniques [236–238] or any other frequency estimation method. The transient performance has been experimentally evaluated in Fig. 4.9, using the generator speed measurement given by a resolver as a reference for red the comparison. Both PLL with low pass filter and FLL are good candidates for the frequency

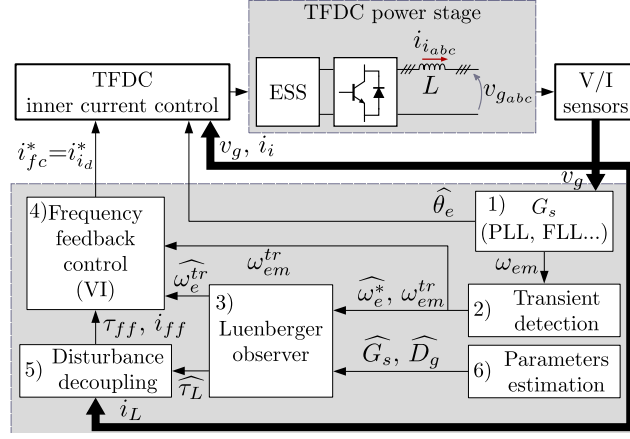


**Figure 4.8:** Control scheme for the proposed transient frequency drift compensator.

estimation. Due to its robustness under distorted grids, a DSOGI-FLL will be used in this proposal. Its dynamic transfer function will be referred henceforth as  $G_s(s)$ , modelled as the 2<sup>nd</sup> order system approximation in (4.9), obtained by curve-fitting methods.

$$G_s(s) = \frac{\omega_{em}}{\omega_e} = \frac{k_s \omega_{ns}^2}{s^2 + 2\xi_s \omega_{ns} s + \omega_{ns}^2} \quad (4.9)$$

Where  $k_s$  is the sensor gain, 1 by default, and  $\omega_{ns}$ ,  $\xi_s$  are the natural frequency and damping factor of the system respectively.

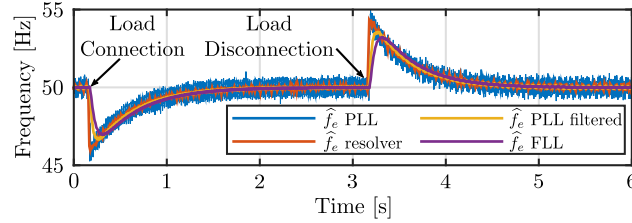


**Figure 4.9:** Experimental results for the frequency drift measurement at the PCC under the connection and disconnection of a resistive load without compensation. The used setup is defined by Fig. 4.6 and Table A.5.

2. Transient detection: To avoid steady-state compensation, the detection of the frequency transients is required and the actual grid frequency command has to be decoupled. The proposed method for obtaining the transient frequency  $\omega_{em}^{tr}$  is detailed at Section 4.3.2.2.

3. Luenberger observer: The Luenberger observer was presented in Section 3.5 of Chapter 3 as a powerful control tool for improving the sensor response, avoiding sensors and observing the disturbance of a system. The observer will play one of the main tasks in the proposed control, compensating the delay introduced by the frequency estimation block (sensor of the system). It will observe the grid frequency before the frequency estimation block ( $\widehat{\omega}_e^{tr}$ ). In addition, it can provide an estimation of the load disturbance.
4. Frequency feedback control: The main block of the control system consists in a feedback regulator able to provide a current or torque reference for the VSI ( $i_{fc}^*$ ), using the error between the frequency reference and the frequency estimation. Details for the feedback based control are given at Section 4.3.2.3.
5. Load disturbance decoupling: When the load disturbance is measured or estimated, it is possible to use it as a feed-forward ( $\tau_{ff}$ ,  $i_{ff}$ ) to improve the dynamic response [143]. Two options have been considered: one is based on the current measurement, developed at Section 4.3.2.4, and another relies on the Luenberger observer, considered at Section 4.3.3.
6. Estimated parameters: The necessary information for the implementation of the Luenberger observer ( $\widehat{D}_g$  and  $\widehat{G}_s$ ) should be estimated either on-line or off-line. In the scope of this thesis all the parameters will be known or obtained off-line.

#### 4.3.2.2 Transient detection algorithm

The transient detection issue has been already covered in previous literature by 1) using a transient detection window [185], and 2) an open loop estimator to extract the frequency reference considering a droop-controlled grid [234]. In the first case, a simple comparison of the feedback frequency and a threshold determines a transient window. However, delays, noise and harmonic distortion in the frequency estimator may lead to incorrect performance. In the second case, the open loop estimator leads to errors with any change in the estimator parameters. In this thesis, a method based on the correlation of the measured frequency with a signal of period  $T$  and zero average is proposed.

The method consists in the comparison of a correlation coefficient with a threshold, resulting in a transient window. The correlation coefficient is obtained as the square of the one period cross-correlation between an input signal  $f(t)$  and a zero average signal  $g(t)$  of period  $T$ , defined by the expression (4.10).

$$C_t(t) = \sum_{i=-\infty}^{\infty} \left( \left( \frac{1}{T} \int_{(i-1)T}^{iT} f(t) \cdot g(t) dt \right)^2 \cdot \text{rect} \left( \frac{t - T/2 - i \cdot T}{T} \right) \right) \quad (4.10)$$

$$g(t) = \sin\left(\frac{2\pi t}{T}\right) \quad (4.11)$$

Where  $C_t$  is the correlation coefficient, that update its value every period  $T$ , and  $g(t)$  can be any periodic signal with zero average over a period as (4.11). The obtained value is maintained over the period  $T$ , indicated mathematically with the rectangular function *rect*. The correlation will give low values during the steady state, while it will lead to significantly larger values during transients. When compared with a configurable threshold, a transient window will be defined by an initial time,  $t_1$ , and a final time,  $t_2$ . The practical discrete implementation in real time of the transient detection algorithm is described in the algorithm defined in Appendix B.1, using a Tustin discretization for the integral, where  $T_s$  is the sampling period used for the implementation. In the present application, the input  $f(t)$  to the transient detector will be the estimated grid frequency ( $f(t) = \omega_{em}(t)$ ).

Assuming that the grid frequency reference will have a slow variation compared to the integration interval,  $T$ , the correlation function will give low values during the steady state. On the other hand, when a transient frequency drift occurs, it will lead to larger values. The resulting behavior is similar to the use of a derivative, but without the associated noise problems. Using the correlation squared value, (4.10), a transient window is generated and any frequency out of that window is considered to be the the grid frequency reference ( $\omega_e^*$ ). The last frequency value before the transient detection is considered as the estimated reference frequency ( $\widehat{\omega_e^*}$ ). The transient detector output is the transient frequency ( $\omega_{em}^{tr}$ ), obtained as  $\omega_{em}^{tr} = \omega_{em} - \widehat{\omega_e^*}$ .

The obtained experimental results for the estimated transient frequency are shown at Fig. 4.10. Two different  $T$  values are used for the estimation:  $T = 40\text{ms}$  and  $T = 70\text{ms}$ . The correlation value is scaled by 10 to simplify the representation. Threshold value is set to 5 and the FLL bandwidth is set to 5Hz. The results are compared with respect to the measured frequency, from which the reference value has been subtracted.

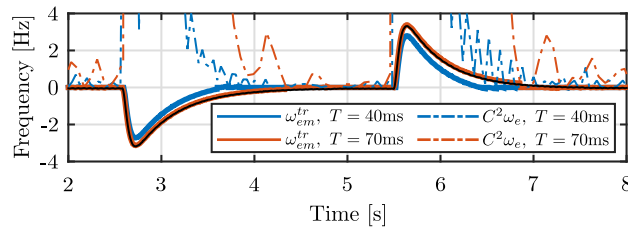


**Figure 4.10:** Experimental results for the transient frequency estimation using the proposed method. Evaluation under connection and disconnection of a resistive load at the PCC without compensation. The setup is defined by Fig. 4.6 and Table A.5.

### 4.3.2.3 Frequency feedback regulator and virtual inertia (VI)

The feedback based frequency control is shown in Fig. 4.11. The TFDC controller  $C_c$ , uses the estimated transient frequency ( $\omega_{em}^{tr}$ ), obtained from the frequency sensor and the transient detection block, to provide a control action by means of an equivalent torque command ( $\tau_{fc}^*$ ).

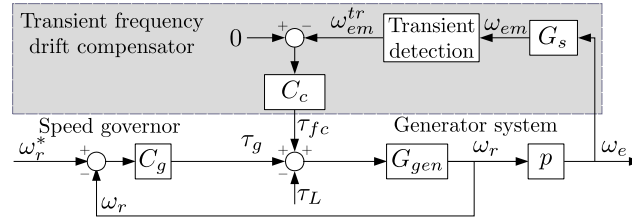


**Figure 4.11:** Proposed controller for transient frequency drift compensation in the grid model block diagram. The speed governor and generator blocks match the system presented in Fig. 4.7.

Once the TFDC is included in the system, the disturbance rejection transfer function  $\frac{\omega_r}{T_L}$  is given by (4.12)

$$D_c(s) = \frac{\omega_r(s)}{T_L(s)} = -\frac{D_g(s)}{1 + D_g(s) \cdot C_c(s) \cdot G'_s(s)} \quad (4.12)$$

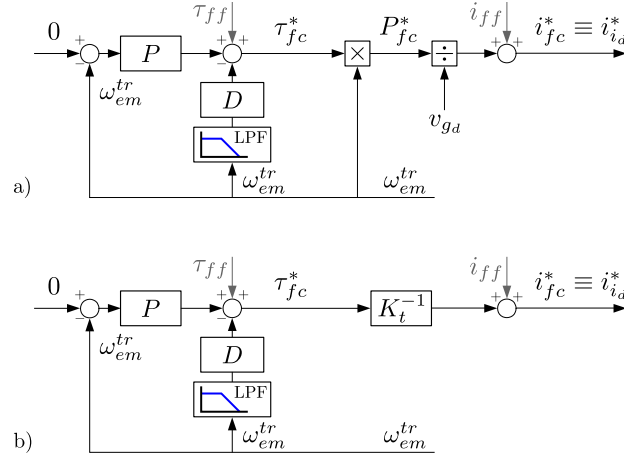
where  $G'_s(s) = G_s(s) \cdot p$ ,  $p$  is the number of pole pairs of the machine and  $G_s(s)$  the sensor transfer function.  $D_g(s)$  is the generator disturbance transfer function in (4.7). The obtained expression only applies during the transient, assuming the grid frequency reference has been already decoupled.

Fig. 4.12 shows the general scheme for the frequency controller  $C_c$ , including the torque to current conversion. The load decoupling feed-forward is considered as an optional functionality ( $\tau_{ff}$ ,  $i_{ff}$ ) to improve the system disturbance rejection. P and D are a proportional gain and derivative term ( $D(t) = K_d \frac{d}{dt}$ ) respectively.

The feedback controller may present PDF topology, defined by (4.13) or a simple P controller with null derivative term (4.14). Regarding the torque to current reference conversion, two options are considered one based on power reference and another based on a torque constant gain. The second one will be used in this section for simplification purposes, using the torque constant of the PMSG used as slack DG.

$$\text{PDF regulator} \rightarrow C_c(s) = K_p + K_d s \frac{2\pi f_{lpf}}{2\pi f_{lpf} + s} = K_{fc} + J_{fc} s \frac{2\pi f_{lpf}}{2\pi f_{lpf} + s} \quad (4.13)$$

$$\text{P regulator} \rightarrow C_c(s) = K_p = K_{fc} \quad (4.14)$$



**Figure 4.12:** Pseudo-derivative feedback (PDF) structure for the TFDC. a) Torque to current reference conversion using power calculation; b) Simplified torque to current reference calculation using a torque constant gain  $K_t$ .

Where  $K_p$  and  $K_d$  are the proportional and derivative gains of the compensator. These two gains are equivalent to the damping coefficient  $K_{fc}$  and the virtual inertia  $J_{fc}$  in (4.8) respectively. The variable  $f_{lpf}$  is the cut-off frequency of the low-pass filter associated to the derivative term.

The different alternatives are compared based on their dynamic stiffness, defined as (4.15).

$$S_c(s) = \frac{T_L(s)}{\omega_r(s)} = \frac{1 + D_g(s) \cdot C_c(s) \cdot G'_s(s)}{D_g(s)} \quad (4.15)$$

Fig. 4.13 shows the dynamic stiffness evaluated in frequency domain and the corresponding transient response in time domain for two different P and PDF settings. Two different proportional gains providing two different gain margins (GM) are used. In the case of the PDF, a minimum phase margin of  $60^\circ$  is set at the open-loop crossover frequency in both cases. The graph shows the benefits of an increased proportional gain and the improved disturbance rejection capability provided by the inclusion of the differential term. As shown in time domain, the predicted benefits for including the differential term are translated to a reduced initial overshoot when compared to the P method.

Finally, the experimental results for the feedback-based compensation are shown in Fig. 4.14. A good agreement with respect to the previous theoretical discussion can be observed.

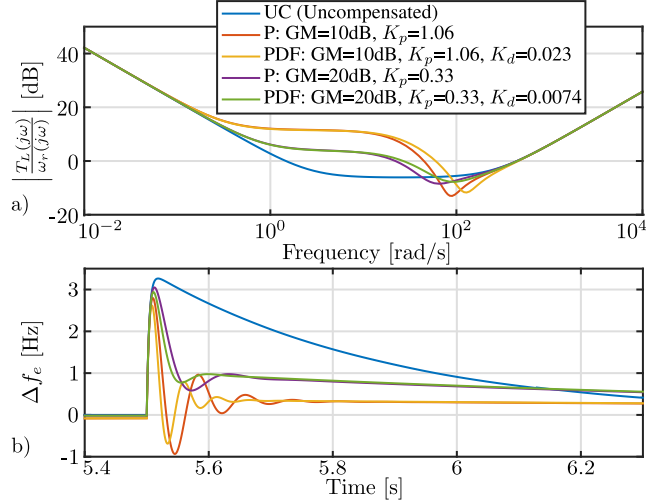


**Figure 4.13:** Performance comparison of the P and PDF methods. a) Dynamic stiffness. b) Transient response.

#### 4.3.2.4 Load feed-forward and estimation

Enhanced dynamic response for the transient frequency drift controller can be obtained by the use of feed-forward disturbance decoupling and the increase of the frequency estimation bandwidth by using a Luenberger type observer.

If the load demand is available, it can be used as a feed-forward for the controller, as shown in Fig. 4.12. Ideally, if the load is fully known, the frequency drift will be eliminated (grey line in Fig. 4.14). However, that solution would lead to the compensation of the whole load power also during steady state. In order to compensate only the transient and keep the grid frequency unalterable, the ESS has to provide the difference between the load power and the power shared by the generator, i.e. the equivalent torque of the compensation system should be  $T_{fc} = T_L - T_g$ . Nevertheless, in the present system, the generator information is not available as none communication links between the frequency compensator and the distributed generator are assumed. However, the load information is still a valuable information as it is a derivative state of the frequency, allowing to anticipate the control reaction.

Fig. 4.14 shows the experimental performance comparison for the different feed-back methods, considering different configurations, and the response when a load feed-forward is used. The shown signals correspond to the DSOGI-FLL frequency signal using a FLL BW = 25Hz. UC stands for the uncompensated case. P+FF and PDF+FF are the combination of P and PDF with a load feed-forward respectively. The feed-forward is filtered by a 2<sup>nd</sup> order high-pass filter with bandwidth=0.5Hz. FC stands for the full load compensation obtained by equaling the D-STATCOM current refer-

ence to the load current. In this example, the load information comes from a load current sensor, which is a valid assumption if the proposed solution is to be coupled to a significant load.

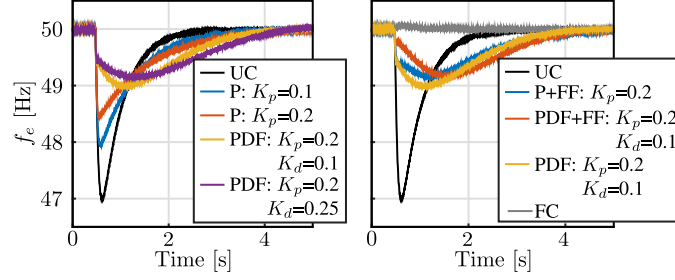


**Figure 4.14:** Transient frequency drift compensation using different control methods under load connection transient. The setup is defined by Fig. 4.6 and Table A.5. Further details on the experimental setup are given at Appendix A.6. The shown signals are estimated by a DSOGI-FLL.

### 4.3.3 Observer-based transient frequency compensator

The main purpose of the observer is to provide a transient frequency drift estimation by providing a nearly zero phase-lag  $\widehat{\omega}_e^{tr}$  estimation within the observer bandwidth. This will boost the response of the TFDC, being able to compensate frequency drift transients usually affected by the PLL/FLL bandwidth restrictions. Additionally, the proposed observer also provides an estimation of the load disturbance that could be used for the feed-forward compensation replacing the  $\tau_{FF}$  measurement by the estimated load  $\widehat{\tau}_L$ . Although the analysis proposes the use of such a load estimation,  $\widehat{\tau}_L$ , it is not used or validated in this study, being part of future development.

#### 4.3.3.1 Observer-based control topology for transient compensation

The proposed Luenberger-based observer control is shown in Fig. 4.15, where  $C_o$  represents the transfer function of the observer regulator. It is worth to point out that in the case the observer is not used,  $\omega_{em}^{tr}$  will be the feedback variable for the close loop frequency controller  $C_c$ .

As the generator and governor parameters are unknown, the  $C_g$  and  $G_{gen}$  transfer functions cannot be explicitly used in the proposed solution. However, the approximations proposed before for the sensor and the generator disturbance transfer functions (4.7), are appealing candidates for the observer implementation. The experimental comparison between the proposed approximations and the real systems are shown in Fig. 4.16. A really good matching is clearly observed.

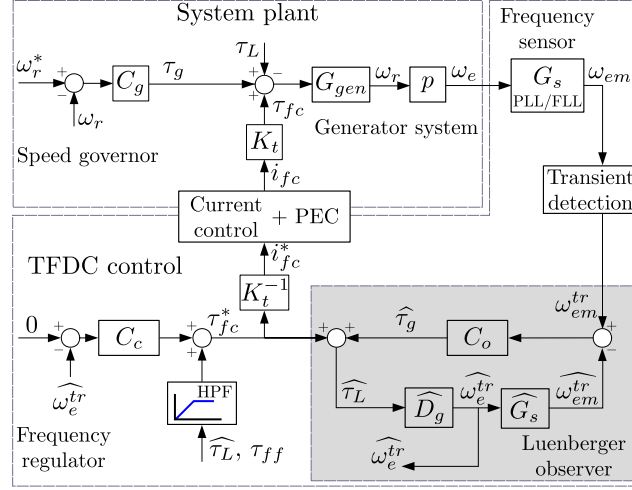


Figure 4.15: Proposed observer-based frequency control structure. The use of  $\widehat{\tau}_L$  is optional.

#### 4.3.3.2 Luenberger observer plant model

The system plant considered for the observer implementation is represented by the state space model shown in Fig. 4.17. The model is defined by the state vector  $\mathbf{x} = [x_1, x_2, x_3, x_4]^T$ , the input vector  $\mathbf{u} = [\tau_L]$  and the output vector  $\mathbf{y} = [\omega_e, \omega_{em}]^T = [p \cdot x_1, x_3]^T$ . The state ( $\mathbf{A}$ ), input ( $\mathbf{B}$ ), output ( $\mathbf{C}$ ) and feed-forward ( $\mathbf{D}$ ) matrices are defined in (4.16) and (4.17).

$$\frac{d}{dt}\mathbf{x}(t) = \mathbf{A} \cdot \mathbf{x}(t) + \mathbf{B} \cdot \mathbf{u}(t) \quad (4.16)$$

$$\mathbf{y}(t) = \mathbf{C} \cdot \mathbf{x}(t) + \mathbf{D} \cdot \mathbf{u}(t) \quad (4.17)$$

$$\mathbf{A} = \begin{bmatrix} -2\xi_g\omega_{ng} & -\omega_{ng}^2 & 0 & 0 \\ 1 & 0 & 0 & 0 \\ 0 & 0 & 0 & 1 \\ k_s p \omega_{ns}^2 & 0 & -\omega_{ns}^2 & -2\xi_s\omega_{ns} \end{bmatrix} \quad \mathbf{B} = \begin{bmatrix} k_g\omega_{ng}^2 \\ 0 \\ 0 \\ 0 \end{bmatrix} \quad (4.18)$$

$$\mathbf{C} = \begin{bmatrix} p & 0 & 0 & 0 \\ 0 & 0 & 1 & 0 \end{bmatrix} \quad \mathbf{D} = \begin{bmatrix} 0 \\ 0 \end{bmatrix} \quad (4.19)$$

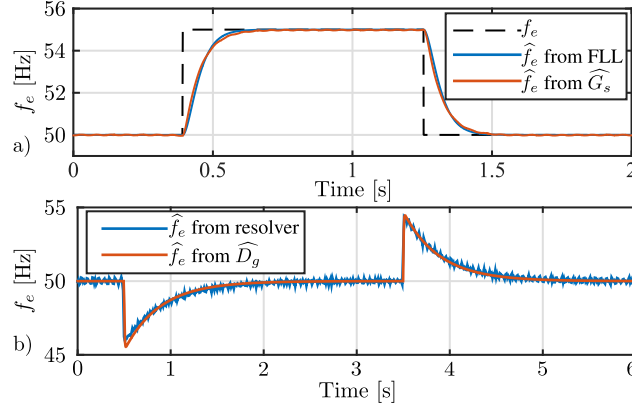


**Figure 4.16:** Experimental results. a) DSOGI-FLL response and its approximation using the 2<sup>nd</sup> order transfer function  $\hat{G}_s$ . b) Open-loop response obtained with the estimation of the disturbance transfer function  $\hat{D}_g$  compared with the frequency measured by the generator resolver.

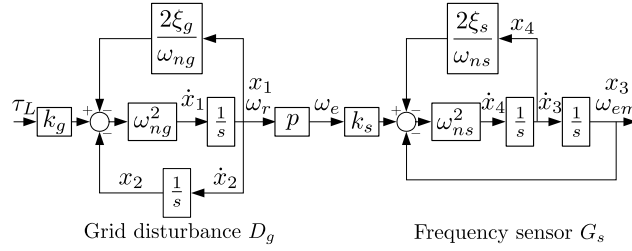


**Figure 4.17:** Block diagram of the observer plant in state space representation.

#### 4.3.3.3 Dynamic analysis of the observer-based frequency compensator

The dynamic stiffness for the proposed observer block diagram, assuming parameters matching between the real and the observed systems, is defined by (4.20).

$$\frac{T_L(s)}{\omega_e(s)} = \frac{1 + \hat{D}_g(s) \cdot C_o \cdot \hat{G}_s(s)}{1 + \hat{D}_g(s)(C_c(s) + C_o(s) \cdot \hat{G}_s(s))} \quad (4.20)$$

The observer controller,  $C_o(s)$ , consists in a 4<sup>th</sup> order transfer function, presenting the same order as the observed plant. It has been tuned in frequency domain using loop-shaping, trying to maximize the bandwidth while giving enough stability margin. The selected values are listed in Table A.5. The resulting frequency and transient responses comparing the proposed observer technique and the FLL feedback technique are shown in Fig. 4.18 and Fig. 4.19. The uncompensated and ideal sensor cases are shown as a reference. Ideal sensor case is defined as frequency feedback control with

$G_s(s) = 1$ , i.e., there is not phase lag introduced by the frequency estimation. As it can be seen, the use of the observer noticeably improves the initial transient response due to the compensated sensor lag. Moreover, in Fig. 4.19, the transient response of the design system (left  $\omega_{ns} = 31.4$  rad/s), is compared with the response when the bandwidth of frequency sensor is reduced by four (right  $\omega_{ns} = 7.85$  rad/s), without changing the observer regulator parameters. The proposed observer-based method still presents a better response than the alternatives.

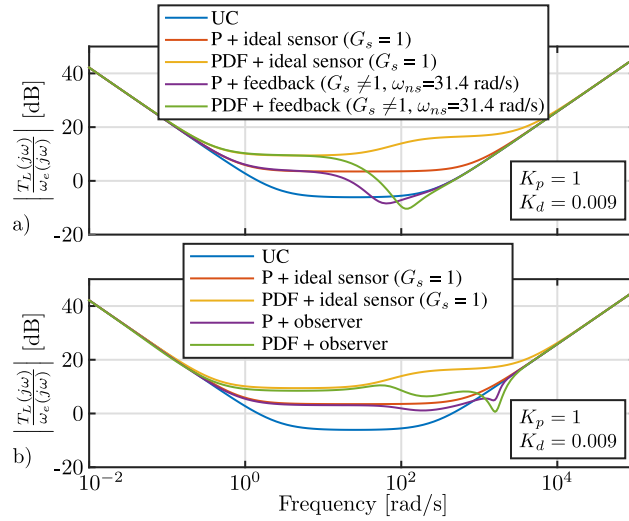


**Figure 4.18:** Dynamic stiffness. a) Results for the feedback-based control. b) Observer-based control. The uncompensated and ideal sensor cases are shown as a reference.

#### 4.3.4 Experimental results

The proposed frequency drift compensator has been experimentally evaluated through the experimental setup described in Appendix A.6. The disturbances created by the different load types in the experimental MG, allow to test the effectiveness of the proposed observer-based compensator under a variety of conditions, enabling the comparison between the different existing methods which have been analyzed in this section. It is worth noting that the grid frequency shown in the experimental results has been obtained using the speed resolver included in the industrial drive.

The experimental results are obtained under two scenarios:

1. In the first scenario, the frequency variation for the evaluation of the TFDC is created by a load disturbance consisting in the connection and disconnection of a three-phase balanced resistive load. This test allows to characterize and compare the different methods evaluating the response under a step disturbance, avoiding to have unwanted disturbances in the middle of a transient.

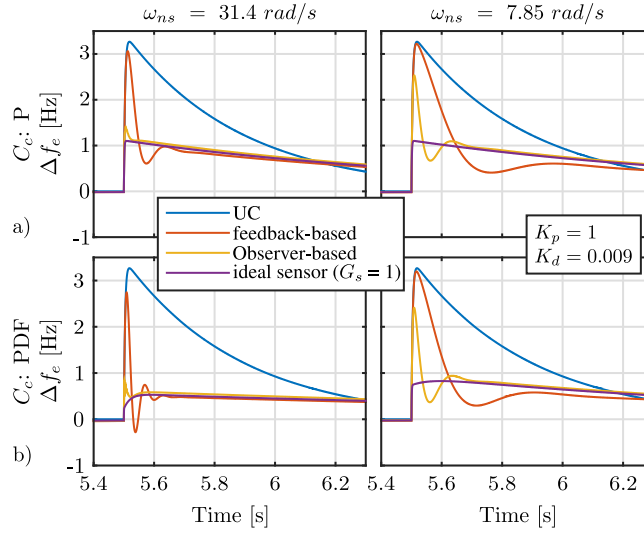


**Figure 4.19:** Transient response comparison for two different DSOGI-FLL bandwidth  $\omega_{ns}$ . a) P controller. b) PDF controller. Both cases are analyzed considering different feedback signals.

2. In the second scenario, a more realistic load behavior is pursued. In this case, the load disturbance is a CPL generated by the PECs-based dynamic load emulator. This second scenario allows to demonstrate the advantages of the proposed observer and its viability in a realistic MG environment, where the PECs operation might be compromised by the transient frequency and voltage magnitude drifts.

#### 4.3.4.1 Experimental case 1: balanced resistive load disturbance

A comparison of the transient response for the feedback and feed-forward methods is shown in Fig. 4.20 for the first scenario. The load feed-forward is implemented using the measured load current, applying a 1<sup>st</sup> order high-pass filter with a cut-off frequency of 0.5Hz. The performance of the proposed observer-based solutions for the first scenario is shown in Fig. 4.21 compared with the feedback methods. As expected, feed-forward and the proposed observer-based methods have the best performance in terms of frequency compensation. Assuming that feed-forward methods need for extra sensors or/and communication, the proposed observer methods, that just depend on the voltage measurements at the PCC, are a promising alternative, offering an extra compensation at the beginning of the transient, reducing the maximum frequency deviation. In this particular case, for the selected parameters, the proposed methods P+Obs and PDF+Obs reduce the maximum frequency deviation in around 1Hz when compared with P and PDF methods without observer, i.e., using  $\omega_e^{tr}$  instead of  $\widehat{\omega}_e^{tr}$ .

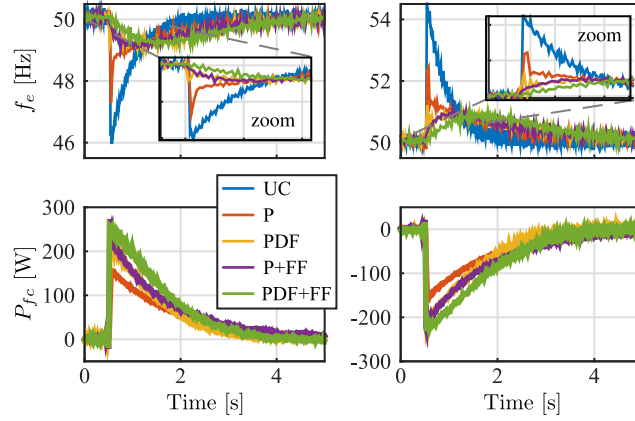


**Figure 4.20:** Experimental results for the first scenario. Top: grid frequency obtained with the resolver. Bottom: power injected by the compensator. Left: load connection. Right: load disconnection.

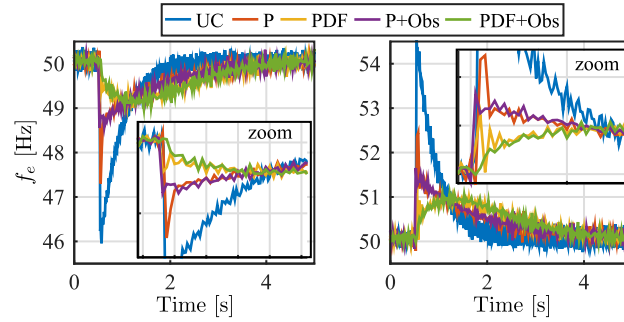


**Figure 4.21:** Experimental results for the first scenario. Results using the proposed observer-based method. Grid frequency obtained with the resolver. Obs stands for observer-based compensation.

Although it has not been applied or tested in this thesis, the observer provides an additional useful information. The observed load current, obtained from the estimation of  $\widehat{\tau}_L$ , is represented in Fig. 4.22. As shown, the transient load disturbance can be estimated by a high-pass filter. This load estimation enables the implementation of a load feed-forward decoupling mechanism without the need for measuring the load current.

#### 4.3.4.2 Experimental case 2: CPL profile disturbance

The results obtained for the second scenario using the PELs-based dynamic load emulator are shown in Fig. 4.23, for P and P+Obs methods, and in Fig. 4.25, for

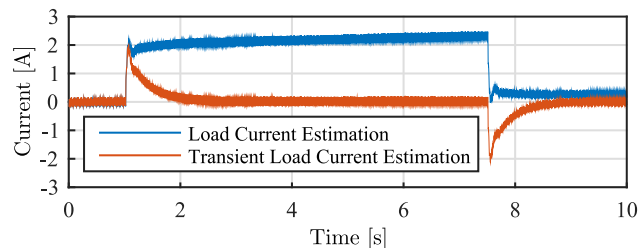


**Figure 4.22:** Experimental results. Load current estimated by the observer. Full load current and transient load disturbance obtained by a 1<sup>st</sup> order high-pass filter with BW = 0.5Hz. The load current is 2.2A.

PDF and PDF+Obs. The frequency, the power drawn by the load emulator and the power injected by the TFDC are represented. It is clearly seen the improvement in the the frequency profile with all methods when compared with the uncompensated case. In order to better compared them, Fig. 4.24 and 4.26 show the detailed view of the critical transients in the system.

The conclusions drawn from the experimental results can be summarized as: 1) for all the cases, the observer-based methods provide a reduction on the maximum frequency deviation when compared with the FLL feedback methods; 2) The maximum deviation is reduced by more than 1Hz in the case of P+Obs when compared with P and 3) when differential action is added, the proposed PDF+Obs method improves the frequency drift by more than 0.5Hz when compared with the PDF. All this conclusions demonstrate the viability and superiority of the proposed methods for fast frequency drift compensation.

Finally, a last test was performed in order to evaluate the limits of the different compensation methods under significant load steps. Fig. 4.27 shows the response of the system under 3 load steps, for five cases: uncompensated, P, P+Obs, PDF and PDF+Obs. The figure does not only show the effect of load disturbances in the frequency but also in the voltage magnitude, which is affected due to the generator impedance and the coupling between its speed and voltage. As shown in Fig. 4.27, at  $t = 0.2s$ , a load step of 600W is applied. Under this load condition, the load emulator trips for the uncompensated scenario due to an overcurrent as a result of the voltage magnitude and frequency distortion. At  $t = 0.6s$ , a load step of 750W is commanded. For this load value. the emulator trips for the P method, while it continues its operation for the rest of the methods. At  $t = 1s$ , when a 1kW load is applied, the emulator trips for the P+Obs and PDF methods, being still responsive when PDF+Obs is used for the compensation. This demonstrates the extended range of operation allowed by the proposed observer-based methods for transient frequency drift compensation.

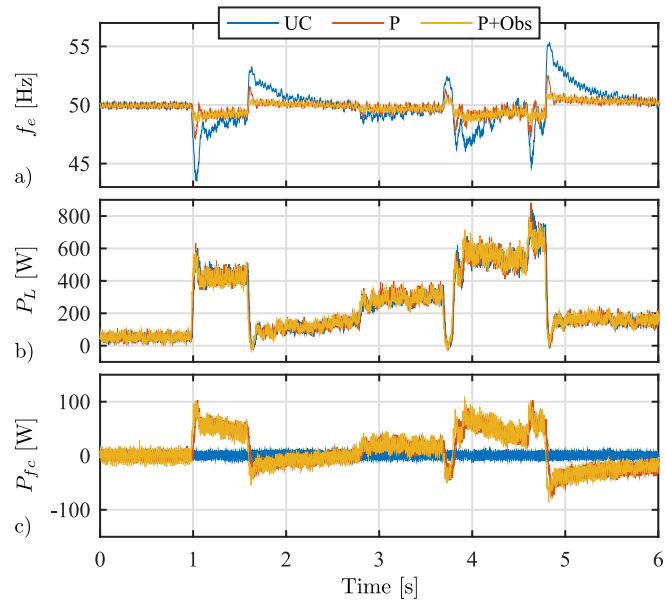


**Figure 4.23:** Experimental results using the dynamic load emulator. a) grid frequency obtained with the drive resolver. b) load power consumption. c) active power injected by the compensator.  $P$  regulator and  $P + Obs$  are compared.

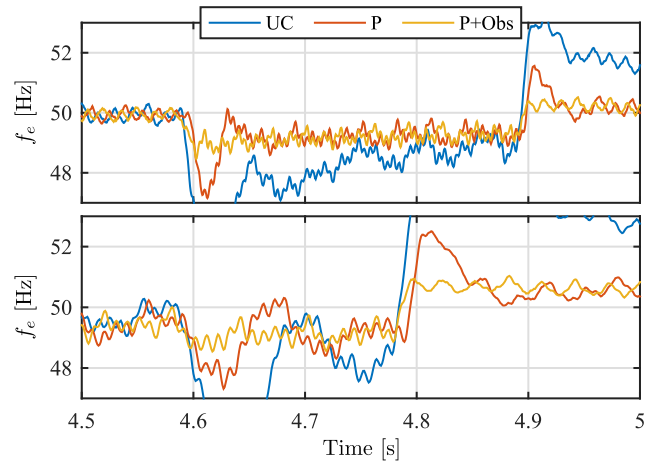


**Figure 4.24:** Detailed view of the experiment in Fig.4.23. Top: time zoom from  $t = 0.5$ s to  $t = 1.5$ s. Bottom: time zoom from  $t = 4.5$ s to  $t = 5$ s.

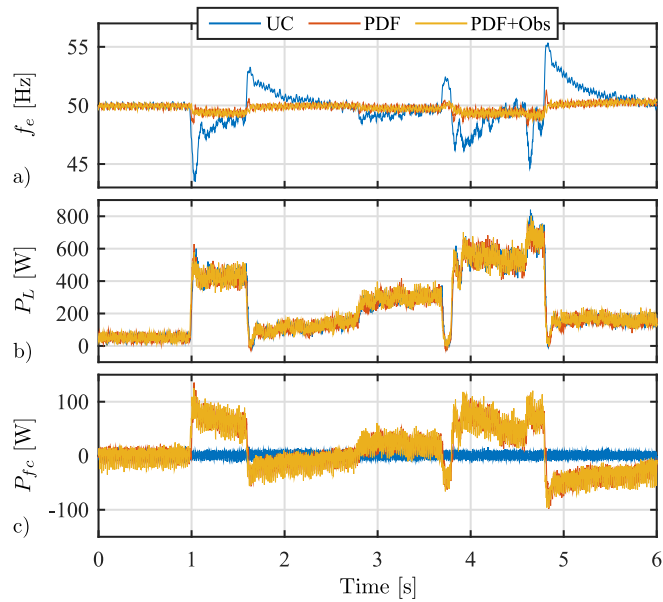


**Figure 4.25:** Experimental results using the dynamic load emulator. a) grid frequency obtained with the drive resolver. b) load power consumption. c) active power injected by the compensator. *PDF* regulator and *PDF + Obs* are compared.

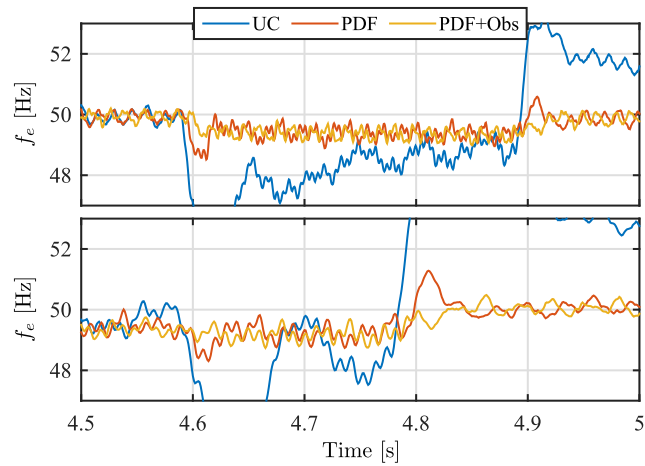


**Figure 4.26:** Detailed view of the experiment in Fig. 4.25. Top: time zoom from  $t = 0.5$ s to  $t = 1.5$ s. Bottom: time zoom from  $t = 4.5$ s to  $t = 5$ s.

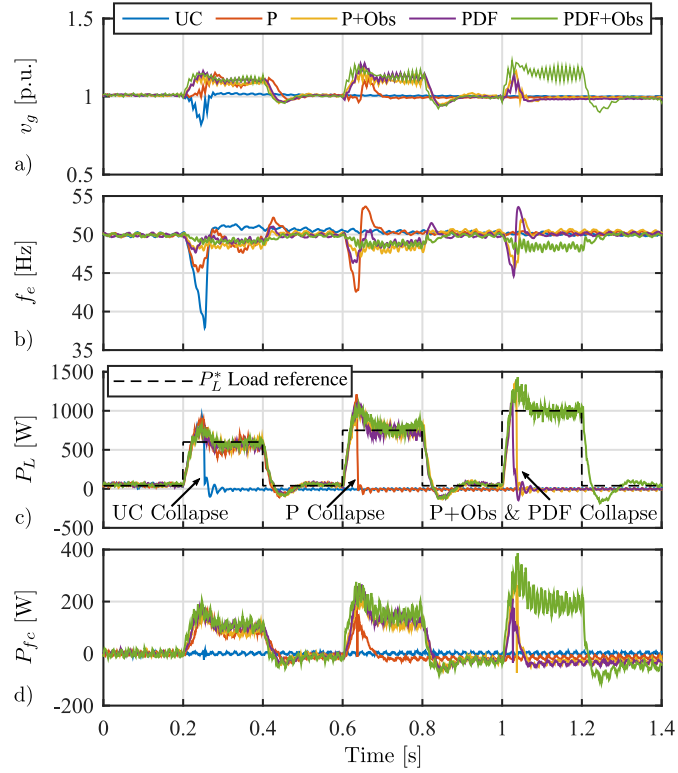


**Figure 4.27:** Performance of the compensation methods under different load step disturbances introduced by the dynamic load emulator in order to evaluate the system robustness. a) Voltage magnitude at the PCC. b) Grid frequency obtained with the drive resolver. c) Load power consumption. d) Active power injected by the compensator.

#### 4.3.4.3 Figures of merit: method comparison for the experimental case 1

As a figure of merit, a comparative evaluation of the analyzed techniques under the first scenario has been done, summarizing their performance in Fig. 4.28. Six indexes have been considered to characterize each method under a load transient using the results exposed in Section 4.3.4.1. They have been normalized with respect to the worst case. The indexes are graphically represented in Fig. 4.28 and are defined as follows:

- $\Delta f_{max}$ : Maximum grid frequency deviation, calculated as the initial frequency minus the frequency nadir.
- RoCoF: Maximum rate of change of frequency, i.e., maximum  $df/dt$ .

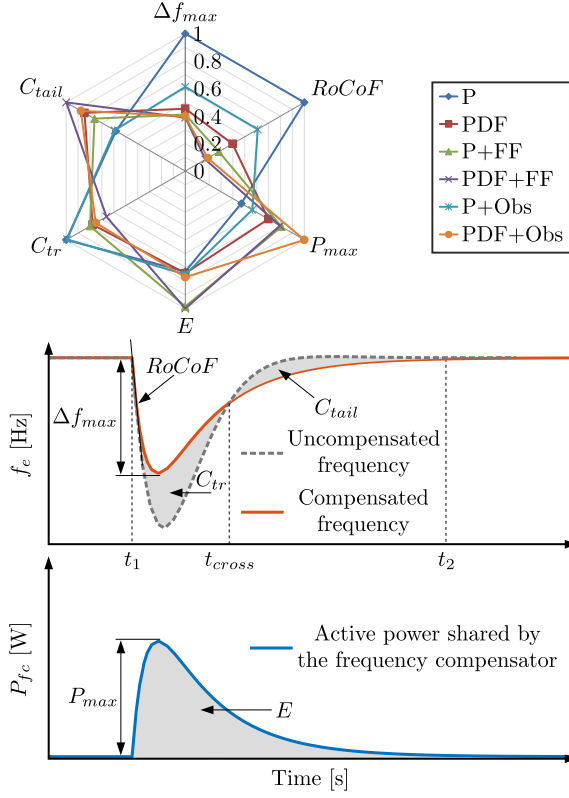


**Figure 4.28:** Figures of merit. Performance comparison for all the considered frequency compensation methods.  $\Delta f_{max}$ : maximum frequency deviation,  $RoCoF$ : maximum  $df/dt$ ,  $P_{max}$ : peak power of the frequency compensator  $E$ : total shared energy by the frequency compensator,  $C_{tr}$ : initial transient deviation coefficient,  $C_{tail}$ : settling time coefficient.

- $P_{max}$ : Maximum peak power shared by the transient frequency drift compensator.
- $E$ : Total energy shared by the frequency compensator during the transient.
- $C_{tr}$ : Initial transient deviation coefficient. It is defined as an index to highlight the initial deviation of frequency when compared with the original uncompensated case. The coefficient is calculated as (4.21), where  $\Delta f_{UC}$  and  $\Delta f_{comp}$  are the frequency deviation in the uncompensated and compensated cases respectively,  $t_1$  is the initial time of the transient and  $t_{cross}$  is the instant at the first crossing of  $\Delta f_{UC}$  and  $\Delta f_{comp}$ .

$$C_{tr} = \left( \int_{t_1}^{t_{cross}} |\Delta f_{UC}| - |\Delta f_{comp}| dt \right)^{-1} \quad (4.21)$$

- $C_{tail}$ : Tail deviation coefficient. It is defined as an index to highlight the settling tail (settling time) after the transient when compared with the original case. The index is calculated as (4.22), where  $t_2$  is the final time of the transient.

$$C_{sett} = - \left( \int_{t_{cross}}^{t_2} |\Delta f_{UC}| - |\Delta f_{comp}| dt \right) \quad (4.22)$$

This last figure has summarized the most important characteristics of each technique and highlights the benefits of the observer-based frequency compensation. It is clearly demonstrated how the maximum frequency deviation and RoCoF are improved (reduced) with the observer-based methods (P+Obs and PDF+Obs) when compared to the FLL sensor-based (P and PDF), presenting the PDF+Obs similar  $\Delta f_{max}$  than the load feed-forward method (PDF+FF). In the case of peak power, the observer-based and feed-forward techniques present a higher power requirement when compared to their basic versions. However, although the feed-forward methods present higher energy consumption, all the rest techniques exhibit a similar energy requirements. Regarding the initial and tail deviation coefficients ( $C_{tr}$  and  $C_{tail}$ ), it is clear how the P and P+Obs methods provides less compensation during the initial transient, but also offer a higher compensation during the transient tail, expecting a reduced settling time when compared to the other methods. At a glance, it is worth to point out that in general, the PDF methods offer lower  $\Delta f_{max}$  and RoCoF at the expense of higher peak power and energy needs.

Considering this discussion and the extended robustness of the observer-based compensation shown previously in 4.27, this section has proposed a solution for transient frequency drift compensation that improves the performance of existing methods based only in the frequency estimation by means of PLLs and FLLs. In addition to the benefits achieved when using similar control gains ( $K_p$  and  $K_d$ ), the increase in phase and gain margins given by the observer estimation is expected to allow higher gains than the existing methods within stability limitations.

#### 4.4 Predictive sequence estimator for control of grid-tied converters under highly distorted conditions

The importance and necessity of an accurate phase estimation in AC grid-tied converters has been discussed during the literature review in Chapter 2, and along the document, being an essential block in all of the covered control strategies applied to AC. The previous section has highlighted the importance of an instantaneous and precise frequency estimation when compensating frequency transients. However, the synchronization with the AC grid becomes necessary in the inner control loops (current

and voltage) for any grid-tied device. As expected in weak systems as MGs, the grid voltage and current can have a higher distortion, within the regulation limits, than traditional distribution systems. This has been already seen in previous section, where the frequency and voltage magnitude was subject to sudden changes when one nanogrid node is isolated from the rest of the MG, becoming a critical weak system that can lead to the miss-operation of grid-tied converters. In addition to voltage magnitude and frequency changes, the distortion can appear as phase jumps, harmonics, and unbalances in the case of single-phase grid-tied devices or contingencies.

This section present a method for the estimation of the phase and magnitude of positive, negative sequence and harmonic components based on the Goertzel algorithm. The method is able to operate under distorted grid conditions. The proposed strategy is suitable for synchronization with a distorted grid, and for closed-loop applications where the positive, negative or additional harmonics have to be tightly controlled, offering a considerably fast response.

#### 4.4.1 The Goertzel algorithm

The proposed method relies on an efficient implementation of the Discrete Fourier Transform (DFT) by using the sliding Goertzel transform (SGT) [290], suitable for the extraction of harmonic components in real-time applications. The algorithm presents a lower computational burden when compared with traditional FFT-based (Fast Fourier Transform) approaches for a low number of harmonics. Specifically, for calculating  $M$  harmonics from an input data vector of length  $N$ , the associated cost of the Goertzel algorithm can be expressed as  $O(N, M)$ , whereas for the FFT is  $O(N, \log_2 N)$ , where  $O$  is the number of operations. Obviously, when the number of calculated harmonics meets  $M \leq \log_2 N$ , the Goertzel approximation becomes the preferred choice. In the scope of this thesis, assuming a 50Hz nominal frequency, and a 10kHz sample rate, one fundamental cycle leads to a time window of 20ms and 200 samples. With the proposed parameters, the calculations using the Goertzel approach are faster than the FFT alternative when the calculated number of frequency components is  $M \leq 8$ . The algorithm description in pseudo-code and the block diagram for the implementation are shown in the Algorithm 2 and Fig. B.1 Appendix B.2.

In order to understand the SGT, it is useful to compare its dynamic response with the one obtained with the standard Goertzel algorithm. The transfer function of the Goertzel algorithm in the  $z$  domain is given by (4.23). The frequency component to be analyzed is defined as  $\omega_h = 2\pi h/N$ , where  $h$  is the harmonic order ( $h = 1$  for the fundamental component). The corresponding frequency response is shown in Fig. 4.29 for  $h = [1, -3, 5, -7]$ . As it can be seen from the frequency response, the Goertzel algorithm works as a resonator at the specified  $\omega_h$  frequencies.

$$H_{gh} = \frac{1 - e^{-j\omega_h} z^{-1}}{1 - 2 \cos(\omega_h) z^{-1} + z^{-2}} \quad (4.23)$$

For the sliding Goertzel implementation, the  $z$  domain expression is given by (4.24).

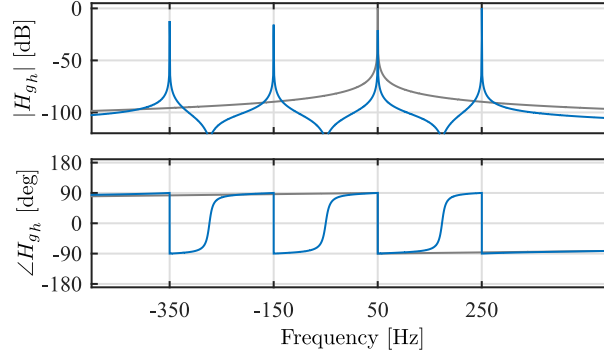


**Figure 4.29:** Goertzel algorithm frequency response for a complex signal with harmonics  $h = [1, -3, 5, -7]$ . In blue the overall response is shown, in gray the response when the algorithm is tuned only for  $h = 1$  (fundamental).

When compared to (4.23), the sliding implementation voids the output after  $N$  samples. This is due to the modified numerator term,  $1 - z^{-N}$ . By splitting the expression in two terms, the first one is equal to  $H_{g_h}$  (standard Goertzel transform) and the second one to  $z^{-N}H_{g_h}$ . The corresponding frequency response is shown in Fig. 4.30. In this case the response present a sidelobe structure with the main lobes located at the specified  $\omega_h$  frequencies.

$$H_{sg_h} = \frac{(1 - e^{-j\omega_h} z^{-1})(1 - z^{-N})}{1 - 2 \cos(\omega_h)z^{-1} + z^{-2}} = H_{g_h} (1 - z^{-N}) \quad (4.24)$$

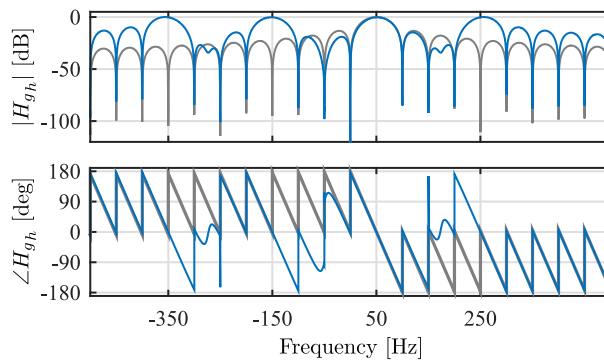


**Figure 4.30:** Sliding Goertzel algorithm frequency response for a complex signal with harmonics  $h = [1, -3, 5, -7]$ . In blue the overall response is shown, in gray the response when the algorithm is tuned only for  $h = 1$ .

The use of Goertzel-based techniques for sequence extraction requires to measure the grid phase to neutral voltages at the PCC of the grid-tied devices ( $v_{g_{abc}}$ ), and to transform them to the stationary reference frame ( $v_{g_{\alpha\beta}}$ ). The real and the imaginary part  $v_{g_{\alpha\beta}} = v_{g_{\alpha}} + jv_{g_{\beta}}$  are used as inputs to the Goertzel algorithm described in Appendix B.2. A comparison for the impulse response and the poles and zeros map in both the standard Goertzel implementation and sliding approach is shown in Fig. 4.31 for the discrete domain. As shown, the differences are related to the duration of the impulse response. For the case of the standard Goertzel approach, the impulse response is a pure resonator at the frequency of the tracked harmonics (only the fundamental is shown for illustration purposes). For the case of the sliding Goertzel, the impulse response duration is limited to the duration of the processing window ( $N$  samples), corresponding in this case to 20ms. The duration of the signal leads to zero padding in the sliding Goertzel transform, explaining the sidelobes in the frequency domain.

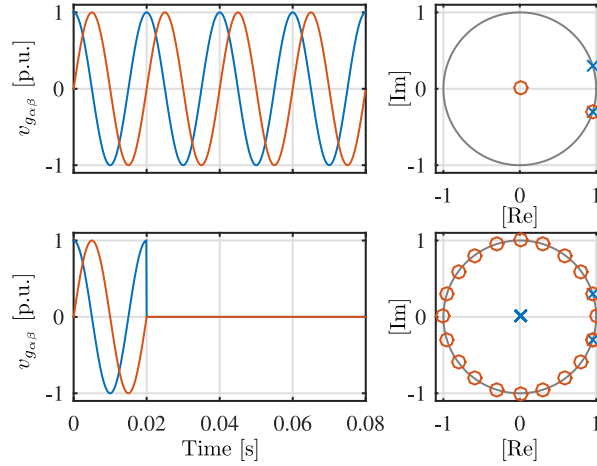


**Figure 4.31:** Impulse response and pole/zero map. Goertzel method on the top and the Sliding Goertzel modification on the bottom. For illustration purposes  $N = 20$  and  $h = 1$  are used.

#### 4.4.2 The predictive sliding Goertzel-based sequence estimator

The proposed sequence estimator will be based on a modification of the SGT, applying predictive techniques. To start with, the Goertzel transform and the SGT will be analyzed for a 3-phase system. A comparison between the estimation given by the standard Goertzel and the SGT with respect to the actual harmonic magnitudes and phases is shown in Fig. 4.32. For the analysis of the system, the harmonics detailed in Table A.6 in Appendix A.7 are used.

As it is shown, when the input signal is at steady state during the selected 20ms

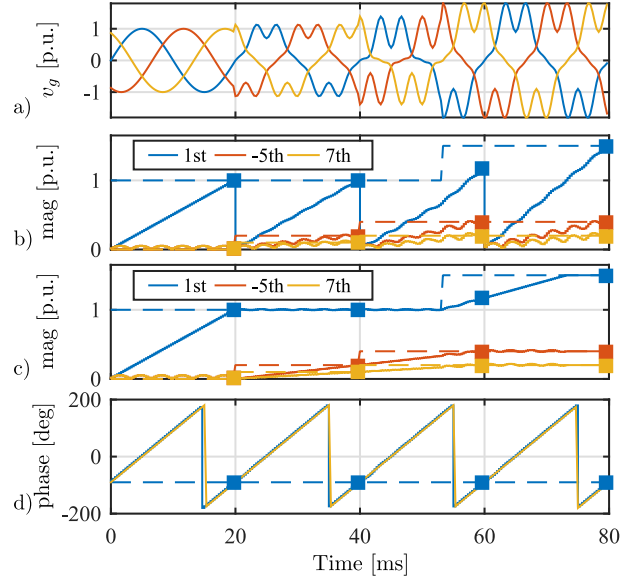


**Figure 4.32:** Sliding Goertzel estimation for a three-phase system with the harmonic contents shown in Table A.6. The dotted lines correspond to the real value of each of the harmonics. The square dots represent the estimated value at the end of each block. a) waveforms, b) Goertzel and c) SGT estimation, d) phase.

window, the SGT estimation converges to the right values. Two important conclusions can be drawn from the represented graphs:

1. For the standard Goertzel represented in Fig. 4.32b), the estimation procedure is discontinuous, being the current harmonic value only reached at the end of the current processing window and restarted at the beginning of the next one. Obviously, this invalidates the method to be directly used in converter real-time control applications. Alternatively, the SGT approach represented in Fig. 4.32c) allows for a continuous estimation. This is the selected choice in this research.
2. The estimated magnitude needs the total number of samples and time,  $N = 200$ ,  $t = 20\text{ms}$ , to converge to the correct value. This would lead to an unacceptable delay when the estimation is used as a feedback signal. However, it can be also seen that the evolution of the fundamental component ( $1^{\text{st}}$  harmonic) estimation is linear during the estimation window and barely affected by the harmonic content.

In order to overcome this last issue, the proposal in this thesis is to incorporate a predictive SGT implementation, named P-SGT, that improves the convergence speed

and, at the same time, avoids the extra calculations derived from the overlapping. The predictive behavior is implemented by a two-step algorithm:

- Firstly, a linear sliding least squares estimation (LSE) is run over the output of each SGT sample. This will lead to a linear representation of the corresponding datapoints, characterized by a slope  $\overline{m}_{le}$ , and an offset  $n_{le}$  updated at the start of each estimation window. It is worth to point out that, as the output values of the SGT are complex, two different least squares estimation can be obtained: one for the module and another one for the phase. Even considering this linear condition both for the magnitude and the phase estimation, an accurate phase estimation can be obtained before each window is completed with the SGT algorithm. Thus, in the scope of this research, the phase estimation will be directly obtained from the SGT algorithm.
- Secondly, the module value at the end of the estimation window is predicted. This is implemented at each step by considering the linear evolution expressed in (4.25).

$$\widehat{y}_N[n] = y[n] + \overline{m}_{le}[n] \cdot [N - n] \quad (4.25)$$

Where  $\overline{m}_{le}[n]$  is the moving average slope estimated by the LSE approach,  $N$  the window size,  $n$  the actual sample,  $y$  the output of the SGT and  $\widehat{y}_N$  the predicted signal at the end of the estimation window. A graphical description for the algorithm is shown in Fig. 4.33.

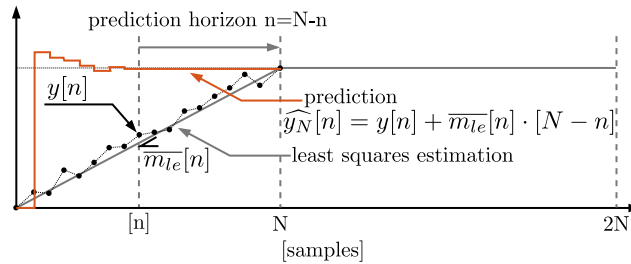


**Figure 4.33:** Graphical representation of the proposed predictive algorithm. The slope at each of the points is filtered by a moving average filter for reducing the derivative noise.

The simulation results for the magnitude estimation with the SGT, the LSE and the P-SGT methods are shown in Fig. 4.34 for a signal of module equal 1.

As shown, the results obtained by the P-SGT approximation notably improve the speed of the estimation convergence. However, even with the averaged slope calculation, a transient can be observed at the beginning of each processing window. This

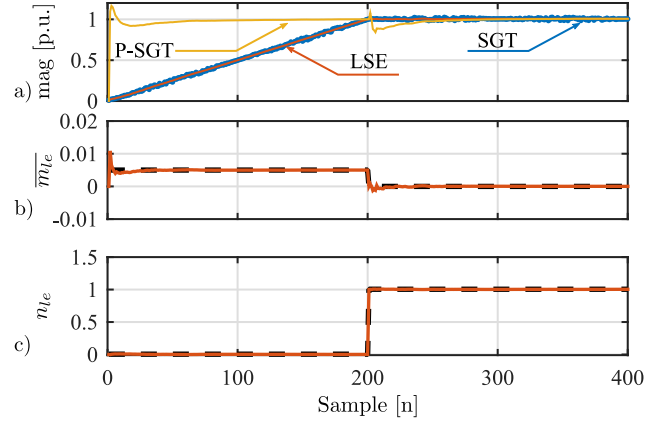


**Figure 4.34:** Proposed P-SGT estimation. a) evolution of the magnitude. SGT in blue, LSE in red and P-SGT in yellow. b) evolution of the predicted slope, c) evolution of the predicted offset. A window of  $N = 200$  has been used for demonstration purposes.

behavior is caused by the inherent derivative process of the P-SGT that enables the fast convergence. On the other hand, the SGT estimation (and the LSE filtered signal) provide smooth transitions. Thus, the used of a mixed approach that fuses the result of both estimations becomes an appealing solution. The combined estimation will be based on the rate of change in the SGT estimation.

#### 4.4.2.1 Combined SGT and P-SGT estimation: the PF-SGT estimation

Considering the performance of both the SGT and the P-SGT strategies shown in Fig. 4.34, a combination of both methods for an enhanced estimation is proposed, leading to the predictive fusion SGT strategy (PF-SGT). The proposed fusion rule is defined by (4.26).

$$y_{h\omega_e}^{pf-sgt} = y_{h\omega_e}^{p-sgt} \cdot (1 - k_{h\omega_e}^f) + y_{h\omega_e}^{sgt} \cdot (k_{h\omega_e}^f) \quad (4.26)$$

Where the value of the fusion gain,  $k_{h\omega_e}^f$ , is given by (4.27).

$$k_{h\omega_e}^f = \exp\left(-\text{abs}\left(\frac{\text{mavg}(\Delta y_{h\omega_e}^{sgt})}{\text{max}(\Delta y_{h\omega_e}^{sgt})}\right)\right) \cdot g_{h\omega_e} \quad (4.27)$$

The variables in (4.26) and (4.27) are defined as follows:

- $y_{h\omega_e}^{pf-sgt}$ : PF-SGT estimation of the harmonic component  $h$  at fundamental frequency  $\omega_e$ .

- $y_{h\omega_e}^{sgt}$ : SGT estimation of the harmonic component  $h$  at fundamental frequency  $\omega_e$ . It is equal to the  $y$  defined before in the SGT algorithm.
- $y_{h\omega_e}^{p-sgt}$ : P-SGT estimation of harmonic component  $h$  at fundamental frequency  $\omega_e$ . It is equal to the  $y_N$  defined in (4.25).
- $\Delta y_{h\omega_e}^{sgt}$ : is the rate of change of the module of the estimated harmonic components by the SGT algorithm. It is calculated as the difference between the module of the actual sample minus the previous one.
- *mavg*: Moving average function. A window of  $N$  samples is used for the calculation.
- *max*: Maximum variation function. For this research a maximum of  $1.1/N = 5.5e - 3$  p.u. is established.
- $g_{h\omega_e}$ : Gain of the exponential function used for tuning the fusion system.

The response of the estimation using the different methods and the evolution of the adaptive gain is shown in Fig. 4.35. As shown, the fusion helps to reduce the transient at the beginning of the processing window ( $n=200$ ).

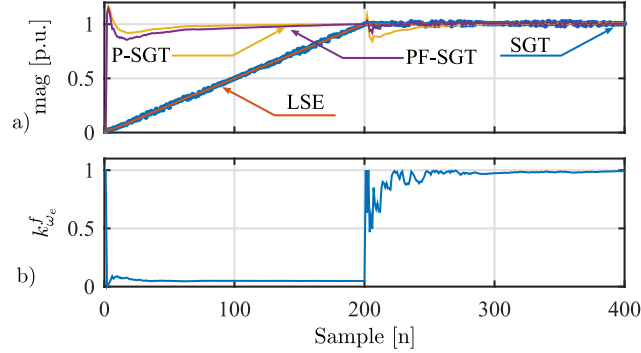


**Figure 4.35:** Proposed fusion mechanism. a) evolution of the module. b) evolution of the gain.  $g_{h\omega_e} = 5$ ,  $\max(\Delta y_{h\omega_e}^{sgt}) = 5.5e - 3$ .

The transient response and settling time for the PF-SGT depending on the value of the fusion gain  $g_{h\omega_e}$  is shown in 4.36. A parameter sweep of  $g_{h\omega_e}$  is performed between 1 and 6. As it can be seen, for the presented magnitude steps, values larger than  $g_{h\omega_e} > 4$  hardly contribute to an improved transient response.

#### 4.4.2.2 Discussion on grid frequency variation

As discussed in previous sections of the present chapter, the frequency variation is a critical challenge in weak MGs. When the proposed PF-SGT method is applied for

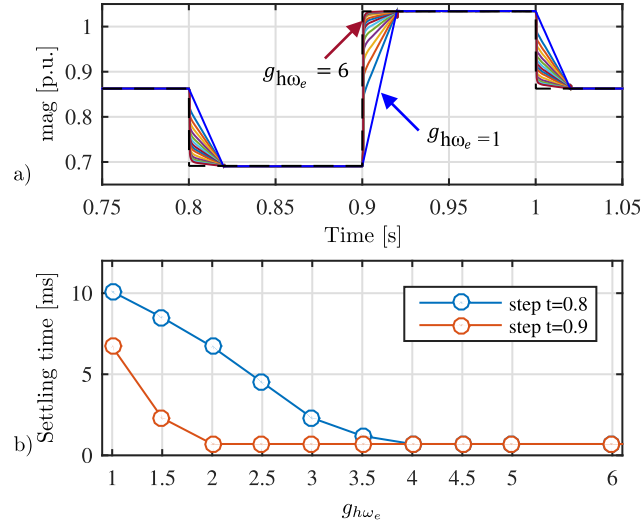


**Figure 4.36:** Variation of the PF-SGT response and settling time with respect to the fusion gain. a) the response of the proposed fusion mechanism to two different step changes is shown, b) the calculated time constant.

the estimation of grid voltages and currents, frequency changes must be considered. As known, frequency domain methods based on the DFT, as the Goertzel transform, assume the periodicity of the signal and are affected by the discrete resolution. However, when used for the analysis of real-time signals in microgrids, this assumption is not longer valid. The effect of the signal being not periodic, together with the discrete resolution, will cause spectral leakage, affecting both the phase and magnitude of the estimated components. Often, windowing techniques (both in time and frequency domain) are applied in order to reduce the impact. Unfortunately, this procedure also affects the magnitude and the phase of the extracted components and often requires for additional compensation. A different approach, is to optimize the number of samples needed for the calculation (200 by default in the present research) depending on the fundamental frequency, so an integer number of cycles is acquired at each processing window. For this research, and considering that only the harmonics of the fundamental frequency (including itself) needs to be isolated, a simple approach has been used. By selecting a coarse spectral resolution of 50Hz (the expected nominal frequency), spectral leakage is avoided when deviations from the fundamental frequency appears. The drawbacks of this procedure are that a bounded steady state error for the phase will appear and that any other disturbance signal falling within the band of [25 – 75]Hz will be affecting the estimation. This effects will be later discussed in Section 4.4.4.2.

#### 4.4.2.3 Magnitude estimation errors due to the LSE algorithm

Due to the slope averaging defined in (4.25), magnitude estimation errors happens when any change in the signal magnitude occurs during the LSE calculation period.

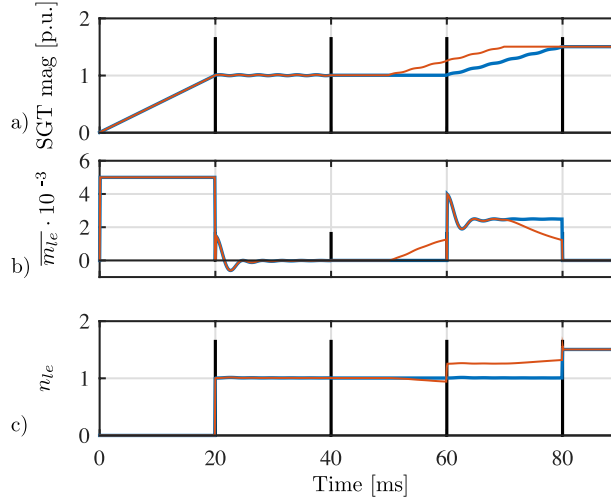


**Figure 4.37:** Prediction errors due to the averaging window problem. a) SGT estimated magnitude for two different cases. Blue: magnitude changes aligned with sample  $n = 0$  at each window. Red: magnitude change at  $t = 50\text{ms}$  at sample  $n = N/2$ . b) and c) estimated slopes and offsets for the two cases.

Fig. 4.37 shows the magnitude estimation for two different cases. In the first one (blue trace), the disturbances occur at  $t = 0$  and  $t = 60$  ms, which corresponds in both cases to the  $n = 0$  sample at the processing windows 1 and 4. Under that conditions, the predicted slope,  $\overline{m}_{l_e}$  and offset,  $n_{l_e}$ , are correctly estimated. In the second case (red trace), the magnitude steps occurs at  $t = [0, 50]\text{ms}$ , corresponding to  $n = [0, N/2]$  samples respectively. As shown, for the  $t = 50\text{ms}$  step, the slope prediction starts to react at the step time but, because of the average calculation, the value by the end of the processing window,  $t = 60\text{ms}$ , is half of the expected value. After that, during the next processing window starting at  $t = 60\text{ms}$ , the slope is correctly adapted until  $t = 70\text{ms}$ , time at which the average calculation makes the slope prediction to decrease, reaching half of the expected value at  $t = 80\text{ms}$ . Similar explanations can be given to the offset calculation. The two explained cases, cover the minimum and maximum estimation errors. The maximum error will happen when a step change happens at half of the processing window and will be equal to half the correct value.

In order to correct these estimation errors, a simple procedure is explained in Fig. 4.38. The fundamental idea is based on the detection of magnitude changes with the SGT algorithm. When a change is detected, the estimation window is restarted so the calculations of the slope and offset are based on the new incoming values. Ideally, this

will make the estimation to converge to the right value despite the instant at which the magnitude varies. The trigger signal  $M_{th}$ , used for the magnitude change detection, is based on the absolute value of the derivative of the slope given by the SGT, and it is shown in Fig. 4.38b) depicted in blue. By comparing with a trigger level, represented by the red dashed line, the processing window can be reset. As shown in Fig. 4.38a), an step change in the value of the fundamental component from 1p.u to 1.5 p.u occurs at  $t = 50\text{ms}$ , corresponding to  $n = N/2$ . In Fig. 4.38b), the output of the slope change detector  $M_{th}$ , instantaneously reacts to the change. The results for the predicted slope and offset are depicted in red in Figs. 4.38c) and 4.38d) respectively, compared to the slope and offset obtained with the standard approach, shown in blue. Finally, the estimated output is shown in Fig. 4.38e). The estimation clearly tracks the correct values in around 5ms, which is an excellent response time. As a comparison, the tracked slope and offset using the standard approach is shown in blue.

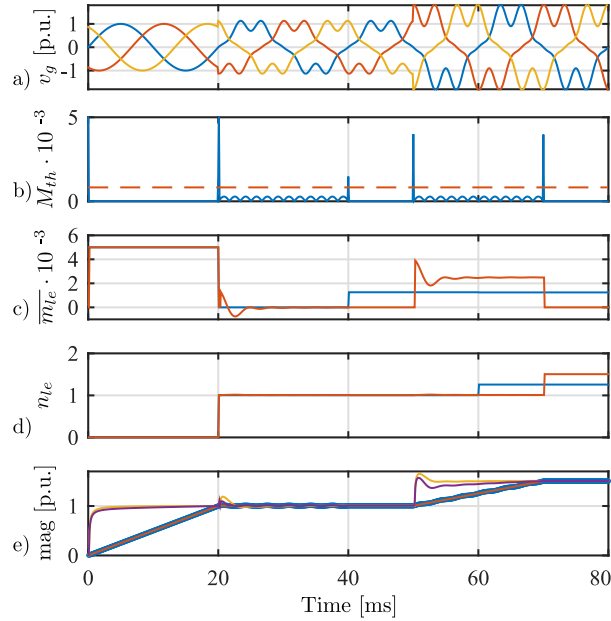


**Figure 4.38:** Correction of window averaging errors. a) voltage to neutral waveforms, b) slope change detector, c) LSE slope, d) LSE offset, e) estimated output. In c) and d) blue and red represents the slope and offset obtained by the LSE without and with the proposed modification respectively.

#### 4.4.2.4 Phase-jump detection and magnitude correction

An adverse effect that noticeably affects to the magnitude estimation is the occurrence of a phase jump. A simple technique that detects a phase-jump and corrects its

effects in the estimated magnitude is proposed. The basic idea is to check if the phase difference between the actual phase estimation and the previous one falls within the grid code limits. An acceptable frequency deviation from the nominal value has been selected to be  $\omega_{err} = 2 \cdot 2\pi$  rad/s ( $\pm 2$  Hz). According to that, the phase difference between the actual phase estimation and the previous one should fall within the phase limits defined by (4.28), where  $T_s$  is the sample time and  $P_s$  the phase difference.

$$(\omega_e - \omega_{err}) \cdot T_s < P_s < (\omega_e + \omega_{err}) \cdot T_s \quad (4.28)$$

Thus, if a phase-jump is detected, the magnitude estimation at the previous sample is used. Alternatively, a low-pass filtered version of the voltage complex vector could be used, but this solution requires more computational effort at no extra advantage. Fig. 4.39 shows the proposed correction mechanism compared to the magnitude variation before the compensation.

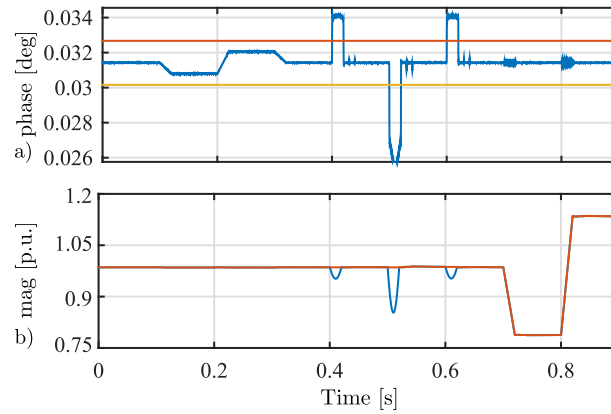


**Figure 4.39:** Compensation of magnitude estimation during three phase-jumps. a) The phase-jumps are represented in blue and the limits given by (4.28) in red and yellow. Phase-jumps occur at  $t = [0.4, 0.5, 0.6]$  s. b) The estimated magnitude without (blue) and with (red) the correction is shown.

#### 4.4.2.5 Implementation of the proposed PF-SGT method

The implementation block diagram of the proposed PF-SGT method as well as its possible use for the current control of a grid-tied converter is depicted in Fig. 4.40. On the left-side, the PF-SGT technique is shown. The input to the algorithm is the  $v_{g_{\alpha\beta}}$  voltage complex vector measured at the PCC. The output of the method are the complex components of the estimated frequency components  $v_{g_{\alpha\beta} h_1 \dots h_n}$  as well as the phase of the fundamental component,  $\theta_{h_1}$ . In case the system is expected to work under different frequencies depending on the situation, and to avoid steady state errors in the voltage phase and magnitude, the frequency can be added as an input to

the PF-SGT block. The estimated frequency  $\widehat{\omega}_e$  can be obtained by an external FLL estimator as the DSOGI approach. However, in the scope of this thesis, this parameter will be used as a constant value equal to the nominal fundamental frequency (50Hz) to avoid the use of additional frequency estimation, with the counterpart of phase steady state errors as will be shown in following sections. On the right-side, the use of the estimated components for the current control implementation is shown. The estimated phase is used as the rotation angle for the  $\alpha\beta \rightarrow dq$  or the  $abc \rightarrow dq$  transformation. The estimated grid voltage harmonic components can be used as a feed-forward added at the output of the current control. In addition, it is worth to point out that the fundamental and harmonic components of the current can also be obtained with the PF-SGT in order to control them independently.

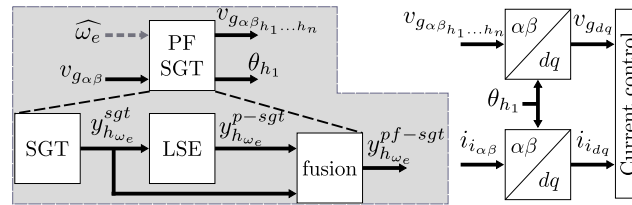


**Figure 4.40:** Digital signal processing. Left-side, estimation of voltage harmonics. Right-side. Use of the estimated voltages in the internal current-loop control.

Regarding the viability for real-time implementation, the computational burden of the proposed method can be calculated by computing the needed floating point operations and the memory needs. The number of floating point operations considering four harmonics is around 2200. As an example, considering the number of cycles for each floating point operation based on the popular TMS320F28335 controller with a 150MHz clock, it leads to a computational time lower than  $60\mu s$ . Regarding the memory needs, a buffer of  $N + 1$  samples is needed for the calculation of the SGT plus some additional room for the scalar variables. Considering together the processing and memory needs, it is concluded that the proposed method has a moderate computational burden for modern digital signal controllers.

### 4.4.3 Offline system evaluation

The initial evaluation of the proposed method is performed offline using the setup described in Appendix A.7. The tests consist in the offline application of the sequence estimation method to a distorted three-phase voltage signal obtained experimentally. Different steps at the magnitude, phase and frequency of the signal have been considered, as well as the behavior with and without additional harmonic content.

The proposed PF-SGT method has been analyzed under different conditions and compared to the extended DSOGI implementation, tuning the DSOGI according to the optimal parameters indicated by the authors in [238]. The results for the tracked grid

voltage magnitude and phase using the PF-SGT are shown in Fig 4.41 and detailed at 4.42. The different events at the voltage signal are repeated twice. During the first interval ( $t = 0 - 1.2$  s), no harmonics are considered. At the second one ( $t = 1.2 - 2.4$  s), the harmonics indicated at Table A.6 in Appendix A.7 are considered. The events are scheduled as follows:

1. **Magnitude:** At  $t = 0.8$ s and  $t = 0.9$ s it changes to 0.8 and 1.2p.u. The same change is observed at  $t = 1.98$ s and  $t = 2.08$ s.
2. **Frequency:** At  $t = 0.2$ s and  $t = 0.3$ s, the rated 50Hz frequency is changed to 49 and 51Hz respectively. Same pattern is reproduced at  $t = 1.38$  s and  $t = 1.48$ s.
3. **Phase:** At  $t = 0.5$ s,  $t = 0.6$ s,  $t = 0.7$ s phase-jumps of 30,  $-60$  and 30 degrees are induced. Same pattern is observed at  $t = 1.68$ s,  $t = 1.78$ s,  $t = 1.88$ s.
4. **DC offset:** Starting at  $t = 1.5$ s, a DC offset is added at the output of the voltage sensors. DC offset values are  $v_{g_{a_{dc}}} = 10$ V,  $v_{g_{b_{dc}}} = 5$ V,  $v_{g_{c_{dc}}} = -5$ V.

As it can be seen, the proposed method shows a better immunity to harmonics and faster response to the considered changes with the exception of the phase change at  $t = 0.6$  and 1.78 s. This is due to the correction explained in (4.28), that have not being explained in (4.28), that have not being considered for this initial evaluation. It is specially remarkable the improvement of the proposed method when DC offset components are considered, becoming the DSOGI more distorted under this condition even in steady state.

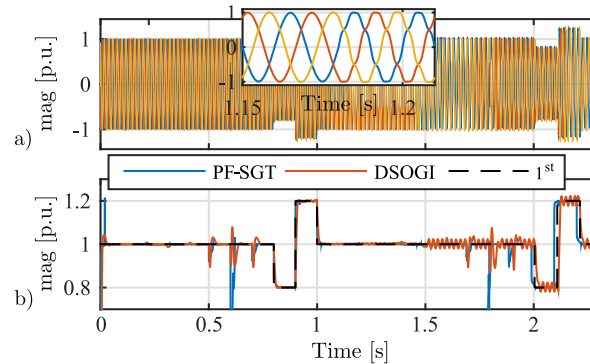


**Figure 4.41:** Offline system evaluation. Comparison of the PF-SGT method with respect to the ideal 1<sup>st</sup> harmonic and the DSOGI implementation. a) time domain waveforms, b) magnitude estimation.

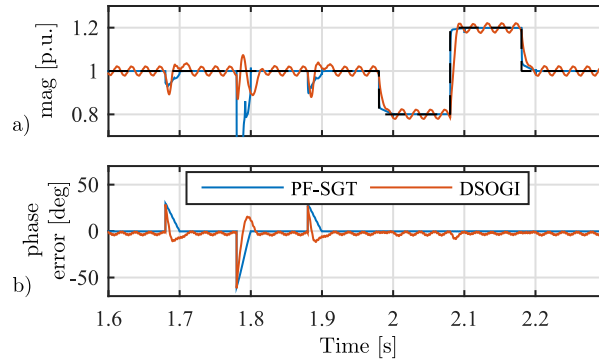


**Figure 4.42:** Offline system evaluation. Detail on the comparison of the PF-SGT method with respect to the ideal 1<sup>st</sup> harmonic (fundamental component) and the DSOGI implementation. a) magnitude, b) phase error

#### 4.4.3.1 Performance under unbalanced conditions

Fig. 4.43 shows the performance of the proposed technique and the DSOGI method under unbalanced conditions. At  $t = 0.2$ s, phase  $b$  of the input three-phase voltage falls to 0.7 p.u.

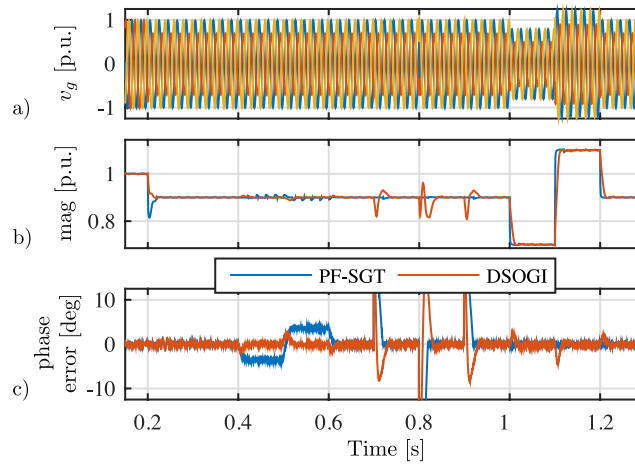


**Figure 4.43:** Offline system evaluation. Comparison between the DSOGI and the proposed PF-SGT method under unbalanced conditions. From top to bottom: a) grid phase voltages, b) grid voltage magnitude, c) grid voltage phase error.

The same disturbances as the previous tests are applied under unbalanced conditions: frequency deviation test is performed between  $t = 0.4$ s and  $t = 0.6$ s, phase jump

test is performed between  $t = 0.7\text{s}$  and  $t = 0.9\text{s}$ , and finally magnitude deviations test is performed between  $t = 1.0\text{s}$  and  $t = 1.2\text{s}$ . The obtained results match with those retrieved in the previous tests. In this regard, the proposed method shows a better tracking capabilities under all tested disturbances.

#### 4.4.3.2 PF-SGT and DSOGI step response comparison

As it has been shown, the PF-SGT present a faster transient response for tracking the magnitude of harmonics and fundamental components than the DSOGI technique. Since both the DSOGI and the PF-SGT methods involve nonlinear systems, their transfer functions have been approximated by the  $2^{\text{nd}}$  order systems shown in Fig. 4.44 in order to compared them under a magnitude step change. The results of the approximation procedure are shown in Table 4.2, where  $\omega_n$  and  $\xi$  are the natural frequency and damping factor of each method respectively.

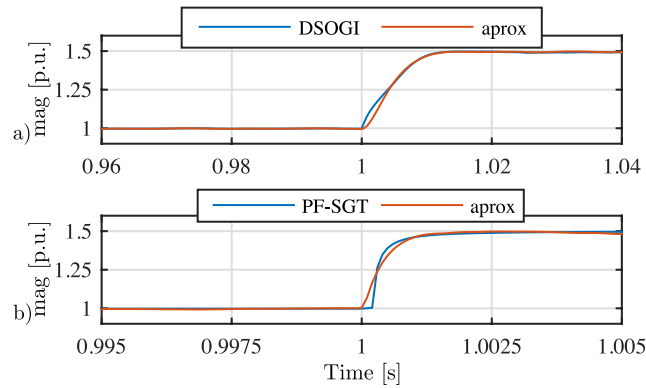


**Figure 4.44:** Approximation of a) DSOGI and b) PF-SGT methods

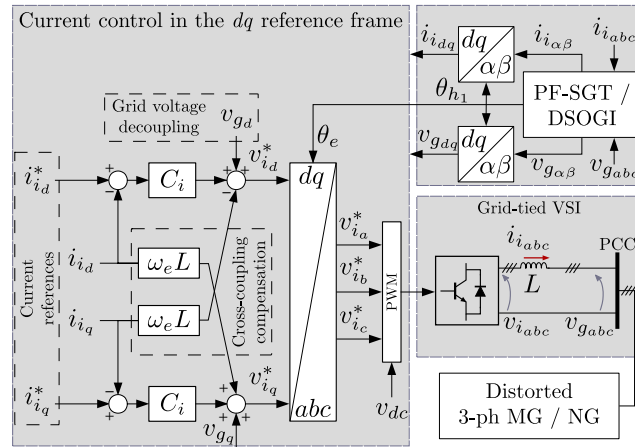
The faster response of the proposed PF-SGT appears as a more appealing method for closed-loop dynamic control of isolated harmonics and fundamental components.

Table 4.2: Approximation parameters.

Method	$f_n$ [Hz]	$\xi$
DSOGI	60.5	$\frac{\sqrt{(2) \cdot 3}}{2}$
PF-SGT	8600	$\sqrt{(2)} \cdot 8$

#### 4.4.3.3 Closed-loop behavior

The impact of the proposed PF-SGT over the closed-loop performance in a grid-tied converter has been compared with respect to the DSOGI. A PI-based current control similar to the one presented in 3.10 in Chapter 3 is used for the closed-loop simulation. However, in this case, the fundamental voltage and current obtained by the PF-SGT and the DSOGI will be used in the control scheme. The modified control diagram using the PF-SGT or the DSOGI for fundamental components control is displayed in Fig. 4.45.



**Figure 4.45:** VSI inner current control topology implemented in the  $dq$  synchronous reference frame using the PF-SGT or DSOGI fundamental voltage and current estimation.

For both techniques, the current control loop is tuned by using a zero-pole cancellation technique and its bandwidth is set to 20Hz. The analytical response has been analyzed using the  $2^{nd}$  order system approximation presented in Section 4.4.3.1. The phase margin of the system is used as a figure of merit to analyze the stability of the current control loop. In this regard, a limit of 60 degrees is usually considered to assure stability.

Fig. 4.46 shows the open-loop  $G(s)H(s)$  Bode plots for a bandwidth in the current control loop of 20Hz. It can be observed that the phase margin of the system using the DSOGI method is 58 deg, while it is  $\approx 87$ deg when the PF-SGT method is used under the same bandwidth. This clearly shows the bandwidth limit of the current control loop when a DSOGI method is used for fundamental current control.

The time domain simulation of the current control in synchronous reference frame has been performed connecting the grid-tied VSI to a voltage source that reproduces the distorted three-phase voltage profile obtained experimentally used along the offline validation. The resulting closed-loop current control relevant signals are shown in Fig. 4.47, testing the reference tracking capabilities in the synchronous reference frame

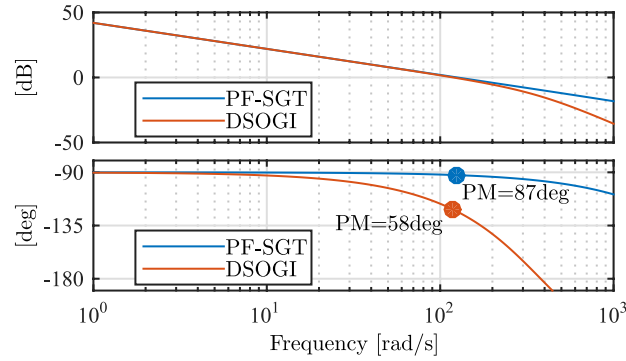


**Figure 4.46:**  $G(s)H(s)$  Bode Plot for DSOGI and proposed methods. Current control bandwidth of 20 Hz.

and the effect of grid voltage distortion. The relevant parameters for the closed-loop simulation setup are included in Appendix A.7 in Table A.7. As clearly shown, the proposed PF-SGT method shows a better transient response and harmonic rejection capabilities than the DSOGI alternative. Moreover, the bandwidth was set to such a low value in order to keep stable the DSOGI-based current control, having still some margin to increase the current control bandwidth in the case of using the PF-SGT estimation.

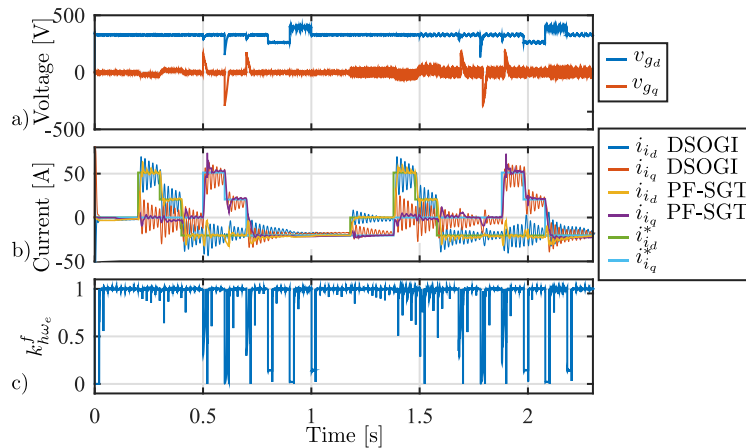


**Figure 4.47:** Offline system evaluation. Close loop comparison between the DSOGI and the proposed PF-SGT methods. a)  $dq$  grid voltages, b)  $dq$  converter currents, c) adaptive fusion gain for the PF-SGT method.

#### 4.4.4 Online system evaluation

The online experimental validation of the proposed sequence estimator is done by using the experimental setup defined in Appendix A.7. The proposed algorithms are processed online in the PM15F42C control unit using the voltage measurements at the point of common coupling (PCC). The experimental results compare the PF-SGT with the DSOGI algorithm as done for the offline evaluation. Additionally, the phase calculation using the inverse tangent function  $atan$  will be applied to the voltage complex vector  $v_{g\alpha\beta}$  to compare it with the other two methods and highlight the need for an accurate and robust phase estimation under distorted conditions.

##### 4.4.4.1 Variation of grid voltage magnitude

In order to evaluate the robustness and tracking capability under voltage magnitude variations, the PF-SGT and the DSOGI methods have been evaluated under the presence of fundamental voltage steps and the presence of harmonics. Fig. 4.48 shows the response under no harmonics, while Fig. 4.49 includes the additional harmonics in Table A.8 of Appendix A.7. A voltage magnitude variation from 1 to 0.8 p.u. at  $t = 0.1$ s and from 0.8 to 1.15 p.u. at  $t = 0.2$ s are considered. As shown, the proposed PF-SGT method presents a faster dynamic response as well as a higher harmonic robustness, both for the magnitude and the phase estimation.

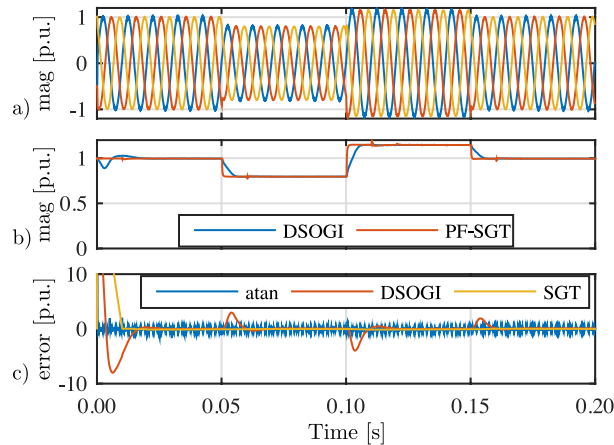


**Figure 4.48:** Online system evaluation. Comparison between the DSOGI and the proposed PF-SGT method for a magnitude step change. No harmonics are injected. From top to bottom: a) grid voltages, b) grid voltage magnitude, c) grid voltage phase error. Note that  $atan$  refers to the inverse-tangent function.

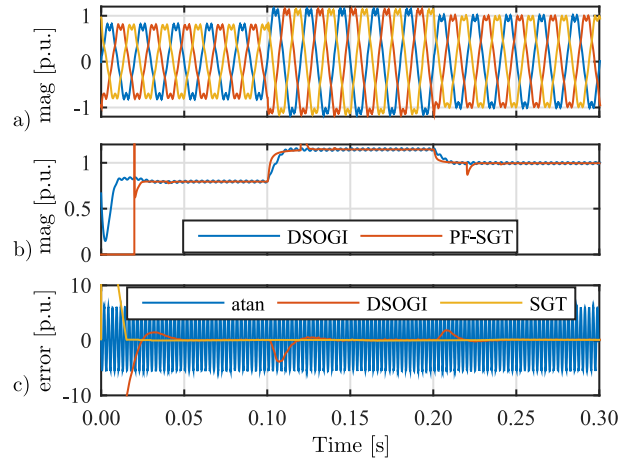


**Figure 4.49:** Online system evaluation. Comparison between the DSOGI and the proposed PF-SGT method for a magnitude step change. Harmonics as listed in Table A.6 are injected. From top to bottom: a) grid voltages, b) grid voltage magnitude, c) grid voltage phase error.

#### 4.4.4.2 Variation of grid voltage frequency

For the evaluation of the PF-SGT under frequency changes, variations of grid voltage frequency have been introduced from 50 to 49 Hz at  $t = 0.1$ s and from 49 to 51 Hz at  $t = 0.2$ s. The results both without and with the additional harmonics specified in Table A.8 are shown in Fig. 4.50 and Fig. 4.51 respectively.

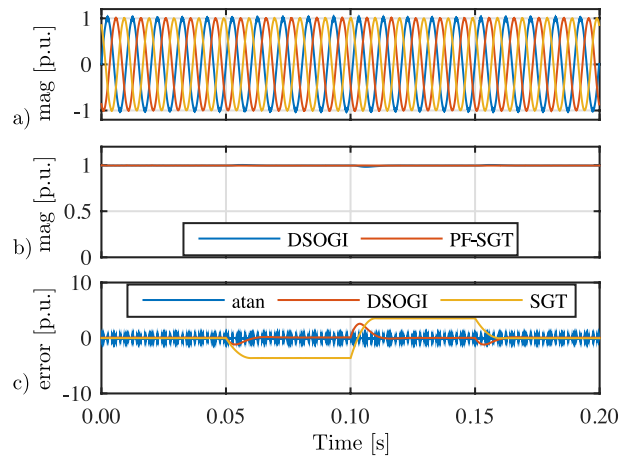


**Figure 4.50:** Online system evaluation. Comparison between the DSOGI and the proposed PF-SGT method for a frequency step change. No harmonics are injected. From top to bottom: a) grid voltages, b) grid voltage magnitude, c) grid voltage phase error.

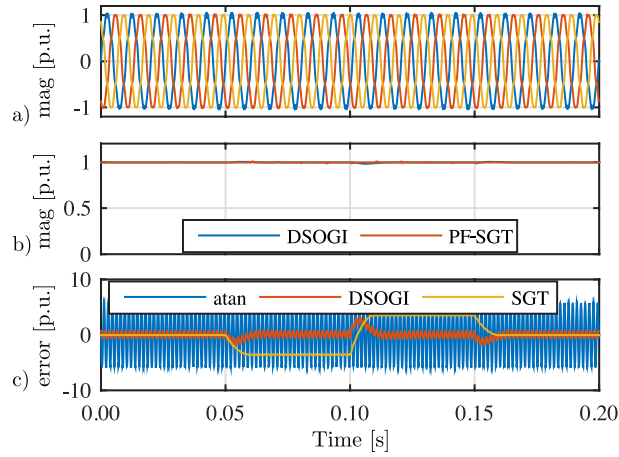


**Figure 4.51:** Online system evaluation. Comparison between the DSOGI and the proposed PF-SGT method for a frequency step change. Harmonics as listed in Table A.6 are injected. From top to bottom: a) grid voltages, b) grid voltage magnitude, c) grid voltage phase error.

As shown, the proposed method has a better magnitude response but a worse phase estimation as it presents an steady state error. The reason is the considered frequency resolution. As explained before in Section 4.4.2.2, a coarse frequency resolution of 50Hz has been selected in the scope of this thesis to avoid the need for a precise frequency estimation. This implies that any deviation smaller than 50Hz can not be measured and the difference between the real grid frequency and the fundamental component is directly coupled to a phase and a magnitude error. The maximum errors have been numerically evaluated as shown in Fig. 4.52. As it can be seen, both the error in magnitude and phase are small for variations between [46, 54]Hz. The maximum phase error can be approximated by the linear expression shown in (4.29), where  $\max(\omega_{err})$  is the maximum expected frequency error in rad/s and  $f_e$  the grid frequency in Hz.

$$\max \theta_{err} = \frac{\max(\omega_{err}) \cdot 180}{f_e \cdot 2\pi} \quad (4.29)$$

The maximum frequency error depends on the frequency resolution and the maximum admissible grid frequency deviation. For the values considered in this validation ( $\max(\omega_{err}) = 1\text{Hz}$  and  $f_e = 50\text{Hz}$ ), the error is bounded to a maximum of 3.6deg. The effect of the frequency error over the estimated magnitude and phase has been validated by the experimental results shown in Fig. 4.53. As expected, the phase is kept within the specified limits and the magnitude is barely affected as expected from the previously seen results in Fig. 4.52. For those applications in which the maximum allowed phase deviation is lower than the limits given by (4.29), a modification in the proposed method can be included, so it becomes frequency adaptive. For that, the number of samples  $N$  used for the calculations is obtained as a function of the

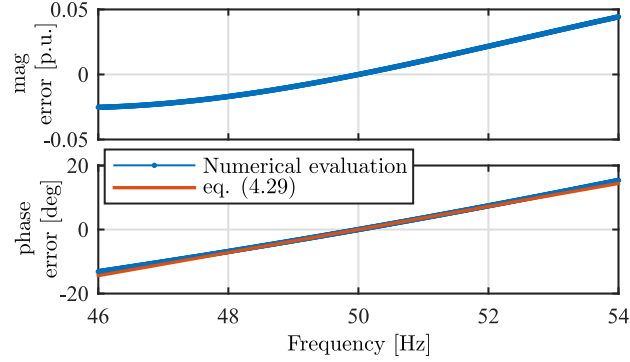


**Figure 4.52:** Effect of grid frequency variation over the estimated magnitude (top) and phase (bottom). Phase error is compared against the linear approximation in (4.29).

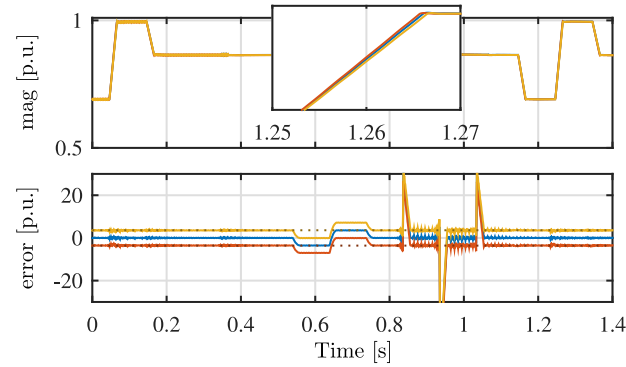


**Figure 4.53:** Online system evaluation. Effect of grid frequency variation over the magnitude (top) and phase (bottom). Goertzel algorithm is tuned for 50Hz and three different cases are represented: 50Hz (blue), 49Hz (yellow), 51Hz (red). Theoretical limits for the phase according to expression (4.29) are marked dotted.

fundamental frequency, according to the expression (4.30).

$$N = \text{round} \left( \frac{2\pi}{\omega_e \cdot T_s} \right) \quad (4.30)$$

In that case, the coefficients for the Goertzel algorithm have to be updated in real-time. The experimental results when the adaptation mechanism is used are shown in Fig. 4.54. For the updating of the frequency  $\widehat{\omega}_e$ , the DSOGI frequency estimation have been used in this test. Comparing the phase error with respect to Fig. 4.51, the phase jump is corrected, achieving a zero phase error in steady state.

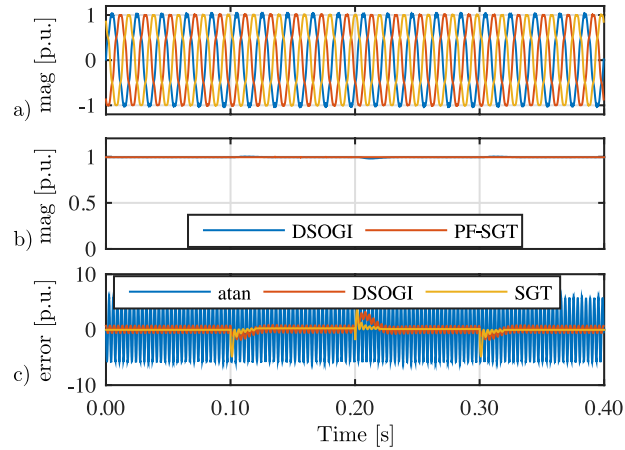


**Figure 4.54:** Online system evaluation. Comparison between the DSOGI and the proposed PF-SGT method for a frequency step change when an adaptive frequency is used. Harmonics as listed in Table A.6 are injected. From top to bottom: a) grid voltages, b) grid voltage magnitude, c) grid voltage phase error.

#### 4.4.4.3 Variation of grid voltage phase

Finally, the effect of grid voltage phase variation and phase-jumps has been analyzed. The results both without harmonics and with the additional harmonics indicated in Table A.8, are shown in Fig. 4.55 and Fig. 4.56 respectively.

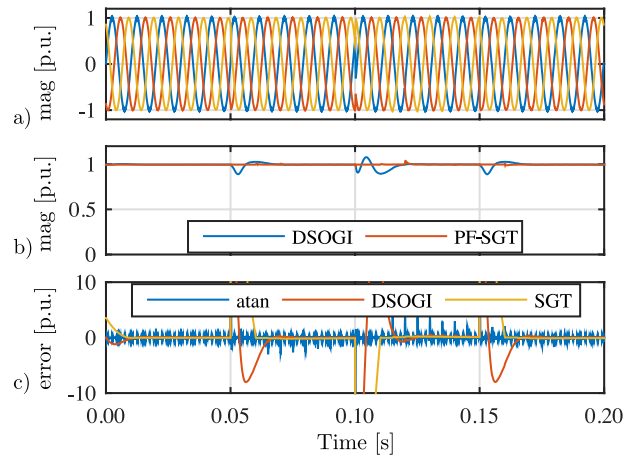


**Figure 4.55:** Online system evaluation. Comparison between the DSOGI and the proposed PF-SGT method for a phase step change. No harmonics are injected. From top to bottom: a) grid voltages, b) grid voltage magnitude, c) grid voltage phase error.

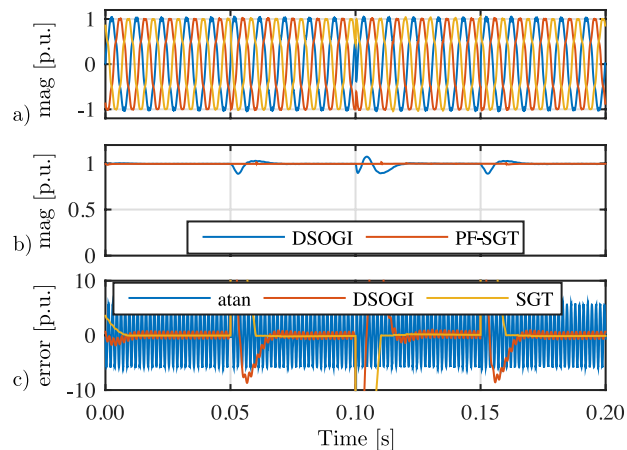


**Figure 4.56:** Online system evaluation. Comparison between the DSOGI and the proposed PF-SGT method for a phase step change. Harmonics as listed in Table A.6 are injected. From top to bottom: a) grid voltages, b) grid voltage magnitude, c) grid voltage phase error.

The variations of grid phase take place at  $t = 0.05\text{s}$  from 0 to 30 deg, at  $t = 0.1\text{s}$  from 30 to  $-30$  deg and at  $t = 0.15\text{s}$  from  $-30$  to 0 deg. The proposed PF-SGT method presents a higher robustness against phase-jumps in regard to the magnitude estimation, while the SGT presents a faster phase tracking response than the DSOGI technique. Under the presence of harmonic components, although the fundamental component magnitude estimation remains similar, the phase estimated by the DSOGI presents a noticeable ripple as happened in the other tested cases.

The results and analysis provided for the proposed PF-SGT sequence estimator demonstrate its viability and robustness in distorted systems as microgrids. Thus, it becomes a valid sequence estimation strategy for its integration in the control of grid-tied converters. Although it remains out of the scope of this research, the proposed method not only becomes a powerful tool for fundamental component control, synchronization or monitoring, but also for a potential application in harmonic and unbalance control.

## 4.5 Conclusions

This chapter has addressed several issues related to active power compensation, frequency estimation delay, synchronization and voltage and current sequence estimation, giving rise to the following contributions:

- The basics of a device able to improve the grid quality by means of dynamic power compensation have been presented. The solution is valid for its implementation in grids with a P/V or P/f relation by modifying the external control loops.

- A transient frequency drift compensation has been proposed based on the use of a nearly-zero lag transient frequency estimation using a Luenberger observer. The proposed solution addresses two of the main limitations of existing frequency compensation methods in the literature: the phase lag on the frequency estimation, and the transient detection for decoupling the grid reference frequency. The performance achieved by feedback control has been improved by the development of a transient observer, formed by a novel transient detection method, based on signal correlation that effectively decouples the grid reference frequency from the compensator inputs, and a Luenberger-based observer that provides a fast frequency estimation and allows to increase the phase margin in the frequency controller. Moreover, the developed observer structure allows to estimate the load current, that can be employed as a feed-forward mechanism for the decoupling of the load disturbance. A detailed comparison, including analytical derivations, simulation and experimental results, have been carried out. The methods have been tested under two different scenarios considering resistive and electronic loads. The analytical derivations, the simulation and the experimental results have demonstrated the effectiveness of the proposed observer-based TFDC. Additionally, it has been demonstrated that the proposed method allows for an extended range operation, withstanding higher disturbances and improving the system stability under the presence of CPLs. The decoupling of the grid frequency reference makes the method suitable for the operation in MGs under droop control. The proposed techniques have been compared with the existing ones, analytically and experimentally, in an isolated MG with resistive and CPLs, evincing the limitations of VI and existing frequency estimators when used for transient frequency compensation. A normalized performance comparison has been derived from the analysis, establishing a benchmark for the selection of the most suitable method depending on the application. Under the conditions used in this thesis, a reduction of 1Hz in the initial frequency drift and a reduced RoCoF compared with the existing techniques is achieved. The contributions in Section 4.3 lead to the possibility of faster frequency compensation in weak grids even with a reduced FLL or PLL bandwidth.
- A new predictive estimation technique for grid-tied converters based on a frequency-based method. To the author's best knowledge, the proposed method using a modification of the sliding Goertzel Transformation has not been used before for grid phase tracking in power converters. The proposed PF-SGT method has been evaluated with respect to a consolidated alternative, the DSOGI, showing a superior performance in terms of dynamic response and disturbance rejection. It is particular remarkable the immunity to DC offsets as well as to changes at the grid frequency. The proposed algorithm has been validated by both simulation and experimental results. The impact of the phase estimation and harmonic decoupling in a closed-loop current control implementation has also been evaluated, being the proposed PF-SGT an important improvement over the DSOGI method.



## Chapter 5

# Cooperative primary control in hybrid AC/DC microgrids

### 5.1 Introduction

The previous chapters have presented strategies and solutions for the current and voltage control implementation of grid-tied converters and the improvement of the dynamic response in weak microgrids. As the background system, the experimental multi-subgrid hybrid AC/DC MG introduced in Section 3.2 has been developed for research purposes in the amenities of the *Laboratory for Electrical Energy Management Unified Research* (LEMUR) group in the University of Oviedo. This chapter seeks to define an scheme for the overall primary control of such a microgrid topology, integrating some of the concepts and proposals presented up to this point.

Apart from the AC and DC buses regulation, it is worth to highlight that the main control concern in hybrid AC/DC MGs, when compared to AC or DC grids, is the power sharing between the AC and DC buses. This is achieved by means of the interlinking converters and depends on their control (they can usually operate in active/reactive power control mode or as AC or DC grid-forming converters). Thus, in the present study, the MG primary control has to consider the regulation of the DC voltage, the AC voltage magnitude and frequency and the interaction between the LVDC bus and the AC nanogrids. This chapter covers two alternatives as an initial approach for primary control in the studied microgrid, applying the basics of master-slave, virtual synchronous generators and DC droop control. Those primary control alternatives are modified to enhance the cooperative active power sharing between the DC and AC subgrids by means of the interlinking converters control.

This chapter leads to the following contributions: 1) A master-slave primary control based on the QVC voltage control, consisting in a centralized LVDC bus voltage control

and a master-slave fixed-frequency nanogrids control where the interlinking converters (NGHCs) operate in grid-forming mode. 2) A primary control based on synchronous generators, consisting in a DC droop controlled LVDC bus by means of a proposed DC virtual generator scheme, and interlinking converters operated as grid-forming virtual synchronous generators. 3) An improvement for each of the presented schemes is proposed for reducing the dependency on the mains and enhancing the AC/DC power sharing, one based on an adaptive power sharing algorithm, and another based on a proposed hybrid AC/DC virtual generator topology for its application to the NGHCs.

## 5.2 Primary control implementation in a hybrid AC/DC microgrid with multiple AC subgrids

The primary control of the microgrid will mainly involve the regulation of the LVDC bus and the control of voltage magnitude and frequency in the AC nanogrids both of them based on master-slave methods. Before proposing the control techniques that integrate the dynamic and primary control in the microgrid, some basic control premises have to be defined for the voltage magnitude and frequency control in the AC nanogrids and the voltage control in the LVDC bus.

The simplified global control diagram of the microgrid is shown in Fig. 5.1. The microgrid control will be based on a centralized approach that considers a central control station located in the microgrid transformation center (MGTC) which functions are the converter inner control loops of the SST (TAB and MGHC), the NGHCs primary control, and the secondary and tertiary control, that remains out of the scope of this thesis. The primary central controller considers the use of fast communication links between the NGHCs' controllers with other NGHCs' and with the SST controller, considering even their implementation in a single control unit. However, as an initial approach, the NGHCs and the SST will be controlled autonomously without exploiting the communication between them, decoupling the NGHCs' control from the LVDC bus regulation. The control tasks regarding the SST and NGHCs converter and primary control is summarized in Fig. 5.2. In this control approach, the communication between the SST and the NGHCs is not used.

Regarding the AC nanogrids control, the NGHCs will act as 3-phase grid-forming converters in their corresponding nanogrid under the assumption of being the highest rated power source in a NG, regulating both the AC voltage magnitude and frequency. Thus, the bus where the NGHC is connected is considered the slack bus of the NG. Then, as a first approach, DGs and dESSs in the NGs will operate in PQ mode or MPPT mode, receiving their commands from the secondary and tertiary controllers (out of the scope of this thesis), while the grid-forming NGHCs will absorb the power transients. Under these assumptions, the elements present in the nanogrids, either loads or generators, are considered an aggregated disturbance to the primary control, i.e., to the grid-forming NGHC. Nonetheless, the use of dESSs to provide ancillary services is considered. The dESSs in the nanogrid could provide local dynamic active

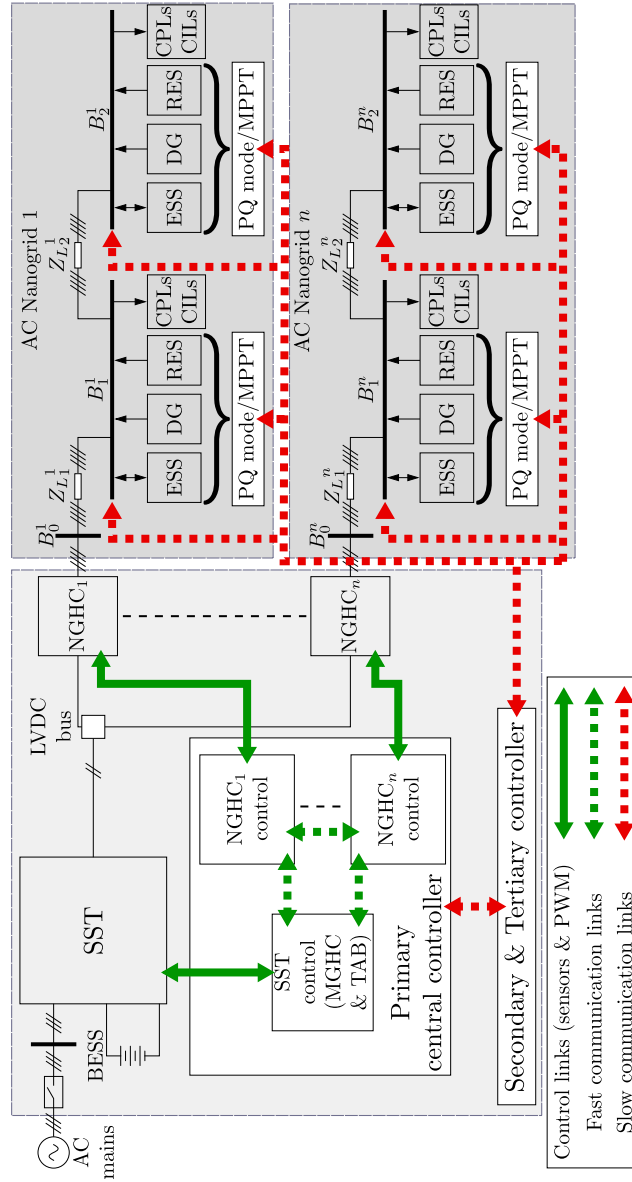
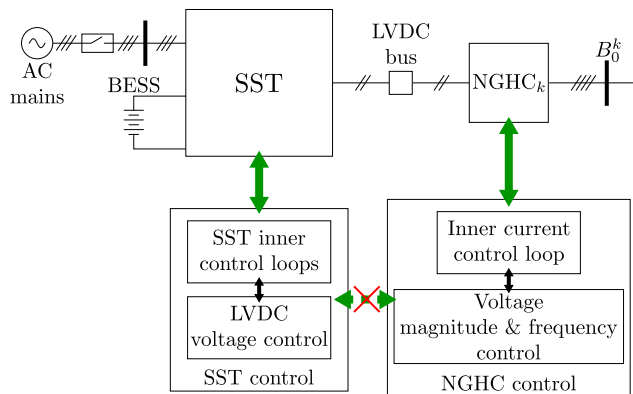


Figure 5.1: Simplified diagram of the microgrid control and communications.



**Figure 5.2:** SST and NGHCs control tasks.

power compensation improving the performance within the nanogrid while reducing the impact in the LVDC bus.

As the NGHCs are operated in grid-forming mode, they are seen as constant power disturbances (load/generation) by the LVDC bus, and do not contribute to the regulation of the DC voltage. Thus, the regulation of the LVDC bus relies on the SST through the power sharing of the MGHC (mains connection) and the central BESS. Depending on the availability of the utility grid, two modes of operations are considered:

1. During *grid-connected* operation, the mains ( $P_{mains}$ ) and the central BESS ( $P_{bess}$ ) can share the effort for controlling the LVDC voltage and absorb the power mismatches in the microgrid. A multiple slack scheme with a centralized controller can be applied to achieved this. The power sharing between the two sources will pursue for a reduced energy dependency on the utility grid during steady state and a reduced stress during transients in the central BESS, establishing an energy shaving strategy. Additionally, the BESS limitations (bandwidth, available power, State of Charge (SoC)...) have to be considered in the power sharing.
2. During *islanded* operation, the MG is disconnected from the utility grid and only the central BESS is available as a power source in the transformation center. In such a case, the central BESS can be operated as a grid-forming to maintain the DC voltage under control.

It is worth noting that under the proposed scenario, the NGHCs are decoupled from the LVDC bus regulation, and the power mismatches supported by the NGHCs are entirely provided by the mains and the central BESS, being the NGs agnostic about each other. This may create an important dependency on the mains and a high stress on the central BESS.

Once these premises are established, the internal structure of the LVDC voltage control and the NGHCs' control has to be defined. This section proposes two alternatives for the implementation of the outer voltage (and frequency in the case of the NGHCs) control loops:

1. The first control approach is based on the use of the quadratic voltage control analyzed in Chapter 3, Section 3.8, and will be referred in advance as QVC-based MG control. The LVDC control consist of a centralized multi-slack based on QVC, while the NGHCs are operated following the proposed QVC-based AC grid-forming structure in Section 3.8.8. This leads to fixed frequency AC nanogrids where the active power is mainly associated to the voltage magnitude.
2. The second control approach is based on the emulation of the properties of synchronous generators used in conventional generation, and will be referred as VG-based MG control. The control of NGCHs will consist of a VSG-based grid-forming control that regulates the frequency according to the active power, leading to non-fixed frequency AC nanogrids where the active power transients might be bounded to frequency variations. As virtual synchronous generators are an AC approach, an adaptation of this concept is proposed, named DC virtual generator (DCVG), for the shared regulation of the LVDC voltage by combining multiple sources.

### 5.2.1 QVC-based microgrid control proposal

The use of a master-slave topology for both the LVDC regulation and the NGHCs control can simplify the implementation of the dynamic control in the microgrid under study. In addition, the QVC alternative presented in 3.8, will be used in the NGHCs voltage control, due to the presence of CPLs in the NGs' nodes, and in the LVDC regulation given that the NGHCs will behave as CPLs for the LVDC bus. Taking advantage of the 3-port SST and the centralized controller, the power references of the mains and the central BESS can be given by a centralized QVC controller. In the case of the NGHCs, the use of a grid-forming strategy that establishes a constant frequency noticeable simplifies the control within the nanogrids.

#### 5.2.1.1 AC nanogrids dynamic control based on QVC grid-forming control

As proposed in Section 3.8.8, the QVC can be applied to the 3-phase AC control under some assumptions. The fixed frequency QVC-based voltage control proposed for the NGHCs in the  $dq$  synchronous reference frame is shown in Fig. 5.3. The complete cascaded control scheme for any of the 3-phase NGHCs is represented, being the term  $k$  the nanogrid identifier. In addition to the scheme presented in Section 3.8.8, a grid current decoupling term can be added to the current command as a feed-forward term to improve the disturbance rejection. However, as a tradeoff, an improved disturbance



within its power limitations, while the mains contribute with the high bandwidth transients unless the battery power is limited for any reason, in which case the mains will participate also in the steady state. The power contribution of the BESS is decided by means of a low pass filter with a determined cut-off frequency that generates the  $P_{bess}^*$  reference, while the mains share the rest of the QVC control action. Alternatively, if a peak-shaving strategy is needed, the power reference to the BESS and the mains can be exchanged without any other implications in the following discussion.

In the case of *islanded* mode, the battery would be the only available power source to maintain the regulation of the LVDC bus. In that case, to maintain the proper operation of the QVC-based voltage regulator, either a back-calculation or a reduction on the QVC bandwidth,  $\omega_n$ , should be applied to fulfill the cascaded control requirements so that the QVC bandwidth is at least ten times lower than the cut-off frequency used in the BESS low pass filter. Those two options are indicated in red within the figure.

### 5.2.2 VG-based microgrid control proposal

The integration of virtual synchronous generator (VSGs) in PEC dominated microgrids allows to imitate the behavior of conventional grids dominated by large synchronous generators (SGs), providing the microgrid with an increased overall virtual inertia, softening the voltage magnitude and frequency rate of change during abrupt active power transients, as well as attaching the active power to the grid frequency. Moreover, VSGs allow the integration of conventional SGs in the microgrid together with DGs, ESS and loads interfaced by PECs. Besides, the VSG scheme can also be combined with distributed droop control in order to manage the steady state power sharing between different sources in the MG, improving the transient response and lack of inertia of the droop control. Although in DC there is not an equivalent approach like synchronous generator dominated DC grid, this thesis proposes to extend the concept of VSG to DC systems, taking advantage of its properties to provide a DC microgrid with inertia and establish a decentralized transient power sharing between different sources. In the microgrid under study, this means that the transient participation of mains and central BESS can be determined by assigning them a different inertia.

This following discussion has to be seen as an alternative to the primary control based on fixed frequency nanogrids and centralized LVDC voltage control presented previously. In this alternative approach the control of the NGHCs is implemented by means of a grid-forming VSG instead of the conventional fixed frequency grid-forming, and an LVDC voltage regulation scheme based on DC virtual generators (DCVGs) and P/V DC droop control. This allows to adapt the participation of the mains and central BESS in the transient and stationary power sharing and, additionally, provides

an automatic transition between the *grid-connected* and *islanded* modes.

### 5.2.2.1 AC nanogrids dynamic control based on virtual synchronous generators (VSGs)

Each NGHC acts as a grid-forming unit with a dynamic control based on a VSG scheme, regulating both the AC voltage magnitude and frequency. The control system assumes the NGHC is the highest rated power converter and the highest inertial source in the NG, absorbing the majority of the power mismatches. As in the previous primary control scheme, the NGHCs' control is decoupled from the LVDC bus regulation, and the power mismatches supported by the NGHCs are entirely provided by the mains and the central BESS, being the NGs agnostic about each other. Although the nanogrids count with a 4 wires topology (3ph+N), as in the previous NGHCs control proposal, a balanced system will be considered, being the effect of unbalances out of the scope of the thesis, simplifying the NGHCs regulation to a 3-phase VSG control.

The VSG control topology proposed for the NGHCs is shown in Fig. 5.5 and it is based on the closed-loop VSG control scheme proposed in [133]. It is implemented in the dq synchronous reference frame and consists of the following parts:

1. **A virtual stator impedance model** (resistance  $R_s^k$  and inductance  $L_s^k$ ) that emulates the VSG stator and generates the current references  $i_{i_d}^*$  and  $i_{i_q}^*$ .
2. **An inner control loop** consisting of a  $dq$  vector current controller similar to the used in the fixed frequency approach (Figs. 3.10 and 5.3).
3. **An emulation of an automatic voltage regulator (AVR)** to regulate the NG voltage in steady state by generating a virtual voltage,  $E_d^k$ ;
4. **A governor model** that regulates the rotor speed,  $\omega_e^k$ , i.e., the grid frequency, according to a given frequency reference  $\omega_e^{k*}$  that in this case will be the nominal grid frequency.
5. **The virtual synchronous generator rotor model** emulating a virtual inertia and damping using the VSG swing function (5.1), where  $b_r^k$  is the rotor damping (viscous friction coefficient),  $J_r^k$  is the inertia, while  $\tau_G^k$  and  $\tau_L^k$  are the governor applied virtual torque and the virtual torque load respectively, being the last one depending on the actual load of the NGHC. This block determines the grid frequency and the synchronization angle  $\theta_e^k$ .

$$\frac{d}{dt}\omega_e^k(t) = \frac{-b_r^k}{J_r^k}\omega_e^k(t) + \frac{1}{J_r^k}(\tau_G^k(t) - \tau_L^k(t)) \quad (5.1)$$

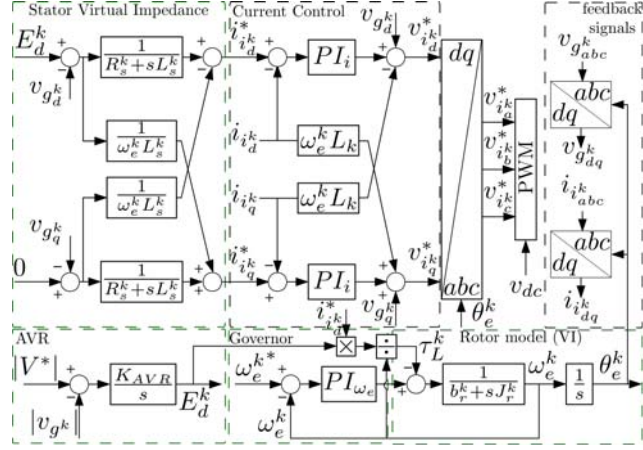


**Figure 5.5:** VSG-based grid-forming control block diagram proposed for the implementation in the NGHCs.  $k$  is the NG identifier.

### 5.2.2.2 LVDC dynamic control based on droop control and DC virtual generators (DCVG)

The proposed LVDC regulation scheme consists in the dynamic power sharing between the mains and the BESS through DC virtual generators (DCVGs) and P/V DC droops. This control topology presents two main characteristics:

- The DC virtual generators enable to modify the DC bus inertia and to define the transient power sharing between the mains and BESS. For instance, in some cases it will be more desirable to provide the high frequency variations with the mains, reducing the stress in the BESS, while in others, it could be the opposite (as in peak saving strategy).
- The P/V droop permits to establish a decentralized sharing mechanism during steady state.

The proposed DCVG control scheme is shown in Fig. 5.6, valid for both the MGHC (mains) and the central BESS, where  $\gamma$  is an identifier that can represent *mains* or *bess*. Its integration in the MG is shown in Fig. 5.7.

The DC virtual generator scheme is divided in 8 blocks:

1. **P/V droop:** where  $m_\gamma$  is the droop gain,  $P_0^\gamma$  is the offset commanded power (for example an steady state power command for charging the battery in the central BESS) and  $P_\gamma$  is the measured output power.
2. **Reference calculation:** the DCVG output voltage reference is calculated based on the P/V droop output, the LVDC bus nominal voltage  $v_{dc}$  and a virtual

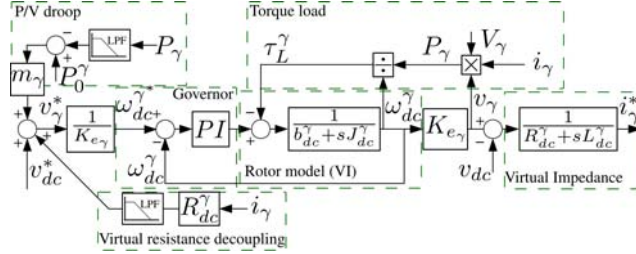


**Figure 5.6:** DC virtual generator (DCVG) proposed for the distributed regulation of DC voltage and the power sharing between the mains and the central BESS. The identifier  $\gamma$  can be substituted by *mains* or *bess*.

- resistance decoupling. After the calculation of  $v_\gamma^*$ , a bmf constant ( $K_{e_\gamma}$ ) is applied to get the frequency ( $\omega_{dc}^\gamma$ ).
3. **Governor:** it consist of a feedback PI regulator which aim is to track the ( $\omega_{dc}^\gamma$ ) reference.
  4. **Rotor model:** is the virtual plant that provides the virtual inertia ( $J_{dc}^\gamma$ ) and friction ( $b_{dc}^\gamma$ ) to the system.
  5. **Torque load:** is the disturbance of the virtual system and is obtained from the instantaneous power shared by the mains or BESS.
  6. **Frequency to voltage conversion:** the virtual generator voltage is obtained from the virtual frequency ( $\omega_{dc}^\gamma$ ), using the constant  $K_{e_\gamma}$ .
  7. **Virtual impedance:** a virtual impedance is used to determined the current reference which feed the inner control loops of the power sources, in this case managed through the SST. The impedance consists of a resistance and an inductance ( $Z_{dc}^\gamma(s) = R_{dc}^\gamma + sL_{dc}^\gamma$ ).
  8. **Virtual resistance decoupling:** suppress the steady state voltage deviation due to the virtual impedance. It is worth to point out that it does not compensate the possible voltage deviations due to the droop control or the presence of DC line impedance.

Unlike the VSG-based grid-forming, the DCVG approach is not an extended solution, being a relatively novel scheme with few similar examples in the recent literature [157, 158]. In order to demonstrate the operation of the proposed sharing scheme in DC, some simulations have been performed in Matlab/Simulink<sup>®</sup>, showing its performance for the LVDC bus regulation of the microgrid under study using the setup described in Appendix A.8.

The power sharing performance for different values of inertia given by the mains and the central BESS is shown in Fig. 5.8. The figure shows the power shared by

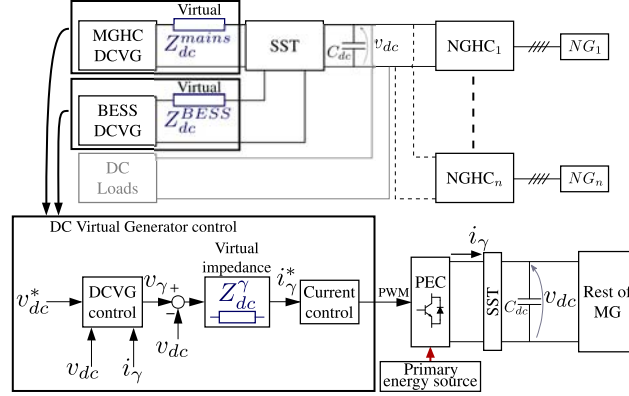


**Figure 5.7:** Integration of the DC virtual generator in the DC bus. The identifier  $\gamma$  can be substituted by mains or bess.

the mains ( $P_{mains}$ ), the BESS ( $P_{bess}$ ), a DC load disturbance ( $P_{L_{dc}}$ ) and the transient power supplied by the LVDC bus capacitor ( $P_{C_{dc}}$ ). Three cases are compared:

1. The mains have a larger inertia, resulting in a higher contribution than the BESS during the transient.
2. The inertia is the same for both, contributing the mains and BESS equally to the initial transient.
3. The BESS presents higher inertia, supporting the transient power mismatch.

In all the cases, the DC bus capacitor supplies the high bandwidth power mismatches. It is worth noting that the stationary power sharing remains unchanged for the 3 cases and depends on the P/V DC droop ( $m_{mains} = 0.02$ ,  $m_{bess} = 0.002$ ).

In the context of this thesis, the first scenario will be assumed for this control alternative. Unlike in the centralized control presented in Section 5.2.1 that minimizes the use of the mains during steady state, in this case the mains will present a higher inertia and power sharing contribution while the BESS remains as a MG back-up in case of contingencies in the mains, especially for *islanded* condition. The BESS inertia is kept low in order to reduce the stress on the battery and increase its life time. Fig. 5.9 illustrates the system behavior in the LVDC side for the selected control under *grid-connected* and *islanded* operation. As shown, once the mains are disconnected at  $t=3.65s$ , the battery has to fully support the DC link regulation. However, due to its low inertia, the DC voltage drop during transients becomes larger. At  $t=4.1s$  the mains are reconnected. It is worth to point out that the transition between *grid-connected* and *islanded* modes is automatic and islanding detection is not needed to maintain the DC bus under regulation. The stationary voltage deviation with respect to the nominal DC voltage ( $v_{dc}^*$ ) is due to the P/V DC droop and should be solved by

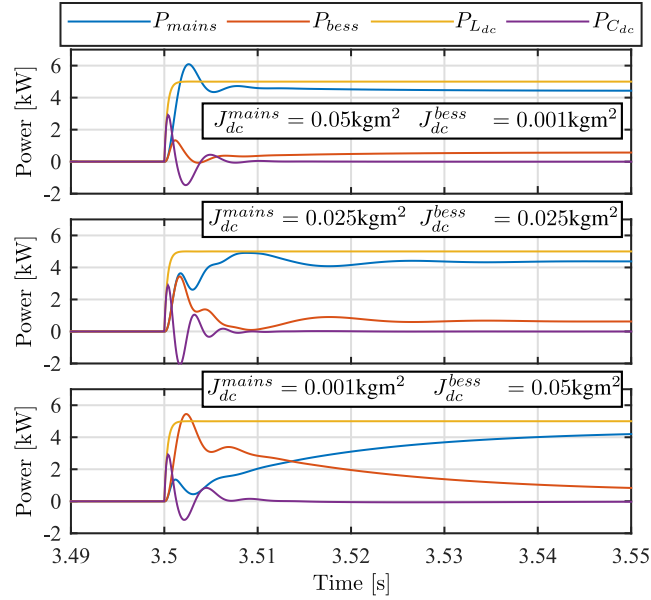


**Figure 5.8:** Power sharing in the DC voltage regulation based on DC virtual generators. Comparison of the performance for different values of inertia in the MGHC (mains) and the BESS under a DC constant power load step disturbance in the DC bus.

the upper secondary controller that should modify the droop parameter  $m_{bess}$  during *islanded*.

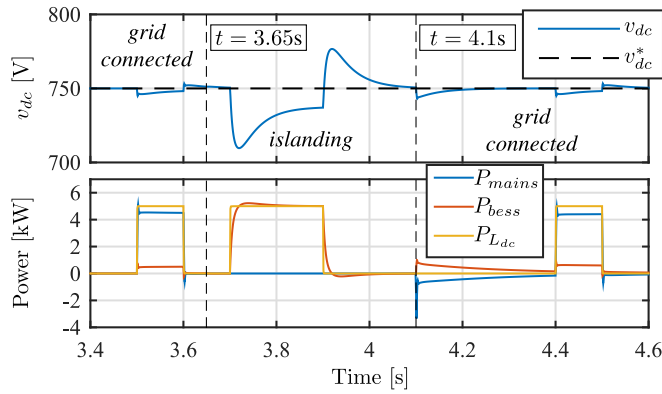


**Figure 5.9:** LVDC control performance and power sharing during *grid-connected* and *islanded* operation. The MG enters in *islanded* mode at  $t=3.65s$  and returns to *grid connected* at  $t=4.1s$

In order to evaluate the functioning of the P/V DC droop and its effects on the system performance, an additional simulation, shown in Fig. 5.10, has been carried

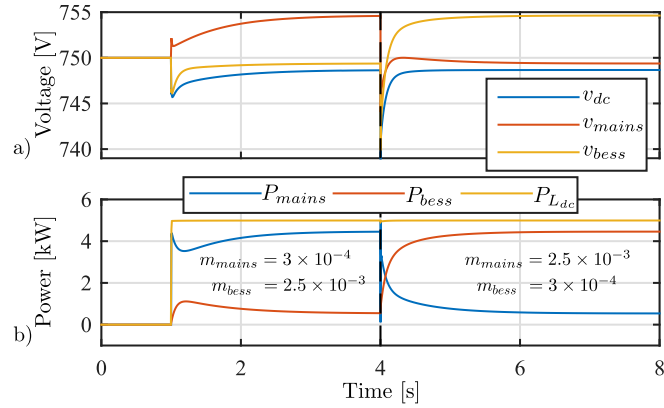


**Figure 5.10:** Simulation results: P/V DC Droop operation. a) LVDC bus voltage and virtual mains and BESS voltages; c) power shared by the mains, BESS and DC load.

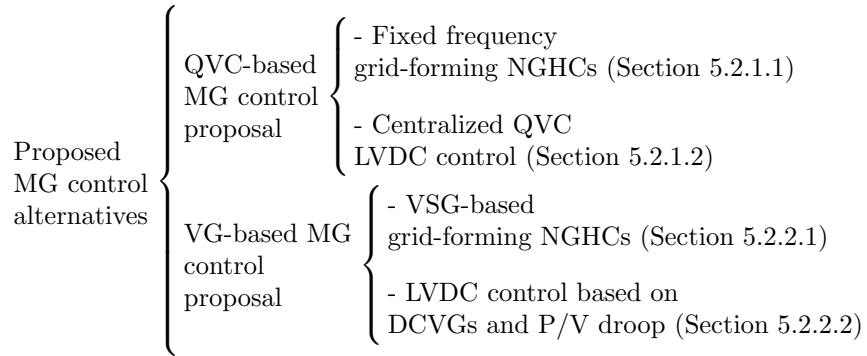
out for illustrating in detail its operation under a DC load step and a sudden change in the mains and BESS droop gains during *grid-connected* mode. At  $t=1$ s a DC load is connected. As a consequence the LVDC voltage drops due to the P/V droop and the mains and BESS virtual generator voltages are modified to provide a determined power sharing. At  $t=4$ s, the droop gains are changed, modifying the power shared by the mains and BESS as well as the virtual voltages.

These simulation results have shown the characteristics of the proposed DC virtual generator, proving its suitability for the application in the system under study, and offering versatility as a solution for low inertial DC grids regulation.

### 5.3 Improved cooperative active power control discussion

The previous section has proposed different scenarios for the control of the voltage in the LVDC, and the regulation of the voltage magnitude and frequency in the nanogrids, summarized in the schema 5.1.

Bridging the differences, in both MG control proposals the regulation of the LVDC and the NGs remain independent and the NGHCs, that play the role of interlinking converters, are operated as AC grid-forming converters. Thus, The NGHCs' control assume the LVDC bus as an ideal DC voltage source while the LVDC bus regulation considers the NGHCs and NGs as a disturbance. Although operating an interlinking converter as an AC grid-forming converter allows to decouple the AC from the DC bus dynamics and contingencies, this might become an issue if the AC side is tightly regulated and the DC side present a low inertia or slow bandwidth regulation. In the case under study, this scenario appears clearly during *islanded* mode, where the regulation



Schema 5.1: Primary control alternatives presented in Section 5.2.

relies entirely on the central BESS and the power mismatches are absorbed/supplied by the BESS and the LVDC capacitor.

Although the NGHCs cannot behave as grid-forming for both the DC and AC voltages at the same time, the solution to avoid dynamic and stability issues, and reduce the central BESS stress during transients may rely on modifying the control of the NGHCs so that they participate also on the regulation of the LVDC bus or ease their dynamic behavior to soften the effect that sudden power changes in the AC NGs produce in the LVDC bus. However, this might present the counterpart of reducing the stiffness and inertia of the AC nanogrids.

In Section 4.2 a solution for compensating active power, based on virtual damping and virtual inertia/capacitance, that can be applied to the nanogrids in both MG control proposals, has been proposed. The use of this solution could compensate the lack of stiffness in the NGHCs control if necessary. The compensators located in the AC nanogrids would be blind to the issues and contingencies in the LVDC bus when the NGHCs are operated as grid-forming for the AC nanogrids. However, involving the NGHCs in the DC regulation could lead to an indirect support for the LVDC bus by means of the devices connected within the nanogrids, improving the active power sharing between the LVDC bus and AC NGs. Thus, a power compensator would react not only to events happening in the LVDC bus but also in other nanogrids, providing flexibility to the microgrid regulation when necessary.

The second part of this chapter proposes two different control approaches for enabling a more flexible and cooperative dynamic active power sharing between the AC nanogrids and the LVDC bus during islanded operation. Each approach consist of a modification of the primary control schemes presented in Chapter 3. They are summarized as follows:

- The first one applies to the QVC-based MG control (1<sup>st</sup> MG control proposal) and is based on a centralized control and an adaptive algorithm that decides the participation of each nanogrid in the transient active power sharing of the

microgrid. This strategy contemplates the integration of a dESS operated as a voltage magnitude compensator within one of the nanogrids.

- The second alternative is a modification of the VG-based MG control (2<sup>nd</sup> MG control proposal). A hybrid DC/AC virtual generator control scheme (HVG), based on the theory of Virtual Synchronous Machines (VSMs), but here extended to include a DC machine mechanically coupled using the virtual shaft concept, is proposed for its implementation in the NGHCs, coupling the control of the LVDC and the NGs. This strategy contemplates the integration of a dESS operated as a frequency compensator within one of the nanogrids.

Thus, the MG control proposals in the thesis sum up to 4 cases, clustered into two main groups as summarized in the schema 5.2, where the *Basic* stands for the control proposals presented in Section 5.2 while *Cooperative* refers to the methods proposed in the following sections.

$$\text{Proposed MG control alternatives} \left\{ \begin{array}{l} \text{QVC-based MG control proposal} \\ \text{VG-based MG control proposal} \end{array} \right\} \left\{ \begin{array}{l} - \textit{Basic} \text{ QVC-based MG control (Section 5.2.1)} \\ - \textit{Cooperative} \text{ QVC-based MG control (Section 5.4)} \\ - \textit{Basic} \text{ VG-based MG control (Section 5.2.2)} \\ - \textit{Cooperative} \text{ VG-based MG control (Section 5.5)} \end{array} \right.$$

Schema 5.2: Primary control alternatives proposed in this thesis.

## 5.4 Hybrid microgrid control based on adaptive dynamic power sharing

The cooperative adaptive dynamic power sharing applied to the QVC-based microgrid control scheme will be based on the centralized control shown in Fig. 5.11, and it is essentially composed by the following elements:

1. A modified version of the LVDC bus voltage control presented in Fig. 5.4 that generate the high bandwidth reference for the NGHCs instead of the mains.
2. An adaptive algorithm that establishes the sharing of the high bandwidth reference between the NGHCs. A sharing coefficient is used to determine the participation of each NGHC.
3. A modified version of the NGHCs grid-forming control presented in Fig. 5.3 that allows to receive external power references that modify their dynamic control action.

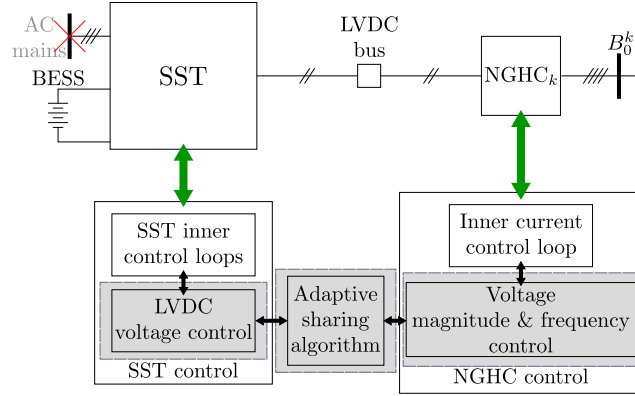


Figure 5.11: Adaptive hybrid dynamic power sharing concept.

### 5.4.1 The DC bus voltage control scheme

The proposed DC bus voltage control scheme is shown in Fig. 5.12. As the originally proposed scheme, it consists in a QVC controller generating a power reference  $P_{C_{dc}}^*$ , which is divided into a low ( $P_{C_{dc_{lf}}}^*$ ) and high ( $P_{C_{dc_{hf}}}^*$ ) bandwidth components by using a low pass filter and saturation. The low frequency command  $P_{C_{dc_{lf}}}^*$  will be given by the BESS, whereas the  $P_{C_{dc_{hf}}}^*$  command will be shared by the NGHCs, dividing it in the commands  $P_{NGHC_1}^*$  to  $P_{NGHC_n}^*$  using sharing coefficients for each NGHC. As *islanded* mode is considered, the utility grid power command in the SST is set to zero ( $P_{main}^* = 0$ ).

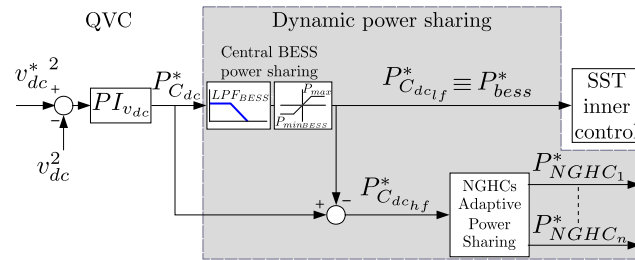


Figure 5.12: Proposed hybrid DC/AC voltage control: DC voltage control scheme based on adaptive power sharing between the different elements in the MG transformation center during *islanded* mode.

### 5.4.2 Adaptive NGs power sharing algorithm

The high frequency power reference shared between the NGHCs will be defined by an adaptive algorithm consisting in the use of complementary sharing coefficients, calculated based on LVDC bus and AC NGs instantaneous conditions. An initial approach was proposed in [2] consisting of a local NGHC coefficient calculation, and a normalization process defined by the equations (5.2), (5.3) and (5.4).

$$\sigma_k(t) = k_{ish} \int \lambda_{dc}^k \Delta v_{dcpu}(t) - \lambda_g^k \Delta v_{g^k pu}(t) dt \quad (5.2)$$

$$\Delta v_{dcpu}(t) = \frac{v_{dc}(t) - v_{dc}^{ss}(t)}{v_{dc}^{ss}(t)} \quad (5.3)$$

$$\Delta v_{g^k pu}(t) = \frac{|v_{g^k}|(t) - |v_{g^k}^{ss}|(t)}{|v_{g^k}^{ss}|(t)} \quad (5.4)$$

Where  $v_{ss}^{eq}$  and  $|v_g^{kss}|$  are the steady-state values of DC voltage and AC voltage magnitude, i.e., the values at the equilibrium point, and  $|v_{g^k}|$  is the AC voltage magnitude at the node  $B_0^k$  of the nanogrids, define as (5.5).

$$|v_{g^k}| = \sqrt{v_{g_d^k}^2 + v_{g_q^k}^2} \quad (5.5)$$

The sharing coefficients for each NGHC,  $\sigma_k$ , were obtained for each NGHC as a function of the DC bus and AC NGs voltage variations in p.u.,  $\Delta v_{dcpu}$  and  $\Delta v_{g^k pu}$ , defined in (5.3) and (5.4). Two constant weighting factors,  $\lambda_{dc}^k$  and  $\lambda_g^k$ , allow to modify the importance of each voltage variation, while the integral gain  $k_{ish}$  determines the adaptation speed.

The continuous integration in this method allows for fast and continuous adaptation. However, this fast adaptation might interfere with the system dynamics, and it relies on high bandwidth communication links between the LVDC voltage controller and the NGHCs controllers for the exchange of the coefficients, becoming non-reliable in case of momentary communications loss or even speed reduction. Moreover, as the variable  $\Delta v_{dcpu}$  is the same in the calculation of the coefficient for both NGHCs, its dependency can be avoided as long as  $\lambda_{dc}^k$  is the same for all the NGHCs. Thus, that adaptation algorithm was modified to overcome the cited potential issues. The adaptive algorithm can be divided in 3 steps summarized in Fig.5.13: 1) a transient detection that triggers the update of the sharing coefficients; 2) the local coefficient calculation; and 3) the normalization of the sharing coefficient that allows to calculate the power command  $P_{NGHC_k}^*$  for each nanogrid.

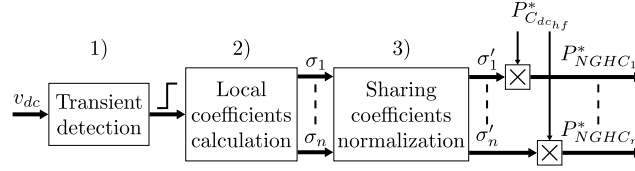


**Figure 5.13:** Simplified representation of the adaptive algorithm for power sharing between the LVDC and the NGHCs.

#### 5.4.2.1 Transient detection

The sharing coefficients will be updated when a significant active power disturbance is demanded to the hybrid MG leading to an asynchronous update of those coefficients. For that purpose, the transient detection mechanism proposed in Section 4.3.2.2 is used for triggering the calculation of the sharing coefficients. As in the proposed MG any active power change (either in the LVDC bus or within the nanogrids) will have an impact in the LVDC bus, the LVDC bus voltage will be the signal used for determining the transient window. The block diagram of the transient detection algorithm for this application is shown in Fig. 5.14.

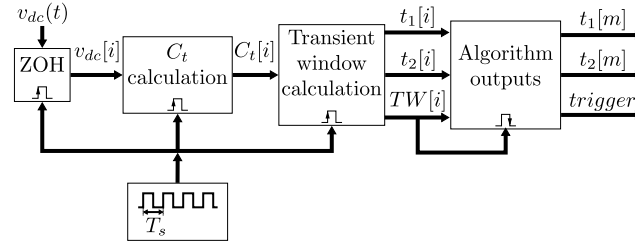


**Figure 5.14:** Simplified representation of the transient detection algorithm applied to the LVDC voltage.

In the present application, the input to the transient detector will be the measured LVDC voltage ( $v_{dc}$ ) and the main purposes of the transient detector is to trigger the update of the sharing coefficient and determine the instants  $t_1$  and  $t_2$  that will be used in the sharing coefficient calculation (5.6).

#### 5.4.2.2 Local coefficient calculation

The sharing coefficient  $\sigma_k$  is calculated after the instant  $t_2$  using the RMS value of the p.u. AC voltage magnitude deviation in the NGHC PCC ( $B_0^k$ ) of each NG, in the interval  $t_1$ - $t_2$ , where  $t_1$  and  $t_2$  are determined by the transient detector. Firstly, the RMS value  $\Delta v_{g_{RMS}^k}$  is obtained within the interval  $t_1$ - $t_2$  as (5.6), where  $m$  refers to the actual iteration of the adaptive power sharing algorithm. Secondly, the RMS value

is saturated,  $\Delta v_{g_{RMS}^k}^{sat}$ , as (5.7), where  $\delta_{max}$  is a tunable parameter that represents the maximum expected RMS value. Then, the sharing coefficient  $\sigma_k$  is obtained as (5.8), where  $\lambda_g^k$  is a configurable weighting factor, limited between 0 and 1, and  $\eta_m$  is a filtering factor that provides the algorithm with memory. Thus, if  $\eta_m > 1$ , the previous values of  $\Delta v_{g_{RMS}^k}^{sat}$  will be necessary for the sharing coefficient calculation.

$$\Delta v_{g_{RMS}^k}[m] = \sqrt{\frac{1}{t_2[m] - t_1[m]} \int_{t_1[m]}^{t_2[m]} |\Delta v_{g_{pu}^k}(t)|^2 dt} \quad (5.6)$$

$$\Delta v_{g_{RMS}^k}^{sat}[m] = \begin{cases} 0 & \text{if } \Delta v_{g_{RMS}^k}[m] \leq 0 \\ \Delta v_{g_{RMS}^k}[m] & \text{if } 0 < \Delta v_{g_{RMS}^k}[m] < \delta_{max} \\ \delta_{max} & \text{if } \Delta v_{g_{RMS}^k}[m] \geq \delta_{max} \end{cases} \quad (5.7)$$

$$\sigma_k[m] = \delta_{max} \cdot \eta_m - \lambda_g^k \sum_{i=0}^{\eta_m-1} \Delta v_{g_{RMS}^k}^{sat}[m-i] \quad (5.8)$$

### 5.4.2.3 Normalization

Finally, the sharing coefficients of each NG are normalized ( $\sigma'_k$ ) as (5.9) and the power reference for each NGHC is calculated as (5.10).

$$\sigma'_k[m] = \frac{\sigma_k[m]}{\sum_{i=1}^2 \sigma_i[m]} \quad (5.9)$$

$$P_{NGHC_k}^* = P_{C_{dc_{hpf}}}^* \sigma'_k[m] \quad (5.10)$$

In order to clarify the relation of the different blocks that composed the adaptive power sharing algorithm and its integration in the MG control, Fig. 5.15 shows a block diagram summarizing the relation between the different elements, describing the steps of the adaptive power sharing algorithm, for a MG with 2 nanogrids.

### 5.4.3 The AC nanogrids cooperative voltage control scheme

The proposed NGHC voltage control scheme for the adaptive dynamic power sharing presented in this section consist of a modified version of the QVC-based NGHC control seen in Section 5.2.1.1 (Fig. 5.3), that allows to process the reference  $P_{NGHC_k}^*$  obtained by the adaptive algorithm. When the hybrid adaptive power sharing is enabled, i.e., during *islanded* mode, the power  $P_{NGHC_k}^*$  is subtracted from  $P_{i_d}^*$ , modifying

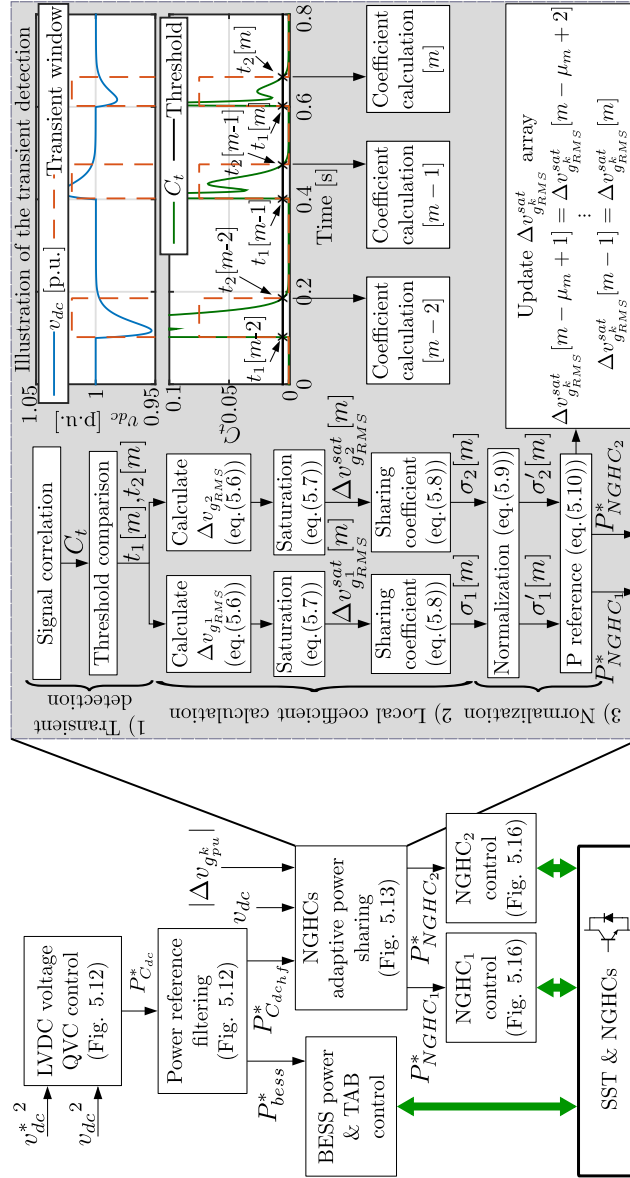


**Figure 5.15:** Simplified diagram of the proposed control topology for the hybrid AC/DC MG and description of the adaptive power sharing algorithm considering two nanogrids ( $n = 2$ ).

the control action, and therefore a soften power sharing with the LVDC bus is expected. The effect of the  $q$ -axis in the active power component will be neglected against the  $d$ -axis, and thus,  $P_{NGHC_k}^*$  is just subtracted from the  $d$ -axis voltage control. This operation implies an adverse modification of the control action, thus, in order to prevent the  $d$ -axis voltage controller from eliminating the effect of  $P_{NGHC_k}^*$  or react to it, a back-calculation anti-windup is applied.

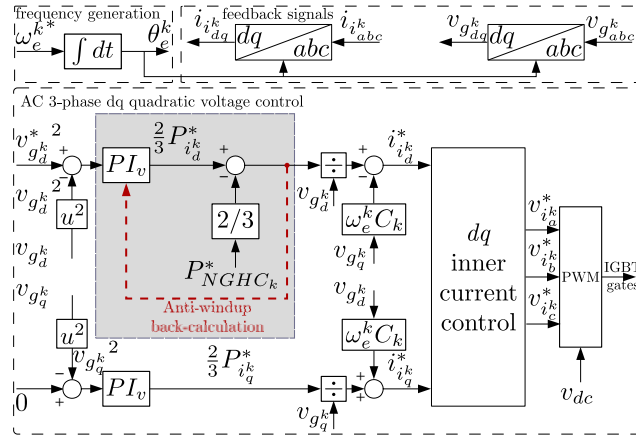


**Figure 5.16:** Modified NGHCs QVC-based AC grid-forming controller to enable the dynamic active power sharing between the LVDC bus and the nanogrids.

As the NGHCs are the NGs grid-forming, a modification in their power reference will lead to a variation in the AC voltage magnitude of the NGs, allowing the exchange of active power between the LVDC and the AC nanogrids. However, this effect is subject to elements in each AC NG providing/absorbing power as a reaction to the voltage magnitude variation. This can be provided by the nanogrid equivalent capacitance ( $C_k$ ), that can support a transient for a limited time without compromising the quality in the AC side. However the equivalent capacitance in AC nanogrids is expected to be low as it will be mainly formed by the capacitance of the LC filters belonging to the grid-tied power converters. Section 4.2 presented a dynamic power compensator as a solution for the lack of damping and inertia/capacitance in AC systems that can be applied as an ancillary service in AC grids. Thus, a solution to maintain the quality and increase the participation in the Hybrid DC/AC NG power sharing may relies on including local dynamic voltage compensation within the NG. In such a case, the voltage compensation not only enhance the operation locally in the nanogrid, but also can provide indirect support during transients to the LVDC bus and other neighboring AC nanogrids. The generic simplified configuration for a nanogrid is shown in Fig. 5.17, where only the NGHC and a possible local dynamic voltage compensator will participate actively in the NG voltage regulation while the rest of devices are treated as disturbances. It is worth to point out that the voltage compensator can be included or not within any of the nanogrids nodes.



manding a  $P_{NGHC_k}^*$  will lead to an adverse effect in the AC NGs voltage controller, being necessary to pursue for a trade-off between the LVDC bus and AC NGs quality based on the conditions of each NG, justifying the use of the adaptive power sharing algorithm.

#### 5.4.4 Simulation and experimental results

The proposed *cooperative* control presented in this section has been evaluated through simulations and experimentally, comparing it with the *basic* control (QVC-based MG control) presented in the Section 5.2.1. The simulation and experimental setup details are summarized in Appendix A.9. Two scenarios are considered to evaluate the performance of the *cooperative* control topology proposed in this section compared with the *basic* configuration:

1. The first scenario consists in applying the proposed adaptive *cooperative* technique for power sharing without any local AC dynamic voltage compensator.
2. In the second scenario, a local voltage compensator is activated in the  $NG_1$ .

The *basic* configuration will be evaluated in *islanded* mode and without local voltage compensation in the NGs. Considering a central BESS power control bandwidth of 75Hz, in the *basic* case the LVDC voltage control bandwidth will be reduced to 10Hz in order to comply with margins of cascaded control requirements. On the other hand, when the *cooperative* technique is applied, the NGHCs participation permits an overall inner control loop bandwidth, and consequently a larger LVDC voltage control bandwidth. The overall inner control loop bandwidth for the LVDC bus voltage control is assumed to be the same as the NGHCs inner control bandwidth (500Hz), and therefore the LVDC voltage QVC controller bandwidth can be increased up to 50Hz.

Considering the increasing penetration of CPLs in the electrical system and their negative effect in the system stability and dynamic response as highlighted in Section 3.8, the system has been evaluated under CPLs, assuming it is the worst possible case, considering them as the most critical disturbance when compared with CILs and CCLs.

##### 5.4.4.1 Simulation results

The proposed methods has been validated through simulations in MATLAB/Simulink<sup>®</sup> following the simulation setup shown in Fig. 5.19. Apart from the converters in the MG transformation center (MGHC, SST, NGHCs) the following devices are considered in the MG: 1) two CPLs are present in the MG, one in each nanogrid, located in the nodes  $B_2^1$  and  $B_2^2$ , 2) a local dynamic voltage compensator supplied by an ESS is connected to the node  $B_1^1$  of  $NG_1$ .

The simulation results are shown in Fig. 5.20, where the *basic* and *cooperative* 1<sup>st</sup> primary control are compared. It shows the LVDC bus voltage, the AC voltage

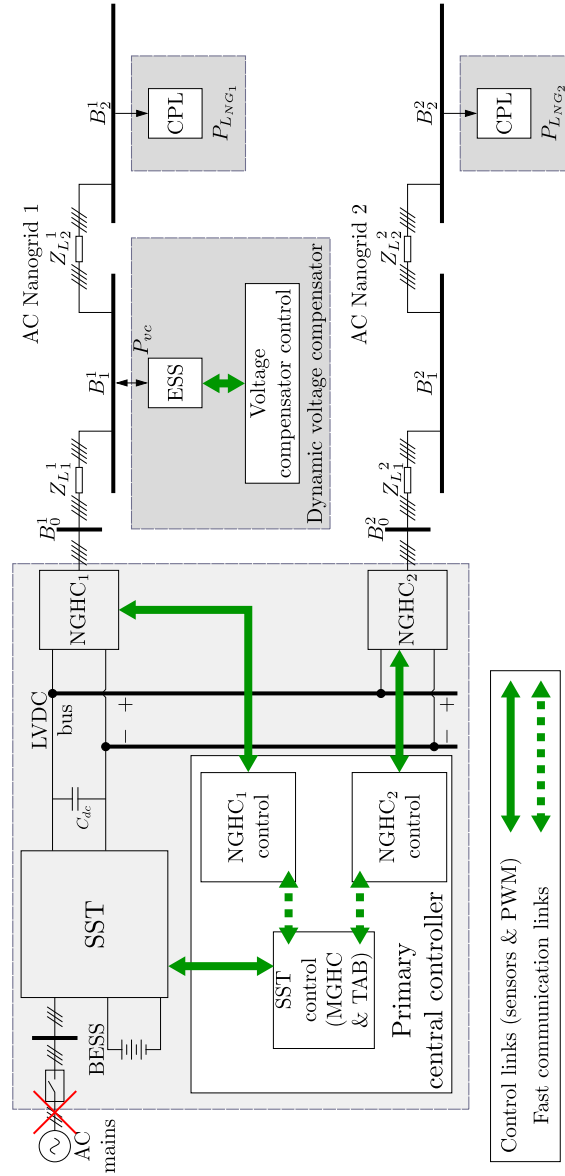


**Figure 5.19:** Simulation setup: 1<sup>st</sup> microgrid primary control strategy and improved adaptive hybrid power sharing.

magnitude in both NGs in p.u. at the node  $B_0^k$  (point of connection of the NGHCs), the normalized sharing coefficients  $\sigma'_k$  and the transient window used for updating the coefficients, the power commands generated by the modified QVC DC controller (Fig. 5.12 and the active power drawn by the CPLs in each NG. The system is tested under multiple steps of CPL disturbances in both NGs. The sequence of events observed in the figure is the following:

- Between  $t = 0\text{s}$  and  $t = 0.25\text{s}$ , the sharing coefficients  $\sigma'_1$  and  $\sigma'_2$  are forced to 0 in the proposed *cooperative* control (the NGHCs do not cooperate with the LVDC bus regulation) and the local AC dynamic voltage compensator is inactive. This scenario present similar conditions to the *basic* control, however, the voltage controller bandwidth is kept to 50Hz while it is 10Hz for the *basic* control. This test allows to illustrate the effect of using excessive voltage control bandwidth with reduced inner control bandwidth (only the central BESS contribute to the LVDC voltage control). The violation of the cascaded control requirements is traduced into oscilations in the LVDC bus voltage and in the central BESS power.
- At  $t = 0.25\text{s}$ , the proposed *cooperative* sharing technique is activated. As expected, the power required by the LVDC voltage controller is now shared between both NGs and central BESS, reacting one NG to the events on the other. As the BESS provides the steady state, the NGHCs only contribute during the transients. Under this control, the LVDC bus voltage transients are improved compared to the *basic* control. However, the AC NGs voltages become distorted as a consequence.
- At  $t = 0.65\text{s}$ , the local dynamic voltage compensator in  $B_1^1$  ( $NG_1$ ) is activated (only in the *cooperative* case). This leads to an overall improvement in both LVDC bus and AC voltages, reducing significantly the voltage variations due to CPL steps.
- At  $t = 1.3\text{s}$ , the total system load exceeds the central BESS maximum power. This leads to an overall MG collapse for the *basic* control at  $t = 1.5\text{s}$ . The LVDC bus voltage becomes unregulated, drops as the LVDC bus capacitor is discharged. As the NGs voltage is only regulated by the NGHCs, the voltage magnitude in the NGs also drops as a consequence. Due to the power topology and modulation of the NGHCs, their terminal output phase voltage can be set up to  $\frac{v_{dc}}{\sqrt{3}}$  (third harmonic injection PWM), decoupling the drop of the DC voltage until that value reaches the nominal AC voltage, explaining the delay between the collapse in the LVDC bus and the NGs. On the other hand, in the *cooperative* control, the use of a local compensator not only improves the transients but also enables the power sharing mechanism to operate during steady state, maintaining the whole microgrid under regulation. Once the central BESS reaches the power limit, the compensator starts to provide power to maintain the LVDC bus and AC NGs at

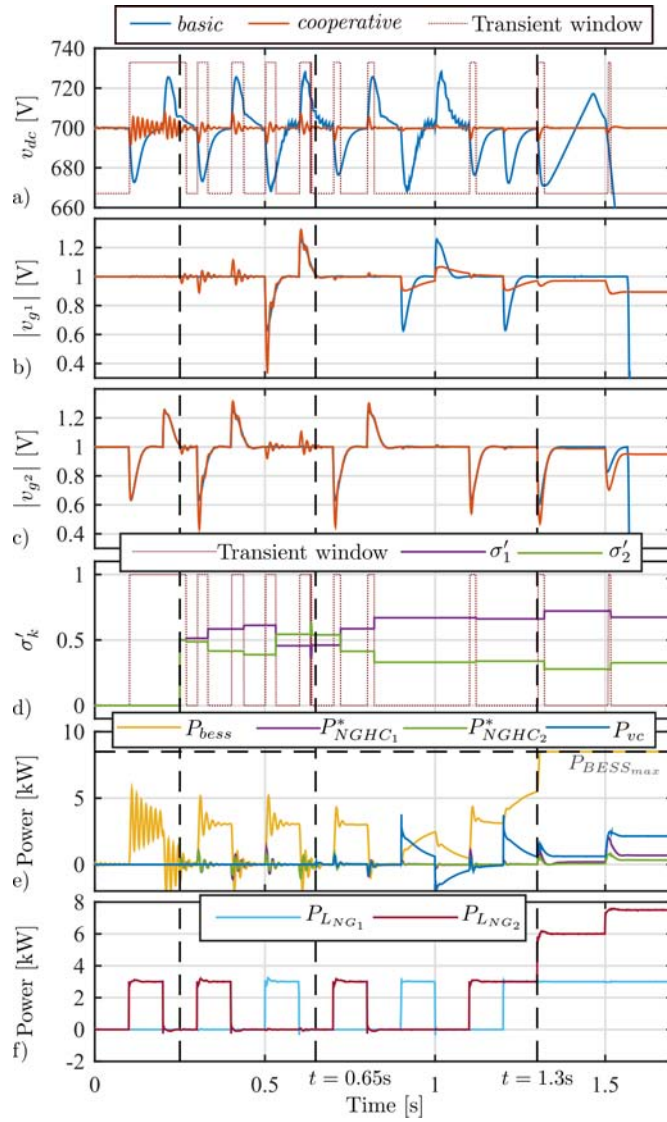


**Figure 5.20:** Simulation results: system performance using the proposed methods. a) LVDC Voltage; b)  $NG_1$  voltage magnitude in p.u., c)  $NG_2$  voltage magnitude in p.u., d) transient window obtained by the transient estimation strategy, and sharing coefficients, e) Power shared by the elements participating in the active power control, f) Load drawn by the CPLs located in the NGs.

the expense of an stationary error in  $v_{g_1}$  and  $v_{g_2}$  caused by the P regulator in the local AC voltage compensator, but avoiding the collapse of the microgrid.

#### 5.4.4.2 Experimental results

The experimental results have been obtained in a full scale hybrid AC/DC microgrid prototype implemented within the facilities of the research group *Laboratory for Electrical Energy Management Unified Research* in the University of Oviedo, Spain. The simplified experimental setup is shown in Fig. 5.21, similar to the configuration used in simulations, but in this case just a CPL, able to act as a load profile emulator, is present in the MG, located in the node  $B_2^2$  in the second nanogrid.

The experimental results are summarized in Fig. 5.22, where the *basic* and the *cooperative* control are compared. It shows the DC voltage, the AC voltage magnitude in both NGs in p.u., the sharing coefficients  $\sigma'_k$ , the CPL in  $NG_2$  and the power shared by the voltage compensator in  $NG_1$ . The system is tested under multiple steps of CPL disturbances in  $NG_2$ . The sequence of events are described as follows:

- Between  $t = 0\text{s}$  and  $t = 0.8\text{s}$ , the proposed cooperative technique (red) is enabled while the local AC voltage compensator is inactive. The power required by the LVDC bus voltage controller is shared between both NGs and the central BESS, reacting  $NG_1$  to the events on  $NG_2$ . As expected, the DC voltage transients are notably improved compared to the *basic* control. However, as a consequence, the voltage in  $NG_1$  is distorted and in  $NG_2$  the transient response might be worsen, depending on the sharing coefficient. Initially,  $\sigma'_1 = \sigma'_2$ , thus the power  $P_{C_{dc_{hf}}}^*$  is shared equally by the NGHCs. As the coefficient change, the transient response in the NGs is modified. As in this results the load steps take place only in  $NG_2$ , with the consequent significant voltage deviations, the adaptive sharing algorithm tends to reduce the collaboration of  $NGHC_2$ , increasing the participation of  $NGHC_1$  until a value of 0.75. However, as the voltage compensator is disabled, the only element providing inertia, i.e. transient active power, in  $NG_1$  is the filter capacitor, thus the participation of  $NGHC_1$  negatively impacts the  $NG_1$  AC voltage profile.
- At  $t = 0.8\text{s}$ , a local voltage compensator in  $NG_1$  is activated providing additional inertia, leading to an overall improvement in both DC and AC voltages as shown before in the simulation results. As soon as the  $NG_1$  voltage profile is improved due to the compensator, the adaptive mechanism keeps increasing the participation of  $NGHC_1$  in the LVDC control, alleviating the effort of  $NGHC_2$ . It is worth to point out how the voltage compensator in  $NG_1$  reacts to active power transients taking place in  $NG_2$ . This behavior is allowed by the proposed control scheme based on cooperative adaptive power sharing.

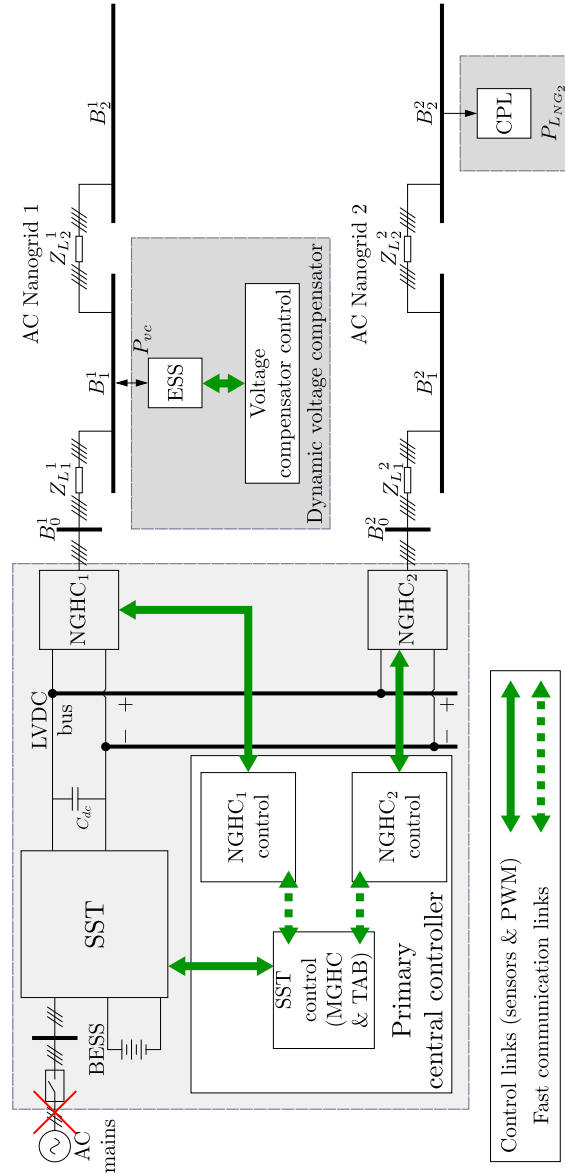


**Figure 5.21:** Experimental setup: 1<sup>st</sup> microgrid primary control strategy and improved adaptive hybrid power sharing.

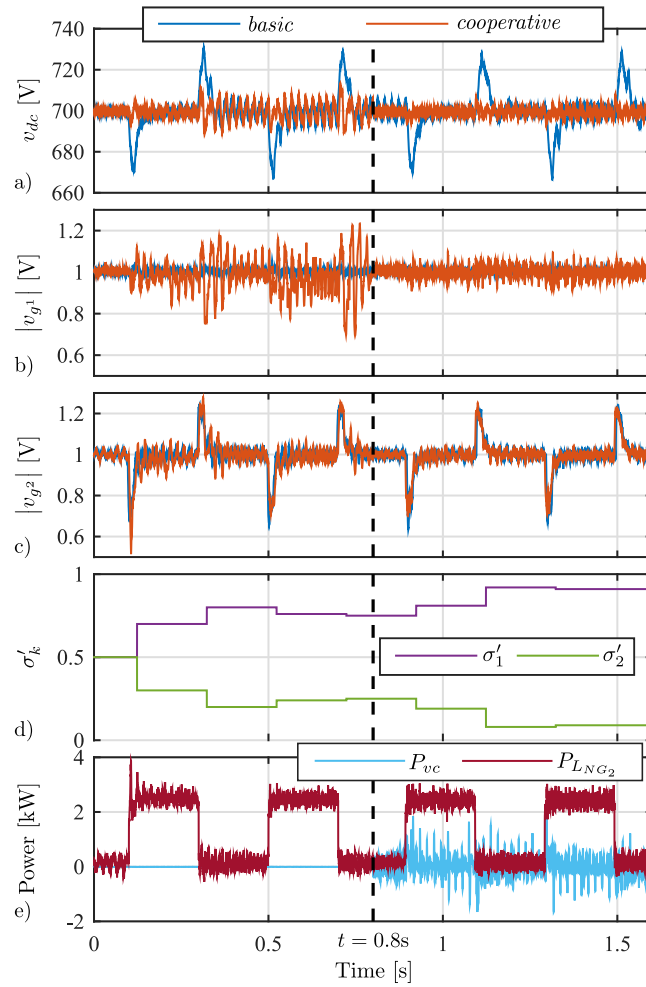


**Figure 5.22:** Experimental results: system performance using the proposed methods. a) LVDC Voltage; b)  $NG_1$  voltage magnitude in p.u., c)  $NG_2$  voltage magnitude in p.u., d) sharing coefficients, e) Load drawn by the CPL located in the  $NG_2$  and power shared by the voltage compensator.

### 5.4.5 Disturbance to output frequency response

In order to further analyze the proposed control methods and highlight the achievements against the *basic* control, the proposed system has been linearized using the MATLAB/Simulink<sup>®</sup> linearization tool. The disturbance to output transfer functions have been analyzed for the LVDC voltage and the nanogrids voltage magnitude. Two disturbances are considered: the CPL variations in the  $NG_1$ ,  $\Delta P_{L_{NG_1}}$ , and in the  $NG_2$ ,  $\Delta P_{L_{NG_2}}(s)$ . Three outputs are taken into account: the LVDC voltage variation,  $\Delta V_{dc}$ , and the NGs voltage magnitude variation,  $\Delta|V_{g1}|$  and  $\Delta|V_{g2}|$ .

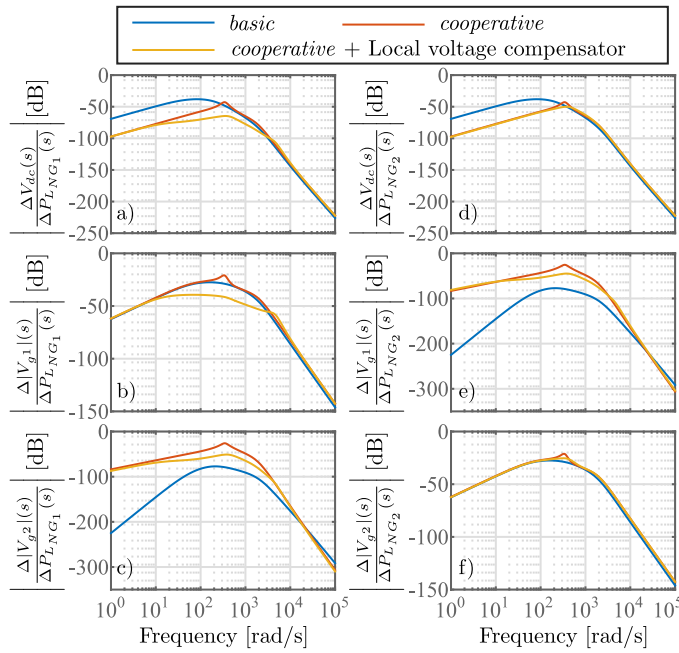


**Figure 5.23:** Bode diagram of the disturbance to output voltage transfer functions. The *basic* and *cooperative* methods are compared. a), b) and c) voltage variation in the LVDC and the NGs ( $\Delta V_{dc}$ ,  $\Delta|V_{g1}|$ ,  $\Delta|V_{g2}|$ ) under a CPLs disturbance in the  $NG_1$ . d), e) and f) voltage variation in the LVDC and the NGs ( $\Delta V_{dc}$ ,  $\Delta|V_{g1}|$ ,  $\Delta|V_{g2}|$ ) under a CPLs in the  $NG_2$ .

Fig. 5.23 shows the Bode diagrams of those transfer functions for 3 different cases: 1) the *basic* control; 2) proposed cooperative adaptive sharing control without local voltage compensators, 3) proposed cooperative adaptive control with a local voltage compensator in the  $NG_1$ . Those 3 cases have been evaluated in 3 equilibrium points ( $t = 0.09s$ ,  $t = 0.29$  and  $t = 0.89$  respectively) of the simulated system in Fig. 5.20. The Bode plots are explained below:

- a) & d): As the proposed cooperative method (red) allows to increase the band-

width of the LVDC voltage controller, the response is clearly improved at low and medium frequencies. In addition, when the voltage compensator is included (yellow), the response is further enhanced, specially in medium frequencies. It is worth noting that, although the local compensator is in  $NG_1$ , the response under  $\Delta P_{L_{NG_2}}$  is also improved thanks to the indirect cooperation between NGs.

- *b) & f)*: Here, the counter part of the power sharing mechanism (red) is shown. In order to improve the overall system operating range and the DC profile, the NGs disturbance rejection is slightly worsen. However, the local voltage compensator (yellow) attenuates this effect in f) ( $NG_2$ ), and improves drastically the response in b) ( $NG_1$ ) against the *basic* control.
- *c) & e)*: In the *basic* control (blue) the two NGs are decoupled from each other, thus  $\Delta P_{L_{NG_2}}$  has a negligible effect in the  $NG_1$  and vice-versa (their coupling is mainly due to sensor errors and delays). The cooperative adaptive sharing method allows to couple both NGs increasing the cross-effect that one has on the other as shown in c) and e). This enables the collaborative power flow between NGs.

Table 5.1: Gain Margins for the transfer functions in Fig. 5.23.

Gain margins [dB]	$\Delta P_{L_{NG_1}}$ disturbance			$\Delta P_{L_{NG_2}}$ disturbance		
	$\Delta V_{dc}$ a)	$\Delta  V_{g1} $ b)	$\Delta  V_{g2} $ c)	$\Delta V_{dc}$ d)	$\Delta  V_{g1} $ e)	$\Delta  V_{g2} $ f)
Basic	38.5	27.6	77.2	38.5	77.2	27.5
Cooperative	46.9	24.9	30.9	46.9	30.5	25.2
Cooperative & volt. comp.	67.2	39.4	54.9	52.4	48.8	26.4
Cooperative vs. basic	8.4	-2.7	-46.3	8.4	-46.7	-2.3
Cooperative & volt. comp. vs. basic	27.6	11.8	-22.3	13.9	-28.4	-1.1

The gain margins of the transfer functions represented in Fig. 5.23 are listed in Table 5.1, where a) to f) refers to each Bode plot. The difference between the *cooperative* method and the *basic* control are included below the gain margins. As shown, by slightly compromising the margins in b) and f), a noticeable improvement appears in the DC link a). In the case of the cross-effect transfer functions c) and e), the gain margins are still higher than in b) and f). It is worth pointing out that in every case the phase margin is infinite and the gain margin is positive, ensuring the global stability in all the analyzed cases.

## 5.5 Hybrid AC/DC microgrid control based on hybrid AC/DC virtual generators

The *cooperative* active power sharing proposed for the VG-based MG control scheme, presented in Section 5.2.2, will be based on a decentralized control in the transformation center, being the control of the mains and central BESS independent of the NGCHs' control. This modified control involves less changes on the *basic* VG-based MG control than the case seen in previous section, and it is essentially composed by the following elements:

1. The LVDC bus voltage control presented in Section 5.2.2.2 remains unchanged.
2. A hybrid virtual AC/DC generator (HVG) is proposed to replace the original VSG-based NGHCs control. The HVG consist of a modification of the VSG control scheme that links the reference frequency to the LVDC voltage.

The conceptual representation of the system based on virtual generators is shown in Fig. 5.24. Unlike in the *basic* control based on virtual generators, in the *cooperative* control once the proposed Hybrid AC/DC virtual generator is implemented in the NGHCs, the LVDC bus voltage behavior is coupled to the grid frequency in the NGs. Thus, the NGHCs become sensitive to disturbances in the LVDC, and therefore, to the active power changes in other NGs, participating automatically in the LVDC regulation. This reduces the dependence on the mains, and alleviates the participation of the central BESS during *islanded* mode as seen with the previous *cooperative* control proposed for the QVC-based MG control. During transients, the stiffness of the NGHCs will be soften and the inertial elements in the NGs (DERs and ESS operated as VSG or frequency compensators) will react to the frequency variation, injecting or absorbing active power. On the other hand, in case the central BESS is not able to provide the required power during steady state, the system, including the LVDC bus, will be supported by those DERs or ESS in the NGs able to provide power during steady state. In order to allow this behavior, and increase the participation of the NGs in the hybrid AC/DC MG power sharing, either in transients or steady state, there should be DERs in the NGs that react to changes in frequency. This can be achieved by using VSG combined with droop controls or by using dedicated frequency compensation devices based on VI. In the scope of this thesis, the master-slave configuration will be maintained for the control of the NGs, thus the NGHCs should still play the role of VSG-based grid-forming converters, considering also the integration of ESSs operated as VI-based dynamic frequency compensators.

### 5.5.1 The proposed hybrid AC/DC virtual generator

The proposed hybrid AC/DC virtual generator for the implementation of the NGHCs control is shown in Fig. 5.25. The proposed control is based on the model of a



DC virtual generator mechanically coupled to a VSG through the rotor shafts. While the AC stator model, the current regulator and the AVR remains the same as in the original VSG-based control proposed in Section 5.2.2.1 (Fig. 5.5), the control related to the frequency regulation is modified to be dependent on the LVDC voltage. The governor is replaced by the model of a DC Virtual Machine (DCVM) and it consist of the following elements:

1. **A DC stator model** ( $R_{dc}^k$  and  $L_{dc}^k$ ) that emulates a DC virtual stator impedance and establishes the electrical torque applied to the DC machine depending on the LVDC voltage  $v_{dc}$  and the bemf  $E_{dc}^k$ .
2. **The mechanical model of the virtual shaft** that couples the DC virtual machine and the VSG, modelled as a virtual inertia  $J_r^k$  and a damping factor  $b_r^k$ .
3. **An steady-state frequency regulator** based on the variation of the rotor flux  $\varphi$  to modify the relation between the rotational speed  $\omega_e^k$  and the bemf  $E_{dc}^k$ . The regulator  $R_{\omega_e^k}$  can be implemented as an slow PI or as an integrator, as the main function of this block is to control the steady state frequency. In order to improve the response during start up, the inverse of the nominal bemf constant  $K_e^{-1}$  is applied as a feed-forward.

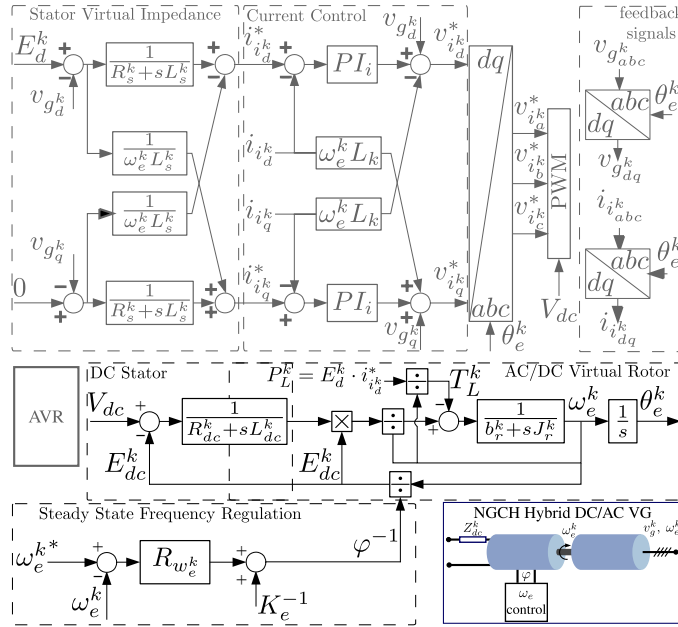


**Figure 5.25:** Block diagram of the proposed Hybrid AC/DC virtual generator for enabling the cooperative power sharing between NGs through the LVDC.

The basic principle of operation consists in the following: in case the LVDC voltage varies, the frequency in the NGs will change, dynamically and proportionally, with the dynamics of the defined AC/DC virtual generator. The frequency regulator will allow to decouple the NGHC frequency  $\omega_e^k$  from the  $V_{dc}$  during steady state, thus the frequency can return to its nominal value even if the  $v_{dc}$  deviates from the nominal LVDC bus voltage.

It is worth to point out that this scheme can be applied to the 2<sup>nd</sup> primary control approach either in *islanded* or *grid-connected* modes, without performing any modification to the control schemes of LVDC bus or NGHCs regulation or their parameters, being the participation of the different elements in the MG dependent on their configured inertia and damping.

### 5.5.2 Simulation results

The proposed *basic* and *cooperative* alternatives for the VG-based microgrid primary control has been tested through simulations in MATLAB/Simulink<sup>®</sup> following the simulation setup shown in Fig. 5.26, where 2 nanogrids have been considered. Apart from the devices in the MG transformation center, the following devices populate the MG: 1) two CPLs are present in the MG, one in each nanogrid, located in the nodes  $B_2^1$  and  $B_2^2$ , 2) a local frequency compensator supplied by an ESS is connected to the node  $B_1^1$  of nanogrid 1 sharing the active power  $P_{fc}$ , and 3) a DC CPL is connected to the LVDC bus.

The system has been evaluated under an illustrative scenario with the setup described in A.10.

Two cases are simulated to evaluate the performance of the proposed MG control:

1. The first case consist in the simulation of the *basic* VG-based control described in Section 5.2.2. The LVDC bus is regulated by the mains (MGHC) and central BESS operated as DCVGs with a P/V DC droop as described in Section 5.2.2.2. The mains (MGHC) provides the majority of the inertia and steady state power sharing while the central BESS is mainly conceived as a back up for contingencies like *islanded* mode, presenting low inertia and reduced participation in the power sharing under normal conditions (*grid-connected*). The NGHCs are controlled as grid-forming according to the VSG topology in Fig. 5.5, presenting a stiff governor response and a high VI.
2. In the second case consist in the simulation of the *cooperative* control based on HVGs. The control in the NGHCs is modified, introducing the hybrid AC/DC virtual generator proposed in Section 5.5.1, shown in Fig. 5.25. The LVDC bus regulation remains the same as in the *basic* case.

In both cases, the parameters in common are the same, and similar conditions are established: 1) two NGs are connected to the LVDC line; 2) in the  $NG_2$  just

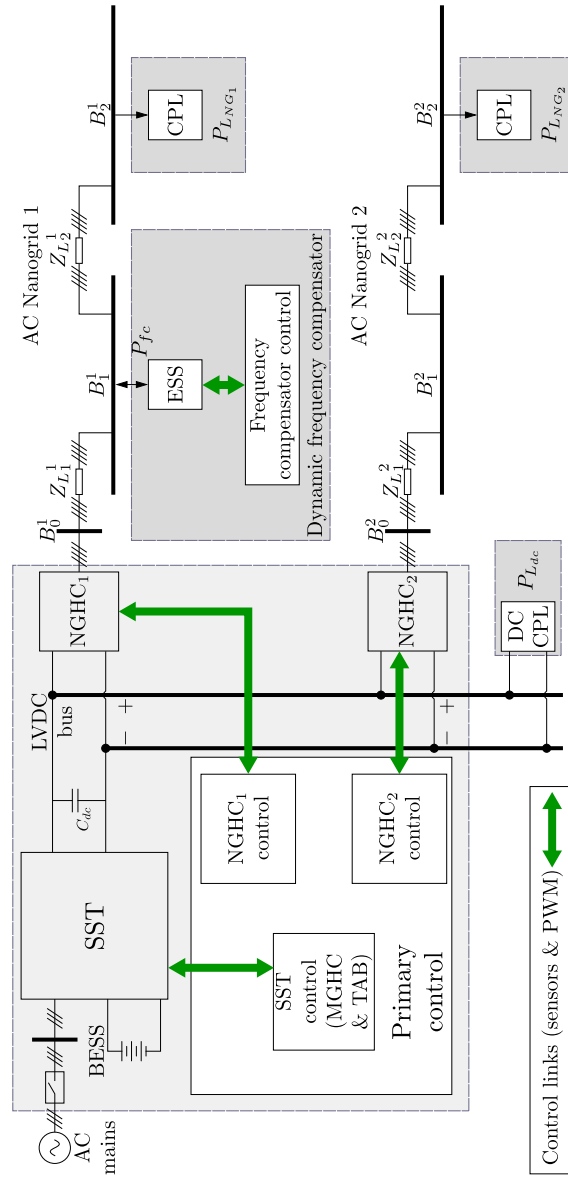


**Figure 5.26:** Simulation setup: 2<sup>nd</sup> microgrid primary control strategy and improved adaptive hybrid power sharing.

CPLs are connected to the grid; 3) a DC load ( $P_{Ldc}$ ) is directly connected to the LVDC bus; 4) in the  $NG_1$  not only CPLs, but also an ESS operated as a frequency compensator is present in the NG. The frequency compensator is operated based on the VI and damping controller presented in Section 4.2.3; 5) two modes of operation are considered in the simulation: *grid-connected* and *islanded* modeds. Under *grid-connected* the power to control the LVDC is shared by the mains and the central BESS. During *islanded*, the LVDC control relies only in the BESS. As the BESS is configured with a reduced inertia, the LVDC voltage profile will be affected during transients. Moreover, due to the power limitations of the central BESS, the system stability can be compromised if an overrated operation is reached i.e. if the maximum power of the BESS is reached either during transients or steady state.

The simulations evaluate the 2 modes of operation under multiple active power steps in the NGs and LVDC bus. The results, comparing the *basic* and *cooperative* control are shown in Fig. 5.27. It shows the DC voltage, the AC voltage in both NGs, grid frequency in each NG, the power delivered by the mains, the central BESS and the frequency compensator, and the AC and DC loads. The figure is described as follows.

From  $t = 0s$  to  $t = 1.2$  the MG operates in *grid-connected* mode. During this mode the  $v_{dc}$  response presents a high stiffness in both cases. For the case 1 (*basic*), the grid frequency is only affected by power changes in the corresponding NG, thus, the NGs does not react to the DC load. Conversely, in the second case (*cooperative*), the frequency in both NGs is sensitive to changes in any NG and the LVDC bus, being slightly disturbed by the DC load connection and disconnection.

From  $t = 1.2s$  to  $t = 3s$  the mains are disconnected and the MG changes to *islanded* mode. In case 1, the operation in the NGs is similar than in *grid-connected*, however, the  $v_{dc}$  profile is notably worsen, presenting the case 2 a better LVDC profile thanks to the proposed *cooperative* control. For case 2, the coupling between NGs and DC bus becomes evident, in both voltage and frequency signals. Thus, the frequency compensator not only helps with the frequency regulation in  $NG_1$ , but also collaborate with the LVDC regulation and the frequency regulation in  $NG_2$  indirectly, reacting to the  $NG_2$  load and the DC load. It is clearly seen how the battery stress is reduced compared with case 1. In both cases, even the load step is similar, a better frequency response is observed in the  $NG_1$  than in  $NG_2$ , due to the presence of the frequency compensator. Despite the  $v_{dc}$  steady state deviation due to P/V DC droop, it is worth noting how in the case 2 the frequency steady state error in both NGs is zero thanks to the steady state frequency regulation block.

At  $t = 3$  the total load in the MG exceeds the central BESS maximum power. In case 1, as the NGHCs are decoupled from the  $v_{dc}$  regulation, the whole system leads to instability and collapses although there is available power in the frequency compensator of  $NG_1$ . In contrast, the proposed *cooperative* control allows to maintain the system operation automatically, although an steady state error in the  $v_{dc}$  and the NGs frequencies is clearly shown. The active power mismatch is sustained by the frequency compensator of  $NG_1$ .

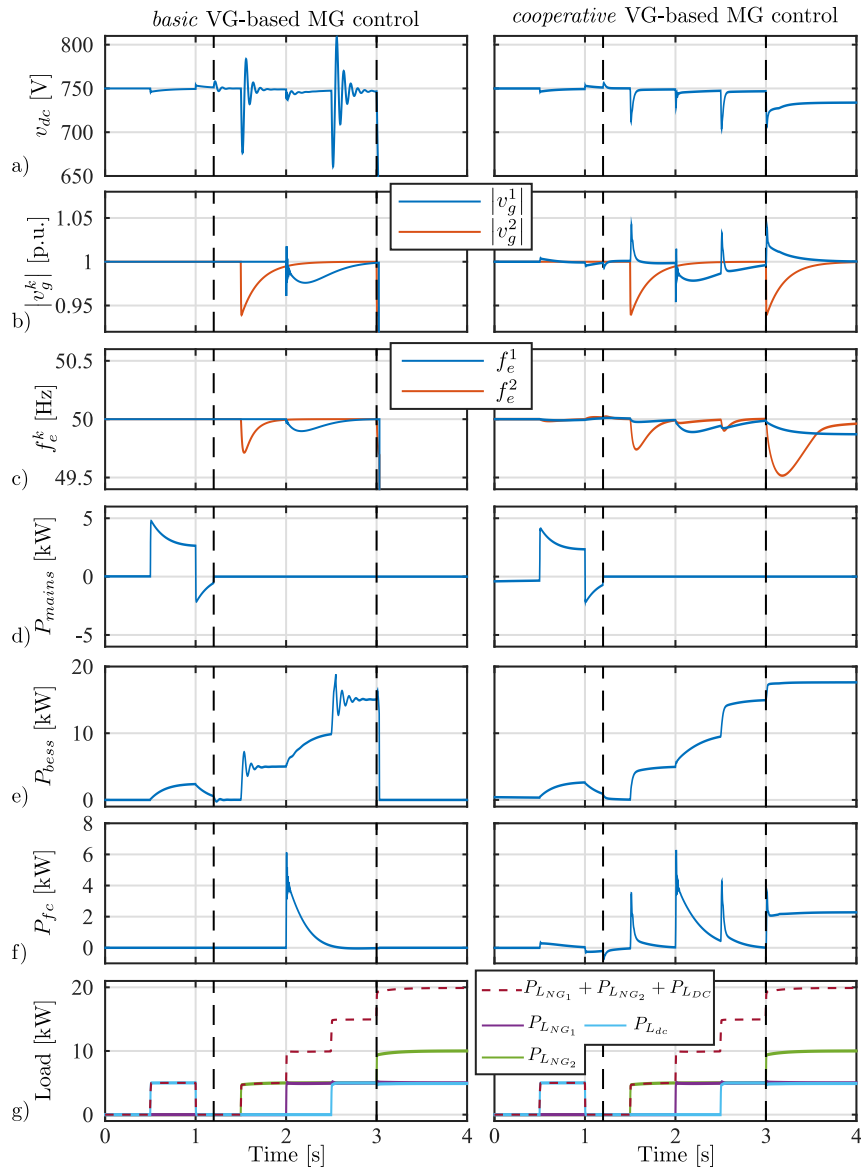


**Figure 5.27:** Simulation results: comparison between the *basic* control (left) and the proposed *cooperative* hybrid MG control (right). a) LVDC bus voltage; b) NGs voltage magnitude; d) NGs frequency; f),g) and h) power shared by the mains, BESS and frequency compensator; i) NGs AC loads and DC load.

This section has presented a *cooperative* alternative to the *basic* VG-based MG control described in Section 5.2.2 and both methods have been compared in simulation under an illustrative scenario. The obtained results match the expected behavior in the theoretical discussion, demonstrating the potential of the *basic* and *cooperative* VG-based MG control schemes as an alternative for hybrid AC/DC MGs control.

## 5.6 Conclusions

This chapter proposes 2 control alternatives for the primary control in a hybrid AC/DC MG with multiple AC subgrids, pursuing for the improvement of the dynamic active power sharing between the AC nanogrids and the LVDC bus:

- Two primary control schemes have been proposed for the control of a hybrid AC/DC microgrid with several AC subgrids (nanogrids), one based on grid-forming quadratic voltage control (QVC) and other based on virtual generators.
- A dynamic voltage control technique is proposed for a fixed frequency hybrid AC/DC microgrid with ESSs, based on the power sharing between the AC NGs and a central BESS to maintain the grid quality in both the LVDC and the AC NGs and increase the flexibility under high penetration of CPLs and PECs. An adaptive power sharing mechanism have being presented for maintaining the LVDC voltage under control, not only reducing the stress in the central BESS system and the dependence in the utility grid, but also demonstrating the extended operation and improved transient response in the LVDC when the central BESS presents bandwidth and power limitations. An automatic cooperative sharing method for the power exchanged between the AC NGs have been proposed. Its operation, together with the use of a local AC dynamic voltage compensator based on a virtual capacitance, positively affects the operation of the microgrid. The theoretical discussion has been supported with simulations, experimental results and a study on the system frequency response.
- A cooperative active power control is proposed for a hybrid AC/DC microgrid with ESS, based on hybrid DC/AC virtual generators that allows the indirect collaboration between the regulation in the AC NGs and the LVDC bus, maintaining the grid quality in both the LVDC and the AC NGs. A control scheme based on DC virtual generators is proposed for the DC voltage regulation and power sharing between the mains and the central BESS. The method allows to adapt the participation of the mains and BESS in the transient and stationary power sharing for DC bus regulation, and enables an automatic transition between *grid connected* and *islanded* modes. Meanwhile, the DC/AC virtual generators allow an automatic power sharing that couples the LVDC voltage and the NGs voltage and frequency, maintaining the power balance in the hybrid MG. The proposed alternative, not only allows reducing the stress in the central BESS and the dependence in the utility grid but also demonstrates the extended operation

and improved transient response in the LVDC when the central BESS presents low inertia and power limitations. The theoretical discussion has been supported with simulations in MATLAB/Simulink<sup>®</sup>.

# Chapter 6

## Conclusions and future work

### 6.1 Conclusiones (Spanish)

La presente tesis ha abordado varios aspectos relevantes en el campo del control dinámico de microrredes híbridas AC/DC, centrándose en el control de convertidores conectados a la red, en la regulación dinámica de tensión DC y tensión/frecuencia AC, y en la mejora de la distribución dinámica de potencia activa considerando el uso de ESSs. Salvo algunas excepciones, las técnicas y estrategias de control propuestas se han orientado principalmente a aplicaciones en DC, a aplicaciones AC trifásicas equilibradas, y a la gestión dinámica de la potencia activa. En el Capítulo 2 se ofrece una visión general de las características, los componentes, los dispositivos conectados a la red, las técnicas de control y los retos que presenta el concepto de microrred, exponiendo varias oportunidades en el campo de las microrredes híbridas AC/DC. Se han explorado estas oportunidades, de las que se desprenden las siguientes conclusiones:

- Se ha propuesto un nuevo esquema de control de corriente sensorless para filtros LCL en convertidores trifásicos AC conectados a red. La solución se basa en el uso de un observador de Luenberger para la estimación de la corriente del lado de red y reduciendo el número de sensores de corriente. La estrategia propuesta permite implementar un control fiable de la corriente de salida en un filtro LCL utilizando únicamente sensores de corriente en el lado del convertidor y sensores de tensión en el punto de conexión con la red, evitando medir la tensión del condensador y la corriente de salida. El método propuesto ha sido modelado teóricamente, implementado en un controlador digital y validado experimentalmente.
- Se ha propuesto un método de estimación de la impedancia de red en tiempo real. El método propuesto se basa en una alternativa de inyección de señal de pulsada (PSI) que induce una perturbación en la corriente y tensión de la red utilizada para una estimación basada en el algoritmo RLS (del inglés *recursive*

*least squares*). Evitando la inyección continua de la señal, el método presenta una mínima distorsión armónica. Esto se logra empleando la acción de control del observador de Luenberger, desarrollado en el punto anterior, como mecanismo de activación. En comparación con otras alternativas, cabe señalar que el sistema propuesto funciona naturalmente en condiciones de red desequilibradas.

- El control de tensión en microrredes de AC y DC en configuración maestro-esclavo ha sido ampliamente analizado considerando la alta penetración de cargas de potencia constante. Se han comparado dos métodos de control basados en PI, el control de tensión con realimentación directa (DVC) y el control de tensión con realimentación cuadrática (QVC), describiendo sus beneficios e inconvenientes. El QVC ha demostrado mejorar el comportamiento dinámico bajo perturbaciones de potencia constante. Las ideas presentadas durante la discusión teórica permiten construir una metodología para el diseño del lazo de control de tensión, incluyendo la selección del valor del condensador de la planta, considerando el comportamiento dinámico. Como se ha demostrado, el método de análisis propuesto puede aplicarse a convertidores con diferentes valores nominales, con lo que tiene el potencial de convertirse en una herramienta de diseño. Cabe destacar que la metodología deja a criterio del diseño la selección de parámetros dependientes de la aplicación, tales como el nivel de carga en el punto de equilibrio, los márgenes de estabilidad y la desviación máxima de tensión bajo perturbaciones.
- El uso de la capacitancia virtual ha sido introducido como una técnica para mejorar la respuesta de control de tensión, y como una herramienta para pronosticar experimentalmente el efecto de redimensionar la capacitancia en sistemas existentes. La capacitancia virtual aparece como una solución simple pero efectiva para mejorar el rechazo de perturbaciones. El método es adecuado para su implementación tanto en aplicaciones DC como en AC.
- Se han propuesto las bases de un dispositivo basado en un sistema de almacenamiento de energía, capaz de mejorar la calidad de la red mediante la compensación dinámica de la potencia activa. La solución es válida para su implementación en redes con relación P/V (potencia activa/magnitud de tensión) o P/f (potencia activa/frecuencia) modificando los lazos de control externos. Por lo tanto, el dispositivo propuesto puede compensar la magnitud de la tensión o la frecuencia en función de las características de la red. Se consideran dos lazos de control externos: 1) la compensación de tensión se consigue mediante un regulador de lazo cerrado basado en capacitancia virtual y amortiguación virtual; 2) la compensación de frecuencia se realiza mediante un regulador de lazo cerrado basado en inercia virtual y amortiguación virtual.
- En microrredes de AC débiles con una relación P/f, las oscilaciones de frecuencia debidas a los desajustes de potencia activa pueden ser críticas, y una solución bien establecida es el uso de almacenamiento de energía para la compensación. Sin embargo, a diferencia de la compensación de tensión, la compensación de frecuencia presenta problemas adicionales debido a la necesidad de la estimación de

la frecuencia de red. Se ha propuesto un compensador de frecuencia transitoria basado en un observador de Luenberger, destacando las siguientes contribuciones: 1) una caracterización exhaustiva del sistema y un análisis de rechazo de perturbaciones de los métodos existentes en comparación con el compensador propuesto, 2) un método novedoso para la detección de la frecuencia transitoria y 3) la implementación de una nueva solución mejorada basada en el uso de un observador de Luenberger para la estimación de la frecuencia de la red que permita una reducción del retardo de fase del compensador, obteniendo una respuesta más rápida e incrementando el margen de fase con respecto a los métodos existentes.

- Se ha propuesto una técnica predictiva de estimación de secuencia de red para convertidores conectados a redes débiles distorsionadas. El método se basa en una modificación de la transformada deslizante de Goertzel (sliding Goertzel transform) que permite estimar la fase y magnitud de cualquier componente de frecuencia (secuencia positiva, secuencia negativa, armónicos), siendo útil para el seguimiento de fase, control fundamental y control de desequilibrios y armónicos. El método propuesto  $PF - SGT$  ha sido evaluado con respecto a una alternativa consolidada, el DSOGI, mostrando un desempeño superior en términos de respuesta dinámica y rechazo de perturbaciones. Es particularmente notable la inmunidad a las desviaciones de DC debidas a los sensores, así como a los cambios en la frecuencia de la red. También se ha evaluado el impacto de la estimación de fase y el desacoplamiento armónico en una implementación de control de corriente en lazo cerrado, siendo la propuesta  $PF - SGT$  una mejora importante sobre el método DSOGI.
- Aunque en la literatura se encuentran varios ejemplos de control de microrredes híbridas de AC/DC, la mayoría de ellas sólo consideran una subred DC, una subred AC y un convertidor de interconexión. Se ha propuesto una arquitectura de control primario basada en un esquema maestro-esclavo centralizado para microrredes híbridas AC/DC que presentan múltiples subredes AC interconectadas por varios convertidores AC/DC. Las ventajas y características del QVC sobre el DVC explorado en el capítulo 3 han sido decisivas para la selección de esta alternativa para el control tanto en el lado DC como en el lado AC de la microrred. El esquema de control consiste en un controlador de tensión continua centralizado basado en QVC para la subred DC y un control de la tensión trifásica basado en QVC y frecuencia fija, implementado en los convertidores de interconexión para la regulación de las subredes de AC. Esta configuración conduce a una regulación independiente y robusta de las subredes de DC y AC.
- Se ha propuesto un esquema de control basado en generadores virtuales de continua y control droop DC para la regulación de la tensión de redes DC que permite adaptar la participación de diferentes fuentes en el reparto de potencia transitoria y estacionaria. El esquema propuesto, basado en generadores virtuales DC, permite ajustar el reparto en régimen estacionario mediante la configuración de un control droop P/V, mientras que la participación transitoria se ajusta modif-

icando la inercia virtual y amortiguando el generador virtual de DC. Además, la estrategia propuesta presenta una transición automática entre el modo conectado a red y el modo isla. La propuesta permite la posibilidad de integrar dispositivos de colaboración adicionales en un bus de DC.

- Se ha propuesto una segunda alternativa para el control primario basado en generadores virtuales (VG) para microrredes híbridas AC/DC con múltiples subredes AC. En este caso, la subred DC está regulada por el esquema propuesto de generadores virtuales DC, mientras que los convertidores de interconexión funcionan como generadores síncronos virtuales (VSG) en modo maestro. El uso de VSGs en redes de DC permite el ajuste de la inercia de la red, permite la compatibilidad con generadores síncronos acoplados directamente e imita los fundamentos de las redes tradicionales a una escala reducida. Además, esto prepara la red para la integración de otros dispositivos participativos operados como VSGs. Hay que señalar que, en comparación con el control primario basado en QVC, los VSGs implican un diseño más complejo debido al mayor número de parámetros a sintonizar. Al igual que en el control primario basado en QVC, la regulación de los lados DC y AC de la microrred permanece independiente.
- Se ha propuesto una estrategia cooperativa de control de tensión para microgrids híbridas AC/DC con múltiples subredes AC operadas bajo el control primario basado en QVC. La estrategia de control consiste en un mecanismo cooperativo de reparto de potencia que mantiene la tensión de subred DC bajo control obligando a los convertidores de interconexión a participar en la regulación de la tensión DC. Se ha propuesto un método de reparto adaptativo para determinar la participación de cada convertidor de interconexión en el intercambio de energía entre las subredes DC y AC. Su funcionamiento, junto con el uso de un compensador de tensión dinámico AC local, afecta positivamente al funcionamiento de la microrred. La propuesta no sólo reduce el estrés en los dispositivos que regulan la subred DC y la dependencia de la red pública, sino que también demuestra la operación extendida y la respuesta transitoria mejorada en la subred DC cuando los recursos de almacenamiento de energía vinculados a la red DC presentan un bajo ancho de banda, baja inercia y limitaciones de potencia, situación propensa a ocurrir durante el funcionamiento en modo isla.
- Se propone un segundo control cooperativo de tensión y potencia activa para microrredes híbridas AC/DC que funcionan bajo el control primario basado en VG. El control cooperativo se basa en el uso de generadores virtuales híbridos AC/DC, implementados en los convertidores de interconexión, que permiten la colaboración indirecta entre las subredes DC y AC. Mientras que la regulación de la subred DC se basa principalmente en el esquema de control de generadores virtuales DC propuesto, los generadores virtuales híbridos AC/DC permiten un reparto automático de potencia que acopla la tensión DC y la tensión y frecuencia de las subredes de AC, manteniendo el equilibrio de potencia en la MG híbrida. Como en el caso anterior, la propuesta permite reducir la dependencia de la red

principal y permite una operación extendida y una mejor respuesta transitoria en la subred DC cuando los recursos energéticos conectados a dicha subred presentan una baja inercia y limitaciones de potencia. A diferencia de la solución cooperativa anterior, en la que se utilizaban compensadores de tensión, esta solución se basa en compensadores de frecuencia localizados dentro de las subredes AC, siendo crítico el retardo y la precisión de la estimación de frecuencia para una implementación práctica adecuada.

## 6.2 Conclusions

This thesis has addressed several relevant aspects in the field of dynamic control of hybrid AC/DC microgrids, focusing on the control of grid-tied converters, the DC voltage and AC voltage/frequency dynamic regulation and the dynamic active power sharing improvement considering the use of ESSs. Despite some exceptions, the proposed techniques and control strategies have been mainly oriented to DC and AC balanced 3-phase applications, and the dynamic management of active power. An overview on characteristics, components, grid-tied devices, control techniques and challenges of microgrids was given in Chapter 2, exposing several opportunities in the field of hybrid AC/DC microgrids. Those opportunities have been explored, giving rise to the following conclusions:

- A novel sensorless current control scheme for LCL filters in grid-tied 3-phase VSIs has been proposed. The solution is based on the use of a Luenberger-based observer for the estimation of the grid current and allows to reduce the number of current sensors. The proposed strategy allows to implement a reliable control of the output current in an LCL filter using only current sensors at the converter side and voltage sensors at the point of connection with the grid, avoiding to measure the LCL capacitor voltage and the output current. The proposed method has been theoretically modelled, implemented in a digital controller and validated experimentally in a grid-tied 3-phase VSI prototype.
- An online grid impedance estimation method based on the premises of minimum disturbance has been proposed. The proposed method is based on a pulsed signal injection alternative that induces a grid-current disturbance used for an RLS-based estimation. The minimum disturbance is achieved by avoiding the continuous signal injection. This is achieved by employing the proposed grid-current Luenberger observer control action as the trigger mechanism. When compared to other alternatives, it is worth noting that the proposed system naturally works under unbalanced grid conditions.
- The voltage control in master-slave AC and DC microgrids with high penetration of CPLs has been extensively analyzed. Two PI-based control methods, the direct voltage control (DVC) and the quadratic-based voltage control (QVC), have been

compared outlining their benefits and drawbacks. The QVC has proved to enhance the dynamic behavior under CPL disturbances. The ideas presented during the theoretical discussion allow for building a methodology for the voltage control loop design, including the selection of the plant capacitor value considering the dynamic performance. As demonstrated, the proposed analytical method can be applied to converters having different rated values, thus having the potential of becoming a design tool. It is worth noting that the methodology leaves up to the designer the selection of parameters which are application dependent, such as the load level in the equilibrium point, the stability margins and the maximum voltage deviation under CPL disturbances.

- The use of the virtual capacitance has been introduced as a technique for voltage control response enhancement, and as a tool to experimentally forecast the effect of resizing the capacitance in existing systems. The virtual capacitance appears as a simple but effective solution for disturbance rejection improvement compared to more complex model-based existing controllers. The method is suitable for its implementation either in DC or AC applications.
- The basics of an ESS-based device able to improve the grid quality by means of dynamic power compensation have been proposed. The solution is valid for its implementation in grids with a P/V (active power/voltage magnitude) or P/f (active power/frequency) relation by modifying the external control loops. Thus, the proposed device can compensate either voltage magnitude or frequency depending on the characteristics of the grid. Two external control loops are considered: 1) the voltage compensation is achieved by means of a closed-loop regulator based on virtual capacitance and virtual damping; 2) the frequency compensation is realized by means of a closed-loop regulator based on virtual inertia and virtual damping.
- In weak AC microgrids with a P/f relation, the frequency oscillations due to active power mismatches can be critical, and a well established solution is the use of ESS for compensation. However, unlike voltage compensation, the frequency compensation present additional issues due to the necessity for frequency estimation. An observer-based frequency drift compensator have been proposed, highlighting the following contributions: 1) an exhaustive system characterization and disturbance rejection analysis of the existing methods compared with the proposed compensator, 2) a novel method for the detection of the transient frequency and 3) the implementation of a novel enhanced solution based on the use of a Luenberger type observer for the grid frequency estimation that allows for a reduction of the compensator phase lag, obtaining a faster response and increasing the phase margin with respect to other existing methods.
- A predictive sequence estimation technique for grid-tied converters has been proposed for its application in weak and distorted microgrids. The method is based on a modification of the sliding Goertzel transformation that allows to estimate

the phase and magnitude of any frequency component (positive sequence, negative sequence, harmonics), being useful for phase tracking, fundamental control, and unbalance and harmonic control. The proposed  $PF - SGT$  method has been evaluated with respect to a consolidated alternative, the DSOGI, showing a superior performance in terms of dynamic response and disturbance rejection. It is particularly remarkable the immunity to DC offsets as well as to changes at the grid frequency. The impact of the phase estimation and harmonic decoupling in a closed-loop current control implementation has also been evaluated, being the proposed  $PF - SGT$  an important improvement over the DSOGI method.

- Although several examples of hybrid AC/DC microgrids control are found in the literature, most of them only consider a DC subgrid, an AC subgrid and an interlinking converter. A primary control architecture based on a centralized master-slave scheme has been proposed for hybrid AC/DC microgrids that present multiple AC subgrids interfaced by several AC/DC interlinking converters. The advantages and characteristics of QVC over the DVC explored in Chapter 3 have been decisive for the selection of such an alternative for the control in both DC and AC sides of the microgrid. The control scheme consists in a centralized QVC-based DC voltage controller for the DC subgrid and a fixed-frequency QVC-based 3-phase grid-forming control implemented in the interlinking converters for the regulation of the AC subgrids. This configuration leads to an independent and robust regulation of the DC and AC subgrids.
- A control scheme based on DC virtual generators and DC droop control has been proposed for the DC bus voltage regulation that allows to adapt the participation of different sources in the transient and stationary power sharing. The proposed scheme based on DC virtual generators permits to adjust the steady state sharing through the configuration of a P/V droop control while the transient participation is adjusted by modifying the virtual inertia and damping of the DC virtual generator. In addition, the proposed strategy presents an automatic transition between *grid-connected* and *islanded* modes. The proposal enables the possibility to integrate additional collaborative devices in a DC bus.
- A second alternative for primary control based on virtual generators has been proposed for multi AC subgrids hybrid AC/DC microgrids. In this case, the DC subgrid is regulated under the DC virtual generators proposed scheme, while the interlinking converters are operated as master virtual synchronous generators. The use of VSGs in AC grids allows the adjustment of grid inertia, enables the compatibility with directly coupled synchronous generators and mimics the basics of traditional grids at a reduced scale. In addition, this prepares the grid for the integration of other participative devices operated as VSGs. It has to be remarked that, when compared with the QVC-based primary control, the VSGs involves a more complex design due to the higher number of parameters to be tuned. As in the QVC-based primary control, the regulation of the DC and AC sides of the microgrid remains independent.

- A cooperative voltage control strategy for hybrid AC/DC microgrids with multiple AC subgrids operated under the QVC-based primary control has been proposed. The control strategy consists in a cooperative power sharing mechanism that maintains the DC subgrid voltage under control by forcing the interlinking converters to participate in the DC voltage regulation. An adaptive sharing method has been proposed for determining the participation of each interlinking converter in the power exchange between the DC and AC subgrids. Its operation, together with the use of a local AC dynamic voltage compensator, positively affects the operation of the microgrid. The proposal not only reduces the stress in the devices regulating the DC subgrid and the dependence in the utility grid, but also demonstrates the extended operation and improved transient response in the DC subgrid when the DC grid-tied energy resources present low bandwidth, low inertia and power limitations, prone to happen during *islanded* operation.
- A second cooperative voltage and active power control is proposed for hybrid AC/DC microgrids operated under the VG-based primary control. The cooperative control is based on the use of hybrid DC/AC virtual generators, implemented in the interlinking converters, that allow the indirect collaboration between the regulation in the DC and AC subgrids. While the DC subgrid regulation mainly relies on the proposed DC virtual generators control scheme, the hybrid AC/DC virtual generators allow an automatic power sharing that couples the DC voltage and the AC subgrids voltage and frequency, maintaining the power balance in the hybrid MG. As in the previous case, the proposal allows to reduce the dependence in the utility grid and permits an extended operation and improved transient response in the DC subgrid when the DC energy resources presents low inertia and power limitations. Unlike the previous cooperative solution where voltage compensators are used, this solution relies on frequency compensators within the AC subgrids, being critical the delay and accuracy of frequency estimation for a suitable practical implementation.

## 6.3 Future work

The contributions and the work conducted during the development of the present thesis open new opportunities for the improvement of microgrids and grid-tied converters control. The following future lines derived from the thesis are suggested:

- In the thesis, a balanced system has been considered for the design of the microgrid control and the strategies proposed for grid-tied converter current and voltage control. Thus, it becomes appealing to adapt the proposed techniques (LCL filter observer, QVC grid-forming control, VSG and HVG...) to a 4-wire solution where the homopolar, harmonics and negative sequence component can be different from zero. Including the rejection of unbalances and harmonics in the NGHCs becomes a necessary task. In this line, the use of the Goertzel-based sequence estimator stands as a potential powerful tool for the compensation of harmonics and unbalances control.
- The effect of CPL has been carried out when PI-based voltage control is used. However, other alternatives such as proportional resonant or repetitive controllers have been proposed in the literature. Extending the carried out analysis to these or other kind of controllers can potentially provide insight in the development of a complete design tool for primary voltage control in AC/DC microgrids applications.
- In this thesis, the design of the voltage control has assumed a perfect infinite bandwidth current regulator, using the premises of cascaded control. However, the effect of additional dynamic terms not perfectly compensated in the current loop will negatively affect the external loops. Integrating this effect in a future analysis has a great potential for understanding all the coupled dynamics.
- Develop a design tool based on the conclusions gathered from the analysis of grid-forming converter voltage control. Such analysis has allowed to establish design boundaries being a starting point for the development of a simple and versatile system design tool for grid-forming applications able to minimize the capacitor size and select the proper control parameters.
- Some of the proposals in this thesis have been tested and demonstrated using illustrative parameters. It becomes interesting to find out optimal tuning for some of the proposed strategies (observer-based frequency compensator, HVG and VSG-based primary control...).
- One of the main issues related with the high presence of PECs in new microgrids and distribution systems is the fault management. The fault location and a rapid actuation becomes critical in order to maintain the integrity of the grid. The proposed impedance estimation and transient detection methods might be suitable for use in this field.

- Regarding the observer-based transient frequency drift compensator, three interesting future lines are proposed: 1) the development of an online strategy for the identification of a simplified transfer function of the grid for its use in the Luenberger observer, 2) the use of the load estimated by the observer as a feed-forward for the frequency compensator, 3) evaluate the potential of the observer for frequency estimation and synchronization in grid-tied converters.
- The proposed HVG-based control has been only validated under simulations. Demonstrate the viability in the experimental microgrid as well as generalize its application to different topologies of AC/DC hybrid microgrids is an interesting topic to be further studied.
- The adaptive algorithm proposed for the cooperative QVC-based primary control can be adapted to the cooperative VG-based control, modifying the inertia and damping parameters of the proposed HVG scheme to optimize the participation of each nanogrid.

# Bibliography

- [1] P. García, P. Arboleya, B. Mohamed, and A. A. C. Vega. Implementation of a Hybrid Distributed/Centralized Real-Time Monitoring System for a DC/AC Microgrid With Energy Storage Capabilities. *IEEE Transactions on Industrial Informatics*, 12(5):1900–1909, Oct 2016.
- [2] Á. Navarro-Rodríguez, P. García, R. Georgious, and J. García. Adaptive active power sharing techniques for DC and AC voltage control in a hybrid DC/AC microgrid. In *2017 IEEE Energy Conversion Congress and Exposition (ECCE)*, pages 30–36, Oct 2017.
- [3] Á. Navarro-Rodríguez, P. García, R. Georgious, and J. García. Adaptive Active Power Sharing Techniques for DC and AC Voltage Control in a Hybrid DC/AC Microgrid. *IEEE Transactions on Industry Applications*, 55(2):1106–1116, March 2019.
- [4] Á. Navarro-Rodríguez, P. García, C. Blanco, R. Georgious, and J. García. Cooperative Control in a Hybrid DC/AC Microgrid based on Hybrid DC/AC Virtual Generators. In *2018 IEEE Energy Conversion Congress and Exposition (ECCE)*, pages 1156–1163, Sep. 2018.
- [5] P. García, J. M. Guerrero, J. García, A. Navarro-Rodríguez, and M. Sumner. Low frequency signal injection for grid impedance estimation in three phase systems. In *2014 IEEE Energy Conversion Congress and Exposition (ECCE)*, pages 1542–1549, Sept 2014. 6953602.
- [6] P. García, M. Sumner, Á. Navarro-Rodríguez, J. M. Guerrero, and J. García. Observer-Based Pulsed Signal Injection for Grid Impedance Estimation in Three-Phase Systems. *IEEE Transactions on Industrial Electronics*, 65(10):7888–7899, Oct 2018.
- [7] A. Navarro-Rodríguez, P. García, J. M. Cano, and M. Sumner. Limits, stability and disturbance rejection analysis of voltage control loop strategies for grid forming converters in DC and AC microgrids with high penetration of constant power loads. In *2017 19th European Conference on Power Electronics and Applications (EPE'17 ECCE Europe)*, pages P.1–P.10, Sept 2017.

- 
- [8] A. Navarro-Rodríguez, P. García, R. Georgious, and J. Garcia. A communication-less solution for transient frequency drift compensation on weak microgrids using a D-statcom with an energy storage system. In *2015 IEEE Energy Conversion Congress and Exposition (ECCE)*, pages 6904–6911, Sept 2015.
- [9] Á. Navarro-Rodríguez, P. García, R. Georgious, J. García, and S. Saeed. Observer-Based Transient Frequency Drift Compensation in AC Microgrids. *IEEE Transactions on Smart Grid*, 10(2):2015–2025, March 2019.
- [10] C. Blanco, P. García, Á. Navarro-Rodríguez, and M. Sumner. Predictive frequency-based sequence estimator for control of grid-tied converters under highly distorted conditions. In *2017 IEEE Energy Conversion Congress and Exposition (ECCE)*, pages 2940–2947, Oct 2017.
- [11] C. B. Charro, P. García-Fernandez, Á. Navarro-Rodríguez, and M. Sumner. Predictive Frequency-Based Sequence Estimator for Control of Grid-Tied Converters Under Highly Distorted Conditions. *IEEE Transactions on Industry Applications*, 54(5):5306–5317, Sep. 2018.
- [12] B. Lasseter. Microgrids [distributed power generation]. In *2001 IEEE Power Engineering Society Winter Meeting. Conference Proceedings (Cat. No.01CH37194)*, volume 1, pages 146–149 vol.1, Jan 2001.
- [13] R. H. Lasseter. MicroGrids. In *2002 IEEE Power Engineering Society Winter Meeting. Conference Proceedings (Cat. No.02CH37309)*, volume 1, pages 305–308 vol.1, Jan 2002.
- [14] R. H. Lasseter and P. Paigi. Microgrid: a conceptual solution. In *2004 IEEE 35th Annual Power Electronics Specialists Conference (IEEE Cat. No.04CH37551)*, volume 6, pages 4285–4290 Vol.6, June 2004.
- [15] Adam Hirsch, Yael Parag, and Josep Guerrero. Microgrids: A review of technologies, key drivers, and outstanding issues. *Renewable and Sustainable Energy Reviews*, 90:402 – 411, 2018.
- [16] Robert H. Lasseter, Abbas A. Akhil, Chris Marnay, John Stephens, Jeffery E. Dagle, Ross T. Guttromson, A. Sakis Meliopoulos, Robert J Yinger, and Joseph H. Eto. Integration of Distributed Energy Resources: The CERTS MicroGrid Concept. Technical report, CERTS, 10/2003 2003.
- [17] F. Martin-Martínez, A. Sánchez-Miralles, and M. Rivier. A literature review of Microgrids: A functional layer based classification. *Renewable and Sustainable Energy Reviews*, 62:1133 – 1153, 2016.
- [18] Huang Jiayi, Jiang Chuanwen, and Xu Rong. A review on distributed energy resources and MicroGrid. *Renewable and Sustainable Energy Reviews*, 12(9):2472 – 2483, 2008.

- [19] Yeliz Yoldaş, Ahmet Önen, S.M. Muyeen, Athanasios V. Vasilakos, and İrfan Alan. Enhancing smart grid with microgrids: Challenges and opportunities. *Renewable and Sustainable Energy Reviews*, 72:205 – 214, 2017.
- [20] Xuan Zhu, Xiao qing Han, Wen ping Qin, and Peng Wang. Past, today and future development of micro-grids in China. *Renewable and Sustainable Energy Reviews*, 42:1453 – 1463, 2015.
- [21] Iván Patrao, Emilio Figueres, Gabriel Garcerá, and Raúl González-Medina. Microgrid architectures for low voltage distributed generation. *Renewable and Sustainable Energy Reviews*, 43:415 – 424, 2015.
- [22] Krishnarajsinh A. Jadav, Hitesh M. Karkar, and I. N. Trivedi. A Review of Microgrid Architectures and Control Strategy. *Journal of The Institution of Engineers (India): Series B*, 98(6):591–598, Dec 2017.
- [23] Lubna Mariam, Malabika Basu, and Michael F. Conlon. Microgrid: Architecture, policy and future trends. *Renewable and Sustainable Energy Reviews*, 64:477 – 489, 2016.
- [24] M. S. Mahmoud, M. Saif Ur Rahman, and F. M. A.L.-Sunni. Review of microgrid architectures – a system of systems perspective. *IET Renewable Power Generation*, 9(8):1064–1078, 2015.
- [25] Yang Zhou and C. Ngai-Man Ho. A review on Microgrid architectures and control methods. In *2016 IEEE 8th International Power Electronics and Motion Control Conference (IPEMC-ECCE Asia)*, pages 3149–3156, May 2016.
- [26] A. M. R. Lede, M. G. Molina, M. Martinez, and P. E. Mercado. Microgrid architectures for distributed generation: A brief review. In *2017 IEEE PES Innovative Smart Grid Technologies Conference - Latin America (ISGT Latin America)*, pages 1–6, Sept 2017.
- [27] G. S. Rawat and Sathans. Survey on DC microgrid architecture, power quality issues and control strategies. In *2018 2nd International Conference on Inventive Systems and Control (ICISC)*, pages 500–505, Jan 2018.
- [28] T. Dragičević, X. Lu, J. C. Vasquez, and J. M. Guerrero. DC Microgrids—Part II: A Review of Power Architectures, Applications, and Standardization Issues. *IEEE Transactions on Power Electronics*, 31(5):3528–3549, May 2016.
- [29] D. Kumar, F. Zare, and A. Ghosh. DC Microgrid Technology: System Architectures, AC Grid Interfaces, Grounding Schemes, Power Quality, Communication Networks, Applications, and Standardizations Aspects. *IEEE Access*, 5:12230–12256, 2017.
- [30] Jackson John Justo, Francis Mwasilu, Ju Lee, and Jin-Woo Jung. AC-microgrids versus DC-microgrids with distributed energy resources: A review. *Renewable and Sustainable Energy Reviews*, 24:387 – 405, 2013.

- [31] D. J. Hammerstrom. AC Versus DC Distribution Systems. Did We Get it Right? In *2007 IEEE Power Engineering Society General Meeting*, pages 1–5, June 2007.
- [32] Estefanía Planas, Jon Andreu, José Ignacio Gárate, Iñigo Martínez de Alegría, and Edorta Ibarra. AC and DC technology in microgrids: A review. *Renewable and Sustainable Energy Reviews*, 43:726 – 749, 2015.
- [33] Peng Wang, Xiong Liu, Chi Jin, Pohchiang Loh, and Fookhoong Choo. A hybrid AC/DC micro-grid architecture, operation and control. In *Power and Energy Society General Meeting, 2011 IEEE*, pages 1–8, July 2011.
- [34] Eneko Unamuno and Jon Andoni Barrera. Hybrid ac/dc microgrids—Part I: Review and classification of topologies. *Renewable and Sustainable Energy Reviews*, 52:1251 – 1259, 2015.
- [35] A. Gupta, S. Doolla, and K. Chatterjee. Hybrid AC-DC Microgrid: Systematic Evaluation of Control Strategies. *IEEE Transactions on Smart Grid*, 9(4):3830–3843, July 2018.
- [36] Junliu Zhang, Diankui Guo, Fengping Wang, Yuechang Zuo, and Haiyan Zhang. Control strategy of interlinking converter in hybrid AC/DC microgrid. In *Renewable Energy Research and Applications (ICRERA), 2013 International Conference on*, pages 97–102, Oct 2013.
- [37] M. N. Ambia, A. Al-Durra, and S. M. Muyeen. Centralized power control strategy for AC-DC hybrid micro-grid system using multi-converter scheme. In *IECON 2011 - 37th Annual Conference on IEEE Industrial Electronics Society*, pages 843–848, Nov 2011. 6119420.
- [38] X. Zhou, Y. Chen, L. Zhou, A. Luo, J. M. Guerrero, W. Wu, L. Yang, and W. Tan. Power coordinated control method with frequency support capability for hybrid single/three-phase microgrid. *IET Generation, Transmission Distribution*, 12(10):2397–2405, 2018.
- [39] C. Mahesh and F. T. Josh. A comprehensive study on distributed energy generation integration technology. In *2017 International Conference on Innovations in Electrical, Electronics, Instrumentation and Media Technology (ICEEIMT)*, pages 49–56, Feb 2017.
- [40] Manzar Ahmed, Uzma Amin, Suhail Aftab, and Zaki Ahmed. Integration of Renewable Energy Resources in Microgrid. *Energy and Power Engineering*, pages 12–29, 2015.
- [41] Ramazan Bayindir, Eklas Hossain, Ersan Kabalci, and Ronald Perez. A Comprehensive Study on Microgrid Technology. *International Journal of Renewable Energy Research*, 2014.

- 
- [42] Lucian Ioan Dulău, Mihail Abrudean, and Dorin Bică. Distributed Generation Technologies and Optimization. *Procedia Technology*, 12:687 – 692, 2014. The 7th International Conference Interdisciplinarity in Engineering, INTER-ENG 2013, 10-11 October 2013, Petru Maior University of Tirgu Mures, Romania.
- [43] Mathew Aneke and Meihong Wang. Energy storage technologies and real life applications – A state of the art review. *Applied Energy*, 179:350 – 377, 2016.
- [44] Xing Luo, Jihong Wang, Mark Dooner, and Jonathan Clarke. Overview of current development in electrical energy storage technologies and the application potential in power system operation. *Applied Energy*, 137:511 – 536, 2015.
- [45] D.O. Akinyele and R.K. Rayudu. Review of energy storage technologies for sustainable power networks. *Sustainable Energy Technologies and Assessments*, 8:74 – 91, 2014.
- [46] P.F. Ribeiro, B.K. Johnson, M.L. Crow, A Arsoy, and Y. Liu. Energy storage systems for advanced power applications. *Proceedings of the IEEE*, 89(12):1744–1756, Dec 2001.
- [47] P.J. Hart, P.J. Kollmeyer, L.W. Juang, R.H. Lasseter, and T.M. Jahns. Modeling of second-life batteries for use in a CERTS microgrid. In *Power and Energy Conference at Illinois (PECI), 2014*, pages 1–8, Feb 2014.
- [48] N. Mukherjee and D. Strickland. Modular ESS with second life batteries operating in grid independent mode. In *Power Electronics for Distributed Generation Systems (PEDG), 2012 3rd IEEE International Symposium on*, pages 653–660, June 2012.
- [49] L. Benadero, R. Cristiano, D. J. Pagano, and E. Ponce. Nonlinear Analysis of Interconnected Power Converters: A Case Study. *IEEE Journal on Emerging and Selected Topics in Circuits and Systems*, 5(3):326–335, Sept 2015.
- [50] M. Cupelli, M. Moghimi, A. Riccobono, and A. Monti. A comparison between synergetic control and feedback linearization for stabilizing MVDC microgrids with constant power load. In *IEEE PES Innovative Smart Grid Technologies, Europe*, pages 1–6, Oct 2014.
- [51] A. Emadi, A. Khaligh, C. H. Rivetta, and G. A. Williamson. Constant power loads and negative impedance instability in automotive systems: definition, modeling, stability, and control of power electronic converters and motor drives. *IEEE Transactions on Vehicular Technology*, 55(4):1112–1125, July 2006.
- [52] T. Dragičević, J. M. Guerrero, J. C. Vasquez, and D. Škrlec. Supervisory Control of an Adaptive-Droop Regulated DC Microgrid With Battery Management Capability. *IEEE Transactions on Power Electronics*, 29(2):695–706, Feb 2014.

- [53] G. Sulligoi, D. Bosich, and G. Giadrossi. Linearizing voltage control of MVDC power systems feeding constant power loads: Stability analysis under saturation. In *2013 IEEE Power Energy Society General Meeting*, pages 1–5, July 2013.
- [54] D. Tran, H. Zhou, and A. M. Khambadkone. A simple design of DC power system with multiple source-side converters to operate stably under constant power load. In *The 2nd International Symposium on Power Electronics for Distributed Generation Systems*, pages 520–525, June 2010.
- [55] T. Dragičević, X. Lu, J. C. Vasquez, and J. M. Guerrero. DC Microgrids-Part I: A Review of Control Strategies and Stabilization Techniques. *IEEE Transactions on Power Electronics*, 31(7):4876–4891, July 2016.
- [56] A. Kwasinski and C. N. Onwuchekwa. Dynamic Behavior and Stabilization of DC Microgrids With Instantaneous Constant-Power Loads. *IEEE Transactions on Power Electronics*, 26(3):822–834, March 2011.
- [57] A. Yazdani and R. Iravani. *Voltage-Sourced Converters in Power Systems: Modelling, Control and Applications*. John Wiley & Sons, Inc., 2010.
- [58] Erika Twining and D. G. Holmes. Grid current regulation of a three-phase voltage source inverter with an LCL input filter. *IEEE Transactions on Power Electronics*, 18(3):888–895, May 2003.
- [59] S. Yang, Q. Lei, F. Z. Peng, and Z. Qian. A Robust Control Scheme for Grid-Connected Voltage-Source Inverters. *IEEE Transactions on Industrial Electronics*, 58(1):202–212, Jan 2011.
- [60] C. Meyer and R. W. De Doncker. Power electronics for modern medium-voltage distribution systems. In *The 4th International Power Electronics and Motion Control Conference, 2004. IPEMC 2004.*, volume 1, pages 58–66 Vol.1, Aug 2004.
- [61] D. Grahame Holmes and Thomas A. Lipo. *Pulse Width Modulation For Power Converters: Principles and Practice*. Wiley-IEEE Press, 2003.
- [62] A. Hintz, U. R. Prasanna, and K. Rajashekara. Comparative Study of the Three-Phase Grid-Connected Inverter Sharing Unbalanced Three-Phase and/or Single-Phase systems. *IEEE Transactions on Industry Applications*, 52(6):5156–5164, Nov 2016.
- [63] P. Rodriguez, R. Pindado, and J. Bergas. Alternative topology for three-phase four-wire PWM converters applied to a shunt active power filter. In *IEEE 2002 28th Annual Conference of the Industrial Electronics Society. IECON 02*, volume 4, pages 2939–2944 vol.4, Nov 2002.

- [64] R. Zhang, D. Boroyevich, V. H. Prasad, H. . Mao, F. C. Lee, and S. Dubovsky. A three-phase inverter with a neutral leg with space vector modulation. In *Proceedings of APEC 97 - Applied Power Electronics Conference*, volume 2, pages 857–863 vol.2, Feb 1997.
- [65] A. Bellini and S. Bifaretti. A simple control technique for three-phase four-leg inverters. In *International Symposium on Power Electronics, Electrical Drives, Automation and Motion, 2006. SPEEDAM 2006.*, pages 1143–1148, May 2006.
- [66] Man-Chung Wong, Zheng-Yi Zhao, Ying-Duo Han, and Liang-Bing Zhao. Three-dimensional pulse-width modulation technique in three-level power inverters for three-phase four-wired system. *IEEE Transactions on Power Electronics*, 16(3):418–427, May 2001.
- [67] R. Zhang, V. H. Prasad, D. Boroyevich, and F. C. Lee. Three-dimensional space vector modulation for four-leg voltage-source converters. *IEEE Transactions on Power Electronics*, 17(3):314–326, May 2002.
- [68] S. Bifaretti, A. Lidozzi, L. Solero, and F. Crescimbin. Modulation With Sinusoidal Third-Harmonic Injection for Active Split DC-Bus Four-Leg Inverters. *IEEE Transactions on Power Electronics*, 31(9):6226–6236, Sep. 2016.
- [69] J. M. Sosa, G. Escobar, P. R. Martínez-Rodríguez, G. Vázquez, M. A. Juárez, and M. Diosdado. Comparative evaluation of L and LCL filters in transformerless grid tied converters for active power injection. In *2014 IEEE International Autumn Meeting on Power, Electronics and Computing (ROPEC)*, pages 1–6, Nov 2014.
- [70] U. P. Yagnik and M. D. Solanki. Comparison of L, LC and LCL filter for grid connected converter. In *2017 International Conference on Trends in Electronics and Informatics (ICEI)*, pages 455–458, May 2017.
- [71] M. Liserre, F. Blaabjerg, and S. Hansen. Design and control of an LCL-filter-based three-phase active rectifier. *IEEE Transactions on Industry Applications*, 41(5):1281–1291, September 2005.
- [72] R. Juntunen, J. Korhonen, T. Musikka, L. Smirnova, O. Pyrhönen, and P. Silventoinen. Identification of resonances in parallel connected grid inverters with LC- and LCL-filters. In *2015 IEEE Applied Power Electronics Conference and Exposition (APEC)*, pages 2122–2127, March 2015.
- [73] H. Xiao, X. Qu, S. Xie, and J. Xu. Synthesis of active damping for grid-connected inverters with an LCL filter. In *2012 IEEE Energy Conversion Congress and Exposition (ECCE)*, pages 550–556, Sep. 2012.
- [74] J. Xu, S. Xie, and T. Tang. Active Damping-Based Control for Grid-Connected LCL-Filtered Inverter With Injected Grid Current Feedback Only. *IEEE Transactions on Industrial Electronics*, 61(9):4746–4758, Sep. 2014.

- 
- [75] Jinming Xu, Shaojun Xie, and Ting Tang. Active Damping-Based Control for Grid-Connected -Filtered Inverter With Injected Grid Current Feedback Only. *IEEE Transactions on Industrial Electronics*, 61(9):4746–4758, September 2014.
- [76] J. Dannehl, M. Liserre, and F.W. Fuchs. Filter-Based Active Damping of Voltage Source Converters With Filter. *IEEE Transactions on Industrial Electronics*, 58(8):3623–3633, August 2011.
- [77] M. Liserre, A.D. Aquila, and F. Blaabjerg. Genetic algorithm-based design of the active damping for an LCL-filter three-phase active rectifier. *IEEE Transactions on Power Electronics*, 19(1):76–86, January 2004.
- [78] Shao Zhang, Shuai Jiang, Xi Lu, Baoming Ge, and Fang Zheng Peng. Resonance Issues and Damping Techniques for Grid-Connected Inverters With Long Transmission Cable. *IEEE Transactions on Power Electronics*, 29(1):110–120, January 2014.
- [79] R. Pena-Alzola, M. Liserre, F. Blaabjerg, R. Sebastian, J. Dannehl, and F.W. Fuchs. Systematic Design of the Lead-Lag Network Method for Active Damping in LCL-Filter Based Three Phase Converters. *IEEE Transactions on Industrial Informatics*, 10(1):43–52, February 2014.
- [80] F. Huerta, E. Bueno, S. Cobrecas, F.J. Rodriguez, and C. Giron. Control of grid-connected voltage source converters with LCL filter using a Linear Quadratic servocontroller with state estimator. In *IEEE Power Electronics Specialists Conference, 2008. PESC 2008*, pages 3794–3800, June 2008.
- [81] M. Malinowski and S. Bernet. A Simple Voltage Sensorless Active Damping Scheme for Three-Phase PWM Converters With an Filter. *IEEE Transactions on Industrial Electronics*, 55(4):1876–1880, April 2008.
- [82] F. Caricchi, F. Crescimbin, G. Noia, and D. Pirolo. Experimental study of a bidirectional DC-DC converter for the DC link voltage control and the regenerative braking in PM motor drives devoted to electrical vehicles. In *Ninth Annual Conference Proceedings Applied Power Electronics Conference and Exposition, APEC*, volume 1, pages 381–386, 1994.
- [83] Xin Guo, Xuhui Wen, and Ermin Qiao. A DSP Based Controller for High Power Dual-Phase DC-DC Converters. In *Power Electronics and Motion Control Conference, 2006. IPERC 2006. CES/IEEE 5th International*, volume 1, pages 1–5, Aug 2006.
- [84] X. She, A. Q. Huang, and R. Burgos. Review of Solid-State Transformer Technologies and Their Application in Power Distribution Systems. *IEEE Journal of Emerging and Selected Topics in Power Electronics*, 1(3):186–198, Sep. 2013.

- [85] Dong-Hyun Ha, Nam ju Park, Kui-Jun Lee, Dong-Gyu Lee, and Dong-Seok Hyun. Interleaved Bidirectional DC-DC Converter for Automotive Electric Systems. In *Industry Applications Society Annual Meeting, 2008. IAS '08. IEEE*, pages 1–5, Oct 2008.
- [86] Sukin Park and Yujin Song. An interleaved half-bridge bidirectional dc-dc converter for energy storage system applications. In *Power Electronics and ECCE Asia (ICPE ECCE), 2011 IEEE 8th International Conference on*, pages 2029–2034, May 2011.
- [87] C. Gu, Z. Zheng, L. Xu, K. Wang, and Y. Li. Modeling and Control of a Multiport Power Electronic Transformer (PET) for Electric Traction Applications. *IEEE Transactions on Power Electronics*, 31(2):915–927, Feb 2016.
- [88] Z. Ding, C. Yang, Z. Zhang, C. Wang, and S. Xie. A Novel Soft-Switching Multiport Bidirectional DC-DC Converter for Hybrid Energy Storage System. *IEEE Transactions on Power Electronics*, 29(4):1595–1609, April 2014.
- [89] H. Tao, A. Kotsopoulos, J. L. Duarte, and M. A. M. Hendrix. Transformer-Coupled Multiport ZVS Bidirectional DC-DC Converter With Wide Input Range. *IEEE Transactions on Power Electronics*, 23(2):771–781, March 2008.
- [90] H. Fan and H. Li. High-Frequency Transformer Isolated Bidirectional DC-DC Converter Modules With High Efficiency Over Wide Load Range for 20 kVA Solid-State Transformer. *IEEE Transactions on Power Electronics*, 26(12):3599–3608, Dec 2011.
- [91] T. Zhao, L. Yang, J. Wang, and A. Q. Huang. 270 kVA Solid State Transformer Based on 10 kV SiC Power Devices. In *2007 IEEE Electric Ship Technologies Symposium*, pages 145–149, May 2007.
- [92] D. De, A. Castellazzi, and A. Lamantia. 1.2kW dual-active bridge converter using SiC power MOSFETs and planar magnetics. In *2014 International Power Electronics Conference (IPEC-Hiroshima 2014 - ECCE ASIA)*, pages 2503–2510, May 2014.
- [93] Z. Wang, A. Castellazzi, S. Saeed, Á. Navarro-Rodríguez, and P. Garcia. Impact of SiC technology in a three-port active bridge converter for energy storage integrated solid state transformer applications. In *2016 IEEE 4th Workshop on Wide Bandgap Power Devices and Applications (WiPDA)*, pages 84–89, Nov 2016.
- [94] P. García, S. Saeed, Á. Navarro-Rodríguez, J. Garcia, and H. Schneider. Switching Frequency Optimization for a Solid State Transformer With Energy Storage Capabilities. *IEEE Transactions on Industry Applications*, 54(6):6223–6233, Nov 2018.
- [95] B. Kroposki, T. Basso, and R. DeBlasio. Microgrid standards and technologies. In *2008 IEEE Power and Energy Society General Meeting - Conversion and Delivery of Electrical Energy in the 21st Century*, pages 1–4, July 2008.

- 
- [96] G.J. Kish and P.W. Lehn. Microgrid design considerations for next generation grid codes. pages 1–8, July 2012.
  - [97] IEEE Standard for the Specification of Microgrid Controllers. *IEEE Std 2030.7-2017*, pages 1–43, April 2018. 8340204.
  - [98] J. Decuir and P. Michael. Draft IEEE standard for DC microgrids for rural and remote electricity access applications. In *2017 IEEE Conference on Technologies for Sustainability (SusTech)*, pages 1–5, Nov 2017.
  - [99] IEEE Guide for Design, Operation, and Integration of Distributed Resource Island Systems with Electric Power Systems. *IEEE Std 1547.4-2011*, pages 1–54, July 2011.
  - [100] IEEE Draft Recommended Practice for the Planning and Design of the Microgrid. *IEEE P2030.9/D9, December 2018*, pages 1–42, Jan 2018. 8577037.
  - [101] IEEE Guide for Design, Operation, and Integration of Distributed Resource Island Systems with Electric Power Systems. *IEEE Std 1547.4-2011*, pages 1–54, July 2011.
  - [102] IEEE Standard for Interconnection and Interoperability of Distributed Energy Resources with Associated Electric Power Systems Interfaces. *IEEE Std 1547-2018 (Revision of IEEE Std 1547-2003)*, pages 1–138, April 2018.
  - [103] IEEE Standard for Interconnecting Distributed Resources with Electric Power Systems - Amendment 1. *IEEE Std 1547a-2014 (Amendment to IEEE Std 1547-2003)*, pages 1–16, May 2014.
  - [104] IEEE Recommended Practice for Utility Interface of Photovoltaic (PV) Systems. *IEEE Std 929-2000*, 2000.
  - [105] IEEE Recommended Practice for Interconnecting Distributed Resources with Electric Power Systems Distribution Secondary Networks. *IEEE Std 1547.6-2011*, pages 1–38, Sept 2011.
  - [106] IEEE Application Guide for IEEE Std 1547(TM), IEEE Standard for Interconnecting Distributed Resources with Electric Power Systems. *IEEE Std 1547.2-2008*, pages 1–217, April 2009.
  - [107] Engineering Recommendation G99: Requirements for the connection of generation equipment in parallel with public distribution networks on or after 27 April 2019.
  - [108] Engineering Recommendation G83: Recommendations for the Connection of Type Tested Small-scale Embedded Generators (Up to 16A per Phase) in Parallel with Low-Voltage Distribution Systems.

- 
- [109] Engineering Recommendation G59: Recommendations for the Connection of Generating Plant to the Distributions Systems of Licensed Distribution Network Operators.
- [110] IEEE Recommended Practice for Monitoring Electric Power Quality. *IEEE Std 1159-2009 (Revision of IEEE Std 1159-1995)*, pages c1–81, June 2009. 5154067.
- [111] IEEE Guide for Identifying and Improving Voltage Quality in Power Systems. *IEEE Std 1250-2011 (Revision of IEEE Std 1250-1995)*, pages 1–70, March 2011.
- [112] IEEE Recommended Practice and Requirements for Harmonic Control in Electric Power Systems. *IEEE Std 519-2014 (Revision of IEEE Std 519-1992)*, pages 1–29, June 2014.
- [113] Y.A.-R.I. Mohamed and E.F. El-Saadany. Adaptive Decentralized Droop Controller to Preserve Power Sharing Stability of Paralleled Inverters in Distributed Generation Microgrids. *Power Electronics, IEEE Transactions on*, 23(6):2806–2816, Nov 2008.
- [114] M.S. Golsorkhi and D.D.C. Lu. A Control Method for Inverter-Based Islanded Microgrids Based on V-I Droop Characteristics. *Power Delivery, IEEE Transactions on*, 30(3):1196–1204, June 2015. 6898026.
- [115] P. Arboleya, C. Gonzalez-Moran, and M. Coto. A hybrid central-distributed control applied to microgrids with droop characteristic based generators. In *Power Electronics and Motion Control Conference (EPE/PEMC), 2012 15th International*, pages LS7a.5–1–LS7a.5–8, Sept 2012.
- [116] D. Chen and L. Xu. Autonomous DC Voltage Control of a DC Microgrid With Multiple Slack Terminals. *IEEE Transactions on Power Systems*, 27(4):1897–1905, Nov 2012.
- [117] J. M. Guerrero, M. Chandorkar, T. Lee, and P. C. Loh. Advanced Control Architectures for Intelligent Microgrids—Part I: Decentralized and Hierarchical Control. *IEEE Transactions on Industrial Electronics*, 60(4):1254–1262, April 2013.
- [118] Xianyong Feng, Aditya Shekhar, Fang Yang, Robert E. Hebner, and Pavol Bauer. Comparison of Hierarchical Control and Distributed Control for Microgrid. *Electric Power Components and Systems*, 45(10):1043–1056, 2017.
- [119] M. C. Chandorkar, D. M. Divan, and R. Adapa. Control of parallel connected inverters in standalone AC supply systems. *IEEE Transactions on Industry Applications*, 29(1):136–143, Jan 1993.
- [120] J. C. Vasquez, R. A. Mastromauro, J. M. Guerrero, and M. Liserre. Voltage Support Provided by a Droop-Controlled Multifunctional Inverter. *IEEE Transactions on Industrial Electronics*, 56(11):4510–4519, Nov 2009.

- [121] J. M. Guerrero, J. C. Vasquez, J. Matas, L. G. de Vicuna, and M. Castilla. Hierarchical Control of Droop-Controlled AC and DC Microgrids—A General Approach Toward Standardization. *IEEE Transactions on Industrial Electronics*, 58(1):158–172, Jan 2011.
- [122] M. Barnes, J. Kondoh, H. Asano, J. Oyarzabal, G. Ventakaramanan, R. Lasseter, N. Hatziargyriou, and T. Green. Real-World MicroGrids-An Overview. In *2007 IEEE International Conference on System of Systems Engineering*, pages 1–8, April 2007.
- [123] Xiongfei Wang, J. M. Guerrero, and Z. Chen. Control of grid interactive AC microgrids. In *2010 IEEE International Symposium on Industrial Electronics*, pages 2211–2216, July 2010.
- [124] I. J. Balaguer, Q. Lei, S. Yang, U. Supatti, and F. Z. Peng. Control for Grid-Connected and Intentional Islanding Operations of Distributed Power Generation. *IEEE Transactions on Industrial Electronics*, 58(1):147–157, Jan 2011.
- [125] F. Katiraei, R. Iravani, N. Hatziargyriou, and A. Dimeas. Microgrids management. *IEEE Power and Energy Magazine*, 6(3):54–65, May 2008.
- [126] Eneko Unamuno and Jon Andoni Barrena. Hybrid ac/dc microgrids—Part II: Review and classification of control strategies. *Renewable and Sustainable Energy Reviews*, 52:1123 – 1134, 2015.
- [127] P. Karlsson and J. Svensson. DC bus voltage control for a distributed power system. *IEEE Transactions on Power Electronics*, 18(6):1405–1412, Nov 2003. 1243700.
- [128] T. L. Vandoorn, B. Meersman, L. Degroote, B. Renders, and L. Vandeveld. A Control Strategy for Islanded Microgrids With DC-Link Voltage Control. *IEEE Transactions on Power Delivery*, 26(2):703–713, April 2011. First mention of VBD 5685286.
- [129] J. Rocabert, A. Luna, F. Blaabjerg, and P. Rodríguez. Control of Power Converters in AC Microgrids. *IEEE Transactions on Power Electronics*, 27(11):4734–4749, Nov 2012.
- [130] J. C. Vasquez, J. M. Guerrero, M. Savaghebi, J. Eloy-Garcia, and R. Teodorescu. Modeling, Analysis, and Design of Stationary-Reference-Frame Droop-Controlled Parallel Three-Phase Voltage Source Inverters. *IEEE Transactions on Industrial Electronics*, 60(4):1271–1280, April 2013.
- [131] P. Rodriguez, I. Candela, C. Citro, J. Rocabert, and A. Luna. Control of grid-connected power converters based on a virtual admittance control loop. In *2013 15th European Conference on Power Electronics and Applications (EPE)*, pages 1–10, Sep. 2013.

- 
- [132] X. Wang, Y. W. Li, F. Blaabjerg, and P. C. Loh. Virtual-Impedance-Based Control for Voltage-Source and Current-Source Converters. *IEEE Transactions on Power Electronics*, 30(12):7019–7037, Dec 2015.
- [133] Hassan Bevrani, Bruno Francois, and Toshifumi Ise. *Microgrid Dynamics and Control*. Wiley, 2017.
- [134] Sohail Khan, Benoit Bletterie, Adolfo Anta, and Wolfgang Gawlik. On Small Signal Frequency Stability under Virtual Inertia and the Role of PLLs. *Energies*, 11(9), 2018.
- [135] N. Mukherjee, D. De, and N. Nandagaoli. Effect of sudden variation of grid voltage in primary frequency control application using converter based energy storage systems for weak grid systems. In *2017 19th European Conference on Power Electronics and Applications (EPE'17 ECCE Europe)*, pages P.1–P.10, Sep. 2017.
- [136] H.-P. Beck and R. Hesse. Virtual synchronous machine. In *Electrical Power Quality and Utilisation, 2007. EPQU 2007. 9th International Conference on*, pages 1–6, Oct 2007.
- [137] J. Liu, Y. Miura, H. Bevrani, and T. Ise. Enhanced Virtual Synchronous Generator Control for Parallel Inverters in Microgrids. *IEEE Transactions on Smart Grid*, 8(5):2268–2277, Sept 2017.
- [138] Qing-Chang Zhong and G. Weiss. Synchronverters: Inverters That Mimic Synchronous Generators. *Industrial Electronics, IEEE Transactions on*, 58(4):1259–1267, April 2011.
- [139] J. Alipoor, Y. Miura, and T. Ise. Distributed generation grid integration using virtual synchronous generator with adoptive virtual inertia. In *Energy Conversion Congress and Exposition (ECCE), 2013 IEEE*, pages 4546–4552, Sept 2013.
- [140] D. J. Hogan, F. Gonzalez-Espin, J. G. Hayes, G. Lightbody, L. Albiol-Tendillo, and R. Foley. Virtual synchronous-machine control of voltage-source converters in a low-voltage microgrid. In *2016 18th European Conference on Power Electronics and Applications (EPE'16 ECCE Europe)*, pages 1–10, Sep. 2016.
- [141] S. Y. Altahir, X. Yan, and A. S. Gadaalla. New Control Scheme for Virtual Synchronous Generators of Different Capacities. In *2017 IEEE International Conference on Energy Internet (ICEI)*, pages 131–135, April 2017.
- [142] S. D'Arco and J. A. Suul. Equivalence of Virtual Synchronous Machines and Frequency-Droops for Converter-Based MicroGrids. *IEEE Transactions on Smart Grid*, 5(1):394–395, Jan 2014.
- [143] I. Serban and C. Marinescu. Control Strategy of Three-Phase Battery Energy Storage Systems for Frequency Support in Microgrids and with Uninterrupted

- Supply of Local Loads. *Power Electronics, IEEE Transactions on*, 29(9):5010–5020, Sept 2014.
- [144] M.A. Torres L, L.A.C. Lopes, L.A. Moran T, and J.R. Espinoza C. Self-Tuning Virtual Synchronous Machine: A Control Strategy for Energy Storage Systems to Support Dynamic Frequency Control. *Energy Conversion, IEEE Transactions on*, 29(4):833–840, Dec 2014.
- [145] Y. Hirase, O. Noro, K. Sugimoto, K. Sakimoto, Y. Shindo, and T. Ise. Effects of suppressing frequency fluctuations by parallel operation of virtual synchronous generator in microgrids. In *Energy Conversion Congress and Exposition (ECCE), 2015 IEEE*, pages 3694–3701, Sept 2015.
- [146] M. Torres and L.A.C. Lopes. Frequency control improvement in an autonomous power system: An application of virtual synchronous machines. In *Power Electronics and ECCE Asia (ICPE ECCE), 2011 IEEE 8th International Conference on*, pages 2188–2195, May 2011.
- [147] S. K. Mazumder, M. Tahir, and K. Acharya. Master–Slave Current-Sharing Control of a Parallel DC–DC Converter System Over an RF Communication Interface. *IEEE Transactions on Industrial Electronics*, 55(1):59–66, Jan 2008.
- [148] S. Anand, B. G. Fernandes, and J. Guerrero. Distributed Control to Ensure Proportional Load Sharing and Improve Voltage Regulation in Low-Voltage DC Microgrids. *IEEE Transactions on Power Electronics*, 28(4):1900–1913, April 2013.
- [149] L. Meng, Q. Shafiee, G. F. Trecate, H. Karimi, D. Fulwani, X. Lu, and J. M. Guerrero. Review on Control of DC Microgrids and Multiple Microgrid Clusters. *IEEE Journal of Emerging and Selected Topics in Power Electronics*, 5(3):928–948, Sept 2017.
- [150] Juan P. Torreglosa, Pablo García-Triviño, Luis M. Fernández-Ramirez, and Francisco Jurado. Control strategies for DC networks: A systematic literature review. *Renewable and Sustainable Energy Reviews*, 58:319 – 330, 2016.
- [151] R. A. F. Ferreira, H. A. C. Braga, A. A. Ferreira, and P. G. Barbosa. Analysis of voltage droop control method for dc microgrids with Simulink: Modelling and simulation. In *2012 10th IEEE/IAS International Conference on Industry Applications*, pages 1–6, Nov 2012.
- [152] Ramy Georgious Zaher. *A hybrid solution for distributed energy storage for microgeneration in microgrids: Design of the electronic power and control system*. PhD thesis, Universidad de Oviedo, 2018.
- [153] N. R. Chaudhuri and B. Chaudhuri. Adaptive Droop Control for Effective Power Sharing in Multi-Terminal DC (MTDC) Grids. *IEEE Transactions on Power Systems*, 28(1):21–29, Feb 2013.

- [154] Y. Yang, M. M. Khan, and J. Yu. An improved cooperative control method of DC microgrid based on nearest neighbors communication. In *IECON 2017 - 43rd Annual Conference of the IEEE Industrial Electronics Society*, pages 792–797, Oct 2017.
- [155] H. Wang, M. Han, R. Han, J. M. Guerrero, and J. C. Vasquez. A Decentralized Current-Sharing Controller Endows Fast Transient Response to Parallel DC–DC Converters. *IEEE Transactions on Power Electronics*, 33(5):4362–4372, May 2018.
- [156] F. Gao, Y. Gu, S. Bozhko, G. Asher, and P. Wheeler. Analysis of droop control methods in DC microgrid. In *2014 16th European Conference on Power Electronics and Applications*, pages 1–9, Aug 2014.
- [157] D. Wu, F. Tang, T. Dragicevic, J. M. Guerrero, and J. C. Vasquez. Coordinated Control Based on Bus-Signaling and Virtual Inertia for Islanded DC Microgrids. *IEEE Transactions on Smart Grid*, 6(6):2627–2638, Nov 2015.
- [158] E. Unamuno and J. A. Barrena. Design and small-signal stability analysis of a virtual-capacitor control for DC microgrids. In *2017 19th European Conference on Power Electronics and Applications (EPE'17 ECCE Europe)*, pages P.1–P.10, Sept 2017.
- [159] E. Unamuno and J. A. Barrena. Primary control operation modes in islanded hybrid ac/dc microgrids. In *IEEE EUROCON 2015 - International Conference on Computer as a Tool (EUROCON)*, pages 1–6, Sep. 2015.
- [160] H. Zhang, J. Zhou, Q. Sun, J. M. Guerrero, and D. Ma. Data-Driven Control for Interlinked AC/DC Microgrids Via Model-Free Adaptive Control and Dual-Droop Control. *IEEE Transactions on Smart Grid*, 8(2):557–571, March 2017.
- [161] R. P. S. Chandrasena, F. Shahnia, S. Rajakaruna, and A. Ghosh. Dynamic operation and control of a hybrid nanogrid system for future community houses. *IET Generation, Transmission Distribution*, 9(11):1168–1178, 2015.
- [162] P. C. Loh, D. Li, Y. K. Chai, and F. Blaabjerg. Autonomous Operation of Hybrid Microgrid With AC and DC Subgrids. *IEEE Transactions on Power Electronics*, 28(5):2214–2223, May 2013.
- [163] T.L. Vandoorn, B. Renders, L. Degroote, B. Meersman, and L. Vandeveldel. Active Load Control in Islanded Microgrids Based on the Grid Voltage. *Smart Grid, IEEE Transactions on*, 2(1):139–151, March 2011. Use of Voltage-droop control 5661889.
- [164] Yao Liu, Xiaochao Hou, Xiaofeng Wang, Chao Lin, and J. M. Guerrero. A Coordinated Control for Photovoltaic Generators and Energy Storages in Low-Voltage AC / DC Hybrid Microgrids under Islanded Mode. 2016.

- [165] D. Chen, Y. Xu, and A. Q. Huang. Integration of DC Microgrids as Virtual Synchronous Machines Into the AC Grid. *IEEE Transactions on Industrial Electronics*, 64(9):7455–7466, Sept 2017.
- [166] Zhihao Zhang, Xinhong Huang, Jin Jiang, and Bin Wu. A load-sharing control scheme for a microgrid with a fixed frequency inverter. *Electric Power Systems Research*, 80(3):311 – 317, 2010.
- [167] A. Kwasinski and C. N. Onwuchekwa. Dynamic Behavior and Stabilization of DC Microgrids With Instantaneous Constant-Power Loads. *IEEE Transactions on Power Electronics*, 26(3):822–834, March 2011.
- [168] M. K. Mishra and K. Karthikeyan. A Fast-Acting DC-Link Voltage Controller for Three-Phase DSTATCOM to Compensate AC and DC Loads. *IEEE Transactions on Power Delivery*, 24(4):2291–2299, Oct 2009. 5235863.
- [169] S. Vazquez, J. A. Sanchez, J. M. Carrasco, J. I. Leon, and E. Galvan. A Model-Based Direct Power Control for Three-Phase Power Converters. *IEEE Transactions on Industrial Electronics*, 55(4):1647–1657, April 2008. 4439209.
- [170] B. N. Singh, P. Rastgoufard, B. Singh, A. Chandra, and K. Al-Haddad. Design, simulation and implementation of three-pole/four-pole topologies for active filters. *IEE Proceedings - Electric Power Applications*, 151(4):467–476, July 2004. 1305516.
- [171] Yang Ye, M. Kazerani, and V. H. Quintana. Modeling, control and implementation of three-phase PWM converters. *IEEE Transactions on Power Electronics*, 18(3):857–864, May 2003. 1198065.
- [172] L. Zhang, L. Harnefors, and H. Nee. Power-Synchronization Control of Grid-Connected Voltage-Source Converters. *IEEE Transactions on Power Systems*, 25(2):809–820, May 2010. 5308285.
- [173] Rolf Ottersten. *On Control of Back-to-Back Converters and Sensorless Induction Machine Drives*. PhD thesis, Chalmers University of Technology, 2003.
- [174] L. Harnefors, M. Bongiorno, and S. Lundberg. Input-Admittance Calculation and Shaping for Controlled Voltage-Source Converters. *IEEE Transactions on Industrial Electronics*, 54(6):3323–3334, Dec 2007. 4384346.
- [175] Joaquín González Norniella. *Aportaciones al Control Directo de Potencia de Rectificadores Activos Trifásicos*. PhD thesis, Universidad de Oviedo, 2012.
- [176] Y. Xia, Y. Peng, P. Yang, M. Yu, and W. Wei. Distributed Coordination Control for Multiple Bidirectional Power Converters in a Hybrid AC/DC Microgrid. *IEEE Transactions on Power Electronics*, 32(6):4949–4959, June 2017.

- [177] R. S. Pena, R. J. Cardenas, J. C. Clare, and G. M. Asher. Control strategies for voltage control of a boost type PWM converter. In *Power Electronics Specialists Conference, 2001. PESC. 2001 IEEE 32nd Annual*, volume 2, pages 730–735 vol.2, 2001.
- [178] M. Di Benedetto, A. Lidozzi, L. Solero, M. Tang, A. Formentini, and P. Zanchetta. Disturbance-Observer Assisted Controller for Stand-Alone Four-Leg Voltage Source Inverter. In *2018 IEEE Energy Conversion Congress and Exposition (ECCE)*, pages 2265–2270, Sep. 2018.
- [179] C. Marinescu and I Serban. About the main frequency control issues in microgrids with renewable energy sources. In *2013 International Conference on Clean Electrical Power (ICCEP)*, pages 145–150, June 2013.
- [180] I Serban, R. Teodorescu, and C. Marinescu. Energy storage systems impact on the short-term frequency stability of distributed autonomous microgrids, an analysis using aggregate models. *IET Renewable Power Generation*, 7(5):531–539, Sept 2013.
- [181] R. Majumder. Some Aspects of Stability in Microgrids. *IEEE Transactions on Power Systems*, 28(3):3243–3252, Aug 2013.
- [182] J. M. Guerrero. Editorial Special Issue on Power Electronics for Microgrids-Part II. *IEEE Transactions on Power Electronics*, 26(3):659–663, March 2011.
- [183] J.M. Guerrero, Poh Chiang Loh, Tzung-Lin Lee, and M. Chandorkar. Advanced Control Architectures for Intelligent Microgrids-Part II: Power Quality, Energy Storage, and AC/DC Microgrids. *IEEE Transactions on Industrial Electronics*, 60(4):1263–1270, April 2013.
- [184] Bhim Singh, K. Al-Haddad, and A Chandra. A review of active filters for power quality improvement. *IEEE Transactions on Industrial Electronics*, 46(5):960–971, Oct 1999.
- [185] A Agbedahunsi, M. Sumner, E. Christopher, A Watson, A Costabeber, and R. Parashar. Frequency control improvement within a microgrid, using enhanced STATCOM with energy storage. In *6th IET International Conference on Power Electronics, Machines and Drives (PEMD 2012)*, pages 1–6, March 2012.
- [186] Alex Taiwo Agbedahunsi. *Frequency Control for Microgrids using Enhanced STATCOM and Supercapacitor Energy Storage*. PhD thesis, The University of Nottingham, May 2013.
- [187] Roger C. Dugan, Mark F. McGranaghan, Surya Santoso, and H. Wayne Beaty. *Electrical Power Systems Quality, Third Edition*. McGraw-Hill Education, 2012.
- [188] IEC 61000-4-30: Electromagnetic compatibility (EMC) - Part 4-30: testing and measurement techniques - power quality measurement methods. Tech. rep. International Electrotechnical Commission, 2001.

- [189] Giel Van den Broeck, Jeroen Stuyts, and Johan Driesen. A critical review of power quality standards and definitions applied to DC microgrids. *Applied Energy*, 229:281 – 288, 2018.
- [190] ETSI EN 300 132-3-1 V2.1.1 (2011-10) Environmental Engineering (EE); Power supply interface at the input to telecommunications and datacom (ICT) equipment; Part 3: Operated by rectified current source, alternating current source or direct current source up to 400 V; Sub-part 1: Direct current source up to 400 V.
- [191] Voltage characteristics of electricity supplied by public electricity networks. *UNE-EN 50160:2011, Royal Degree 2011-7603*, 2011.
- [192] Ali Al-Shetwi, Muhamad Sujod, and Noor Lina Ramli. A review of the fault ride through requirements in different grid codes concerning penetration of PV system to the electric power network. *ARPJ Journal of Engineering and Applied Sciences*, 10:9906–9912, 10 2015.
- [193] Florin Iov, Daniela Anca, Poul Sorensen, and Nicolaos Cutululis. Mapping of Grid Faults and Grid Codes. *Riso-R-1617 (EN)*, 01 2007.
- [194] Ying Cheng, Chang Qian, M.L. Crow, S. Pekarek, and Stan Atcitty. A Comparison of Diode-Clamped and Cascaded Multilevel Converters for a STATCOM With Energy Storage. *Industrial Electronics, IEEE Transactions on*, 53(5):1512–1521, Oct 2006. 1705642.
- [195] A Arulampalam, J.B. Ekanayake, and N. Jenkins. Application study of a STATCOM with energy storage. *IEEE Proceedings on Generation, Transmission and Distribution*, 150(3):373–384, May 2003.
- [196] M. Beza and M. Bongiorno. Comparison of two control approaches for stability enhancement using STATCOM with active power injection capability. In *Energy Conversion Congress and Exposition (ECCE), 2015 IEEE*, pages 4721–4728, Sept 2015.
- [197] Duck-Su Lee, Soo-Nam Kim, Young-Chan Choi, Byung-San Baek, and Jong-Sung Hur. Development of wind power stabilization system using BESS and STATCOM. In *Innovative Smart Grid Technologies (ISGT Europe), 2012 3rd IEEE PES International Conference and Exhibition on*, pages 1–5, Oct 2012.
- [198] J.A Barrado, R. Grino, and H. Valderrama-Blavi. Power-Quality Improvement of a Stand-Alone Induction Generator Using a STATCOM With Battery Energy Storage System. *Power Delivery, IEEE Transactions on*, 25(4):2734–2741, Oct 2010.
- [199] M.G. Molina, P.E. Mercado, and E.H. Watanabe. Analysis of Using FACTS Controllers with Superconducting Magnetic Energy Storage in the Primary Frequency Control of Power Systems. In *Transmission Distribution Conference and Exposition: Latin America, 2006. TDC '06. IEEE/PES*, pages 1–7, Aug 2006.

- [200] A Arulampalam, M. Barnes, N. Jenkins, and J.B. Ekanayake. Power quality and stability improvement of a wind farm using STATCOM supported with hybrid battery energy storage. *Generation, Transmission and Distribution, IEE Proceedings-*, 153(6):701–710, November 2006.
- [201] Z. Yang, C. Shen, L. Zhang, M.L. Crow, and S. Atcitty. Integration of a StatCom and battery energy storage. *Power Systems, IEEE Transactions on*, 16(2):254–260, May 2001.
- [202] P. Srithorn, M. Sumner, L. Yao, and R. Parashar. A STATCOM with supercapacitors for enhanced power system stability. In *Power Electronics, Machines and Drives, 2008. PEMD 2008. 4th IET Conference on*, pages 96–100, April 2008.
- [203] Zhengping Xi, B. Parkhideh, and S. Bhattacharya. Improving distribution system performance with integrated STATCOM and supercapacitor energy storage system. In *Power Electronics Specialists Conference, 2008. PESC 2008. IEEE*, pages 1390–1395, June 2008.
- [204] Lirong Zhang, Yi Wang, Heming Li, and Pin Sun. Hybrid power control of cascaded STATCOM/BESS for wind farm integration. In *Industrial Electronics Society, IECON 2013 - 39th Annual Conference of the IEEE*, pages 5288–5293, Nov 2013.
- [205] S.K. Balibani, G. Gurralla, and I Sen. Power system stability enhancement using a STATCOM with ESS. In *India Conference (INDICON), 2013 Annual IEEE*, pages 1–6, Dec 2013.
- [206] R. Kuiava, R.A Ramos, and N.G. Bretas. Control design of a STATCOM with Energy Storage System for stability and power quality improvements. In *Industrial Technology, 2009. ICIT 2009. IEEE International Conference on*, pages 1–6, Feb 2009.
- [207] M.E. Baran, S. Teleke, L. Anderson, A Huang, S. Bhattacharya, and S. Atcitty. STATCOM with energy storage for smoothing intermittent wind farm power. In *Power and Energy Society General Meeting - Conversion and Delivery of Electrical Energy in the 21st Century, 2008 IEEE*, pages 1–6, July 2008.
- [208] J. Mundackal, AC. Varghese, P. Sreekala, and V. Reshmi. Grid power quality improvement and battery energy storage in wind energy systems. In *Emerging Research Areas and 2013 International Conference on Microelectronics, Communications and Renewable Energy (AICERA/ICMiCR), 2013 Annual International Conference on*, pages 1–6, June 2013.
- [209] A Sattar, A Al Durra, C. Caruana, S.M. Muyeen, and J. Tamura. Real time implementation of the BESS to smoothen the output power fluctuation of the variable speed wind turbine generator. In *Electrical Machines and Systems (ICEMS), 2012 15th International Conference on*, pages 1–6, Oct 2012.

- [210] M. R I Sheikh, F. Eva, M. A Motin, and M. A Hossain. Wind generator output power smoothing and terminal voltage regulation by using STATCOM/SMES. In *Developments in Renewable Energy Technology (ICDRET), 2012 2nd International Conference on the*, pages 1–5, Jan 2012.
- [211] M.C. Falvo, L. Martirano, and D. Sbordone. D-STATCOM with energy storage system for application in Smart Micro-Grids. In *2013 International Conference on Clean Electrical Power (ICCEP)*, pages 571–576, June 2013.
- [212] M.T. Holmberg, M. Lahtinen, J. McDowall, and T. Larsson. SVC Light with energy storage for frequency regulation. In *2010 IEEE Conference on Innovative Technologies for an Efficient and Reliable Electricity Supply (CITRES)*, pages 317–324, Sept 2010.
- [213] V. Fernão Pires, Enrique Romero-Cadaval, D. Vinnikov, I. Roasto, and J.F. Martins. Power converter interfaces for electrochemical energy storage systems – A review. *Energy Conversion and Management*, 86:453 – 475, 2014.
- [214] Deepak Ravi, Bandi Mallikarjuna Reddy, Shimi S.L, and Paulson Samuel. Bidirectional dc to dc Converters: An Overview of Various Topologies, Switching Schemes and Control Techniques. *International Journal of Engineering & Technology*, 2018.
- [215] Sudipta Chakraborty, Bill Kramer, and Benjamin Kroposki. A review of power electronics interfaces for distributed energy systems towards achieving low-cost modular design. *Renewable and Sustainable Energy Reviews*, 13(9):2323 – 2335, 2009.
- [216] J. Li-Jun, Y. Guang-Yao, J. Miao-Miao, C. Yi-Fan, Z. Hai-Peng, and Z. Ke. Study of bi-directional DC-DC converter of micro-grid hybrid energy storage system. In *2015 IEEE 10th Conference on Industrial Electronics and Applications (ICIEA)*, pages 1166–1169, June 2015.
- [217] F. Zhang, Y. Yang, C. Ji, W. Wei, Y. Chen, C. Meng, Z. Jin, and G. Zhang. Power management strategy research for DC microgrid with hybrid storage system. In *2015 IEEE First International Conference on DC Microgrids (ICDCM)*, pages 62–68, June 2015.
- [218] N. Eghtedarpour and E. Farjah. Control strategy for distributed integration of photovoltaic and energy storage systems in DC micro-grids. *Renewable Energy*, 45:96 – 110, 2012.
- [219] Y. Guo, W. Ma, J. Meng, and Y. Wang. A Virtual Inertia Control Strategy for Dual Active Bridge DC-DC Converter. In *2018 2nd IEEE Conference on Energy Internet and Energy System Integration (EI2)*, pages 1–5, Oct 2018.
- [220] A. Lana, P. Nuutinen, J. Karppanen, P. Peltoniemi, T. Kaipia, and J. Partanen. Control of directly connected energy storage in LVDC distribution network. In

- 11th IET International Conference on AC and DC Power Transmission*, pages 1–6, Feb 2015.
- [221] Ramy Georgious, Jorge Garcia, Pablo García, and Angel Navarro-Rodriguez. A Comparison of Non-Isolated High-Gain Three-Port Converters for Hybrid Energy Storage Systems. *Energies*, 11:658, 03 2018.
- [222] R. Georgious, J. García, Á. Navarro-Rodríguez, and P. García. A Study on the Control Design of Nonisolated Converter Configurations for Hybrid Energy Storage Systems. *IEEE Transactions on Industry Applications*, 54(5):4660–4671, Sep. 2018.
- [223] M. Ayar, S. Obuz, R. Trevizan, A. Bretas, and H. Latchman. A Distributed Control Approach for Enhancing Smart Grid Transient Stability and Resilience. *IEEE Transactions on Smart Grid*, PP(99):1–1, 2017.
- [224] E. Hammad, A. Farraj, and D. Kundur. On Effective Virtual Inertia of Storage-Based Distributed Control for Transient Stability. *IEEE Transactions on Smart Grid*, PP(99):1–1, 2017.
- [225] Seung-Ki Sul. *Control of Electric Machine Drive Systems*. Wiley IEEE press, 2011.
- [226] D.Y. Ohm. Analysis of PID and PDF compensators for motion control systems. In *Conference Record of the 1994 IEEE Industry Applications Society Annual Meeting, 1994*, pages 1923–1929 vol.3, Oct 1994.
- [227] C.M. Liaw, Y. K. Chen, K.H. Chao, and H.C. Chen. Quantitative design and implementation of PI-D controller with model-following response for motor drive. *IEEE Proceedings - Electric Power Applications*, 145(2):98–104, Mar 1998.
- [228] T. Piraisoodi and S. Sadhu. Characteristic Analysis of High Order Disturbance Observer. In *2005 Annual IEEE INDICON*, pages 431–436, Dec 2005.
- [229] Thao Tran Phuong, R. Furusawa, C. Mitsantisuk, and K. Ohishi. Force sensing considering periodic disturbance suppression based on high order disturbance observer and Kalman-filter. In *2011 4th International Conference on Human System Interactions (HSI)*, pages 336–341, May 2011.
- [230] E. Saito and S. Katsura. A filter design method in disturbance observer for improvement of robustness against disturbance in time delay system. In *2012 IEEE International Symposium on Industrial Electronics (ISIE)*, pages 1650–1655, May 2012.
- [231] Du Limin, Zhang Ke, and Jin Guang. Linear auto disturbance rejection controller for vector-controlled PMSM drive system. In *2011 International Conference on Transportation, Mechanical, and Electrical Engineering (TMEE)*, pages 879–882, Dec 2011.

- [232] George Ellis. *Observer in Control Systems: A practical guide*. Academic Press, an imprint of Elsevier Science, 2002.
- [233] S. Pulendran and J. E. Tate. Energy Storage System Control for Prevention of Transient Under-Frequency Load Shedding. *IEEE Transactions on Smart Grid*, 8(2):927–936, March 2017.
- [234] M.A. Torres L. *Dynamic Frequency Control in Diesel-Hybrid Autonomous Power Systems using Virtual Synchronous Machines*. PhD thesis, Concordia University, Montreal, Quebec, Canada, May 2013.
- [235] Gene F. Franklin, J. David Powell, and Abbas Emami-Naeini. *Feedback Control of Dynamic Systems*. Prentice Hall, fourth edition edition, 2002.
- [236] Se-Kyo Chung. A phase tracking system for three phase utility interface inverters. *IEEE Transactions on Power Electronics*, 15(3):431–438, May 2000.
- [237] P. Roncero-Sanchez, X. del Toro Garcia, AP. Torres, and V. Feliu. Fundamental Positive- and Negative-Sequence Estimator for Grid Synchronization Under Highly Disturbed Operating Conditions. *IEEE Transactions on Power Electronics*, 28(8):3733–3746, Aug 2013.
- [238] P. Rodriguez, A. Luna, M. Ciobotaru, R. Teodorescu, and F. Blaabjerg. Advanced Grid Synchronization System for Power Converters under Unbalanced and Distorted Operating Conditions. In *IECON 2006 - 32nd Annual Conference on IEEE Industrial Electronics*, pages 5173–5178, Nov 2006.
- [239] Bo Wen. *Stability Analysis of Three-phase AC Power Systems Based on Measured D-Q Frame Impedances*. PhD thesis, Virginia Polytechnic Institute and State University, 2014.
- [240] D. Dong, B. Wen, D. Boroyevich, P. Mattavelli, and Y. Xue. Analysis of Phase-Locked Loop Low-Frequency Stability in Three-Phase Grid-Connected Power Converters Considering Impedance Interactions. *IEEE Transactions on Industrial Electronics*, 62(1):310–321, Jan 2015.
- [241] W. Wu, Y. Chen, A. Luo, L. Zhou, X. Zhou, L. Yang, Y. Dong, and J. M. Guerrero. A Virtual Inertia Control Strategy for DC Microgrids Analogized With Virtual Synchronous Machines. *IEEE Transactions on Industrial Electronics*, 64(7):6005–6016, July 2017.
- [242] H. Qiu, J. Fang, and Y. Tang. Explore the Capability of Power Electronic Converters in Providing Power System Virtual Inertia. In *2018 IEEE Energy Conversion Congress and Exposition (ECCE)*, pages 215–221, Sep. 2018.
- [243] P. A. Dahono and R. Mulyadi. A new control method of DC-DC converters based on virtual capacitance concept. In *4th IEEE International Conference on Power Electronics and Drive Systems. IEEE PEDS 2001 - Indonesia. Proceedings (Cat. No. 01TH8594)*, volume 1, pages 121–125 vol.1, Oct 2001.

- [244] Christopher James Rose. *An adaptive D-STATCOM control scheme utilising impedance estimation*. PhD thesis, The University of Nottingham, 2015.
- [245] Guo Xiaoqiang, Wu weiyang, Gu Herong, and San Guocheng. DC injection control for grid-connected inverters based on virtual capacitor concept. In *2008 International Conference on Electrical Machines and Systems*, pages 2327–2330, Oct 2008.
- [246] V. Natarajan and G. Weiss. Synchronverters With Better Stability Due to Virtual Inductors, Virtual Capacitors, and Anti-Windup. *IEEE Transactions on Industrial Electronics*, 64(7):5994–6004, July 2017.
- [247] H. Xu, X. Zhang, F. Liu, R. Shi, C. Yu, W. Zhao, Y. Yu, and W. Cao. A reactive power sharing method based on virtual capacitor in islanding microgrid. In *2014 International Power Electronics Conference (IPEC-Hiroshima 2014 - ECCE ASIA)*, pages 567–572, May 2014.
- [248] A. Micalef, M. Apap, C. Spiteri-Staines, and J. M. Guerrero. Selective virtual capacitive impedance loop for harmonic voltage compensation in islanded MicroGrids. In *IECON 2013 - 39th Annual Conference of the IEEE Industrial Electronics Society*, pages 7968–7973, Nov 2013.
- [249] Huafeng Xiao, Xiaohui Qu, Shaojun Xie, and Jinming Xu. Synthesis of active damping for grid-connected inverters with an LCL filter. In *2012 IEEE Energy Conversion Congress and Exposition (ECCE)*, pages 550–556, September 2012.
- [250] J. He and Y. W. Li. Generalized Closed-Loop Control Schemes with Embedded Virtual Impedances for Voltage Source Converters with LC or LCL Filters. *IEEE Transactions on Power Electronics*, 27(4):1850–1861, April 2012.
- [251] Poh Chiang Loh and D. G. Holmes. Analysis of multiloop control strategies for LC/CL/LCL-filtered voltage-source and current-source inverters. *IEEE Transactions on Industry Applications*, 41(2):644–654, March 2005.
- [252] J. Kukkola, M. Hinkkanen, and K. Zenger. Observer-Based State-Space Current Controller for a Grid Converter Equipped With an LCL Filter: Analytical Method for Direct Discrete-Time Design. *Industry Applications, IEEE Transactions on*, PP(99):1–1, 2015.
- [253] A. Ghanem, M. Rashed, M. Sumner, M. A. Elsayes, and I. I. I. Mansy. Grid impedance estimation for islanding detection and adaptive control of converters. *IET Power Electronics*, 10(11):1279–1288, 2017.
- [254] Cristian Blanco Charro. *Synchronization, islanding detection and power quality improvement in distributed power generation systems*. PhD thesis, Universidad de Oviedo, 2015.

- [255] M. Sumner, B. Paethorpe, and D.W.P. Thomas. Impedance measurement for improved power quality-Part 2: a new technique for stand-alone active shunt filter control. *IEEE Transactions on Power Delivery*, 19(3):1457–1463, 2004.
- [256] J.R. Massing, M. Stefanello, H.A. Grundling, and H. Pinheiro. Adaptive Current Control for Grid-Connected Converters With LCL Filter. *IEEE Transactions on Industrial Electronics*, 59(12):4681–4693, 2012.
- [257] Z. Staroszczyk. A method for real-time, wide-band identification of the source impedance in power systems. *IEEE Transactions on Instrumentation and Measurement*, 54(1):377–385, Feb 2005.
- [258] M. Sumner, B. Paethorpe, D. W. P. Thomas, P. Zanchetta, and M. C. Di Piazza. A technique for power supply harmonic impedance estimation using a controlled voltage disturbance. *IEEE Transactions on Power Electronics*, 17(2):207–215, Mar 2002.
- [259] M. Liserre, F. Blaabjerg, and R. Teodorescu. Grid Impedance Estimation via Excitation of LCL -Filter Resonance. *IEEE Transactions on Industry Applications*, 43(5):1401–1407, 2007.
- [260] A. Vidal, A. G. Yepes, F. D. Freijedo, Ó. López, J. Malvar, F. Baneira, and J. Doval-Gandoy. A Method for Identification of the Equivalent Inductance and Resistance in the Plant Model of Current-Controlled Grid-Tied Converters. *IEEE Transactions on Power Electronics*, 30(12):7245–7261, Dec 2015.
- [261] A. K. Broen, M. Amin, E. Skjong, and M. Molinas. Instantaneous frequency tracking of harmonic distortions for grid impedance identification based on Kalman filtering. In *2016 IEEE 17th Workshop on Control and Modeling for Power Electronics (COMPEL)*, pages 1–7, June 2016.
- [262] A. Bechouche, D. Ould Abdeslam, H. Seddiki, and A. Rahoui. Estimation of equivalent inductance and resistance for adaptive control of three-phase PWM rectifiers. In *IECON 2016 - 42nd Annual Conference of the IEEE Industrial Electronics Society*, pages 1336–1341, Oct 2016.
- [263] D. Martin and E. Santi. Auto tuning of digital deadbeat current controller for grid tied inverters using wide bandwidth impedance identification. In *2012 Twenty-Seventh Annual IEEE Applied Power Electronics Conference and Exposition (APEC)*, pages 277–284, 2012.
- [264] L. Asiminoaei, R. Teodorescu, F. Blaabjerg, and U. Borup. A digital controlled PV-inverter with grid impedance estimation for ENS detection. *IEEE Transactions on Power Electronics*, 20(6):1480–1490, Nov 2005.
- [265] D.D. Reigosa, F. Briz, C.B. Charro, P. Garcia, and J.M. Guerrero. Active Islanding Detection Using High-Frequency Signal Injection. *IEEE Transactions on Industry Applications*, 48(5):1588–1597, 2012.

- [266] D. Reigosa, F. Briz, C. Blanco, P. Garcia, and J. Manuel Guerrero. Active Islanding Detection for Multiple Parallel-Connected Inverter-Based Distributed Generators Using High-Frequency Signal Injection. *IEEE Transactions on Power Electronics*, 29(3):1192–1199, 2014.
- [267] T. Roinila, M. Vilkkko, and J. Sun. Online grid impedance measurement using discrete-interval binary sequence injection. In *2013 IEEE 14th Workshop on Control and Modeling for Power Electronics (COMPEL)*, pages 1–8, June 2013.
- [268] M. Cespedes and J. Sun. Three-phase impedance measurement for system stability analysis. In *2013 IEEE 14th Workshop on Control and Modeling for Power Electronics (COMPEL)*, pages 1–6, June 2013.
- [269] M. A. Azzouz and E. F. El-Saadany. Multivariable Grid Admittance Identification for Impedance Stabilization of Active Distribution Networks. *IEEE Transactions on Smart Grid*, 8(3):1116–1128, May 2017.
- [270] M. Cespedes and J. Sun. Adaptive Control of Grid-Connected Inverters Based on Online Grid Impedance Measurements. *IEEE Transactions on Sustainable Energy*, 5(2):516–523, April 2014.
- [271] M. Céspedes and J. Sun. Online grid impedance identification for adaptive control of grid-connected inverters. In *2012 IEEE Energy Conversion Congress and Exposition (ECCE)*, pages 914–921, Sept 2012.
- [272] M. Sumner, B. Palethorpe, and D.W.P. Thomas. Impedance measurement for improved power quality-Part 1: the measurement technique. *IEEE Transactions on Power Delivery*, 19(3):1442–1448, 2004.
- [273] N. Hoffmann and F.W. Fuchs. Minimal Invasive Equivalent Grid Impedance Estimation in Inductive and Resistive Power Networks Using Extended Kalman Filter. *IEEE Transactions on Power Electronics*, 29(2):631–641, 2014.
- [274] Xiaoqiang Guo, Zhigang Lu, Xiaofeng Sun, Herong Gu, and Weiyang Wu. New grid impedance estimation technique for grid-connected power converters. *Journal of Engineering Research*, 2(3):19, 2014.
- [275] L. Asiminoaei, R. Teodorescu, F. Blaabjerg, and U. Borup. Implementation and Test of an Online Embedded Grid Impedance Estimation Technique for PV Inverters. *IEEE Transactions on Industrial Electronics*, 52(4):1136–1144, 2005.
- [276] A.V. Timbus, P. Rodriguez, R. Teodorescu, and M. Ciobotaru. Line Impedance Estimation Using Active and Reactive Power Variations. In *IEEE Power Electronics Specialists Conference, 2007. PESC 2007*, pages 1273–1279, 2007.
- [277] A. Riccobono, S. K. A. Naqvi, A. Monti, T. Caldognetto, J. Siegers, and E. Santi. Online wideband identification of single-phase AC power grid impedances using an existing grid-tied power electronic inverter. In *2015 IEEE 6th International*

- Symposium on Power Electronics for Distributed Generation Systems (PEDG)*, pages 1–8, June 2015.
- [278] T. Roinila, T. Messo, and A. Aapro. Impedance measurement of three phase systems in DQ-domain: Applying MIMO-identification techniques. In *2016 IEEE Energy Conversion Congress and Exposition (ECCE)*, pages 1–6, Sept 2016.
- [279] S. Golestan, J. M. Guerrero, and J. C. Vasquez. Three-Phase PLLs: A Review of Recent Advances. *IEEE Transactions on Power Electronics*, 32(3):1894–1907, March 2017.
- [280] F. D. Freijedo, J. Doval-Gandoy, O. Lopez, and E. Acha. A Generic Open-Loop Algorithm for Three-Phase Grid Voltage/Current Synchronization With Particular Reference to Phase, Frequency, and Amplitude Estimation. *IEEE Transactions on Power Electronics*, 24(1):94–107, Jan 2009.
- [281] S. Golestan, A. Vidal, A. G. Yepes, J. M. Guerrero, J. C. Vasquez, and J. Doval-Gandoy. A True Open-Loop Synchronization Technique. *IEEE Transactions on Industrial Informatics*, 12(3):1093–1103, June 2016.
- [282] P. Rodriguez, R. Teodorescu, I. Candela, A.V. Timbus, M. Liserre, and F. Blaabjerg. New Positive-sequence Voltage Detector for Grid Synchronization of Power Converters under Faulty Grid Conditions. In *2006 37th IEEE Power Electronics Specialists Conference*, pages 1–7, June 2006.
- [283] A. M. Gole and V. K. Sood. A static compensator model for use with electromagnetic transients simulation programs. *IEEE Transactions on Power Delivery*, 5(3):1398–1407, Jul 1990.
- [284] C. Blanco, D. Reigosa, F. Briz, and J. M. Guerrero. Synchronization in highly distorted three-phase grids using selective notch filters. In *2013 IEEE Energy Conversion Congress and Exposition*, pages 2641–2648, Sept 2013.
- [285] Xiaoqiang Guo, Weiyang Wu, and Zhe Chen. Multiple-Complex Coefficient-Filter-Based Phase-Locked Loop and Synchronization Technique for Three-Phase Grid-Interfaced Converters in Distributed Utility Networks. *Industrial Electronics, IEEE Transactions on*, 58(4):1194–1204, April 2011.
- [286] C. Blanco, D. Reigosa, F. Briz, J. M. Guerrero, and P. Garcia. Grid synchronization of three-phase converters using cascaded complex vector filter PLL. In *2012 IEEE Energy Conversion Congress and Exposition (ECCE)*, pages 196–203, Sept 2012.
- [287] F. D. Freijedo, A. G. Yepes, O. Lopez, A. Vidal, and J. Doval-Gandoy. Three-Phase PLLs With Fast Postfault Retracking and Steady-State Rejection of Voltage Unbalance and Harmonics by Means of Lead Compensation. *IEEE Transactions on Power Electronics*, 26(1):85–97, Jan 2011.

- 
- [288] S. Golestan, J. M. Guerrero, A. Vidal, A. G. Yepes, and J. Doval-Gandoy. PLL With MAF-Based Prefiltering Stage: Small-Signal Modeling and Performance Enhancement. *IEEE Transactions on Power Electronics*, 31(6):4013–4019, June 2016.
- [289] C. Blanco, D. Reigosa, F. Briz, and J. M. Guerrero. Quadrature signal generator based on all-pass filter for single-phase synchronization. In *2014 IEEE Energy Conversion Congress and Exposition (ECCE)*, pages 2655–2662, Sept 2014.
- [290] Gerald Goertzel. An Algorithm for the Evaluation of Finite Trigonometric Series. *The American Mathematical Monthly*, 65(1):34–35, 1958.
- [291] E. Jacobsen and R. Lyons. An update to the sliding DFT. *IEEE Signal Processing Magazine*, 21(1):110–111, Jan 2004.
- [292] C. A. Busada, S. Gomez Jorge, and J. A. Solsona. Full-State Feedback Equivalent Controller for Active Damping in LCL -Filtered Grid-Connected Inverters Using a Reduced Number of Sensors. *IEEE Transactions on Industrial Electronics*, 62(10):5993–6002, Oct 2015.
- [293] A.J. Arriagada, J.R. Espinoza, J.R. Rodriguez, and L.A. Moran. On-line filtering reactance identification in voltage-source three-phase active-front-end rectifiers. In *The 29th Annual Conference of the IEEE Industrial Electronics Society, 2003. IECON '03*, volume 1, pages 192–197 vol.1, November 2003.
- [294] F. Briz, P. García, M. W. Degner, D. Díaz-Reigosa, and J. M. Guerrero. Dynamic Behavior of Current Controllers for Selective Harmonic Compensation in Three-Phase Active Power Filters. *IEEE Transactions on Industry Applications*, 49(3):1411–1420, May 2013.
- [295] Yongsug Suh and T. A. Lipo. Control scheme in hybrid synchronous stationary frame for PWM AC/DC converter under generalized unbalanced operating conditions. *IEEE Transactions on Industry Applications*, 42(3):825–835, May 2006.



# Appendix



## Appendix A

# Simulation and experimental implementation



## A.1 Clarke-Park transform

The Clarke-Park transformation consists in a coordinate change from the stationary 3-phase system to a 2 components rotating reference frame. In 3-phase system, the 3-phase stationary components of an arbitrary electrical variable  $x$  can be represented as a rotating vector  $\mathbf{x}_s$ , which speed is the electrical frequency. That vector can be expressed as a complex number and represented with two orthogonal components, that can be stationary ( $\alpha\beta$  reference frame) or synchronous ( $dq$  reference frame). In this thesis, for the  $dq$  reference frame, the  $d$ -axis component will be aligned with the positive real axis and  $q$ -axis with the positive imaginary-axis, being the rotating frame align 90 degrees behind the  $a$ -axis. The vector representation of the synchronous reference frame is shown in Fig. A.1 and defined by the equation (A.1), where  $\theta = \omega t$  is the frame phase and  $\omega$  the frame rotational speed.

$$\mathbf{x}_s = x_d + jx_q = (x_\alpha + jx_\beta)e^{-j(\theta - \frac{\pi}{2})} = \frac{2}{3} \left( x_a + x_b e^{-\frac{j2\pi}{3}} + x_c e^{\frac{j2\pi}{3}} \right) e^{-j(\theta - \frac{\pi}{2})} \quad (\text{A.1})$$

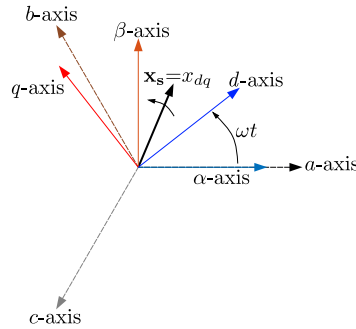


**Figure A.1:** Reference frame vector representation.

Additionally, if the system is not balanced, an orthogonal component to the complex plane named homopolar or zero sequence allows for a close transformation between the natural  $abc$  and the  $\alpha\beta 0$  and  $dq$  references frames.

The scalar transformations from the  $abc$  reference frame to the  $\alpha\beta$  and  $\alpha\beta$  to  $abc$  can be expressed by equations (A.2) and (A.3) respectively, where  $x$  denotes any of the electrical variables in the system (current or voltage), and  $x_0$  is the homopolar component.

$$\begin{bmatrix} x_\alpha \\ x_\beta \\ x_0 \end{bmatrix} = \begin{bmatrix} \frac{2}{3} & -\frac{1}{3} & -\frac{1}{3} \\ 0 & \frac{1}{\sqrt{3}} & -\frac{1}{\sqrt{3}} \\ \frac{1}{3} & \frac{1}{3} & \frac{1}{3} \end{bmatrix} \begin{bmatrix} x_a \\ x_b \\ x_c \end{bmatrix} \quad (\text{A.2})$$

$$\begin{bmatrix} x_a \\ x_b \\ x_c \end{bmatrix} = \begin{bmatrix} 1 & 0 & 1 \\ -\frac{1}{2} & \frac{\sqrt{3}}{2} & 1 \\ -\frac{1}{2} & -\frac{\sqrt{3}}{2} & 1 \end{bmatrix} \begin{bmatrix} x_\alpha \\ x_\beta \\ x_0 \end{bmatrix} \quad (\text{A.3})$$

The scalar transformations from the  $\alpha\beta$  reference frame to the  $dq$  and  $\alpha\beta$  to  $dq$  can be expressed by equations (A.4) and (A.5) respectively, where  $x$  denotes any of the electrical variables in the system (current or voltage),  $\theta$  is the phase of the complex vector in the stationary reference frame, and  $x_0$  is the homopolar component.

$$\begin{bmatrix} x_d \\ x_q \\ x_0 \end{bmatrix} = \frac{2}{3} \begin{bmatrix} \sin(\theta) & -\cos(\theta) & 0 \\ \cos(\theta) & \sin(\theta) & 0 \\ 0 & 0 & 1 \end{bmatrix} \begin{bmatrix} x_\alpha \\ x_\beta \\ x_0 \end{bmatrix} \quad (\text{A.4})$$

$$\begin{bmatrix} x_\alpha \\ x_\beta \\ x_0 \end{bmatrix} = \begin{bmatrix} \sin(\theta) & \cos(\theta) & 0 \\ -\cos(\theta) & \sin(\theta) & 0 \\ 0 & 0 & 1 \end{bmatrix} \begin{bmatrix} x_d \\ x_q \\ x_0 \end{bmatrix} \quad (\text{A.5})$$

The scalar transformations from the  $abc$  reference frame to the  $dq$  and  $dq$  to  $abc$  can be expressed by equations (A.6) and (A.7) respectively, where  $x$  denotes any of the electrical variables in the system (current or voltage),  $\theta$  is the phase of the complex vector in the stationary reference frame, and  $x_0$  is the homopolar component.

$$\begin{bmatrix} x_d \\ x_q \\ x_0 \end{bmatrix} = \frac{2}{3} \begin{bmatrix} \sin(\theta) & \sin(\theta - \frac{2\pi}{3}) & \sin(\theta - \frac{4\pi}{3}) \\ \cos(\theta) & \cos(\theta - \frac{2\pi}{3}) & \cos(\theta - \frac{4\pi}{3}) \\ \frac{1}{2} & \frac{1}{2} & \frac{1}{2} \end{bmatrix} \begin{bmatrix} x_a \\ x_b \\ x_c \end{bmatrix} \quad (\text{A.6})$$

$$\begin{bmatrix} x_a \\ x_b \\ x_c \end{bmatrix} = \begin{bmatrix} \sin(\theta) & \cos(\theta) & 1 \\ \sin(\theta - \frac{2\pi}{3}) & \cos(\theta - \frac{2\pi}{3}) & 1 \\ \sin(\theta - \frac{4\pi}{3}) & \cos(\theta - \frac{4\pi}{3}) & 1 \end{bmatrix} \begin{bmatrix} x_d \\ x_q \\ x_0 \end{bmatrix} \quad (\text{A.7})$$

The instantaneous active ( $P$ ) and reactive ( $Q$ ) power calculated using the voltage ( $x = v$ ) and current ( $x = i$ ) in the synchronous reference frame are defined by (A.8) and (A.9) respectively.

$$P(t) = \frac{3}{2} (v_d(t)i_d(t) + v_q(t)i_q(t) + 2v_0(t)i_0(t)) \quad (\text{A.8})$$

$$Q(t) = \frac{3}{2} (v_q(t)i_d(t) - v_d(t)i_q(t)) \quad (\text{A.9})$$

## A.2 Digital control implementation

The real time implementation of control systems in the present thesis is done in discrete domain via digital signal controllers (DSCs). The generic diagram for the control of converters is shown in Fig. A.2 . The PI controllers, Luenberger-observers and discrete algorithms used along the thesis is discretized applying bilinear approximation (Tustin). The relation between the  $z$  domain and Laplace domain using the bilinear transform is defined by A.10, where  $T_s$  is the sampling time of the analog to digital conversion and the control system. The discretization of the PI regulators is described below.

$$s = \frac{2}{T_s} \frac{1 - z^{-1}}{1 + z^{-1}} \quad (\text{A.10})$$

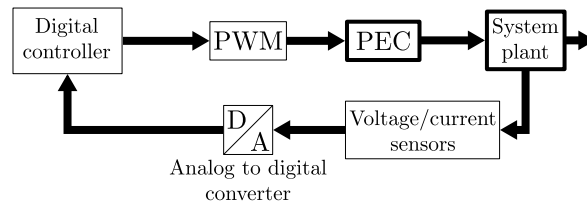


**Figure A.2:** Generic control diagram for the converter control in the scope of this thesis.

The Proportional Integral (PI) regulators proposed in the system control scheme should be defined for the digital implementation. The PI transfer function in time and Laplace domain is denoted in (A.11) and (A.12) respectively, where  $U$  is the controller action and  $E$  is the input error. This continuous expressions should be obtained in the discrete domain using the  $z$  transformation.

$$u(t) = k_p \left( e(t) + \frac{1}{T_i} \int e(t) dt \right) \quad (\text{A.11})$$

$$\frac{U(s)}{E(s)} = k_p \left( 1 + \frac{1}{T_i s} \right) \quad (\text{A.12})$$

Using the Tustin method for the discretization, a transfer function of the form shown in (A.13) is obtained.

$$\frac{U(z)}{E(z)} = \frac{b_0 z + b_1}{a_0 z - 1} \quad (\text{A.13})$$

Dividing the expression by  $z$ , the resulting equation is that shown in (A.14).

$$\frac{U(z)}{E(z)} = \frac{b_0 + b_1 z^{-1}}{a_0 - a_1 z^{-1}} \quad (\text{A.14})$$

Substituting the factor  $z^{-1}$  in (A.15) by the corresponding previous sample of U and E, and clearing U and E, the equation results in (A.16), where  $k$  and  $k - 1$  stand for the actual and previous sample respectively.

$$U(a_0 - a_1 z^{-1}) = E(b_0 + b_1 z^{-1}) \quad (\text{A.15})$$

$$U[k]a_0 - U[k-1]a_1 = E[k]b_0 + E[k-1]b_1 \quad (\text{A.16})$$

Then, the expression which should be implemented in digital controller is the one shown in (A.17), where U[k] and E[k] are the present values while E[k-1] and U[k-1] are the values obtained in previous sample. As  $a_0$  and  $a_1$  are 1, they can be skipped from the equation.

$$U[k] = E[k]b_0 + E[k-1]b_1 + U[k-1] \quad (\text{A.17})$$

Concerning the PI parameters  $b_0$  and  $b_1$ , they are dependent on the proportional and integral gains of the PI as well as the sample period, following the relation shown in (A.18) and (A.19).

$$b_0 = k_p \frac{T_s}{2T_i} + 1 \quad (\text{A.18})$$

$$b_1 = k_p \frac{T_s}{2T_i} - 1 \quad (\text{A.19})$$

The saturation of PI controllers require an anti wind-up technique. In this thesis, the anti wind-up of PI regulators is implemented based on back-calculation, which consists in uploading the variable E[k-1] with the limited PI output as shown in (A.20).

$$E[k-1] = (U[k] - E[k]b_0 - U[k-1]a_1)b_1 \quad (\text{A.20})$$

### A.3 Simulation and experimental setup: evaluation of the observer-based LCL filter control

The proposed observer-based LCL filter has been evaluated through simulations and experimental results using the parameters in Table A.1. The analytical analysis and the time domain simulations have been performed in MATLAB<sup>®</sup> and

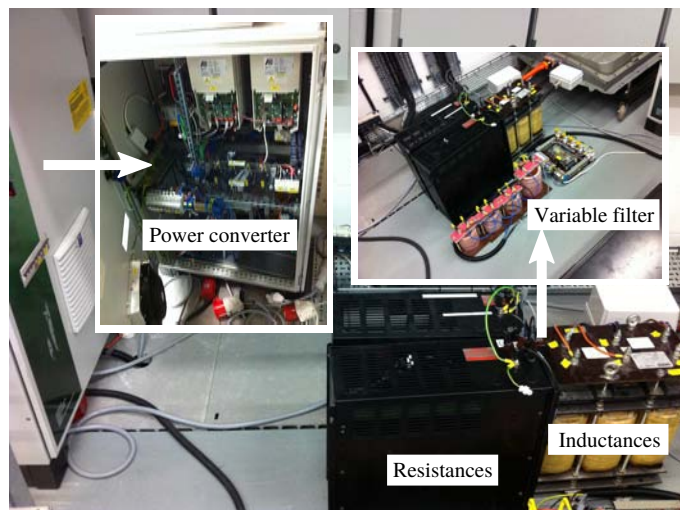
MATLAB/Simulink<sup>®</sup> respectively. For the time domain simulations the toolbox SimPowerSystems<sup>™</sup> has been used, using an ideal VSI. The experimental results have been obtained using a 3-phase AC inverter developed prototype consisting in a MTL-CBI0060F121XHF power converter rated at 15 kVA from GUASCH rectifiers, and a control system based on the TMS320F28335 DSC from Texas Instruments.

Table A.1: Observer-based LCL filter control parameters

Nominal parameters	Value
$R_1$	0.2 $\Omega$
$R_2$	0.2 $\Omega$
$L_1$	7 mH
$L_2$	7 mH
$C$	6 $\mu F$
$C_i$ BW	300 Hz
$k_{p_i}$	26.4
$T_{i_i}$	0.035
$k_a$	50
$C_o$ BW	1000 Hz
$k_{p_o}$	87.9
$T_{i_o}$	0.035
$T_s$	100 $\mu s$

## A.4 Simulation and experimental setup: evaluation of the grid impedance estimation method based on pulsed signal injection

The proposed impedance estimation method has been evaluated through simulations and experimental results using the parameters in Table A.2. The simulations have been obtained in MATLAB<sup>®</sup> and MATLAB/Simulink<sup>®</sup>. The experimental results have been obtained using a PM15F42C power module from Triphase, rated at 15kVA at the facilities of The University of Nottingham. The power module is interfaced to the AC grid through a LCL filter. The converter is coupled directly to the grid, without an isolation transformer. For the experiments carried out, the  $L_2$  inductance is bypassed and the voltage is measured at the filter capacitor. The power converter running the RLS algorithm is connected to the grid by a set of different impedances, with inductance [0.5, 1, 2.5]mH ([0.0833, 0.1667, 0.4167]p.u) and resistance [0.2, 0.15, 0.15] $\Omega$  ([0.1083, 0.0812, 0.0812]p.u). A 10 $\Omega$  three-phase balanced resistive load is connected in parallel to the converter output. A picture for the experimental setup can be seen in Fig. A.3. In order to check the accuracy of the method under a controlled environment, initial results have been obtained by disconnecting the grid and interfacing the converter to a balanced resistive load while varying the series impedance.



**Figure A.3:** Experimental setup. Photo for the Setup#1 described in Table A.2. Left-side, a picture for the PM15F42C power module, at the right, a set of inductances used for the variable grid impedance, as well as the resistive loads.

Table A.2: Parameters

Nominal parameters	Value
$R_1$	0.2 $\Omega$
$R_2$	0.2 $\Omega$
$L_1$	2.3 mH
$L_2$	0.93 mH
$C$	10 $\mu$ F
pulse mag.	0.1 pu
pulse width.	1 ms
$\lambda$	0.9
$Z_{base}$ (150kVA, 400V)	1.85 $\Omega$
$L_{base}$	6mH
$T_s$	125 $\mu$ s

## A.5 Simulation and experimental setup: analysis of DVC and QVC

The analysis of DVC and QVC voltage control has been supported with simulations and experimental results using the parameters in Table A.3 and Table A.4 respectively. The analytical analysis and the time domain simulations have been performed in MATLAB<sup>®</sup> and MATLAB/Simulink<sup>®</sup> respectively, using a continuous model in

both cases.

Table A.3: System parameters used for the analytical and simulation examples

Parameter	Scenario 1	Scenario 2
Nominal Voltage $V_n$	325 V	650 V
Capacitor $C$	40 $\mu$ F	10 $\mu$ F
Nominal Active Power $P_n$	50kW	50kW
$\omega_n$	2 $\pi$ 50 rad/s	2 $\pi$ 50 rad/s
$\zeta$	1	1

The experimental results have been obtained in the facilities of the PEMC research group at The University of Nottingham, using the Triphase power modules PM15F42C ( $T_s = 125\mu$ s) and PM90F60C ( $T_s = 62.5\mu$ s). The experimental parameters are included in Table A.4.

Table A.4: System parameters used for voltage control analysis

System Parameters	Experimental Setup	
	DC MG	AC MG
Voltage reference $V^*$	680 $V_{DC}$	230 $V_{AC_{rms}}$
Nominal Frequency	DC	50 Hz
Nominal Active Power $P$	11 kW	90 kW
Capacitor $C$	1000 $\mu$ F	40 $\mu$ F
AC Filter Inductance $L$	-	500 $\mu$ H
Switching frequency $f_{sw}$	8 kHz	8/16 kHz
Current control bandwidth	2 $\pi$ 500 rad/s	2 $\pi$ 500 rad/s
Voltage control loop $\omega_n / \zeta$	2 $\pi$ 6 rad/s / 1	2 $\pi$ 50 rad/s / 1

## A.6 Simulation and experimental setup: evaluation of the observer-based transient frequency compensation

The proposed observer based frequency-drift compensator has been evaluated through simulations and experimental results using the parameters in Table A.5. The analytical analysis and the time domain simulations have been performed in MATLAB<sup>®</sup> and MATLAB/Simulink<sup>®</sup> respectively. The experimental results have been obtained using a 3-phase AC inverter developed prototype consisting in a MTL-CBI0060F121XHF power converter rated at 15 kVA from GUASCH rectifiers, and a control system based on the TMS320F28335 DSC from Texas Instruments. The equipment used to implement the experimental setup is shown in Fig. A.4. The MG generator is emulated using 2 coupled PMSMs one acting as generator and other as

the governor motor controlled by a commercial drive. The grid frequency shown in the experimental results have been obtained using the speed resolver included in the industrial drive.

Table A.5: System Parameters

MG Voltage ph-ph / $f_n$	98V <sub>rms</sub> / 50Hz
3-phase load	32 $\Omega$
BEMF / Torque constant / Poles	98V/krmp / 1.6Nm/A / 3 pairs
Mechanical parameters	$J = 0.0019\text{kg} \cdot \text{m}^2$ , $b = 0.2\text{Nms}$
Electrical parameters	$L_g = 6\text{mH}$ , $R_g = 2.1\Omega$
Power / ESS Voltage	20kW / 140V
DC link voltage / Capacitor	300V / 2mF
Grid connected AC filter	$R = 0.2\Omega$ , $L = 7.18\text{mH}$
DC/DC converter filter	$R = 0.1\Omega$ , $L = 7.18\text{mH}$
TFDC DC/DC Current control	BW=500Hz, $k_{pi}=22$ , $T_{ii}=1/13$
TFDC DC link Voltage control	BW=50Hz, $k_{pv}=1$ , $T_{iv}=1/175$
TFDC AC/DC Current control	BW=400Hz, $k_{pi}=22$ , $T_{ii}=1/50$
TFDC Control Gains	P: $K_p = 0.2$ PDF: $K_p = 0.2$ , $K_d = 0.1$
Observer parameters	$k_g = 0.78$ , $\omega_{ng} = 25.6$ , $\xi_g = 4.96$ $k_s = 1$ , $\omega_{ns} = 31.4$ , $\xi_s = 1$
Observer $C_o$ coefficients	$K_o = 10$ , zeros=[10, 10, 5, 3.4] $\cdot 10^{-3}$ poles=[20, 10, 10, 6.67] $\cdot 10^{-4}$
Dynamic Load Emulator	Current BW = 500Hz Power BW = 50Hz Current limit = 10A Nominal Power = 1kW
$T_s$	100 $\mu\text{s}$

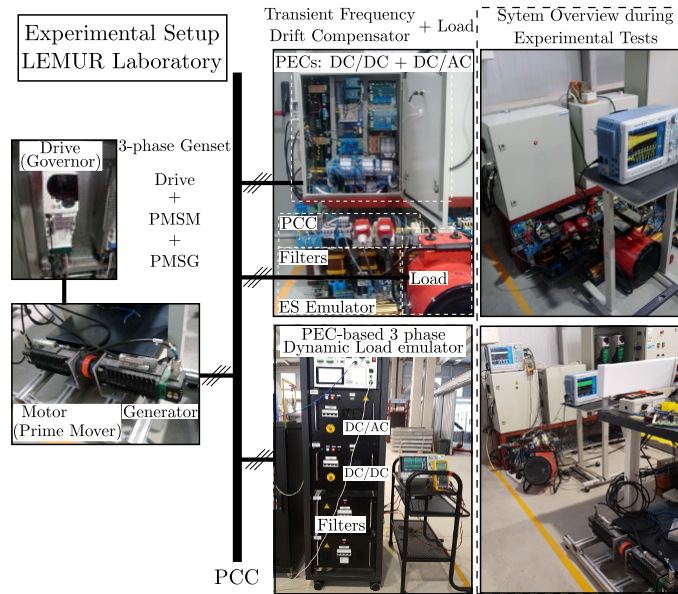


**Figure A.4:** Experimental prototype. Left: generator and drive used as the governor and the prime mover. Top center: TFDC and resistive load. Bottom center: dynamic load emulator based on PECs. Right: the setup during operation.

## A.7 Simulation and experimental setup: evaluation of the predictive sequence estimator

The proposed Goertzel-based sequence estimator has been evaluated through simulations and experimental results. The simulations have been done using MATLAB<sup>®</sup> and MATLAB/Simulink<sup>®</sup>. For the experimental results, two different scenarios have been used, always considering a fundamental grid frequency of 50Hz:

- **Offline evaluation:** The offline evaluation of the proposed sequence estimator has been done using a programmable voltage source (2210 TC-ACS-50-480-400 from Regatron located in the facilities of the LEMUR group at the University of Oviedo) to create different grid voltage profiles. The data is acquired at 1Ms/s sample rate by an scope and later down-sampled to 10kHz. The down-sampled signal is processed in Matlab/Simulink<sup>®</sup> using the different analyzed estimation methods.
- **Online evaluation:** The online experimental validation of the proposed sequence estimator is done by using the experimental setup shown in Fig. A.5, located at the facilities of PEMC group at The University of Nottingham. The setup

is composed by two Triphase power modules PM15F42C and PM90F60C and a set of passive loads. The PM90F60C module is used as a grid voltage emulator for creating the different grid scenarios (grid profiles), modifying the magnitude, phase, frequency and harmonic content of the voltage signal. The proposed algorithms are processed online in the PM15F42C control unit using the voltage measurements at the point of common coupling (PCC).

Both the offline and online tests use the same code implementation in Matlab/Simulink<sup>®</sup>.

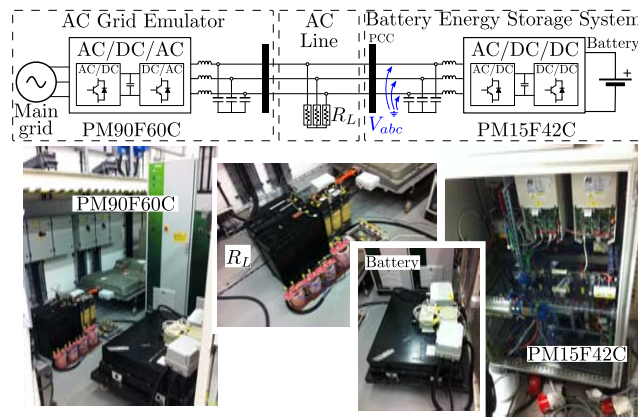


**Figure A.5:** Setup used for the experimental validation. Two converters are coupled together, PM90F60C unit is used to create the varying grid conditions and PM15F42C runs the proposed estimation method.

The harmonic components considered for the simulations and the offline experimental validation are listed in Table A.6.

Table A.6: Considered harmonics in the simulation and offline implementation.

Harmonic order $h$	Magnitude (p.u.)
-5	0.2
7	0.2

The relevant parameters used for the closed-loop current control simulation are listed in Table A.7.

The harmonic components considered for the online experimental validation are listed in Table A.8.

Table A.7: Closed-loop current control parameters.

Parameter $h$	Value
(VSI filter) L	5mH
(VSI filter) R	0.2 $\Omega$
Switching frequency $f_{sw}$	10kHz
Current control BW	20Hz

Table A.8: Considered harmonics in the online implementation.

Harmonic order $h$	Magnitude (p.u.)
5	0.05
7	0.05

## A.8 Simulation setup: LVDC control based on droop control and DCVGs

The simulation validation of the LVDC control proposed in Section 5.2.2 has been performed in MATLAB/Simulink<sup>®</sup>. The relevant parameters used for the simulation are given in Table A.9.

Table A.9: System Parameters

LVDC Parameters	Values
DC Nominal Voltage ( $V_{dc}^*$ )	750 V
SST inner control BW (mains & BESS)	500Hz
LVDC bus Capacitor ( $C_{dc}$ )	750 $\mu$ F
bemf $K_{emains}$ and $K_{ebess}$	2.38 V·s/rad
DCVGs virtual impedance $L_{dc}^\gamma/R_{dc}^\gamma$	0mH / 1 $\Omega$
mains droop gain $m_{mains}$	$2.5 \times 10^{-5}$
BESS droop gain $m_{bess}$	$2.08 \times 10^{-4}$
mains Virtual Inertia ( $J_{dc}^{mains}, b_{dc}^{mains}$ )	0.005kgm <sup>2</sup> / 0.01Nms
BESS Virtual Inertia ( $J_{dc}^{bess}, b_{dc}^{bess}$ )	0.001kgm <sup>2</sup> / 0.015Nms
mains and BESS governor BW	50Hz

## A.9 Simulation and experimental setup: evaluation of the *basic* and *cooperative* QVC-based MG control

The proposed *basic* and *cooperative* QVC-based MG control have been evaluated through simulations and experimental results using the parameters in Table A.10. The simulations have been performed in and MATLAB/Simulink<sup>®</sup> using the toolbox SimPowerSystems<sup>™</sup>. The experimental results have been obtained using the experimental hybrid AC/DC microgrid developed in the facilities of the LEMUR group at the University of Oviedo.

Table A.10: Simulation and experimental system parameters

AC Nanogrids Parameters	Values
AC Nominal Voltage ( $v_{g1}^*, v_{g2}^*$ )	212 $V_{AC_{rms}}$ / 50 Hz
NGHCs AC inner control loop BW	$2\pi 500$ rad/s
NGHCs AC QVC voltage control $\omega_n / \zeta$	$2\pi 37.5$ rad/s / 2
NGHCs Filter Capacitor ( $C_1, C_2$ )	80 $\mu F$
NGHCs Filter Inductance ( $L_1, L_2$ )	1 mH
NGHCs rated power	50 kVA
NGs line impedance ( $Z_1^k, Z_2^k$ )	$0.02\Omega$ / $1.5\mu H$
AC voltage compensator gains $K_{vc} / C_{vc}$	$0.2 / 5 \cdot 10^{-4}$
AC voltage compensator inner control BW	$2\pi 500$ rad/s
AC CPL power control BW	$2\pi 500$ rad/s
LVDC bus and DC voltage control	
DC Nominal Voltage ( $v_{dc}^*$ )	700 V
DC inner control loop BW	$2\pi 500$ rad/s
DC equivalent Capacitor ( $C_{dc}$ )	1100 $\mu F$
DC Voltage control loop $\omega_n / \zeta$	$2\pi 50$ / 1
Central BESS $BW / P_{max}$	75 Hz / 8.5 kW
Adaptive power sharing algorithm	
Power Sharing $\lambda_g^1 / \lambda_g^2 / \delta_{max} / \eta_m$	1 / 1 / 0.5 / 2
Transient detection $T / \text{threshold}$	2 ms / $5 \cdot 10^{-3}$

## A.10 Simulation setup: evaluation of the *basic* and *cooperative* VG-based MG control

The proposed *basic* and *cooperative* VG-based MG control have been evaluated through simulations in MATLAB/Simulink<sup>®</sup>. The system has been evaluated under an illustrative scenario with the parameters using the parameters in Table A.11.

Table A.11: System Parameters

AC NGs and NGHCs Parameters	Values
AC Nominal Voltage ( $v_g^{k*}, \omega_e^{k*}$ )	230 $V_{AC_{rms}}$ / 50Hz
NGHCs Filter ( $L_k, C_k$ )	1mH / 80 $\mu$ F
NGHCs Virtual Impedance ( $L_s^k, R_s^k$ )	0.1mH / 2 $\Omega$
NGHCs AVR integral gain ( $K_{AVR}^k$ )	5
NGHCs Virtual Inertia ( $J_r^k, b_r^k$ )( <i>basic</i> )	0.1kgm <sup>2</sup> / 1Nms
NGHCs Virtual Inertia ( $J_r^k, b_r^k$ )( <i>cooperative</i> )	3kgm <sup>2</sup> / 0.01Nms
NGHCs Governor BW (case 1)	50Hz
NGHCs DC Virtual Impedance ( $L_{dc}^k, R_{dc}^k$ )	0mH / 1 $\Omega$
NGHCs freq reg $R_{\omega_e^k}$ ( $k_{p_{\omega_e^k}}, T_{i_{\omega_e^k}}$ )	0.01 / 100
$NG_2$ Frequency compensator ( $K_{vi}, J_{vi}$ )	6 / 1kgm <sup>2</sup>
LVDC Parameters	Values
DC Nominal Voltage ( $v_{dc}^*$ )	750 V
Current control BW (mains & BESS)	500Hz
DC bus Capacitor ( $C_{dc}$ )	750 $\mu$ F
$K_{e_{mains}}$ and $K_{e_{bess}}$	2.38 V·s/rad
DCVGs Virtual impedance $L_{dc}^\gamma/R_{dc}^\gamma$	0mH / 1 $\Omega$
mains droop gain $m_{mains}$	$2.5 \times 10^{-5}$
BESS droop gain $m_{bess}$	$2.08 \times 10^{-4}$
mains Virtual Inertia ( $J_{dc}^{mains}, b_{dc}^{mains}$ )	0.005kgm <sup>2</sup> / 0.01Nms
BESS Virtual Inertia ( $J_{dc}^{bess}, b_{dc}^{bess}$ )	0.001kgm <sup>2</sup> / 0.015Nms
mains and BESS Governor BW	50Hz



## Appendix B

# Algorithms pseudo-code and diagrams



## B.1 Transient detection algorithm

---

**Algorithm 1** Transient detection algorithm implementation.

---

```

1:  $x[i], x[i - 1] \leftarrow [0, 0]$ 
2:  $y[i], y[i - 1] \leftarrow [0, 0]$ 
3:  $C_t[i], C_t[i - 1] \leftarrow [0, 0]$ 
4: for  $i \leftarrow 1$ , end of execution (real time) do
5:    $f[i] \leftarrow \text{actual sample}$ 
6:    $x[i] = f[i] * g[i]$ 
7:    $y[i] = \frac{T_s}{2} (x[i] + x[i - 1]) + y[i - 1]$ 
8:    $x[i - 1] = x[i]$ 
9:    $y[i - 1] = y[i]$ 
10:  if  $i == \frac{T}{T_s}$  then
11:     $C_t[i] = (\frac{1}{T}y[i])^2$ 
12:     $x[i] \leftarrow 0$ 
13:     $x[i - 1] \leftarrow 0$ 
14:     $y[i] \leftarrow 0$ 
15:     $y[i - 1] \leftarrow 0$ 
16:  else
17:     $C_t[i] = C_t[i - 1]$ 
18:  end if
19:   $C_t[i - 1] = C_t[i]$ 
20:  if  $C_t[i] > \text{Threshold}$  then
21:    if  $\text{Transient Window}[i] == \text{OFF}$  then
22:       $t_1[i] \leftarrow \text{actual time } t$ 
23:    end if
24:     $\text{Transient Window}[i] \leftarrow \text{ON}$ 
25:  else
26:    if  $\text{Transient Window}[i] == \text{ON}$  then
27:       $t_2[i] \leftarrow \text{actual time } t$ 
28:      send trigger to local coefficient calculation
29:    end if
30:     $\text{Transient Window}[i] \leftarrow \text{OFF}$ 
31:  end if
32: end for

```

---

## B.2 Sliding Goertzel transform algorithm

Fig. B.1 shows the block of the IIR Goertzel algorithm, where  $h$  stands for the harmonic order, that can adopt positive and negative values and includes the fundamental component ( $h=1$ ). The black traces are the operations computed at each sample. The blue traces represent the operations to be done at the last step ( $n = N$ ) for the standard Goertzel, corresponding to lines 11 and 12 in Algorithm 2. Green lines represent the additional operations for the sliding Goertzel transform implementation. It has to be remarked, that for the case of SGT, the output equation is calculated at each sample (line 7 in Algorithm 2).

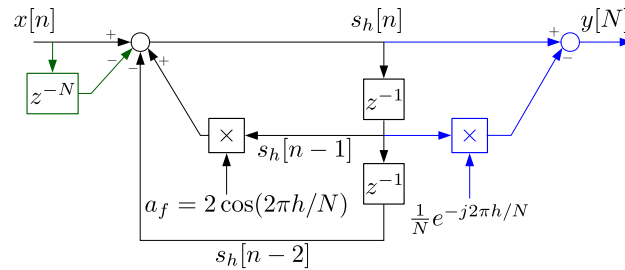


Figure B.1: IIR implementation of the Goertzel algorithm for a single harmonic  $h$ .

---

### Algorithm 2 Goertzel and SGT algorithm implementation.

---

```

1:  $f_{bin} \leftarrow 2\pi h/N$ 
2:  $a_f \leftarrow 2 \cos(f_{bin})$ 
3:  $b_f \leftarrow e^{-j f_{bin}}$ 
4: for  $h \leftarrow 1, \text{number of elements in } f_{bin}$  (harmonics) do
5:   for  $n \leftarrow 1, N - 1$  do
6:      $s_h[h, n] = x[n] - x[n - N] + a_f[h] \cdot s_h[h, n - 1] - s_h[h, n - 2]$ 
7:      $y(h, n) = (s_h[h, n] - s_h[h, n - 1] \cdot b_f[h])/N$ 
8:      $s_h[h, n - 2] = s_h[h, n - 1]$ 
9:      $s_h[h, n - 1] = s_h[h, n]$ 
10:  end for
11:   $s_h[h, n] = a_f[h] \cdot s_h[h, n - 1] - s_h[h, n - 2]$ 
12:   $y[h, N] = (s_h[h, n] - s_h[h, n - 1] \cdot b_f[h])/N$ 
13: end for

```

---

## Appendix C

### Journal publications



## C.1 Observer-based Transient Frequency Drift Compensation in AC Microgrids

Á. Navarro-Rodríguez, P. García, R. Georgious, J. García and S. Saeed, "Observer-Based Transient Frequency Drift Compensation in AC Microgrids," in *IEEE Transactions on Smart Grid*, vol. 10, no. 2, pp. 2015-2025, March 2019. doi: 10.1109/TSG.2017.2786085.



This is the author's version of an article that has been published in this journal. Changes were made to this version by the publisher prior to publication.  
The final version of record is available at <http://dx.doi.org/10.1109/TSG.2017.2786085>

1

## Observer-based Transient Frequency Drift Compensation in AC Microgrids

Ángel Navarro-Rodríguez, *Student Member, IEEE*, Pablo García, *Member, IEEE*, Ramy Georgious, *Student Member, IEEE*, Jorge García, *Senior Member, IEEE*, and Sarah Saeed, *Student Member, IEEE*

**Abstract**—This paper proposes a novel solution for transient frequency compensation in weak 3-phase Microgrids (MGs) based on a Luenberger observer and a transient frequency detector. Unlike in conventional grids, the low inertia of the generators coupled to a MG could make their rotor speeds to be affected by load changes, varying the grid frequency and compromising the grid quality and stability. This problem has been approached in the literature by the Virtual Inertia (VI) concept. However, the existing solutions are affected by the decoupling of the grid frequency reference and the frequency estimation bandwidth. The proposed paper addresses these problems by the use of a transient frequency drift estimator based on a transient detector and a Luenberger type observer that provides a nearly-zero lag frequency estimation. The proposed alternative is analytically compared with the existing techniques and validated through simulation and exhaustive experimental results in an islanded MG. The developed method enables a 1Hz reduction in the transient frequency deviation when compared with the existing alternatives and improves the system stability.

**Index Terms**—AC-DC, DC-DC power converters, Energy storage, Frequency control, Microgrids, Observers, Power control, Power quality, Power system dynamics.

### I. INTRODUCTION

THE weakness, quality and stability problems associated to Microgrids (MGs) have been considered since they emerged, demanding a significant research effort [1]–[3]. Distribution Static Synchronous Compensator (D-STATCOM) with Energy Storage, or simply Energy Storage System (ESS), are the preferred solution for power quality enhancement involving active power exchange in MGs [4]–[6].

Some examples of ESS use can be found for frequency profile enhancement [7], [8]. In these applications, the ESS works in coordination with a power plant, using a communication link and providing access to the system variables. Often, the ESS participates both in the power sharing during steady state and transients. In [3], an ESS system was proposed for frequency compensation limited to the operation during transients. However, the proposed solution relies on the commu-

nication with the generation system. The communication-less frequency compensation in MGs has been already proposed, being one of the most common solutions the Virtual Inertia (VI) [9]–[16].

The absence of communications leads to three main constraints: 1) The grid frequency must be estimated from the voltage signals at the point of common coupling (PCC). Methods such as Phase-Locked Loop (PLL) [17], [18], or more robust techniques as Frequency-Locked Loop (FLL) [19], can be used. However, they are characterized by relatively slow dynamics which limits the compensator controller bandwidth. 2) Improved load-disturbance rejection capability needs for a derivative action to fasten the controller response, however this is prone to noise in the estimated frequency signal. 3) Avoiding power sharing during steady state might be compromised with varying grid frequency reference.

The present paper will focus on the design of an improved transient frequency drift compensator (TFDC) for its application in weak MGs. The TFDC will be implemented by means of a D-STATCOM with ESS, being the proposed method agnostic with respect to the ESS technology. Although other enhanced solutions appear in the literature [20]–[24], in the present study, two of the main existing limitations for frequency compensation are addressed: the decoupling of the grid frequency reference and the low bandwidth of grid frequency estimators. The performance achieved by existing feedback control has been improved by the development of a transient observer, formed by a novel transient detection method based on signal correlation that effectively decouples the grid reference frequency from the compensator inputs, and a Luenberger-based observer that provides a nearly-zero lag frequency estimation and allows to increase the phase margin in the frequency controller. Among the contributions in the present paper, it is worth to highlight: 1) an exhaustive system characterization and disturbance rejection analysis of the existing methods compared with the proposed TFDC, 2) a novel method for the detection of the transient frequency and 3) the implementation of a novel enhanced solution based on the use of a Luenberger type observer [25] for the grid frequency estimation that allows for a reduction of the compensator phase lag, mitigating the dependence on the derivative factor associated to VI.

The proposed techniques have been compared with the existing ones, analytically and experimentally, in an isolated MG with resistive and Constant Power Loads (CPL), evincing the limitations of VI and existing frequency estimators when used for transient frequency compensation. A normalized

The present work has been partially supported by the predoctoral grants program Severo Ochoa for the formation in research and university teaching of Principado de Asturias PCTI-FICYT under grants ID BP13-138, BP14-135 and BP16-133. This work also was supported in part by the Research, Technological Development and Innovation Program Oriented to the Society Challenges of the Spanish Ministry of Economy and Competitiveness under grants ENE2013-44245-R and ENE2016-77919-R and by the European Union through ERFD Structural Funds (FEDER).

A. Navarro-Rodríguez, P. García, R. Georgious, J. García and S. Saeed are with the Department of Electrical, Computer and System Engineering, University of Oviedo, Gijón, 33204, Spain (e-mail: navarroangel@uniovi.es, garciaf-pablo@uniovi.es, georgiousramy@uniovi.es, garciajorge@uniovi.es, hazkial-sarah.uo@uniovi.es).

This is the author's version of an article that has been published in this journal. Changes were made to this version by the publisher prior to publication.  
The final version of record is available at <http://dx.doi.org/10.1109/TSG.2017.2786085>

2

performance comparison has been derived from the analysis, establishing a benchmark for the selection of the most suitable method depending on the application. Under the conditions used in this paper, a reduction of 1Hz in the initial frequency drift compared with the existing techniques is achieved. Thus, the contributions in this paper lead to the possibility of faster frequency compensation in weak grids even with a reduced FLL or PLL bandwidth.

The paper is organized as follows. Section II formulates the dynamic frequency drift problem. Section III covers the control structure of the TFDC. Section IV details the model and use of the Luenberger based observer. Section V shows the experimental results.

## II. PROBLEM DEFINITION AND SYSTEM MODELING

Deviations on power grid nominal parameters can lead to non-optimal operation or malfunction of grid connected elements. Moreover, the violation of regulations could trigger the system protections, compromising the grid power quality and stability. As a reference, the default IEEE regulation for distributed resources is summarized in Table I, where  $f_e$  and  $f_n$  are the instantaneous grid frequency and the nominal grid frequency respectively.

TABLE I  
DEFAULT CLEARING TIMES UNDER ABNORMAL FREQUENCY OPERATION  
BASED ON IEEE STD 1547A-2014 [26]

Frequency [Hz]	Clearing Time [s]
$f_e < f_n - 3$	0.16
$f_e < f_n - 0.5$	2
$f_e > f_n + 0.5$	2
$f_e > f_n + 2$	0.16

### A. Problem description

MGs and distribution networks are often governed by low inertia synchronous generators, being the grid active power related to their rotating speed. In weak grids, the connection and disconnection of the different grid elements, as power generators and loads, may cause variations on the voltage magnitude and grid frequency. This problem is illustrated in Fig. 1, where the load power disturbance and the induced frequency drift is shown. This issue can be mitigated by using a solution capable of injecting power to the grid with a much faster dynamic response than the grid generators, thus compensating the power mismatch.

### B. Integration of the proposed solution in the MG

Fig. 1 shows the proposed solution integrated in an experimental isolated weak MG. The MG consists in a single node isolated 3-phase MG, governed by a distributed synchronous generator, feeding both passive and active loads. Such a generator operates in slack mode when the MG is disconnected from the utility grid, and presents a high output impedance ( $R_g$ ,  $L_g$ ) and low mechanical inertia. The synchronous generator is implemented by a permanent magnet synchronous generator (PMSG) mechanically coupled to a

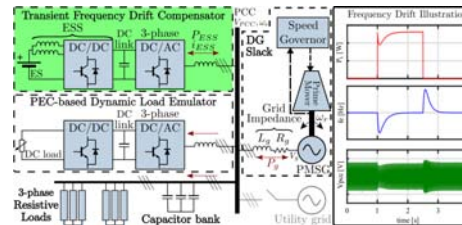


Fig. 1. Integration of the system under study in an isolated MG governed by a distributed synchronous generator operating in slack mode. The frequency drift contingency is illustrated on the right.

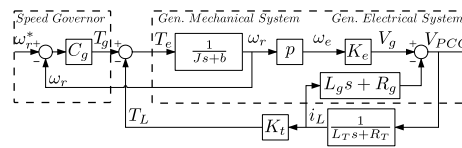


Fig. 2. Equivalent block diagram of a PM synchronous generator supplying constant-impedance type loads.

permanent magnet synchronous motor (PMSM), acting as a speed governor. In order to make the setup to be as close as possible to a generic MG, both passive load, consisting of 3-phase resistors, and tightly regulated dynamic loads operated in Constant Power Load (CPL) mode, are present in the MG. CPL are emulated by a grid tied AC/DC IGBT inverter coupled to a DC/DC converter that feeds a DC load.

The proposed compensating solution, highlighted in green, is integrated into a D-STATCOM, consisting of a 3-phase IGBT inverter coupled through a DC link to an ESS, and a bidirectional DC/DC boost IGBT converter in 2 branch interleaved configuration. The proposed topology is able to both inject or absorb active/reactive power, thus being able to assist the distributed generator during transients due to load disturbances, smoothing the frequency dynamic response. During steady state operation, the TFDC algorithm should be idle, being the stationary control out of the scope of this paper.

### C. Generator model

For high-performance frequency compensation, the system dynamics must be deeply analyzed. Moreover, the system dynamic modeling becomes mandatory when using observer-based techniques. Fig. 2 shows the equivalent system of a synchronous generator coupled to a speed governor.  $\omega_r$  is the rotor mechanical speed,  $C_g$  the governor controller,  $T_g$  the governor injected torque,  $J$  and  $b$  the generator inertia and friction coefficients,  $K_e$  and  $K_t$  the generator back EMF and torque constant and  $p$  the number of pole pairs. The electrical load is represented by the parameters  $R_T$  and  $L_T$ ,  $i_L$  is the load current and  $T_L$  is the equivalent load torque.  $R_g$  and  $L_g$  represent the grid impedance, in this case, the generator stator impedance.



This is the author's version of an article that has been published in this journal. Changes were made to this version by the publisher prior to publication.  
The final version of record is available at <http://dx.doi.org/10.1109/TSG.2017.2786085>

4

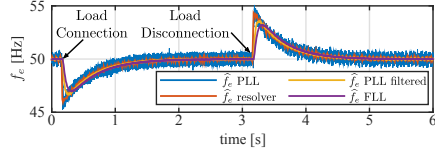


Fig. 4. Experimental results for the frequency drift measurement at the PCC under the connection and disconnection of a resistive load without compensation. The used setup is defined by Fig. 1 and Table II.

3) *Frequency control*: The main block of the control system consist in a feedback regulator able to provide a current or torque reference for the D-STATCOM ( $i_{ESS}^*$ ,  $T_{ESS}^*$ ), using the error between the frequency reference and the frequency estimation. Details for the feedback based control are given at section III-C.

4) *Load disturbance estimation*: When grid parameters are known or estimated, it is possible to generate a load estimation and use it as a feed-forward, either in terms of power, torque or current ( $T_{FF}$ ,  $I_{FF}$ ) to improve the dynamic response [8]. In this study, two options have been considered. One is based on the current measurement, developed at section III-D, and another relying on a Luenberger-based observer, considered at section IV.

5) *Estimated parameters*: The necessary information for the implementation of the load disturbance observer should be estimated either on-line or off-line. In the scope of this paper all the parameters will be known or obtained off-line.

### B. Transient detection

The transient detection issue has been already covered in previous literature by 1) using a transient detection window [3], and 2) an open loop estimator to extract the frequency reference considering a droop-controlled grid [28]. In the first case, a simple comparison of the feedback frequency and a threshold determines a transient window. However, delays, noise and harmonic distortion in the frequency estimator may lead to incorrect performance. In the second case, the open loop estimator leads to errors with any change in the estimator parameters. In this paper, a method based on the correlation of the measured frequency with a signal of period  $T$  and zero average is proposed (5).

$$C\omega_e(t) = \int_0^T x(t)f(t)dt \rightarrow C^2\omega_e(t) = \left( \int_0^T x(t)f(t)dt \right)^2 \quad (5)$$

where  $C\omega_e$  is the correlation result,  $x(t)$  is  $\omega_{em}$  and  $f(t)$  could be any function having zero average. For the sake of simplicity, a sine type function is used.

Assuming that the grid frequency reference will have a slow variation compared to the integration interval,  $T$ , the correlation function will give low values during the steady state. On the other hand, when a transient frequency drift occurs, it will lead to larger values. The resulting behavior is similar to the use of a derivative, but without the associated

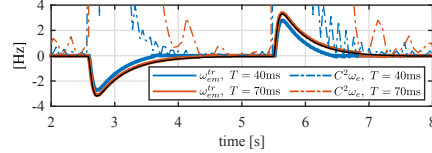


Fig. 5. Experimental results for the transient frequency estimation using the proposed method. Evaluation under connection and disconnection of a resistive load at the PCC without compensation. The setup is defined by Fig. 1 and Table II.

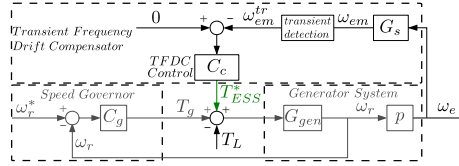


Fig. 6. Proposed controller for transient frequency drift compensation in the grid model block diagram. The speed governor and generator blocks match the system presented in Fig. 2. The torque provided by the TFDC is highlighted in green.

noise problems. Using the correlation squared value, (5), a transient window is generated and any frequency out of that window is considered to be the the grid frequency reference ( $\omega_e^*$ ). The last frequency value before the transient detection is considered as the estimated reference frequency ( $\hat{\omega}_e^*$ ). The transient detector output is the transient frequency ( $\omega_{em}^{tr}$ ), obtained as  $\omega_{em}^{tr} = \omega_{em} - \hat{\omega}_e^*$ .

The obtained experimental results for the estimated transient frequency are shown at Fig. 5. Two different  $T$  values are used for the estimation:  $T = 40\text{ms}$  and  $T = 70\text{ms}$ . The correlation value is scaled by 10 to simplify the representation. Threshold value is set to 5 and the FLL bandwidth is set to 5Hz. The results are compared with respect to the measured frequency, from which the reference value has been subtracted.

### C. Frequency feedback based control

The feedback based frequency control is shown in Fig. 6. The TFDC controller  $C_c$ , uses the estimated transient frequency ( $\omega_{em}^{tr}$ ), obtained from the frequency sensor and the transient detection block, to provide a control action by means of an equivalent torque command ( $T_{ESS}^*$ ).

Once the TFDC is included in the system, the disturbance rejection transfer function  $\frac{\omega_e}{T_L}$  is given by (6)

$$D_c(s) = \frac{\omega_e(s)}{T_L(s)} = -\frac{D_g(s)}{1 + D_g(s) \cdot C_c(s) \cdot G_s'(s)} \quad (6)$$

where  $G_s'(s) = G_s(s) \cdot p$ ,  $p$  is the number of pole pairs of the machine and  $G_s(s)$  the sensor transfer function.  $D_g(s)$  is the generator disturbance transfer function in (2). The obtained expression only applies during the transient, assuming the grid frequency reference has been already decoupled.

This is the author's version of an article that has been published in this journal. Changes were made to this version by the publisher prior to publication.  
The final version of record is available at <http://dx.doi.org/10.1109/TSG.2017.2786085>

5

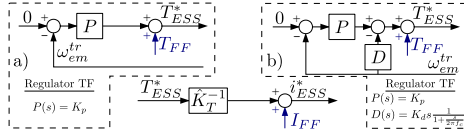


Fig. 7. Control structure for frequency drift compensation. a) Proportional (P) regulator; b) Pseudo-derivative feedback (PDF) structure. An optional load feed-forward can be applied either in terms of torque,  $T_{FF}$ , or current,  $I_{FF}$ .

Fig. 7 shows the general scheme for the frequency controller  $C_c$ , including the torque to current conversion. A feed-forward to improve the control is considered as an optional functionality ( $T_{FF}$ ,  $I_{FF}$ ).

It is worth noting that PI regulators are not considered in this study as the use of an integral action in the controller, even if it can improve the steady state disturbance rejection drastically, would also lead to the unavoidable share of power during steady state. P and PDF options will be analyzed. The two alternative transfer functions of the feedback frequency controller  $C_c(s)$  are defined by (7), P, and (8), PDF regulator, assuming the input as  $-\omega_{em}^{tr}$ .

$$C_c(s) = K_p \quad (7) \quad C_c(s) = K_p + K_d s \frac{2\pi f_c}{2\pi f_c + s} \quad (8)$$

Where  $K_p$  and  $K_d$  are the proportional and derivative gains of the compensator. These two gains are equivalent to the damping coefficient  $k_{pESS}$  and the virtual inertia gain  $J_{ESS}$  in (3) respectively. The variable  $f_c$  is the cut-off frequency of the low-pass filter associated to the derivative term.

The different alternatives are compared based on their dynamic stiffness, defined as (9).

$$S_c(s) = \frac{T_L(s)}{\omega_r(s)} = \frac{1 + D_g(s) \cdot C_c(s) \cdot G'_s(s)}{D_g(s)} \quad (9)$$

Fig. 8 shows the dynamic stiffness evaluated in frequency domain and the corresponding transient response in time domain for two different P and PDF settings. Two different proportional gains providing two different gain margins (GM) are used. In the case of the PDF, a minimum phase margin of  $60^\circ$  is set at the open-loop crossover frequency in both cases. The graph shows the benefits of an increased proportional gain and the improved disturbance rejection capability provided by the inclusion of the differential term. As shown in time domain, the predicted benefits for including the differential term are translated to a reduced initial overshoot when compared to the P method.

Finally, the experimental results for the feedback-based compensation are shown in Fig. 9. A good agreement with respect to the previous theoretical discussion can be observed.

#### D. Load feed-forward and state observation

Enhanced dynamic response for the transient frequency drift controller can be obtained by the use of feed-forward disturbance decoupling and the increase of the frequency estimation bandwidth by using a Luenberger type observer.

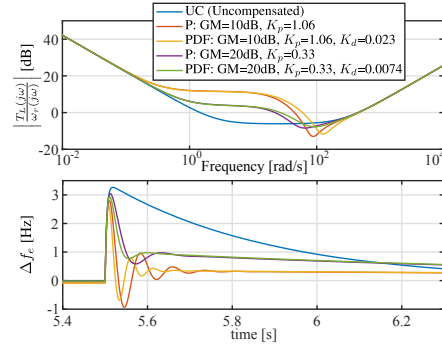


Fig. 8. Performance comparison of the P and PDF methods. Top: dynamic stiffness. Bottom: transient response.

If the load demand is available, it can be used as a feed-forward for the controller, as shown in Fig. 7. Ideally, if the load is fully known, the frequency drift will be eliminated (grey line in Fig. 9). However, that solution would lead to the compensation of the whole load power also during steady state. In order to compensate only the transient and keep the grid frequency unalterable, the ESS has to provide the difference between the load power and the power drawn by the generator, i.e. the equivalent torque of the compensation system should be  $T_{ESS} = T_L - T_g$ . Nevertheless, in a communication-less system, the generator information is not available. However, the load information is still a valuable information as it is a derivative state of the frequency, allowing to anticipate the control reaction.

Fig. 9 shows the experimental performance comparison for the different feedback methods, considering different configurations, and the response when a load feed-forward is used. The shown signals correspond to the DSOGI-FLL frequency signal using a FLL BW = 25Hz. UC stands for the uncompensated case. P+FF and PDF+FF are the combination of P and PDF with a load feed-forward respectively. The feed-forward is filtered by a  $2^{nd}$  order high-pass filter with bandwidth=0.5Hz. FC stands for the full load compensation obtained by equaling the D-STATCOM current reference to the load current. In this example, the load information comes from a load current sensor, which is a valid assumption if the proposed solution is to be coupled to a significant load.

#### IV. TRANSIENT FREQUENCY-DRIFT OBSERVER

The main purpose of the observer is to provide a transient frequency-drift estimation by providing a nearly zero phase-lag  $\omega_{em}^{tr}$  estimation within the observer bandwidth. This will boost the response of the TFDC, being able to compensate frequency drift transients usually affected by the PLL/FLL bandwidth restrictions. Additionally, the proposed observer also provides an estimation of the load disturbance that could be used for the feed-forward compensation replacing the  $T_{FF}$  measurement

This is the author's version of an article that has been published in this journal. Changes were made to this version by the publisher prior to publication.  
The final version of record is available at <http://dx.doi.org/10.1109/TSG.2017.2786085>

6

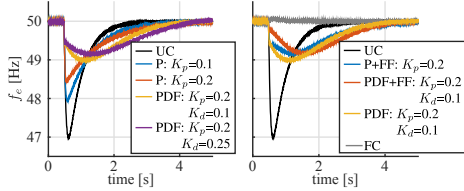


Fig. 9. Transient frequency drift compensation using different control methods under load connection transient. The setup is defined by Fig. 1 and Table II. Further details on the experimental setup are given at section V.

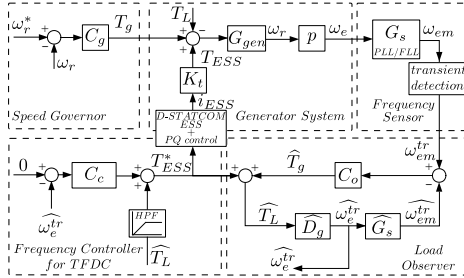


Fig. 10. Proposed observer control structure. The use of  $\hat{T}_L$  is optional.

by the estimated load  $\hat{T}_L$ . Although the paper proposes the use of such a load estimation,  $\hat{T}_L$ , it is not used or validated in this study, being part of future development. The proposed Luenberger-based observer control is shown in Fig. 10, where  $C_o$  represents the transfer function of the observer regulator. It is worth to point out that in the case the observer is not used,  $\omega_{em}^{tr}$  will be the feedback variable for the close loop frequency controller  $C_c$ .

As the generator and governor parameters are unknown, the  $C_g$  and  $G_{gen}$  transfer functions cannot be explicitly used in the proposed solution. However, the approximations proposed before for the sensor and the generator disturbance transfer functions (2), are appealing candidates for the observer implementation. The experimental comparison between the proposed approximations and the real systems are shown in Fig. 11. A really good matching is clearly observed. The observer is implemented using the state-space formulation corresponding to the model shown in Fig. 12. The model is defined by the state vector  $x = [x_1, x_2, x_3, x_4]^T$ , the input vector  $u = [T_L]$  and the output vector  $y = [\omega_e, \omega_{em}]^T = [p \cdot x_1, x_3]^T$ . The state, input, output and feed-forward matrices are defined in (10).

$$A = \begin{bmatrix} -2\xi_g\omega_{ng} & -\omega_{ng}^2 & 0 & 0 \\ 1 & 0 & 0 & 0 \\ 0 & 0 & 0 & 1 \\ k_s p \omega_{ns}^2 & 0 & -\omega_{ns}^2 & -2\xi_s\omega_{ns} \end{bmatrix}, B = \begin{bmatrix} k_g \omega_{ng}^2 \\ 0 \\ 0 \\ 0 \end{bmatrix}$$

$$C = \begin{bmatrix} p & 0 & 0 & 0 \\ 0 & 0 & 1 & 0 \end{bmatrix}, D = \begin{bmatrix} 0 \\ 0 \end{bmatrix} \quad (10)$$

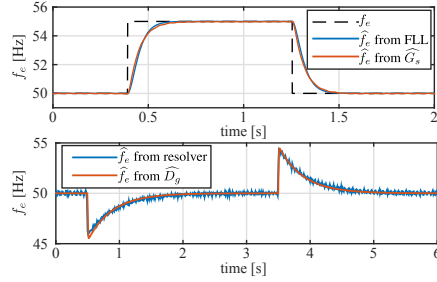


Fig. 11. Experimental results. Top: DSOGI-FLL response and its approximation using the 2<sup>nd</sup> order transfer function  $\hat{G}_s$ . Bottom: Open-loop response obtained with the estimation of the disturbance transfer function  $\hat{D}_g$  compared with the frequency measured by the generator resolver.

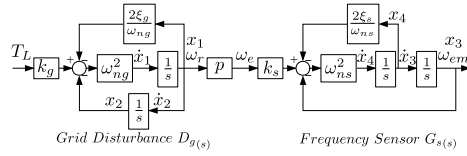


Fig. 12. Observer block diagram in state space form.

The dynamic stiffness for the proposed observer block diagram, assuming parameters matching between the real and the observed systems, is defined by (11).

$$\frac{T_L(s)}{\omega_e(s)} = \frac{1 + \hat{D}_g(s) \cdot C_o \cdot \hat{G}_s(s)}{1 + \hat{D}_g(s)(C_c(s) + C_o(s) \cdot \hat{G}_s(s))} \quad (11)$$

The observer controller,  $C_o(s)$ , consists in a 4<sup>th</sup> order transfer function, presenting the same order as the observed plant. It has been tuned in frequency domain using loop-shaping, trying to maximize the bandwidth while giving enough stability margin. The selected values are listed in Table II. The resulting frequency and transient responses comparing the proposed observer technique and the FLL feedback technique are shown in Fig. 13 and Fig. 14. The uncompensated and ideal sensor cases are shown as a reference. Ideal sensor case is defined as frequency feedback control with  $G_s(s) = 1$ , i.e., there is not phase lag introduced by the frequency estimation. As it can be seen, the use of the observer noticeably improves the initial transient response due to the compensated sensor lag. Moreover, in Fig. 14, the transient response of the design system (left  $\omega_{ns} = 31.4$  rad/s), is compared with the response when the bandwidth of frequency sensor is reduced by four (right  $\omega_{ns} = 7.85$  rad/s), without changing the observer regulator parameters. The proposed observer-based method still presents a better response than the alternatives.

## V. EXPERIMENTAL RESULTS

The proposed frequency-drift compensation have been experimentally evaluated. The experimental grid has been presented in Section II, Fig. 1, and the relevant parameters

This is the author's version of an article that has been published in this journal. Changes were made to this version by the publisher prior to publication.  
The final version of record is available at <http://dx.doi.org/10.1109/TSG.2017.2786085>

7

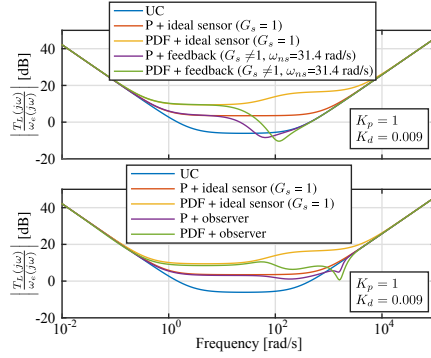


Fig. 13. Dynamic stiffness. Top: results for the feedback-based control. Bottom: observer-based control. The uncompensated and ideal sensor cases are shown as a reference.

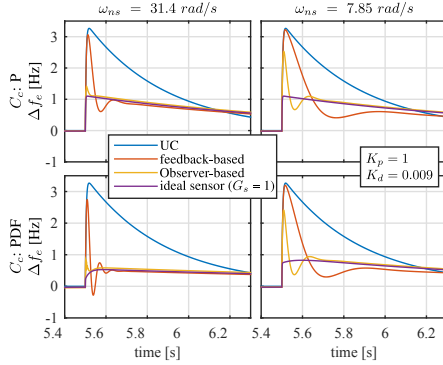


Fig. 14. Transient response comparison for different DSOGI-FLL bandwidth. Top: P controller. Bottom: PDF controller. Both cases are analyzed considering different feedback signals.

are given in Table II, including the P and PDF as well as the observer parameters used in the experimental tests. The equipment used to implement the experimental setup is shown in Fig. 15. The control system of the TFDC has been implemented in a TMS320F28335 DSC from Texas Instruments. The MG generator is emulated using 2 coupled PMSMs one acting as generator and other as the governor motor controlled by a commercial drive. The disturbances created by the different load types in the experimental MG, allow to test the effectiveness of the proposed observer-based compensator under a variety of conditions, enabling the comparison between the different existing methods which have been analyzed in this paper. It is worth noting that the grid frequency shown in the experimental results have been obtained using the speed resolver included in the industrial drive. The experimental results are obtained under two scenarios:

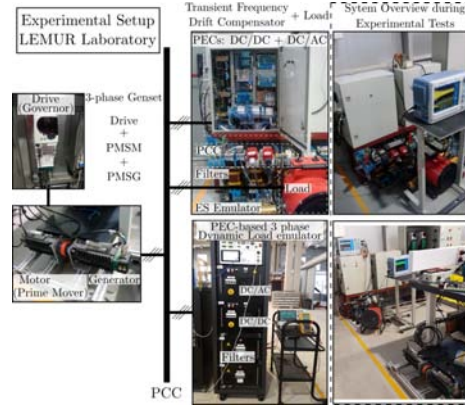


Fig. 15. Experimental prototype. Left: generator and drive used as the governor and the prime mover. Top center: TFDC and resistive load. Bottom center: dynamic load emulator based on PECs. Right: the setup during operation.

- 1) In the first scenario, the frequency variation for the evaluation of the TFDC is created by a load disturbance consisting in the connection and disconnection of a three-phase balanced resistive load. This test allows to characterized and compare the different methods evaluating the response under a step disturbance, avoiding to have unwanted disturbances in the middle of a transient.
- 2) In the second scenario, a more realistic load behavior is pursued. In this case, the load disturbance is a CPL generated by the PECs-based dynamic load emulator. This second scenario allows to demonstrate the advantages of the proposed observer and its viability in a realistic MG environment, where the PECs operation might be compromised by the transient frequency and voltage magnitude drifts.

A comparison of the transient response for the feedback and feed-forward methods is shown in Fig. 16 for the first scenario. The load feed-forward is implemented using the measured load current, applying a 1<sup>st</sup> order high-pass filter with a cut-off frequency of 0.5Hz. The performance of the proposed observer-based solutions for the first scenario is shown in Fig. 17 compared with the feedback methods. As expected, feed-forward and the proposed observer-based methods have the best performance in terms of frequency compensation. Assuming that feed-forward methods need for extra sensors or/and communication, the proposed observer methods, that just depend on the voltage measurements at the PCC, are a promising alternative, offering an extra compensation at the beginning of the transient, reducing the maximum frequency deviation. In this particular case, for the selected parameters, the proposed methods P+Obs and PDF+Obs reduce the maximum frequency deviation in around 1Hz when compared with P and PDF methods without observer, i.e., using  $\omega_{em}^{tr}$  instead

This is the author's version of an article that has been published in this journal. Changes were made to this version by the publisher prior to publication.  
The final version of record is available at <http://dx.doi.org/10.1109/TSG.2017.2786085>

8

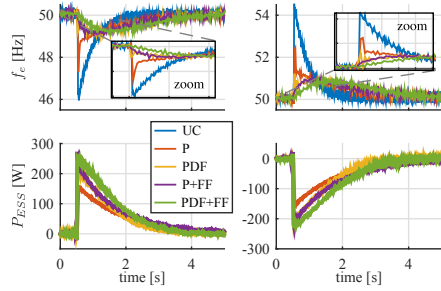


Fig. 16. Experimental results for the first scenario. Top: grid frequency obtained with the resolver. Bottom: power injected by the compensator. Left: load connection. Right: load disconnection.

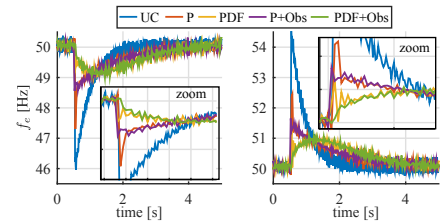


Fig. 17. Experimental results for the first scenario. Results using the proposed observer-based method. Grid frequency obtained with the resolver. Obs stands for observer-based compensation.

of  $\hat{\omega}_c^{dr}$ .

Although it has not been applied or tested in this paper, the observer provides an additional useful information. The observed load current, obtained from the estimation of  $\hat{T}_L$ , is represented in Fig. 18. As shown, the transient load disturbance can be estimated by a high-pass filter. This load estimation enables the implementation of a load feed-forward mechanism without the need for measuring the load current.

The results obtained for the second scenario using the PELs-based dynamic load emulator are shown in Fig. 19, for P and P+Obs methods, and in Fig. 21, for PDF and PDF+Obs. The frequency, the power drawn by the load emulator and the

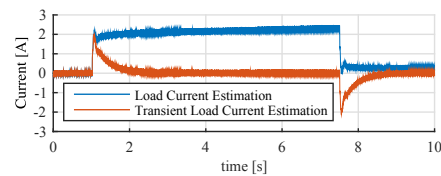


Fig. 18. Experimental results. Load current estimated by the observer. Full load current and transient load disturbance obtained by a  $1^{st}$  order high-pass filter with BW = 0.5Hz. The load current is 2.2A.

TABLE II  
SYSTEM PARAMETERS

MG Voltage ph-ph / $f_n$	98V <sub>rms</sub> / 50Hz
3-phase load	32 $\Omega$
BEMF / Torque constant / Poles	98V/krpm / 1.6Nm / 3 pairs
Mechanical parameters	$J = 0.0019\text{kg} \cdot \text{m}^2$ , $b = 0.2\text{Nm/s}$
Electrical parameters	$L_g = 6\text{mH}$ , $R_g = 2.1\Omega$
Power / ESS Voltage	20kW / 140V
DC link voltage / Capacitor	300V / 2mF
Grid connected AC filter	$R = 0.2\Omega$ , $L = 7.18\text{mH}$
DC/DC converter filter	$R = 0.1\Omega$ , $L = 7.18\text{mH}$
TFDC DC/DC Current control	BW=500Hz, $K_{pi}=22$ , $K_{ii}=13$
TFDC DC link Voltage control	BW=50Hz, $K_{pi}=1$ , $K_{ii}=175$
TFDC AC/DC Current control	BW=400Hz, $K_{pi}=22$ , $K_{ii}=50$
TFDC Control Gains	P: $K_p = 0.2$
Observer parameters	PDF: $K_p = 0.2$ , $K_d = 0.1$ $k_g = 0.78$ , $\omega_{ng} = 25.6$ , $\xi_g = 4.96$ $k_s = 1$ , $\omega_{ns} = 31.4$ , $\xi_s = 1$
Observer $C_o$ coefficients	$K_o = 10$ , zeros=[10, 10, 5, 3.4] $\cdot 10^{-3}$ poles=[20, 10, 10, 6.67] $\cdot 10^{-4}$
Dynamic Load Emulator	Current BW = 500Hz Power BW = 50Hz Current limit = 10A Nominal Power = 1kW

power injected by the TFDC are represented. It is clearly seen the improvement in the the frequency profile with all methods when compared with the uncompensated case. In order to better compared them, Fig. 20 and 22 show the detailed view of the critical transients in the system.

The conclusions drawn from the experimental results can be summarized as: 1) for all the cases, the observer-based methods provide a reduction on the maximum frequency deviation when compared with the FLL feedback methods; 2) The maximum deviation is reduced by more than 1Hz in the case of P+Obs when compared with P and 3) when differential action is added, the proposed PDF+Obs method improves the frequency drift by more than 0.5Hz when compared with the PDF. All this conclusions demonstrate the viability and superiority of the proposed methods for fast frequency drift compensation.

Finally, a last test was performed in order to evaluate the limits of the different compensation methods under significant load steps. Fig. 23 shows the response of the system under 3 load steps, for five cases: uncompensated, P, P+Obs, PDF and PDF+Obs. The figure does not only show the effect of load disturbances in the frequency but also in the voltage magnitude, which is affected due to the generator impedance and the coupling between its speed and voltage. As shown in Fig. 23, at  $t = 0.2\text{s}$ , a load step of 600W is applied. Under this load condition, the load emulator trips for the uncompensated scenario due to an overcurrent as a result of the voltage magnitude and frequency distortion. At  $t = 0.6\text{s}$ , a load step of 750W is commanded. For this load value, the emulator trips for the P method, while it continues its operation for the rest of the methods. At  $t = 1\text{s}$ , when a 1kW load is applied, the emulator trips for the P+Obs and PDF methods, being still responsive when PDF+Obs is used for the compensation. This demonstrates the extended range of operation allowed by the proposed observer-based methods for transient frequency drift compensation.

This is the author's version of an article that has been published in this journal. Changes were made to this version by the publisher prior to publication.  
The final version of record is available at <http://dx.doi.org/10.1109/TSG.2017.2786085>

9

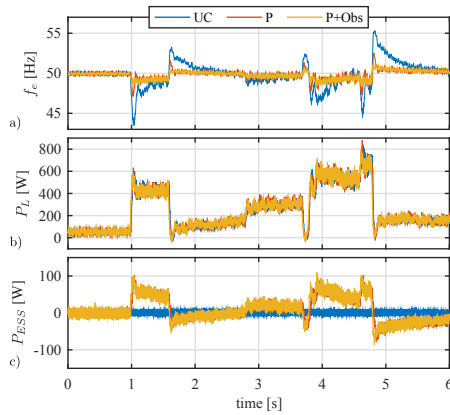


Fig. 19. Experimental results using the dynamic load emulator. a) grid frequency obtained with the drive resolver. b) load power consumption. c) active power injected by the compensator.  $P$  regulator and  $P + Obs$  are compared.

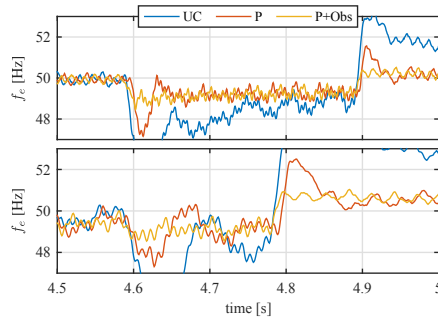


Fig. 20. Detailed view of the experiment in Fig. 19. Top: time zoom from  $t = 0.5s$  to  $t = 1.5s$ . Bottom: time zoom from  $t = 4.5s$  to  $t = 5s$ .

## VI. CONCLUSION

In this paper, a transient frequency drift compensation has been proposed based on the use of a nearly-zero lag transient frequency estimation using a Luenberger observer. The proposed solution addresses two of the main limitations of existing frequency compensation methods in the literature: the phase lag on the frequency estimation, and the transient detection for decoupling the grid reference frequency. The performance achieved by feedback control has been improved by the development of a transient observer, formed by a novel transient detection method, based on signal correlation that effectively decouples the grid reference frequency from the compensator inputs, and a Luenberger-based observer that provides a fast frequency estimation and allows to increase the phase margin in the frequency controller. Moreover, the de-

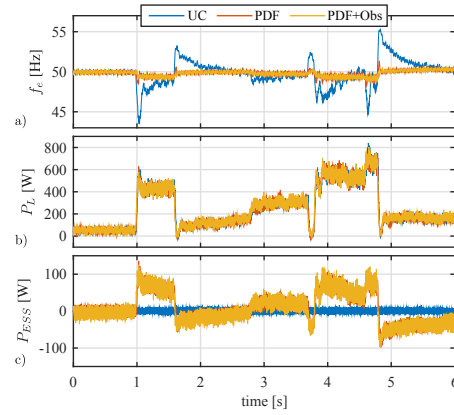


Fig. 21. Experimental results using the dynamic load emulator. a) grid frequency obtained with the drive resolver. b) load power consumption. c) active power injected by the compensator.  $PDF$  regulator and  $PDF + Obs$  are compared.

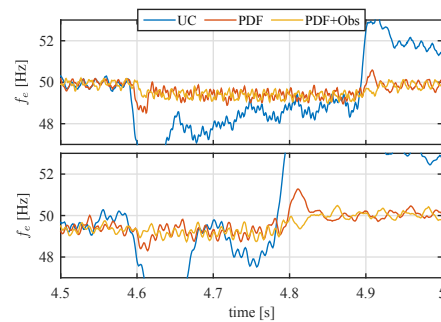


Fig. 22. Detailed view of the experiment in Fig. 21. Top: time zoom from  $t = 0.5s$  to  $t = 1.5s$ . Bottom: time zoom from  $t = 4.5s$  to  $t = 5s$ .

veloped observer structure allows to estimate the load torque, that can be employed as a feed-forward mechanism for the decoupling of the load disturbance. A detailed comparison, including analytical derivations, simulation and experimental results, have been carried out. The methods have been tested under two different scenarios considering passive and active loads based on resistors and PEC respectively. The analytical derivations, the simulation and the experimental results have demonstrated the effectiveness of the proposed observer-based TFDC. Additionally, it has been demonstrated that the proposed method allows for an extended range operation, withstanding higher disturbances and improving the system stability. The decoupling of the grid frequency reference makes the method suitable for the operation in weak grids under droop control. Finally, a comparative evaluation of

This is the author's version of an article that has been published in this journal. Changes were made to this version by the publisher prior to publication.  
The final version of record is available at <http://dx.doi.org/10.1109/TSG.2017.2786085>

10

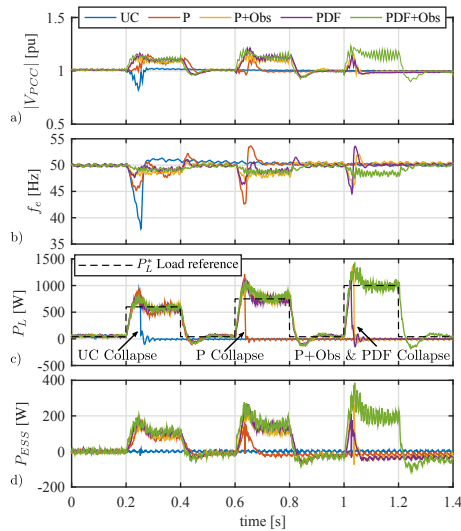


Fig. 23. Evaluation of the compensation methods under different load step disturbances introduced by the dynamic load emulator. a) Voltage magnitude at the PCC. b) Grid frequency obtained with the drive resolver. c) Load power consumption. d) Active power injected by the compensator.

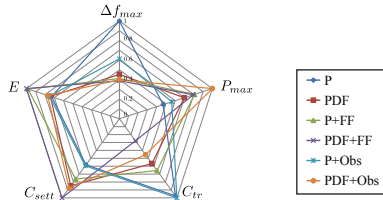


Fig. 24. Merit figure. Performance evaluation for all the considered methods.  $\Delta f_{max}$ : maximum frequency deviation,  $P_{max}$ : peak power  $E$ : total shared energy,  $C_{tr}$ : initial transient deviation,  $C_{sett}$ : settling time for transient frequency drift.

the analyzed techniques has been done, summarizing their performance in Fig. 24. Five indexes are considered. The indexes have been derived from the data obtained in the first scenario using a resistive load and are normalized in p.u., being all of them the higher the worst.

#### REFERENCES

- [1] J. M. Guerrero, "Editorial Special Issue on Power Electronics for Microgrids-Part II," *IEEE Transactions on Power Electronics*, vol. 26, no. 3, pp. 659–663, March 2011.
- [2] J. Guerrero, P. C. Loh, T.-L. Lee, and M. Chandorkar, "Advanced Control Architectures for Intelligent Microgrids-Part II: Power Quality, Energy Storage, and AC/DC Microgrids," *IEEE Transactions on Industrial Electronics*, vol. 60, no. 4, pp. 1263–1270, April 2013.
- [3] A. Agbedahunsi, M. Sumner, E. Christopher, A. Watson, A. Costabeber, and R. Parashar, "Frequency control improvement within a microgrid, using enhanced STATCOM with energy storage," in *6th IET International Conference on Power Electronics, Machines and Drives (PEMD 2012)*, March 2012, pp. 1–6.
- [4] A. Arulampalam, J. Ekanayake, and N. Jenkins, "Application study of a STATCOM with energy storage," *IEEE Proceedings on Generation, Transmission and Distribution*, vol. 150, no. 3, pp. 373–384, May 2003.
- [5] M. Falvo, L. Martirano, and D. Sbordone, "D-STATCOM with energy storage system for application in Smart Micro-Grids," in *2013 International Conference on Clean Electrical Power (ICCEP)*, June 2013, pp. 571–576.
- [6] M. Beza and M. Bongiorno, "Comparison of two control approaches for stability enhancement using STATCOM with active power injection capability," in *Energy Conversion Congress and Exposition (ECCE), 2015 IEEE*, Sept 2015, pp. 4721–4728.
- [7] M. Holmberg, M. Lahtinen, J. McDowall, and T. Larsson, "SVC Light with energy storage for frequency regulation," in *2010 IEEE Conference on Innovative Technologies for an Efficient and Reliable Electricity Supply (CITRES)*, Sept 2010, pp. 317–324.
- [8] I. Serban and C. Marinescu, "Control Strategy of Three-Phase Battery Energy Storage Systems for Frequency Support in Microgrids and with Uninterrupted Supply of Local Loads," *Power Electronics, IEEE Transactions on*, vol. 29, no. 9, pp. 5010–5020, Sept 2014.
- [9] H.-P. Beck and R. Hesse, "Virtual synchronous machine," in *Electrical Power Quality and Utilisation, 2007. EPQU 2007. 9th International Conference on*, Oct 2007, pp. 1–6.
- [10] Q.-C. Zhong and G. Weiss, "Synchronverters: Inverters That Mimic Synchronous Generators," *Industrial Electronics, IEEE Transactions on*, vol. 58, no. 4, pp. 1259–1267, April 2011.
- [11] M. Torres and L. Lopes, "Frequency control improvement in an autonomous power system: An application of virtual synchronous machines," in *Power Electronics and ECCE Asia (ICPE ECCE), 2011 IEEE 8th International Conference on*, May 2011, pp. 2188–2195.
- [12] Y. Hirase, O. Noro, K. Sugimoto, K. Sakimoto, Y. Shindo, and T. Ise, "Effects of suppressing frequency fluctuations by parallel operation of virtual synchronous generator in microgrids," in *Energy Conversion Congress and Exposition (ECCE), 2015 IEEE*, Sept 2015, pp. 3694–3701.
- [13] A. Navarro-Rodriguez, P. Garcia, R. Georgious, and J. Garcia, "A communication-less solution for transient frequency drift compensation on weak microgrids using a d-statcom with an energy storage system," in *2015 IEEE Energy Conversion Congress and Exposition (ECCE)*, Sept 2015, pp. 6904–6911.
- [14] M. Ayar, S. Obuz, R. Trevizan, A. Bretas, and H. Latchman, "A distributed control approach for enhancing smart grid transient stability and resilience," *IEEE Transactions on Smart Grid*, vol. PP, no. 99, pp. 1–1, 2017.
- [15] E. Hammad, A. Farraj, and D. Kundur, "On effective virtual inertia of storage-based distributed control for transient stability," *IEEE Transactions on Smart Grid*, vol. PP, no. 99, pp. 1–1, 2017.
- [16] S. D'Arco and J. A. Suul, "Equivalence of virtual synchronous machines and frequency-droops for converter-based microgrids," *IEEE Transactions on Smart Grid*, vol. 5, no. 1, pp. 394–395, Jan 2014.
- [17] S.-K. Chung, "A phase tracking system for three phase utility interface inverters," *IEEE Transactions on Power Electronics*, vol. 15, no. 3, pp. 431–438, May 2000.
- [18] P. Roncero-Sanchez, X. del Toro Garcia, A. Torres, and V. Feliu, "Fundamental Positive- and Negative-Sequence Estimator for Grid Synchronization Under Highly Disturbed Operating Conditions," *IEEE Transactions on Power Electronics*, vol. 28, no. 8, pp. 3733–3746, Aug 2013.
- [19] P. Rodriguez, A. Luna, M. Ciobotaru, R. Teodorescu, and F. Blaabjerg, "Advanced Grid Synchronization System for Power Converters under Unbalanced and Distorted Operating Conditions," in *32nd Annual Conference on IEEE Industrial Electronics, IECON 2006*, Nov 2006, pp. 5173–5178.
- [20] M. Torres L. L. Lopes, L. Moran T, and J. Espinoza C, "Self-Tuning Virtual Synchronous Machine: A Control Strategy for Energy Storage Systems to Support Dynamic Frequency Control," *Energy Conversion, IEEE Transactions on*, vol. 29, no. 4, pp. 833–840, Dec 2014.
- [21] L.-Y. Lu and C.-C. Chu, "Consensus-Based Secondary Frequency and Voltage Droop Control of Virtual Synchronous Generators for Isolated AC Micro-Grids," *Emerging and Selected Topics in Circuits and Systems, IEEE Journal on*, vol. 5, no. 3, pp. 443–455, Sept 2015.
- [22] J. Alipoor, Y. Miura, and T. Ise, "Distributed generation grid integration using virtual synchronous generator with adoptive virtual inertia," in

This is the author's version of an article that has been published in this journal. Changes were made to this version by the publisher prior to publication.  
The final version of record is available at <http://dx.doi.org/10.1109/TSG.2017.2786085>

11

*Energy Conversion Congress and Exposition (ECCE), 2013 IEEE*, Sept 2013, pp. 4546–4552.

- [23] S. Pulendran and J. E. Tate, "Energy storage system control for prevention of transient under-frequency load shedding," *IEEE Transactions on Smart Grid*, vol. 8, no. 2, pp. 927–936, March 2017.
- [24] J. Liu, Y. Miura, H. Bevrani, and T. Ise, "Enhanced virtual synchronous generator control for parallel inverters in microgrids," *IEEE Transactions on Smart Grid*, vol. 8, no. 5, pp. 2268–2277, Sept 2017.
- [25] D. Luenberger, "Observing the State of a Linear System," *IEEE Transactions on Military Electronics*, vol. 8, no. 2, pp. 74–80, April 1964.
- [26] "IEEE Standard for Interconnecting Distributed Resources with Electric Power Systems - Amendment 1," *IEEE Std 1547a-2014 (Amendment to IEEE Std 1547-2003)*, pp. 1–16, May 2014.
- [27] S.-K. Sul, *Control of Electric Machine Drive Systems*. Wiley IEEE press, 2011.
- [28] M. Torres L., "Dynamic frequency control in diesel-hybrid autonomous power systems using virtual synchronous machines," Ph.D. dissertation, Concordia University, Montreal, Quebec, Canada, May 2013.



**Ángel Navarro-Rodríguez** (S'15) received the B.Sc. degree in telecommunications engineering with honors from the University of Castilla La-Mancha, Spain in 2012 and the M.Sc. degree in Electrical Energy Conversion and Power Systems from the University of Oviedo, Gijón, Spain in 2014. Nowadays he is Ph.D student in the Department of Electrical, Computer, and Systems Engineering in the University of Oviedo, granted by the government of Principado de Asturias. He is part of the LEMUR research team in University of Oviedo since 2014

and his research interests include Energy Storage Systems, Control Systems, Electronics, Power Electronic Converters, Microgrids, power quality and Renewable Energies.



**Pablo García** (S01-A06-M09) received the M.S. and Ph.D. degrees in electrical engineering and control from the University of Oviedo, Gijón, Spain, in 2001 and 2006, respectively. In 2004, he was a Visitor Scholar at the University of Madison-Wisconsin, Madison, WI, USA, Electric Machines and Power Electronics Consortium. In 2013 he was a visiting scholar at The University of Nottingham, UK. He is the co-author of more than 20 IEEE journals and 50 international conferences. He is currently an Associate Professor within the Department of Electrical, Electronics, Computer, and Systems Engineering at the University of Oviedo. His research interests include control of grid-tied converters, parameter estimation, energy conversion, AC drives, sensorless control, AC machines diagnostics and signal processing.



**Ramy Georgious** (S'15) received the B.Sc. degree from Port Said University, Port Said, Egypt, in May 2010, in Electrical Engineering with average appreciation Excellent with honors degree. He received the M.Sc. degree from University of Oviedo, Gijón, Asturias, Spain, in June 2014, in Electrical Energy Conversion and Power Systems (EECPs). He worked as a teacher assistant in the Electrical Engineering department in Port Said University from March 2011 to September 2012. He joined LEMUR research team in University of Oviedo in July 2014.

He was granted by the government of Principado de Asturias to do his Ph.D. in the University of Oviedo. His research interests include Energy Storage Systems, Control Systems, Power Electronic Converters, Microgrids, Renewable Energy, Design and Simulation.



**Jorge García** (S'01-M'05-SM'11), received the M.Sc. and Ph.D. degrees in electrical engineering from the University of Oviedo, Asturias, Spain, in 2000 and 2003, respectively. In December 1999, he joined the Electrical and Electronic Engineering Department of the University of Oviedo, where he is currently an Associate Professor. He works with the LEMUR research team; his current research interests include power electronics and control for industrial, grid support and lighting applications. Dr. García is co-author of more than 40 journal papers and more than 80 international conference papers in power and industrial electronics. Dr. García was a recipient of the University of Oviedo Outstanding PhD. Thesis Award in 2005.



**Sarah Saeed** (S'16) Received B.Sc. degree in Electrical Engineering from the University of Ain Shams, Egypt, in 2013. She received her M.Sc. degree in Electrical Energy Conversion and Power Systems in 2015. She received the first prize for her master thesis awarded by the chair of Mobility in the University of Oviedo in 2016. She is currently working towards her PhD degree from the University of Oviedo as an investigator within LEMUR research group, and granted by the government of the Principado de Asturias. Her research interests

include: power electronic converters modeling and digital control, design and construction of DC/DC converter topologies, integration of energy storage systems in power electronic applications, and nonlinear magnetics.



## **C.2 Adaptive Active Power Sharing Techniques for DC and AC Voltage Control in a Hybrid DC/AC Microgrid**

Á. Navarro-Rodríguez, P. García, R. Georgious and J. García, "Adaptive Active Power Sharing Techniques for DC and AC Voltage Control in a Hybrid DC/AC Microgrid," in *IEEE Transactions on Industry Applications*, vol. 55, no. 2, pp. 1106-1116, March-April 2019. doi: 10.1109/TIA.2018.2873543



This is the author's version of an article that has been published in this journal. Changes were made to this version by the publisher prior to publication.  
The final version of record is available at <http://dx.doi.org/10.1109/TIA.2018.2873543>

# Adaptive Active Power Sharing Techniques for DC and AC Voltage Control in a Hybrid DC/AC Microgrid

Ángel Navarro-Rodríguez, Pablo García, Ramy Georgious and Jorge García  
Dept. of Electrical, Electronics, Systems & Computers Engineering  
University of Oviedo, LEMUR Group  
Gijón, 33204, Spain

Email: [navarroangel@uniovi.es](mailto:navarroangel@uniovi.es), [garciapablo@uniovi.es](mailto:garciapablo@uniovi.es), [georgiousramy@uniovi.es](mailto:georgiousramy@uniovi.es), [garciajorge@uniovi.es](mailto:garciajorge@uniovi.es)

**Abstract**—This paper deals with the AC and DC dynamic voltage control in a hybrid DC/AC Microgrid (MG) with central and distributed Battery Energy Storage Systems (BESSs), applying a power sharing mechanism between the different devices in the MG. The MG is composed by a multiport transformation center and two fixed frequency 3 phase AC Nanogrids (NGs) coupled to a DC bus through 3-phase Power Electronic Converters (PECs). The system pursues to minimize the dependence on the utility grid and the stress in the MGs central BESS, while increasing the power handling capability and the overall system stability during islanding condition. In order to approach the proposed aim, two main concerns are studied in this paper: an adaptive power sharing mechanism between the DC bus and the AC NGs for DC voltage control, and the design and implementation of an AC dynamic local voltage compensator based on Distributed Energy Storage System (DESS). The proposed techniques are validated through simulations and experimental results.

## I. INTRODUCTION

The increasing concern about environmental issues and the rising popularity of concepts as local generation and self-consumption have led to an increasing interest on alternatives to the conventional utility grid as Microgrids (MGs), Nanogrids (NGs) and Smart grids (SGs). Despite its advantages, the weakness and stability problems associated to MGs have been considered since its appearance, demanding significant research interests, specially regarding the power quality improvement [1], [2]. Furthermore, with the appearance of hybrid DC/AC MGs, where distributed energy resources (DERs) and loads may share/draw power in both the AC grid and the DC lines, new MG issues appears as the stability and grid quality in DC and AC [3], [4].

Several topologies for hybrid MGs have been proposed during the last years, classified by the interconnection with the mains and the connection between the DC and the AC

networks [5]. However, most of the examples in the literature are based on a direct connection with the mains in the AC grid and an interlinking converter between the DC and AC buses, being susceptible to contingencies in the mains [3], [4], [6], [7]. In contrast, the MG topology proposed in [8] and shown in Fig. 1, consist in a two-stage completely isolated topology with multiple AC Nanogrids (NGs) that allows to decouple the DC and AC buses from the utility grid through a MG head converter (MGHC). This reduces the impact of distributed generation (DG) in the mains and the sensitivity of the MG to contingencies in the utility grid, being the selected topology for this study. Moreover, the required modification to the already existing infrastructure is minimized, since there are no changes in the distribution system downstream of the transformation center.

Regarding the control system, several control schemes (central controller, master-slave, droop-based control, hybrid approaches ...) are found in the literature to ensure the voltage/frequency control and power sharing in AC distribution networks [6], [9]–[11], and DC grids [12], [13]. In the particular application of hybrid MGs, some control solutions have been proposed [14]. However, most of them are based on a DC/AC interlinking converter operated in grid following mode [3], [4], [6], [7].

Conversely, the topology in [8] is based on DC/AC 3-phase 2-level interlinking converters operated in grid forming mode (slack mode). Compared to droop control strategies, grid forming control methods based on master-slave or multi-slack grid control, with fixed frequency, can simplify the MG design with high presence of DERs interfaced by power electronic converters (PECs), and renewable sources operated under maximum power point tracking (MPPT) [12], [13], [15].

This tight regulation in the interlinking converters, hereinafter referred to as Nanogrid head converters (NGHCs) [8], allows for decoupling the AC from the DC bus dynamics, thus, the NGs behave as CPLs for the LVDC. Counter-intuitive, this might become an issue if the LVDC present a low inertia, for instance during *islanding mode* or under low DC bus capacitance. Therefore, the solution to avoid critical dynamic

The present work has been partially supported by the predoctoral grants program Severo Ochoa for the formation in research and university teaching of Principado de Asturias PCTI-FICYT under the grant ID BP14-135. This work also was supported in part by the Research, Technological Development and Innovation Program Oriented to the Society Challenges of the Spanish Ministry of Economy and Competitiveness under grant ENE2016-77919-R and by the European Union through ERFD Structural Funds (FEDER).

and stability issues relies on making the NGHCs participate on the regulation of the LVDC, involving a dynamic power sharing between DC and AC buses. However, the dynamic power sharing between DC and AC buses in a hybrid MG when the coupling converters are operated in slack mode, is not yet exploited. In [16], an study on cascaded converters stability is carried out, presenting an analogous problem. A power balancing mechanism between AC and DC using a  $V_g/V_{dc}$  droop is also proposed in [17]. However, the first method is related to a pure DC MG while the second is implemented in AC/DC/AC grid tied converters operated in droop-based grid feeding. The aim of the present study is to implement a dynamic sharing mechanism to the MG under study.

Concerning the dynamic voltage control and active power sharing in AC grids, many studies can be found in the literature based on the variation of the frequency with the active power ( $P/f$ ), being the stiffness determined by the system inertia [18]–[22]. However, when the fixed frequency approach is used instead, active power variations will affect mainly the voltage magnitude ( $P/V$ ) being the grid inertia dependent on the grid equivalent capacitance as in DC grids [23]. In addition, the high presence of PECs, that reduces the system inertia, and the challenges imposed by the high presence of constant power loads (CPLs) [16], make the grid prone to stability and dynamic response issues. The concepts of Quadratic Voltage Control (QVC) and virtual capacitance, studied in [23], seems to be a promising solution to this problems applicable in both DC and AC.

In summary, this paper deals with the AC and DC voltage control in a hybrid DC/AC MG considering central and distributed Battery Energy Storage Systems (BESSs), which topology is based on the MG presented in [8]. A power sharing mechanism between the AC NGs and the DC bus is proposed. The system will have as main constraints the reduced dependency on the utility grid (mains), the islanded operation and the optimization of the ESS usage. The main contributions are related with the two main concerns that are studied: 1) the design of an adaptive method for the dynamic power sharing between the DC bus and the AC NGs for an enhanced DC voltage control, improving the overall MG performance; and 2) the implementation of an AC voltage compensator for the NG-based distribution system. The compensation will rely on the use of virtual capacitor for an improved system stiffness.

This paper follows the study presented in [24]. The changes incorporated respect to the conference paper are the improvement of the adaptive power sharing algorithm and the experimental verification of the proposed methods. The paper is organized as follows. Section II introduces the hybrid DC/AC Microgrid topology under study. Section III explains the basics of the proposed voltage control loops in DC and AC systems. Section IV covers the proposed adaptive voltage control in the hybrid DC/AC MG. Section V presents the simulation and experimental results. Section VI contains the dynamic characterization of the system through the frequency response

analysis. Finally, section VII states the conclusions.

## II. SYSTEM DESCRIPTION AND ANALYSIS

The hybrid MG under study, shown in Fig. 1, is based on the topology presented in [8], and is composed by a MG transformation center (MGTC) and two 3-phase AC NGs based on fixed frequency Master-Slave topology. The MGTC consists of a central BESS (battery + DC/DC converter) and a connection to the mains interconnected by a common Low Voltage DC bus (LVDC) to two NG Head Converters (NGHCs) feeding the AC NGs. The BESS and the mains are interfaced with the LVDC by a three-port solid-state transformer (SST). Likewise, the mains are interfaced with the SST by means of an AC/DC MG head converter (MGHC). It is worth to point out that the SST operation is out of the scope of this paper, considering it as an ideal connection that provides galvanic isolation. The MG is designed as follows. The NGHC acts as a slack, both for the AC voltage magnitude and frequency. The MGs loads, constant power loads (CPLs) and Constant Impedance Loads (CILs), are only located at the 3 phase NGs. Under this configuration, the load as seen by the LVDC is drawn by the NGHCs. Additionally, different distributed resources such as Distributed Generation (DG) and ESSs can be installed at NG level. A central controller governs the MGTC and low bandwidth communications are considered in the NGs between the DGs, ESSs and NGHCs. The central BESS and the MGHC connected to the mains are operated in power control mode, receiving commands from the central controller.

Power mismatches in conventional grids are absorbed by the high inertia of generators. However, in the case under study, they have to be supported by the energy storage elements, including capacitances, installed at the MG. As a first approach, DGs and DESS in the NG will operate with constant PQ commands while the slack NGHCs will absorb the power transients, controlling the voltage magnitude and frequency. Additionally a local dynamic voltage compensator able to share active power might be considered in the NGs ( $P_{vc}$ ). Depending on the MG being connected/disconnected to the main grid, two modes of operation are defined: 1) During *non-islanding* operation, the mains  $P_{mains}$  and the BESS  $P_{BESS}$  can share the effort; 2) During *islanding*, the MG is disconnected from the utility grid and only the BESS is available as a power source in the transformation center.

In any case, the voltage in DC and AC NGs should remain under control within regulation limits. Additionally, two constraints are established: 1) The dependence on the utility grid should be minimized; 2) The BESS limitations (bandwidth, available power, State of Charge (SoC)) have to be considered in the power sharing. This paper is focused on the operation during *islanding* mode.

Although the DGs in the NG could be used to provide ancillary services, most of DERs in the NG either present a low response or should be operated in Maximum Power Point Tracking (MPPT). However, DESSs in the NG can be used, providing local compensation while reducing the conduction

This is the author's version of an article that has been published in this journal. Changes were made to this version by the publisher prior to publication.  
The final version of record is available at <http://dx.doi.org/10.1109/TIA.2018.2873543>

$$\frac{d}{dt} \begin{bmatrix} i_{i^k d} \\ v_{g^k d} \\ i_{i^k q} \\ v_{g^k q} \end{bmatrix} = \begin{bmatrix} -\frac{R_k}{L_k} & \frac{1}{L_k} & 0 & 0 \\ \frac{1}{C_k} & 0 & 0 & 0 \\ 0 & 0 & -\frac{R_k}{L_k} & \frac{1}{L_k} \\ 0 & 0 & \frac{1}{C_k} & 0 \end{bmatrix} \begin{bmatrix} i_{i^k d} \\ v_{g^k d} \\ i_{i^k q} \\ v_{g^k q} \end{bmatrix} + \begin{bmatrix} \omega_{e^k} & 0 & 0 & 0 \\ 0 & \omega_{e^k} & 0 & 0 \\ 0 & 0 & -\omega_{e^k} & 0 \\ 0 & 0 & 0 & -\omega_{e^k} \end{bmatrix} \begin{bmatrix} i_{i^k d} \\ v_{g^k d} \\ i_{i^k q} \\ v_{g^k q} \end{bmatrix} + \begin{bmatrix} \frac{1}{L_k} & 0 & 0 & 0 \\ 0 & -\frac{1}{C_k} & 0 & 0 \\ 0 & 0 & \frac{1}{L_k} & 0 \\ 0 & 0 & 0 & -\frac{1}{C_k} \end{bmatrix} \begin{bmatrix} v_{g^k d} \\ i_{g^k d} \\ v_{g^k q} \\ i_{g^k q} \end{bmatrix} \quad (1)$$

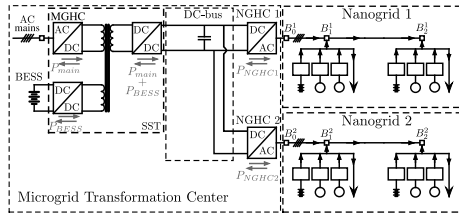


Fig. 1. Topology of the Hybrid DC/AC Microgrid under study.

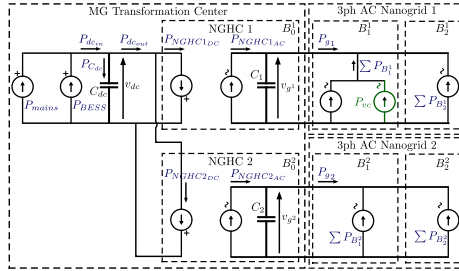


Fig. 2. Simplified power sharing scheme within the Hybrid DC/AC MG.

losses. As a first approach, in this study one local ESSs will be used for transient compensation located at the first node of NG1 ( $B_1^1$ ). Fig. 2 shows a simplified scheme of the MG illustrating the different elements participating on the power sharing, where  $\sum P_{B_j^k}$  ( $k$  denotes the NG, while  $j$  the node) is the total power share between DGs, DESS and active power loads within a node,  $\sum P_{B_j^k} = \sum (P_{DG_j^k} + P_{DESS_j^k} - P_{L_j^k})$ .

The system model for the voltage control, both in AC and DC, is simplified to a capacitor, neglecting line impedances and approximating the current control loops of the PECs to a low-pass filter. 3-phase balanced AC NGs are assumed.

The modeling of the system under study will be based on the simplified power scheme for one of the NGHCs shown in Fig. 3. Thus, the AC system modeled in  $dq$  synchronous reference frame is defined by (1), where  $k$  is the NG identifier,  $v_{g^k}$  is the NG voltage at node  $B_0^k$ ,  $i_{g^k}$  is the current drawn by the NGHCs into the NGs (i.e. the control action of NGHCs),  $\omega_{e^k}$  is the grid frequency and  $i_{g^k}$  is the total current drawn by the buses  $B_1^k$  and  $B_2^k$ , i.e., the system disturbance.

The DC link can be modeled in terms of active power as (2),

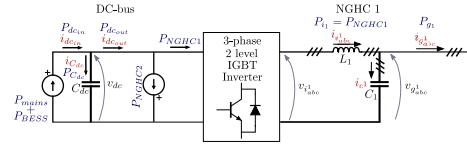


Fig. 3. Simplified equivalent power scheme of one of the NGHCs.

where  $C_{dc}$  is the LVDC capacitor,  $P_{dcin}$  is the power shared by the main and the central BESS, and  $P_{dcout}$  is the power drawn by the NGHCs ( $P_{dcout} = P_{NGHC_1}(t) + P_{NGHC_2}(t)$ ), being defined by (3) and (4), assuming  $v_{g_0} = 0$ . Thus, the NGHCs are seen as CPLs by the DC link. The power flowing into the capacitor is defined as  $P_{C_{dc}} = P_{dcin} - P_{dcout}$ .

$$\frac{dv_{dc}(t)}{dt} = \frac{1}{C_{dc}v_{dc}(t)} \left( P_{dcin}(t) - \underbrace{(P_{NGHC_1}(t) + P_{NGHC_2}(t))}_{P_{dcout}} \right) \quad (2)$$

$$P_{dcout}(t) = \sum_{k=1}^2 P_{NGHC_k}(t) \quad (3)$$

$$P_{NGHC_k}(t) = \frac{3}{2} \left( v_{g_d^k}(t) i_{g_d^k}(t) + v_{g_q^k}(t) i_{g_q^k}(t) \right) \quad (4)$$

### III. VOLTAGE CONTROL: CONTROLLER DESIGN

The MGTC control will involve the dynamic control of both DC link and AC NGs voltages. The closed loop voltage controllers, both in AC and DC, will be based on a feedback PI regulator, implemented in  $dq$  synchronous reference frame in the case of the AC NGs. Two alternatives for the basic voltage control are considered in this paper, following the analysis and discussion proposed in [23]. Fig. 4 shows the generic representation of those alternatives for DC voltage control (or each of the axis of the  $dq$  synchronous reference frame voltage control), where  $i_{L(t)}$ ,  $p_{L(t)}$  and  $g_{L(t)}$  are the time dependent disturbances drawn by constant current loads (CCLs), constant power loads (CPLs) and constant impedance loads (CILs) respectively. It is necessary to point out that  $g_{L(t)}$  is the conductance that represents the inverse of the real part of a CIL. According to this, the system plant is defined by (5), being a non-linear system.

$$\frac{dv(t)}{dt} = \frac{1}{C} \left( i(t) - \underbrace{\left( i_{L(t)} + \frac{p_{L(t)}}{v(t)} + g_{L(t)}v(t) \right)}_{Disturbance} \right) \quad (5)$$

This is the author's version of an article that has been published in this journal. Changes were made to this version by the publisher prior to publication.  
The final version of record is available at <http://dx.doi.org/10.1109/TIA.2018.2873543>

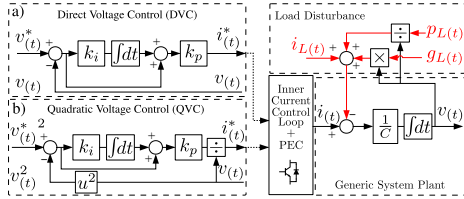


Fig. 4. Voltage control schemes, based on cascaded control. a) Direct Voltage Control (DVC), b) Quadratic Voltage Control (QVC).

Pursuant to this expression, the conventional voltage control, referred in [23] as Direct Voltage Control (DVC), will present a non linear behavior under the presence of CGLs and CPLs. Alternatively, Quadratic Voltage Control (QVC) can be used instead. Although it has been proposed before in the literature referred as energy based controller, its applications has been limited to the DC link control of DC/AC converters [25], [26]. Nonetheless, its application can be generalized to any cascade-based voltage control as slack converters in both DC and AC MGs. It is worth to point out that this assumption is valid provided that the inner power and current control loops, including the converter and current filter, behave as an ideal  $2^{nd}$  order low-pass filter with a much higher bandwidth than the outer voltage control loop. The details for its implementation in AC are given later in this section. The QVC generic expression is defined in (6).

$$P_{(t)}^* = k_p \left( (v_{(t)}^*)^2 - v_{(t)}^2 \right) + k_i \int (v_{(t)}^*)^2 - v_{(t)}^2 dt \quad (6)$$

Where  $k_p$  and  $k_i$  are the ideal PI regulator gains.

Despite the fact that the QVC also presents a non-linear relation between the voltage and the load disturbance, the relation between the square voltage and the CPLs is linear considering the system plant in (7), where  $P^*$  is the control action and  $P_{C(t)}$  is the power flowing into the capacitor.

$$v_{(t)} \frac{dv_{(t)}}{dt} = \frac{1}{C} P_{C(t)} \Rightarrow \frac{dv_{(t)}^2}{dt} = \frac{2}{C} P_{C(t)} \quad (7)$$

The main feature of the voltage control for the application presented in this paper is the disturbance rejection capability. In order to analyze how the disturbance rejection of each method is affected by the type of load, their disturbance to output transfer functions were obtained and analyzed in [23]. The expressions for the DVC are shown in (8), (9) and (10).

$$\frac{\Delta V_{(s)}}{\Delta I_{L(s)}} \approx \frac{-sV_0^2}{s^2V_0^2C + s(k_pV_0^2 - P_{L0} + G_{L0}V_0^2) + k_ik_pV_0^2} \quad (8)$$

$$\frac{\Delta V_{(s)}}{\Delta P_{L(s)}} \approx \frac{-sV_0}{s^2V_0^2C + s(k_pV_0^2 - P_{L0} + G_{L0}V_0^2) + k_ik_pV_0^2} \quad (9)$$

$$\frac{\Delta V_{(s)}}{\Delta G_{L(s)}} \approx \frac{-sV_0^3}{s^2V_0^2C + s(k_pV_0^2 - P_{L0} + G_{L0}V_0^2) + k_ik_pV_0^2} \quad (10)$$

Where  $V_0$ ,  $P_{L0}$  and  $G_{L0}$  are the voltage magnitude, the CPL level, and the CIL level at the equilibrium point respectively.

The expressions for the QVC are stated in (11), (12) and (13), where  $I_{L0}$  is the CCL level at the equilibrium point.

$$\frac{\Delta V_{(s)}}{\Delta I_{L(s)}} \approx \frac{-sV_0}{s^2V_0C + s(2k_pV_0 + I_{L0} + 2G_{L0}V_0^2) + 2k_ik_pV_0^2} \quad (11)$$

$$\frac{\Delta V_{(s)}}{\Delta P_{L(s)}} \approx \frac{-s}{s^2V_0C + s(2k_pV_0 + I_{L0} + 2G_{L0}V_0^2) + 2k_ik_pV_0^2} \quad (12)$$

$$\frac{\Delta V_{(s)}}{\Delta G_{L(s)}} \approx \frac{-sV_0^2}{s^2V_0C + s(2k_pV_0 + I_{L0} + G_{L0}V_0^2) + 2k_ik_pV_0^2} \quad (13)$$

These expressions demonstrate a clear dependence of the disturbance to output transfer functions on the CPL, CIL and CCL levels in both the DVC and QVC. However, the DVC presents a critical negative dependency on CPL level,  $P_{L0}$ , for any kind of load disturbance, which can compromise the system stability. On the contrary, the QVC eliminates the dependency on CPL level. Fig. 5 shows an example of system response comparing the DVC and QVC under the same conditions, for different CPL levels at the equilibrium point  $P_{L0}$ , assuming  $I_{L0} = 0$  A and  $G_{L0} = 0 \Omega^{-1}$ . As shown, the DVC response is worsen as  $P_{L0}$  increases, decreasing its gain margin, tending to instability, while the QVC response remains constant.

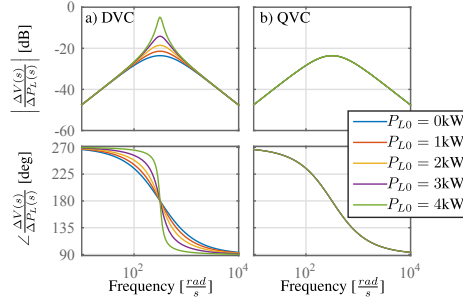


Fig. 5. Bode diagram of the CPL disturbance to output transfer function  $\frac{\Delta V_{(s)}}{\Delta P_{L(s)}}$  for different values of  $P_{L0}$ , assuming  $I_{L0} = 0$  A and  $G_{L0} = 0 \Omega^{-1}$ . a) DVC response, b) QVC response. The parameters for both are:  $V_0 = 300$  V,  $C = 1$ ,  $\omega_n = 2\pi 50 \frac{rad}{s}$ .

Further analysis and comparison of DVC and QVC are provided in [23]. Due to the high presence of PECs, CPLs and constant power generation expected in the grid under analysis,

This is the author's version of an article that has been published in this journal. Changes were made to this version by the publisher prior to publication.  
The final version of record is available at <http://dx.doi.org/10.1109/TIA.2018.2873543>

a control based on the QVC is proposed for the application presented in this paper.

In order to tune the voltage regulator, a tuning method based on the linearized reference tracking transfer function is used. Applying linearization, the close loop system defined by (6) and (7) can be approximated as (14), where  $V_0^*$  and  $V_0$  are the voltage reference and the voltage in the equilibrium point respectively. Considering operation near the equilibrium point and  $V_0^* = V_0$ , (14) can be approximated by a second order system with a determined natural frequency  $\omega_n$  and a damping factor  $\zeta$  as (15). Thus, the PI regulator parameters of QVC are tuned according to (16). The units of  $k_p$  and  $k_i$  are  $[\Omega^{-1}]$  and  $[s^{-1}]$  respectively, behaving the PI as an admittance. The natural frequency  $\omega_n$ , should be selected according to the cascaded control premises, while the damping factor,  $\zeta$ , can be selected as a trade-off between overshoot and settling time.

$$\frac{V(s)}{V_0^*} \approx \frac{s2k_pV_0^* + 2k_pk_iV_0^*}{s^2CV_0 + s2k_pV_0 + 2k_pk_iV_0} \quad (14)$$

$$\frac{V(s)}{V_0^*} \approx \frac{2\zeta\omega_n s + \omega_n^2}{s^2 + 2\zeta\omega_n s + \omega_n^2} \quad (15)$$

$$k_p = \zeta\omega_n C; \quad k_i = \frac{\omega_n^2 C}{2k_p} \quad (16)$$

#### A. QVC applied to the LVDC voltage control

The described QVC scheme can be applied directly as shown in 4(b), considering the control action of the PI regulator as the active power reference required by the DC bus capacitor. The specific basic DC bus voltage control is shown in Fig. 6.

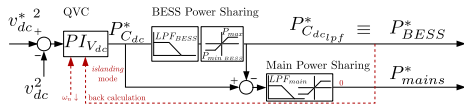


Fig. 6. DC bus slack controller based on Quadratic Voltage Control. *islanding mode* modifications highlighted in red.

As specified before, during *non-islanding* both the BESS and the main grid participate in the control. To reduce the dependence on the main grid, the BESS provides the low bandwidth variations, within its power limitations, while the main contribute with the high bandwidth transients unless the battery power is limited for any reason, in which case the main will participate also in the steady state. In the case of *islanding*, the battery would be the only available power source to maintain the regulation of the DC link. In that case, to maintain the proper operation of the voltage regulator, either a back calculation or a reduction on the control bandwidth,  $\omega_n$ , should be applied to fulfill the cascaded control requirements.

#### B. QVC applied to the 3-phase AC voltage control

The QVC can be applied to the 3-phase AC control considering the following assumptions:

- If the control is implemented in the  $dq$  synchronous reference frame, and assuming the system plant (3-phase capacitor) is balanced and decoupled cross-coupling terms in the control scheme, voltage control loop can be defined by two independent DC systems one for  $d$ -axis and another for the  $q$ -axis.
- The scaling factor of the  $dq$  reference frame,  $\frac{3}{2}$  in the case of using magnitude conservative transformation, should be considered.
- The active power is calculated as a sum of a  $d$ -axis power component,  $P_d$ , and  $q$ -axis power component  $P_q$ , according to the general expression in (17), considering the term  $P_q \ll P_d$ .

$$P(t) = \underbrace{\frac{3}{2}v_d(t)i_d(t)}_{P_d} + \underbrace{\frac{3}{2}v_q(t)i_q(t)}_{P_q} \quad (17)$$

Under these assumptions, the differential equation for the plant can be simplified as (18).

$$\frac{dv_{g_x^k}(t)}{dt} = \frac{1}{C_k} \left( i_{i_x^k}(t) - \underbrace{\left( i_{L_x^k}(t) + \frac{2}{3}P_{L_x^k}(t) + g_{L_x^k}(t)v_{g_x^k}(t) \right)}_{\text{Disturbance } i_{g_x^k}} \right) \quad (18)$$

Where  $x$  indicates the reference frame  $d$ -axis or  $q$ -axis. Under a balanced load  $g_{L_x^k}$  is assumed to be the same in the  $d$ -axis and  $q$ -axis.

The PI expression for the QVC in (6) is also modified by (19) for the AC  $dq$  implementation.

$$\frac{2}{3}P_x^*(t) = k_p \left( v_{x(t)}^{*2} - v_{x(t)}^2 \right) + k_i \int \left( v_{x(t)}^{*2} - v_{x(t)}^2 \right) dt \quad (19)$$

The PI parameters  $k_p$  and  $k_i$  are tuned as in the DC application (16). It is worth noting that under the described assumptions, the expressions (8)-(13) are also valid for each of the  $dq$  axis substituting  $P_{L0}$  by  $\frac{2}{3}P_{L0}$  and  $\Delta P_L$  by  $\frac{2}{3}\Delta P_L$ .

Considering all the above, a voltage control in the  $dq$  reference frame is proposed based on QVC and fixed frequency. The complete cascaded control scheme for a 3-phase AC slack converter is shown in Fig. 7. A grid current decoupling term could be added in order to improve the disturbance rejection, drawn in green color. However, an improved disturbance rejection could increase the stress in the DC side for the proposed MG topology, which is translated in an increased stress in the BESS during an *islanding* scenario.

#### IV. HYBRID DC/AC VOLTAGE CONTROL

The proposed hybrid MG should maintain the power quality and reliability in both the LVDC bus and the AC NGs. This paper deals with the specific task of managing the dynamic



This is the author's version of an article that has been published in this journal. Changes were made to this version by the publisher prior to publication.  
The final version of record is available at <http://dx.doi.org/10.1109/TIA.2018.2873543>

to the LVDC voltage. The method, defined by equation (24), is based on the squared correlation of the measured LVDC voltage ( $v_{dc}$ ), with a signal of period  $T$  and zero average ( $\sin(\frac{2\pi t}{T})$ ).

$$C_t(t) = \left( \frac{1}{T} \int_0^T v_{dc}(t) \sin\left(\frac{2\pi t}{T}\right) dt \right)^2 \quad (24)$$

Where  $C_t$  is the correlation result used as trigger. The correlation function will give low values during the steady state, while it will lead to significantly larger values during transients. When compared with a configurable threshold, the transient window will be defined by an initial time,  $t_1$ , and a final time,  $t_2$ . The purpose of the transient detector is to determine the instants  $t_1$  and  $t_2$  that will be used in the sharing coefficient calculation (25).

2) *Local coefficient calculation*: The sharing coefficient  $\sigma_k$  is calculated after the instant  $t_2$  using the RMS value of the p.u. AC voltage magnitude deviation in the NGHC PCC ( $B_k^i$ ) of each NG, in the interval  $t_1$ - $t_2$ , where  $t_1$  and  $t_2$  are determined by the transient detector. Firstly, the RMS value  $\Delta v_{g_{RMS}}^k$  is obtained as (25), where  $n$  refers to the actual iteration of the described algorithm. Secondly, the RMS value is saturated,  $\Delta v_{g_{RMS}}^{sat}$ , as (26), where  $\delta_{max}$  is a tunable parameter that represents the maximum expected RMS value. Then, the sharing coefficient  $\sigma_k$  is obtained as (27), where  $\lambda_g$  is a configurable weighting factor, limited between 0 and 1, and  $\eta_m$  is a filtering factor that provides the algorithm with memory. Thus, if  $\eta_m < 1$ , the previous values of  $\Delta v_{g_{RMS}}^{sat}$  will be necessary for the sharing coefficient calculation.

$$\Delta v_{g_{RMS}}^k[n] = \sqrt{\frac{1}{t_2[n] - t_1[n]} \int_{t_1[n]}^{t_2[n]} |\Delta v_{g_{pu}}^k(t)|^2 dt} \quad (25)$$

$$\Delta v_{g_{RMS}}^{sat}[n] = \begin{cases} 0 & \text{if } \Delta v_{g_{RMS}}^k[n] \leq 0 \\ \Delta v_{g_{RMS}}^k[n] & \text{if } 0 < \Delta v_{g_{RMS}}^k[n] < \delta_{max} \\ \delta_{max} & \text{if } \Delta v_{g_{RMS}}^k[n] \geq \delta_{max} \end{cases} \quad (26)$$

$$\sigma_k[n] = \delta_{max} \cdot \eta_m - \lambda_g \sum_{i=0}^{\eta_m-1} \Delta v_{g_{RMS}}^{sat}[n-i] \quad (27)$$

3) *Normalization*: Finally, the sharing coefficients of each NG are normalized ( $\sigma'_k$ ) and the power reference for each NGHC is calculated as (28).

$$\sigma'_k[n] = \frac{\sigma_k[n]}{\sum_{i=1}^2 \sigma_i[n]}; P_{NGHC_k}^* = P_{C_{dc,hpf}}^* \sigma'_k[n] \quad (28)$$

In order to clarify the integration of the different control blocks and the power sharing technique, Fig. 9 shows a block diagram summarizing the relation between the different elements of the control system, describing the steps of the adaptive power sharing algorithm.

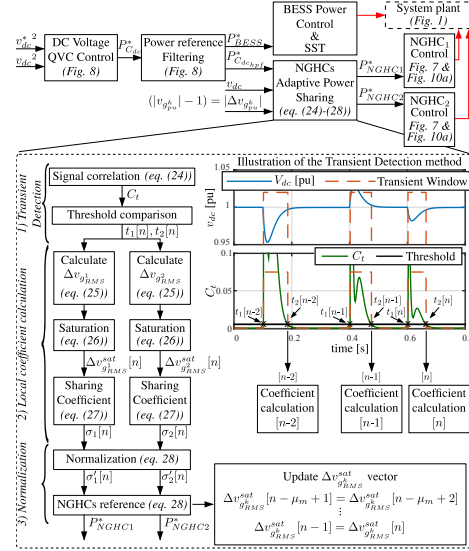


Fig. 9. Simplified block diagram of the proposed control topology for the Hybrid DC/AC MG, including the description of the adaptive power sharing technique.

### C. The AC Nanogrids voltage control scheme

The proposed AC NG voltage control scheme is represented in Fig. 10, where just the  $d$ -axis has been represented for simplicity. The slack control in the NGHC (Fig. 10a)) relies on a modification of the control scheme presented in Fig. 7. When the hybrid adaptive power sharing is enabled, the power reference  $P_{NGHC_k}^*$  obtained by (28) is subtracted from  $P_{ik}^*$ , modifying the control action. The  $q$ -axis power component is neglected against the  $d$ -axis, thus  $P_{NGHC_k}^*$  is just subtracted from the  $d$ -axis for simplicity. To prevent the voltage controller from eliminating the effect of  $P_{NGHC_k}^*$ , back calculation is applied. As the NGHC is the NG slack, a modification in its power reference will lead to a variation in the voltage magnitude, thus allowing the exchange of power between the DC and AC systems. However, this effect is subject to elements in the AC NG providing/absorbing power as a reaction to the voltage variation. This can be provided by the grid equivalent capacitance, enabling a limited participation during the transients, or by introducing ancillary services for such a purpose in the NG.

A solution to maintain the quality and increase the participation in the Hybrid DC/AC NG power sharing is to include local dynamic voltage compensation within the NG. It can be addressed by any local DG or DBESS available in the NG, able to provide active power. The proposed generic

This is the author's version of an article that has been published in this journal. Changes were made to this version by the publisher prior to publication.  
The final version of record is available at <http://dx.doi.org/10.1109/TIA.2018.2873543>

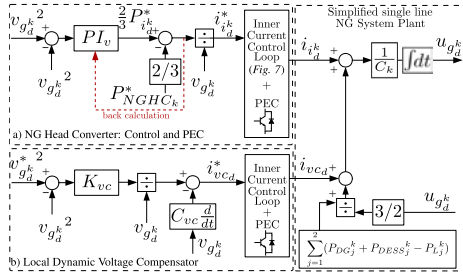


Fig. 10. Proposed hybrid DC/AC voltage control: decentralized AC NG voltage control scheme. a) NGHC control; b) Local voltage compensator.

control topology for the local dynamic voltage compensator is shown in Fig. 10b) and defined by (29). A virtual capacitance ( $C_{vc} \frac{d}{dt}$ ) increases the grid equivalent capacitance, enhancing the initial transient response and improving the participation during transients in the hybrid sharing mechanism. A low pass filter is needed in the practical implementation of the derivative term. A P quadratic regulator ( $K_{vc}$ ) improves the grid voltage damping, and enable the participation during steady state in the hybrid DC/AC power sharing during abnormal conditions, for instance, if the central BESS is overloaded during *islanding*. Both parts of the controller can be implemented independently or combined depending on the limitations of the DG or DBESS providing that service.

$$i_{vcda}^*(t) = \underbrace{\frac{K_{vc} \cdot (v_{gd}^*(t)^2 - v_{gdq}(t)^2)}{v_{gdq}(t)}}_{\text{damping factor}} - \underbrace{C_{vc} \cdot \frac{d}{dt} v_{gdq}(t)}_{\text{Virtual Capacitor}} \quad (29)$$

## V. SIMULATION AND EXPERIMENTAL RESULTS

The proposed system has been validated through simulations in MATLAB/Simulink<sup>®</sup> and experimentally in a Hybrid DC/AC MG full scale prototype implemented within the facilities of the research group *Laboratory for Electrical Energy Management Unified Research* in the University of Oviedo, Spain. The system parameters are summarized in Table I, valid for both the simulation and the experimental setup. Two scenarios are considered to evaluate the performance of the control topology proposed in this paper compared with the *base case* operation. The first scenario consists on applying the proposed adaptive technique for power sharing without local AC voltage compensation. In the second scenario, a local voltage compensator is activated in the  $NG_1$ . Considering the increasing penetration of CPLs and their negative effect in the system stability and dynamic response [12], [23], the system has been evaluated under CPLs, considering them as the most critical disturbance when compared with CILs and CCLs.

The *base case* consists in the operation when the control schemes presented in Fig. 8 and 10 are used, by disabling the

TABLE I  
SIMULATION AND EXPERIMENTAL SYSTEM PARAMETERS

AC Nanogrids Parameters	Values
AC Nominal Voltage ( $V_{g1}^*$ , $V_{g2}^*$ )	212 V <sub>AC,rms</sub> / 50 Hz
NGHCs AC inner control loop BW	2π500 rad/s
NGHCs AC voltage control $\omega_n / \zeta$	2π37.5 rad/s / 2
NGHCs Filter Capacitor ( $C_1$ , $C_2$ )	80 μF
NGHCs Filter Inductance ( $L_1$ , $L_2$ )	1 mH
NGHCs rated power	50 kVA
AC voltage compensator gains $K_{vc} / C_{vc}$	0.2 / 5 · 10 <sup>-4</sup>
AC voltage compensator BW	2π500 rad/s
AC CPL current control BW	2π500 rad/s
DC link and adaptive power sharing	Values
DC Nominal Voltage ( $V_{dc}^*$ )	700 V
DC inner control loop BW	2π500 rad/s
DC equivalent Capacitor ( $C_{dc}$ )	1100 μF
DC Voltage control loop $\omega_n / \zeta$	2π50 / 1
Central BESS $BW / P_{max}$	75 Hz / 8.5 kW
Power Sharing $\lambda_1^2 / \lambda_2^2 / \delta_{max} / \eta_m$	1 / 1 / 0.5 / 2
Transient detection $T / \text{threshold}$	2 ms / 5 · 10 <sup>-3</sup>

power sharing in DC ( $\sigma_1' = \sigma_2' = 0$ ) and without local voltage compensation in the NGs. Considering a BESS bandwidth of 75Hz, in the base case the DC voltage control bandwidth is reduced to 10Hz in order to comply with the cascaded control requirements for stability reasons.

On the other hand, when the proposed technique is applied, the overall inner control loop bandwidth is assumed to be 500Hz thanks to the NGHCs participation, and the DC voltage controller bandwidth can be increased up to 50Hz.

### A. Simulation Results

The simulation results are shown in Fig. 11, where the *base case* and the proposed method are compared. It shows the DC voltage, the AC voltage in both NGs in p.u., the sharing coefficients  $\sigma_k'$  and the transient window used for updating the coefficients, the power commands generated by the DC controller in Fig. 8 and the CPL in each NG. The system is tested under multiple steps of CPL disturbances in both NGs. The sequence of events for the proposed method is as follows:

- Between  $t = 0$ s and  $t = 0.25$ s, the proposed sharing technique and the local AC voltage compensator are inactive. The effect of using excessive voltage control bandwidth with reduced inner control bandwidth is illustrated.
- At  $t = 0.25$ s, the proposed sharing technique is activated. As expected, the power required by the DC voltage controller is now shared between both NGs and central BESS, reacting one NG to the events on the other. As the BESS provides the steady state, the power shared operates only during the transients. The DC voltage transients are improved compared to the *base case*, however the AC NGs voltages are distorted as a consequence.
- At  $t = 0.65$ s, a local voltage compensator in  $B_1^1$  ( $NG_1$ ) is activated. This leads to an overall improvement in both DC and AC voltages reducing significantly the voltage variations under CPL steps.
- At  $t = 1.3$ s, the total system load exceeds the central BESS maximum power, leading to an overall MG collapse for the *base case* at  $t = 1.5$ s. On the other

This is the author's version of an article that has been published in this journal. Changes were made to this version by the publisher prior to publication.  
The final version of record is available at <http://dx.doi.org/10.1109/TIA.2018.2873543>

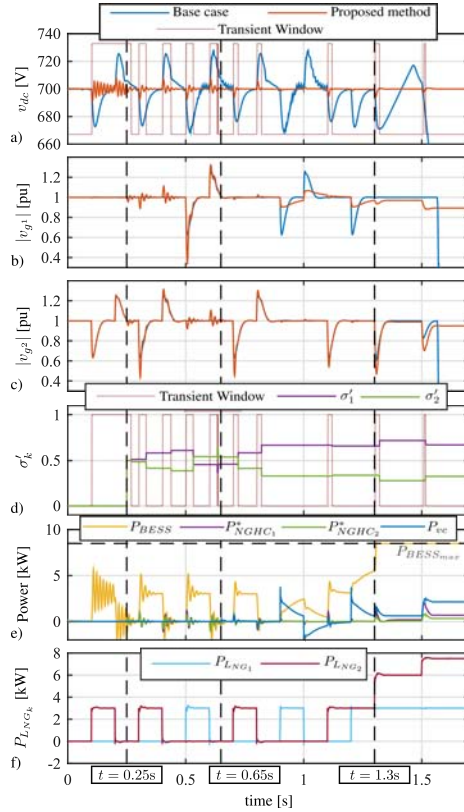


Fig. 11. Simulation results: system performance using the proposed methods. a) LVDC Voltage; b)  $NG_1$  voltage magnitude in p.u., c)  $NG_2$  voltage magnitude in p.u., d) transient window obtained by (24), and sharing coefficients, e) Power shared by the elements participating in the active power control, f) Load drawn by the CPLs located in the NGs.

hand, the use of a local compensator not only improves the transients but also enables the sharing mechanism to operate during steady state. Once the BESS limits, the compensator starts to provide power to maintain the DC and AC NGs at the expense of an stationary error in  $V_{g1}$  caused by the P regulator in the local AC voltage compensator.

### B. Experimental Results

The experimental setup follows the scheme in Fig. 1. The NGs are populated as follows: 1) A tightly regulated CPL, that acts as a load profile emulator, has been connected in the node  $B_2^2$  of  $NG_2$ ; 2) A voltage compensator supplied by

a BESS has been located at the node  $B_1^1$  of  $NG_1$ . For the sake of simplicity, only this two elements, together with the converters in the transformation center, will be considered in this paper.

The experimental results are summarized in Fig. 12, where the *base case* and the proposed method are compared. It shows the DC voltage, the AC voltage in both NGs in p.u., the sharing coefficients  $\sigma'_k$ , the CPL in  $NG_2$  and the power shared by the voltage compensator in  $NG_1$ . The system is tested under multiple steps of CPL disturbances in  $NG_2$ . The sequence of events are described as follows:

- Between  $t = 0$ s and  $t = 0.8$ s, the proposed sharing technique is enabled while the local AC voltage compensator is inactive. The power required by the DC voltage controller is shared between both NGs and the central BESS, reacting  $NG_1$  to the events on  $NG_2$ . As expected, the DC voltage transients are notably improved compared to the *base case*. However, as a consequence, the voltage in  $NG_1$  is distorted and in  $NG_2$  the transient response might be worsen, depending on the sharing coefficient. Initially,  $\sigma'_1 = \sigma'_2$ , thus the power  $P_{C_{active}}^*$  is shared equally by the NGHCs. As the coefficient change, the transient response in the NGs is modified. As in this example the load steps take place only in  $NG_2$ , with the consequent significant voltage deviations, the adaptive sharing algorithm tends to reduce the collaboration of  $NGHC_2$ , increasing the participation of  $NGHC_1$  until an steady value of 0.75. However, as the voltage compensator is disabled, the only element providing inertia, i.e. active power, in  $NG_1$  is the filter capacitor, thus the participation of  $NGHC_1$  negatively impacts the  $NG_1$  AC voltage.
- At  $t = 0.8$ s, a local voltage compensator in  $NG_1$  is activated providing additional inertia, leading to an overall improvement in both DC and AC voltages as shown before in the simulation results. As soon as the  $NG_1$  voltage profile is improved due to the compensator, the adaptive mechanism keeps increasing the participation of  $NGHC_1$  in the LVDC control, alleviating the effort of  $NGHC_2$ . It is worth to point out how the voltage compensator in  $NG_1$  reacts to active power transients taking place in  $NG_2$ . This behavior is allowed by the proposed control scheme based on adaptive power sharing.

## VI. DISTURBANCE TO OUTPUT FREQUENCY RESPONSE

In order to further prove the feasibility of the proposed methods and highlight the achievements against the *base case*, the proposed system has been linearized. Its disturbance to output transfer functions have been analyzed. Two disturbances are considered: the CPL variations in the  $NG_1$ ,  $\Delta P_{L_{NG_1}}$ , and in the  $NG_2$ ,  $\Delta P_{L_{NG_2}}(s)$ . Three outputs are taken into account: the LVDC voltage variation,  $\Delta V_{dc}$ , and the NGs voltage magnitude variation,  $\Delta |V_{g1}|$  and  $\Delta |V_{g2}|$ .

Fig. 13 shows the Bode diagrams of those transfer functions for 3 different cases: 1) the *base case*; 2) proposed adaptive

This is the author's version of an article that has been published in this journal. Changes were made to this version by the publisher prior to publication.  
The final version of record is available at <http://dx.doi.org/10.1109/TIA.2018.2873543>

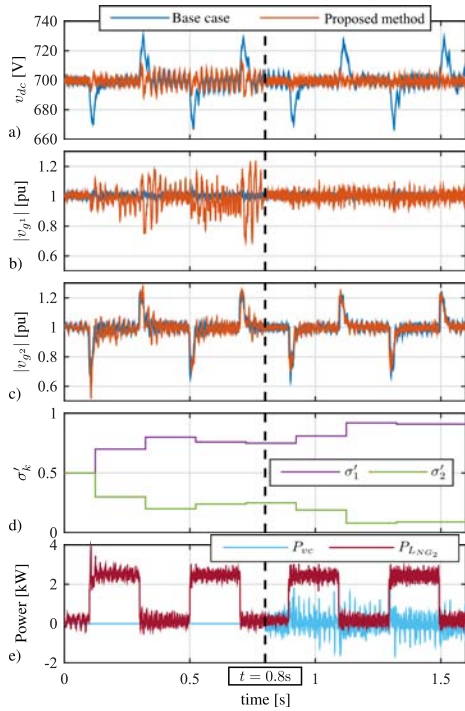


Fig. 12. Experimental results: system performance using the proposed methods. a) LVDC Voltage; b)  $NG_1$  voltage magnitude in p.u., c)  $NG_2$  voltage magnitude in p.u., d) sharing coefficients, e) Load drawn by the CPL located in the  $NG_2$  and power shared by the voltage compensator.

sharing method without local compensators, 3) proposed adaptive method with a local voltage compensator in the  $NG_1$ . Those 3 cases have been evaluated in 3 equilibrium points ( $t = 0.09s$ ,  $t = 0.29$  and  $t = 0.89$  respectively) of the simulated system in Fig. 11. The Bode plots are explained as follows:

- a) & d): As the proposed adaptive method (red) allows to increase the bandwidth of the DC voltage controller, the response is clearly improved at low and medium frequencies. In addition, when the voltage compensator is included (yellow), the response is further enhanced, specially in medium frequencies. It is worth noting that, although the local compensator is in  $NG_1$ , the response under  $\Delta P_{LNG_2}$  is also improved thanks to the indirect cooperation between NGs.
- b) & f): Here, the counter part of the power sharing mechanism (red) is shown. In order to improve the overall system operating range and the DC profile, the

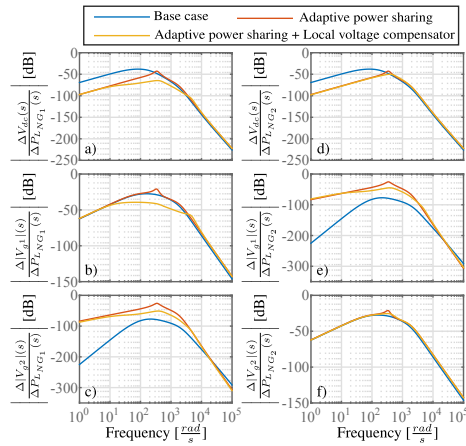


Fig. 13. Bode diagram of the disturbance to output voltage transfer functions. The *base case* and the proposed methods are compared. a), b) and c) voltage variation in the LVDC and the NGs ( $\Delta V_{dc}$ ,  $\Delta |V_{g1}|$ ,  $\Delta |V_{g2}|$ ) under a CPLs disturbance in the  $NG_1$ . d), e) and f) voltage variation in the LVDC and the NGs ( $\Delta V_{dc}$ ,  $\Delta |V_{g1}|$ ,  $\Delta |V_{g2}|$ ) under a CPLs in the  $NG_2$ .

NGs disturbance rejection is slightly worsen. However, the local compensator (yellow) attenuates this effect in f) ( $NG_2$ ), and improves drastically the response in b) ( $NG_1$ ) against the *base case*.

- c) & e): In the *base case* (blue) the two NGs are decoupled from each other, thus  $\Delta P_{LNG_2}$  has a negligible effect in the  $NG_1$  and vice-versa (their coupling is mainly due to sensor errors and delays). The adaptive sharing method allows to couple both NGs increasing the cross-effect that one has on the other as shown in c) and e). This enables the collaborative power flow between NGs.

The gain margins of the transfer functions represented in Fig. 13 are listed in Table II, where a) to f) refers to each Bode plot. The difference between the proposed methods and the *base case* are included below the gain margins. As shown, by slightly compromising the margins in b) and f), a noticeable improvement appears in the DC link a). In the case of the cross-effect transfer functions c) and e), the gain margins are still higher than in b) and f). It is worth pointing out that in every case the phase margin is infinite and the gain margin is positive, ensuring the global stability in all the analyzed cases.

## VII. CONCLUSIONS

In this paper, a dynamic voltage control technique is proposed for a fixed frequency hybrid AC/DC Microgrid with ESSs, based on the power sharing between the AC NGs and a central BESS to maintain the grid quality in both the LVDC and the AC NGs and increase the flexibility under high penetration of CPLs and PECs. An adaptive power sharing

This is the author's version of an article that has been published in this journal. Changes were made to this version by the publisher prior to publication.  
The final version of record is available at <http://dx.doi.org/10.1109/TIA.2018.2873543>

TABLE II  
GAIN MARGINS FOR THE TRANSFER FUNCTIONS IN FIG. 13.

Gain margins (dB)	$\Delta P_{L_{NG_1}}$ disturbance			$\Delta P_{L_{NG_2}}$ disturbance		
	$\Delta V_{dc}$ a)	$\Delta  V_{g1} $ b)	$\Delta  V_{g2} $ c)	$\Delta V_{dc}$ d)	$\Delta  V_{g1} $ e)	$\Delta  V_{g2} $ f)
Base case	38.5	27.6	77.2	38.5	77.2	27.5
Adaptive	46.9	24.9	30.9	46.9	30.5	25.2
Adaptive & comp.	67.2	39.4	54.9	52.4	48.8	26.4
Adaptive vs. base case	8.4	-2.7	-46.3	8.4	-46.7	-2.3
Adaptive & comp. vs. base case	27.6	11.8	-22.3	13.9	-28.4	-1.1

mechanism have being presented for maintaining the LVDC voltage under control, not only reducing the stress in the central BESS system and the dependence in the utility grid, but also demonstrating the extended operation and improved transient response in the LVDC when the central BESS presents bandwidth and power limitations. An automatic cooperative sharing method for the power exchanged between the AC NGs have been proposed. Its operation, together with the use of a local AC dynamic voltage compensator based on a virtual capacitance, positively affects the operation of the Microgrid. The theoretical discussion has been supported with simulations, experimental results and a study on the system frequency response.

#### REFERENCES

- J. M. Guerrero, "Editorial Special Issue on Power Electronics for Microgrids 2014:Part II," *IEEE Transactions on Power Electronics*, vol. 26, no. 3, pp. 659–663, March 2011.
- J. Guerrero, P. C. Loh, T.-L. Lee, and M. Chandorkar, "Advanced Control Architectures for Intelligent Microgrids 2014:Part II: Power Quality, Energy Storage, and AC/DC Microgrids," *IEEE Transactions on Industrial Electronics*, vol. 60, no. 4, pp. 1263–1270, April 2013.
- P. Wang, X. Liu, C. Jin, P. Loh, and F. Choo, "A hybrid AC/DC microgrid architecture, operation and control," in *Power and Energy Society General Meeting, 2011 IEEE*, July 2011, pp. 1–8.
- J. Zhang, D. Guo, F. Wang, Y. Zhuo, and H. Zhang, "Control strategy of interlinking converter in hybrid AC/DC microgrid," in *Renewable Energy Research and Applications (ICRERA), 2013 International Conference on*, Oct 2013, pp. 97–102.
- E. Unamuno and J. A. Barrena, "Hybrid ac/dc microgridspart i: Review and classification of topologies," *Renewable and Sustainable Energy Reviews*, vol. 52, pp. 1251 – 1259, 2015. [Online]. Available: <http://www.sciencedirect.com/science/article/pii/S1364032115008412>
- M. Ambia, A. Al-Durra, and S. Mueyen, "Centralized power control strategy for AC-DC hybrid micro-grid system using multi-converter scheme," in *IECON 2011 - 37th Annual Conference on IEEE Industrial Electronics Society*, Nov 2011, pp. 843–848.
- X. Zhou, Y. Chen, L. Zhou, A. Luo, J. M. Guerrero, W. Wu, L. Yang, and W. Tan, "Power coordinated control method with frequency support capability for hybrid single/three-phase microgrid," *IET Generation, Transmission Distribution*, vol. 12, no. 10, pp. 2397–2405, 2018.
- P. Garca, P. Arbolea, B. Mohamed, and A. A. C. Vega, "Implementation of a hybrid distributed/centralized real-time monitoring system for a dc/ac microgrid with energy storage capabilities," *IEEE Transactions on Industrial Informatics*, vol. 12, no. 5, pp. 1900–1909, Oct 2016.
- Y.-R. Mohamed and E. El-Saadany, "Adaptive Decentralized Droop Controller to Preserve Power Sharing Stability of Paralleled Inverters in Distributed Generation Microgrids," *Power Electronics, IEEE Transactions on*, vol. 23, no. 6, pp. 2806–2816, Nov 2008.
- M. Golsorkhi and D. Lu, "A Control Method for Inverter-Based Isolated Microgrids Based on V-I Droop Characteristics," *Power Delivery, IEEE Transactions on*, vol. 30, no. 3, pp. 1196–1204, June 2015.
- P. Arbolea, C. Gonzalez-Moran, and M. Coto, "A hybrid central-distributed control applied to microgrids with droop characteristic based generators," in *Power Electronics and Motion Control Conference (EPE/PEMC), 2012 15th International*, Sept 2012, pp. LS7a.5–1–LS7a.5–8.
- T. Dragievi, X. Lu, J. C. Vasquez, and J. M. Guerrero, "DC Microgrids-Part I: A Review of Control Strategies and Stabilization Techniques," *IEEE Transactions on Power Electronics*, vol. 31, no. 7, pp. 4876–4891, July 2016.
- D. Chen and L. Xu, "Autonomous dc voltage control of a dc microgrid with multiple slack terminals," *IEEE Transactions on Power Systems*, vol. 27, no. 4, pp. 1897–1905, Nov 2012.
- E. Unamuno and J. A. Barrena, "Hybrid ac/dc microgridspart ii: Review and classification of control strategies," *Renewable and Sustainable Energy Reviews*, vol. 52, pp. 1123 – 1134, 2015. [Online]. Available: <http://www.sciencedirect.com/science/article/pii/S1364032115008333>
- Z. Zhang, X. Huang, J. Jiang, and B. Wu, "A load-sharing control scheme for a microgrid with a fixed frequency inverter," *Electric Power Systems Research*, vol. 80, no. 3, pp. 311 – 317, 2010.
- L. Benadero, R. Cristiano, D. J. Pagano, and E. Ponce, "Nonlinear analysis of interconnected power converters: A case study," *IEEE Journal on Emerging and Selected Topics in Circuits and Systems*, vol. 5, no. 3, pp. 326–335, Sept 2015.
- T. Vandoom, B. Renders, L. Degroote, B. Meersman, and L. Vanvelde, "Active Load Control in Isolated Microgrids Based on the Grid Voltage," *Smart Grid, IEEE Transactions on*, vol. 2, no. 1, pp. 139–151, March 2011, use of Voltage-droop control.
- A. Navarro-Rodriguez, P. Garcia, R. Georgious, and J. Garcia, "A communication-less solution for transient frequency drift compensation on weak microgrids using a D-statcom with an energy storage system," in *Energy Conversion Congress and Exposition (ECCE), 2015 IEEE*, Sept 2015, pp. 6904–6911.
- I. Serban and C. Marinescu, "Control Strategy of Three-Phase Battery Energy Storage Systems for Frequency Support in Microgrids and with Uninterrupted Supply of Local Loads," *Power Electronics, IEEE Transactions on*, vol. 29, no. 9, pp. 5010–5020, Sept 2014.
- M. Torres L. L. Lopes, L. Moran T. and J. Espinoza C, "Self-Tuning Virtual Synchronous Machine: A Control Strategy for Energy Storage Systems to Support Dynamic Frequency Control," *Energy Conversion, IEEE Transactions on*, vol. 29, no. 4, pp. 833–840, Dec 2014.
- Y. Hirase, O. Noro, K. Sugimoto, K. Sakimoto, Y. Shindo, and T. Ise, "Effects of suppressing frequency fluctuations by parallel operation of virtual synchronous generator in microgrids," in *Energy Conversion Congress and Exposition (ECCE), 2015 IEEE*, Sept 2015, pp. 3694–3701.
- A. Navarro-Rodriguez, P. Garcia, R. Georgious, J. Garcia, and S. Saeed, "Observer-based transient frequency drift compensation in ac microgrids," *IEEE Transactions on Smart Grid*, vol. PP, no. 99, pp. 1–1, 2017.
- A. Navarro-Rodriguez, P. Garcia, J. M. Cano, and M. Sumner, "Limits, stability and disturbance rejection analysis of voltage control loop strategies for grid forming converters in dc and ac microgrids with high penetration of constant power loads," in *2017 19th European Conference on Power Electronics and Applications (EPE'17 ECCE Europe)*, Sept 2017, pp. P.1–P.10.
- A. Navarro-Rodriguez, P. Garcia, R. Georgious, and J. Garcia, "Adaptive active power sharing techniques for DC and AC voltage control in a hybrid DC/AC microgrid," in *2017 IEEE Energy Conversion Congress and Exposition (ECCE)*, Oct 2017, pp. 30–36.
- M. K. Mishra and K. Karthikeyan, "A fast-acting dc-link voltage controller for three-phase dstatcom to compensate ac and dc loads," *IEEE Transactions on Power Delivery*, vol. 24, no. 4, pp. 2291–2299, Oct 2009.
- S. Vazquez, J. A. Sanchez, J. M. Carrasco, J. I. Leon, and E. Galvan, "A model-based direct power control for three-phase power converters," *IEEE Transactions on Industrial Electronics*, vol. 55, no. 4, pp. 1647–1657, April 2008.

This is the author's version of an article that has been published in this journal. Changes were made to this version by the publisher prior to publication.  
The final version of record is available at <http://dx.doi.org/10.1109/TIA.2018.2873543>



**Ángel Navarro-Rodríguez** (S'15) received the B.Sc. degree in telecommunications engineering with honors from the University of Castilla La-Mancha, Spain in 2012 and the M.Sc. degree in Electrical Energy Conversion and Power Systems from the University of Oviedo, Gijón, Spain in 2014. Nowadays he is Ph.D student in the Department of Electrical, Computer, and Systems Engineering in the University of Oviedo, granted by the government of Principado de Asturias. In 2016 and 2017, he was a visitor researcher at The University of Nottingham, UK, in the Power Electronics, Machines and Control (PEMC) research group. He is part of the LEMUR research group in University of Oviedo since 2014 and his research interests include Energy Storage Systems, Control Systems, Electronics, Power Electronic Converters, Microgrids, power quality and Renewable Energies.



**Pablo García** (S01-A06-M09) received the M.S. and Ph.D. degrees in electrical engineering and control from the University of Oviedo, Gijón, Spain, in 2001 and 2006, respectively. In 2004, he was a Visitor Scholar at the University of Madison-Wisconsin, Madison, WI, USA, Electric Machines and Power Electronics Consortium. In 2013 he was a visiting scholar at The University of Nottingham, UK. He is the co-author of more than 20 IEEE journals and 50 international conferences. He is currently an Associate Professor within the Department of Electrical, Electronics, Computer, and Systems Engineering at the University of Oviedo. His research interests include control of grid-tied converters, parameter estimation, energy conversion, AC drives, sensorless control, AC machines diagnostics and signal processing.



**Ramy Georgious** (S'15) received the B.Sc. degree from Port Said University, Port Said, Egypt, in May 2010, in Electrical Engineering with average appreciation Excellent with honors degree, and the M.Sc. degree in Electrical Energy Conversion and Power Systems (EECPs) and the Ph.D. degree in electrical engineering from the University of Oviedo, Gijón, Asturias, Spain, in June 2014 and July 2018, respectively. He worked as a teacher assistant in the Electrical Engineering department in Port Said University from March 2011 to September 2012. He joined LEMUR research team in University of Oviedo in July 2014. In 2015, he was a visitor researcher with Power Electronics, Machines and Control (PEMC) research group at the University of Nottingham, United Kingdom. He was granted by Erasmus Mundus (MEDASTAR) to do his Master in 2012 and by the government of Principado de Asturias to do his Ph.D. in 2013 in the University of Oviedo. His research interests include Energy Storage Systems, Control Systems, Power Electronic Converters, Microgrids, Renewable Energy, Design and Simulation.



**Jorge García** (S'01-M'05-SM'11), received the M.Sc. and Ph.D. degrees in electrical engineering from the University of Oviedo, Asturias, Spain, in 2000 and 2003, respectively. In December 1999, he joined the Electrical and Electronic Engineering Department of the University of Oviedo, where he is currently an Associate Professor. He works with the LEMUR research team; his current research interests include power electronics and control for industrial, grid support and lighting applications. Dr. García is co-author of more than 40 journal papers and more than 80 international conference papers in power and industrial electronics. Dr. García was a recipient of the University of Oviedo Outstanding Ph.D. Thesis Award in 2005.



### **C.3 Observer-Based Pulsed Signal Injection for Grid Impedance Estimation in Three-Phase Systems**

P. García, M. Sumner, Á. Navarro-Rodríguez, J. M. Guerrero and J. García, "Observer-Based Pulsed Signal Injection for Grid Impedance Estimation in Three-Phase Systems," in *IEEE Transactions on Industrial Electronics*, vol. 65, no. 10, pp. 7888-7899, Oct. 2018. doi: 10.1109/TIE.2018.2801784.



This is the author's version of an article that has been published in this journal. Changes were made to this version by the publisher prior to publication.  
The final version of record is available at <http://dx.doi.org/10.1109/TIE.2018.2801784>

# Observer-Based Pulsed Signal Injection for Grid Impedance Estimation in Three Phase Systems

Pablo García, *Member IEEE*, Mark Sumner, *Senior Member IEEE*, Ángel Navarro-Rodríguez, *Student Member IEEE*, Juan M. Guerrero, *Member IEEE*, and Jorge Garcia, *Senior Member IEEE*

**Abstract**—This paper addresses the estimation of the grid impedance and the control of grid-tied converters by combining pulsed-signal injection and observer based techniques. A Luenberger based observer is used for controlling the grid-side current of an LCL filter by only measuring the converter-side currents and the grid-side voltage. This configuration mitigates the effects of parameter variation at the LCL filter. Under grid impedance changes, the observer control signal will be used for triggering the signal injection. A Pulsed Signal Injection (PSI) approach is employed for estimating online the grid impedance using an RLS algorithm. Compared with existing grid-impedance estimation techniques, the proposed method can: 1) identify a generic RL grid impedance, even under unbalanced conditions; 2) reduce the distortion induced by the excitation signal by relying on the observer to triggering the injection when a grid impedance change is detected; 3) Identify grid impedance values much lower than the converter filter impedance, which is the usual situation when the converter rated power is well below the grid rating. Finally, it is worth pointing out that the proposed estimation technique is well suited to be incorporated into an adaptive current controller scheme.

## I. INTRODUCTION

THE use of Voltage Source Converters (VSC) interfaced to the AC grid requires the control of the current delivered to the grid. In order to accurately design the current controller, it is critical to understand the dynamic model between the converter output voltage and the resulting grid current. The model will affect the converter performance in different ways, depending on the sensors used and the filter topology, i.e. L, LC, LCL, connecting the converter to the grid. When using an LCL filter for the interface, are several options for the placement of the current and voltage sensors, each one with their advantages and drawbacks [1], [2]. When AC voltage

This work has been partially funded by the Campus of International Excellence (CEI) of the University of Oviedo, Spain, in the framework of Mobility Grants for Academics in 2013. Also partially supported by the predoctoral grants program Severo Ochoa for the formation in research and university teaching of Principado de Asturias PCTI-FICYT under the grant ID BP14-135. This work also was supported in part by the Research, Technological Development and Innovation Program Oriented to the Society Challenges of the Spanish Ministry of Economy and Competitiveness under grants ENE2013-44245-R, ENE2016-77919-R and by the European Union through ERFD Structural Funds (FEDER).

P. García, A. Navarro-Rodríguez, Juan M. Guerrero and J. García are with the Department of Electrical, Computer and System Engineering, University of Oviedo, Gijón, 33204, Spain (e-mail: garcia-pablo@uniovi.es, navarroangel@uniovi.es, guerrero@uniovi.es, garcia-jorge@uniovi.es). Mark Sumner is with the Department of Electrical and Electronic Engineering, The University of Nottingham, University Park, Nottingham, NG7 2RD, UK. (email: Mark.Sumner@nottingham.ac.uk)

control at the converter output is needed, it is common to measure the voltage at the filter capacitor. However, this will make the current controller dynamics dependent on the grid side impedance [3]. An improved decoupling mechanism for the grid impedance variation can be implemented by placing the voltage sensor in the Point of Common Coupling (PCC). However, this will require either the measurement or the estimation of the capacitor voltage/current to effectively damp the current controller response [4]. This issue is more critical when the power converter is connected to weak networks having a non negligible grid impedance, thus affecting the total output impedance. In order to overcome this problem there are two different alternatives: 1) to force the known output filter to be the dominant dynamic system in any grid situation by implementing passive/active damping or virtual impedance techniques [5], [6], and, 2) to implement an adaptive current controller [7], [8], in which controller gains change depending on the grid impedance.

For the second option, the grid impedance must be estimated online as well as the variations of the LCL filter parameters. Methods for the identification of the grid impedance can be classified into those requiring the use of dedicated devices and those that can be implemented without any additional hardware. Methods in the first group are often able to estimate the impedance over a wide frequency range using signal injection and frequency based techniques [9], [10]. Regarding the second group, impedance estimation could be implemented using two different approaches: 1) model-based techniques and, 2) signal-injection based techniques. Model-based techniques use the transfer function between the voltage and the current for parameter estimation. In [11], the use of the LCL filter resonance is proposed in order to perform the estimation. As pointed out by the authors, the main issue of this technique is the existence of two resonance frequencies when reactive power passive compensation is added at the PCC. Recently, the identification of the equivalent grid inductance and resistance using closed-loop transient response has been proposed [12]. The method looks appealing and it is well supported with experimental validation, but it does not include the operation under unbalanced grid conditions and does not show the response to sudden changes on the grid impedance, which is critical for islanding detection. In [13], the use of the existing grid harmonics is proposed for the impedance estimation at different frequencies using a Kalman filter. However, only simulation results are provided. A similar approach is proposed in [14]. The estimated model coefficients are online updated using an adaptive linear neuron (ADALINE)

This is the author's version of an article that has been published in this journal. Changes were made to this version by the publisher prior to publication.  
The final version of record is available at <http://dx.doi.org/10.1109/TIE.2018.2801784>

algorithm. The results are experimentally confirmed. However, all the electrical variables (grid current and voltages) need to be measured and operation under unbalanced conditions is not demonstrated. In [15], grid inductance is estimated using two consecutive samples of the grid current within a switching period. The estimation method is based on the discrete-time model at the grid frequency and, as recognized by the authors, the method is only valid for the inductive component. Moreover, the operation is only demonstrated for two different inductance values and unbalanced conditions are not considered.

Signal-injection based methods use an additional excitation in order to track the system response [16]–[23]. For the excitation signal, several approaches have been proposed: 1) Pulsed Signal Injection (PSI) [9], [23]–[25]; 2) High Frequency Signal Injection (HFSI) at constant high frequency [18], [19], [26]–[28]; 3) current regulator reaction [19]; 4) Low Frequency Signal Injection (LFSI) [20], [29], [30]; 5) Binary Sequence Signal Injection (BSSI) [21], [31], [32].

Regarding the PSI methods, the results presented in [9] are obtained in the absence of fundamental excitation and the pulses are injected period-to-period. The results in [24] are related to the ones presented in this paper, but they are only focused on a pure inductive three phase balanced impedance. The method proposed in [23] is based on parameter identification using the pulse response and an adaptive model approach. The authors claim the method is able to estimate the grid admittance even with the presence of other power converters connected to the grid. The injected pulse magnitude and duration are similar to the one proposed in this paper. However, the activation of the pulse injection is not fully described and the results are only tested under real-time emulation provided by an OPAL-RT simulator. The method shown in [25] uses a current-pulse injection with the peak of the sinusoidal trajectory of 2 p.u. For the method proposed in our research, the peak pulsed current is around 0.03 p.u. Moreover, the use of the observer will allow the reduction of the current THD to below 1%. Furthermore, the signal processing is based on the DFT, increasing the computational burden and the memory requirements.

HFSI methods and current regulator reaction present some issues: 1) The selection of the high frequency requires the consideration of the possible reaction of any active power filter (APF) connected to the same PCC, compensating the high frequency voltage/current harmonics; 2) the estimated impedance is not the transient impedance, which determines the grid current response to the voltage changes imposed by the power converter, which is the one needed for current controller tuning.

LFSI methods can be separated into those adding an additional excitation signal, similar to HFSI methods, and those using the changes in the commands delivered by the power converter. Using the first approach, a current/voltage excitation signal of a given frequency, often an inter-harmonic, is injected into the grid. The grid voltage/current response at that frequency is analysed and the impedance at the injection frequency is obtained, often using frequency based methods. In [17], [29] a 75Hz current signal is used. The same comments

as mentioned before for the HFSI methods apply: the disturbance signal is continuously injected and the impedance is only estimated at the injection frequency. Additionally, due to the low-frequency signal injection, the reaction of the current regulators can compensate for the disturbance signal, thus reducing the effectiveness of the method. A solution given by the authors is to inject the excitation signal as a current reference, but then the bandwidth of the current controller can compromise the accuracy of the estimation. The second class of methods, require modifying the converter fundamental command. In [30], the  $P$  and  $Q$  commands are altered and both the inductive and resistive part of the impedance are estimated. The main drawback of this method is the coupling between the induced changes in the fundamental command used for the estimation from those due to the regular operation of the converter. The results are only verified by simulation and there is no discussion of the estimation under unbalanced conditions.

BSSI methods are based on the injection of a pulse-train whose response is processed using frequency-based methods. They allow the grid impedance to be identified over a wide-range of frequencies. However, compared to PSI methods, they require a longer processing time because of the time required to inject the test signal and the calculations needed for the identification in the frequency domain. Moreover, most of the proposed methods are only validated for the estimation of the inductance term under balanced grid conditions.

In order to overcome the aforementioned problems, this paper proposes a hybrid strategy based on both an observer and a PSI. A Luenberger style observer will be used for controlling the grid-side current and detecting coarse grid impedance changes, only relying on the converter-side current and the voltage at the PCC. The proposed PSI, consisting of the injection of a pulse synchronized with the zero crossing of each three phase voltages, will allow the accurate measurement of the grid impedance by using a Recursive Least Square (RLS) algorithm. The proposed PSI method improves the THD when compared to other alternatives by constraining the injection of the pulses to those time intervals in which a change in the grid impedance is detected by the observer. As it will be demonstrated, the proposed technique allows for the estimation of both the resistive and inductive terms under unbalanced grid conditions. Thus, the contributions of this work can be summarized as: 1) identification of a generic RL grid impedance, including unbalance conditions; 2) reduction of the distortion induced by the excitation signal by relying on the observer to triggering the injection when a grid impedance change is detected; 3) identification of grid impedance values much lower than the converter filter impedance, which is the usual situation when the converter rated power is well below the grid rating.

The paper is organized as follows. Section II explains the state-space model of the LCL filter and the grid impedance, the design of the observer and the digital implementation of the control system. Section III shows the injection mechanism, including the selection of the injection pulse. Section IV covers the RLS adaptive procedure used for the grid impedance estimation. Finally, simulation and experimental results are

This is the author's version of an article that has been published in this journal. Changes were made to this version by the publisher prior to publication.  
The final version of record is available at <http://dx.doi.org/10.1109/TIE.2018.2801784>

shown in Section V.

## II. SYSTEM MODELING AND CONTROL

### A. System modeling

The state space representation of an LCL filter (Fig. 1) in an arbitrary reference frame is given by (1), (2); where  $\mathbf{x} = [i_i, v_c, i_g]^T$  is the state vector and  $\mathbf{u} = [v_i, v_g]^T$  the input vector, corresponding to the current and voltages in Fig. 1. Each component at the state and input vectors is a complex variable that can be split into the real,  $x_x$ , and the imaginary,  $x_y$ , parts. Equations (1) and (2) could be particularized for the stationary ( $\alpha, \beta$ ) or to the synchronous ( $d, q$ ) reference frames by making  $\omega_e = 0$  or  $\omega_e = \omega_{grid}$  respectively. A compact representation is given at (3), (4). The corresponding block diagram using complex vector notation is shown in Fig. 2.

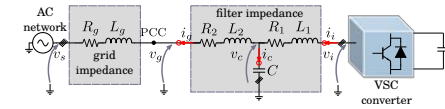


Fig. 1. Connection of the LCL filter to the output of the VSC.

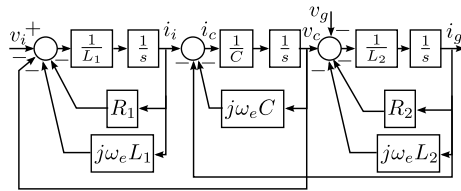


Fig. 2. LCL filter block diagram in complex-vector form.

$$\begin{aligned} \frac{d}{dt} \mathbf{x}_x &= \begin{pmatrix} -R_1/L_1 & -1/L_1 & 0 \\ 1/C & 0 & -1/C \\ 0 & 1/L_2 & -R_2/L_2 \end{pmatrix} \cdot \mathbf{x}_x \\ &+ \omega_e \begin{pmatrix} 1 & 0 & 0 \\ 0 & 1 & 0 \\ 0 & 0 & 1 \end{pmatrix} \cdot \mathbf{x}_y + \begin{pmatrix} 1/L_1 & 0 \\ 0 & 0 \\ 0 & -1/L_2 \end{pmatrix} \cdot \mathbf{u}_x \end{aligned} \quad (1)$$

$$\begin{aligned} \frac{d}{dt} \mathbf{x}_y &= \begin{pmatrix} -R_1/L_1 & -1/L_1 & 0 \\ 1/C & 0 & -1/C \\ 0 & 1/L_2 & -R_2/L_2 \end{pmatrix} \cdot \mathbf{x}_y \\ &- \omega_e \begin{pmatrix} 1 & 0 & 0 \\ 0 & 1 & 0 \\ 0 & 0 & 1 \end{pmatrix} \cdot \mathbf{x}_x + \begin{pmatrix} 1/L_1 & 0 \\ 0 & 0 \\ 0 & -1/L_2 \end{pmatrix} \cdot \mathbf{u}_y \end{aligned} \quad (2)$$

$$\frac{d}{dt} \mathbf{x}_x = \mathbf{A}_x \cdot \mathbf{x}_x + \omega_e \mathbf{I} \cdot \mathbf{x}_y + \mathbf{B}_x \cdot \mathbf{u}_x \quad (3)$$

$$\frac{d}{dt} \mathbf{x}_y = \mathbf{A}_y \cdot \mathbf{x}_y - \omega_e \mathbf{I} \cdot \mathbf{x}_x + \mathbf{B}_y \cdot \mathbf{u}_y \quad (4)$$

### B. Grid-side current observer

The superior filtering performance of the LCL structure when compared to the L or LC alternatives has also important shortcomings in the design of the current controller [33]. This situation is even worse when harmonic compensation is considered [34]. Current control using a LCL filter is a challenging task due to the resonance created by the capacitor and the inductances and often an attenuation method is needed. There are several alternatives in the literature which can be separated into passive and active damping techniques. On one side, passive damping techniques require the use of additional passive elements, such as series or parallel resistances which increase the system losses [33]. On the other, active damping methods often need for additional current or voltage sensors. Lately, some researchers have addressed active damping implementation methods not needing any extra elements [2], [35]–[40]. The methods in that group could be split in those requiring to estimate the capacitor current or the inductance voltage from those that rely on digital filtering of the control signal. The first approach requires the use of time derivatives which are normally noisy or require the use of complicated control algorithms. The second alternative places a notch filter at the current controller output, in order not to react at the LCL resonance frequency [35]. However, the bandwidth of the current controller must be often decreased.

In this paper, a control strategy based on a Luenberger type observer will be used [41]. The observer is similar to the one developed in [42], where direct discrete-time domain design is used instead. The simplicity of the design in the continuous-time domain and the small difference in the performance for the parameters used in this research makes the solution in [41] appealing. It is also related with [43], but the more convenient converter side current is used instead of the grid side one. The proposed control strategy will estimate the grid-side current by using the converter-side current sensors and the voltage sensors at the PCC.

The observer-based current control block diagram is shown in Fig. 3. The observer performance, at the synchronous reference frame, is shown at Fig. 4 when the estimated LCL filter parameters match the real ones. As shown, the grid current is correctly tracked and the dynamic performance is comparable to the one obtained when the grid side sensors are used. A detailed explanation about the working principles is provided in [41].

### C. Digital control implementation

For the digital implementation, the Luenberger observer and the current controller designs must be translated to the discrete-time domain. Several options exist for the discretization. Considering that the method should be suitable for an adaptive implementation, the use of complicated matrices' operations must be reduced. As a compromise between the accuracy and the computational burden, Tustin method is selected. The resulting expressions are shown in (5), (6), where

This is the author's version of an article that has been published in this journal. Changes were made to this version by the publisher prior to publication.  
The final version of record is available at <http://dx.doi.org/10.1109/TIE.2018.2801784>

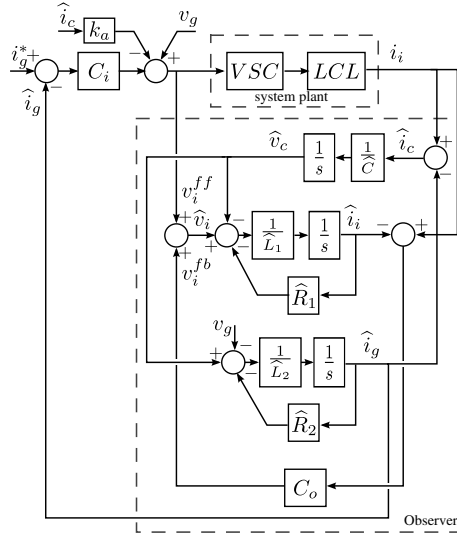


Fig. 3. Grid-current observer structure in an arbitrary reference frame.

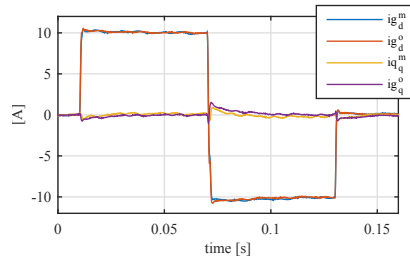


Fig. 4. Experimental results for the grid-current observer transient response. The results show a comparison of the observer-based control with respect to the sensor-based using an additional grid-side current sensor. Superscript  $m$  is for the sensor-based control, whereas  $o$  is for the observer-based control.

$[k]$  and  $[k-1]$  correspond to the present and previous samples and  $T_s$  is the sample time.

$$\mathbf{x}_x[k] = \mathbf{K}_{ix} \cdot \left( \mathbf{K}_{ax} \cdot \mathbf{x}_x[k-1] + \frac{T_s}{2} \mathbf{B}_x (\mathbf{u}_x[k] + \mathbf{u}_x[k-1]) \right) + \frac{T_s}{2} \omega_e \mathbf{I} (\mathbf{x}_y[k] + \mathbf{x}_y[k-1]) \quad (5)$$

$$\mathbf{x}_y[k] = \mathbf{K}_{iy} \cdot \left( \mathbf{K}_{ay} \cdot \mathbf{x}_y[k-1] + \frac{T_s}{2} \mathbf{B}_y (\mathbf{u}_y[k] + \mathbf{u}_y[k-1]) \right) - \frac{T_s}{2} \omega_e \mathbf{I} (\mathbf{x}_x[k] + \mathbf{x}_x[k-1]) \quad (6)$$

where  $\mathbf{K}_{ax}$ ,  $\mathbf{K}_{ay}$ ,  $\mathbf{K}_{ix}$ ,  $\mathbf{K}_{iy}$  being the values of  $\mathbf{K}_a = \mathbf{I} + \frac{T_s}{2} \mathbf{A}$

and  $\mathbf{K}_i = (\mathbf{I} - \frac{T_s}{2} \mathbf{A})^{-1}$  for either the  $x$ - or  $y$ - axes. The observer controller ( $C_o$ ) is also discretized using Tustin approximation. Proportional-Integral (PI) or Proportional-Resonant (PR) controllers can be selected depending on the implementation being at the synchronous or the stationary reference frame respectively. In this study, a synchronous reference frame has been selected.

As explained in [41], the observer feedback signal,  $v_i^{fb}$ , reacts to any change in the grid impedance. That variation can be used for triggering the pulse injection, thus avoiding the injection of a continuous disturbance into the grid. Fig. 5 shows the experimental results when a sudden change in the grid impedance occurs for two different reactive current levels. As it can be seen, even if the changes in the fundamental command affect the observer signal, the variation due to the grid impedance change is for the shown cases more than 100% larger.

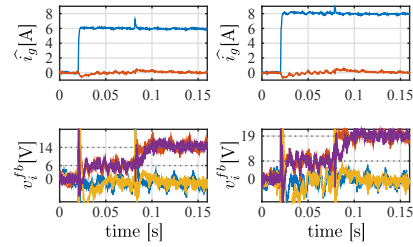


Fig. 5. Experimental results for the transient detection. Top row: fundamental grid currents components at the synchronous reference frame for two different current references, 6 and 8. Blue color is used for  $d$  and red for  $q$ -axis. The transient at 0.08 seconds is due to the change of the grid impedance. Bottom row: observer feedback signal components at the synchronous reference frame. At each of the graphs representing the observer feedback signals, four traces are depicted. Blue and red colors are used for the  $d$  and  $q$  components, respectively while magenta and yellow show the filtered signals with a 2<sup>nd</sup> order Butterworth filter tuned with a cut-off frequency of 75Hz.

### III. PULSED SIGNAL INJECTION

There are different PSI alternatives related with the injection parameters which can be adjusted. As shown in Fig. 6, the signal is centered at the zero crossing of the phase to neutral voltages. Zero crossing is detected by the PLL also used for grid synchronization. This instant has been selected in order to minimize the voltage distortion, as it will be discussed later.

In this paper, three different pulse injection alternatives are investigated. Two of them are implemented in the  $abc$  reference frame, while the third one is in the  $dq$  reference frame. The pulses are injected by modifying the duty cycle provided by the current controller. During the pulse injection, the fundamental voltage command is disabled for the case of  $abc$  injection (see Fig. 6) whereas is added to the injected pulse in the  $dq$  reference frame implementation. As seen in Fig. 6, both the pulse width and the magnitude can be changed. Obviously, larger pulses will help in the estimation procedure,

This is the author's version of an article that has been published in this journal. Changes were made to this version by the publisher prior to publication.  
The final version of record is available at <http://dx.doi.org/10.1109/TIE.2018.2801784>

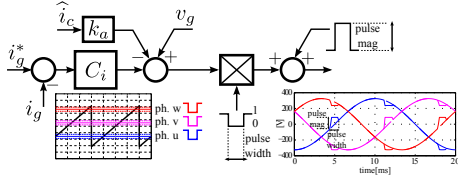


Fig. 6. PSI implementation. The pulse injection is synchronized and centered with respect to the grid voltage zero crossing and the fundamental voltage command is blanked during the injection time. On the phase representation ( $ph.u, v, w$ ), dashed lines show the starting and end of each phase pulse and solid ones the zero crossing of the respective phase.

but will also increase the resulting current THD. The values shown in Table I have been used. Resulting waveforms for the inverter commands and the applied voltages are shown in Fig. 7. The corresponding currents in the synchronous reference frame are depicted in Fig. 8. The three alternatives are described following:

- 1) **Method#1.** Pulse width is set to the desired value and the magnitude is set to zero. Under these conditions, the fundamental voltage command is clamped to zero during the pulse injection time. In the  $dq$  reference frame, even if the pulse is mostly applied at the  $q$ -axis, both components are modified. The pulses exhibit a triangular shape at the  $q$ -axis and the resulting current has a sinusoidal waveform.
- 2) **Method#2.** Fundamental command is held at the corresponding value at the beginning of the pulse injection and when the phase crosses the zero is changed to the symmetrical value with respect to zero. In the  $dq$  reference frame,  $d$ -axis component is also affected, although in a less noticeable way than for Method#1. The pulses at the  $q$ -axis are also transformed to a triangular shape, but the resulting current has a triangular waveform of opposite phase when compared to previous method.
- 3) **Method#3.** Pulses are directly injected at the  $q$ -,  $d$ -, or both axes by adding the pulses to the fundamental command delivered by the current controller. When compared to the pulse injection in the  $dq$  reference frame for both Method#1 and Method#2, the resulting excitation is stepwise in the  $abc$  reference frame but has triangular form in the  $dq$  reference frame. Even if the RLS algorithm is to be implemented in the  $\alpha\beta$  reference frame, in order to allow the identification to work under unbalanced conditions it has been tested that the results are improved when square pulses are applied in the  $dq$  reference frame.

It must be remarked that all the pulse injection strategies share the fact that the applied distortion to the voltage command is symmetrical with respect to the zero crossing, thus resulting in a zero average voltage error. Selecting one method or the other is based on the sensitivity of the current response and on the implementation burden. For this paper, Method#3 is considered, with the injection kept at the  $q$ -axis.

Experimental results of the system operating in closed-loop using the observer estimated grid current with a 500 Hz bandwidth are shown in Fig. 9. The results show that, even if the current controller reaction is affecting the pulses injection, they are clearly visible on the grid voltage and thus could potentially be used for the RLS estimation. It is also remarkable the close matching compared to the simulated results shown in Fig. 8. At this point, it is needed to

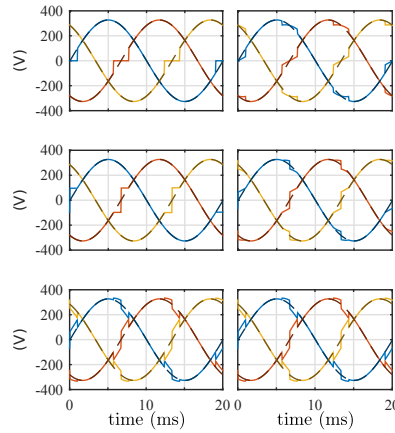


Fig. 7. PSI waveforms for the three proposed methods in the  $abc$  reference frame. From top to bottom, Method#1, Method#2 and Method#3. Left column shows the generated phase voltage command and right column the phase to neutral voltages. Dashed lines show the variables if the pulse injection is disabled.

comment on the additional THD distortion induced by the pulse injection. As it has been explained, pulse injection is disabled until a change in the impedance is detected by the observer. Whenever this happens, three pulses are injected (one at the zero crossing of each of the phases). The expected result is that the THD distortion is notably reduced with respect to existing techniques. In order to corroborate that, first a suitable procedure for the THD definition for pulsating signal has been carried out. As provided by the IEC61000-4-7 standard, ten fundamental periods of the voltage and current signals for 50Hz of nominal frequency are analyzed. Considering the pulsating and discontinuous nature of the proposed injection mechanism, the THD is calculated in time domain using (7).

$$THD[\%] = \frac{\sqrt{\sum_{t=0}^{t=200ms} \mathbf{x}_{\alpha\beta}^{si}{}^2}}{\sqrt{\sum_{t=0}^{t=200ms} \mathbf{x}_{\alpha\beta}{}^2}} \cdot 100 \quad (7)$$

where  $\mathbf{x}_{\alpha\beta}^{si}$  is the isolated injection voltage signal or the corresponding current response in the  $\alpha\beta$  reference frame and  $\mathbf{x}_{\alpha\beta}$  the overall voltage/current signal. The calculation of the THD is restricted to 200ms that corresponds to 10 fundamental cycles at 50Hz. The THD calculations are done for selected references corresponding to all the methods compared in this paper, i.e: LFSI, HFSI, PSI and BSSI. The calculations are

This is the author's version of an article that has been published in this journal. Changes were made to this version by the publisher prior to publication.  
The final version of record is available at <http://dx.doi.org/10.1109/TIE.2018.2801784>

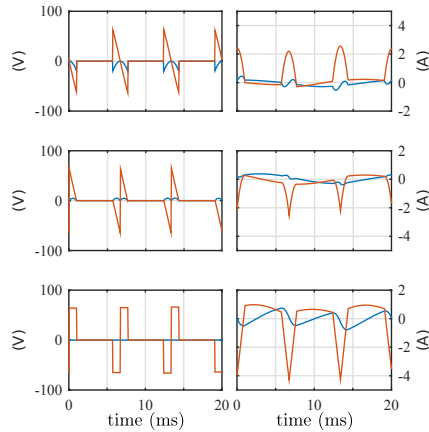


Fig. 8. PSI waveforms for the three proposed methods in the  $dq$  reference frame. Fundamental component is removed in order to zoom on the injected pulsed components. Left column is for the  $v_{dq}$  voltages and right for the  $i_{dq}$  current.  $d$ -axis and  $q$ -axis are represented in blue and red respectively. From top to bottom, Method#1, Method#2 and Method#3.

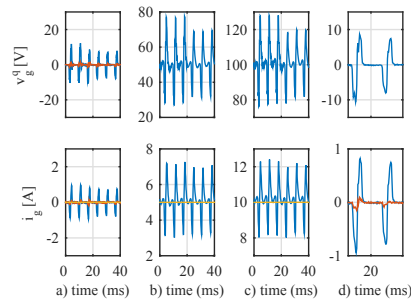


Fig. 9. Experimental results using Method#3. System is operated in closed-loop with a bandwidth of 500Hz using the observed grid current. Top row shows the  $q$ -axis component of the grid voltage, whereas bottom row is for the observed grid current components in the synchronous reference frame. Different levels of  $q$ -axis current commanded: a) 0A, b) 5A, c) 10A, d) zoom for 0A conditions. Blue color is used for  $q$ -axis component and red for  $d$ -axis. At  $t = 20$ ms, the 2.4mH inductance series connected at the output of the LCL filter is changed to 0.6mH.

carried out using the same simulation models, with same grid conditions and using the signal injection parameters as indicated by the authors. Results for the comparison are summarized in Fig. 10. As it can be seen, the proposed method has the lowest THD for the grid voltage, both for the 2ms and the 1ms cases. Considering the grid current THD, the proposed observer-based method is the second best for the 2ms case, just after the HFSI method, and the best one for the case of 1ms. It is also worth noting that the comparison conditions represent the worst case scenario for our proposal.

The calculated THD value assumes 3 pulses will be injected each 10 cycles, meaning that the observer is reacting to a change in the impedance each 10 cycles. However, the most important advantage of the observer-based method is the fact that the pulse injection is discontinuous, making the THD to be improved when the grid impedance is kept stable. Fig. 11 shows an interesting comparison between the observer-based injection and the HFSI method. There, the THD results for the 2ms case are calculated as a function of the percentage of cycles in which the injection is applied. As it can be seen, the break-even point at which the proposed method improves the HFSI injection occurs when the ratio is lower than 4%. This condition is met after 40 grid cycles (0.8s).

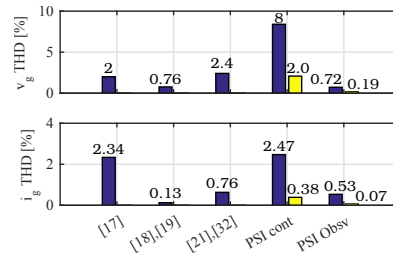


Fig. 10. THD comparison for the different methods analyzed in this paper. Both the grid voltage,  $v_g$  and the grid current,  $i_g$  are shown. Numbers are for the references as cited in the bibliography. PSI cont. and PSI Obsv. are the continuous and observer-based pulse injection for two different pulses duration (blue for 2ms and yellow for 1ms).

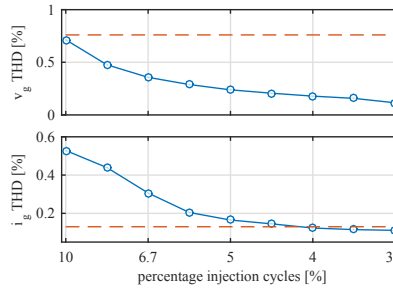


Fig. 11. THD comparison for the PSI observer-based method (blue) and the HFSI method (dashed red) as a function of the percentage of cycles in which the injection is applied. Top, voltage at the PCC. Bottom, grid current.

#### IV. RLS ALGORITHM IMPLEMENTATION

Measurement of the the grid impedance in real time requires an online estimation procedure. The existing literature approaches, as discussed before, rely on the injection of a voltage/current signal and measuring the resulting current/voltage [18], [28]; the use of the closed-loop current response for implementing a MRAS strategy [12]; or the use of observers

This is the author's version of an article that has been published in this journal. Changes were made to this version by the publisher prior to publication.  
The final version of record is available at <http://dx.doi.org/10.1109/TIE.2018.2801784>

or estimators [27]. In this paper, the estimation of the system parameters is carried out by using an RLS approach [24], [44]. For that purpose, the differential voltage equation for the equivalent grid impedance in the stationary reference frame is discretized using Tustin method. The stationary reference frame is selected for the estimation in order to enable the system to work under unbalanced grid impedance conditions.

In a stationary reference frame aligned with the spatial angle orientation of the impedance, each individual term contributing to the equivalent grid impedance as seen by the converter, i.e. cable impedance and loads, can be represented in matrix form by (8).

$$\mathbf{Z}_{\alpha\beta i} = \mathbf{R}_{\alpha\beta i} + \mathbf{j}\omega_e \mathbf{L}_{\alpha\beta i} = \begin{pmatrix} Z_{\alpha\alpha i} & Z_{\alpha\beta i} \\ Z_{\alpha\beta i} & Z_{\beta\beta i} \end{pmatrix} \quad (8)$$

In (8), the  $i$  subscript is related to each individual impedance seen from the PCC. When the impedance is balanced,  $Z_{\alpha\alpha i}$  equals  $Z_{\beta\beta i}$ . Non diagonal terms ( $Z_{\alpha\beta i}$ ) represent the cross coupling between phases. Rotating the impedance matrix to a common  $\alpha\beta$  reference frame and considering  $n$  impedance elements, leads to (9).

$$\mathbf{Z}_{\alpha\beta} = \sum_{i=1}^n \left[ \Sigma Z_i \begin{pmatrix} 1 & 0 \\ 0 & 1 \end{pmatrix} + \Delta Z_i \begin{pmatrix} \cos \theta_e^i & \sin \theta_e^i \\ \sin \theta_e^i & -\cos \theta_e^i \end{pmatrix} + Z_{\alpha\beta i} \begin{pmatrix} -\sin \theta_e^i & \cos \theta_e^i \\ \cos \theta_e^i & \sin \theta_e^i \end{pmatrix} \right] \quad (9)$$

where  $\Sigma Z_i = \frac{Z_{\alpha\alpha i} + Z_{\beta\beta i}}{2}$ ,  $\Delta Z_i = \frac{Z_{\alpha\alpha i} - Z_{\beta\beta i}}{2}$ , and  $\theta_e^i$  is the spatial angular phase of the unbalance impedance. For example, for single-phase loads at phases  $u$ ,  $v$ ,  $w$ ,  $\theta_e^i$  equals  $0$ ,  $2\pi/3$  or  $4\pi/3$  respectively. In the case the system is balanced, only the matrix terms depending on  $\Sigma Z_i$  will remain. The relationship with the phase impedances can be obtained by using the definitions:  $\Sigma Z_i = \frac{z_{a1} + z_{b1} + z_{c1}}{3}$  and  $\Delta Z_i = \frac{z_{a1} + a z_{b1} + a^2 z_{c1}}{3}$ , where  $a = e^{j2\pi/3}$ .

By considering the overall grid impedance dominated by the resistance and inductance terms, (9) can be expressed as (10).

$$\mathbf{Z}_{\alpha\beta} = \sum_{i=1}^n \left[ (\Sigma R_i + \mathbf{j}\omega_e \Sigma L_i) \begin{pmatrix} 1 & 0 \\ 0 & 1 \end{pmatrix} + (\Delta R_i + \mathbf{j}\omega_e \Delta L_i) \begin{pmatrix} \cos \theta_e^i & \sin \theta_e^i \\ \sin \theta_e^i & -\cos \theta_e^i \end{pmatrix} + (R_{\alpha\beta i} + \mathbf{j}\omega_e L_{\alpha\beta i}) \begin{pmatrix} -\sin \theta_e^i & \cos \theta_e^i \\ \cos \theta_e^i & \sin \theta_e^i \end{pmatrix} \right] \quad (10)$$

where,  $\Sigma R_i = \frac{R_{\alpha\alpha i} + R_{\beta\beta i}}{2}$ ,  $\Sigma L_i = \frac{L_{\alpha\alpha i} + L_{\beta\beta i}}{2}$ ,  $\Delta R_i = \frac{R_{\alpha\alpha i} - R_{\beta\beta i}}{2}$ ,  $\Delta L_i = \frac{L_{\alpha\alpha i} - L_{\beta\beta i}}{2}$ . From here, the voltage equation given by (11) can be obtained,

$$\mathbf{v}_{z_{eq}}^{\alpha\beta} = \mathbf{v}_g^{\alpha\beta} - \mathbf{v}_s^{\alpha\beta} = \mathbf{R}_{\alpha\beta} \mathbf{i}_g^{\alpha\beta} + \mathbf{L}_{\alpha\beta} \frac{d\mathbf{i}_g^{\alpha\beta}}{dt} \quad (11)$$

where  $\mathbf{v}_{z_{eq}}^{\alpha\beta}$  is the voltage drop vector across the overall equivalent impedance,  $\mathbf{v}_g^{\alpha\beta}$  and  $\mathbf{v}_s^{\alpha\beta}$  are the PCC voltage and the grid voltage vectors (see Fig. 1), and  $\mathbf{i}_g^{\alpha\beta}$  is the grid current vector.  $\mathbf{L}_{\alpha\beta}$  and  $\mathbf{R}_{\alpha\beta}$  are, respectively, the sum of the inductance and resistance matrices for the different grid impedances as expressed in (10).

In the proposed estimation method, it is assumed that the  $\mathbf{L}_{\alpha\beta}$  is constant at the different harmonic frequencies, being the grid impedance the only variable affected by frequency according to (8) [45]. This has been experimentally validated by injecting harmonic components in the grid and measuring the corresponding harmonic impedance by calculating the Fast Fourier Transform (FFT) of the voltages and grid currents at the different frequencies. The results are shown in Fig. 12. As it is clearly shown, the inductance term remains almost constant around  $L = 0.5\text{mH}$ , whereas the impedance is clearly increasing with frequency due to the inductive behavior of the grid at that frequencies. At this research, none of the following effects are considered regarding the inductance variation: 1) inductance variation with saturation due to the fundamental command when the converter fundamental current is decoupled from load variations, 2) variations due to parasitic effects such as skin, proximity, and parasitic capacitance effects and, 3) equivalent impedance in distribution grids dominated by active elements (power converters), being this last topic focus of attention of current research.

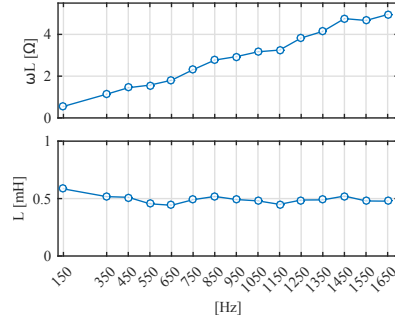


Fig. 12. Experimental results. Measurement of the harmonic impedance of the grid by injecting a distorted converter voltage. Voltages and currents at the PCC are measured and registered and the data is calculated in frequency domain. Sample rate is set to 1Ms/s and spectral resolution is set to 1Hz.

From (11), the discrete approximation for the grid current  $\alpha\beta$  components using Tustin method with a sampling period  $T_s$  can be expressed according to (12), (13).

$$i_g^{\alpha}[k] = a_1^{\alpha} \cdot i_g^{\alpha}[k-1] + a_2^{\alpha} \cdot i_g^{\beta}[k] + a_3^{\alpha} \cdot i_g^{\beta}[k-1] + b_0^{\alpha} (v_{\alpha}[k] + v_{\alpha}[k-1]) \quad (12)$$

$$i_g^{\beta}[k] = a_1^{\beta} \cdot i_g^{\beta}[k-1] + a_2^{\beta} \cdot i_g^{\alpha}[k] + a_3^{\beta} \cdot i_g^{\alpha}[k-1] + b_0^{\beta} (v_{\beta}[k] + v_{\beta}[k-1]) \quad (13)$$

where  $a_1^{\alpha} = \frac{\frac{2}{T_s} L_{\alpha\alpha} - R_{\alpha\alpha}}{\frac{2}{T_s} L_{\alpha\alpha} + R_{\alpha\alpha}}$ ,  $a_2^{\alpha} = -\frac{\frac{2}{T_s} L_{\alpha\beta} + R_{\alpha\beta}}{\frac{2}{T_s} L_{\alpha\alpha} + R_{\alpha\alpha}}$ ,  $a_3^{\alpha} = \frac{\frac{2}{T_s} L_{\alpha\beta} + R_{\alpha\beta}}{\frac{2}{T_s} L_{\alpha\alpha} + R_{\alpha\alpha}}$ ,  $b_0^{\alpha} = \frac{1}{\frac{2}{T_s} L_{\alpha\alpha} + R_{\alpha\alpha}}$ ,  $a_1^{\beta} = \frac{\frac{2}{T_s} L_{\beta\beta} - R_{\beta\beta}}{\frac{2}{T_s} L_{\beta\beta} + R_{\beta\beta}}$ ,  $a_2^{\beta} = -\frac{\frac{2}{T_s} L_{\beta\alpha} + R_{\beta\alpha}}{\frac{2}{T_s} L_{\beta\beta} + R_{\beta\beta}}$ ,  $a_3^{\beta} = \frac{\frac{2}{T_s} L_{\beta\alpha} + R_{\beta\alpha}}{\frac{2}{T_s} L_{\beta\beta} + R_{\beta\beta}}$ ,  $b_0^{\beta} = \frac{1}{\frac{2}{T_s} L_{\beta\beta} + R_{\beta\beta}}$  and  $v_{\alpha}$ ,  $v_{\beta}$  represent the components of the difference between the PCC and the grid voltages.

This is the author's version of an article that has been published in this journal. Changes were made to this version by the publisher prior to publication.  
The final version of record is available at <http://dx.doi.org/10.1109/TIE.2018.2801784>

From (12), (13) the values for the resistance and inductance terms can be obtained as (14).

$$\begin{aligned} R_{xx} &= \frac{1 - a_1^x}{2b_0^x}, & L_{xx} &= \frac{T_s}{4} \frac{1 + a_1^x}{b_0^x}, \\ R_{xy} &= -\frac{a_2^x + a_3^x}{2b_0^x}, & L_{xy} &= \frac{T_s}{4} \frac{a_3^x - a_2^x}{b_0^x} \end{aligned} \quad (14)$$

where  $x, y$  could be either  $\alpha$  or  $\beta$ .

The RLS algorithm will allow to estimate the resistances and inductances in (14) by determining the values of the coefficients  $a_i^x$  and  $b_j^x$ . The error driving the RLS update is obtained as the difference between the observed grid current,  $i_{g[k]}^x$ , as calculated by the observer, and the one estimated by the RLS algorithm,  $\hat{i}_{g[k]}^x$ . Decoupling of the unknown grid voltage,  $v_s^{\alpha\beta}$ , is achieved by only considering the current induced by the pulse injection. This is done by subtracting the fundamental current reference from the overall current. It is then assumed that the grid voltage is stiff enough to neglect any effect on it due to the injected pulses and thus it could be removed from the equation.

The least squares problem is formulated in recursive form using the equations (15)-(18). The system equations are represented by defining the variables and coefficients vectors,  $\mathbf{X}_{[k]}^x$ ,  $\mathbf{W}_{[k]}^x$ , as (19) and (20) respectively, where superscript  $x$  could be either  $\alpha$  or  $\beta$ . The estimated RLS current,  $\hat{i}_{g[k]}^x$ , is determined by the product  $\mathbf{W}_{[k-1]}^x \cdot \mathbf{X}_{[k]}^x$  in (15). All the variables names are referred to those shown in Fig. 1.

$$\alpha_{[k]}^x = i_{g[k]}^x - \mathbf{W}_{[k-1]}^x \cdot \mathbf{X}_{[k]}^x \quad (15)$$

$$\mathbf{g}_{[k]}^x = \mathbf{P}_{[k-1]}^x \cdot \mathbf{X}_{[k]}^x \cdot \left[ \lambda + \mathbf{X}_{[k]}^x T \cdot \mathbf{P}_{[k-1]}^x \cdot \mathbf{X}_{[k]}^x \right]^{-1} \quad (16)$$

$$\mathbf{P}_{[k]}^x = \lambda^{-1} \cdot \mathbf{P}_{[k-1]}^x - \mathbf{g}_{[k]}^x \cdot \mathbf{X}_{[k]}^x T \lambda^{-1} \cdot \mathbf{P}_{[k-1]}^x \quad (17)$$

$$\mathbf{W}_{[k]}^x = \mathbf{W}_{[k-1]}^x + \left( \alpha_{[k]}^x \cdot \mathbf{g}_{[k]}^x \right)^T \quad (18)$$

$$\mathbf{X}_{[k]}^x = \left[ i_{g[k-1]}^x, i_{g[k]}^x, i_{g[k-1]}^y, v_{g[k]}^x, v_{g[k-1]}^x \right]^T \quad (19)$$

$$\mathbf{W}_{[k]}^x = \left[ a_{1[k]}^x, a_{2[k]}^x, a_{3[k]}^x, b_{0[k]}^x, b_{0[k]}^x \right] \quad (20)$$

where  $\mathbf{P}_{(5 \times 5)}$  is the covariance matrix and it is initialized to  $\mathbf{P} = 0.01 \cdot \mathbf{I}_{(5 \times 5)}$ ;  $\mathbf{g}_{(5 \times 1)}$  is the adaptation gain, and  $\lambda = [0, 1]$  is the forgetting factor, which need to be selected as a tradeoff of the expected estimation bandwidth and the signal to noise ratio. Values between 0.95 and 1 are often selected. For this paper, the values shown in Table I have been used. After the injection of a new pulse, the estimation of the  $\mathbf{W}$  components for both the  $\alpha$  and the  $\beta$  components is updated and a new estimation for  $\mathbf{R}_{\alpha\beta}$  and  $\mathbf{L}_{\alpha\beta}$  is obtained using (14).

Regarding the computational burden of the proposed approach, the number of needed floating operations have been determined by using a Matlab based tool. A total of 632 floating operations (multiplications and additions) are needed. Considering the number of cycles for each floating point operation based on a TMS320F28335 controller with a 150Mhz clock, it leads to a computational time lower than 20 $\mu$ s. Thus, it is considered that the implementation is feasible and fast enough on medium performance digital signal controllers.

TABLE I  
PARAMETERS

Nominal parameters	Value (Setup#1/Setup#2)
$r_1$ [ $\Omega$ ]	0.2/0.2
$r_2$ [ $\Omega$ ]	0.2/0.2
$L_1$ [mH]	2.3/7
$L_2$ [mH]	0.93/7
$C$ [ $\mu$ F]	10/6
pulse mag. [p.u]	0.1/0
pulse width. [ms]	1/2
$\lambda$	0.9/0.8
$Z_{base}$ [ $\Omega$ ] (150kVA, 400V)	1.85
$L_{base}$ [mH]	6

## V. SIMULATION AND EXPERIMENTAL RESULTS

In order to illustrate the performance of the method under different balanced and unbalanced conditions, the simulation shown in Fig. 13 has been carried out. Different RL impedances have been connected in series between the output of the converter and the grid. Additionally, a balanced resistive load has been connected in parallel to the converter output. Every 0.1s, a transient is generated, changing the equivalent grid impedance. At  $t = 0.5s$ , an unbalance on the series impedance in phase- $a$  is induced. At  $t = 0.7s$ , phase- $a$  resistive load is reduced by 25%. Fast convergence and detection of asymmetries in the  $\alpha$  and  $\beta$  components are shown. Phase voltages at the PCC and estimated grid-side currents during the load transient are shown in Fig. 14. As clearly shown, the injection of the  $q$ -axis pulses is reflected at the PCC phase voltages and, consequently, at the estimated grid-side currents.

Experimental results were obtained using a PM15F42C power module from Triphase. The power module is interfaced to the AC grid through a LCL filter, which parameters are listed in Table I under Setup#1. Rated power of the converter is 15kVA, switching frequency is 8kHz. The converter is coupled directly to the grid, without an isolation transformer. In Table I,  $L_1$  and  $L_2$  are the converter side and the grid side inductances respectively. For the experiments carried out, the  $L_2$  inductance is bypassed and the voltage is measured at the filter capacitor. The power converter running the RLS algorithm is connected to the grid by a set of different impedances, with inductance  $[0.5, 1, 2.5]$ mH ( $[0.0833, 0.1667, 0.4167]$ p.u) and resistance  $[0.2, 0.15, 0.15]$  $\Omega$  ( $[0.1083, 0.0812, 0.0812]$ p.u). A 10 $\Omega$  three-phase balanced resistive load is connected in parallel to the converter output. A picture for the experimental setup can be seen in Fig. 15. In order to check the accuracy of the method under a controlled environment, initial results have been obtained by disconnecting the grid and interfacing the converter to a balanced resistive load while varying the series impedance.

Results for the estimated parameters during several transient conditions are shown in Fig. 16. As it can be seen, the estimated parameters are in close agreement with the actual impedance values. The unbalance condition is introduced between  $t = 5s$  and  $t = 15s$  by varying the series impedance at phase  $a$ , which is reflected into different values for the diagonal terms in the  $\mathbf{Z}_{\alpha\beta}$  matrix, as predicted by the theoretical analysis. The value for the connected parallel resistive

This is the author's version of an article that has been published in this journal. Changes were made to this version by the publisher prior to publication.  
The final version of record is available at <http://dx.doi.org/10.1109/TIE.2018.2801784>

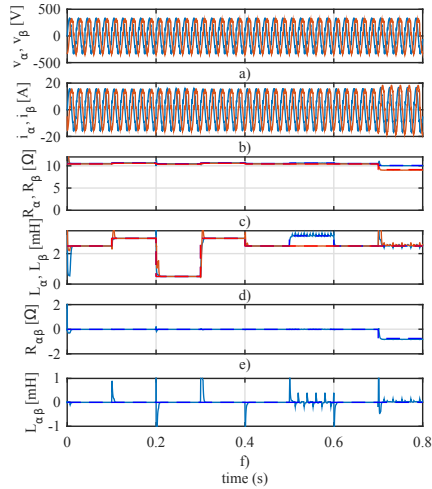


Fig. 13. Simulation results. Transient response. From top to bottom: a)  $v_{\alpha}, v_{\beta}$ . b)  $i_{\alpha}, i_{\beta}$ . c), d)  $R_{\alpha\alpha}, R_{\beta\beta}$ . and  $L_{\alpha\alpha}, L_{\beta\beta}$  components for the matrices at the  $\alpha\beta$  reference frame. e) and f), the corresponding out-diagonal  $R_{\alpha\beta}$  and  $L_{\alpha\beta}$ . Every 0.1s a new condition is evaluated by varying the equivalent phase resistances and inductances using the following sequence:  
 $R_a = [10.55, 10.7, 10.5, 10.7, 10.55, 10.7, 10.55, 10.55]\Omega$ ,  
 $L_a = [2.5, 3, 0.5, 3.0, 2.5, 3.5, 2.5, 2.5]mH$ ,  
 $R_b = [10.5, 10.6, 10.4, 10.6, 10.5, 10.5, 10.5, 10.5]\Omega$ ,  
 $L_b = [2.5, 3, 0.5, 3.0, 2.5, 2.5, 2.5, 2.5]mH$ ,  $R_c = [10.4, 10.55, 10.35, 10.55, 10.4, 10.4, 10.4, 7.85]\Omega$ ,  $L_c = [2.5, 3, 0.5, 3.0, 2.5, 3.5, 2.5, 2.5]mH$ .  $L_{base} = 6mH$ ,  $R_{base} = 1.85\Omega$ .

load is also accurately determined, being the small variations on the resistance terms due to the changes of the associated inductance series resistances. The injected pulses in the  $\alpha\beta$  reference frame as well as the real and estimated currents are shown in Fig. 17. A good match between both signals can be observed.

Finally, experimental results with a grid-tied converter have been obtained. The method is tested with two different levels of reactive current,  $i_q = [0, 2.5]A$ . The commanded value of the fundamental current has been kept at low level compared to the converter rated current (30A) in order to analyze the performance of the current control when the pulses are injected. The grid voltages in Fig. 18 show a noticeable harmonic content, which will allow to demonstrate the operation of the method under distorted grid conditions. In Fig. 18, the grid voltages at the instant the three pulses are injected following a change in the impedance are shown. The effect of the pulse injection over the grid voltage is clearly visible, as well as the effect in the grid-side current.

Before the RLS estimation, the grid voltage and the fundamental current are online decoupled. For the case of the voltage, the average value of the  $v_d$  and  $v_q$  components is subtracted. Being the pulse magnitude centered at zero, it does not affect the average value and thus the contribution

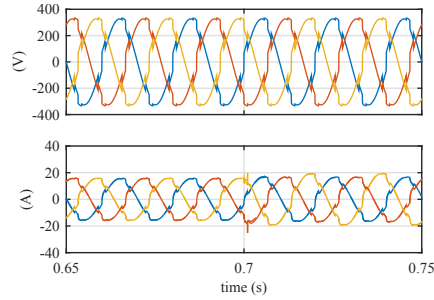


Fig. 14. Simulation results. Transient response. On top the injected voltages by the converter at the PCC, on bottom the corresponding currents. The waveforms correspond to the same conditions explained in Fig. 13. At  $t = 0.7s$  the load transient causes an unbalanced condition.

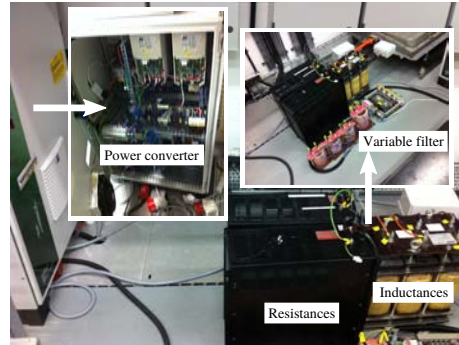


Fig. 15. Experimental setup. Photo for the Setup#1 described in Table I. Left-side, a picture for the PM15F42C power module, at the right, a set of inductances used for the variable grid impedance, as well as the resistive loads.

of the grid can be easily removed. The resulting signal is rotated back to the stationary reference frame to be used in the estimation procedure. For the current signal, the current reference is subtracted from the overall current. Fig. 19 shows the estimation of the grid impedance during two different transients. The impedance values are filtered with a 5Hz low pass filter to remove the high frequency noise affecting the  $a_i$  and  $b_j$  values. As shown, the convergence of the method is really fast, arriving to the final value just after the injection of the last pulse.

## VI. CONCLUSION

This paper has proposed the use of a RLS based technique to online estimate the grid impedance with a moderate computational burden. The proposed system is triggered from the error signal coming from a Luenberger observer used for the control of the grid current in a LCL filter. The triggering scheme avoids the continuous injection of pulses, thus improving the

This is the author's version of an article that has been published in this journal. Changes were made to this version by the publisher prior to publication.  
The final version of record is available at <http://dx.doi.org/10.1109/TIE.2018.2801784>

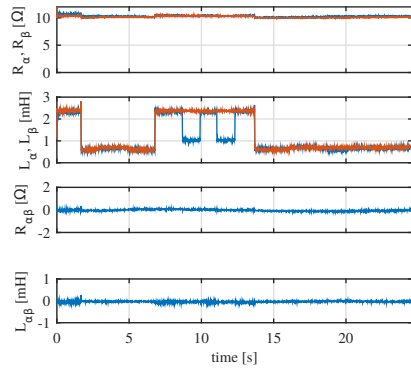


Fig. 16. Experimental results. Transient response of the RLS algorithm. From bottom to top: a), b) the diagonal terms for the  $R_{\alpha\alpha}, R_{\beta\beta}$  and  $L_{\alpha\alpha}, L_{\beta\beta}$  matrices at the  $\alpha\beta$  reference frame are shown, c), d) the corresponding out-diagonal  $R_{\alpha\beta}$  and  $L_{\alpha\beta}$ . A change is introduced into the series impedance connected to phase  $a$  from 2.5mH to 0.5mH ([0.4167, 0.0833]p.u.) The small variations on the resistance terms correspond to the resistive changes due to the connection/disconnection of the inductances.

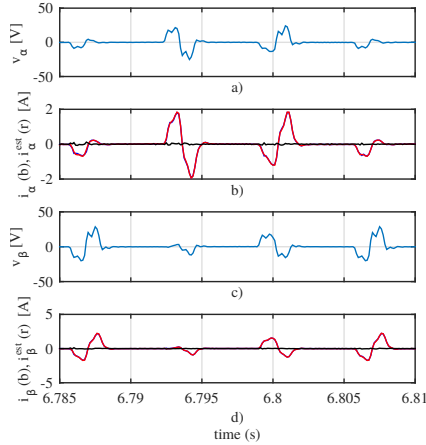


Fig. 17. Experimental results. Transient response of the RLS algorithm. a) and c) show a zoom on the injected pulses, whereas b) and d) show the corresponding grid-side current response. In b) and c) the measured and estimated current components are depicted in blue and red. Estimation error is depicted in black.

efficiency and the THD compared to other approaches relying on signal injection. The observer and the estimation method have been tested through simulation and experimental results. Different methods for the signal injection have been compared and the  $q$ -axis injection in the synchronous reference frame has been finally selected for an increased sensitivity. The RLS algorithm is implemented in the  $\alpha\beta$  reference frame to

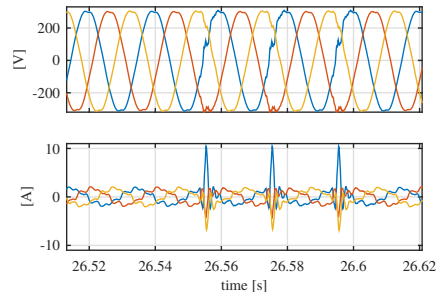


Fig. 18. Experimental results. Injection of the pulses when the power converter is connected to the grid. The upper graph shows the grid voltages and the lower one the corresponding grid currents. The converter was operated with a fundamental current command  $i_q = 2.5A$ .

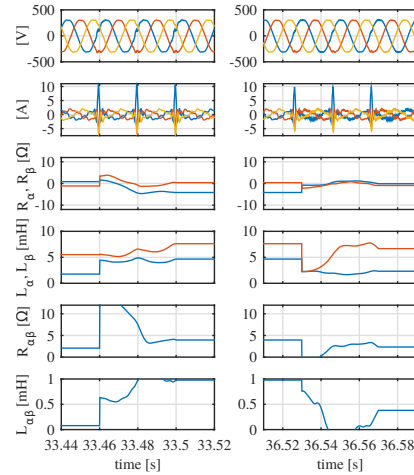


Fig. 19. Experimental results. RLS results with the converter interfaced to the grid. From top to bottom: a) voltages at the filter capacitor. b) grid currents. c)  $R_{\alpha}, R_{\beta}$ . d)  $L_{\alpha}, L_{\beta}$ . e)  $R_{\alpha\beta}$ . f)  $L_{\alpha\beta}$ . The converter is current controlled with a reference  $i_q^* = 2.5A$ .

enable the operation both under balanced and unbalanced grid conditions. The proposed system is a suitable method for a different number of applications, including adaptive control, islanding detection and fault detection.

REFERENCES

[1] H. Xiao, X. Qu, S. Xie, and J. Xu, "Synthesis of active damping for grid-connected inverters with an LCL filter," in *2012 IEEE Energy Conversion Congress and Exposition (ECCE)*, Sep. 2012, pp. 550-556.  
[2] J. Xu, S. Xie, and T. Tang, "Active Damping-Based Control for Grid-Connected-Filtered Inverter With Injected Grid Current Feedback Only," *IEEE Transactions on Industrial Electronics*, vol. 61, no. 9, pp. 4746-4758, Sep. 2014.

This is the author's version of an article that has been published in this journal. Changes were made to this version by the publisher prior to publication.  
The final version of record is available at <http://dx.doi.org/10.1109/TIE.2018.2801784>

- [3] J. He and Y. W. Li, "Generalized closed-loop control schemes with embedded virtual impedances for voltage source converters with lcl filters," *IEEE Transactions on Power Electronics*, vol. 27, no. 4, pp. 1850–1861, April 2012.
- [4] P. C. Loh and D. G. Holmes, "Analysis of multiloop control strategies for lcl/lcl-filtered voltage-source and current-source inverters," *IEEE Transactions on Industry Applications*, vol. 41, no. 2, pp. 644–654, March 2005.
- [5] W. Yao, M. Chen, J. Matas, J. Guerrero, and Z.-m. Qian, "Design and Analysis of the Droop Control Method for Parallel Inverters Considering the Impact of the Complex Impedance on the Power Sharing," *IEEE Transactions on Industrial Electronics*, vol. 58, no. 2, pp. 576–588, 2011.
- [6] J. He, Y. W. Li, J. Guerrero, F. Blaabjerg, and J. Vasquez, "An Islanding Microgrid Power Sharing Approach Using Enhanced Virtual Impedance Control Scheme," *IEEE Transactions on Power Electronics*, vol. 28, no. 11, pp. 5272–5282, 2013.
- [7] M. Sumner, B. Palethorpe, and D. Thomas, "Impedance measurement for improved power quality-Part 2: a new technique for stand-alone active shunt filter control," *IEEE Transactions on Power Delivery*, vol. 19, no. 3, pp. 1457–1463, 2004.
- [8] J. Massing, M. Stefanello, H. Grundling, and H. Pinheiro, "Adaptive Current Control for Grid-Connected Converters With LCL Filter," *IEEE Transactions on Industrial Electronics*, vol. 59, no. 12, pp. 4681–4693, 2012.
- [9] Z. Staroszczyk, "A method for real-time, wide-band identification of the source impedance in power systems," *IEEE Transactions on Instrumentation and Measurement*, vol. 54, no. 1, pp. 377–385, Feb 2005.
- [10] M. Sumner, B. Palethorpe, D. W. P. Thomas, P. Zanchetta, and M. C. D. Piazza, "A technique for power supply harmonic impedance estimation using a controlled voltage disturbance," *IEEE Transactions on Power Electronics*, vol. 17, no. 2, pp. 207–215, Mar 2002.
- [11] M. Liserre, F. Blaabjerg, and R. Teodorescu, "Grid Impedance Estimation via Excitation of LCL-Filter Resonance," *IEEE Transactions on Industry Applications*, vol. 43, no. 5, pp. 1401–1407, 2007.
- [12] A. Vidal, A. G. Yepes, F. D. Freijedo, O. López, J. Malvar, F. Baneira, and J. Doval-Gandoy, "A method for identification of the equivalent inductance and resistance in the plant model of current-controlled grid-tied converters," *IEEE Transactions on Power Electronics*, vol. 30, no. 12, pp. 7245–7261, Dec 2015.
- [13] A. K. Broen, M. Amin, E. Skjong, and M. Molinas, "Instantaneous frequency tracking of harmonic distortions for grid impedance identification based on kalman filtering," in *2016 IEEE 17th Workshop on Control and Modeling for Power Electronics (COMPEL)*, June 2016, pp. 1–7.
- [14] A. Bechouche, D. O. Abdeslam, H. Seddiki, and A. Rahoui, "Estimation of equivalent inductance and resistance for adaptive control of three-phase pwm rectifiers," in *IECON 2016 - 42nd Annual Conference of the IEEE Industrial Electronics Society*, Oct 2016, pp. 1336–1341.
- [15] A. Ghanem, M. Rashed, M. Sumner, M. A. Elsayes, and I. I. I. Mansy, "Grid impedance estimation for islanding detection and adaptive control of converters," *IET Power Electronics*, vol. 10, no. 11, pp. 1279–1288, 2017.
- [16] D. Martin and E. Santi, "Auto tuning of digital deadbeat current controller for grid tied inverters using wide bandwidth impedance identification," in *2012 Twenty-Seventh Annual IEEE Applied Power Electronics Conference and Exposition (APEC)*, 2012, pp. 277–284.
- [17] L. Asiminoaei, R. Teodorescu, F. Blaabjerg, and U. Borup, "A digital controlled PV-inverter with grid impedance estimation for ENS detection," *IEEE Transactions on Power Electronics*, vol. 20, no. 6, pp. 1480–1490, 2005.
- [18] D. Reigosa, F. Briz, C. Charro, P. Garcia, and J. Guerrero, "Active Islanding Detection Using High-Frequency Signal Injection," *IEEE Transactions on Industry Applications*, vol. 48, no. 5, pp. 1588–1597, 2012.
- [19] D. Reigosa, F. Briz, C. Blanco, P. Garcia, and J. Manuel Guerrero, "Active Islanding Detection for Multiple Parallel-Connected Inverter-Based Distributed Generators Using High-Frequency Signal Injection," *IEEE Transactions on Power Electronics*, vol. 29, no. 3, pp. 1192–1199, 2014.
- [20] L. Asiminoaei, R. Teodorescu, F. Blaabjerg, and U. Borup, "A digital controlled pv-inverter with grid impedance estimation for ens detection," *IEEE Transactions on Power Electronics*, vol. 20, no. 6, pp. 1480–1490, Nov 2005.
- [21] T. Roinila, M. Viikko, and J. Sun, "Online grid impedance measurement using discrete-interval binary sequence injection," in *2013 IEEE 14th Workshop on Control and Modeling for Power Electronics (COMPEL)*, June 2013, pp. 1–8.
- [22] M. Cespedes and J. Sun, "Three-phase impedance measurement for system stability analysis," in *2013 IEEE 14th Workshop on Control and Modeling for Power Electronics (COMPEL)*, June 2013, pp. 1–6.
- [23] M. A. Azzouz and E. F. El-Saadany, "Multivariable grid admittance identification for impedance stabilization of active distribution networks," *IEEE Transactions on Smart Grid*, vol. 8, no. 3, pp. 1116–1128, May 2017.
- [24] M. Cespedes and J. Sun, "Adaptive control of grid-connected inverters based on online grid impedance measurements," *IEEE Transactions on Sustainable Energy*, vol. 5, no. 2, pp. 516–523, April 2014.
- [25] M. Cespedes and J. Sun, "Online grid impedance identification for adaptive control of grid-connected inverters," in *2012 IEEE Energy Conversion Congress and Exposition (ECCE)*, Sept 2012, pp. 914–921.
- [26] M. Sumner, B. Palethorpe, and D. Thomas, "Impedance measurement for improved power quality-Part 1: the measurement technique," *IEEE Transactions on Power Delivery*, vol. 19, no. 3, pp. 1442–1448, 2004.
- [27] N. Hoffmann and F. Fuchs, "Minimal Invasive Equivalent Grid Impedance Estimation in Inductive  $\pi$ -Resistive Power Networks Using Extended Kalman Filter," *IEEE Transactions on Power Electronics*, vol. 29, no. 2, pp. 631–641, 2014.
- [28] X. Guo, Z. Lu, X. Sun, H. Gu, and W. Wu, "New grid impedance estimation technique for grid-connected power converters," *Journal of Engineering Research*, vol. 2, no. 3, p. 19, 2014. [Online]. Available: <http://dx.doi.org/10.7603/s40632-014-0019-7>
- [29] L. Asiminoaei, R. Teodorescu, F. Blaabjerg, and U. Borup, "Implementation and Test of an Online Embedded Grid Impedance Estimation Technique for PV Inverters," *IEEE Transactions on Industrial Electronics*, vol. 52, no. 4, pp. 1136–1144, 2005.
- [30] A. Timbus, P. Rodriguez, R. Teodorescu, and M. Ciobotaru, "Line Impedance Estimation Using Active and Reactive Power Variations," in *IEEE Power Electronics Specialists Conference, 2007. PESC 2007*, 2007, pp. 1273–1279.
- [31] A. Riccobono, S. K. A. Naqvi, A. Monti, T. Caldognetto, J. Siegers, and E. Santi, "Online wideband identification of single-phase ac power grid impedances using an existing grid-tied power electronic inverter," in *2015 IEEE 6th International Symposium on Power Electronics for Distributed Generation Systems (PEDG)*, June 2015, pp. 1–8.
- [32] T. Roinila, T. Messo, and A. Aapro, "Impedance measurement of three phase systems in dq-domain: Applying mimo-identification techniques," in *2016 IEEE Energy Conversion Congress and Exposition (ECCE)*, Sept 2016, pp. 1–6.
- [33] M. Liserre, F. Blaabjerg, and S. Hansen, "Design and control of an LCL-filter-based three-phase active rectifier," *IEEE Transactions on Industry Applications*, vol. 41, no. 5, pp. 1281–1291, Sep. 2005.
- [34] D. Wojciechowski, "Novel predictive control of 3-phase LCL-based active power filter," in *Compatibility and Power Electronics, 2009. CPE '09*, May 2009, pp. 298–305.
- [35] J. Dannehl, M. Liserre, and F. Fuchs, "Filter-Based Active Damping of Voltage Source Converters With Filter," *IEEE Transactions on Industrial Electronics*, vol. 58, no. 8, pp. 3623–3633, Aug. 2011.
- [36] M. Liserre, A. Aquila, and F. Blaabjerg, "Genetic algorithm-based design of the active damping for an LCL-filter three-phase active rectifier," *IEEE Transactions on Power Electronics*, vol. 19, no. 1, pp. 76–86, Jan. 2004.
- [37] S. Zhang, S. Jiang, X. Lu, B. Ge, and F. Z. Peng, "Resonance Issues and Damping Techniques for Grid-Connected Inverters With Long Transmission Cable," *IEEE Transactions on Power Electronics*, vol. 29, no. 1, pp. 110–120, Jan. 2014.
- [38] R. Pena-Alzola, M. Liserre, F. Blaabjerg, R. Sebastian, J. Dannehl, and F. Fuchs, "Systematic Design of the Lead-Lag Network Method for Active Damping in LCL-Filter Based Three Phase Converters," *IEEE Transactions on Industrial Informatics*, vol. 10, no. 1, pp. 43–52, Feb. 2014.
- [39] F. Huerta, E. Bueno, S. Cobreces, F. Rodriguez, and C. Giron, "Control of grid-connected voltage source converters with LCL filter using a Linear Quadratic servocontroller with state estimator," in *IEEE Power Electronics Specialists Conference, 2008. PESC 2008*, June 2008, pp. 3794–3800.
- [40] M. Malinowski and S. Bernet, "A Simple Voltage Sensorless Active Damping Scheme for Three-Phase PWM Converters With an Filter," *IEEE Transactions on Industrial Electronics*, vol. 55, no. 4, pp. 1876–1880, Apr. 2008.
- [41] P. Garcia, J. M. Guerrero, J. Garcia, A. Navarro-Rodríguez, and M. Sumner, "Low frequency signal injection for grid impedance estimation in three phase systems," in *2014 IEEE Energy Conversion Congress and Exposition (ECCE)*, Sept 2014, pp. 1542–1549.

This is the author's version of an article that has been published in this journal. Changes were made to this version by the publisher prior to publication.  
The final version of record is available at <http://dx.doi.org/10.1109/TIE.2018.2801784>

- [42] J. Kukkola, M. Hinkkanen, and K. Zenger, "Observer-Based State-Space Current Controller for a Grid Converter Equipped With an LCL Filter: Analytical Method for Direct Discrete-Time Design," *Industry Applications, IEEE Transactions on*, vol. PP, no. 99, pp. 1–1, 2015.
- [43] C. A. Busada, S. G. Jorge, and J. A. Solsona, "Full-state feedback equivalent controller for active damping in lcl-filtered grid-connected inverters using a reduced number of sensors," *IEEE Transactions on Industrial Electronics*, vol. 62, no. 10, pp. 5993–6002, Oct 2015.
- [44] A. Arriagada, J. Espinoza, J. Rodriguez, and L. Moran, "On-line filtering reactance identification in voltage-source three-phase active-front-end rectifiers," in *The 29th Annual Conference of the IEEE Industrial Electronics Society, 2003. IECON '03*, vol. 1, Nov. 2003, pp. 192–197 vol.1.
- [45] F. Briz, P. García, M. W. Degner, D. Díaz-Reigosa, and J. M. Guerrero, "Dynamic behavior of current controllers for selective harmonic compensation in three-phase active power filters," *IEEE Transactions on Industry Applications*, vol. 49, no. 3, pp. 1411–1420, May 2013.



**Ángel Navarro-Rodríguez** (S'15) received the B.Sc. degree in telecommunications engineering with honors from the University of Castilla La-Mancha, Spain in 2012 and the M.Sc. degree in Electrical Energy Conversion and Power Systems from the University of Oviedo, Gijón, Spain in 2014. Nowadays he is Ph.D student in the Department of Electrical, Computer, and Systems Engineering in the University of Oviedo, granted by the government of Principado de Asturias.

He is part of the LEMUR research team in University of Oviedo since 2014 and his research interests include Energy Storage Systems, Control Systems, Electronics, Power Electronic Converters, Microgrids, power quality and Renewable Energies.



**Pablo García** (S'01-A'06-M'09) received the M.S. and Ph.D. degrees in electrical engineering and control from the University of Oviedo, Gijón, Spain, in 2001 and 2006, respectively. In 2004, he was a Visitor Scholar at the University of Madison-Wisconsin, Madison, WI, USA, Electric Machines and Power Electronics Consortium. In 2013 he was a visiting scholar at The University of Nottingham, UK.

He is the co-author of more than 20 IEEE journals and 50 international conferences. He is currently an Associate Professor within the Department of Electrical, Electronics, Computer, and Systems Engineering at the University of Oviedo. His research interests include control of grid-tied converters, parameter estimation, energy conversion, AC drives, sensorless control, AC machines diagnostics and signal processing.



**Juan M. Guerrero** (S'00-A'01-M'04) received the M.E. degree in industrial engineering and the Ph.D. degree in Electrical and Electronic Engineering from the University of Oviedo, Gijón, Spain, in 1998 and 2003, respectively.

Since 1999, he has occupied different teaching and research positions with the Department of Electrical, Computer and Systems Engineering, University of Oviedo, where he is currently an Associate Professor. From February to October 2002, he was a Visiting Scholar at the

University of Wisconsin, Madison. From June to December 2007, he was a Visiting Professor at the Tennessee Technological University, Cookeville. His research interests include control of electric drives and power converters, smart grids and renewable energy generation.

Dr. Guerrero received an award from the College of Engineers of Asturias and León, Spain, for his M.E. thesis in 1999, four IEEE Industry Applications Society Conference Prize Paper Awards, and the University of Oviedo Outstanding Ph.D. Thesis Award in 2004.



**Mark Sumner** (M'92-SM'05) Mark Sumner received the B.Eng degree in Electrical and Electronic Engineering from Leeds University in 1986 and then worked for Rolls Royce Ltd in Ansty, UK. Moving to the University of Nottingham, he completed his PhD in induction motor drives in 1990, and after working as a research assistant, was appointed Lecturer in October 1992. He is now Professor of Electrical Energy Systems.

His research interests cover control of power electronic systems including sensorless motor drives, diagnostics and prognostics for drive systems, power electronics for enhanced power quality and novel power system fault location strategies.



**Jorge García** (S'01-M'05-SM'11), received the M.Sc. and Ph.D. degrees in electrical engineering from the University of Oviedo, Asturias, Spain, in 2000 and 2003, respectively. In December 1999, he joined the Electrical and Electronic Engineering Department of the University of Oviedo, where he is currently an Associate Professor. He works with the LEMUR research team; his current research interests include power electronics and control for industrial, grid support and lighting applications. Dr.

García is co-author of more than 40 journal papers and more than 80 international conference papers in power and industrial electronics.



## C.4 Predictive Frequency-Based Sequence Estimator for Control of Grid-Tied Converters Under Highly Distorted Conditions

C. B. Charro, P. García-Fernandez, Á. Navarro-Rodríguez and M. Sumner, "Predictive Frequency-Based Sequence Estimator for Control of Grid-Tied Converters Under Highly Distorted Conditions," in *IEEE Transactions on Industry Applications*, vol. 54, no. 5, pp. 5306-5317, Sept.-Oct. 2018. doi: 10.1109/TIA.2018.2846552.



This is the author's version of an article that has been published in this journal. Changes were made to this version by the publisher prior to publication.  
The final version of record is available at <http://dx.doi.org/10.1109/TIA.2018.2846552>

1

## Predictive frequency-based sequence estimator for control of grid-tied converters under highly distorted conditions

Cristian Blanco\*, Pablo García\*, Ángel Navarro-Rodríguez\*, and Mark Sumner†

\*University of Oviedo. Dept. of Elec., Computer & System Engineering  
Gijón, 33204, Spain

e-mail: blancocristian@uniovi.es, garciafpablo@uniovi.es, navarroangel@uniovi.es  
†The University of Nottingham. Department of Electrical and Electronic Engineering  
University Park, Nottingham. NG7 2RD, UK  
e-mail: Mark.Sumner@nottingham.ac.uk

**Abstract**—This paper proposes a novel frequency-based predictive sequence estimator that allows for the isolation of voltages and currents harmonic components needed for the control of grid-tied converters. The proposed method relies on an enhanced Sliding Goertzel Transformation (SGT) by adding a predictive estimator with a prediction horizon equal to the SGT processing window. The performance of the proposed method is compared with the well-established DSOGI alternative, proving a higher estimation bandwidth as well as improved immunity to changes in the magnitude, frequency and phase of the tracked signals. Additionally, the close-loop performance in a current-controlled grid-tied inverter using the proposed sequence extractor is analyzed. The presented results allow to quantitatively measure the estimator impact over the power converter performance in a real application.

### I. INTRODUCTION

Distributed power generation (DPG) is expected to play an important role in the short and medium term design of the electricity generation, transmission and distribution systems. This is due to the increasing penetration of renewable generation units at distribution level which must also provide ancillary services such as harmonic compensation [1] and magnitude and frequency restoration [2]. DPG systems based on renewable generation can help to decrease CO<sub>2</sub> emissions since the DPG units are placed near to where the power is consumed. On the other hand, the use of DPG increases the complexity of the whole system due to the coexistence of several systems with different characteristics (nominal power, output impedance, duty cycle, transient response...)

DPG units are usually connected to the utility grid by using electronic power converters (mainly PWM voltage source inverters, (VSI) [3], [4]). VSI control strategies are mainly composed of an inner current control loop, an outer voltage

control loop and an external power control loop [5] usually based on proportional-integral (PI [3], [4]) or proportional-resonant (PRES [5]) controllers. To perform an accurate control of the fundamental component of the current, voltage or power, the use of PI and PRES controllers requires the estimation of the magnitude, frequency and phase of the fundamental component of the utility grid. Furthermore, if harmonic content is present in the grid voltage or current, the estimation of frequency, phase and magnitude for these additional harmonics is a desirable feature. This, combined with suitable synchronization methods, has been the focus of much research over recent years. In this regard, the utility grid voltage may be polluted with harmonic components (due to the use of nonlinear loads) or unbalanced conditions (due to single-phase loads) and therefore the utility grid magnitude and frequency may vary between values defined in the grid codes as load conditions change. Phase jumps may also occur and also grid voltage measurements may be incorrect, especially with respect to the DC components, due to the used voltage sensors [6]. The VSI control is required to be fast and accurate under all of these polluted conditions, being the synchronization technique a key feature of the DPG control.

Synchronization techniques can be divided into two categories: open-loop [7], [8] or closed-loop [9]–[14]. Open-loop methods estimate the PCC voltage magnitude, frequency and phase without any feedback while closed-loop methods are based on locking one characteristic of the input signal, e.g. the frequency (frequency-locked-loop, FLL [9]) or phase (phase-locked-loop, PLL [11]). Closed-loop techniques are preferred as they tend to have better performance. However, most techniques are challenged by grid disturbances (mainly additional harmonics), which can affect parameter estimation. One possible solution is to reduce the closed-loop controller bandwidth. However, this is at the price of a degradation in transient response, which is not an acceptable solution in most applications. Alternatively, a filtering stage can be implemented – pre-filter and filter in the loop techniques are the most acceptable solutions [12].

A pre-filter stage feeds the closed-loop method with a

The present work has been partially supported by the predoctoral grants program Severo Ochoa for the formation in research and university teaching of Principado de Asturias PCTI-FICYT under the grant ID BP14-135. This work also was supported in part by the Research, Technological Development and Innovation Program Oriented to the Society Challenges of the Spanish Ministry of Economy and Competitiveness under grant ENE2016-77919-R and by the European Union through ERFD Structural Funds (FEDER).

This is the author's version of an article that has been published in this journal. Changes were made to this version by the publisher prior to publication.  
The final version of record is available at <http://dx.doi.org/10.1109/TIA.2018.2846552>

2

filtered version of the grid voltage that contains only the fundamental component. DSOGI-FLL [9], MCCF-PLL [13], DSOGI-PLL [10], or CCCF-PLL [14] are examples of pre-filter stage methods. Filter in the loop techniques, [12], [15], remove the unwanted effects of harmonics and unbalances within the closed loop. In both cases, filters can be implemented by using second-order generalized integrators [9], [10], notch filters [12], complex-coefficient filters [13], [14], lead compensator [15] or moving average filters [16].

When using filtering stages, some aspects must be carefully considered: filters introduce phase delays that must be estimated and compensated in real time [17]; transient response is impaired [6]; filters need to adapt their central frequency during frequency deviations [13] and magnitude and phase jumps affect the estimation of frequency, magnitude and phase [12]. In order to deal with these drawbacks, this paper proposes the use of a sliding method in frequency domain, known as the sliding Goertzel transform (SGT) [18]–[20], to estimate the fundamental and harmonic components of the utility grid.

This paper expands on the work presented in [21] to include 1) a more detailed theoretical derivation, 2) an improved signal processing algorithm and 3) more extensive experimental results to validate the proposed technologies. Predictive techniques are proposed to boost the SGT transient response while a wide frequency resolution is used to compute the algorithm, increasing the system robustness to frequency variations. Experimental verification is provided to test the proposed method performance for different grid disturbances, including magnitude changes, frequency deviations, the presence of harmonic components and phase jumps. The paper is organized as follows: in section II, the mathematical approach based on the SGT algorithm is explained. Following, in section III, the proposed predictive algorithm is introduced, including simulation results to demonstrate its effectiveness. In III-A, the use of a fusion method for an estimation based both on the sliding implementation and on the predictive proposal is included. Section III-B describes the proposed method for the frequency estimation and the impact of frequency variation on the estimation of the voltage magnitude and phase. In section IV, the evaluation of the method using a programmable voltage supply is included. Finally, in V, the experimental results with a grid-tied converter are included, thus validating the approach of the proposed method.

## II. GOERTZEL ALGORITHM ANALYSIS

The basics of the proposed method rely on an efficient implementation of the Discrete Fourier Transform (DFT) by using the sliding Goertzel implementation [22], suitable for the extraction of harmonic components in real-time applications. The implementation has a lower computational burden when compared with traditional FFT-based approach for a low number of harmonics. Specifically, for calculating  $M$  harmonics from an input data vector of length  $N$ , the associated cost of the Goertzel algorithm can be expressed as  $O(N, M)$ , whereas for the FFT is  $O(N, \log_2 N)$ . Obviously, when the number of calculated harmonics meets  $M \leq \log_2 N$ , then the Goertzel approximation is the preferred choice. In this paper,

### Algorithm 1 Goertzel and SGT algorithm implementation.

```

1:  $f_{bin} \leftarrow 2\pi h/N$ 
2:  $a_f \leftarrow 2 \cos(f_{bin})$ 
3:  $b_f \leftarrow e^{-j f_{bin}}$ 
4: for  $h \leftarrow 1, \text{number of elements in } f_{bin}$  (harmonics) do
5:   for  $n \leftarrow 1, N - 1$  do
6:      $s_h(h, n) = x(n) - x(n - N) + a_f(h) \cdot s_h(h, n - 1) - s_h(h, n - 2)$ 
7:      $y(h, n) = (s_h(h, n) - s_h(h, n - 1) \cdot b_f(h))/N$ 
8:      $s_h(h, n - 2) = s_h(h, n - 1)$ 
9:      $s_h(h, n - 1) = s_h(h, n)$ 
10:   end for
11:    $s_h(h, n) = a_f(h) \cdot s_h(h, n - 1) - s_h(h, n - 2)$ 
12:    $y(h, N) = (s_h(h, n) - s_h(h, n - 1) \cdot b_f(h))/N$ 
13: end for

```

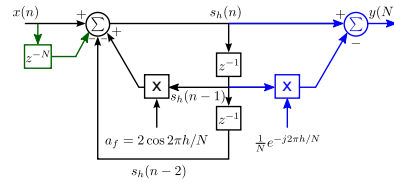


Fig. 1. IIR implementation of the Goertzel algorithm for a single harmonic  $h$ . Black traces are the operations computed at each sample. For the standard Goertzel, blue traces represent the operations to be done at the last step ( $n = N$ ), corresponding to lines 11 and 12 in Algorithm 1. Green lines represent the additional operations for the SGT implementation. It has to be remarked, that for the case of the SGT, the output equation needs to be calculated at each sample (line 7 in Algorithm 1).

one fundamental cycle, assuming a 50Hz nominal frequency, is considered at 10kHz sample rate, leading to a time window of 20ms and 200 samples. With the proposed parameters, the calculations using the Goertzel approach are faster than the FFT alternative when the calculated number of harmonics is  $M \leq 8$ . The algorithm description in pseudo-code and the block diagram for the implementation are shown in Algorithm 1 and Fig. 1 respectively. At the implementation, the  $h$  input variable contains the harmonic order of the sequences being analyzed.

In order to fully understand the SGT, it is useful to compare its dynamic response with respect to the standard Goertzel algorithm. The transfer function of the Goertzel algorithm in the  $z$  domain is given by (1), where  $\omega_h = 2\pi h/N$ , being  $h$  the harmonic order. The corresponding frequency response is shown in Fig. 2. As it can be seen from the frequency response, the Goertzel algorithm works as a resonator at the specified  $\omega_h$  frequencies.

$$H_{gh} = \frac{1 - e^{-j\omega_h} z^{-1}}{1 - 2 \cos(\omega_h) z^{-1} + z^{-2}} \quad (1)$$

For the sliding Goertzel implementation, the  $z$  domain expression is given by (2). When compared to (1), the sliding implementation voids the output after  $N$  samples. This is due to the modified numerator term,  $1 - z^{-N}$ . By splitting the expression into two fractional terms, the first one is equal

This is the author's version of an article that has been published in this journal. Changes were made to this version by the publisher prior to publication.  
The final version of record is available at <http://dx.doi.org/10.1109/TIA.2018.2846552>

3

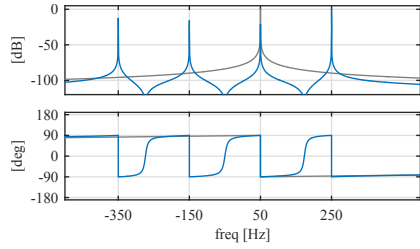


Fig. 2. Goertzel algorithm frequency response for a complex signal with harmonics  $h = [1, -3, 5, -7]$ . In blue the overall response is shown, in gray the response when the algorithm is tuned only for  $h = 1$ .

to  $H_{g_h}$  and the second one to  $z^{-N}H_{g_h}$ . The corresponding frequency response is shown in Fig. 3.

$$H_{sg_h} = \frac{(1 - e^{-j\omega_h} z^{-1})(1 - z^{-N})}{1 - 2 \cos(\omega_h) z^{-1} + z^{-2}} = H_{g_h} (1 - z^{-N}) \quad (2)$$

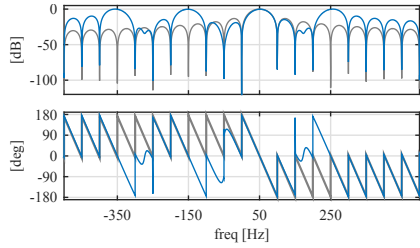


Fig. 3. Sliding Goertzel algorithm frequency response for a complex signal with harmonics  $h = [1, -3, 5, -7]$ . In blue the overall response is shown, in gray the response when the algorithm is tuned only for  $h = 1$ .

### III. SEQUENCE EXTRACTOR IMPLEMENTATION

Use of Goertzel-based techniques for sequence extraction requires to measure the grid phase voltages ( $v_{an}, v_{bn}, v_{cn}$ ), and to transform them to the stationary reference frame ( $v_{\alpha\beta}$ ). From there, the real and the imaginary part  $v_{\alpha\beta} = v_{\alpha} + jv_{\beta}$  are used as inputs to the Goertzel algorithm. A comparison for both the impulse response and the poles and zeros map for the standard Goertzel implementation and sliding approach is shown in Fig. 4. As it has been discussed, the differences are related to the duration of the impulse response. For the case of the standard Goertzel approach, the impulse response is a pure resonator at the frequency of the tracked harmonics. For the case of the sliding Goertzel, the impulse response duration is limited to the duration of the processing window ( $N$  samples), in the shown case corresponding to 20ms.

For the validation of the system, the harmonics detailed in Table I are used. A comparison between the estimation given by the standard Goertzel and the SGT with respect to the

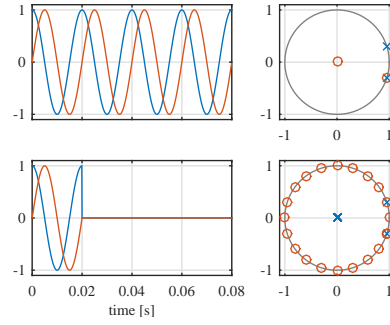


Fig. 4. Impulse response and pole/zero map for the Goertzel method (top) and the Sliding Goertzel modification (bottom).  $N = 20$ ,  $h = 1$  for a simpler representation.

TABLE I  
CONSIDERED HARMONICS.

Harmonic Order	Mag (p.u.)
1	1
-5	0.2
7	0.2

actual harmonic magnitudes and phases is shown in Fig. 5. As it can be seen, when the input signal is at steady state

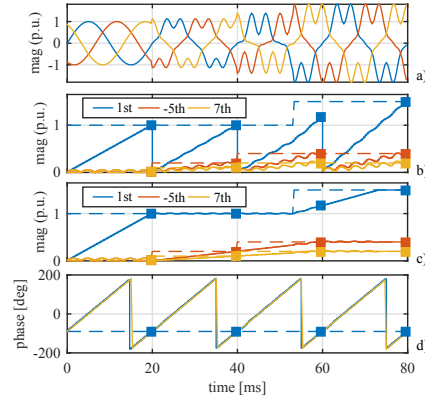


Fig. 5. Sliding Goertzel estimation for a three phase system with the harmonic contents shown in Table I. The dotted lines correspond to the real value of each of the harmonics. The square dots represent the estimated value at the end of each block. a) waveforms, b) Goertzel and c) SGT estimation, d) phase.

during the selected 20ms window, the estimation converges to the right values. By looking at the represented graphs, two important conclusions can be drawn: 1) For the standard Goertzel represented in Fig. 5b), the estimation procedure is

This is the author's version of an article that has been published in this journal. Changes were made to this version by the publisher prior to publication.  
The final version of record is available at <http://dx.doi.org/10.1109/TIA.2018.2846552>

4

discontinuous, being the current harmonic value only reached at the end of the current processing window and restarted at the beginning of the next one. Obviously, this invalidates the method to be directly used in converter real-time control applications, as the one proposed in this paper. Alternatively, the *SGT* approach represented in Fig. 5c) allows for a continuous estimation. This is the selected choice for our investigations. 2) The estimated magnitude needs the total number of samples and time,  $N = 200$ ,  $t = 20\text{ms}$ , to converge to the correct value. This would raise an unacceptable delay when the estimation is used as a feedback signal. However, it can be also seen that the evolution of the fundamental component ( $1^{\text{st}}$  harmonic) estimation is linear during the estimation window and barely affected by the harmonic content.

In order to overcome 2), this paper proposes to incorporate a predictive *SGT* implementation, namely *P-SGT*, that improves the convergence speed and, at the same time, avoids the extra calculations derived from the overlapping. The predictive behavior is implemented by a two-step algorithm. Firstly, a linear sliding least squares estimation (*LSE*) is run over the output of each *SGT* sample. This will lead to a linear representation of the corresponding datapoints. It must be remarked that being the output values of the *SGT* complex, two different least squares estimation can be obtained: one for the module and another one for the phase. Even considering this linear condition both for the magnitude and the phase estimation, at this paper the phase estimation is directly obtained from the *SGT* algorithm due to the fact that an accurate phase estimation can be obtained before each window is completed. Secondly, the module value at the end of the estimation window is predicted. This last step is implemented at each step by again considering the linear evolution expressed in (3)

$$\hat{y}[N] = y[n] + \overline{m}_{le}[n] \cdot [N - n] \quad (3)$$

, where  $\overline{m}_{le}[n]$  is the moving average slope estimated by the *LSE* approach,  $N$  the window size and  $n$  the actual sample. A graphical description for the algorithm is shown in Fig. 6.

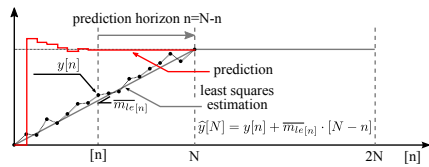


Fig. 6. Graphical representation of the proposed predictive algorithm. The slope at each of the points is filtered by a moving average filter for reducing the derivative noise.

The simulation results for the proposed methods are shown in Fig. 7. As it can be seen, the results obtained by the *P-SGT* approximation notably improve the convergence estimation speed. However, even with the averaged slope calculation, a transient can be observed at the beginning of each processing window. This behavior is inherent to the involved derivative process. By comparing the smooth transitions given by the *SGT*, it can be deduced that both estimations can work

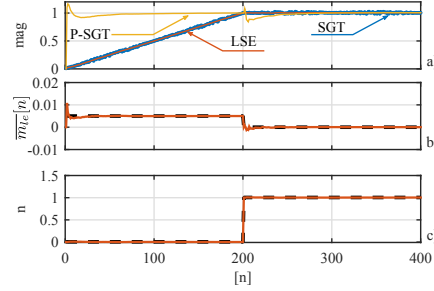


Fig. 7. Proposed *P-SGT* implementation. a) evolution of the magnitude. *SGT* in blue, *LSE* in red and *P-SGT* in yellow. b) evolution of the predicted slope, c) evolution of the predicted offset. A window of  $N = 200$  has been used for demonstration purposes.

in a complementary approach. The combined estimation will be based on the rate of change in the *SGT* estimation. As previously discussed, during the *SGT* convergence time, the estimation will exhibit a mostly linear change. On the contrary, once the estimation has reached the final value, it will have a mostly zero variation. Based on that, the *P-SGT* will be favored during the transients, whereas the classical *SGT* will be mostly used at the steady state. This idea will be mathematically developed and numerically evaluated during the next section.

#### A. Combined *SGT* and *P-SGT* estimation

Considering the performance of both the *SGT* and the *P-SGT* strategies shown in Fig. 7, it is proposed to combine both methods, leading to the so called *PF-SGT*, for getting an enhanced estimation. For the fusion rule, (4) is proposed.

$$X_{h\omega_e}^{pf-sgt} = X_{h\omega_e}^{p-sgt} \cdot (1 - k_{h\omega_e}^f) + X_{h\omega_e}^{sgt} \cdot (k_{h\omega_e}^f) \quad (4)$$

The value of the fusion gain,  $k_{h\omega_e}^f$ , in (4) is given by (5).

$$k_{h\omega_e}^f = \exp\left(-\text{abs}\left(\frac{\text{mavg}(\Delta X_{h\omega_e}^{sgt})}{\text{max}(\Delta X_{h\omega_e}^{sgt})}\right)\right) \cdot g_{h\omega_e} \quad (5)$$

Variables in (4), (5) are defined as follows:

- $X_{h\omega_e}^{sgt}$ . *SGT* estimation of harmonic component  $h$  at fundamental frequency  $\omega_e$  for variable  $X$ .
- $X_{h\omega_e}^{p-sgt}$ . *P-SGT* estimation of harmonic component  $h$  at fundamental frequency  $\omega_e$  for variable  $X$ .
- $X_{h\omega_e}^{pf-sgt}$ . *PF-SGT* estimation of the harmonic component  $h$  at fundamental frequency  $\omega_e$  for variable  $X$ .
- $\Delta X_{h\omega_e}^{sgt}$  is the rate of change of the module of the estimated harmonic components by the *SGT* algorithm. It is calculated as the difference between the module of the actual sample minus the previous one.
- *mavg*. Moving average function. A window of  $N$  samples is used for the calculation.
- *max*. Maximum variation function. For this research a maximum of  $1.1/N = 5.5e - 3$  p.u. is established.

This is the author's version of an article that has been published in this journal. Changes were made to this version by the publisher prior to publication.  
The final version of record is available at <http://dx.doi.org/10.1109/TIA.2018.2846552>

5

- $g_{h\omega_c}$ . Gain of the exponential function used for tuning the fusion system.

Evolution of the estimation and the adaptive gain is shown in Fig. 8. As clearly shown, the fusion helps on removing the transient at the beginning of each of the processing windows. Time constant for the fusion estimation depending on the value of the fusion gain  $g_{h\omega_c}$  is shown in 9, where a parameter sweep of  $g_{h\omega_c}$  (between 1 and 6) is performed. As it can be seen, for the selected magnitude steps, values larger than  $g_{h\omega_c} > 4$  do not contribute to an improved transient response.

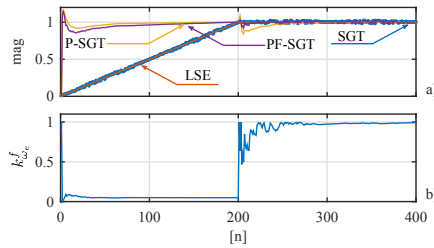


Fig. 8. Proposed fusion mechanism. a) evolution of the module. b) evolution of the gain.  $g_{h\omega_c} = 5$ ,  $\max(\Delta X_{h\omega_c}^{sgt}) = 5.5e-3$

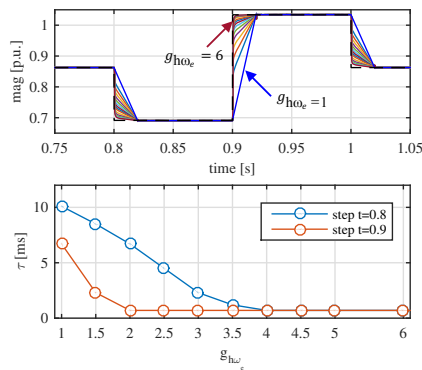


Fig. 9. Variation of the fusion time constant with respect to the fusion gain. On top, the response of the proposed fusion mechanism to two different step changes is shown, on bottom the calculated time constant.

### B. Frequency estimation

When the proposed *PF-SGT* method is applied for the estimation of grid voltages and currents, frequency changes must be considered. As known, frequency domain methods based on the DFT assume the periodicity of the signal and are affected by the discrete resolution. However, when used for the analysis of signals coming from a real-time application, this assumption is not longer valid. The effect of the signal being not periodic, together with the discrete resolution, will

cause spectral leakage, affecting both the phase and magnitude of the estimated components. Often, windowing techniques (both in time and frequency domain) are applied in order to reduce the impact. Unfortunately, this procedure also affects the magnitude and the phase of the extracted components and often additional compensation is needed. A different approach, is to optimize the number of samples needed for the calculation (200 by default in our implementation) depending on the fundamental frequency, so an integer number of cycles is acquired at each processing window. For this paper, and considering that only the harmonics of the fundamental frequency needs to be isolated, an even simpler approach has been used. By selecting a coarse spectral resolution of 50Hz, spectral leakage is avoided when deviations from the fundamental frequency appears. The drawbacks of this procedure are that, as commented in Section V-B, a bounded steady state error for the phase will appear and that any other disturbance signal falling within the band of [25 – 75]Hz will be affecting the estimation. Additionally, also in Section V-B, an adaptive frequency method is considered for those applications requiring a zero-steady-state phase error.

### C. Magnitude estimation errors due to the LSE algorithm

The magnitude estimation using the proposed *LSE* method over a  $N$ -length window depends on the sample where the disturbance occurs ( $0 < n < N - 1$ ). This is due to the slope averaging define in (3). The average leads to magnitude estimation errors if any change in the signal magnitude occurs during the *LSE* calculation period. Fig. 10 shows the magnitude estimation for two different cases. In the first one (blue trace), the disturbances occur at  $t = [0, 60]$ ms, which correspond in both cases to  $n = 0$  sample at processing windows 1 and 4. Under that conditions, the predicted slope,  $m$  and offset,  $n$ , are correctly estimated. In the second case (red trace), the magnitude steps are commanded at  $t = [0, 50]$ ms, corresponding to  $n = [0, N/2]$  samples respectively. As shown, for the  $t = 50$ ms step, the slope prediction starts to react at the step time but, because of the average calculation, the value by the end of the processing window,  $t = 60$ ms, is half of the expected value. After that, during the next processing window starting at  $t = 60$ ms, the slope is correctly adapted until  $t = 70$ ms, time at which the average calculation makes the prediction to decrease, reaching half of the expected value at  $t = 80$ ms. Similar explanations can be given to the offset calculation. The two explained cases, cover the minimum and maximum estimation errors. The maximum error will happen when an step change happens at half the processing window and will be equal to half the correct value.

In order to correct these estimation errors, a simple procedure is explained in Fig. 11. The underpinning idea is based on the detection of magnitude changes from the *SGT* algorithm. When a change is detected, the estimation window is restarted so the calculations of the slope and offset are based on the new incoming values. Ideally, this will make the estimation to converge to the right value despite the instant at which the magnitude varies. As shown in Fig. 11a), an step change in

This is the author's version of an article that has been published in this journal. Changes were made to this version by the publisher prior to publication.  
The final version of record is available at <http://dx.doi.org/10.1109/TIA.2018.2846552>

6

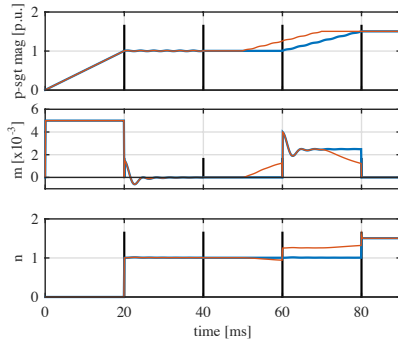


Fig. 10. Prediction errors due to the averaging window problem. a) *SGT* estimated magnitude for two different cases. Blue: magnitude changes aligned with sample  $n = 0$  at each window. Red: magnitude change at  $t = 50$ ms at sample  $n = N/2$ . b) and c) estimated slopes and offsets for the two cases.

the value of the fundamental component from 1p.u to 1.5 p.u is commanded at  $t = 50$ ms, corresponding to  $n = N/2$ . As shown in Fig. 11b), the output of a slope change detector instantaneously reacts to the change. This fact will be used as a trigger mechanism for resetting the estimation window. The trigger signal is based on the absolute value of the derivative of the slope given by the *SGT*, and it is shown in Fig. 11b) depicted in blue. By comparing with a trigger level, represented by the red slashed line, the processing window can be reset. The results for the predicted slope and offset are depicted in red in Figs. 11c) and 11d) respectively. Finally, the estimated output is shown in Fig. 11e). Clearly the estimation tracks the correct values in around 5ms, which is an excellent response time. As a comparison, the tracked slope and offset using the standard approach is shown in blue.

#### D. Phase-jump detection and magnitude correction

An adverse effect that noticeably affects to the magnitude and frequency estimation is the occurrence of a phase jump. This subsection shows a simple technique that detects a phase jump and corrects its effects in the estimated magnitude. The main underpinning idea is to check if the phase difference between the actual phase angle estimation and the previous one falls within the grid code limits. An acceptable frequency deviation from the nominal value has been selected to be  $\omega_{err} = 2 \cdot 2\pi$ rad/s. According to that, the phase difference between the actual phase estimation and the previous one should fall within the phase limits defined by (6), where  $T_s$  is the sample time and  $P_s$  the phase difference.

$$(\omega_e - \omega_{err}) \cdot T_s < P_s < (\omega_e + \omega_{err}) \cdot T_s \quad (6)$$

Thus, if a phase jump is detected, the magnitude estimation at the previous sample is used. Alternatively, a low-pass version of the voltage complex vector could be used, but this solution requires more computational effort at no extra advantage. Fig. 12 shows the proposed correction mechanism

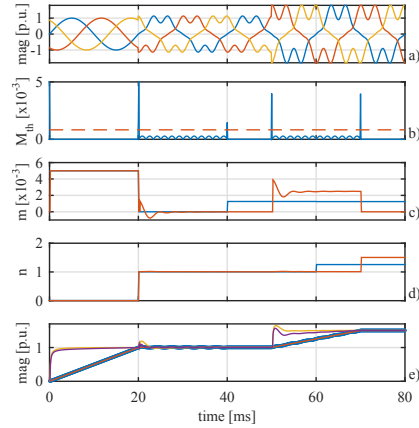


Fig. 11. Correction of window averaging errors. a) voltage to neutral waveforms, b) slope change detector, c) *LSE* slope, d) *LSE* offset, e) estimated output. In c) and d) blue and red represents the slope and offset obtained by the *LSE* without and with the proposed modification respectively.

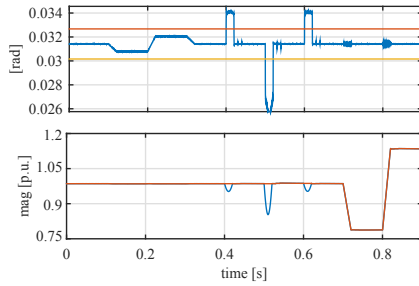


Fig. 12. Compensation of magnitude estimation during three phase-jumps. On top, the phase-jumps are represented in blue and the limits given by (6) in red and yellow. Phase-jumps occur at  $t = [0.4, 0.5, 0.6]$  s. On bottom, the estimated magnitude before (blue) and after (red) the correction is implemented.

compared to the magnitude variation before the compensation.

#### E. Digital signal processing

The digital signal processing needed for the implementation of the proposed *PF-SGT* method as well as its use for the current control of a grid-tied converter is explained in Fig. 13. On the left-side, the input to the algorithm is the  $v_{\alpha\beta}$  voltage complex vector measured at the point of common coupling. The output of the method are the complex components of the estimated harmonics  $v_{\alpha\beta h_1 \dots h_n}$  as well as the phase of the main harmonic,  $\angle v_{\alpha\beta h_1}$ . In the case an adaptive frequency estimation is needed, the estimated frequency,  $\hat{\omega}_e$ , shall be added as an input to the *PF-SGT* block. On the right-side,

This is the author's version of an article that has been published in this journal. Changes were made to this version by the publisher prior to publication.  
The final version of record is available at <http://dx.doi.org/10.1109/TIA.2018.2846552>

7

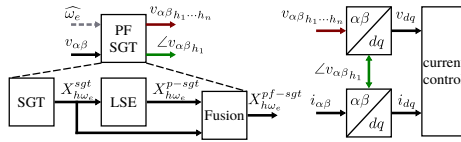


Fig. 13. Digital signal processing. Left-side, estimation of voltage harmonics. Right-side, Use of the estimated voltages in the internal current-loop control.

the use of the estimated components for the current control implementation is shown. The estimated phase is used as the rotation angle for the  $\alpha\beta \rightarrow dq$  transformation. The estimated grid voltage harmonic components can be used as a feed-forward added at the output of the current control.

The computation burden of the proposed method can be calculated by computing the needed floating point operations and the memory needs. The number of floating point operations considering four harmonics is around 2200. Considering the number of cycles for each floating point operation based on a *TMS320F28335* controller with a 150MHz clock, it leads to a computational time lower than  $60\mu\text{s}$ . Regarding the memory needs, a buffer of  $N + 1$  samples is needed for the calculation of the *SGT* plus some additional room for the scalar variables. Considering together the processing and memory needs, it is concluded that the proposed method has a moderate computational burden for modern digital signal controllers.

#### IV. OFF-LINE SYSTEM EVALUATION

The initial evaluation of the proposed sequence estimator has been done using a programmable voltage source (2210 TC-ACS-50-480-400 from Regatron) to create the different grid conditions. Different steps at the magnitude, phase and frequency of the signal are considered as well as the behavior with and without additional harmonic content. The data is acquired at 1Ms/s sample rate by an scope and later down-sampled to 10kHz. The down-sampled signal is processed in Matlab/Simulink using the same code implementation later to be used during the on-line test.

The results for the tracked grid voltage's magnitude and phase using the *PF-SGT* are shown in Fig 14 and 15. The different events at the source signal are repeated twice. During the first interval ( $t = 0 - 1.2$  s), no harmonics were included. At the second one, the harmonics indicated at Table I are considered. Moreover, starting at  $t = 1.5$  s, a dc offset is added at the output of the voltage sensors. De-offset values are  $V_u = 10$  V,  $V_v = 5$  V,  $V_w = -5$  V. The events are scheduled as follows: 1) **Magnitude**. At  $t = 0.8$  s and  $t = 0.9$  s it changes to 0.8 and 1.2 p.u. The same change is observed at  $t = 1.98$  s and  $t = 2.08$  s. 2) **Frequency**. At  $t = 0.2$  s and  $t = 0.3$  s, the rated 50 Hz frequency is changed to 49 and 51 Hz respectively. Same pattern is reproduced at  $t = 1.38$  s and  $t = 1.48$  s. 3) **Phase**. At  $t = 0.5$ ,  $t = 0.6$ ,  $t = 0.7$  s phase jumps of 30,  $-60$ , 30 deg. are induced. Same pattern is observed at  $t = 1.68$ , 1.78, 1.88 s. At the graph, the behavior of the proposed method is tested compared to the DSOGI implementation. The

tuning of the DSOGI has been done according to the optimal parameters indicated by its authors [9]. As it can be seen, the proposed method shows a better immunity to harmonics and faster response to the considered changes with the exception of the phase change at  $t = 0.6$  and 1.78 s. This is due to the correction explained in (6) not being considered for the initial evaluation. It is specially remarkable the improvement of the proposed method when DC components are considered.

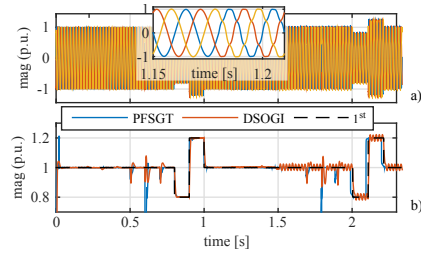


Fig. 14. Off-line system evaluation. Comparison of the *PF-SGT* method with respect to the ideal  $1^{st}$  harmonic and the DSOGI implementation. a) time domain waveforms, b) module estimation.

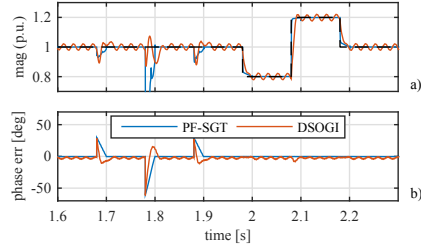


Fig. 15. Off-line system evaluation. Detail on the comparison of the *PF-SGT* method with respect to the ideal  $1^{st}$  harmonic and the DSOGI implementation. a) module, b) phase error

#### A. Performance under unbalanced conditions

Fig. 16 shows the performance of the proposed technique and the DSOGI method under unbalanced conditions. At  $t = 0.2$  s, phase *b* of the input three-phase voltage falls to 0.7 p.u. (Fig. 16). The same disturbances as the previous tests are applied under unbalanced conditions: frequency deviation test is performed between  $t = 0.4$  s and  $t = 0.6$  s, phase jump test is performed between  $t = 0.7$  s and  $t = 0.9$  s and finally magnitude deviations test is performed between  $t = 1.0$  s and  $t = 1.2$  s. As it can be observed, the obtained results match with that retrieved in the previous tests. In this regard, the proposed method shows a better tracking capabilities under all tested disturbances.

#### B. Closed-loop behavior

The impact of the proposed *PF-SGT* over the closed-loop performance has been compared with respect to the DSOGI. A

This is the author's version of an article that has been published in this journal. Changes were made to this version by the publisher prior to publication.  
The final version of record is available at <http://dx.doi.org/10.1109/TIA.2018.2846552>

8

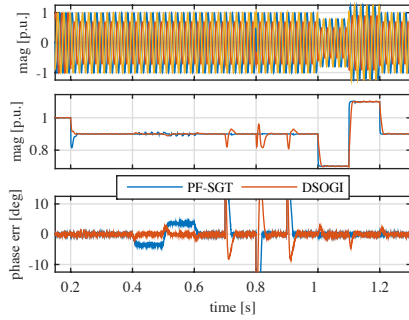


Fig. 16. Off-line system evaluation. Comparison between the DSOGI and the proposed  $PF-SGT$  method under unbalanced conditions. From top to bottom: a) grid voltages, b) grid voltage magnitude, c) grid voltage phase error.

TABLE II  
APPROXIMATION PARAMETERS.

Method	$f_n$ (Hz)	$\xi$
DSOGI	60.5	$\frac{\sqrt{(2) \cdot 3}}{2}$
PF-SGT	8600	$\frac{\sqrt{(2) \cdot 8}}{2}$

PI controller is used while the plant has been modeled as a RL circuit. Since both the DSOGI and the PF-SGT methods involve nonlinear systems, their transfer functions have been approximated by  $2^{nd}$  order systems as shown in Fig. 17. The results of the approximation procedure are shown in Table II, where  $\omega_n$  and  $\xi$  are the natural frequency and damping factor of each method respectively.

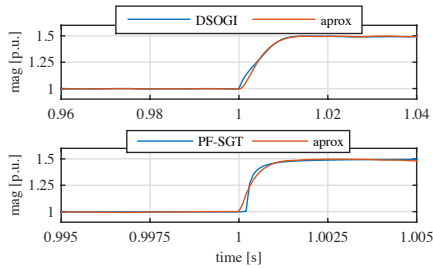


Fig. 17. Approximation of a) DSOGI and b) PF-SGT methods

For both techniques, the current control loop is tuned by using a zero-pole cancellation technique, its bandwidth being set to (20 Hz). The phase margin of the system is used as a figure of merit to analyze the stability of the current control loop. In this regard, a limit of 60 deg will be considered to assure stability.

Fig. 18 shows the  $G(s)H(s)$  Bode plots for a bandwidth in the current control loop of 20 Hz. It can be observed that the

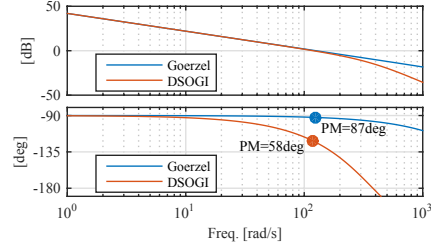


Fig. 18.  $G(s)H(s)$  Bode Plot for DSOGI and proposed methods. Current Control Bandwidth  $BW_I = 20\text{Hz}$

phase margin of the system including the DSOGI method is  $58\text{deg}$ , while it is  $\approx 87\text{deg}$  when the PF-SGT method is used under the same bandwidth (see Fig. 18). This clearly shows the bandwidth limit of the current control loop when a DSOGI method is used.

The closed-loop current control relevant signals are shown in Fig. 19. Reference tracking capabilities in the synchronous reference frame has been tested. The grid voltage was acquired as previously explained and the down-sampled voltage data was used in a real-time Simulink simulation. The same sequence than for the open-loop results shown in Fig. 14 has been used. The relevant parameters for the setup are: filter values:  $L = 5\text{mH}$ ,  $R = 0.2\Omega$ , switching frequency  $f_{sw} = 10\text{kHz}$ , current control bandwidth 20Hz. As clearly shown, the proposed method shows a better transient response and harmonic rejection capabilities than the DSOGI alternative. Moreover, the bandwidth was set to such a low value in order to keep stable the DSOGI-based current control.

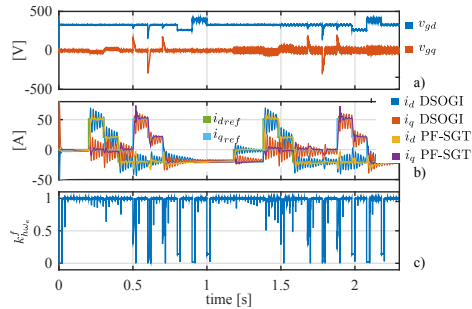


Fig. 19. Off-line system evaluation

. Close loop comparison between the DSOGI and the proposed  $PF-SGT$  methods. a) grid voltages, b) grid currents, c) adaptive fusion gain for the  $PF-SGT$  method.

## V. ON-LINE SYSTEM EVALUATION

The on-line experimental validation of the proposed sequence estimator is done by using the experimental grid shown

This is the author's version of an article that has been published in this journal. Changes were made to this version by the publisher prior to publication.  
The final version of record is available at <http://dx.doi.org/10.1109/TIA.2018.2846552>

9

in Fig. 20. The setup is composed by two Triphase power modules PM15F42C and PM90F60C and a set of passive loads. The PM90F60C module is used as a grid voltage emulator for creating the different grid scenarios, modifying the magnitude, phase, frequency and harmonic content of the voltage signal. The PM15F42C module is integrated in the system operating as a constant power controlled battery energy storage system. The proposed algorithms are processed online in the PM15F42C control unit using the voltage measurements at the point of common coupling (PCC). The experimental results use the DSOGI algorithm as the base case for the comparison.

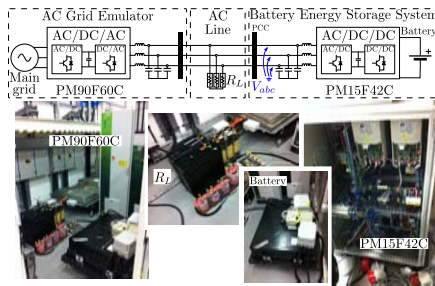


Fig. 20. Setup used for the experimental validation. Two converters are coupled together, PM90F60C unit is used to create the varying grid conditions and PM15F42C runs the proposed estimation method.

#### A. Variation of grid voltage magnitude

Variations of the grid voltage magnitude from 1 to 0.8 p.u. at  $t = 0.1$  s and from 0.8 to 1.15 p.u. at  $t = 0.2$  are considered. Results both without and with the  $h_5 = 5\%$ ,  $h_7 = 5\%$  additional harmonics are shown in Fig. 21 and Fig. 22 respectively. As shown, the proposed method has a faster dynamic response as well as a higher harmonic robustness, both for the magnitude and the phase estimation.

#### B. Variation of grid voltage frequency

Variations of grid voltage frequency from 50 to 49 Hz at  $t = 0.1$  s and from 49 to 51 Hz at  $t = 0.2$  are considered. Results both without and with the  $h_5 = 5\%$ ,  $h_7 = 5\%$  additional harmonics are shown in Fig. 24 and Fig. 25 respectively. As shown, the proposed method has a better magnitude response but a worse phase as there is an steady state error in the phase estimation. The reason is the considered frequency resolution. As explained before, a coarse frequency resolution of 50Hz. has been selected for this work. This implies that any deviation smaller than 50Hz can not be measured and the difference between the real grid frequency and the fundamental harmonic is directly coupled to a phase and a magnitude error. The maximum errors have been numerically evaluated as shown in Fig. 23. As it can be seen, both the error in magnitude and phase are small for variations between [46, 54]Hz. The maximum phase error can

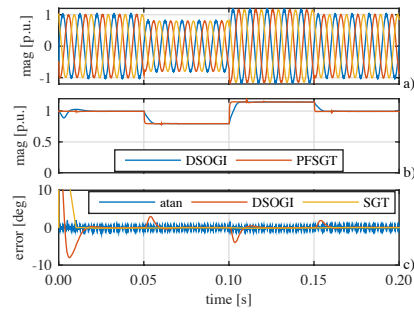


Fig. 21. On-line system evaluation. Comparison between the DSOGI and the proposed  $PF-SGT$  method for a magnitude step change. No harmonics are injected. From top to bottom: a) grid voltages, b) grid voltage magnitude, c) grid voltage phase error. Note that *atan* refers to the inverse-tangent function.

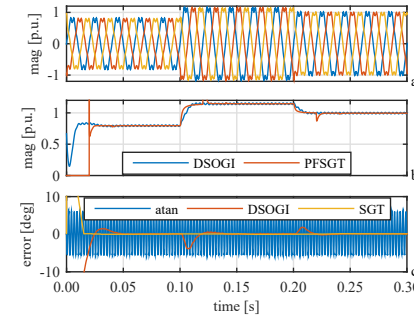


Fig. 22. On-line system evaluation. Comparison between the DSOGI and the proposed  $PF-SGT$  method for a magnitude step change. Harmonics as listed in Table I are injected. From top to bottom: a) grid voltages, b) grid voltage magnitude, c) grid voltage phase error.

be approximated by the linear expression shown in (7), where  $\max(\omega_{err})$  is the maximum frequency error in rad/s and  $f_e$  the grid frequency in Hz.

$$\max \theta_{err} = \frac{\max(\omega_{err}) \cdot 180}{f_e \cdot 2\pi} \quad (7)$$

The maximum frequency error depends on the frequency resolution and the maximum admissible grid frequency deviation. For the values considered at this paper, the error is bounded to a maximum of 3.6deg. The effect of the frequency error over the estimated magnitude and phase has been validated by the experimental results shown in Fig. 26. As expected, the phase is kept within the specified limits and the magnitude is barely affected. For those applications in which the maximum phase deviation is lower than the limits given by (7), a modification in the proposed method can be added, so it become frequency adaptive. For that, the number of samples  $N$  used for the calculations is obtained in function of the fundamental frequency, according to (8). In that case,

This is the author's version of an article that has been published in this journal. Changes were made to this version by the publisher prior to publication.  
The final version of record is available at <http://dx.doi.org/10.1109/TIA.2018.2846552>

10

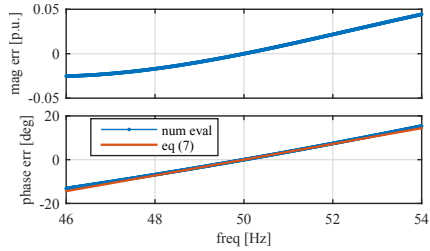


Fig. 23. Effect of grid frequency variation over the estimated magnitude (top) and phase (bottom). Phase error is compared against the linear approximation in (7).

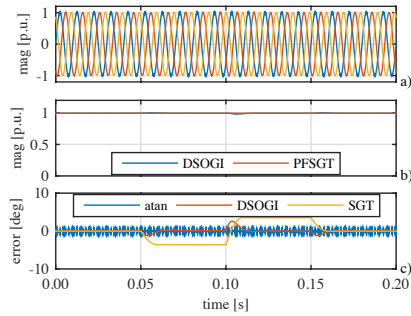


Fig. 24. On-line system evaluation . Comparison between the DSOGI and the proposed  $PF - SGT$  method for a frequency step change. No harmonics are injected. From top to bottom: a) grid voltages, b) grid voltage magnitude, c) grid voltage phase error.

the coefficients for the Goertzel algorithm have to be updated in real time. The experimental results when the adaptation mechanism is used are shown in Fig. 27. Comparing the phase error with respect to Fig. 25, the phase jump is corrected, achieving a zero phase error in steady state.

$$N = \text{round} \left( \frac{2\pi}{\omega_c \cdot T_s} \right) \quad (8)$$

### C. Variation of grid voltage phase

Variations of grid voltage phase from 0 to 30 deg. at  $t = 0.05$  s, from 30 to  $-30$  deg at  $t = 0.1$  and from  $-30$  to 0 deg at  $t = 0.15$  s are considered. Results both without and with the  $h_5 = 5\%$ ,  $h_7 = 5\%$  additional harmonics are shown in Fig. 28 and Fig. 29 respectively. The proposed method has similar results compared to DSOGI when no additional harmonics are considered and an improved response under harmonic conditions.

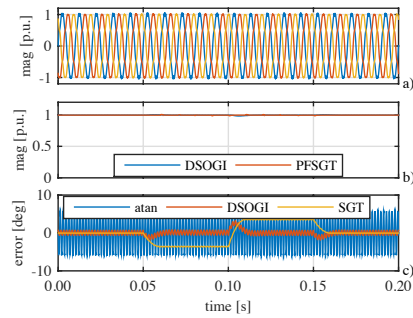


Fig. 25. On-line system evaluation. Comparison between the DSOGI and the proposed  $PF - SGT$  method for a frequency step change. Harmonics as listed in Table I are injected. From top to bottom: a) grid voltages, b) grid voltage magnitude, c) grid voltage phase error.

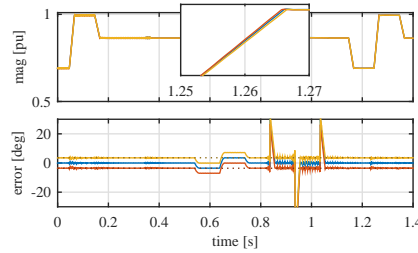


Fig. 26. On-line system evaluation. Effect of grid frequency variation over the magnitude (top) and phase (bottom). Goertzel algorithm is tuned for 50Hz and three different cases are represented: 50Hz (blue), 49Hz (yellow), 51Hz (red). Theoretical limits for the phase according to expression (7) are marked dotted.

## VI. CONCLUSION

This paper has introduced a new predictive estimation technique for grid-tied converters based on a frequency-based method. To the author's best knowledge, the proposed method using a modification of the Sliding Goertzel Transformation has not been used before for grid phase tracking in power converters. The proposed  $PF - SGT$  method has been evaluated with respect to a consolidated alternative, the DSOGI, showing a superior performance in terms of dynamic response and disturbance rejection. It is particularly remarkable the immunity to DC offsets as well as to changes at the grid frequency. The proposed algorithm has been validated by both simulation and experimental results. The impact of the phase estimation and harmonic decoupling in a closed-loop current control implementation has also been evaluated, being the proposed  $PF - SGT$  an important improvement over the DSOGI method.

This is the author's version of an article that has been published in this journal. Changes were made to this version by the publisher prior to publication.  
The final version of record is available at <http://dx.doi.org/10.1109/TIA.2018.2846552>

11

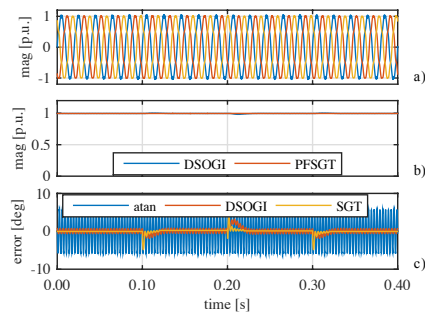


Fig. 27. On-line system evaluation. Comparison between the DSOGI and the proposed  $PF - SGT$  method for a frequency step change when an adaptive frequency is used. Harmonics as listed in Table I are injected. From top to bottom: a) grid voltages, b) grid voltage magnitude, c) grid voltage phase error.

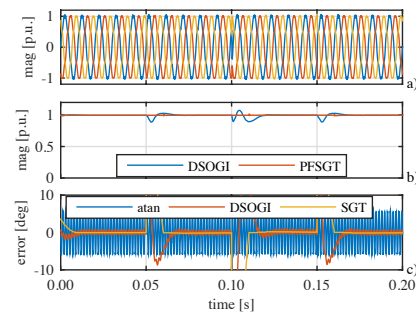


Fig. 29. On-line system evaluation. Comparison between the DSOGI and the proposed  $PF - SGT$  method for a phase step change. Harmonics as listed in Table I are injected. From top to bottom: a) grid voltages, b) grid voltage magnitude, c) grid voltage phase error.

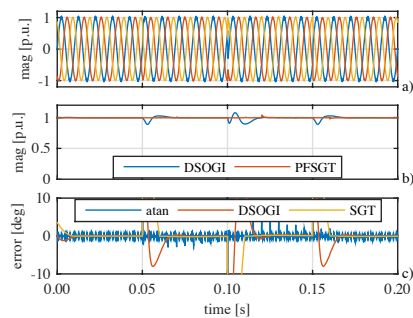


Fig. 28. On-line system evaluation. Comparison between the DSOGI and the proposed  $PF - SGT$  method for a phase step change. No harmonics are injected. From top to bottom: a) grid voltages, b) grid voltage magnitude, c) grid voltage phase error.

#### REFERENCES

- [1] C. Blanco, D. Reigosa, J. C. Vasquez, J. M. Guerrero, and F. Briz, "Virtual admittance loop for voltage harmonic compensation in microgrids," *IEEE Transactions on Industry Applications*, vol. 52, no. 4, pp. 3348–3356, July 2016.
- [2] J. W. Simpson-Porco, Q. Shafiq, F. Dörfler, J. C. Vasquez, J. M. Guerrero, and F. Bullo, "Secondary frequency and voltage control of islanded microgrids via distributed averaging," *IEEE Transactions on Industrial Electronics*, vol. 62, no. 11, pp. 7025–7038, Nov 2015.
- [3] E. Twining and D. G. Holmes, "Grid current regulation of a three-phase voltage source inverter with an lcl input filter," *IEEE Transactions on Power Electronics*, vol. 18, no. 3, pp. 888–895, May 2003.
- [4] S. Yang, Q. Lei, F. Z. Peng, and Z. Qian, "A robust control scheme for grid-connected voltage-source inverters," *IEEE Transactions on Industrial Electronics*, vol. 58, no. 1, pp. 202–212, Jan 2011.
- [5] J. C. Vasquez, J. M. Guerrero, M. Savaghebi, J. Eloy-Garcia, and R. Teodorescu, "Modeling, analysis, and design of stationary-reference-frame droop-controlled parallel three-phase voltage source inverters," *IEEE Transactions on Industrial Electronics*, vol. 60, no. 4, pp. 1271–1280, April 2013.
- [6] S. Golestan, J. M. Guerrero, and J. C. Vasquez, "Three-phase pll's: A review of recent advances," *IEEE Transactions on Power Electronics*, vol. 32, no. 3, pp. 1894–1907, March 2017.
- [7] F. D. Freijedo, J. Doval-Gandoy, O. Lopez, and E. Acha, "A generic open-loop algorithm for three-phase grid voltage/current synchronization with particular reference to phase, frequency, and amplitude estimation," *IEEE Transactions on Power Electronics*, vol. 24, no. 1, pp. 94–107, Jan 2009.
- [8] S. Golestan, A. Vidal, A. G. Yepes, J. M. Guerrero, J. C. Vasquez, and J. Doval-Gandoy, "A true open-loop synchronization technique," *IEEE Transactions on Industrial Informatics*, vol. 12, no. 3, pp. 1093–1103, June 2016.
- [9] P. Rodriguez, A. Luna, M. Ciobotaru, R. Teodorescu, and F. Blaabjerg, "Advanced grid synchronization system for power converters under unbalanced and distorted operating conditions," in *IECON 2006 - 32nd Annual Conference on IEEE Industrial Electronics*, Nov 2006, pp. 5173–5178.
- [10] P. Rodriguez, R. Teodorescu, I. Candela, A. Timbus, M. Liserre, and F. Blaabjerg, "New positive-sequence voltage detector for grid synchronization of power converters under faulty grid conditions," in *2006 37th IEEE Power Electronics Specialists Conference*, June 2006, pp. 1–7.
- [11] A. M. Gole and V. K. Sood, "A static compensator model for use with electromagnetic transients simulation programs," *IEEE Transactions on Power Delivery*, vol. 5, no. 3, pp. 1398–1407, Jul 1990.
- [12] C. Blanco, D. Reigosa, F. Briz, and J. M. Guerrero, "Synchronization in highly distorted three-phase grids using selective notch filters," in *2013 IEEE Energy Conversion Congress and Exposition*, Sept 2013, pp. 2641–2648.
- [13] X. Guo, W. Wu, and Z. Chen, "Multiple-complex coefficient-filter-based phase-locked loop and synchronization technique for three-phase grid-interfaced converters in distributed utility networks," *Industrial Electronics, IEEE Transactions on*, vol. 58, no. 4, pp. 1194–1204, April 2011.
- [14] C. Blanco, D. Reigosa, F. Briz, J. M. Guerrero, and P. Garcia, "Grid synchronization of three-phase converters using cascaded complex vector filter pll," in *2012 IEEE Energy Conversion Congress and Exposition (ECCE)*, Sept 2012, pp. 196–203.
- [15] F. D. Freijedo, A. G. Yepes, O. Lopez, A. Vidal, and J. Doval-Gandoy, "Three-phase pll's with fast postfault retracking and steady-state rejection of voltage unbalance and harmonics by means of lead compensation," *IEEE Transactions on Power Electronics*, vol. 26, no. 1, pp. 85–97, Jan 2011.
- [16] S. Golestan, J. M. Guerrero, A. Vidal, A. G. Yepes, and J. Doval-Gandoy, "Pll with maf-based prefiltering stage: Small-signal modeling and performance enhancement," *IEEE Transactions on Power Electronics*, vol. 31, no. 6, pp. 4013–4019, June 2016.
- [17] C. Blanco, D. Reigosa, F. Briz, and J. M. Guerrero, "Quadrature signal generator based on all-pass filter for single-phase synchronization," in *2014 IEEE Energy Conversion Congress and Exposition (ECCE)*, Sept 2014, pp. 2655–2662.
- [18] K. Duda, "Accurate, guaranteed stable, sliding discrete fourier transform [dsp tips amp; tricks]," *IEEE Signal Processing Magazine*, vol. 27, no. 6, pp. 124–127, Nov 2010.

This is the author's version of an article that has been published in this journal. Changes were made to this version by the publisher prior to publication.  
The final version of record is available at <http://dx.doi.org/10.1109/TIA.2018.2846552>

12

- [19] E. Jacobsen and R. Lyons, "The sliding dft," *IEEE Signal Processing Magazine*, vol. 20, no. 2, pp. 74–80, Mar 2003.
- [20] —, "An update to the sliding dft," *IEEE Signal Processing Magazine*, vol. 21, no. 1, pp. 110–111, Jan 2004.
- [21] C. Blanco, P. García, A. Navarro-Rodríguez, and M. Sumner, "Predictive frequency-based sequence estimator for control of grid-tied converters under highly distorted conditions," in *2017 IEEE Energy Conversion Congress and Exposition (ECCE)*, Oct 2017, pp. 2940–2947.
- [22] G. Goertzel, "An Algorithm for the Evaluation of Finite Trigonometric Series," *The American Mathematical Monthly*, vol. 65, no. 1, pp. 34–35, 1958.

## Appendix D

### Conference publications



## **D.1 Low frequency signal injection for grid impedance estimation in three phase systems**

P. García, J. M. Guerrero, J. García, Á. Navarro-Rodríguez and M. Sumner, "Low frequency signal injection for grid impedance estimation in three phase systems," 2014 IEEE Energy Conversion Congress and Exposition (ECCE), Pittsburgh, PA, 2014, pp. 1542-1549.



# Low Frequency Signal Injection for Grid Impedance Estimation in Three Phase Systems

Pablo García, Juan M. Guerrero, Jorge García,  
 Ángel Navarro-Rodríguez  
 Dept. of Elec., Computer & System Engineering  
 University of Oviedo  
 Gijón, 33204, Spain  
 Email: garciafpablo@uniovi.es, guerrero@uniovi.es,  
 garciajorge@uniovi.es, angelnr23@gmail.com

Mark Sumner  
 Department of Electrical and Electronic Engineering  
 The University of Nottingham  
 Nottingham, NG7 2RD, UK  
 Email: Mark.Sumner@nottingham.ac.uk

**Abstract**—This paper deals with the estimation and decoupling of grid impedance and LCL filter parameters variation using signal injection techniques and Luenberger type observer. When integrating a power converter in the AC grid as an interface for any Distributed Generation Systems (DGS) or other grid quality compensator like Active Power Filters (APF) or STATCOM, inner control loop normally requires current control. Current controller performance is greatly affected by the filter and grid impedance values. Although normally the filter impedance dominates the dynamics of the current controller, in weak networks the impedance of the grid can not be neglected. Additionally, other often required functions, as islanding detection, also rely on the estimation of the grid impedance. For this paper, a Luenberger based observer is proposed for controlling the grid current when a LCL filter is used. The proposed method will rely on measuring the converter side current and the grid voltage and will cope with parameter variation at the filter transfer function. For variations at the grid impedance, the control action deliver by the observer feedback path will be used for triggering an injection mechanism. A Low Frequency Signal Injection (LFSI) approach is proposed for online estimating the grid impedance using an RLS algorithm. The proposed estimation technique is well suited to be incorporated into an adaptive current controller scheme.

## I. INTRODUCTION

Use of Voltage Source Converters (VSC) interfaced to the AC grid requires to control the current deliver to the grid. In order to accurately design the current controller, it is critical to understand the existing dynamic model between the applied converter output voltage and the resulting grid current. The dynamic model will affect in different ways the performance, depending on the used sensors and the filter used for the connection of the converter to the grid. When using a LCL filter for the interface, there exist multiple options for the placement of the current and voltage sensors, each of those with their advantages and drawbacks [1], [2]. When the control of the AC voltage at the output of the converter is needed, it is

This work has been partially funded by the Campus of International Excellence (CEI) of the University of Oviedo, Spain, in the framework of Mobility Grants for Academics in 2013. This work also was supported in part by the Research, Technological Development and Innovation Program Oriented to the Society Challenges of the Spanish Ministry of Economy and Competitiveness under grant ENE2013-44245-R and by the European Union through ERFD Structural Funds (FEDER).

usual to measure the voltage at the filter capacitor. However, this will make the current controller dependent on the grid side impedance. The variation is effectively decoupled by moving the voltage sensor to the Point of Common Coupling (PCC), but then the capacitor voltage/current needs to be estimated in order to damp the current controller. The issue is more critical when interfacing the power converter to weak networks having a non negligible grid impedance, thus affecting the total output impedance. In order to overcome this problem there are two different alternatives: 1) to force the known output filter to be the dominant dynamic system in any grid situation by implementing passive/active damping or virtual impedance techniques [3], [4] and, 2) to implement and adaptive current controller [5], [6] which parameters change depending on the grid impedance.

For this second option, it is needed to online estimate the grid impedance and the variations at the LCL filter parameters. Impedance estimation could be implemented using two different approaches: 1) model based techniques and, 2) signal injection based techniques. Model based techniques, use the transfer function between the applied voltage and the current for estimating the parameters. In [7], the use of the resonance of a LCL filter is proposed in order to make the estimation. As commented by the authors, the principal issue of this technique is the existence of two resonance peaks when passive reactive power compensation is added at the Point of Common Coupling (PCC).

Signal injection based methods use an additional excitation in order to track the response of the system [8]–[11]. For the signal excitation, several approaches can be followed. 1) High Frequency Signal Injection (HFSI) [10]–[13], 2) current regulator reaction [11], 3) Low Frequency Signal Injection (LFSI) [14], [15]. 1) and 2) are based on the same physical explanation. When injecting a voltage at a given high frequency, the resulting current includes a component at that frequency. By analyzing those current components, it is possible to obtain the impedance. However, there are some issues with this high frequency injection techniques: 1) selection of the high frequency must be done by asserting that the reaction of any APF connected to the same PCC is not removing the high

$$\frac{d}{dt}\mathbf{x} = \begin{pmatrix} -R_1^x/L_1^x & \omega_e & -1/L_1^x & 0 & 0 & 0 \\ -\omega_e & -R_1^y/L_1^y & 0 & -1/L_1^y & 0 & 0 \\ 1/C & 0 & 0 & \omega_e & -1/C & 0 \\ 0 & 1/C & -\omega_e & 0 & 0 & -1/C \\ 0 & 0 & 1/L_2^x & 0 & -R_2^x/L_2^x & 0 \\ 0 & 0 & 0 & 1/L_2^y & 0 & -R_2^y/L_2^y \end{pmatrix} \cdot \mathbf{x} + \begin{pmatrix} 1/L_1^x & 0 & 0 & 0 & 0 \\ 0 & 1/L_1^y & 0 & 0 & 0 \\ 0 & 0 & 0 & 0 & 0 \\ 0 & 0 & 0 & 0 & 0 \\ 0 & 0 & -1/L_2^x & 0 & 0 \\ 0 & 0 & 0 & -1/L_2^y & 0 \end{pmatrix} \cdot \mathbf{u} \quad (1)$$

frequency current harmonic; 2) the estimated impedance is not the transient impedance, which is the one needed for tuning the current regulator, but the impedance at the injection frequency.

In order to overcome the aforementioned problems, in this paper a mixed strategy based on an observer and LFSI is proposed. By one side, a Luenberger style observer will be used for controlling the grid current with a reduced number of sensors. By the other, the proposed LFSI, consisting on the injection of a pulse aligned with the zero crossing of each three phase voltages, will allow to detect changes at the grid impedance. The pulse is open loop injected by modifying the voltage command delivered by the current controller. In order to reduce the disturbance in the grid, injection of the pulse is restricted to those time intervals in which a change in the grid impedance is detected by the observer. Errors in the feedback path of the observer are proposed to trigger the signal injection mechanism.

When compared with HFSI, the following differences are found: 1) the estimation of the grid transient impedance could be directly obtained, whereas when using the high frequency signal injection just the impedance at a given frequency is estimated; 2) the LFSI is more rich in harmonic content. This could help in reducing the impact of any APF connected in parallel with the converter injecting the low frequency signal; 3) signal processing is more complicated with the LFSI. In the case of HFSI, the estimation could be directly estimated from the isolated components at the injection frequency. Isolating the components just require the use of band-pass or low-pass filters in the stationary or carrier signal frequency respectively. For the LFSI, a model approach estimation based on Recursive Least Square (RLS) method is used. However, there is no need for any additional filter stage; 4) HFSI is affected by the transients in the fundamental current, being quite challenging to remove the transient harmonics using digital filters. In [16], the use of a fundamental current observer is proposed in order to mitigate the effect. On the contrary, using the proposed LFSI, fundamental transient currents could also be used for the impedance estimation.

The paper is organized as follows. Section II explains the state space model of the LCL filter and grid impedance, the design of the observer and the digital implementation of the control system. Section III shows the injection mechanism, including the selection of the injection pulse and Section IV the RLS adaptive procedure used for the grid impedance estimation. Finally, simulation and experimental results are shown at Section V.

## II. SYSTEM MODELING AND CONTROL

This section describes the system modeling in a generic reference frame as well as the theoretical background for the implemented control. It also includes the details for the digital implementation of the designed Luenberger observer.

### A. System modeling

The state space representation of a LCL filter (Fig. 1) in an arbitrary reference frame is given by (1), where  $\mathbf{x} = [i_x, v_c, i_y]^T$  is the state vector and  $\mathbf{u} = [v_x, v_y]^T$  the input vector. Also note that each component at the state and input vectors is a complex variable with two elements; the real and imaginary components, i.e  $\mathbf{v} = (v_x, v_y)$ . Equation (1) could be particularized for the stationary  $(\alpha, \beta)$  or to the synchronous  $(d, q)$  references frames by making  $\omega_e = 0$  or  $\omega_e = \omega_{grid}$  respectively. An alternative representation of (1), separating the  $x$  and  $y$  terms, is shown at (2), (3) and in compact form at (4), (5). That form will be used for an easier digital implementation of the observer structure. Finally, the corresponding block diagram representation in compact complex notation is shown at Fig. 2.

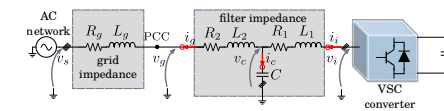


Fig. 1. Connection of the LCL filter to the output of the VSC converter.

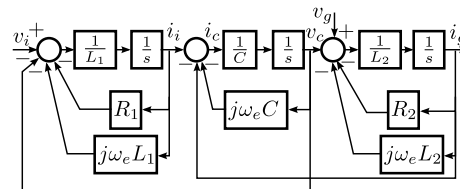


Fig. 2. LCL filter block diagram in state space form.

$$\begin{aligned} \frac{d}{dt} \mathbf{x}_x = & \begin{pmatrix} -R_1/L_1 & -1/L_1 & 0 \\ 1/C & 0 & -1/C \\ 0 & 1/L_2 & -R_2/L_2 \end{pmatrix}_x \cdot \mathbf{x}_x \\ & + \omega_c \begin{pmatrix} 1 & 0 & 0 \\ 0 & 1 & 0 \\ 0 & 0 & 1 \end{pmatrix} \cdot \mathbf{x}_y + \begin{pmatrix} 1/L_1 & 0 \\ 0 & 0 \\ 0 & -1/L_2 \end{pmatrix}_x \cdot \mathbf{u}_x \end{aligned} \quad (2)$$

$$\begin{aligned} \frac{d}{dt} \mathbf{x}_y = & \begin{pmatrix} -R_1/L_1 & -1/L_1 & 0 \\ 1/C & 0 & -1/C \\ 0 & 1/L_2 & -R_2/L_2 \end{pmatrix}_y \cdot \mathbf{x}_y \\ & - \omega_c \begin{pmatrix} 1 & 0 & 0 \\ 0 & 1 & 0 \\ 0 & 0 & 1 \end{pmatrix} \cdot \mathbf{x}_x + \begin{pmatrix} 1/L_1 & 0 \\ 0 & 0 \\ 0 & -1/L_2 \end{pmatrix}_y \cdot \mathbf{u}_y \end{aligned} \quad (3)$$

$$\frac{d}{dt} \mathbf{x}_x = \mathbf{A}_x \cdot \mathbf{x}_x + \omega_c \mathbf{I} \cdot \mathbf{x}_y + \mathbf{B}_x \cdot \mathbf{u}_x \quad (4)$$

$$\frac{d}{dt} \mathbf{x}_y = \mathbf{A}_y \cdot \mathbf{x}_y - \omega_c \mathbf{I} \cdot \mathbf{x}_x + \mathbf{B}_y \cdot \mathbf{u}_y \quad (5)$$

### B. Control implementation

The superior filtering performance of the LCL structure when compared to the L or LC alternatives has also important shortcomings in the design of the current controller [17]. This situation is even worsened when harmonic compensation is considered [18]. Current control for a LCL filter is a challenging task due to the resonance appearing between the capacitor and the inductances and normally an attenuation method is needed. The basic idea is to compensate or attenuate the capacitor current within the bandwidth of the current controller, but still keeping the filtering capability for frequencies at and above the switching frequency.

In the literature there are several alternatives which can be separated into passive and active damping techniques. By one side, passive damping techniques require the use of additional passive elements, such as a series or parallel resistances which increase the system losses [17]. By the other, active damping methods often need additional current or voltage sensors. Lately, some publications have addressed the implementation of active damping methods which do not need any extra elements [2], [19]–[24]. The methods in that group could be separated into those which require to estimate the capacitor current or the inductance voltage, thus relying on calculating derivatives which are normally noisy or require the use of complicated control algorithms. More appealing because of their simplicity are those methods relying on digital filtering of the control signal in order not to react at the resonance frequency. However, often the bandwidth of the current controller must be decreased.

For this paper, a structure based on a Luenberger type observer is proposed [25]. The proposed system will control the grid side current by using the converter side current sensors and the voltage sensors at the PCC as the solely sensing elements. This configuration has some advantages in terms of 1) costs, only the current sensors usually provided

by the power stage need to be used; 2) safety, the current sensors on the converter side are also suitable for protection of the power stage; 3) performance, PCC voltage measurement allows for measuring and decoupling the effects of a varying grid impedance but also to real power factor measurement and; 4), reliability as a reduced number of sensors reduces the fault probability.

The proposed observer and current control block diagram are shown at Fig 3. The control system works as follows. The estimated values for the converter side inductance ( $\hat{L}_1$ ), filter capacitor ( $\hat{C}$ ) and grid side inductance ( $\hat{L}_2$ ) are used for building the dynamic model previously shown in (1). Inputs to the observer are the commanded voltage from the converter ( $v_i^{ff}$ ) and the measured converter side current ( $i_i$ ). The estimated capacitor current ( $\hat{i}_c$ ) is obtained from the difference of the measured converter side current and the estimated grid current ( $\hat{i}_g$ ).  $\hat{i}_c$  is later used at the output of the current controller to implement the active damping mechanism and  $\hat{i}_g$  is used as the feedback signal for the current controller. The feedback path of the observer is generated from the estimation error of the converter side current ( $e_i = i_i - \hat{i}_i$ ). The error signal is the input to the observer controller ( $C_o$ ) which, depending on the reference frame of the implementation, will be a PI (synchronous reference frame) or a PR for the stationary reference frame. The output of the feedback path ( $v_i^{fb}$ ) is added to the feedforward value to the commanded voltage in order to compensate for any unknown in the system. The feedback voltage will also be used for triggering the low frequency pulse injection. Finally, for the current controller implementation ( $C_i$ ), PI or PR structures are used depending on the selected reference frame. The active damping term and the measured PCC voltage are after added in order to damp the oscillations and to effectively reject the effects on the grid current due to any change in the grid impedance.

### C. Digital control implementation

For the online implementation, the Luenberger observer and the current controller designs must be translated to the digital domain. The Luenberger observer is discretized using the Euler approximation, as shown in (6), (7), where  $[k]$  corresponds to the actual sample time,  $[k-1]$  to the previous one and  $T_s$  is the sample time. It is worth noting that even if here the matrix formulation is shown for the sake of simplicity, the discrete observer equations can be implemented in scalar form, more suitable for the online implementation.

$$\begin{aligned} \mathbf{x}_x[k] = & (\mathbf{I} - T_s \mathbf{A}_x)^{-1} \cdot (\mathbf{x}_x[k-1] + T_s \mathbf{B}_x \cdot \mathbf{u}_x[k]) \\ & + T_s \omega_c \mathbf{I} \cdot \mathbf{x}_y[k-1] \end{aligned} \quad (6)$$

$$\begin{aligned} \mathbf{x}_y[k] = & (\mathbf{I} - T_s \mathbf{A}_y)^{-1} \cdot (\mathbf{x}_y[k-1] + T_s \mathbf{B}_y \cdot \mathbf{u}_y[k]) \\ & - T_s \omega_c \mathbf{I} \cdot \mathbf{x}_x[k-1] \end{aligned} \quad (7)$$

For the controller discretization, Tustin approximation is used. PI or PR structures are used depending on performing the implementation at the synchronous or the stationary reference frame respectively.

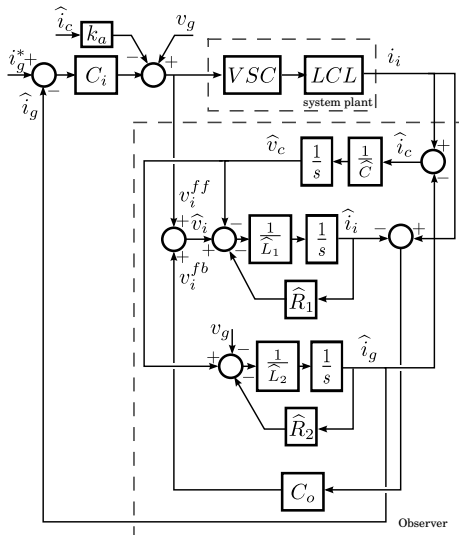


Fig. 3. Proposed observer structure in an arbitrary reference frame.

The observer performance, at the synchronous reference frame, is shown at Fig. 4 when the estimated LCL filter parameters match the real ones. As shown, the grid current is correctly tracked.

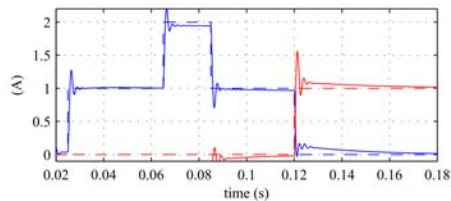


Fig. 4. Transient response for the presented observer structure in digital form.

### III. LOW FREQUENCY SIGNAL INJECTION

For the LFSI, there are different alternatives and parameters which can be adjusted. As represented in Fig. 5, the signal is injected centered at the zero crossing of the phase to neutral voltages. Zero crossing is detected by using the calculated phase from the PLL used for grid synchronization. This point has been selected in order to minimize the voltage distortion, as demonstrated later in the discussion.

At this paper, three different alternatives for the pulse injection are investigated, the first two are implemented at the

$abc$  reference frame, while the third one is at the  $dq$  reference frame. The pulses are injected as a duty modifications to the output of the current controller and, during the pulse injection, the fundamental voltage command is disabled for the case of the  $abc$  injection (see Fig. 6) whereas is just an addition when implemented in the  $dq$  reference frame. This will enable both a sharper excitation but also a quite simple implementation of the signal injection. As seen in Fig. 5, both the pulse width and the magnitude can be changed. As wider is the pulse and as larger the magnitude, the bigger the disturbance delivered to the system would be. Obviously, increased disturbance values will help in the estimation procedure, but also will increase the THD of the resulting currents. For this paper, the values shown in Table I have been used. Resulting waveforms for the inverter commands and the applied voltages are shown at Fig. 7 whereas the corresponding currents at the synchronous reference frame are shown at Fig. 8. The three tested alternatives are following described:

- 1) **Method#1.** Pulse width is established to the desired value and the the magnitude is set to zero. Under that condition, the fundamental voltage command is clamped to zero during the pulse injection time. The implementation of this strategy is straightforward, since it is just a multiplication of the duty commands times a time window set to zero during the pulse duration. When translating to the  $dq$  reference frame, even if the pulse is mostly at the  $q$  axis, both components are modified. The pulses are transformed to a triangular shape at the  $q$  axis and the resulting current has a sinusoidal waveform.
- 2) **Method#2.** Fundamental command is hold at the corresponding value at the beginning of the pulse injection and when the phase crosses the zero is changed to the opposite value. Transformed to the  $dq$  reference frame,  $d$  component is also modified, although in a less noticeable way than for Method#1. The pulses at the  $q$  axis are also transformed to a triangular shape, but the resulting current has a triangular waveform of opposite phase when compared to previous method.
- 3) **Method#3.** When looking at the pulse result in the  $dq$  reference frame for both Method#1 and Method#2, the resulting excitation is affecting the  $d$  and  $q$  axis and, even if the pulse is an stepwise in the  $abc$  reference frame, is having a triangular form on the  $dq$  reference frame. Because the RLS algorithm will be implemented in the synchronous reference frame, it is desirable to have an step shape in that reference. This could be easily achieved by using the same strategy than for Method#2 but injecting the pulses directly in the synchronous reference frame at the  $q$  axis.

It must be remarked that all pulse injection strategies share the fact that the applied distortion to the voltage command is symmetrical, thus resulting in the voltage average error being zero. Selecting one or the other is based on the sensitivity of the current response and on the implementation burden. For this paper, Method#3 is considered because of the advantages



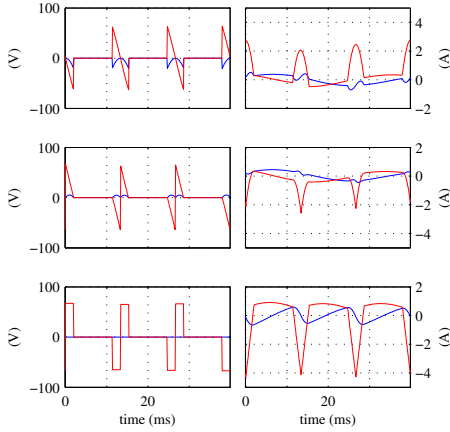


Fig. 8. LFSI waveforms for the three proposed methods in the  $dq$  reference frame. Fundamental component is removed in order to zoom on the high frequency components. From top to bottom, Method#1, Method#2 and Method#3.

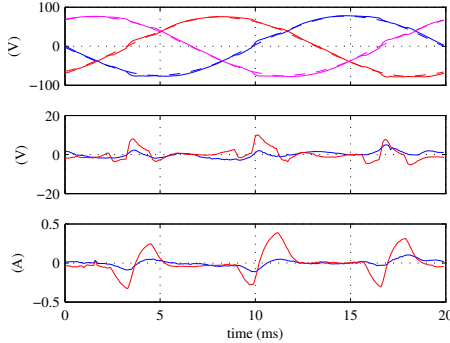


Fig. 9. Experimental results for Method#3. The system is operated in close loop with a bandwidth of  $200\text{Hz}$ . Filter capacitor is removed and current commands were set to zero. From top to bottom it is shown the phase to neutral voltages at the PCC, the voltage commands, and the grid currents at the synchronous reference frame. Blue color is used for the  $d$  component and red for the  $q$ .

thus could be removed from the estimation. The system equations are represented in state-space form by defining the state vector  $\mathbf{X}_{[k]} = \begin{bmatrix} \mathbf{i}_{g[k-1]}, \mathbf{v}_{g[k]} \end{bmatrix}^T$  and coefficients vector  $\mathbf{W}_{[k]} = [\mathbf{a}_{1[k]}, \mathbf{b}_{0[k]}]$

TABLE I  
PARAMETERS

Nominal parameters	Value (Setup#1/Setup#2)
$r_1$ [ $\Omega$ ]	0.2/0.2
$r_2$ [ $\Omega$ ]	0.2/0.2
$L_1$ [ $mH$ ]	2.3/7
$L_2$ [ $mH$ ]	0.93/7
$C$ [ $\mu F$ ]	10/6
pulse mag. [ $p.u$ ]	0.1/0
pulse width. [ $ms$ ]	1/2
$\lambda$	0.998/0.8

$$\mathbf{e}_{[k]} = \mathbf{i}_{g[k]} - \hat{\mathbf{i}}_{g[k]} \quad (12)$$

The least square problem is formulated in recursive form using the equations (13) - (16).  $P_{(2 \times 2)}$  is the covariance matrix and it is initialized to  $P = 0.01 \begin{pmatrix} 1 & 0 \\ 0 & 1 \end{pmatrix}$ ,  $g_{(2 \times 1)}$  the adaptation gain and  $\lambda = [0, 1]$  is the forgetting factor, which need to be selected as a tradeoff of the expected estimation bandwidth and the signal to noise ratio. Frequently, values between 0.95 and 1 are selected. For this paper, the value shown in Table I has been selected. At each sample time, the estimation of the parameters  $\mathbf{b}_0, \mathbf{a}_1$  is updated and a new estimation for  $\mathbf{R}$  and  $\mathbf{L}$  is obtained.

$$\alpha_{[k]} = \mathbf{i}_{[k]} - \mathbf{W}_{[k-1]} \cdot \mathbf{X}_{[k]} \quad (13)$$

$$g_{[k]} = P_{[k-1]} \cdot \mathbf{X}_{[k]} \cdot \left[ \lambda + \mathbf{X}_{[k]}^T \cdot P_{[k-1]} \cdot \mathbf{X}_{[k]} \right]^{-1} \quad (14)$$

$$P_{[k]} = \lambda^{-1} \cdot P_{[k-1]} - g_{[k]} \cdot \mathbf{X}_{[k]}^T \cdot \lambda^{-1} \cdot P_{[k-1]} \quad (15)$$

$$\mathbf{W}_{[k]} = \mathbf{W}_{[k-1]} + (\alpha_{[k]} \cdot g_{[k]})^T \quad (16)$$

## V. SIMULATION AND EXPERIMENTAL RESULTS

For the simulation results, Simulink has been used for the implementation and Matlab for the analysis. All the simulation results were obtained using real time signal processing. The parameters' estimation and adaptation is continuously calculated at each simulation step. Fig. 10 shows a transient in the grid inductance from  $7mH$  to  $14mH$  and on the grid resistance from 0.2 to  $0.25\Omega$ . The figure shows the estimation of the inductance and resistance for a balanced grid, the modified voltages with the pulse injection and the estimated and real currents. As it can be seen, the parameter estimation converges in a fraction of a fundamental cycle. It is also shown that the resistance estimation drops before reaching the final value. Explanation for that behavior is related with a peak in the estimation of the  $a_1$  coefficient. Still the problem is not too important due to the high convergence speed.

Initial experimental results were obtained using a PM15F42C power module from Triphase. The power modules is directly programmed from Simulink environment, thus allowing for easily test the simulation results. The power module is interfaced to the AC grid trough a LCL filter, which parameters are listed in Table I under Setup#1. In that table, the

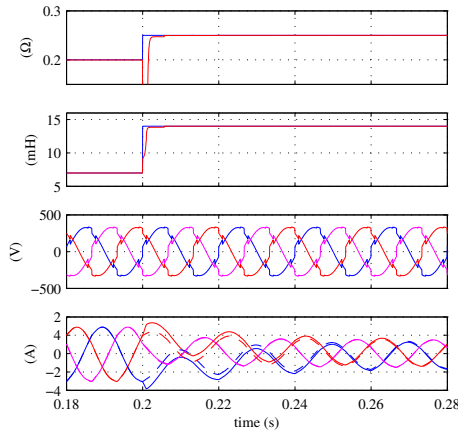


Fig. 10. Simulation results. Transient response. From top to bottom: a) resistance estimation, b) inductance estimation, c) applied voltages, d) resulting grid currents. Measured currents are shown in dashed lines, whereas estimated are in bold.

converter side inductance is  $L_1$  and the grid side inductance  $L_2$ . An additional inductance of  $L_l = 5mH$  has been placed in series after  $L_2$  in order to simulate a weak network. During these experiments, grid impedance estimation using Method#1 were tested.

Fig. 11 shows the obtained waveforms and the corresponding currents during the experiments. By looking at the phase voltages it is clear that the pulse injection is working as expected.

Fig. 12 shows the estimated resistance and inductance during the experimental tests. By looking at the results, the inductance value is really well estimated (the sum of  $L_1 + L_2 + L_l = 8.4mH$ ). The value of the obtained resistance seems to be too high when compared to the measured one (around  $0.5\Omega$ ). A possible explanation could be the effect of the filter capacitance, which is reducing the amount of pulsating current reaching the grid side current sensor.

Additional experiments, including the online implementation of the observer, the development and testing of Method#3 and the RLS implementation in the synchronous reference frame have been taken using a MTL-CBI0010N12IXFE power stage from Rectificadores Guash and the control being implemented in a TMS320F28335 DSC from Texas Instruments. The details about the grid filter and pulse injection parameters are shown at Table I under Setup#2.

Experimental results for the the observer reference tracking capability are shown at Fig. 13. Fig. 14 shows the estimated and real currents using Method#3 for the pulse injection and RLS at the synchronous reference frame at steady state con-

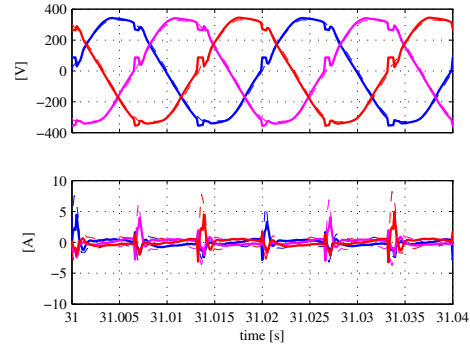


Fig. 11. Experimental results. a) LFSI and b) current response. Measured currents are shown in dashed lines and estimated in bold.

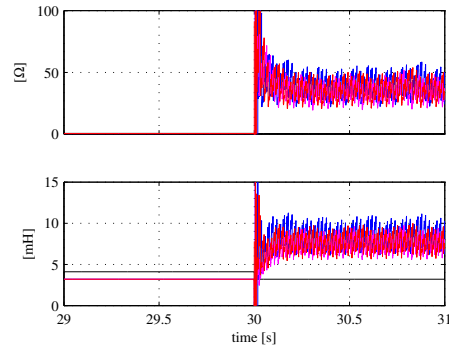


Fig. 12. Experimental results. Parameter estimation during a transient in the grid impedance. RLS estimation is enabled at  $t = 30s$ . a) Resistance estimation. b) Inductance estimation.

ditions. A good match between both components is obtained.

## VI. CONCLUSION

Estimation of the grid impedance is a key factor for improving the performance in weak networks. This paper has proposed the use of a LFSI technique to online estimate the impedance with a moderate computational burden for online implementation. The proposed system is triggered from the error signal coming from a Luenberger observer used for the control of the grid current in a LCL filter. The proposed observer and the estimation method have been tested through simulation and experimental results. Different methods for the LFSI have been compared and an the injection in the

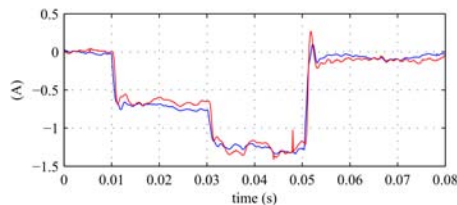


Fig. 13. Experimental results. Proposed observer working under different steps at the  $i_q$  component. Active damping gain  $K_d = 10$ .

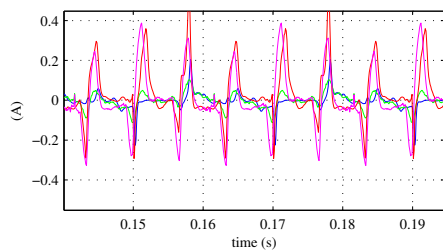


Fig. 14. Experimental results. Estimation of  $i_d$  and  $i_q$  currents using RLS at the synchronous reference frame and pulse injection based on Method#3. The system was operated in close loop with both components having reference 0.

synchronous reference frame has been selected based on an increased sensitivity and reduced cross-coupling.

#### REFERENCES

- [1] H. Xiao, X. Qu, S. Xie, and J. Xu, "Synthesis of active damping for grid-connected inverters with an LCL filter," in *2012 IEEE Energy Conversion Congress and Exposition (ECCE)*, Sep. 2012, pp. 550–556.
- [2] J. Xu, S. Xie, and T. Tang, "Active Damping-Based Control for Grid-Connected-Filtered Inverter With Injected Grid Current Feedback Only," *IEEE Transactions on Industrial Electronics*, vol. 61, no. 9, pp. 4746–4758, Sep. 2014.
- [3] W. Yao, M. Chen, J. Matas, J. Guerrero, and Z.-m. Qian, "Design and Analysis of the Droop Control Method for Parallel Inverters Considering the Impact of the Complex Impedance on the Power Sharing," *IEEE Transactions on Industrial Electronics*, vol. 58, no. 2, pp. 576–588, 2011.
- [4] J. He, Y. W. Li, J. Guerrero, F. Blaabjerg, and J. Vasquez, "An Islanding Microgrid Power Sharing Approach Using Enhanced Virtual Impedance Control Scheme," *IEEE Transactions on Power Electronics*, vol. 28, no. 11, pp. 5272–5282, 2013.
- [5] M. Sumner, B. Palethorpe, and D. Thomas, "Impedance measurement for improved power quality-Part 2: a new technique for stand-alone active shunt filter control," *IEEE Transactions on Power Delivery*, vol. 19, no. 3, pp. 1457–1463, 2004.
- [6] J. Massing, M. Stefanello, H. Grundling, and H. Pinheiro, "Adaptive Current Control for Grid-Connected Converters With LCL Filter," *IEEE Transactions on Industrial Electronics*, vol. 59, no. 12, pp. 4681–4693, 2012.
- [7] M. Liserre, F. Blaabjerg, and R. Teodorescu, "Grid Impedance Estimation via Excitation of LCL-Filter Resonance," *IEEE Transactions on Industry Applications*, vol. 43, no. 5, pp. 1401–1407, 2007.
- [8] D. Martin and E. Santi, "Auto tuning of digital deadbeat current controller for grid tied inverters using wide bandwidth impedance identification," in *2012 Twenty-Seventh Annual IEEE Applied Power Electronics Conference and Exposition (APEC)*, 2012, pp. 277–284.
- [9] L. Asiminoaei, R. Teodorescu, F. Blaabjerg, and U. Borup, "A digital controlled PV-inverter with grid impedance estimation for ENS detection," *IEEE Transactions on Power Electronics*, vol. 20, no. 6, pp. 1480–1490, 2005.
- [10] D. Reigosa, F. Briz, C. Charro, P. Garcia, and J. Guerrero, "Active Islanding Detection Using High-Frequency Signal Injection," *IEEE Transactions on Industry Applications*, vol. 48, no. 5, pp. 1588–1597, 2012.
- [11] D. Reigosa, F. Briz, C. Blanco, P. Garcia, and J. Manuel Guerrero, "Active Islanding Detection for Multiple Parallel-Connected Inverter-Based Distributed Generators Using High-Frequency Signal Injection," *IEEE Transactions on Power Electronics*, vol. 29, no. 3, pp. 1192–1199, 2014.
- [12] M. Sumner, B. Palethorpe, and D. Thomas, "Impedance measurement for improved power quality-Part 1: the measurement technique," *IEEE Transactions on Power Delivery*, vol. 19, no. 3, pp. 1442–1448, 2004.
- [13] N. Hoffmann and F. Fuchs, "Minimal Invasive Equivalent Grid Impedance Estimation in Inductive  $\pi$ -Resistive Power Networks Using Extended Kalman Filter," *IEEE Transactions on Power Electronics*, vol. 29, no. 2, pp. 631–641, 2014.
- [14] L. Asiminoaei, R. Teodorescu, F. Blaabjerg, and U. Borup, "Implementation and Test of an Online Embedded Grid Impedance Estimation Technique for PV Inverters," *IEEE Transactions on Industrial Electronics*, vol. 52, no. 4, pp. 1136–1144, 2005.
- [15] A. Timbus, P. Rodriguez, R. Teodorescu, and M. Ciobotaru, "Line Impedance Estimation Using Active and Reactive Power Variations," in *IEEE Power Electronics Specialists Conference, 2007. PESC 2007*, 2007, pp. 1273–1279.
- [16] F. Briz, A. Diez, and M. W. Degner, "Dynamic operation of carrier-signal-injection-based sensorless direct field-oriented AC drives," *IEEE Transactions on Industry Applications*, vol. 36, no. 5, pp. 1360–1368, Oct. 2000.
- [17] M. Liserre, F. Blaabjerg, and S. Hansen, "Design and control of an LCL-filter-based three-phase active rectifier," *IEEE Transactions on Industry Applications*, vol. 41, no. 5, pp. 1281–1291, Sep. 2005.
- [18] D. Wojciechowski, "Novel predictive control of 3-phase LCL-based active power filter," in *Compatibility and Power Electronics, 2009. CPE '09*, May 2009, pp. 298–305.
- [19] J. Dannehl, M. Liserre, and F. Fuchs, "Filter-Based Active Damping of Voltage Source Converters With Filter," *IEEE Transactions on Industrial Electronics*, vol. 58, no. 8, pp. 3623–3633, Aug. 2011.
- [20] M. Liserre, A. Aquila, and F. Blaabjerg, "Genetic algorithm-based design of the active damping for an LCL-filter three-phase active rectifier," *IEEE Transactions on Power Electronics*, vol. 19, no. 1, pp. 76–86, Jan. 2004.
- [21] S. Zhang, S. Jiang, X. Lu, B. Ge, and F. Z. Peng, "Resonance Issues and Damping Techniques for Grid-Connected Inverters With Long Transmission Cable," *IEEE Transactions on Power Electronics*, vol. 29, no. 1, pp. 110–120, Jan. 2014.
- [22] R. Pena-Alzola, M. Liserre, F. Blaabjerg, R. Sebastian, J. Dannehl, and F. Fuchs, "Systematic Design of the Lead-Lag Network Method for Active Damping in LCL-Filter Based Three Phase Converters," *IEEE Transactions on Industrial Informatics*, vol. 10, no. 1, pp. 43–52, Feb. 2014.
- [23] F. Huerta, E. Bueno, S. Cobrecas, F. Rodriguez, and C. Giron, "Control of grid-connected voltage source converters with LCL filter using a Linear Quadratic servocontroller with state estimator," in *IEEE Power Electronics Specialists Conference, 2008. PESC 2008*, Jun. 2008, pp. 3794–3800.
- [24] M. Malinowski and S. Bernet, "A Simple Voltage Sensorless Active Damping Scheme for Three-Phase PWM Converters With an Filter," *IEEE Transactions on Industrial Electronics*, vol. 55, no. 4, pp. 1876–1880, Apr. 2008.
- [25] D. Luenberger, "Observing the State of a Linear System," *IEEE Transactions on Military Electronics*, vol. 8, no. 2, pp. 74–80, Apr. 1964.
- [26] A. Arriagada, J. Espinoza, J. Rodriguez, and L. Moran, "On-line filtering reactance identification in voltage-source three-phase active-front-end rectifiers," in *The 29th Annual Conference of the IEEE Industrial Electronics Society, 2003. IECON '03*, vol. 1, Nov. 2003, pp. 192–197 vol.1.



## **D.2 A Communication-less Solution for Transient Frequency Drift Compensation on Weak Microgrids using a D-Statcom with an Energy Storage System**

A. Navarro-Rodriguez, P. Garcia, R. Georgious and J. Garcia, "A communication-less solution for transient frequency drift compensation on weak microgrids using a D-statcom with an energy storage system," 2015 IEEE Energy Conversion Congress and Exposition (ECCE), Montreal, QC, 2015, pp. 6904-6911.



# A Communication-less Solution for Transient Frequency Drift Compensation on Weak Microgrids using a D-Statcom with an Energy Storage System

Ángel Navarro-Rodríguez, Pablo García, Ramy Georgious and Jorge García  
 Dept. of Elec., Computer & System Engineering  
 University of Oviedo  
 Gijón, 33204, Spain

Email: navarroangel@uniovi.es, garciafpablo@uniovi.es, georgiousramy@uniovi.es, garciajorge@uniovi.es

**Abstract**—This paper proposes a solution for the transient grid frequency drift that occurs when active power transients take place in weak grids. Microgrids (MGs) are by definition weak grids, exhibiting a low inertia and high impedance which make them prone to contingencies that compromise the grid quality and stability. Particularly, the low inertia of the generators coupled to a MG could make the rotor speed to be affected by load changes, thus affecting the grid frequency. When compared with previous works, this research proposes a method for the estimation of the steady state reference frequency and the use of a Luenberger type observer for the estimation of the load current, leading to an improvement in the dynamics and the mitigation of the compensator phase lag due to the grid frequency estimator. Different control strategies are compared during the analytical discussion and validated through experimental results.

## I. INTRODUCTION

The weakness and stability problems associated to a MG have been considered since the apparition of this grid concept, demanding significant research interests. Studies for different types of contingencies have been carried out with the aim of mitigation of unbalances, harmonics, frequency variations, and power quality improvement [1]–[3]. The most extended solution for power quality enhancement involving active power exchange in DG's and MGs, is referred in the literature as Distribution Static Synchronous Compensator (D-STATCOM) with ESS, or simply ESS [4], [5].

Several examples can be found about the use of ESS assisting power generation in DG's for frequency profile enhancement [6], [7]. Nevertheless, in these applications, the ESS works coordinated with a power plant using a communication link, providing access to the system parameters and variables. Often, the ESS participates both in the power share during steady state and transients. In the specific application of dynamic compensation it is worth mentioning the study in [3], where an ESS system was proposed for frequency compensation limited to the operation during transients. However

such a solution presented a very bounded conditions. It relies on the communication with the generation system and the applied droop control may lead to insufficient performance in other applications. Being a relatively novel concept, the communication-less dynamic frequency drift compensation on MG's has been already presented, being one of the most studied solution the Virtual Inertia (VI) concept [8].

The absence of communication leads to three main constraints : 1) The use of grid frequency feedback based control requires the estimation of the frequency. Methods as Phase Lock Loop (PLL) [9], [10], based on angle estimation, or more robust techniques as Frequency Lock Loop (FLL) [11], focused on frequency estimation, can be used. However, they are characterized by relatively slow dynamics which limits the compensator controller bandwidth. 2) In communicated systems, the power reference and the power share of the generators is known, being a useful information for improving the disturbance rejection of the controller. As an alternative, in communication-less solutions, derivative action is commonly used to fasten the response by increasing the controller phase margin. However, it is affected by noise and oscillations on the estimated frequency signal. 3) The grid frequency reference, which may vary governed by droops in the grid, is unknown; leading to power share during steady state if the reference used in the compensation does not match the frequency command.

The present paper will focus on the design of an improved transient frequency drift compensator. For that purpose, the existing methods are analyzed and some enhancements are proposed concerning the commented problems. Among the contributions, it is proposed the use of a Luenberger type observer [12] for the estimation of the load current and the reduction of the compensator phase lag due to the grid frequency estimator.

The paper is organized as follows. Section II formulates the dynamic frequency drift problem. Section III covers the proposed control algorithms and the existing limitations. Section IV details the use of the Luenberger based observer for load estimation. Finally, the experimental results are shown at Section V.

The present work has been partially supported by the predoctoral grants program Severo Ochoa for the formation in research and university teaching of Principado de Asturias PCTI-FICYT under the grant ID BP14-135. This work also was supported in part by the Research, Technological Development and Innovation Program Oriented to the Society Challenges of the Spanish Ministry of Economy and Competitiveness under grant ENE2013-44245-R and by the European Union through ERFD Structural Funds (FEDER).

## II. PROBLEM DEFINITION AND SYSTEM MODELING

Deviations on power grid nominal parameters can lead to non-optimal operation or malfunction of grid connected elements. Moreover, the violation of regulations could trigger the system protections, compromising the grid power quality and stability. As a reference, the default IEEE regulation for Distributed Resources is summarized in Table I.

TABLE I. DEFAULT CLEARING TIMES UNDER ABNORMAL VOLTAGE AND FREQUENCY OPERATION BASED ON IEEE STD 1547A-2014 [13]

Voltage range (% of base voltage)	Clearing Time (s)
$V < 45$	0.16
$45 \leq V < 45$	1
$60 \leq V < 88$	2
$110 \leq V < 120$	1
$V \geq 120$	0.16
Frequency (Hz)	Clearing Time (s)
$f_n < f_n - 3$	0.16
$f_n < f_n - 0.5$	2
$f_n > f_n + 0.5$	2
$f_n > f_n + 2$	0.16

MGs and Distribution Networks are often governed by low inertia synchronous generators, being the grid active power related to their rotating speed. On weak grids, the connection and disconnection of the different elements presented in the grid as power generators and loads may cause variations on the voltage magnitude and frequency. This problem, illustrated in Fig. 1, can be mitigated by using a solution capable of injecting power to the grid with a much faster dynamic response than the grid generators, compensating the power mismatch.

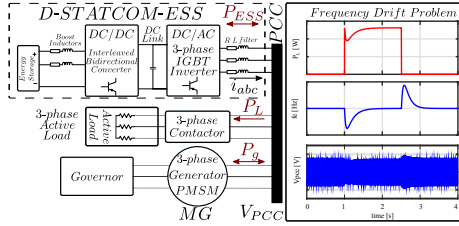


Fig. 1. Integration of the system under study in a simplified MG model for experimental purpose. The frequency drift contingency is illustrated as a graph showing the load power and the consequent grid frequency disturbance.

Fig. 1 shows the proposed solution integrated in an experimental simplified 1 node set-up, emulating a simplified MG, composed by a synchronous generator acting as the main supply and a pure active 3-phase load. The compensation solution will be based on an autonomous system constituted by a D-STATCOM, consisting on a 3-phase 2-level IGBT inverter, coupled through a DC link to an ESS formed by a battery, or any other bidirectional DC supply, and a bidirectional DC/DC boost IGBT converter in 2 branch interleaved configuration. The figure shows the power flow in the system, being  $P_g$ ,  $P_L$  and  $P_{ESS}$  the generator, the load and the proposed solution power respectively. The proposed topology will be able to both inject or consume power, thus, it will assist the generator sharing active power only during transients due to load connections and disconnections, smoothing the frequency dynamic response. On the other hand, during steady state operation, the ESS should be idle unless the battery needs to be charged.

## A. Generator model

For an optimal frequency compensation, the system dynamic model must be known. Moreover, the system modeling becomes mandatory when observation techniques are used. Fig. 2 shows the equivalent system of a synchronous generator coupled to a governor which controls the shaft speed with a certain speed control loop. In the figure,  $\omega_r$  is the rotor mechanical speed in rad/s,  $C_g$  is the governor controller,  $T_g$  is the torque injected by the governor,  $J$  and  $b$  are the generator mechanical parameters (inertia and friction coefficient),  $K_e$  and  $K_t$  are the generator back EMF and torque constant and  $p$  is the number of pole pairs. The electrical load is represented by the parameters  $R_T$  and  $L_T$  being  $i_L$  the load current and  $T_L$  the equivalent torque load.  $T_{ESS}$  is the equivalent torque of the proposed compensating solution.  $R_g$  and  $L_g$  represent the grid impedance, in this case the generator stator impedance.

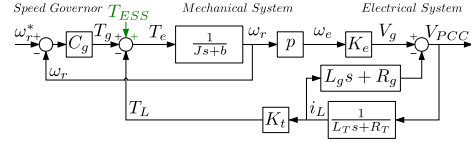


Fig. 2. Equivalent system diagram of a PM synchronous generator supplying constant-impedance type loads.

The mechanical system of the generator is coupled to its electrical one, thus any change or disturbance in the electrical grid will be reflected in its mechanical system. In the case an electrical active load,  $R_T$ , is suddenly connected to the grid, it will generate an equivalent torque load  $T_L$  proportional to the load current  $i_L$  at the generator's shaft. This torque, will be seen as a disturbance by the governor, causing a speed variation which depends on the mechanical inertia and the governor control system. Considering the control system of governor as a PI in the ideal form and neglecting the effect of electrical subsystem of the generator, the generator disturbance transfer function  $D_g$  is expressed by (1).

$$D_g(s) = -\frac{\omega_r(s)}{T_L(s)} = \frac{1}{C_g(s) + Js + b} = \frac{\frac{1}{J}s}{s^2 + \frac{K_p + b}{J}s + \frac{K_p}{T_I J}} \quad (1)$$

Attending to the generator system, it is worth noting that the generator voltage is proportional to the mechanical speed through the back electromotive force constant ( $K_e$ ). Thus, as well as the frequency, the voltage magnitude will vary proportionally. Fig. 1 illustrates the behavior of the synchronous generator when a load is connected/disconnected. As it can be seen, both the frequency and the voltage are affected. Therefore, depending on the grid  $X/R$  ratio, the compensation could positively affect the active and reactive power.

## III. TRANSIENT FREQUENCY DRIFT COMPENSATION

The basic idea of the dynamic frequency drift compensation consists on maintaining the active power balance between the grid elements during transients. In the case under study, the transient active power mismatch between the generation and consumption in the grid will depend on the grid equivalent inertia determined by the synchronous generators and their

associated power source characteristics. Thus, one of the first ideas that emerged consisted on the modification of such grid inertia by introducing a virtual inertia using an ESS that emulates the behavior of a synchronous generator, known in the literature as Virtual Synchronous Machine (VSM) [8]. Although in the literature the expression is commonly referred as a relation between injected power and frequency, in this case an expression in terms of torque and frequency seems to be more appropriate. The law of control is summarized in (2)

$$T_{ESS}(t) = k_{pESS}(w_e^*(t) - w_e(t)) - J_{ESS} \cdot s \cdot w_e(t) \quad (2)$$

where  $T_{ESS}$  is the equivalent torque,  $k_{pESS}$  is a damping coefficient that emulates a governor with proportional regulator,  $J_{ESS}$  is the virtual inertia gain that emulates a machine inertia,  $w_e$  is the instantaneous grid frequency in rad/s and  $w_e^*$  the frequency reference. At this point it is worth to notice that for the case of a single generator grid at which all the machine parameters are known and the frequency is perfectly measured, the term related to the inertia  $J_{ESS} \cdot s \cdot w_e(s)$  would be sufficient to completely compensate the transient response. However, in a real situation, and considering no communications are used, the parameters uncertainty, changes at the operating conditions as well as limited sensor bandwidth and digital control delay, make necessary the use of techniques to improve the control for frequency compensation. The possible enhancements go from the use of a proportional term  $k_{pESS}$  used in VSGs, to advanced techniques as the ones proposed in [8]. The present study, covers improvements based on the use of the available system information in order to estimate the unknown parameters and to enhance the overall performance, taking special concern on the frequency sensor effects. The conditions and constraints of the proposed communication-less solution are the following:

- There is not communication between the proposed solution and any other system at the grid.
- The available measurements will consist only on electric variables (currents and voltages) at the PCC.
- The control relies on the feedback of grid frequency, thus, frequency estimation methods are needed.
- The power exchange between the proposed system and the grid should take place only during transients. The charge cycles of the ESS are not covered in this study.
- Actual frequency command in the MG is unknown.
- The possibility of binding the proposed solution to a significant load in the grid, gaining access to the load current is also considered.

Under these constraints, the main problems to be tackled are summarized as:

- The frequency has to be estimated from electrical variables. The effects of measurement noise and delays as well as grid distortion over the used frequency estimation techniques must be considered.
- The transient state should be detected in order to avoid any possible power share during steady state.
- The frequency command is unknown while is one of the variables involved. Its effects must be either estimated or decoupled.

- The digital implementation of the control introduces constraints relative to delay, bandwidth limitation and noise that can affect the performance being specially critical the use of derivatives.

#### A. Proposed Control System

A simplified version of the proposed control system scheme is shown in Fig. 3. Besides the internal active and reactive current control loops of the converter, five blocks can be identified forming the communication-less solution.

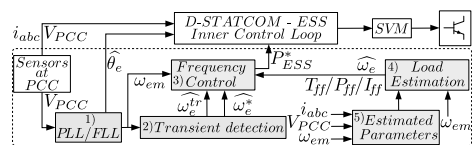


Fig. 3. Simplified control scheme for the proposed system.

1) *Grid synchronization and frequency estimation*: It provides the estimated grid angle ( $\theta_e$ ) for the current coordinate transformation, and the estimated grid frequency ( $\hat{\omega}_e$ ) for its use as control feedback signal, based on PLL or FLL techniques. An experimental comparison of both PLL and FLL frequency measurements with respect to the reading giving by an observer is shown at Fig. 4. As it is readily seen, both PLL with low pass filter and FLL are good candidates for the frequency estimation. However, considering the robustness of FLL under distorted grids, this last solution will be used on all the subsequent experiments.

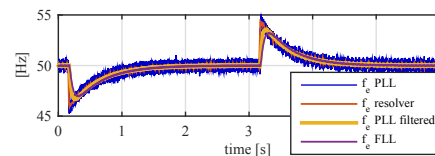


Fig. 4. Experimental results for the measurement of the frequency drift. As a reference the signals are compared with the one given by a resolver. For this work, an FLL is considered.

2) *Transient detection*: As the power exchange during steady state should be avoided, the detection of frequency transients is required. Moreover, the actual grid command should be decoupled from the transient in order to not react to variations of the frequency grid reference. The proposed method is detailed at section III-B.

3) *Frequency control*: The main block of the control system consist on a regulator able to provide a power reference for the D-STATCOM ( $P_{ESS}^*$ ), using the error between the frequency reference and the feedback frequency estimation. Details for the control tuning are giving at section III-C.

4) *Load disturbance estimation*: When grid parameters are known or estimated, it is possible to generate a load estimation and use it as a feedforward either in terms of power, torque or current ( $P_{FF}$ ,  $T_{FF}$ ,  $I_{FF}$ ) to improve the response. In this study

two options have been contemplated one based on current measurement, developed at section III-D, and another relying on a Luenberger-based observer, considered at section IV.

5) *Estimated parameters*: The necessary information for the implementation of the load disturbance estimator should be estimated either online or offline. In the scope of this paper all the parameters will be known or in any case offline obtained.

### B. Transient detection

As it has been said before, it is needed to detect a frequency change with respect to the reference. With the proposed communication-less approach, there is no possibility of getting the grid frequency reference and the detection must be completely carried out autonomously. The obvious solution is to apply a high-pass filter and, over the resulting signal, to calculate the absolute value, which compared with a threshold level will be used for triggering the power injection. However, those kind of methods will still need to subtract from the measured grid frequency the estimated reference. For this reason, the method is prone to errors due to small variations on the reference frequency.

In this paper, a method based on the correlation of the measured frequency with a signal of period  $T$  and zero average is proposed (3).

$$u(t) = \left( \int_0^T x(t)f(t)dt \right)^2 \quad (3)$$

where  $x(t)$  is  $\hat{\omega}_e$  and  $f(t)$  could be a sine or cosine.

The correlation is digitally calculated in two steps: 1) At each sample time, the value for the inner integral is calculated and the result is stored in a variable in memory

$$C\omega_{e[k]} = C\omega_{e[k-1]} + \hat{\omega}_{e[k]} \cdot \sin(2\pi kT) \quad (4)$$

2) After completing the samples for one correlation signal period, the square of the integral is calculated and the result saved:

$$C^2\omega_{e[k]} = (C\omega_{e[k]})^2 \quad (5)$$

Following, the last calculated value for the  $C^2\omega_{e[k]}$  variable is compared with a selected threshold. In the case the value is smaller than the threshold, meaning the system is at steady state, the reference frequency is updated to the measured one. When the value exceeds the threshold, the transient condition is activated and the reference frequency hold to the last updated value. Finally, the estimated transient frequency is obtained as

$$\hat{\omega}_{e^r}[k] = \hat{\omega}_{e[k]} - \hat{\omega}_{e^*}[k] \quad (6)$$

The obtained experimental results for the estimated transient frequency are shown at Fig. 5. The results are compared with respect to the measured frequency, from which the reference value has been subtracted. The curves are presented using two different values for the period of the base sinusoidal signal. As it can be seen, the selection of the period greatly affect the accuracy of the method. Still, the results are really promising while keeping the computational burden very low.

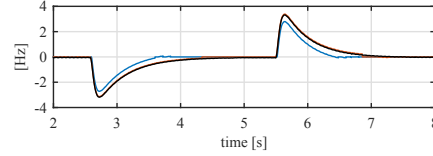


Fig. 5. Experimental results for the transient frequency estimation using the correlation method. The FLL estimated frequency with the reference value subtracted is shown in black. The estimated transient is shown using two different values for the sinusoidal signal period, blue curve is for  $T = 40ms$ , red one for  $T = 70ms$ . Threshold value is set for both cases to 5.

### C. Frequency feedback based control

The basic idea for the feedback based control is shown at Fig. 6. The feedback frequency controller,  $C_c$ , uses the estimated frequency reference ( $\hat{\omega}_e^*$ ) and the measured value ( $\hat{\omega}_e$ ) to provide a control action that could be interpreted either as a power ( $P_{ESS}^*$ ) or equivalent torque command ( $T_{ESS}^*$ ). In this paper, the use of the torque command is proposed.

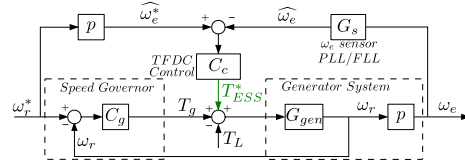


Fig. 6. Block diagram of the transient frequency drift compensator based on feedback control. The provided torque reference is highlighted in green.

The analysis of the dynamic performance of the feedback system it is based on the the disturbance rejection transfer functions. As it has been explained before, for the governor system without any external compensation, the  $T_L$  to  $\omega_r$  transfer function is given by the expression of  $D_{g(s)}$  (1). When the external compensation is added, the resulting transfer function is given by (7)

$$D_c(s) = \frac{\omega_r}{T_L} = -\frac{D_{g(s)}}{1 + D_{g(s)} \cdot C_c(s) \cdot G'_s(s)} \quad (7)$$

where  $G'_s(s) = G_s(s) \cdot p$ , being  $p$  the number of pole pairs of the machine. For the analysis, the generator disturbance transfer function and the frequency sensor are approximated by second order transfer functions as shown in (8). These expressions will be also later used during the development of the observer-based compensation.

$$D_{g(s)} = \frac{k_g \omega_{ng}^2 s}{s^2 + 2\xi_g \omega_{ng} s + \omega_{ng}^2}, \quad G_s(s) = \frac{k_s \omega_{ns}^2}{s^2 + 2\xi_s \omega_{ns} s + \omega_{ns}^2} \quad (8)$$

where the gain  $k_g$  is the  $D_g$  gain, and  $k_s$  is the sensor gain, 1 by default, while  $\omega$  and  $\xi$  are the natural frequency and damping factor of each system. If the governor is considered as a PI regulator, the parameters are equivalent to  $k_g = \frac{T_i}{K_p}$ ,

$$\omega_{ng} = \sqrt{\frac{K_p}{T_i J}} \quad \text{and} \quad \xi_{ng} = \frac{b + K_p}{2J\omega_{ng}}$$

Fig. 7 shows the general scheme for the frequency controller  $C_c$ , including the torque and power alternatives. The  $R$  and  $H$  functions can be substituted by the common regulators terms, P, PI, PD and PDF (pseudo-derivative feedback [14]). It is highlighted in the figure the possibility for adding a feed-forward to improve the control. Detailed explanation about those modifications will be shown in III-D. where  $u(s)$  is the

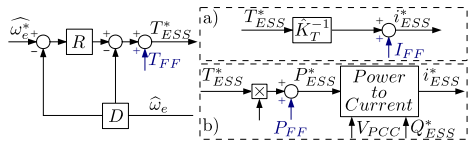


Fig. 7. Control structure for frequency drift compensation.  $R$  could be a P, PI or PD regulator and  $D$  is 0 or derivative regulator (PDF). a) Torque alternative, b) Power alternative.

control action ( $T_{ESS}^*$ ) and  $e(s)$  the error ( $\omega_{e(s)}^* - \omega_{e(s)}$ ).

Before starting with the evaluation of each method, it is worth noting that PI and PD methods are less appealing for this application. The use of an integral action in the controller, even if it can improve the disturbance rejection drastically, would lead to the unavoidable share of power during steady state. On the other hand, the inclusion of a differential action in the direct chain, will boost noise problems in the case there are changes at the commanded frequency. Moreover, PDF topology not only offers derivative action in a smarter way than a classical PD but also, as seen before, has a physical meaning and has been used before in similar frequency control applications [8]. Even being a limited option, P regulator appears as a simpler solution that might be enough for some applications.

The method selected for the comparison of the feedback alternatives is based on the evaluation of the dynamic stiffness. Being the proposed control system oriented to the disturbance rejection, the method will provide a clear view on the expected performance. For the analyzed problem, the dynamic stiffness is defined as (9)

$$S_{c(s)} = \frac{T_L}{\omega_r} = \frac{1 + D_{g(s)} \cdot C_c(s) \cdot G'_s(s)}{D_{g(s)}} \quad (9)$$

When the dynamic stiffness transfer function is evaluated in frequency domain for different P and PDF settings, the results shown in 8 are obtained. The graph clearly indicates the benefits of an increased proportional gain and also the additional disturbance rejection capability bandwidth because of the inclusion of the differential term. The corresponding transient responses in time domain for the same design cases shown at Fig. 8, are depicted at Fig. 9. As shown, the predicted benefits for including the differential term are translated to a reduced initial overshoot when compared to the P design. Finally, the experimental results for the feedback-based compensation is shown at Fig. 10. A good agreement with respect to the previous theoretical discussion can be observed.

#### D. Improving the basic control: Load feed-forward and state observation

Given the limitations due to phase lag on the frequency estimation algorithm, some solutions could be applied to

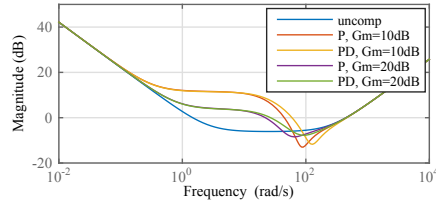


Fig. 8. Dynamic stiffness for PD and PDF methods with two different proportional gains. For the case of PDF methods, a minimum phase margin of 40 deg. is set at the open loop crossover frequency.

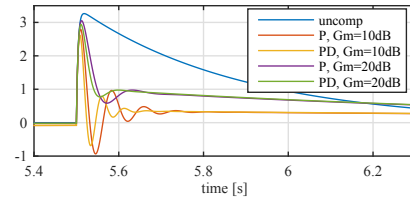


Fig. 9. Compared transient responses for PD and PDF methods with two different proportional gains. For the case of PDF methods, a minimum phase margin of 60 deg.

increase the phase and gain margins, improving the response of the dynamic frequency controller. Two ideas are proposed, the use of a load disturbance feed-forward and the compensation of the frequency estimation effect.

If the load information is available either through load current measurement, or any other method, it can be used as a feed-forward for the controller, as shown in Fig. 7, considering the load feed-forward either in terms of current, power or torque. Ideally, if the load is known and it is fully compensated by the ESS, the frequency drift will be eliminated. However that solution would inject the whole load power during steady state. In order to compensate only the transient and keep the grid frequency unalterable, the ESS has to share only the power load minus the power drawn by the governor, i.e. the equivalent torque of the compensation system should be  $T_{ESS} = T_L - T_g$  in order to reach an optimal balance between compensation and injected energy. The relation between  $T_g$  and  $T_L$  is written in (10) being the transfer function for the ideal case  $\frac{T_{ESS}}{T_L} = 1 - \frac{T_g(s)}{T_L(s)}$ .

$$\frac{T_g(s)}{T_L(s)} = \frac{C_{g(s)}}{C_{g(s)} + Js + b} = \frac{K_p s + K_p / T_i}{Js^2 + (K_p + b)s + K_p / T_i} \quad (10)$$

Nevertheless, unlike  $D_{g(s)}$ , obtaining  $\frac{T_g(s)}{T_L(s)}$  is not easy in a communication-less system if the system parameters are unknown. However, the load information is still a valuable information as it is a derivative state of the frequency, allowing to anticipate the control reaction, i.e. to reduce the phase delay gaining phase margin. In order to eliminate the share during

steady state instead of TF in (10), a high pass filter (HPF) can be applied to the load information.

Fig. 10 shows the experimental performance comparison of the different feedback methods and the response when a load information is used. The load information comes from a load current sensor, which is a valid assumption considering the proposed solution is based on a significant load. The full load compensation is also shown. It has been obtained by equaling the D-STATCOM current reference to the load measured current.

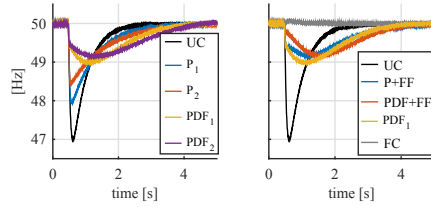


Fig. 10. Transient frequency drift compensation using different control methods. a) Grid frequency, b) Injected Power. UC: uncompensated,  $P_1$ : P controller,  $K_p = 0.1$ ,  $P_2$ : P controller,  $K_p = 0.2$ ,  $PDF_1$ : PDF controller,  $K_p = 0.2$ ,  $K_d = 0.1$ ,  $PDF_2$ : PDF controller,  $K_p = 0.2$ ,  $K_d = 0.25$ ,  $PDF + FF$ : PDF with load feedforward, 2nd order high-pass filter, bandwidth=0.5Hz, and same gains as  $PDF_1$ .

#### IV. LOAD OBSERVER MODELLING

The proposed Luenberger-based observer control is shown in Fig. 11. In this scheme, the speed governor and the generator will be considered as the system and the PLL/FLL the sensor. Considering that the generator and governor param-

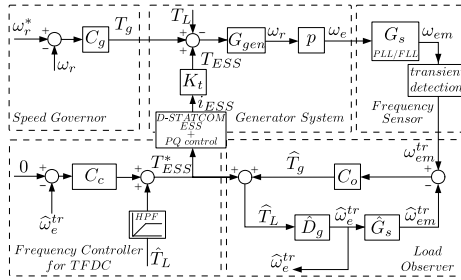


Fig. 11. Proposed observer control structure.

eters are unknown, the systems  $C_g$  and  $G_{gen}$  can not be used explicitly in the proposed solution. However, the second order approximations proposed before for both the sensor and the generator disturbance transfer functions (8), are appealing candidates to the observer implementation. The experimental comparison for the proposed sensor and generator disturbance transfer functions with respect to the real systems are shown in Fig. 12. For the observer implementation, state space modeling is considered. The observer plant state space model

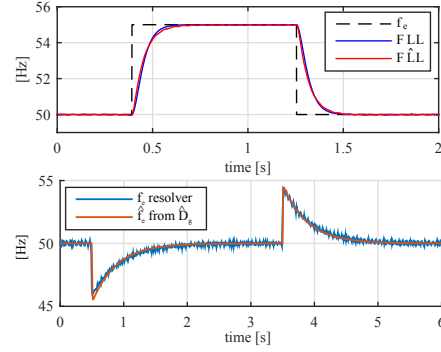


Fig. 12. Experimental results. Top, DSOGI FLL response and its approximation using the 2<sup>nd</sup> order TF in (8). Bottom, Open-loop response obtained with the estimation of the disturbance TF  $\hat{D}_g$ . The estimated frequency is compared with the value obtained by the generator resolver.

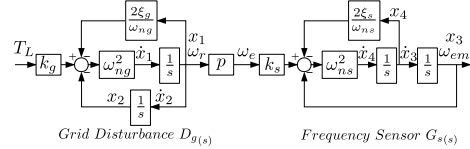


Fig. 13. Observer system plant block diagram in state space form.

is shown in Fig. 13. The model is defined by the state vector  $x = [x_1, x_2, x_3, x_4]^T$ , the input vector  $u = [T_L]$  and the output vector  $y = [\omega_e, \omega_{em}]^T = [p \cdot x_1, x_3]^T$ . The state, input, output and feedforward matrices are defined in (11).

$$A = \begin{bmatrix} -2\xi_g\omega_{ng} & -\omega_{ng}^2 & 0 & 0 \\ 1 & 0 & 0 & 0 \\ 0 & 0 & 0 & 1 \\ k_s p \omega_{ns}^2 & 0 & -\omega_{ns}^2 & -2\xi_s\omega_{ns} \end{bmatrix}, B = \begin{bmatrix} k_g \omega_{ng}^2 \\ 0 \\ 0 \\ 0 \end{bmatrix} \\ C = \begin{bmatrix} p & 0 & 0 & 0 \\ 0 & 0 & 1 & 0 \end{bmatrix}, D = \begin{bmatrix} 0 \\ 0 \end{bmatrix} \quad (11)$$

$$x[k+1] = A_d x[k] + B_d u[k], \quad y[k] = C_d x[k] + D_d u[k] \quad (12)$$

For the digital implementation the difference equations in (12) are used, where  $A_d$ ,  $B_d$ ,  $C_d$  and  $D_d$  are the discretized versions of the state space matrices using zero order hold (ZOH). The discrete matrices are obtained as  $A_d = e^{A T_s}$ ,  $B_d = A^{-1}(A_d - I)B$ ,  $C_d = C$  and  $D_d = D$  being  $T_s$  the sampling time and  $I$  the identity matrix of  $A_d$ . The values used for the listed parameters are shown in Table II.

For the observer analysis, as previously done for the feedback-based control, the dynamic stiffness is used. From the proposed observer block diagram, and assuming parameters matching between the real system and the observer equations, (13) can be obtained.

$$\frac{T_L}{\omega_e} = \frac{1 + \hat{D}_g \cdot C_o \cdot \hat{G}_s}{1 + \hat{D}_g (C_c + C_o \cdot \hat{G}_s)} \quad (13)$$

The resulting frequency plots and transient response is shown in Fig. 14 and Fig. 15. The curves are compared with the uncompensated, ideal sensor and feedback compensation. As it can be seen, the use of the observer improves in a noticeable way the initial transient response due to the compensated sensor lag. Tuning of the observer has been done using loop shaping techniques in frequency domain. The order of the controller has been kept equal to the number of poles of  $\widehat{D}_g \cdot \widehat{G}_s$ , ( $4^{th}$ ). Values for the observer feedback controller are listed in Table II.

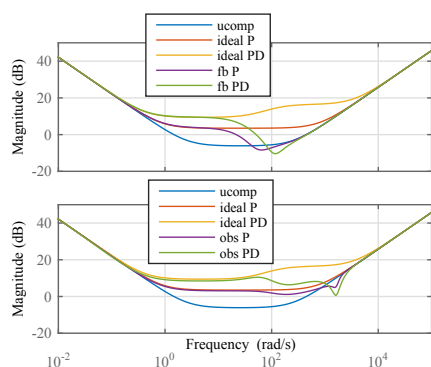


Fig. 14. Dynamic stiffness. Top axes, results for the feedback-based control. Bottom axes, observer-based control. The uncompensated and ideal sensor cases are shown as a reference.

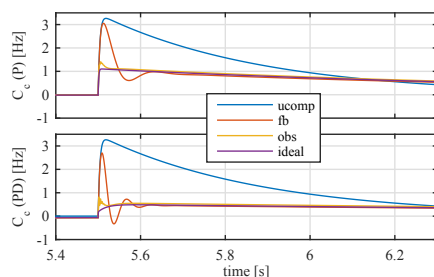


Fig. 15. Transient response. Top axes, results when a P controller is used as the transient frequency controller  $C_c$ . Bottom axes, results when a PD is used instead. The uncompensated and ideal sensor cases are shown as a reference.

## V. EXPERIMENTAL RESULTS

The proposed solutions has been tested both simulated and experimentally, following the setup presented in Section II and in Fig. 1, and the parameters in Table II. In the experimental setup, for the implementation of the DC/DC converter and the inverter, two MTL-CB10060F121XHF power converters rated at 25kW have been used. The control system has been implemented in a TMS320F28335 DSC from Texas Instruments. The MG generator is emulated using 2 coupled

TABLE II. SYSTEM PARAMETERS

Power System Parameters		Value
Nominal Voltage ph-ph[V <sub>rms</sub> ]		98
Nominal Frequency[Hz]		50
Three phase balance load[Ω]		32
Generator Parameters		Value
BEMF constant[V/krpm]		98
Torque constant[Nm]		1.6
Pole pairs		3
Mechanical parameters		$J = 0.0019 kg \cdot m^2$ , $b = 0.2 Nms$
Electrical parameters		$L = 6 mH$ , $R = 2.1 \Omega$
Converter Parameters		Value
Power[kW]		10
Nominal Battery voltage[V]		140
Controlled DC link voltage[V]		300
DC bus capacitor[mF]		2
Grid connected AC filter		$R=0.2 \Omega$ , $L = 7.18 mH$
DC/DC converter boost inductors		$R=0.1 \Omega$ , $L=7.18 mH$
Switching frequency[Hz]		10000
DC/DC converter Control Tuning		Value
Current control loop		$BW=500Hz$ , $K_p=22.5$ , $K_i=13.9276$
DC link Voltage loop		$BW=5Hz$ , $K_p=1$ , $K_i=175$
AC/DC converter Control Tuning		Value
Current control loop		$BW=400Hz$ , $K_p=22.5$ , $K_i=50$
Observer parameters		$k_g=0.78$ , $\omega_{ng}=25.6$ , $\xi_g=4.96$
		$k_s=1$ , $\omega_{ns}=31.4$ , $\xi_s=1$
Observer $C_o$ coefficients		$K_o=10$ , zeros=0.01, 0.01, 0.005, 0.0034 poles=0.002, 0.001, 0.001, 6.67e-4

PMSMs one acting as generator and other as governor motor controlled by a commercial drive.

The grid currents and voltages are shown at Fig. 16, a comparison for the feedback and feedforward methods at Fig. 17 and the observer based results compared with respect to the other analyzed method as well as the estimated load are shown in Fig. 18 and Fig. 19. As expected, feedforward and observer based methods have the best performance in terms of frequency compensation. The use of observation techniques also allows to estimate the load current.

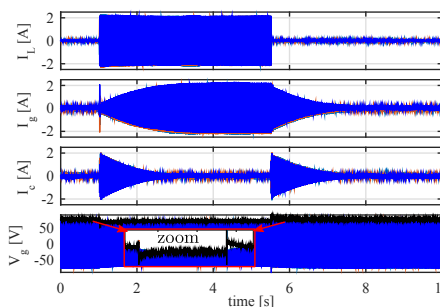


Fig. 16. Experimental results showing the current and voltages. From top to bottom, load current, generator current, compensation current and grid voltage.

## VI. CONCLUSIONS

In this paper, an autonomous system has been proposed for transient frequency drift compensation. The proposed solution has addressed some of the limitations of existing literature. The performance achieved by feedback control has been improved by the employment of feedforward current and the development of a Luenberger-based observer. A detailed comparison

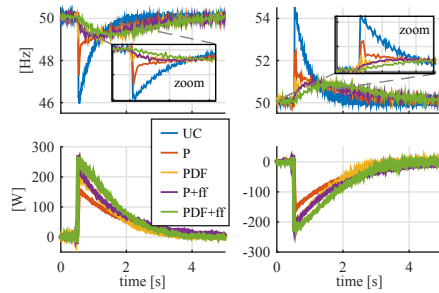


Fig. 17. Experimental results. Grid frequency and Injected Power. UC: uncompensated,  $P$ : P controller,  $K_p = 0.2$ ,  $PDF$ : PDF controller,  $K_p = 0.2$ ,  $K_d = 0.1$ ,  $P + FF$  and  $PDF + FF$ : P, PDF controllers with load feedforward 1st order high-pass filter,  $bw=0.5\text{Hz}$ , and same gains as  $P$  and  $PDF$ .

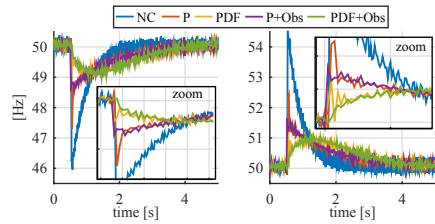


Fig. 18. Experimental results. Observer results. UC: uncompensated,  $P$  and  $PDF$  same than at Fig. 16.  $P + Obs$ ,  $PDF + Obs$  observer bases estimation with the parameters shown at Table II.

including analytical derivations, simulation and experimental results have been carried out. The proposed signal processing for removing of the steady state frequency reference, based on the use of a correlation signal, enables the method to work on weak grids operated under droop control.

Finally, a comparative evaluation of the analyzed techniques has been done summarizing their performance in Fig. 20. Five indexes are considered. The maximum frequency deviation  $\Delta f_{max}$ , the peak power ( $P_{max}$ ), the total shared energy ( $E$ ) and two coefficients  $C_{comp}$  and  $C_{sett}$  are defined to evaluate the initial compensation and the enlargement of settling time compared to the original response respectively. The indexes are shown normalized in pu, being all of them the higher the worst, except  $C_{comp}$  that represent an advantage when tends towards one.

#### REFERENCES

- [1] J. M. Guerrero, "Editorial special issue on power electronics for microgrids 2014; part ii," *IEEE Transactions on Power Electronics*, vol. 26, no. 3, pp. 659–663, March 2011.
- [2] J. Guerrero, P. C. Loh, T.-L. Lee, and M. Chandorkar, "Advanced control architectures for intelligent microgrids 2014; part ii: Power quality, energy storage, and ac/dc microgrids," *IEEE Transactions on Industrial Electronics*, vol. 60, no. 4, pp. 1263–1270, April 2013.

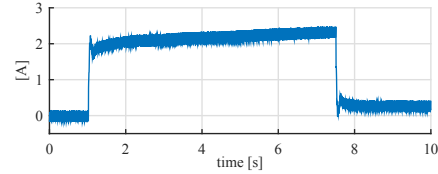


Fig. 19. Experimental results. Observer estimated load. The real current load was 2.2A.

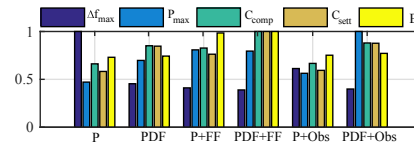


Fig. 20. Merit figure. Performance evaluation for all the considered methods.

- [3] A. Agbedahunsi, M. Sumner, E. Christopher, A. Watson, A. Costabeber, and R. Parashar, "Frequency control improvement within a microgrid, using enhanced statcom with energy storage," in *6th IET International Conference on Power Electronics, Machines and Drives (PEMD 2012)*, March 2012, pp. 1–6.
- [4] A. Arulampalam, J. Ekanayake, and N. Jenkins, "Application study of a statcom with energy storage," *IEEE Proceedings on Generation, Transmission and Distribution*, vol. 150, no. 3, pp. 373–384, May 2003.
- [5] M. Falvo, L. Martirano, and D. Sbordone, "D-statcom with energy storage system for application in smart micro-grids," in *2013 International Conference on Clean Electrical Power (ICCEP)*, June 2013, pp. 571–576.
- [6] M. Holmberg, M. Lahtinen, J. McDowall, and T. Larsson, "Svc light with energy storage for frequency regulation," in *2010 IEEE Conference on Innovative Technologies for an Efficient and Reliable Electricity Supply (CITRES)*, Sept 2010, pp. 317–324.
- [7] I. Serban and C. Marinescu, "Control strategy of three-phase battery energy storage systems for frequency support in microgrids and with uninterrupted supply of local loads," *IEEE Transactions on Power Electronics*, vol. 29, no. 9, pp. 5010–5020, Sept 2014.
- [8] M. Torres L, L. Lopes, L. Moran T, and J. Espinoza C, "Self-tuning virtual synchronous machine: A control strategy for energy storage systems to support dynamic frequency control," *Energy Conversion, IEEE Transactions on*, vol. 29, no. 4, pp. 833–840, Dec 2014.
- [9] S.-K. Chung, "A phase tracking system for three phase utility interface inverters," *IEEE Transactions on Power Electronics*, vol. 15, no. 3, pp. 431–438, May 2000.
- [10] P. Roncero-Sanchez, X. del Toro Garcia, A. Torres, and V. Feliu, "Fundamental positive- and negative-sequence estimator for grid synchronization under highly disturbed operating conditions," *IEEE Transactions on Power Electronics*, vol. 28, no. 8, pp. 3733–3746, Aug 2013.
- [11] P. Rodriguez, A. Luna, M. Ciobotaru, R. Teodorescu, and F. Blaabjerg, "Advanced grid synchronization system for power converters under unbalanced and distorted operating conditions," in *32nd Annual Conference on IEEE Industrial Electronics, IECON 2006*, Nov 2006, pp. 5173–5178.
- [12] D. Luenberger, "Observing the state of a linear system," *IEEE Transactions on Military Electronics*, vol. 8, no. 2, pp. 74–80, April 1964.
- [13] "Ieee standard for interconnecting distributed resources with electric power systems - amendment 1," *IEEE Std 1547a-2014 (Amendment to IEEE Std 1547-2003)*, pp. 1–16, May 2014.
- [14] S.-K. Sul, *Control of Electric Machine Drive Systems*. Wiley IEEE press, 2011.



### **D.3 Limits, stability and disturbance rejection analysis of voltage control loop strategies for grid forming converters in DC and AC microgrids with high penetration of constant power loads**

A. Navarro-Rodríguez, P. García, J. M. Cano and M. Sumner, "Limits, stability and disturbance rejection analysis of voltage control loop strategies for grid forming converters in DC and AC microgrids with high penetration of constant power loads", 2017 19th European Conference on Power Electronics and Applications (EPE'17 ECCE Europe), Warsaw, 2017, pp. P.1-P.10.



### **Limits, Stability and Disturbance Rejection Analysis of Voltage Control Loop Strategies for Grid Forming Converters in DC and AC Microgrids with High Penetration of Constant Power Loads**

A. Navarro-Rodríguez, P. García, J. M. Cano  
LEMUR Group, University of Oviedo  
Campus of Viesques s/n 33204  
Gijón, Spain  
Email: navarroangel@uniovi.es,  
garciafpablo@uniovi.es,  
jmcano@uniovi.es  
URL: <http://lemur.dieecs.com>

M. Sumner  
PEMC Research Group  
Faculty of Engineering  
University of Nottingham  
University Park, NG7 2RD  
Nottingham, UK  
Email: [Mark.Sumner@nottingham.ac.uk](mailto:Mark.Sumner@nottingham.ac.uk)  
URL: <http://www.nottingham.ac.uk>

#### **Acknowledgments**

The present work has been partially supported by the predoctoral grants program Severo Ochoa for the formation in research and university teaching of Principado de Asturias PCTI-FICYT under the grant ID BP14-135. This work was also supported in part by the Research, Technological Development and Innovation Program Oriented to the Society Challenges of the Spanish Ministry of Economy and Competitiveness under grant ENE2013-44245-R and ENE2016-77919-R and by the European Union through ERFD Structural Funds (FEDER).

#### **Keywords**

«Control methods for electrical systems», «Microgrid», «Non-linear control», «Power quality».

#### **Abstract**

This paper extensively analyzes the operation limits, system stability and disturbance rejection capability of the voltage control loops used in master-slave AC and DC Microgrids (MGs). Two different control schemes are studied analytically, simulated and experimentally tested, focusing on Constant Power Loads (CPL). Additionally, the use of the virtual capacitance (VC) as a tool for response enhancement is introduced. The study pursues the proper selection of the controllers gains and minimization of capacitance values by considering the dynamic behavior.

#### **Introduction**

The increasing concern about environmental issues and concepts as renewable energies, distributed generation and self-consumption have led to the necessity of alternatives to the conventional power grid. Moreover, the fast development of power semiconductor devices and digital control systems have made power electronic converters (PECs) the most suitable interface for both generation, energy storage and dimmable loads. Due to the high penetration of renewable generation operating under a maximum power point tracking (MPPT) scheme, one of the adopted voltage control methods in these converter dominated MGs is based on the Master-Slave strategy. This approach requires a grid forming converter controlling the voltage magnitude (and the frequency in the case of AC MGs) [1, 2, 3]. Other alternatives, as droop-based or multiple slack control have been also proposed [4, 5]. Unlike the conventional grid, these kind of MGs are defined as weak. They have a low inertia that should be compensated by a stiff voltage control, and a low line X/R ratio that couples active power and voltage magnitude. Moreover,

the high presence of tightly regulated CPL contribute negatively to that low inertia, in contrast to the self-regulating effect given by conventional loads as Constant Impedance Loads (CIL). In addition, the disturbance rejection response of the voltage control schemes usually implemented in PECs depends on the type of load disturbance, becoming in some cases non-linear and load-state-dependent.

The challenges imposed by CPLs and the non-linearity and stability issues related with the voltage control schemes based on voltage feedback and PI controllers, have been already addressed in the literature [6, 7, 8, 9, 10]. Nonetheless, the dynamics, stability limitations and selection of both the passive elements and the controller parameters for a slack control under CPL have been poorly discussed. Some alternative feedback control topologies have been proposed based on the capacitor energy storage capability as an approach to linearize the relation between the voltage and the power at the DC link [11, 12, 13, 14]. However, those techniques have not been further exploited for grid forming converter applications, existing few examples in the literature focused on the analysis of the dynamic performance.

This paper analyzes the dynamic behavior of the voltage control loop used in grid forming voltage source converters (VSCs) integrated in AC and DC MGs. Due to its wide acceptance in converter control applications, a cascaded voltage-current control scheme is used in this study. Both the conventional voltage feedback control, referred as Direct Voltage Control (DVC) in this document, and the control based on squared voltage, referred as Quadratic Voltage Control (QVC), will be addressed, considering CPLs as the main disturbance. Taking advantage of the cascaded control premises, the inner control loop dynamics will be neglected. Thus, the analysis becomes valid for different applications such as AC slack, DC slack or DC link control. An analytical study on the conventional voltage control schemes is performed based on system linearization methods and validated through simulations and experimentally. In addition, the use of virtual capacitance (VC) is introduced as a tool for disturbance rejection enhancement as well as to experimentally forecast the effect of resizing the capacitance in existing systems. The study will deal with operation limits, the system stability and the disturbance rejection of the voltage control, leading not only to the proper selection of the control scheme and control parameters, but also to the sizing of the passive elements of the converter.

### Problem Definition and System Modeling

In most of the MG applications requiring a voltage regulation, the system plant to be controlled consists of a capacitor whose voltage derivative is proportional to its current. Thus, the control is performed by a closed loop cascaded controller consisting of an inner current control loop and an outer voltage control loop. Assuming the current control loop is fast enough, its dynamics can be neglected. Thus, the voltage control can be assumed as a voltage regulator, which input is the error,  $\epsilon$ , between the voltage reference,  $V^*$ , and the measured voltage,  $\tilde{V}$ , while the control action is the current,  $I$ , entering the system plant. Considering the existence of disturbance loads, the system plant is defined by (1), where  $V_{(t)}$  is the capacitor voltage,  $I_{(t)}$  is the control action of the voltage control loop, and  $I_{d(t)}$  is the load disturbance. According to (1), the controller can be tuned using LTI system properties.

$$\frac{dV_{(t)}}{dt} = \frac{1}{C}(I_{(t)} - I_{d(t)}) \quad (1) \quad \frac{dV_{(t)}}{dt} = \frac{1}{C} \left( I_{(t)} - \underbrace{\left( I_{L(t)} + \frac{P_{L(t)}}{V_{(t)}} + G_{L(t)}V_{(t)} \right)}_{I_{d(t)}} \right) \quad (2)$$

Nevertheless, Constant Current Loads (CCL) are rarely found in power systems. More and more electrical appliances and industrial equipment behaves as CPLs, presenting a tight control of load power, or as CILs. Thus, the system in (1) must be reformulated as the non-linear system in (2), where  $I_L$ ,  $P_L$  and  $G_L$  are the current, power and conductance disturbances drawn by CCLs, CPLs, and CILs respectively. Negative values of  $P_L$  and  $I_L$  are considered as generation. Fig. 1(a) shows the single line representation of the defined non-linear system. The behavior of the different loads existing in a MG are illustrated in Fig. 1(b). The non-linearities due to CPL and CIL will affect the voltage regulation design and performance. Moreover, unlike CILs, it is well known that CPLs are prone to compromise the system stability. In the literature, several attempts have been carried out for obtaining a linear approximation by defining a neg-

ative impedance [8, 9, 4]. In this paper, the effect of non-linear loads is approached by the linearization of the close loop system.

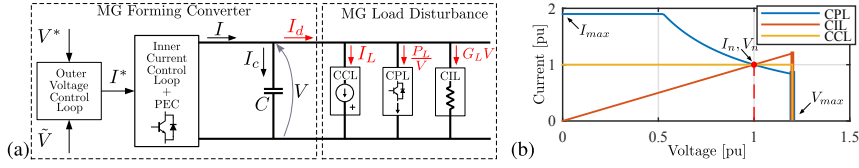


Fig. 1: (a) Simplified single line representation of the grid forming converter and load disturbance in a DC or AC MG. (b) Voltage-Current curves of the different types of loads in MGs.

### The Voltage Controller: Control Topologies, Analytical Models and Analysis

The voltage controller models are analyzed in this section using linearized models. Two control schemes are considered, the direct voltage control (DVC) and the quadratic voltage control (QVC).

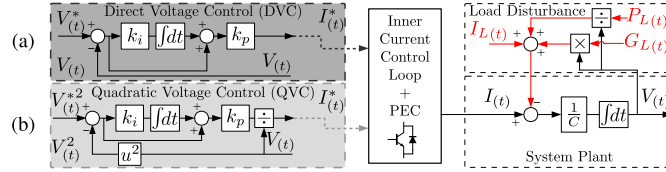


Fig. 2: Voltage control schemes for the different types of loads in MGs. (a) DVC; (b) QVC.

#### The Direct Voltage Controller (DVC)

The DVC control scheme is shown in Fig. 2(a). A PI regulator in the standard form has been selected for the analysis, defined by (3), where  $I^*$  is the control action,  $V^*$  the voltage reference,  $V$  the actual voltage, and  $k_p$  and  $k_i$  are the proportional and integral PI gains respectively. In this paper, the effect of the sensors is neglected. This controller is based on the linear relationship between the voltage and the current at the capacitor. Despite its apparent simplicity, achieving good dynamic behavior is not straightforward, as already reported in the literature [11]. This is due to the fact that even the reference tracking capability for the voltage control is linear, as shown in (4), the voltage reaction to both CPL and CIL disturbances is not.

$$I_{(t)}^* = k_p(V_{(t)}^* - V_{(t)}) + k_p k_i \int (V_{(t)}^* - V_{(t)}) dt \quad (3) \quad \frac{V_{(s)}}{V_{(s)}^*} = \frac{k_p s + k_p k_i}{s^2 C + s k_p + k_i k_p} \quad (4)$$

#### The Quadratic Voltage Controller (QVC)

An alternative to the DVC has been proposed in the literature referred as fast-acting DC link voltage controller and energy based controller, in the context of applications for the DC link control of DC/DC/AC and AC/DC/AC converters [11, 12, 13, 14]. Nonetheless, its application can be generalized to any cascaded-based voltage control such as grid forming converters in both DC and AC MGs. The control scheme is shown in Fig. 2(b) and the controller differential equation is given by (5).

$$I_{(t)}^* = \frac{k_p(V_{(t)}^{*2} - V_{(t)}^2) + k_p k_i \int (V_{(t)}^{*2} - V_{(t)}^2) dt}{V_{(t)}} \quad (5) \quad V_{(t)} \frac{dV_{(t)}}{dt} = \frac{1}{C} P_{c(t)} \Rightarrow \frac{dV_{(t)}^2}{dt} = \frac{2}{C} P_{c(t)} \quad (6)$$

The control is based on the linear relation between the power flowing into the capacitor,  $P_{c(t)}$ , and the voltage module squared,  $V_{(t)}^2$ , as stated in (6). In [11, 13], its design is realized by exploiting the relation between voltage variations and the energy stored in the capacitor,  $W_c$ . However, the tuning method used

in those papers is oriented to the regulation of the DC link of an AFE exposed to the steady state disturbances produced by AC grid unbalances. Here, we include a general approach based on disturbance rejection analysis, considering a meaningful comparison between DVC and QVC dynamic response.

One of the main advantages of QVC, concerning the disturbance rejection and stability analysis, is that the relation between  $V_{(t)}$  and  $P_{L(t)}$  becomes linear, unlike in the case of DVC. This fact facilitates the delimitation of the stable region. However, the controlled variable is still  $V_{(t)}$  and, considering other kind of disturbances that may be present in the grid, as CIL, the system performance should be evaluated according to the  $V_{(t)}$  dynamics. For that reason the system linearization is also needed. Leaving the disturbances aside, unlike in the DVC, the relation between  $V$  and  $V^*$  is non-linear, (5). The linearized approximation of the reference tracking transfer function is proposed in (7), where  $V_0^*$  and  $V_0$  are the voltage reference and the actual voltage at the equilibrium point, respectively. Assuming  $V_0 = V_0^*$ , the transfer function is approximated by (8).

$$\frac{V_{(s)}}{V_{(s)}^*} \approx \frac{s2k_p V_0^* + 2k_p k_i V_0^*}{s^2 C V_0 + s2k_p V_0 + 2k_p k_i V_0} \quad (7) \quad \frac{V_{(s)}}{V_{(s)}^*} \approx \frac{s2k_p + 2k_p k_i}{s^2 C + s2k_p + 2k_p k_i} \quad (8)$$

Among the controllers tuning techniques available for linear systems, an analytical approach has been selected, aimed at simplifying the selection of PI regulator parameters [5]. The close loop system can be simplified as a second order system with natural frequency  $\omega_n$  and damping factor  $\xi$ . Equations (4) and (8), can be expressed as (9), and assuming linearity, the system poles,  $\omega_n$  and  $\xi$ , will be the same for disturbance rejection transfer functions. Thus, the PI regulator gains for DVC and QVC are tuned according to (10) and (11) respectively, leading to a similar bandwidth.

$$\frac{V_{(s)}}{V_{(s)}^*} = \frac{2\xi\omega_n s + \omega_n^2}{s^2 + 2\xi\omega_n s + \omega_n^2} \quad (9) \quad k_p = 2\xi\omega_n C; \quad k_i = \frac{\omega_n^2 C}{k_p} \quad (10) \quad k_p = \xi\omega_n C; \quad k_i = \frac{\omega_n^2 C}{2k_p} \quad (11)$$

According to cascaded control theory, the bandwidth of the inner loop is assumed to be at least one decade higher than  $\omega_n$ . The damping factor,  $\xi$ , can be selected as a trade-off between overshoot and settling time. For this paper the parameters shown in Table I have been selected.

The main requirement of a grid forming converter is a stiff voltage control under disturbances. To analyze the effect of the type of load in the disturbance rejection capability, the  $\frac{\Delta V_{(s)}}{\Delta P_{L(s)}}$  disturbance rejection transfer function for DVC and QVC have been obtained by linearization and are shown in (12) and (13) respectively. In these equations, the equilibrium point is defined by  $x_0 = [V_0^*, V_0, P_{L0}, G_{L0}]$  for DVC and  $x_0 = [V_0^*, V_0, P_{L0}, G_{L0}]$  for QVC.  $V_0^*$  and  $V_0$  are the voltage reference and the steady state voltage at the equilibrium point.  $P_{L0}$  and  $G_{L0}$  are the load in terms of power associated to CPLs and the load in terms of conductance given by CILs at the equilibrium point respectively. An operation close to the equilibrium point is assumed, considering  $V_0 = V_0^*$ .

$$\frac{\Delta V_{(s)}}{\Delta P_{L(s)}} \approx \frac{-sV_0}{s^2 V_0^2 C + s k_p V_0^2 - P_{L0} + G_{L0} V_0^2 + k_i k_p V_0^2} \quad \frac{\Delta V_{(s)}}{\Delta P_{L(s)}} \approx \frac{-s}{s^2 V_0 C + s2k_p V_0 + I_{L0} + 2G_{L0} V_0 + 2k_i k_p V_0} \quad (12) \quad (13)$$

To verify the linearized models, the response of  $\frac{\Delta V_{(s)}}{\Delta P_{L(s)}}$  is compared in Fig. 3 with the simulation of the non-linear system, using Matlab/Simulink, for both DVC and QVC.

The error between the actual response and the linear approximation validates the linear models near the equilibrium point. However, when the load level at the equilibrium point is not considered, the linear model considerably deviates from the actual response as the system deviates from the equilibrium point. To analyze the effect of the load level at the equilibrium point, the root-contour of the DVC for  $P_{L0}$  and  $G_{L0}$ , (14) and (15), and the root-contour of QVC for  $I_{L0}$  and  $G_{L0}$ , (16) and (17), have been obtained.

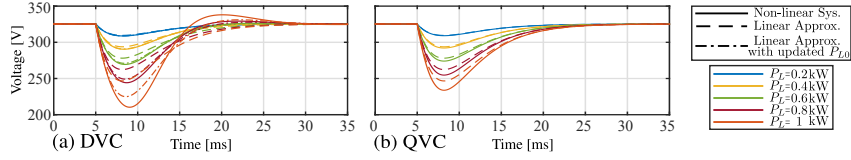


Fig. 3: Non-linear simulated response compared with the linear approximation of  $\frac{\Delta V(s)}{\Delta P_{L(s)}}$  under increasing active power steps. (a) DVC; (b) QVC. Results using the data in Table I.

$$\begin{aligned} \text{DVC root contour } P_{L0} \rightarrow 1 + P_{L0}G(s)H(s) &\approx \frac{-s}{s^2V_0^2C + sk_pV_0^2 + G_{L0}V_0^2 + k_ik_pV_0^2} & \text{DVC root contour } G_{L0} \rightarrow 1 + G_{L0}G(s)H(s) &\approx \frac{V_0^2s}{1 + G_{L0}(s^2V_0^2C + sk_pV_0^2 - P_{L0} + k_ik_pV_0^2)} \end{aligned} \quad (14)$$

$$\begin{aligned} \text{QVC root contour } I_{L0} \rightarrow 1 + I_{L0}G(s)H(s) &\approx \frac{s}{1 + I_{L0}(s^2V_0C + s2k_pV_0 + 2G_{L0}V_0 + 2k_ik_pV_0)} & \text{QVC root contour } G_{L0} \rightarrow 1 + G_{L0}G(s)H(s) &\approx \frac{2V_0s}{1 + G_{L0}(s^2V_0C + s2k_pV_0 + I_{L0} + 2k_ik_pV_0)} \end{aligned} \quad (16)$$

It is worth noting that the response of DVC is non-linear and depends on the load level,  $P_{L0}$  and  $G_{L0}$ , thus conditioning the system behavior and the accuracy of the linear approximation. Moreover, load dependent poles lead to system instability as shown in Fig. 4(a), where the root-contour plot for  $P_{L0}$  is represented. On the other hand, negative values of  $P_{L0}$ , i.e. power generation, can affect positively to the voltage damping.

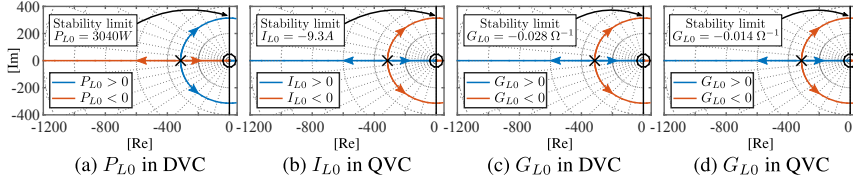


Fig. 4: Root-contour for DVC and QVC depending on  $P_{L0}$ ,  $I_{L0}$  and  $G_{L0}$ . (a) parameter  $P_{L0}$  in DVC; (b) parameter  $I_{L0}$  in QVC; (c) parameter  $G_{L0}$  in DVC; (d) parameter  $G_{L0}$  in QVC.

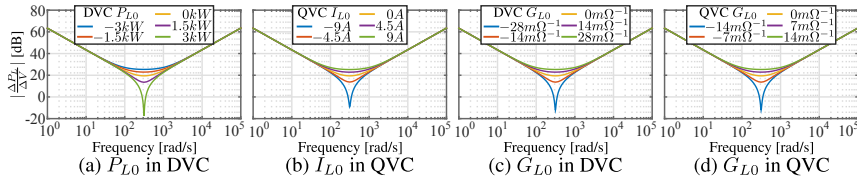


Fig. 5: Dynamic stiffness evaluation depending on  $P_{L0}$ ,  $I_{L0}$  and  $G_{L0}$ . (a) Influence of  $P_{L0}$  in DVC; (b) Influence of  $I_{L0}$  in QVC; (c) Influence of  $G_{L0}$  in DVC; (d) Influence of  $G_{L0}$  in QVC.

In the case of QVC, the term  $P_{L0}$  does not even appear in the equation, which is one of the main advantages of this method over the widely used DVC. It is worth to point out that such an advantage has not been reported yet in the literature. Nonetheless, a dependency on CCLs appears represented by the load level at the equilibrium point  $I_{L0}$ . Although positive load currents,  $I_{L0} \geq 0$ , does not present sta-

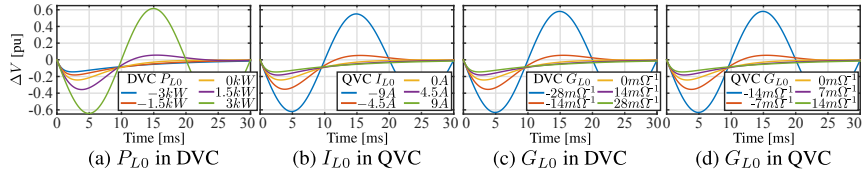


Fig. 6: Step response under a CPL step disturbance of 1kW. (a) Influence of  $P_{L0}$  in DVC; (b) Influence of  $I_{L0}$  in QVC; (c) Influence of  $G_{L0}$  in DVC; (d) Influence of  $G_{L0}$  in QVC.

bility problems, a potential issue appears when  $I_{L0} \leq 0$ , i.e. when constant current generation (CCG) is injected into the grid. The root-contour of the QVC system as a function of  $I_{L0}$  is shown in Fig. 4(b).  $G_{L0}$  appears in both methods and has a positive impact in the system damping of both DVC and QVC as shown in Fig 4(c) and 4(d). However, if  $G_{L0} < 0$ , i.e., when some equipment in the grid behaves as a negative resistor, like a generator operating in voltage/current droop mode, the system response can be worsen until instability. The impact of  $P_{L0}$ ,  $I_{L0}$  and  $G_{L0}$  on the dynamic stiffness, defined as the inverse of the disturbance rejection, and step response of DVC and QVC are shown in Fig 5 and 6. It is worth to point out that the higher is the dynamic stiffness the better is the disturbance rejection capabilities. The effect of  $P_{L0}$  in the time domain response is illustrated in Fig. 7, where the behaviour of DVC and QVC methods are compared under CPL increasing steps. Unlike in the QVC, for the same load step, the response in the DVC method is altered for the worse at higher load levels.

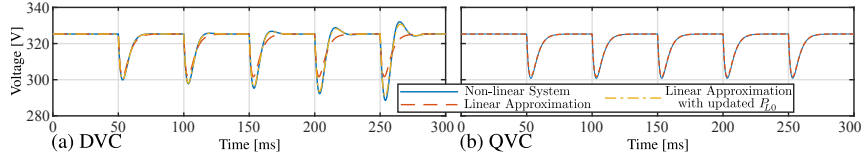


Fig. 7: Disturbance response under increasing CPL. Load is increased by steps of 300W every 50ms. Dashed lines show the linear approximations. (a) DVC; (b) QVC. Results using the data in Table I.

The voltage level also represents a potential cause of instability as it deviates from the equilibrium point. The voltage collapse for both controllers is represented in Fig. 8 for a CPL disturbance. As it is shown, the QVC is not only independent of the CPL load level at the equilibrium point,  $P_{L0}$ , but also withstands higher CPL step disturbance before it collapses. This demonstrates that the QVC can withstand higher CPL variations than the DVC method under the same conditions, as shown in Fig. 8(c), which is a clear advantage of the former controller.

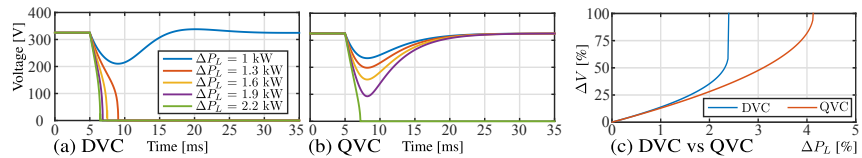


Fig. 8: Voltage collapse for the DVC and QVC methods under CPL steps. (a) DVC performance for an initial  $P_{L0} = 0$ ; (b) QVC performance; (c) DVC and QVC maximum voltage deviation as a function of the CPL step shown in percentage. Results using the data in Table I.

### Effect of system Capacitor and the Virtual Capacitance concept

The capacitor and controller bandwidth take an important role in the system behavior. While the bandwidth is limited by the inner control loop, the size of the capacitor depends on the application. In DC voltage control applications, such as those found in DC links, the capacitor is usually sized according to the expected oscillations caused by stationary power fluctuations, which in some cases leads to over-sizing [13]. Regarding AC grid forming converters, the capacitor is often determined by the filtering requirements of switching frequency harmonics, leading to small capacitor values. It is obvious that increasing the capacitor size while maintaining  $\omega_n$  and  $\xi$ , will lead to an improved disturbance rejection without compromising the system stability. Fig. 9 shows the dynamic stiffness in the frequency domain and the time domain 1kW step response of the disturbance rejection transfer function  $\frac{\Delta V(s)}{\Delta P_L(s)}$  for different capacitor values using DVC and QVC. The QVC and DVC performance is the same if  $P_{L0} = 0W$ .

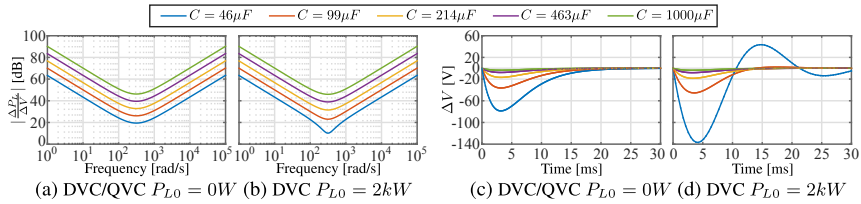


Fig. 9: Evaluation of the capacitor size effect in the disturbance rejection capabilities. (a) QVC dynamic stiffness,  $\frac{\Delta V(s)}{\Delta P_L(s)}$ , for different capacitor values; (b) step response for the transfer function  $\frac{\Delta V(s)}{\Delta P_L(s)}$ .

As expected, the disturbance rejection is improved as the capacitor increases. The size of the capacitor has a direct influence on the maximum disturbance the system can withstand. To compare the performance of both control techniques, the maximum voltage deviation under CPL disturbance has been obtained by non-linear simulation in Simulink as a function of the capacitor size,  $C$ , and the power step disturbance,  $\frac{\Delta P_L}{P_n}$ , with  $P_n = 50kW$ . The results comparing both methods for two different bandwidth,  $\omega_n$ , are shown in Fig. 10, where  $\Delta V_{pu} = 1$  represents the system voltage collapse. As a main conclusion, the QVC extends the region of operation, allowing a better disturbance rejection and avoiding voltage collapse with lower capacitor values compared with the DVC method.

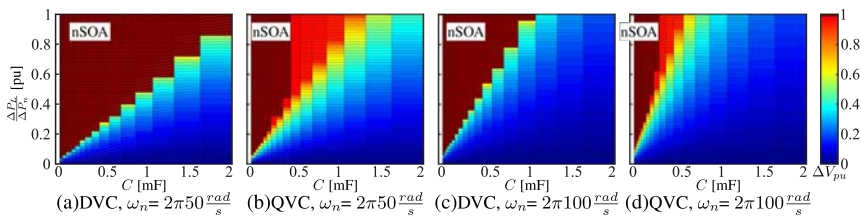


Fig. 10: Maximum voltage deviation depending on the CPL step disturbance and the capacitor value. Data for two different controller bandwidth values is given. (a) DVC,  $\omega_n=2\pi 50rad/s$ ; (b) QVC,  $\omega_n=2\pi 50rad/s$ ; (c) DVC,  $\omega_n=2\pi 100rad/s$ ; (d) QVC,  $\omega_n=2\pi 100rad/s$ . Dark red is considered as the non-Safe Operating Area (nSOA).

As shown, the voltage control bandwidth plays also an important role in the maximum voltage deviation. As an example of its effect, Fig. 11 shows the maximum supported CPL step,  $\frac{\Delta P_L}{P_n}$ , with  $P_n = 50kW$ , as a function of the capacitor size,  $C$ , and the controller bandwidth,  $\omega_n$ , for a maximum voltage deviation of 0.65pu. Fig. 11(c) shows the combinations for which the QVC offers a better performance (represented in green) in the particular data shown in 11(a) and (b). The cases in red represent an operation similar in both DVC and QVC. In this case, the DVC does not offer a better performance than the QVC for any.

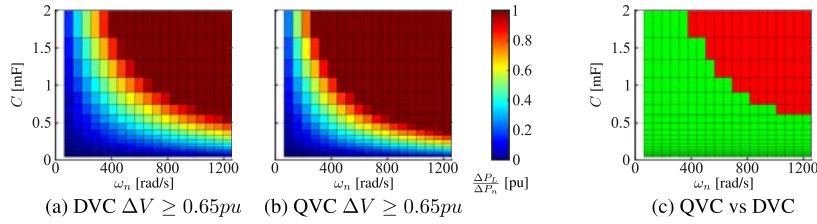
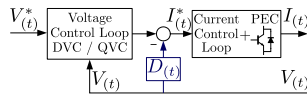


Fig. 11: Maximum CPL step disturbance for a maximum voltage deviation of 0.65 pu, depending on the capacitor value and the voltage control bandwidth,  $\omega_n$ . (a) DVC; (b) QVC; (c) DVC.

Unlike the controller parameters, the modification of the hardware of the system is more restricted. Other techniques for voltage control disturbance rejection enhancement have been proposed in the past, mainly based on load decoupling through measurements, observers or estimators [15]. A simpler alternative is presented in Fig. 12, where  $D(t) = C_v \frac{d}{dt}$ . Using a pseudo-derivative feedback control, it is possible to add a virtual capacitance  $C_v$ , which ideally will be added to the passive capacitance  $C$ , improving the disturbance rejection. The DVC and QVC regulators are now defined by (18) and (19) respectively.



$$I^*(t) = k_p(V(t)^* - V(t)) + k_i \int (V(t)^* - V(t)) dt - C_v \frac{dV(t)}{dt} \quad (18)$$

Fig. 12: Modified Voltage control scheme using PDF structure and  $C_v$ .

$$I^*(t) = \frac{k_p(V(t)^* - V(t)) + k_i \int (V(t)^* - V(t)) dt}{V(t)} - C_v \frac{dV(t)}{dt} \quad (19)$$

Thus, assuming an ideal derivative and ideal sensors, the transfer functions for DVC and QVC, as well as the PI parameters,  $k_p$  and  $k_i$ , can be modified by substituting the parameter  $C$  for  $C + C_v$ . It is worth noting that the virtual capacitance does not only allow to improve the dynamic stiffness but can also be used to emulate low capacitance systems by applying a negative value, i.e.  $C_v < 0$ .

## Experimental Results

The control models presented in this paper have been tested experimentally under 2 different scenarios, covering the application of voltage control in both DC and AC grids. The experimental results have been obtained using the Triphase power modules PM15F42C and PM90F60C. The experimental parameters are included in Table I.

Table I: System parameters used for voltage control analysis

System Parameters	Simulation and Analytical	Experimental Setup	
		DC MG	AC MG
Voltage reference $V^*$	325 V	680 $V_{DC}$	230 $V_{AC_{rms}}$
Nominal Frequency	-	DC	50 Hz
Nominal Active Power $P$	50 kW	11 kW	90 kW
Capacitor $C$	46 $\mu$ F	1000 $\mu$ F	46 $\mu$ F
Switching frequency $f_{sw}$	8 kHz	8 kHz	8/16 kHz
Current control loop bandwidth	$2\pi 500$ rad/s	$2\pi 500$ rad/s	$2\pi 500$ rad/s
Voltage control loop $\omega_n / \xi$	$2\pi 50$ rad/s / 1	$2\pi 5$ rad/s / 1	$2\pi 50$ rad/s / 1

Fig. 13 illustrates the simplified scheme of the experimental setups. For the DC voltage control, a D-Statcom with a battery energy storage system (BESS) has been used (PM15F42C). The DC link voltage is controlled by a DC/DC forming converter fed by a battery, while a DC/AC 3-phase grid tied converter operates as a DC CPL. In order to test the AC voltage control, the PM90F60C 3-ph converter has been

used as the AC grid forming converter while the D-Statcom with BESS (PM15F42C) plays the role of an AC CPL. An additional  $56 \Omega$  resistive load,  $R_L$ , has been included in the MG. The AC control has been implemented in the  $dq$  synchronous reference frame applying the QVC and DVC to both  $d$  and  $q$  axis.

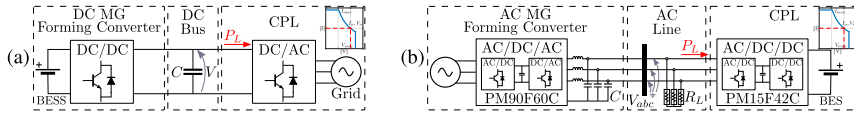


Fig. 13: Experimental setup. (a) DC MG; (b) AC MG.

Fig. 14(a) shows the response of both DVC and QVC under increasing CPL steps for several capacitor values in the DC MG setup. Due to the experimental setup limitations, the capacitor have been resized using virtual capacitance (Fig. 12), being the physical capacitor value  $1000 \mu F$ . In order to better illustrate the effect, the voltage regulator bandwidth has been set to 5Hz.

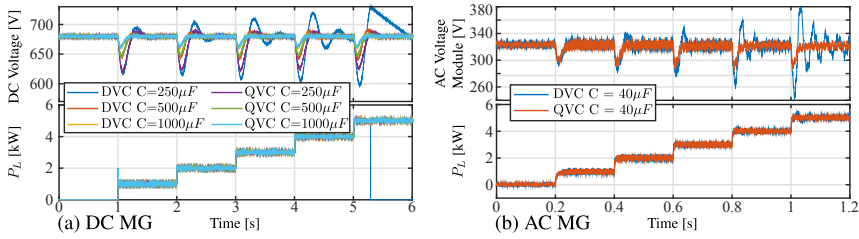


Fig. 14: Experimental Results. DVC and QVC are compared under multistep  $P_L$ . (a) DC grid forming converter performance for different capacitor values. (b) AC grid forming converter performance.

Fig. 14(b) shows the performance comparison between DVC and QVC in the AC 3-ph MG with an increasing CPL. The instantaneous voltage magnitude is represented. As expected from simulations, the DVC dependency on the load level makes its response to be worsen with increased CPL. It is worth noting that the local resistive load provides an improved damping, allowing to move the stability limit from  $P_{L0} \simeq 3 \text{ kW}$  to  $P_{L0} \simeq 6 \text{ kW}$ . The performance of virtual capacitance control applied to AC is shown in Fig. 15 comparing the step response of DVC and QVC. The improved response of the QVC with respect to the DVC should be highlighted, specially when low capacitance values are used.

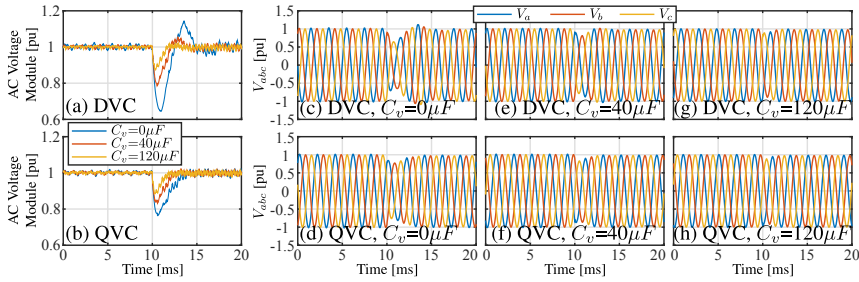


Fig. 15: AC Experimental Setup. DVC and QVC responses using virtual capacitance. Step of  $P_L = 2.5 \text{ kW}$  at  $t = 0.1 \text{ s}$ . (a) DVC voltage module for different  $C_v$  values; (b) QVC voltage module for different  $C_v$  values; (c) DVC phase voltages for  $C_v = 0 \mu F$ ; (d) QVC phase voltages for  $C_v = 0 \mu F$ ; (e) DVC phase voltages for  $C_v = 40 \mu F$ ; (f) QVC phase voltages for  $C_v = 40 \mu F$ ; (g) DVC phase voltages for  $C_v = 120 \mu F$ ; (h) QVC phase voltages for  $C_v = 120 \mu F$ .

## Conclusions

The paper extensively analyzes the voltage control in master-slave AC/DC microgrids with high penetration of CPLs. DVC and QVC have been compared outlining their benefits and drawbacks. The QVC has proved to be a promising alternative under CPL presence. Additionally, the use of the virtual capacitance as a tool for response enhancement has been introduced. The system linearization enables the stability and dynamic analysis for the proper selection of passive elements. The conducted study analyzes the voltage control schemes under a controlled environment valid as a starting point for simplifying the proper selection of the controller scheme, gains and the minimization of capacitance values, establishing the basics for the development of a simple procedure that takes the dynamic behavior into consideration.

## References

- [1] M. N. Ambia, A. Al-Durra, and S. M. Mueeen, "Centralized power control strategy for AC-DC hybrid micro-grid system using multi-converter scheme," in *IECON 2011 - 37th Annual Conference on IEEE Industrial Electronics Society*, Nov 2011, pp. 843–848.
- [2] P. Karlsson and J. Svensson, "DC bus voltage control for a distributed power system," *IEEE Transactions on Power Electronics*, vol. 18, no. 6, pp. 1405–1412, Nov 2003.
- [3] T. L. Vandoorn, B. Meersman, L. Degroote, B. Renders, and L. Vandeveldde, "A Control Strategy for Islanded Microgrids With DC-Link Voltage Control," *IEEE Transactions on Power Delivery*, vol. 26, no. 2, pp. 703–713, April 2011.
- [4] T. Dragievi, X. Lu, J. C. Vasquez, and J. M. Guerrero, "DC Microgrids-Part I: A Review of Control Strategies and Stabilization Techniques," *IEEE Transactions on Power Electronics*, vol. 31, no. 7, pp. 4876–4891, July 2016.
- [5] D. Chen and L. Xu, "Autonomous DC Voltage Control of a DC Microgrid With Multiple Slack Terminals," *IEEE Transactions on Power Systems*, vol. 27, no. 4, pp. 1897–1905, Nov 2012.
- [6] L. Benadero, R. Cristiano, D. J. Pagano, and E. Ponce, "Nonlinear Analysis of Interconnected Power Converters: A Case Study," *IEEE Journal on Emerging and Selected Topics in Circuits and Systems*, vol. 5, no. 3, pp. 326–335, Sept 2015.
- [7] M. Cupelli, M. Moghimi, A. Riccobono, and A. Monti, "A comparison between synergetic control and feedback linearization for stabilizing MVDC microgrids with constant power load," in *IEEE PES Innovative Smart Grid Technologies, Europe*, Oct 2014, pp. 1–6.
- [8] A. Emadi, A. Khaligh, C. H. Rivetta, and G. A. Williamson, "Constant power loads and negative impedance instability in automotive systems: definition, modeling, stability, and control of power electronic converters and motor drives," *IEEE Transactions on Vehicular Technology*, vol. 55, no. 4, pp. 1112–1125, July 2006.
- [9] T. Dragievi, J. M. Guerrero, J. C. Vasquez, and D. Krlec, "Supervisory Control of an Adaptive-Droop Regulated DC Microgrid With Battery Management Capability," *IEEE Transactions on Power Electronics*, vol. 29, no. 2, pp. 695–706, Feb 2014.
- [10] G. Sulligoi, D. Bosich, and G. Giadrossi, "Linearizing voltage control of MVDC power systems feeding constant power loads: Stability analysis under saturation," in *2013 IEEE Power Energy Society General Meeting*, July 2013, pp. 1–5.
- [11] M. K. Mishra and K. Karthikeyan, "A Fast-Acting DC-Link Voltage Controller for Three-Phase DSTATCOM to Compensate AC and DC Loads," *IEEE Transactions on Power Delivery*, vol. 24, no. 4, pp. 2291–2299, Oct 2009.
- [12] S. Vazquez, J. A. Sanchez, J. M. Carrasco, J. I. Leon, and E. Galvan, "A Model-Based Direct Power Control for Three-Phase Power Converters," *IEEE Transactions on Industrial Electronics*, vol. 55, no. 4, pp. 1647–1657, April 2008.
- [13] B. N. Singh, P. Rastgoufard, B. Singh, A. Chandra, and K. Al-Haddad, "Design, simulation and implementation of three-pole/four-pole topologies for active filters," *IEE Proceedings - Electric Power Applications*, vol. 151, no. 4, pp. 467–476, July 2004.
- [14] Y. Ye, M. Kazerani, and V. H. Quintana, "Modeling, control and implementation of three-phase PWM converters," *IEEE Transactions on Power Electronics*, vol. 18, no. 3, pp. 857–864, May 2003.
- [15] R. S. Pena, R. J. Cardenas, J. C. Clare, and G. M. Asher, "Control strategies for voltage control of a boost type PWM converter," in *Power Electronics Specialists Conference, 2001. PESC. 2001 IEEE 32nd Annual*, vol. 2, 2001, pp. 730–735 vol.2.



## **D.4 Adaptive active power sharing techniques for DC and AC voltage control in a hybrid DC/AC microgrid**

A. Navarro-Rodríguez, P. García, R. Georgious and J. García, "Adaptive active power sharing techniques for DC and AC voltage control in a hybrid DC/AC microgrid," 2017 IEEE Energy Conversion Congress and Exposition (ECCE), Cincinnati, OH, 2017, pp. 30-36.



# Adaptive Active Power Sharing Techniques for DC and AC Voltage Control in a Hybrid DC/AC Microgrid

Ángel Navarro-Rodríguez, Pablo García, Ramy Georgious and Jorge García

Dept. of Electrical, Electronics, Systems & Computers Engineering

University of Oviedo, LEMUR Group

Gijón, 33204, Spain

Email: navarroangel@uniovi.es, garciafpablo@uniovi.es, georgiousramy@uniovi.es, garciajorge@uniovi.es

**Abstract**—This paper deals with the AC and DC dynamic voltage control in a hybrid DC/AC Microgrid (MG) with central and distributed Battery Energy Storage Systems (BESSs), applying a power sharing mechanism between the different devices in the MG. The MG is composed by a multiport transformation center and two fixed frequency 3 phase AC Nanogrids (NGs) coupled to a DC bus through 3-phase Power Electronic Converters (PECs). The system pursues to minimize the dependence on the utility grid, the needed DC capacitance and the stress in the MGs central BESS, while increasing the power handling capability and the overall system stability during islanding condition. In order to approach the proposed aim, two main concerns are studied in this paper: an adaptive power sharing mechanism between the DC bus and the AC NGs for DC voltage control, and the design and implementation of an AC dynamic local voltage compensator based on Distributed Energy Storage System (DESS).

## I. INTRODUCTION

The increasing concern about environmental issues and the rising popularity of concepts as local generation and self-consumption have led to an increasing interest on alternatives to the conventional utility grid as Microgrids (MGs), Nanogrids (NGs) and Smart grids (SGs). Despite its advantages, the weakness and stability problems associated to a MG have been considered since its apparition, demanding significant research interests. Studies for different types of contingencies have been carried out, pursuing the power quality improvement [1], [2]. Furthermore, with the apparition of hybrid DC/AC MGs, where the Power Electronic Converters (PECs) may share power not only in the AC grid but also in the DC lines, new MG issues appears as the stability and quality maintenance in both DC and AC [3]–[5].

Different methods and control topologies have been presented in the literature to ensure the distribution network (DN) voltage control and power flow, as the central controller, the

master-slave, the Q/V and P/f droops, and hybrid approaches [6]–[9]. The fast development of power semiconductor devices and digital control systems have made PECs the most suitable interface for both generation, Energy Storage Systems (ESS) and loads leading to MGs dominated by PECs. Moreover, due to the high penetration of renewable generation operating at its maximum power point tracking (MPPT), the control methods based on master-slave or multiple slack, with fixed frequency in the case of AC, can simplify the MGs design [10]–[12].

Concerning the dynamic active power sharing improvement in AC grids, many studies can be found in the literature based on the variation of the frequency with the active power (P/f droop), being the stiffness determined by the system inertia [13]–[16]. However, when the fixed frequency approach is used instead, active power variations will affect the voltage magnitude (P/V droop) being the grid inertia dependent on the grid equivalent capacitance. Regarding the dynamic power sharing between hybrid AC/DC MGs when AC slack converters are used for the coupling between the Low Voltage DC line (LVDC) and the AC grid, few discussion is found in the literature. Some studies have been proposed based on cascaded converters stability [17], and power balancing between AC and DC using a  $V_g/V_{dc}$  droop [18]. However, these methods have been proposed for AC/DC/AC grid tied converters and they can not be directly applied to the AC/DC voltage control of a hybrid MG.

Thus, this paper deals with the AC and DC voltage control in a hybrid DC/AC MG with central and distributed Battery Energy Storage Systems (BESSs). A power sharing mechanism between the different distributed energy resources (DERs) is proposed. The system will have as main constraints the reduced dependency on the main grid, the islanded operation and the optimization of the ESS usage. Two main concerns are studied in this paper: 1) designing an adaptive method for the dynamic power sharing between the DC bus and the AC NGs for an enhanced DC voltage control; and 2) the implementation of an AC voltage compensator for the NG-based distribution system. The compensation will rely on the use of virtual capacitor for an improved system stiffness.

The present work has been partially supported by the predoctoral grants program Severo Ochoa for the formation in research and university teaching of Principado de Asturias PCTI-FICYT under the grant ID BP14-135. This work also was supported in part by the Research, Technological Development and Innovation Program Oriented to the Society Challenges of the Spanish Ministry of Economy and Competitiveness under grant ENE2016-77919-R and by the European Union through ERFD Structural Funds (FEDER).

The paper is organized as follows. Section II introduces the proposed hybrid DC/AC Microgrid topology. Section III explains the basics of the proposed voltage control loops in DC and AC systems. Section IV covers the proposed adaptive voltage control in the hybrid DC/AC MG. Finally, section V presents the simulation results.

## II. THE PROPOSED HYBRID DC/AC MG

The hybrid MG under study, shown in Fig. 1, is composed by a MG transformation center (MGTC) and two 3-phase AC NGs based on fixed frequency Master-Slave topology. The MGTC consists of a BESS and a connection to the main grid interconnected by a common Low Voltage DC bus (LVDC) to two NG Head Converters (NGHCs) feeding the AC NGs. The BESS and main grid are interfaced with the LVDC by a three-port solid-state transformer (SST). It is worth to point out that the SST operation is out of the scope of this paper. The MG is designed as follows. The NGHC acts as an slack, both for the AC voltage magnitude and frequency. The MGs loads, Constant Power Loads (CPLs) and Constant Impedance Loads (CILs), are only located at the 3 phase NGs. Under this configuration, the load as seen by the LVDC is drawn by the NGHCs. Additionally, different distributed resources such as Distributed Generation (DG) and ESSs can be installed at NG level. A central controller governs the MGTC and low bandwidth communications are considered in the NGs between the DGs, ESSs and NGHCs.

Power mismatches in conventional grids are absorbed by the high inertia of generators. However, in the case under study, they have to be supported by the energy storage elements, including capacitances, installed at the MG. As a first approach, DGs and DESS in the NG will operate with constant PQ commands while the slack NGHCs will absorb the power transients, controlling the voltage magnitude and frequency. Additionally a local dynamic voltage compensator able to share active power might be considered in the NGs. Depending on the MG being connected/disconnected to the main grid, two modes of operation are defined: 1) During *non-landing* operation, the utility grid  $P_{main}$  and the BESS  $P_{BESS}$  can share the effort; 2) During *landing*, the proposed MG is disconnected from the utility grid and only the BESS is available as a power source in the transformation center.

In any case, the voltage in DC and AC NGs should remain under control within regulation limits. Additionally, two constraints are established: 1) The dependence on the utility grid should be minimized; 2) The BESS limitations (Bandwidth, available power, State of Charge (SoC)) have to be considered in the power sharing. This paper is focused on the operation during *landing* mode.

Although the DGs in the NG could be used to provide ancillary services, most of DERs in the NG either present a low response or should be operated in Maximum Power Point Tracking (MPPT). However, DESSs in the NG can be used, providing local compensation while reducing the conduction losses. As a first approach, in this study one local ESSs will

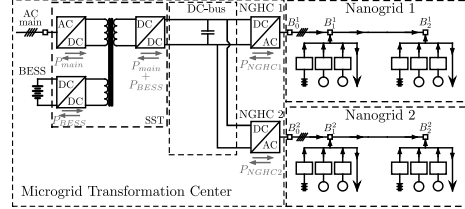


Fig. 1. Topology of the Hybrid DC/AC Microgrid under study.

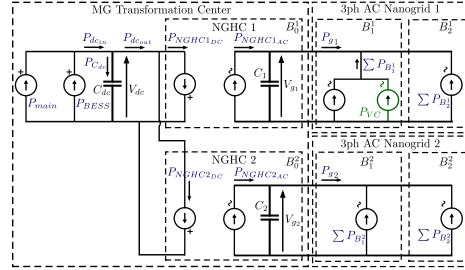


Fig. 2. Simplified power sharing scheme within the Hybrid DC/AC MG.

be used for transient compensation located at the first node of NG1 ( $B_1^1$ ). Fig. 2 shows a simplified scheme of the MG illustrating the different elements participating on the power sharing, where  $\sum P_{B_j^k}$  ( $k$  denotes the NG, while  $j$  the node) is the total power share between DGs, DESS and active power loads within a node,  $\sum P_{B_j^k} = \sum (P_{DG_j^k} + P_{DESS_j^k} - P_{L_j^k})$ .

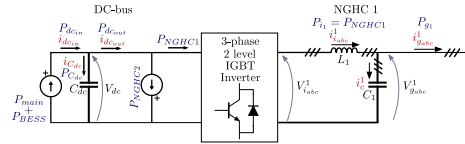


Fig. 3. Simplified equivalent power scheme of one of the NGHCs.

The system model for the voltage control, both in AC and DC, is simplified to a capacitor, neglecting line impedances and approximating the current control loops of the PECs to a low pass filter (LPF). 3-phase balanced AC NGs are assumed.

The modeling of the proposed system will be based on the simplified power scheme for one of the NGHCs shown in Fig. 3. Thus, the AC system modeled in dq synchronous reference frame is defined by (1), where  $k$  is the NG identifier,  $v_g^k$  is the NG voltage at node  $B_0^k$ ,  $i_g^k$  is the current drawn by the NGHCs into the NGs (i.e. the control action of NGHCs),  $\omega_e^k$  is the grid frequency and  $i_g^k$  is the total current drawn by the

$$\frac{d}{dt} \begin{bmatrix} i_{i,d}^k \\ v_{g,d}^k \\ i_{i,q}^k \\ v_{g,q}^k \end{bmatrix} = \begin{bmatrix} -\frac{R_k}{L_k} & \frac{1}{L_k} & 0 & 0 \\ \frac{1}{C_k} & 0 & 0 & 0 \\ 0 & 0 & -\frac{R_k}{L_k} & \frac{1}{L_k} \\ 0 & 0 & \frac{1}{C_k} & 0 \end{bmatrix} \begin{bmatrix} i_{i,d}^k \\ v_{g,d}^k \\ i_{i,q}^k \\ v_{g,q}^k \end{bmatrix} + \begin{bmatrix} \omega_e^k & 0 & 0 & 0 \\ 0 & \omega_e^k & 0 & 0 \\ 0 & 0 & -\omega_e^k & 0 \\ 0 & 0 & 0 & -\omega_e^k \end{bmatrix} \begin{bmatrix} i_{i,q}^k \\ v_{g,q}^k \\ i_{i,d}^k \\ v_{g,d}^k \end{bmatrix} + \begin{bmatrix} \frac{1}{L_k} & 0 & 0 & 0 \\ 0 & \frac{-1}{C_k} & 0 & 0 \\ 0 & 0 & \frac{1}{L_k} & 0 \\ 0 & 0 & 0 & \frac{-1}{C_k} \end{bmatrix} \begin{bmatrix} v_{g,d}^k \\ i_{i,q}^k \\ v_{g,q}^k \\ i_{i,d}^k \end{bmatrix} \quad (1)$$

buses  $B_1^k$  and  $B_2^k$ , i.e., the system disturbance. The DC link can be modeled in terms of active power as (2), where  $C_{dc}$  is the LVDC capacitor,  $P_{dcin}$  is the power shared by the main and the central BESS, and  $P_{dcout}$  is the power drawn by the NGHCs ( $P_{dcout} = P_{NGHC_1(t)} + P_{NGHC_2(t)}$ ), being defined by (3), assuming  $v_{gq} = 0$ . Thus, the NGHCs are seen as CPLs by the DC link. The power flowing into the capacitor is defined as  $P_{C_{dc}} = P_{dcin} - P_{dcout}$ .

$$\frac{dV_{dc}(t)}{dt} = \frac{1}{C_{dc}V_{dc}(t)} \left( P_{dcin} - \underbrace{(P_{NGHC_1(t)} + P_{NGHC_2(t)})}_{P_{dcout}} \right) \quad (2)$$

$$P_{dcout(t)} = \sum_{k=1}^2 P_{NGHC_k(t)} = \sum_{k=1}^2 \frac{3}{2} \left( v_{g,d(t)}^k i_{i,d(t)}^k \right) \quad (3)$$

### III. VOLTAGE CONTROL: CONTROLLER DESIGN

The MGTC control will involve the dynamic control of both DC link and AC NGs voltages. The closed loop voltage controllers, both in AC and DC, will be based on a feedback PI regulator. Two alternatives for the basic voltage control are considered in this paper. Fig. 4 shows the generic representation of those alternatives valid for both DC and AC voltage control, where  $I_{L(t)}$ ,  $P_{L(t)}$  and  $G_{L(t)}$ , are the time dependent disturbances drawn by constant current loads/generation (CCLs), constant power loads/generation (CPLs) and constant impedance loads/generation (CILs) respectively. According to

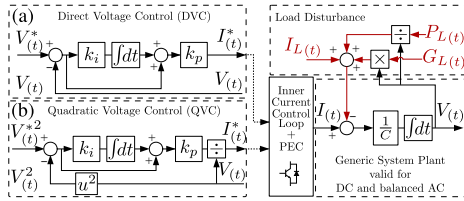


Fig. 4. Voltage control schemes, based on cascaded control, valid for the DC bus and the AC NGHCs. (a) conventional voltage control, namely DVC; (b) proposed alternative, QVC

this, the system plant is defined by (4), defining a non-linear system.

$$\frac{dV(t)}{dt} = \frac{1}{C} \left( I(t) - \underbrace{\left( I_{L(t)} + \frac{P_{L(t)}}{V(t)} + G_{L(t)}V(t) \right)}_{Disturbance} \right) \quad (4)$$

According to this expression, the conventional voltage control, referred in this paper as Direct Voltage Control (DVC), will present a non linear behavior under the presence of CGLs and CPLs. The use of an alternative control based on squared voltage is proposed for the system in this paper. Although it has been proposed before in the literature referred as energy based controller, its applications has been limited to the DC link control of DC/AC converters [19], [20]. Nonetheless, its application can be generalized to any cascade-based voltage control as slack converters in both DC and AC MGs. It will be referred as quadratic voltage control (QVC) in this paper. The QVC is defined by (5), valid for both AC and DC applications.

$$P_{(t)}^* = k_p(V_{(t)}^* - V_{(t)}^2) + k_i \int (V_{(t)}^* - V_{(t)}^2) dt \quad (5)$$

Where  $k_p$  and  $k_i$  are the ideal PI regulator gains. Despite the fact that the QVC also presents a non-linear relation between the voltage and the load disturbance, the relation between the square voltage and the CPLs is linear considering the system plant in (6), where  $P^*$  is the control action and  $P_{c(t)}$  is the power flowing into the capacitor.

$$V_{(t)} \frac{dV_{(t)}}{dt} = \frac{1}{C} P_{c(t)} \Rightarrow \frac{dV_{(t)}^2}{dt} = \frac{2}{C} P_{c(t)} \quad (6)$$

The main feature of the voltage control for the application presented in this paper is the disturbance rejection capability. In order to analyze how the disturbance rejection of each method is affected by the type of load, their disturbance rejection transfer functions are obtained by linearization. The expressions for the DVC are shown in (7), (8) and (9).

$$\frac{\Delta V(s)}{\Delta I_L(s)} \approx \frac{-sV_0^2}{s^2V_0^2C + sk_pV_0^2 - P_{L0} + G_{L0}V_0^2 + k_ik_pV_0^2} \quad (7)$$

$$\frac{\Delta V(s)}{\Delta P_L(s)} \approx \frac{-sV_0}{s^2V_0^2C + sk_pV_0^2 - P_{L0} + G_{L0}V_0^2 + k_ik_pV_0^2} \quad (8)$$

$$\frac{\Delta V(s)}{\Delta G_L(s)} \approx \frac{-sV_0^3}{s^2V_0^2C + sk_pV_0^2 - P_{L0} + G_{L0}V_0^2 + k_ik_pV_0^2} \quad (9)$$

Where  $V_0$ ,  $P_{L0}$  and  $G_{L0}$  are the voltage magnitude, the CPL level, and the CIL level at the equilibrium point respectively.

The expressions for the QVC are stated in (10), (11) and (12), where  $I_{L0}$  is the CCL level at the equilibrium point.

$$\frac{\Delta V(s)}{\Delta I_L(s)} \approx \frac{-sV_0}{s^2V_0C + s2k_pV_0 + I_{L0} + 2G_{L0}V_0^2 + 2k_ik_pV_0^2} \quad (10)$$

$$\frac{\Delta V(s)}{\Delta P_L(s)} \approx \frac{-s}{s^2 V_0 C + s 2k_p V_0 + I_{L0} + 2G_{L0} V_0^2 + 2k_i k_p V_0^2} \quad (11)$$

$$\frac{\Delta V^3(s)}{\Delta G_L(s)} \approx \frac{-s V_0^2}{s^2 V_0 C + s 2k_p V_0 + I_{L0} + G_{L0} V_0^2 + 2k_i k_p V_0^2} \quad (12)$$

These expressions demonstrate a clear dependency of the disturbance rejection transfer functions on the CPL, CIL and CCL levels in both the DVC and QVC. However, the DVC presents a critical negative dependency on CPL level,  $P_{L0}$ , for any kind of load disturbance, which can compromise the system stability. On the contrary, the QVC eliminates the dependency on CPL level. Due to the high presence of PECS, CPLs and constant power generation expected in the grid under analysis, a control based on the QVC is proposed for the application presented in this paper.

In order to tune the voltage regulator, a tuning method based on the linearized reference tracking transfer function is used. Applying linearization, the close loop system defined by (5) and (6) can be approximated as (13), where  $V_0^*$  and  $V_0$  are the voltage reference and the voltage in the equilibrium point respectively. Considering operation near the equilibrium point and  $V_0^* = V_0$ , (13) can be approximated by a second order system with a determined natural frequency  $\omega_n$  and a damping factor  $\xi$  as (14). Thus, the PI regulator gains of QVC are tuned according to (15). The natural frequency  $\omega_n$ , should be selected according to the cascaded control premises, while the damping factor,  $\xi$ , can be selected as a trade-off between overshoot and settling time.

$$\frac{V(s)}{V^*(s)} \approx \frac{s 2k_p V_0^* + 2k_p k_i V_0^*}{s^2 C V_0 + s 2k_p V_0 + 2k_p k_i V_0} \quad (13)$$

$$\frac{V(s)}{V^*(s)} \approx \frac{2\xi\omega_n s + \omega_n^2}{s^2 + 2\xi\omega_n s + \omega_n^2} \quad (14)$$

$$k_p = \xi\omega_n C; \quad k_i = \frac{\omega_n^2 C}{2k_p} \quad (15)$$

#### A. QVC applied to DC voltage control

The described QVC scheme can be applied directly as shown in 4(b), considering the control action of the PI regulator as the active power reference required by the DC bus capacitor. The specific basic DC bus voltage control is shown in Fig. 5. As specified before, during *non-islanding* both the BESS and the main grid participate in the control. To reduce the dependence on the main grid, the BESS provides the low bandwidth variations, within its power limitations, while the main contribute with the high bandwidth transients unless the battery power is limited for any reason, in which case the main will participate also in the steady state. In the case of *islanding*, the battery would be the only available power source to maintain the regulation of the DC link. In that case, to

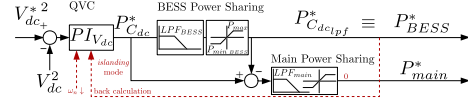


Fig. 5. DC bus slack controller based on Quadratic Voltage Control. *islanding* mode modifications highlighted in red.

maintain the proper operation of the voltage regulator, either a back calculation or a reduction on the control bandwidth,  $\omega_n$ , should be applied to fulfill the cascaded control requirements.

#### B. QVC applied to 3-phase AC voltage control

In the case of AC, a voltage control in the  $dq$  reference frame is proposed based on QVC and fixed frequency. The complete cascaded control scheme for a 3-phase AC slack converter is shown in Fig. 6. A grid current decoupling term could be added in order to improve the disturbance rejection response, drawn in green color. However, an improved disturbance rejection could increase the stress in the DC side for the proposed MG topology, which is translated in an increased stress in the BESS during an *islanding* scenario.

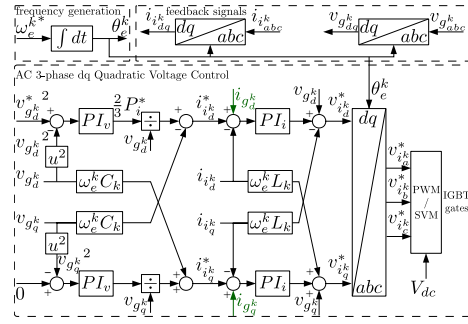


Fig. 6. NGHCs basic AC slack controller based on AC quadratic voltage control implemented in the  $dq$  reference frame.

### IV. HYBRID DC/AC VOLTAGE CONTROL: ADAPTIVE POWER SHARING IN THE LVDC AND LOCAL DYNAMIC VOLTAGE COMPENSATION IN THE AC NGs

The proposed hybrid MG should maintain the power quality and reliability in both the LVDC bus and the AC NGs. This paper deals with the specific task of managing the dynamic active power sharing between the elements present in the grid in order to keep the voltage magnitude quality, and the frequency in the case of the AC NGs. The proposed power topology allows to decouple the events and contingencies happening in the LVDC bus from the voltage control in the NGs, as long as the DC voltage remains within certain levels. However, the NGHCs control is not decoupled from the



the limitations of the DG or DBESS providing that service.

$$v_{vc,dq}^* = \underbrace{\frac{K_{vc,dq} \cdot (v_{g,dq}^* - v_{g,dq}^k)^2}{v_{g,dq}^k}}_{\text{damping factor}} - \underbrace{C_{vc} \cdot \frac{d}{dt} v_{g,dq}^k}_{\text{Virtual Capacitor}} \quad (18)$$

### V. SIMULATION RESULTS

The proposed system has been validated through simulations in MATLAB/Simulink<sup>®</sup>. The parameters are summarized in Table I. Two scenarios are simulated to evaluate the performance of the control topology proposed in this paper compared with the original case. The first test applies the proposed adaptive technique for power sharing without the local voltage compensator, while in the second test a local voltage compensator is included in the first NG with the  $K_{vc}$  and  $C_{vc}$  parameters in Table I. The results are shown in Fig. 9 and 10 respectively. They show the DC voltage, the AC voltage in both NGs, the sharing coefficients, the power commands generated by the DC controller in Fig. 7 and the CPL in each NG. The original case consists on the control presented in Fig. 7 and 8 by disabling the power sharing in DC ( $\sigma_n^1 = \sigma_n^2 = 0$ ) and without local voltage compensation in the NGs. Considering a BESS bandwidth of 100Hz (Table I), in the original case the DC voltage control bandwidth is reduced to 20Hz in order to extend the system stability. On the contrary, when the proposed technique is applied the overall current bandwidth is 500Hz and the DC voltage controller bandwidth can be increased up to 50Hz. The system is tested under multiple steps of CPL disturbances in both NGs. In both tests, the proposed sharing technique (and the voltage compensator in the second case) is activated at  $t = 0.3s$ . Between  $t = 0$  and  $t = 0.3s$ , the effect of using excessive voltage control bandwidth with reduced current bandwidth is illustrated. From  $t = 0.3$  to  $t = 0.7$  the proposed techniques are operating. As expected, the power required by the DC voltage controller is now shared between both NGs and central BESS, reacting one NG to the events on the other. As the BESS provides the steady state, the power shared operates only during the transients. In the first case, the DC voltage transients are improved compared to the original, however the AC NGs voltages are distorted as a consequence. In the second case, under the same conditions, the use of a local voltage compensator leads to an overall improvement in both DC and AC voltages, reducing significantly the voltage variations under CPL steps. At the instant  $t = 0.7s$ , the total system load exceeds the central BESS maximum power leading to an overall MG collapse in the first case and in the original (Fig. 9). On the other hand, the use of a local compensator not only improves the transients but also enables the sharing mechanism to operate during steady state. As shown in Fig. 10, once the BESS limits, the compensator start providing the power to maintain the DC and AC NGs stable at the expense of an stationary error in  $V_{g1}$  caused by the P regulator in the local compensator.

TABLE I  
SYSTEM PARAMETERS

AC Nanogrids Parameters	Values
AC Nominal Voltage ( $V_{g1}^n, V_{g2}^n$ )	230 $V_{AC,rms}/50Hz$
NGHCs AC voltage control $\omega_n / \lambda_i$	2 $\pi$ 50 rad/s / 1
NGs equivalent Capacitor ( $C_1, C_2$ )	300 $\mu F$
AC Voltage compensator gains $K_{vc} / C_{vc}$	0.3/0.001
DC Link Parameters	Values
DC Nominal Voltage ( $V_{dc}^n$ )	700 V
DC Current control loop $\omega_{ni}$	2 $\pi$ 500 rad/s
DC equivalent Capacitor ( $C_{dc}$ )	300 $\mu F$
DC Voltage control loop $\omega_n / \lambda_i$	2 $\pi$ 50 / 1
Central BESS $BW / P_{max}$	100 Hz / 17.5 kW
Power Sharing $k_{i,h} / \lambda_{dc} / \lambda_{ac1} / \lambda_{ac2}$	30 / 2 / 1 / 1

### VI. CONCLUSIONS

In this paper, a dynamic voltage control technique is proposed for a fixed frequency hybrid AC/DC Microgrid with ESS, based on the power sharing between the AC NGs and a central BESS to maintain the grid quality in both the LVDC and the AC NGs with high penetration of CPLs and PECs. An adaptive power sharing mechanism have being presented for maintaining the LVDC voltage under control, not only reducing the stress in the central BESS system and the dependence in the utility grid but also demonstrating the extended operation and improved transient response in the LVDC when the central BESS presents bandwidth and power limitations. In addition, a local AC dynamic voltage compensator has been proposed for AC voltage control support based on virtual capacitance. The theoretical discussion has been supported with simulations. Further investigation on the local compensator tuning and effects, considering the use of adaptive techniques, the enhancement of the adaptive algorithm, considering other factors as the load level or the grid capacitance, and the experimental validation are part of an on-going research.

### REFERENCES

- [1] J. M. Guerrero, "Editorial Special Issue on Power Electronics for Microgrids 2014:Part II," *IEEE Transactions on Power Electronics*, vol. 26, no. 3, pp. 659–663, March 2011.
- [2] J. Guerrero, P. C. Loh, T.-L. Lee, and M. Chandorkar, "Advanced Control Architectures for Intelligent Microgrids 2014:Part II: Power Quality, Energy Storage, and AC/DC Microgrids," *IEEE Transactions on Industrial Electronics*, vol. 60, no. 4, pp. 1263–1270, April 2013.
- [3] P. Wang, X. Liu, C. Jin, P. Loh, and F. Choo, "A hybrid AC/DC microgrid architecture, operation and control," in *Power and Energy Society General Meeting, 2011 IEEE*, July 2011, pp. 1–8.
- [4] J. He, Y. W. Li, and F. Blaabjerg, "Flexible Microgrid Power Quality Enhancement Using Adaptive Hybrid Voltage and Current Controller," *Industrial Electronics, IEEE Transactions on*, vol. 61, no. 6, pp. 2784–2794, June 2014.
- [5] J. Zhang, D. Guo, F. Wang, Y. Zuo, and H. Zhang, "Control strategy of interlinking converter in hybrid AC/DC microgrid," in *Renewable Energy Research and Applications (ICRERA), 2013 International Conference on*, Oct 2013, pp. 97–102.
- [6] M. Ambia, A. Al-Durra, and S. Mueen, "Centralized power control strategy for AC-DC hybrid micro-grid system using multi-converter scheme," in *IECON 2011 - 37th Annual Conference on IEEE Industrial Electronics Society*, Nov 2011, pp. 843–848.

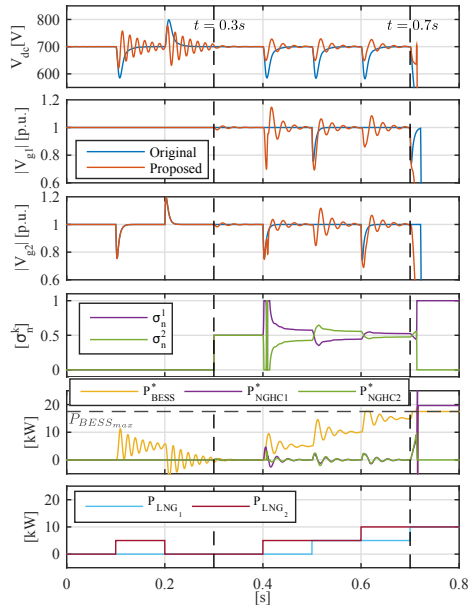


Fig. 9. Simulation results: performance using the proposed adaptive control method. Case 1: Without dynamic voltage compensator in the AC NGs. At  $t=0.3s$  the proposed adaptive mechanism is enabled. At  $t=0.7s$  the total load exceeds the maximum BESS available power, leading to global instability.

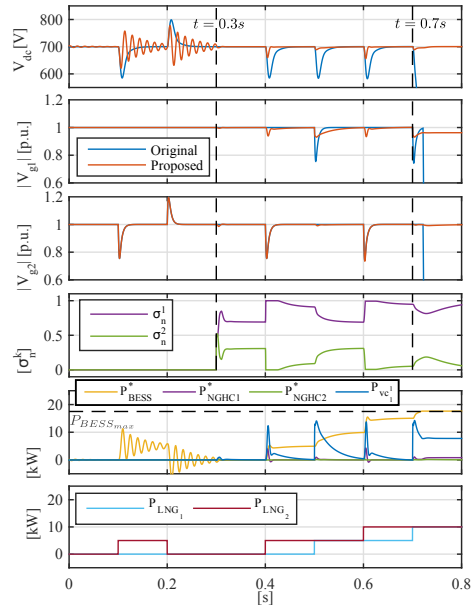


Fig. 10. Simulation results: performance using the proposed adaptive control method. Case 2: With dynamic voltage compensator in the AC NG 1 (Node  $B_1^1$ ). At  $t=0.3s$  the proposed adaptive mechanism is enabled. At  $t=0.7s$  the total load exceeds the maximum BESS power and the compensator share the power during steady state.

- [7] Y.-R. Mohamed and E. El-Saadany, "Adaptive Decentralized Droop Controller to Preserve Power Sharing Stability of Paralleled Inverters in Distributed Generation Microgrids," *Power Electronics, IEEE Transactions on*, vol. 23, no. 6, pp. 2806–2816, Nov 2008.
- [8] M. Golsorkhi and D. Lu, "A Control Method for Inverter-Based Islanded Microgrids Based on V-I Droop Characteristics," *Power Delivery, IEEE Transactions on*, vol. 30, no. 3, pp. 1196–1204, June 2015.
- [9] P. Arbolea, C. Gonzalez-Moran, and M. Coto, "A hybrid central-distributed control applied to microgrids with droop characteristic based generators," in *Power Electronics and Motion Control Conference (EPE/PEMC), 2012 15th International*, Sept 2012, pp. LS7a.5–1–LS7a.5–8.
- [10] T. Dragievi, X. Lu, J. C. Vasquez, and J. M. Guerrero, "Dc microgrids-part i: A review of control strategies and stabilization techniques," *IEEE Transactions on Power Electronics*, vol. 31, no. 7, pp. 4876–4891, July 2016.
- [11] D. Chen and L. Xu, "Autonomous dc voltage control of a dc microgrid with multiple slack terminals," *IEEE Transactions on Power Systems*, vol. 27, no. 4, pp. 1897–1905, Nov 2012.
- [12] Z. Zhang, X. Huang, J. Jiang, and B. Wu, "A load-sharing control scheme for a microgrid with a fixed frequency inverter," *Electric Power Systems Research*, vol. 80, no. 3, pp. 311–317, 2010.
- [13] A. Navarro-Rodriguez, P. Garcia, R. Georgious, and J. Garcia, "A communication-less solution for transient frequency drift compensation on weak microgrids using a D-statcom with an energy storage system," in *Energy Conversion Congress and Exposition (ECCE), 2015 IEEE*, Sept 2015, pp. 6904–6911.
- [14] I. Serban and C. Marinescu, "Control Strategy of Three-Phase Battery

- Energy Storage Systems for Frequency Support in Microgrids and with Uninterrupted Supply of Local Loads," *Power Electronics, IEEE Transactions on*, vol. 29, no. 9, pp. 5010–5020, Sept 2014.
- [15] M. Torres L., L. Lopes, L. Moran T., and J. Espinoza C., "Self-Tuning Virtual Synchronous Machine: A Control Strategy for Energy Storage Systems to Support Dynamic Frequency Control," *Energy Conversion, IEEE Transactions on*, vol. 29, no. 4, pp. 833–840, Dec 2014.
- [16] Y. Hirase, O. Noro, K. Sugimoto, K. Sakimoto, Y. Shindo, and T. Ise, "Effects of suppressing frequency fluctuations by parallel operation of virtual synchronous generator in microgrids," in *Energy Conversion Congress and Exposition (ECCE), 2015 IEEE*, Sept 2015, pp. 3694–3701.
- [17] L. Benadero, R. Cristiano, D. J. Pagano, and E. Ponce, "Nonlinear analysis of interconnected power converters: A case study," *IEEE Journal on Emerging and Selected Topics in Circuits and Systems*, vol. 5, no. 3, pp. 326–335, Sept 2015.
- [18] T. Vandoorn, B. Renders, L. Degroote, B. Meersman, and L. Vandevelde, "Active Load Control in Islanded Microgrids Based on the Grid Voltage," *Smart Grid, IEEE Transactions on*, vol. 2, no. 1, pp. 139–151, March 2011, use of Voltage-droop control.
- [19] M. K. Mishra and K. Karthikeyan, "A fast-acting dc-link voltage controller for three-phase dstatcom to compensate ac and dc loads," *IEEE Transactions on Power Delivery*, vol. 24, no. 4, pp. 2291–2299, Oct 2009.
- [20] S. Vazquez, J. A. Sanchez, J. M. Carrasco, J. I. Leon, and E. Galvan, "A model-based direct power control for three-phase power converters," *IEEE Transactions on Industrial Electronics*, vol. 55, no. 4, pp. 1647–1657, April 2008.



## **D.5 Predictive frequency-based sequence estimator for control of grid-tied converters under highly distorted conditions**

C. Blanco, P. García, Á. Navarro-Rodríguez and M. Sumner, "Predictive frequency-based sequence estimator for control of grid-tied converters under highly distorted conditions," 2017 IEEE Energy Conversion Congress and Exposition (ECCE), Cincinnati, OH, 2017, pp. 2940-2947.



# Predictive frequency-based sequence estimator for control of grid-tied converters under highly distorted conditions

Cristian Blanco\*, Pablo García\*, Ángel Navarro-Rodríguez\*, and Mark Sumner†

\*University of Oviedo. Dept. of Elec., Computer & System Engineering  
Gijón, 33204, Spain

e-mail: blancocristian@uniovi.es, garciafpablo@uniovi.es, navarroangel@uniovi.es

†The University of Nottingham. Department of Electrical and Electronic Engineering

University Park, Nottingham. NG7 2RD, UK

e-mail: Mark.Sumner@nottingham.ac.uk

**Abstract**—This paper proposes a novel frequency-based predictive sequence extractor that allows to isolate the harmonic components of both voltages and currents needed for the control of grid-tied converters. The proposed method is based on a modification of the Sliding Goertzel Transformation (SGT) that allows to include a predictive behavior with a prediction horizon equal to the processing window needed for the algorithm. The technique performance is compared with the well-established DSOGI alternative, allowing for a higher bandwidth in the estimation as well as improved immunity to changes in the magnitude, frequency and phase of the tracked signals. Additionally, the impact of the proposed method on the closed-loop performance of the current controlled converter is proposed as a metric, thus enabling other researches to have a clear view about the expected real impact of the different existing methods.

## I. INTRODUCTION

Distributed power generation (DPG) is expected to play an important role in the short and medium term design of the generation, transport and distribution system. This is due to the penetration of renewable generation units that allows to produce power, providing at the same time ancillary services (harmonic compensation [1], magnitude and frequency restoration [2],...) An engaging characteristic of the DPG systems based in renewable generation is that they help to decrease the emissions since the DPG units are placed near the power is consumed. On the other hand, the use of DPG increases the complexity of the whole system due to the coexistence of several systems with different characteristics (nominal power, output impedance, workload, transient response ...)

DPG units are usually connected to the utility grid by using electronic power converters (mainly PWM voltage source

inverters, VSI [3], [4]). VSI control strategies are mainly composed by an inner current control loop, an outer voltage control loop and an external power control loop [5] based, all of them in general, on proportional-integral (PI [3], [4]) or proportional-resonant (PRES [5]) controllers. To perform an accurate control of the fundamental component of the current, voltage or power, the use of PI and PRES controllers requires to estimate the magnitude, frequency and phase of the fundamental component of the utility grid. Furthermore, if a highly harmonic content is present on the grid, the estimation of frequency, phase and magnitude for additional harmonics is a desirable feature.

During last decades, several authors have been working on the development of synchronization techniques able to work under a wide range of working conditions. In this regard, the utility grid voltage may be polluted with harmonic components (due to the use of nonlinear loads) or unbalanced conditions (due to single-phase loads). At the same time, the utility grid magnitude and frequency may oscillate between values defined in the grid codes. Phase jumps could also occur while grid voltage measurements could be incorrect, especially in terms of DC components due to the voltage sensors [6]. The VSI control is required to be fast and accurate under all of these disturbances, the synchronization technique being a key point of the DPG control.

Synchronization techniques can be divided in open-loop [7], [8] or closed-loop [9]–[14]. Open-loop methods estimate the PCC voltage magnitude, frequency and phase without any feedback while closed-loop methods are based on locking one characteristic of the input signal, e.g. the frequency (frequency-locked-loop, FLL [9]) or phase (phase-locked-loop, PLL [11]). Nowadays, closed-loop techniques are preferred due to their better performance, a common concern being how to deal with grid disturbances that affect to the parameter estimation. The operation of closed-loop methods makes them to naturally adapt their magnitude and frequency estimations

The present work has been partially supported by the predoctoral grants program Severo Ochoa for the formation in research and university teaching of Principado de Asturias PCTI-FICYT under the grant ID BP14-135. This work also was supported in part by the Research, Technological Development and Innovation Program Oriented to the Society Challenges of the Spanish Ministry of Economy and Competitiveness under grant ENE2016-77919-R and by the European Union through ERFD Structural Funds (FEDER).

when these parameters deviate from their nominal values. Thus, research efforts have been traditionally focused in the development of techniques to remove the unwanted effects of additional harmonic components. One possible solution is to reduce the controller bandwidth of the closed-loop structure. However, this is at the price of a transient response degradation, which is not an acceptable solution in most cases. Alternatively, a filtering stage can be implemented, pre-filter and filter in the loop techniques being the most acceptable solutions [12].

A pre-filter stage feeds the closed-loop method with a filtered version of the grid voltage that contains only the fundamental component. DSOGI-FLL [9], MCCF-PLL [13], DSOGI-PLL [10], or CCCF-PLL [14] are examples of pre-filter stage methods. At the same time, filter on the loop techniques ([12], [15]) remove the unwanted effects of harmonics and unbalances inside the closed loop. In both cases, filters can be implemented by using second-order generalized integrators [9], [10], notch filters [12], complex-coefficient filters [13], [14], lead compensators [15] or moving average filters [16].

When using filtering stages, some aspects must be carefully taken into account: filters introduce phase delays that must be online estimated and compensated [17], transient response is affected [6], filters need to adapt their central frequency under frequency deviations [13] and magnitude and phase jumps affect to the frequency, magnitude and phase estimation [12].

In order to deal with these drawbacks, this paper proposes the use of the SGT [18] to estimate the fundamental and harmonic components of the utility grid. Predictive techniques are proposed to boost the Goertzel transient response while a wide frequency resolution is used to compute the algorithm, making the system frequency-adaptive. Experimental verification is provided to test the performance of the proposed method under several grid disturbances, including magnitude changes, frequency deviations, harmonic components and phase jumps.

This paper is organized as follows, in section II, the mathematical approach based on the sliding Goertzel algorithm is explained. Following, the proposed predictive algorithm is detailed, including simulation results to demonstrate its effectiveness. In II-A, the use of a fusion method for an estimation based both on the sliding implementation and on the predictive proposal is included. Section II-B describes the proposed method for the frequency estimation and the impact of frequency variation over the voltage magnitude and phase estimated values. In section III, the evaluation of the method using a programmable voltage supply is included. Finally, in IV, the obtained experimental results are included, thus validating the approach of the proposed method.

## II. IMPLEMENTATION

The basics of the proposed method rely on an efficient implementation of the Discrete Fourier Transform (DFT) by using the recursive Goertzel implementation [19], valid for the extraction of harmonic components in real-time applications. The implementation has a lower computational burden when

TABLE I  
CONSIDERED HARMONICS.

Harmonic Order	Mag (p.u.)
1	1
-5	0.2
7	0.2

compared with traditional FFT-based approach for a low number of harmonics. Specifically, for calculating  $M$  harmonics from an input data vector of length  $N$ , the associated cost of the Goertzel algorithm can be expressed as  $O(N, M)$ , whereas for the FFT is  $O(N, \log_2 N)$ . Obviously, when the number of calculated harmonics meets  $M \leq \log_2 N$ , then the Goertzel approximation is the preferred choice. In this paper, one fundamental cycle, assuming a  $50Hz$  nominal frequency, is considered at  $10kHz$  sample rate, leading to a time window of  $20ms$  and 200 samples. With the proposed parameters, the calculations using the Goertzel approach are faster than the FFT alternative when the calculated number of harmonics is  $M \leq 8$ . For the validation of the system, the harmonics detailed in Table I are used. The implementation is detailed in pseudo-code in Algorithm 1 and the corresponding block diagram is shown in Fig. 1. At the implementation, the  $h$  input variable contains the harmonic order of the sequences being analyzed.

---

### Algorithm 1 Sequence extractor using Goertzel algorithm.

---

```

1:  $f_{bin} \leftarrow 2\pi h/N$ 
2:  $a_f \leftarrow 2 \cos(f_{bin})$ 
3:  $b_f \leftarrow e^{-j f_{bin}}$ 
4:  $sk \leftarrow$  Initialize to zero
5:  $k \leftarrow 1, k1 \leftarrow 2, k2 \leftarrow 3$ 
6: for  $hh \leftarrow 1, \text{number of elements in } f_{bin}$  (harmonics) do
7:   for  $n \leftarrow 1, N - 1$  do
8:      $sk(hh, k) = x(n) + a_f(hh) * sk(hh, k1) -$   

        $sk(hh, k2)$ 
9:      $sk(hh, k2) = sk(hh, k1)$ 
10:     $sk(hh, k1) = sk(hh, k)$ 
11:   end for
12:    $sk(hh, k) = a_f(hh) * sk(hh, k1) - sk(hh, k2)$ 
13:    $y(hh, N) = (sk(hh, k) - sk(hh, k1) * b_f(hh))/N$ 
14: end for

```

---

An example of the evolution in time domain of the recursive Goertzel estimation, compared to the actual magnitudes of the harmonics is shown in Fig. 2. As it can be seen, when the input signal is at steady state during the  $20ms$  needed for the completion of the algorithm, the estimation converges to the desired values. By looking at the represented graphs, two important conclusions can be obtained: 1) The estimation procedure is discontinuous, being the computed harmonic values restarted at each processing window. Obviously, this must be addressed for using the method for converter control application, as the one proposed in this paper. Often, overlapping is used for improving the situation (see Fig. 2c).

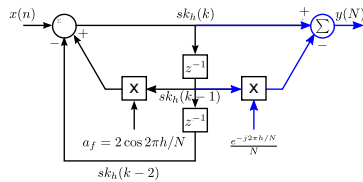


Fig. 1. IIR implementation of the Goertzel algorithm. Black traces are for the recursive part implementation. Blue traces represent the operations to be done at the last step ( $k = N$ ).

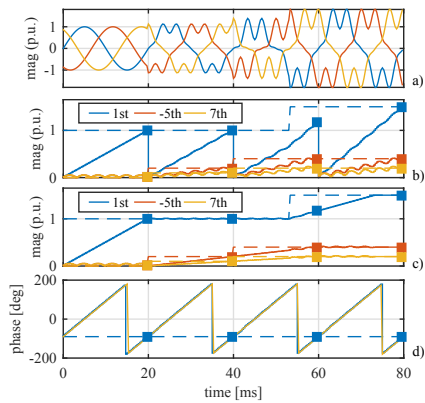


Fig. 2. Recursive Goertzel estimation for a three phase system with the harmonic contents shown in Table 1. The dotted lines correspond to the real value of the harmonics. The square dots represent the estimated value at the end of each block. a) waveforms, b) and c) recursive Goertzel estimation with 0 and  $N-1$  overlap, d) phase error.

However, this comes with an additional cost due to the number of operations required at each sample being multiplied by the number of overlapping samples. Alternatively, an efficient sliding approach of the algorithm (SGT) has been proposed for real-time signal processing applications, being the selected choice for our investigations [18]. 2) The estimated magnitude needs the total number of samples and time,  $N = 200$ ,  $t = 20ms$ , to converge to the correct value. This would raise an unacceptable delay when the estimation is used as a feedback signal. However, it can be also seen that the evolution of the fundamental component ( $1^{st}$  harmonic) estimation is linear during the estimation window and barely affected by the harmonic content.

According to 2), this paper proposes to incorporate a predictive SGT implementation (P-SGT) that improves the convergence speed and, at the same time, avoids the extra calculations of the overlapping. The predictive behavior is implemented by a two-step algorithm. Firstly, a linear recursive least squares estimation (LSE) is run over the output of each

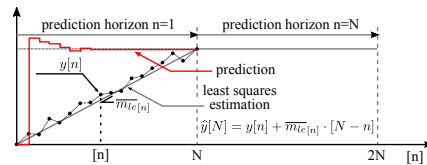


Fig. 3. Graphical representation of the proposed predictive algorithm. The slope at each of the points is filtered by a moving average filter for reducing the derivative noise.

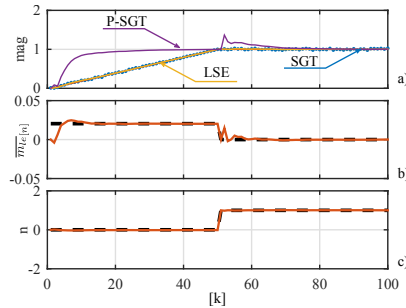


Fig. 4. Proposed P-SGT implementation. a) evolution of the magnitude. Actual samples are represented by blue dots, the output of the SGT by the red line and the prediction by the purple line. b) evolution of the predicted slope, c) evolution of the predicted offset. A window of  $N = 50$  have been used for demonstration purposes.

sample of the SGT. This will lead to a linear representation of the corresponding datapoints. It must be remarked that being the output values of the SGT complex, two different least squares estimation can be obtained: one for the module and another one for the phase. Even considering this linear condition both for the magnitude and the phase estimation, at this paper the phase estimation is directly obtained from the Goertzel algorithm due to the fact that an accurate phase estimation can be obtained before each window is completed. Secondly, the module value at the end of each of the estimation windows is predicted. This last step is implemented at each step by again considering the linear evolution (1)

$$\hat{y}[N] = y[n] + \overline{m}_e[n] \cdot [N - n] \quad (1)$$

, where  $\overline{m}_e[n]$  is the moving average slope estimated by the LSE approach,  $N$  the window size and  $n$  the actual sample. A graphical description for the algorithm is shown in Fig. 3.

The simulation results with the proposed methods is shown in Fig. 4. As it can be seen, the results obtained by the P-SGT approximations notably improves the convergence speed of the estimation. However, even with the averaged slope calculation, some peak transients can be observed at the beginning of each processing window. This behavior is inherent to the involved derivative process. By comparing the smooth transitions using

the SGT, it is clear that both estimations can work in a complementary approach. For that reason, the final proposal for the estimation method will use a combination of both alternatives. The combined estimation will be based on the rate of change in the SGT estimation. As previously discussed, during the convergence time for the SGT, the estimation will exhibit a mostly linear change. On the contrary, once the estimation has reached the final value it will have a mostly zero variation. Based on that, the P-SGT will be favored during the transients, whereas the classical SGT will be mostly used at the steady state. Next section shows the mathematical formulation of the fusion algorithm as well as a numerical evaluation about the method performance.

#### A. Combined SGT and P-SGT estimation

Considering the performance of both the SGT and P-SGT strategies shown in Fig. 4, it is proposed to combine both methods, leading to the so called PF-SGT, for getting the final expression. For the fusion rule, an equation on the form (2) is proposed, where the value of the fusion gain ( $k_{h\omega_e}^f$ ) is given by (3).

$$X_{h\omega_e}^{pf-sgt} = X_{h\omega_e}^{p-sgt} \cdot (1 - k_{h\omega_e}^f) + X_{h\omega_e}^{sgt} \cdot (k_{h\omega_e}^f) \quad (2)$$

$$k_{h\omega_e}^f = \exp\left(-\text{abs}\left(\frac{\text{avg}(\Delta X_{h\omega_e}^{sgt})}{\text{max}(\Delta X_{h\omega_e}^{sgt})}\right)\right) \cdot g_{h\omega_e} \quad (3)$$

Where the presented variables are defined as follows:

- $X_{h\omega_e}^{pf-sgt}$ . Estimation of harmonic component  $h$  at fundamental frequency  $\omega_e$  for variable  $X$  using the PF-SGT method.
- $X_{h\omega_e}^{p-sgt}$ . Estimation of harmonic component  $h$  at fundamental frequency  $\omega_e$  for variable  $X$  using the P-SGT method.
- $X_{h\omega_e}^{sgt}$ . Estimation of harmonic component  $h$  at fundamental frequency  $\omega_e$  for variable  $X$  using the SGT method.
- $\Delta X_{h\omega_e}^{sgt}$  is the rate of change of the module of the estimated harmonic components by the SGT algorithm.
- *avg.*. Moving average function.
- *max.*. Maximum variation function.
- $g_{h\omega_e}$ . Gain of the exponential function used for tuning the fusion system.

Evolution of the estimation and the adaptive gain is shown in Fig. 5. As clearly shown, the fusion helps on removing the transient at the beginning of each of the processing windows. Ongoing work is being carried out for the selection of the optimal fusion gain.

#### B. Frequency estimation

When the proposed PF-SGT method is applied for the estimation of grid voltages and currents, variations at the frequency must be considered. As known, frequency domain methods based on the DFT assume the periodicity of the signal and by the discrete resolution. However, when used for the analysis of signals coming from a real application, this assumption is not longer valid. The effect of the signal

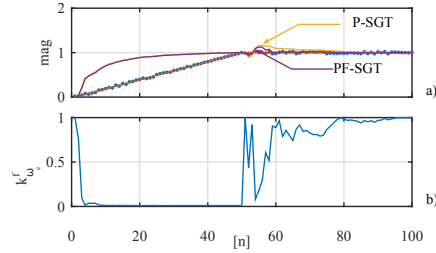


Fig. 5. Proposed fusion mechanism. a) evolution of the module. b) evolution of the gain.  $g_{h\omega_e} = 5$ ,  $\text{max}(\Delta X_{h\omega_e}^{sgt}) = 1.1$

being not periodic, together with the discrete resolution, will cause spectral leakage, affecting both the phase and magnitude of the estimated components. Often, windowing techniques (both in time and frequency domain) are applied in order to reduce the impact. Unfortunately, the procedure also affects the magnitude and the phase of the extracted components and additional compensation is needed. A different approach is to optimize the parameters for the calculation by adjusting the number of needed samples (200 by default in our implementation) depending on the fundamental frequency, so a complete number of cycles is acquired at each processing window. For this paper, and considering that only the harmonics of the fundamental frequency needs to be isolated, an even simpler approach has been used by selecting a coarse spectral resolution of  $50Hz$ . This avoids the spectral leakage when deviations from the fundamental frequency appears, at the cost of any other disturbance signal falling within the band of  $[25 - 75]Hz$  to be affecting the estimation.

#### C. Magnitude estimation errors due to the LSE algorithm

The use of the proposed LSE method over a  $N$ -length window could affect to the magnitude estimation depending on the sample where the disturbance occurs ( $0 < n < N - 1$ ). This is due to the fact that the same slope is assumed over the whole LSE period. This will lead to magnitude estimation errors if any change in the signal magnitude occurs during the LSE calculation period.

In order to test the behavior of the LSE method, Fig. 6 shows the magnitude error when the sample at which the disturbance happens is continuously varied from 0 to  $N=200$ . Different disturbances are considered: a 0.4 p.u. magnitude step, a frequency step from 49 to 51Hz and a phase jump of 60 deg. Two different signals are shown in each graphic: the mean value of the magnitude error over two 200 samples periods is shown in blue color, whereas the magnitude error at the end of the first period is shown in red. As it can be observed, magnitude and phase jumps both affect to the magnitude estimation depending on the sample when they occur.

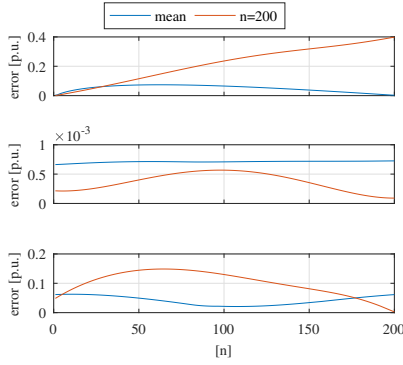


Fig. 6. Effect on the magnitude estimation when the disturbance occurs along the N-length window: a) Magnitude step (0.4 p.u.), b) Frequency Step (2 Hz.) c) Phase Jump (60 deg).

In order to deal with these unwanted errors, what is proposed here is to restart the LSE calculation by looking for a noticeable variation in the estimated magnitude between two consecutive LSE samples, as shown in (4). A threshold ( $M_{th}$ ) of a 15% of the fundamental positive-sequence magnitude has been selected.

$$|X_{\omega_e}^{p-sgt}(n) - X_{\omega_e}^{p-sgt}(n-1)| > M_{th} \quad (4)$$

#### D. Phase-jump detection and magnitude correction

An adverse effect that noticeably affects to the magnitude and frequency estimation is the occurrence of a phase jump. This subsection shows a basic technique that detects a phase jump and corrects its effects in the estimated magnitude. The main working principle of this technique is to check if the phase difference between the actual phase angle estimation and the previous one falls inside the grid code. An acceptable frequency deviation from the nominal value has been selected to be  $\omega_{err} = 2 \cdot 2\pi \text{rad/s}$ . Thus, the phase difference between the actual phase estimation and the previous one ( $P_s$  in (5)) should fall inside the phase advance defined by (5), being  $T_s$  the sampling time. Thus, if a phase jump is detected, the magnitude estimation at the previous sample is used. Note that a low-pass version of the voltage complex vector could be used, but this solution requires more computational effort at no extra advantage. Fig. 7 shows the proposed correction mechanism compared to the magnitude variation before the compensation.

$$(\omega_e - \omega_{err}) \cdot T_s < P_s < (\omega_e + \omega_{err}) \cdot T_s \quad (5)$$

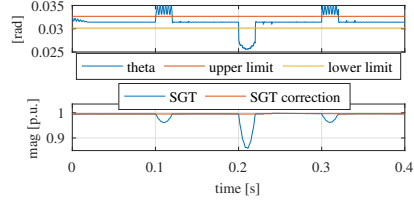


Fig. 7. System evaluation. Compensation of magnitude estimation during a phase-jump.

### III. SYSTEM EVALUATION

The initial evaluation of the proposed sequence estimator has been done using a programmable voltage source (2210 TC-ACS-50-480-400 from Regatron) to create the different grid conditions. Different steps at the magnitude, phase and frequency of the signal are considered as well as the behavior with and without additional harmonic content. The data is acquired by an scope at  $1Ms/s$  and later down-sampled to  $10kHz$ . The down-sampled signal is processed in Matlab/Simulink using a real-time implementation.

The results for the tracked grid voltage's magnitude and phase using the PF-SGT are shown in Fig 8 and 9. The different events at the source signal are repeated twice. During the first interval ( $t = 0 - 1.2s$ ), no harmonics were included. At the second part, the harmonics indicated at Table I are considered. Moreover, starting at  $t = 1.5s$ , a dc offset is included at the output of the voltage sensors. Dc-offset values are  $V_u = 10V$ ,  $V_v = 5V$ ,  $V_w = -5V$ . The events are scheduled as follows: 1) **Magnitude**. At  $t = 0.8s$  and  $t = 0.9s$  it changes to 0.8 and 1.2 p.u. The same change is observed at  $t = 1.98s$  and  $t = 2.08s$ . 2) **Frequency**. At  $t = 0.2s$  and  $t = 0.3s$ , the rated  $50Hz$  frequency is changed to 49 and 51Hz respectively. The same is done  $t = 1.38s$  and  $t = 1.48s$ . 3) **Phase**. At  $t = 0.5s$ ,  $t = 0.6s$ ,  $t = 0.7s$  phase jumps of 30, -60, 30deg. are induced. Same pattern is observed at  $t = 1.68s$ ,  $1.78s$ ,  $1.88s$ . At the graph, the behavior of the proposed method is tested compared to the DSOGI implementation. The tuning of the DSOGI has been done according to the optimal parameters indicated by its authors [9]. As it can be seen, the proposed method shows a better immunity to harmonics and faster response to the considered changes with the exception of the phase change at  $t = 0.6s$  and  $1.78s$ . This is due to the correction explained in (5) not being considered for the initial evaluation. It is special remarkable the improvement of the proposed method when DC components are considered. Finally, the compared experimental results for the dynamics of the closed-loop current control using the DSOGI and the proposed PF-SGT method are shown in Fig. 10. For the initial evaluation of the method, the closed-loop current control of a three phase power converter connected to the grid has been used. The current control has been implemented at the synchronous reference frame and different current references,

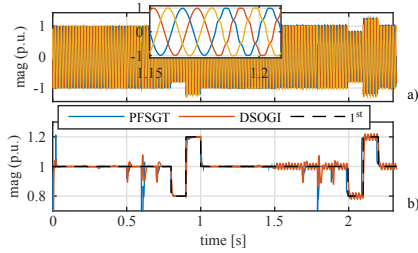


Fig. 8. System evaluation. Comparison of the PF-SGT method with respect to the ideal 1<sup>st</sup> harmonic and the DSOGI implementation. a) evolution of time domain waveforms, b) evolution of the module estimation.

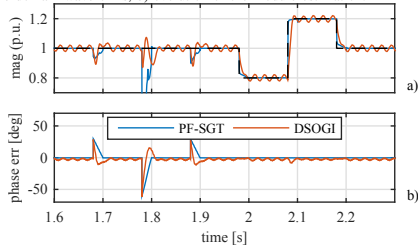


Fig. 9. System evaluation. Detail on the comparison of the PF-SGT method with respect to the ideal 1<sup>st</sup> harmonic and the DSOGI implementation. a) module, b) phase.

both at the  $d$  and  $q$  axis were commanded. The grid voltage was acquired as previously explained and the downsampled voltage data was used in a real-time Simulink simulation. The same sequence than for the open-loop results shown in Fig. 8 has been used. The relevant parameters for the setup are: filter values:  $L = 5mH$ ,  $R = 0.2\Omega$ , switching frequency  $f_{sw} = 10kHz$ , current control bandwidth  $20Hz$ . As clearly shown, the proposed method shows a better transient

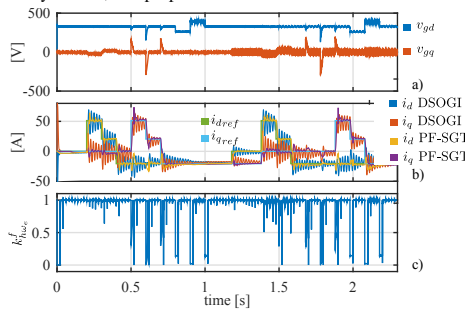


Fig. 10. System evaluation. Close loop comparison between the DSOGI and the proposed PF-SGT methods. a) grid voltages, b) grid currents, c) adaptive fusion gain for the PF-SGT method.

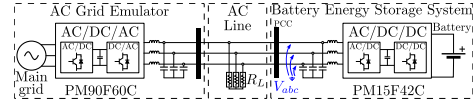


Fig. 11. Setup used for the experimental validation. Two converters are coupled together, PM90F60C unit is used to create the varying grid conditions and PM15F42C runs the proposed estimation method.

response and harmonic rejection capabilities than the DSOGI alternative. Moreover, the bandwidth was set to such a low value in order to keep stable the DSOGI-based current control.

#### IV. EXPERIMENTAL RESULTS

For this paper, the evaluation of the proposed sequence estimator is done using the experimental grid shown in Fig. 11. The setup is composed by Triphase power modules PM15F42C and PM90F60C, and a set of passive loads. The module PM90F60C is used as a grid voltage emulator. It creates the different grid scenarios, modifying the magnitude, phase, frequency and harmonic content of the voltage signal. The module PM15F42C is integrated in the system operating as a constant power controlled battery energy storage system. The proposed algorithms are processed online in the PM15F42C control unit using the voltage measurements at the point of common coupling (PCC). The experimental results use the DSOGI algorithm as the base case for the comparison.

##### A. Variation of grid voltage magnitude

Variations of grid voltage magnitude from 1 to 0.8 p.u. at  $t = 0.1s$  and from 0.8 to 1.15 p.u. at  $t = 0.2$  are considered. Results both without and with  $h_5 = 5\%$ ,  $h_7 = 5\%$  additional harmonics are shown in Fig. 12 and Fig. 13 respectively. As shown, the proposed method have a faster dynamic response as well as higher harmonic robustness, both for the magnitude and the phase estimation.

##### B. Variation of grid voltage frequency

Variations of grid voltage frequency from 50 to 49 Hz. at  $t = 0.1s$  and from 49 to 51 Hz. at  $t = 0.2$  are considered. Results both without and with  $h_5 = 5\%$ ,  $h_7 = 5\%$  additional harmonics are shown in Fig. 14 and Fig. 15 respectively. As shown, the proposed method have a better magnitude response. However, an steady state error in the phase appears with the proposed method. The reason is the considered frequency resolution. As explained before, a frequency resolution of 50 Hz. has been selected for this work. This implies that any deviation smaller than 50Hz can not be measured and the difference between the real grid frequency and the fundamental harmonic is directly coupled to a phase error. However, the maximum possible error under the maximum considered frequency deviation is bounded and given by the expression (6). Where  $\max(\omega_{err})$  is the maximum frequency error and  $f_c$  the grid frequency in Hz. The maximum frequency error depends on the frequency resolution and the maximum admissible grid

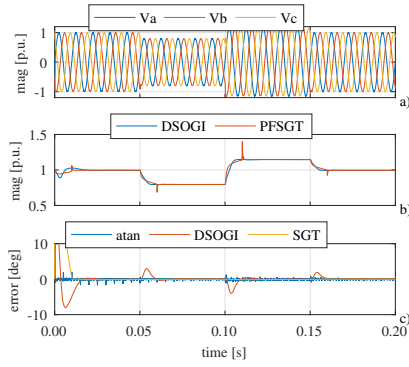


Fig. 12. Experimental results. Comparison between the DSOGI and the proposed PF-SGT methods for a magnitude step change. No harmonics are injected. From top to bottom: a) grid voltages, b) grid voltage magnitude, c) grid voltage phase error.

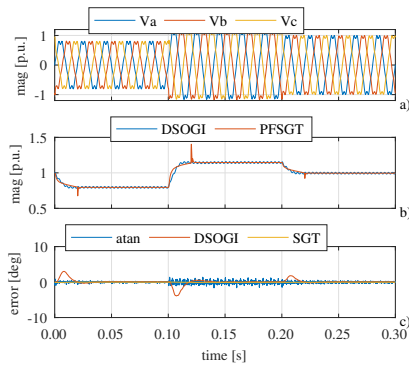


Fig. 13. Experimental results. Comparison between the DSOGI and the proposed PF-SGT methods for a magnitude step change. Harmonics as listed in Table I are injected. From top to bottom: a) grid voltages, b) grid voltage magnitude, c) grid voltage phase error.

frequency deviation. For the values considered at this paper, the error is bounded to a maximum of 3.6deg.

$$\max \theta_{err} = \frac{\max(\omega_{err})2\pi}{f_e} \cdot \frac{180}{2\pi} \quad (6)$$

### C. Variation of grid voltage phase

Variations of grid voltage phase from 0 to 30 deg. at  $t = 0.05$ s, from 30 to -30 deg. at  $t = 0.1$  and from -30 to 0 at  $t = 0.15$ s are considered. Results both without and with  $h_5 = 5\%$ ,  $h_7 = 5\%$  additional harmonics are shown in Fig. 16 and Fig. 17 respectively. As shown, the proposed method have a similar

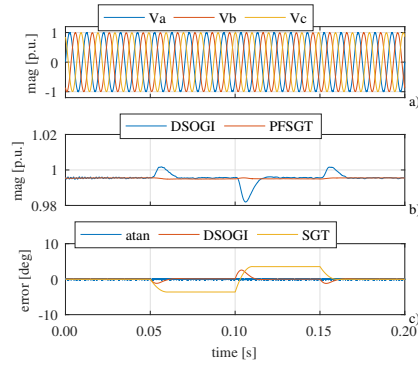


Fig. 14. Experimental results. Comparison between the DSOGI and the proposed PF-SGT methods for a frequency step change. No harmonics are injected. From top to bottom: a) grid voltages, b) grid voltage magnitude, c) grid voltage phase error.

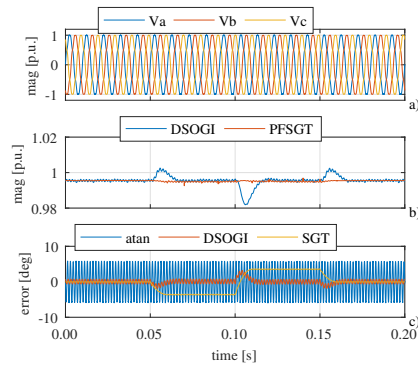


Fig. 15. Experimental results. Comparison between the DSOGI and the proposed PF-SGT methods for a frequency step change. Harmonics as listed in Table I are injected. From top to bottom: a) grid voltages, b) grid voltage magnitude, c) grid voltage phase error.

results compared to DSOGI when no additional harmonics are considered and a clearly improve response under harmonic conditions.

### V. CONCLUSION

This paper has introduced a new predictive estimation technique for grid-tied converters based on a frequency-based method. To the author's best knowledge, the proposed method using a modification of the Sliding Goertzel Transformation (SGT) which includes a predictive modification has not been used before for grid phase tracking in power converters. The proposed PF-SGT method has been evaluated with respect to

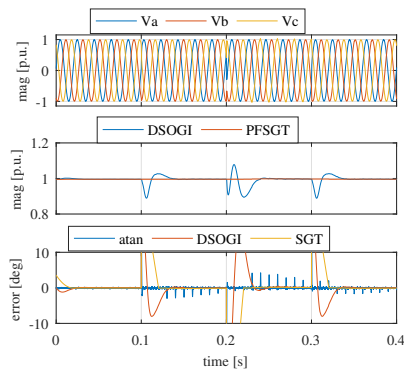


Fig. 16. Experimental results. Comparison between the DSOGI and the proposed PF-SGT methods for a phase step change. No harmonics are injected. From top to bottom: a) grid voltages, b) grid voltage magnitude, c) grid voltage phase error.

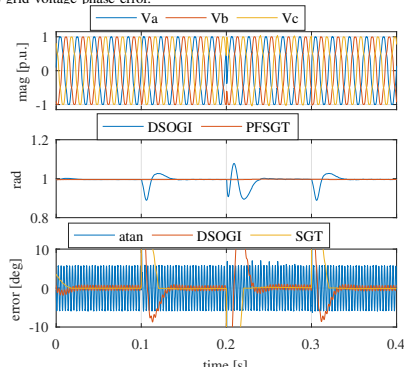


Fig. 17. Experimental results. Comparison between the DSOGI and the proposed PF-SGT methods for a phase step change. Harmonics as listed in Table I are injected. From top to bottom: a) grid voltages, b) grid voltage magnitude, c) grid voltage phase error.

a consolidated alternative, the DSOGI, showing a superior performance in terms of dynamic response and disturbance rejection. It is particular remarkable the immunity to DC offsets as well as to changes at the grid frequency. The proposed algorithm has been validated by both simulation and experimental results. The impact of the phase estimation and harmonic decoupling in a closed-loop current control implementation has also been evaluated, being the proposed PF-SGT an important improvement over the DSOGI method.

#### REFERENCES

- [1] C. Blanco, D. Reigosa, J. C. Vasquez, J. M. Guerrero, and F. Briz, "Virtual admittance loop for voltage harmonic compensation in micro-

- grids," *IEEE Transactions on Industry Applications*, vol. 52, no. 4, pp. 3348–3356, July 2016.
- [2] J. W. Simpson-Porco, Q. Shafiq, F. Dörfler, J. C. Vasquez, J. M. Guerrero, and F. Bullo, "Secondary frequency and voltage control of islanded microgrids via distributed averaging," *IEEE Transactions on Industrial Electronics*, vol. 62, no. 11, pp. 7025–7038, Nov 2015.
- [3] E. Twining and D. G. Holmes, "Grid current regulation of a three-phase voltage source inverter with an lcl input filter," *IEEE Transactions on Power Electronics*, vol. 18, no. 3, pp. 888–895, May 2003.
- [4] S. Yang, Q. Lei, F. Z. Peng, and Z. Qian, "A robust control scheme for grid-connected voltage-source inverters," *IEEE Transactions on Industrial Electronics*, vol. 58, no. 1, pp. 202–212, Jan 2011.
- [5] J. C. Vasquez, J. M. Guerrero, M. Savaghebi, J. Eloy-Garcia, and R. Teodorescu, "Modeling, analysis, and design of stationary-reference-frame droop-controlled parallel three-phase voltage source inverters," *IEEE Transactions on Industrial Electronics*, vol. 60, no. 4, pp. 1271–1280, April 2013.
- [6] S. Golestan, J. M. Guerrero, and J. C. Vasquez, "Three-phase pll's: A review of recent advances," *IEEE Transactions on Power Electronics*, vol. 32, no. 3, pp. 1894–1907, March 2017.
- [7] F. D. Freijedo, J. Doval-Gandoy, O. Lopez, and E. Acha, "A generic open-loop algorithm for three-phase grid voltage/current synchronization with particular reference to phase, frequency, and amplitude estimation," *IEEE Transactions on Power Electronics*, vol. 24, no. 1, pp. 94–107, Jan 2009.
- [8] S. Golestan, A. Vidal, A. G. Yepes, J. M. Guerrero, J. C. Vasquez, and J. Doval-Gandoy, "A true open-loop synchronization technique," *IEEE Transactions on Industrial Informatics*, vol. 12, no. 3, pp. 1093–1103, June 2016.
- [9] P. Rodriguez, A. Luna, M. Ciobotaru, R. Teodorescu, and F. Blaabjerg, "Advanced grid synchronization system for power converters under unbalanced and distorted operating conditions," in *IECON 2006 - 32nd Annual Conference on IEEE Industrial Electronics*, Nov 2006, pp. 5173–5178.
- [10] P. Rodriguez, R. Teodorescu, I. Candela, A. Timbus, M. Liserre, and F. Blaabjerg, "New positive-sequence voltage detector for grid synchronization of power converters under faulty grid conditions," in *2006 37th IEEE Power Electronics Specialists Conference*, June 2006, pp. 1–7.
- [11] A. M. Gole and V. K. Sood, "A static compensator model for use with electromagnetic transients simulation programs," *IEEE Transactions on Power Delivery*, vol. 5, no. 3, pp. 1398–1407, Jul 1990.
- [12] C. Blanco, D. Reigosa, F. Briz, and J. M. Guerrero, "Synchronization in highly distorted three-phase grids using selective notch filters," in *2013 IEEE Energy Conversion Congress and Exposition*, Sept 2013, pp. 2641–2648.
- [13] X. Guo, W. Wu, and Z. Chen, "Multiple-complex coefficient-filter-based phase-locked loop and synchronization technique for three-phase grid-interfaced converters in distributed utility networks," *Industrial Electronics, IEEE Transactions on*, vol. 58, no. 4, pp. 1194–1204, April 2011.
- [14] C. Blanco, D. Reigosa, F. Briz, J. M. Guerrero, and P. Garcia, "Grid synchronization of three-phase converters using cascaded complex vector filter pll," in *2012 IEEE Energy Conversion Congress and Exposition (ECCE)*, Sept 2012, pp. 196–203.
- [15] F. D. Freijedo, A. G. Yepes, O. Lopez, A. Vidal, and J. Doval-Gandoy, "Three-phase pll's with fast postfault retracking and steady-state rejection of voltage unbalance and harmonics by means of lead compensation," *IEEE Transactions on Power Electronics*, vol. 26, no. 1, pp. 85–97, Jan 2011.
- [16] S. Golestan, J. M. Guerrero, A. Vidal, A. G. Yepes, and J. Doval-Gandoy, "pll with maf-based prefiltering stage: Small-signal modeling and performance enhancement," *IEEE Transactions on Power Electronics*, vol. 31, no. 6, pp. 4013–4019, June 2016.
- [17] C. Blanco, D. Reigosa, F. Briz, and J. M. Guerrero, "Quadrature signal generator based on all-pass filter for single-phase synchronization," in *2014 IEEE Energy Conversion Congress and Exposition (ECCE)*, Sept 2014, pp. 2655–2662.
- [18] E. Jacobsen and R. Lyons, "An update to the sliding dft," *IEEE Signal Processing Magazine*, vol. 21, no. 1, pp. 110–111, Jan 2004.
- [19] G. Goertzel, "An Algorithm for the Evaluation of Finite Trigonometric Series," *The American Mathematical Monthly*, vol. 65, no. 1, pp. 34–35, 1958.



## **D.6 Cooperative Control in a Hybrid DC/AC Microgrid based on Hybrid DC/AC Virtual Generators**

Á. Navarro-Rodríguez, P. García, C. Blanco, R. Georgious and J. García, "Cooperative Control in a Hybrid DC/AC Microgrid based on Hybrid DC/AC Virtual Generators," 2018 IEEE Energy Conversion Congress and Exposition (ECCE), Portland, OR, 2018, pp. 1156-1163.



## Cooperative Control in a Hybrid DC/AC Microgrid based on Hybrid DC/AC Virtual Generators

Ángel Navarro-Rodríguez  
*Dept. of Electrical Engineering*  
*University of Oviedo, LEMUR Group*  
 Gijón, Spain  
 navarroangel@uniovi.es

Pablo García  
*Dept. of Electrical Engineering*  
*University of Oviedo, LEMUR Group*  
 Gijón, Spain  
 garciafpablo@uniovi.es

Cristian Blanco  
*Dept. of Electrical Engineering*  
*University of Oviedo, LEMUR Group*  
 Gijón, Spain  
 blancocristian@uniovi.es

Ramy Georgious  
*Dept. of Electrical Engineering*  
*University of Oviedo, LEMUR Group*  
 Gijón, Spain  
 georgiousramy@uniovi.es

Jorge García  
*Dept. of Electrical Engineering*  
*University of Oviedo, LEMUR Group*  
 Gijón, Spain  
 garciajorge@uniovi.es

**Abstract**—This paper deals with the dynamic control of the DC bus voltage and the AC voltage magnitude and frequency in a hybrid DC/AC Microgrid (MG). In order to allow a high penetration of renewable energies, provide an increased system reliability during islanding and reduce the dependency on the mains, Energy Storage Systems (ESSs) are included in both the DC and AC grids. The MG is composed by a multiport solid-state-based transformation center, with connexion to the mains and a central battery energy storage system (BESS), and a flexible number of AC Nanogrids (NGs) coupled to a Low Voltage DC bus (LVDC) through DC/AC 3-phase Power Electronic Converters (PECs) operated as grid forming, hereinafter referred as Nanogrid Head Converters (NGHCs). The MG control presents two main characteristics: 1) A DC bus regulation scheme is proposed based on DC virtual generators and P/V DC droop that allows to adapt the participation in the power sharing for DC bus regulation and provides with an automatic transition between *grid connected* and *islanding* modes; 2) In order to provide a cooperative operation between the different AC NGs, allowing the automatic power sharing between them through the DC bus, a DC/AC virtual generator control scheme, based on the theory of Virtual Synchronous Machines (VSM), is proposed for its implementation in the NGHCs, thus coupling the control of the LVDC and the NGs. The theoretical discussion is supported with simulations.

**Index Terms**—DC/AC Hybrid Microgrid, MG control, Virtual Inertia, Virtual Synchronous Generator

### I. INTRODUCTION

The increasing concern about environmental issues, the problematic of renewable energies integration, and the rising popularity of concepts such as local generation and self-

The present work has been partially supported by the predoctoral grants program Severo Ochoa for the formation in research and university teaching of Principado de Asturias PCTI-FICYT under the grant ID BP14-135. This work has been also partially supported by the government of Principality of Asturias, under IDEPA grant 2017 Thyssen SV-PA-17-RIS3-3, by the Research, Technological Development and Innovation Program Oriented to the Society Challenges of the Spanish Ministry of Economy and Competitiveness under grant ENE2016-77919-R and by the European Union through ERFD Structural Funds (FEDER).

consumption have led to an increasing interest on alternatives to the conventional utility grid as Microgrids (MGs), Nanogrids (NGs) and Smart grids. Despite its advantages, the weakness and stability problems associated to a MG, due to its low inertia and the presence of renewable energy systems (RES), have demanded a significant research interest since its apparition. Studies for different types of contingencies have been carried out, pursuing the power quality improvement [1], [2]. Furthermore, with the apparition of hybrid DC/AC MGs, where the Power Electronic Converters (PECs) may share power not only in the AC grid but also in the DC lines, new MG issues appears as the stability, voltage regulation and quality maintenance in both DC and AC grids [3]–[5].

Several methodologies and control topologies for distribution network (DN) and MGs have been presented in the literature to ensure the voltage control and power flow, as the central controller, the master-slave, the Q/V and P/f droops, the virtual impedance, and hybrid approaches [6]–[9]. In addition, during the recent years a relatively novel approach for MGs distributed control is becoming popular, consisting on the emulation of Synchronous Generators through PECs leading to the well-known terms of Virtual Synchronous Generators (VSG), Virtual Synchronous Machines (VSM), Synchronverters and Virtual Inertia (VI). The integration of VSGs in the MGs allows to imitate the behavior of conventional grids dominated by Synchronous Generators (SG), providing the MG with an additional inertia, softening the frequency and magnitude rate of change during active power transients. Moreover, VSGs avoid the use of frequency or phase detectors for synchronization and allows the integration of conventional SGs in the MGs together with DGs, RESs, ESS and loads interfaced by PECs. Additionally, the stability and dynamic active power balance in the grid can be improved by adding a VI using ESSs, increasing the grid inertia and damping, adding flexibility to the system [10]–[14]. Besides, the VSG scheme can also be combined with Q/V and P/f droops in order to

manage the steady state power sharing in the MG.

Regarding the dynamic power sharing between hybrid DC/AC MGs when 3-phase inverters operated as grid forming are used for the coupling between the Low Voltage DC line (LVDC) and the AC grid, few discussion is found in the literature. Some studies have been proposed based on cascaded converters stability [15], and power balancing between AC and DC using a  $V_g/V_{dc}$  droop [16]. However, these methods have been proposed for AC/DC/AC grid tied converters and they can not be directly applied to the AC/DC voltage control of a hybrid MG. In [17], an adaptive power sharing scheme for hybrid DC/AC is proposed for a MG where fixed frequency slack voltage-controlled converters are used to couple the AC grids to a LVDC, based on a central controller for the LVDC regulation and distributed compensation in the AC grids. Another approach related to the proposal in this paper is found in [18], where a VSM is proposed as an interface between a DC grid and a non-islanded AC grid. However, although the methods can be useful for the present study, the model is demonstrated only for a single phase grid and just consider the connection to one AC grid that operates as a grid feeding converter.

Thus, this paper deals with the dynamic control of the LVDC bus voltage and the AC voltage magnitude and frequency in a hybrid DC/AC MG with ESSs. The MG is composed by a multiport solid-state-based transformation center, with connection to the mains, a central Battery Energy Storage System (BESS), and multiple AC NGs coupled to a LVDC through DC/AC 3-phase PECs. They are referred as Nanogrid Head Converters (NGHCs), and play the role of grid forming converters in their corresponding NGs. The paper proposed two main strategies: 1) A DC voltage regulation scheme based on DC virtual generators and P/V DC droop that allows to adapt the participation of the mains and BESS in the transient and stationary power sharing for DC bus regulation, providing with an automatic transition between *grid connected* and *islanding* modes. 2) in order to provide a cooperative operation of the different AC NGs and the LVDC bus, allowing the automatic power sharing between them, a DC/AC virtual generator control scheme, based on the theory of Virtual Synchronous Machines (VSMs), but here extended to include a DC machine mechanically coupled using the virtual shaft concept, is proposed for its implementation in the NGHCs, coupling the control of the LVDC and the NGs. The proposal pursues a reduced dependency on the mains and the reduction of stress in the central BESS.

It is worth to point out that the transition between *grid connected* and *islanding* modes is automatic and no islanding detection is needed to maintain the DC bus under regulation.

The paper is organized as follows. Section II introduces the hybrid DC/AC Microgrid topology under study and the set-point control regarding DC bus and AC NGs regulation. Section III describes the proposed Hybrid DC/AC virtual generator. Section IV explains the basics of the proposed cooperative DC/AC MG control. Section V describes the operation of DERs for grid frequency support. Section VI

presents the simulation results. Finally, section VII states the conclusions.

## II. HYBRID MG DESCRIPTION AND PROPOSED SET-POINT CONTROL

The hybrid MG under study, shown in Fig. 1, is composed by a MG transformation center (MGTC) and multiple 3-phase 4-wires AC NGs based on VSG control topology. The MGTC consists of a BESS and a MG head converter (MGHC) coupled to the mains, interconnected by a common DC bus (LVDC) to the NG Head Converters (NGHCs) that interface the LVDC with the AC NGs. The BESS and MGHC are interfaced with the LVDC by a three-port solid-state transformer (SST). It is necessary to point out that, in the present study, the main aim of the SST is to provide galvanic isolation between the mains, BESS and LVDC bus and it operates at a high bandwidth compared to the rest of elements in the MG. Thus, its dynamics are neglected and, from the point of view of the MG control it is assumed to behave as a unitary gain.

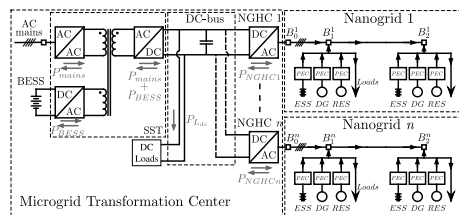


Fig. 1: Topology of the Hybrid DC/AC Microgrid under study.

As a starting point, the MG control is designed as follows: 1) The NGHC acts as Grid Forming converters with a dynamic control based on VSG scheme, regulating both the AC voltage magnitude and frequency, assuming they are the highest rated power source in each NG. As starting scenario, the MGs loads are located at the AC NGs and the LVDC bus. Under this configuration, the load as seen by the LVDC bus is drawn by the NGHCs and the DC loads. 2) Additionally, different distributed energy resources (DERs) such as Distributed Generation (DGs) and ESSs can be installed within the AC NGs. Those DERs can operate in a stiff PQ basis, P/f Q/V droop mode or as VSG or VI providing additional inertia to the grid. The power commands for the DGs and ESSs can be determined by the droop control, by a central controller performing a high level optimal power flow, or by the Maximum Power Point Tracking (MPPT) in the case of RESs. 3) The LVDC bus voltage is regulated by the MGHC (mains) and the BESS under a proposed control scheme based on DC virtual generators and P/V DC droop. During *islanding*, the DC voltage regulation relies only on the BESS.

In conventional grids, the power mismatches are absorbed by the high inertia of generators. However, in MGs, which are usually dominated by PECs or low inertia SGs, the grid inertia must be provided by the energy storage elements present in

the grid, including the DC link capacitors, and the inertia of generators in PEC based DERs. Nonetheless, the use of PECs as interface with the grid involves a decoupling from the generation system and energy storage devices, being the use of the inertial elements dependent on the PEC control. Applying the model of VSGs to the PEC control in DGs and DESS allows to increase the overall MG inertia and attach the active power to the grid frequency. Moreover, in the proposed MG scheme any DER can provide additional VI as an ancillary service taking advantage of its inherent inertia, and ESSs can be integrated in the NGs to improve the dynamic response by frequency compensation, adding flexibility to the grid [10]. As an initial set-point in the proposed MG, the DGs and DESS in the NG might contribute to the grid regulation or might operate with constant PQ commands, while the NGHCs, operated as a VSG, will regulate the voltage and frequency, being the highest inertial source in the NG, and thus absorbing the main part of the power mismatches in its corresponding NG. Under this scenario, the NGHCs are decoupled from the LVDC bus regulation, and the power mismatches supported by the NGHCs are entirely provided by the mains and the central BESS, being the NGs agnostic about each other. This creates an important dependency in the mains and a high stress on the central BESS.

Fig. 2 shows the simplified power scheme of one of the NGHCs including the different elements participating on the power sharing, where  $k$  is the NG identifier and  $n$  is the total number of AC NGs. Considering the given power topology for the NGHCs, it is worth noting that under a control based on grid forming, the NGHC cannot participate directly in the LVDC regulation.

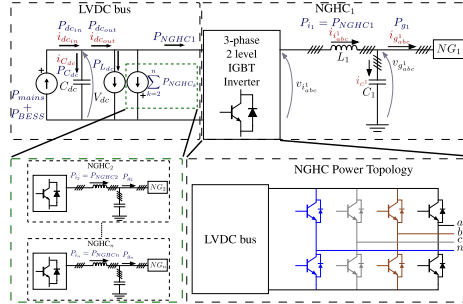


Fig. 2: Power sharing within the Hybrid DC/AC MG: NGCH topology and simplified equivalent power scheme for one of the NGHCs.

In this paper, some assumptions are established for simplification. 1) The DC bus is simplified to a capacitor. 2) The inner current control loop of the PECs interfacing the mains and the central BESS will be approximated by a low pass filter (LPF). 3) Although the application is implemented with 4

wires NGHCs (3ph+N), a balanced system will be considered, being the effect of unbalances out of the scope of this paper.

#### A. Grid forming VSG-based NGHC control

The set-point VSG control topology proposed for the NGHCs is shown in 3. It is implemented in the dq synchronous reference frame and consists of: 1) a virtual stator impedance model (resistance  $R_s^k$  and inductance  $L_s^k$ ) that emulates the VSG stator and generates the current reference  $i_{i_k}^*$ ; 2) a vector current controller; 3) an emulation of an Automatic Voltage Regulator (AVR) to regulate the NG voltage in steady state by generating a virtual voltage,  $E_d^k$ ; 4) a governor model that regulates the rotor speed,  $\omega_e^k$ , i.e., the frequency; and 5) the rotor model emulating a VI with the VSG swing function (damping  $b_s^k$ , inertia  $J_s^k$ ) that determines the grid frequency and the synchronization angle  $\theta_e^k$ .

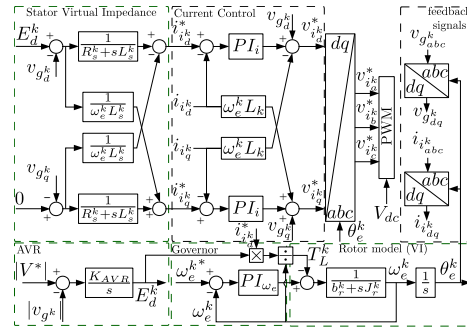


Fig. 3: Set-point grid forming VSG control block diagram proposed for the implementation in the NGHCs.  $k$  is the NG identifier.

#### B. DC voltage regulation: The DC Virtual Generator

The DC link can be modeled as (1), where  $C_{dc}$  is the LVDC capacitor,  $P_{dcin}$  is the power shared by the SST (BESS & mains) (2) and  $P_{dcout}$  is the power drawn by the NGHCs and the DC loads. The power related to the NGHCs is defined by (3), assuming  $v_{gq} = 0$ . Thus, the NGHCs are seen as CPLs by the DC link. The power flowing into the capacitor is defined as  $P_{C_{dc}} = P_{dcin} - P_{dcout}$ .

$$\frac{dV_{dc}(t)}{dt} = \frac{1}{C_{dc}V_{dc}(t)} \left( P_{dcin}(t) - \underbrace{\left( \sum_{k=1}^n P_{NGHC_k}(t) + P_{Ldc}(t) \right)}_{P_{dcout}} \right) \quad (1)$$

$$P_{dcin}(t) = P_{mains}(t) + P_{BESS}(t) = V_{dc}(t)(I_{mains}(t) + I_{BESS}(t)) \quad (2)$$

$$\sum_{k=1}^n P_{NGHC_k}(t) = \sum_{k=1}^n \frac{3}{2} \left( v_{gd}^k(t) \dot{v}_{id}^k(t) \right) \quad (3)$$

The proposed LVDC regulation scheme consists in the dynamic power sharing between the mains and the BESS through DC virtual generators (DCVGs) and P/V DC droops. This control topology presents two main characteristics: 1) The DC virtual generators enable to modify the DC bus inertia and to define the transient power sharing between the mains and BESS. For instance, in some cases it will be more desirable to provide the high frequency variations with the mains, reducing the stress in the BESS, while in others, it could be the opposite. 2) The P/V droop permits to establish a decentralized sharing mechanism during steady state.

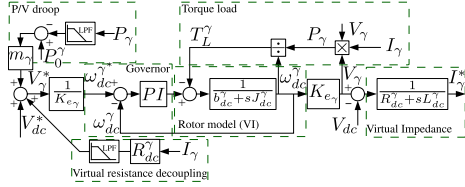


Fig. 4: DC virtual generator (DCVG) proposed for the distributed regulation of DC voltage and the power sharing between the mains and the central BESS. The identifier  $\gamma$  can be substituted by mains or BESS.

The proposed DCVG control scheme and its integration in the MG topology are shown in Fig. 4 and Fig. 5 respectively, valid for both the MGHC (mains) and the BESS.  $\gamma$  is a identifier that can represent mains or BESS. The scheme can be divided in 8 blocks:

- 1) *P/V droop*: where  $m_\gamma$  is the droop gain,  $P_0^\gamma$  is the offset commanded power and  $P_\gamma$  is the measured output power.
- 2) *Reference calculation*: the DCVG output voltage reference is calculated based on the P/V droop output, the LVDC bus nominal voltage  $V_{dc}$  and a virtual resistance decoupling. After the calculation of  $V_\gamma^*$ , a back electromotive force (bemf) constant ( $K_{e_\gamma}$ ) is applied to convert voltage to frequency ( $\omega_{dc}^\gamma$ ).
- 3) *Governor*: it consist of a feedback PI regulator which aim is to track the ( $\omega_{dc}^\gamma$ ) reference.
- 4) *Rotor model*: is the virtual plant that provides the virtual inertia ( $J_{dc}^\gamma$ ) and friction ( $b_{dc}^\gamma$ ) to the system.
- 5) *Torque load*: is the disturbance of the virtual system and is obtained from the instantaneous power shared by the mains or BESS.
- 6) *Frequency to voltage conversion*: the virtual generator voltage is obtained from the virtual frequency ( $\omega_{dc}^\gamma$ ), using the constant  $K_{e_\gamma}$ .
- 7) *Virtual Impedance*: a virtual impedance is used to determined the current reference which feed the inner control

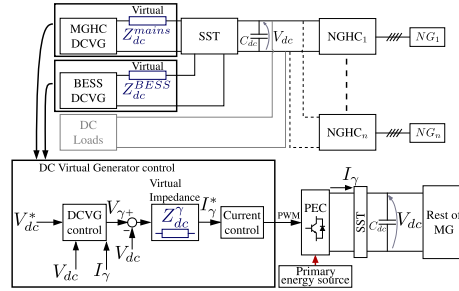


Fig. 5: Integration of the DC virtual generator in the DC bus. The identifier  $\gamma$  can be substituted by mains or BESS.

loops of the MGHC and BESS. The impedance consists of a resistance and an inductance ( $Z_{dc}^\gamma(s) = R_{dc}^\gamma + sL_{dc}^\gamma$ ).

- 8) *Virtual resistance decoupling*: suppress the voltage deviation during steady state due to the virtual impedance.

In order to demonstrate the operation of the proposed sharing scheme in DC, the power sharing performance for different values of inertia in the MGHC and the BESS is shown in Fig. 6. The figure shows the power shared by the mains ( $P_{mains}$ ), the BESS ( $P_{BESS}$ ), the load disturbance ( $P_{L_{dc}}$ ) and the power supplied by the LVDC bus capacitor ( $P_{C_{dc}}$ ). Three cases are compared: 1) the mains have a larger inertia, resulting in a higher contribution than the BESS during the transient; 2) both inertias are the same, contributing the mains and BESS equally to the initial transient; 3) the BESS presents higher inertia, supporting the transient power mismatch. In all the cases, the DC bus capacitor supplies the high bandwidth power mismatches. The stationary power sharing remains unchanged for the 3 cases and depends on the P/V DC droop ( $m_{mains} = 0.02$ ,  $m_{BESS} = 0.002$ ).

In this paper, the first scenario will be assumed, presenting the MGHC (mains) a higher inertia and power sharing contribution while the BESS remains as a MG back-up in case of contingencies in the mains, especially for *islanding* condition. The BESS inertia is kept low in order to reduce the stress on the battery and increase its life time. Fig. 7 illustrates the system behavior in the DC side for the set-point control under *grid connected* and *islanding* operation. As shown, once the mains is disconnected at  $t=3.65s$ , the battery has to fully support the DC link regulation, however, due to its low inertia, the DC voltage drop during transients becomes larger. At  $t=4.1s$  the mains is reconnected. It is worth to point out that the transition between *grid connected* and *islanding* modes is automatic and no *islanding* detection is needed to maintain the DC bus under regulation. The stationary voltage deviation with respect to the nominal DC voltage ( $V_{dc}^*$ ) is due to the P/V DC droop.

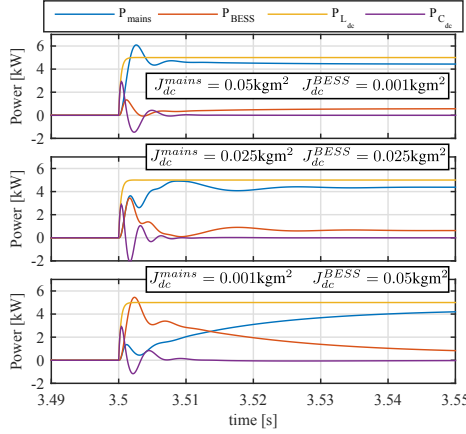


Fig. 6: Power sharing in the DC voltage regulation based on DC virtual generators. Comparison of the performance for different values of inertia in the MGHC (mains) and the BESS under a DC constant power load step disturbance in the DC bus.

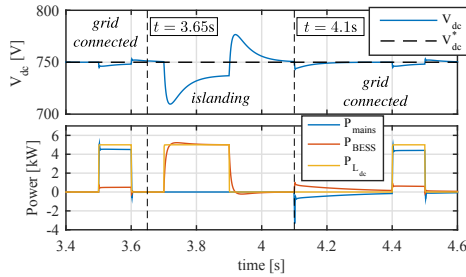


Fig. 7: LVDC control performance and power sharing during *grid connected* and *islanding* operation. The MG enters in *islanding* mode at  $t=3.65s$  and returns to *grid connected* at  $t=4.1s$

### III. VIRTUAL DC/AC GENERATOR SCHEME

The proposed Hybrid DC/AC virtual generator for the implementation of the NGHCs control is shown in Fig. 8. The proposed control is based on the model of a virtual DC generator mechanically coupled to a VSG through the rotor shafts. While the AC stator model, the current regulator and the AVR remains the same as in Fig. 3, the control related to the frequency regulation is modified to be dependent on the LVDC voltage. The governor is replaced by the model of a DC Virtual Machine (DCVM) and it consist of: 1) a DC

stator model ( $R_{dc}^k$  and  $L_{dc}^k$ ) that emulates a DC virtual stator impedance and establish the electrical torque applied to the DC machine depending on the LVDC voltage  $V_{dc}$  and a back electromotive force(bemf)  $E_{dc}^k$ ; 2) an AC/DC virtual rotor that provides the VI to the NGHC, determining the grid frequency; and 3) a frequency regulator based on the variation of the rotor flux  $\varphi$  to modify the relation between the rotational speed  $\omega_e^k$  and the bemf  $E_{dc}^k$ . The regulator  $R_{\omega_e^k}$  can be implemented as a slow PI or as an integrator, as the main function of this block is regulating the steady state frequency. In order to improve the response during start up, the inverse of the nominal bemf constant  $K_e^{-1}$  is applied as a feed-forward.

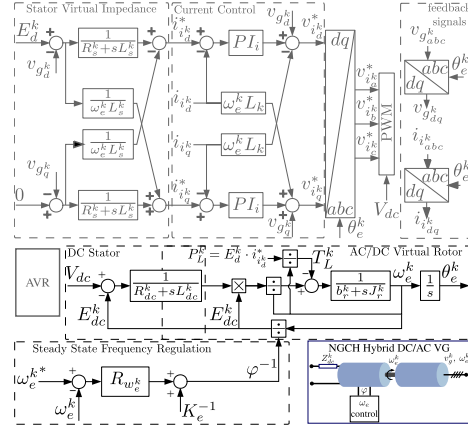


Fig. 8: Block diagram of the proposed Hybrid DC/AC virtual generator for enabling the cooperative power sharing between NGs through the LVDC.

The basic principle of operation consists on the following: in case the LVDC voltage varies, the frequency in the NGs will change, dynamically and proportionally, with the dynamics of the defined DC/AC virtual generator. The frequency regulator will allow to decouple the NGHC frequency  $\omega_e^k$  from the  $V_{dc}$  during steady state, thus the frequency can return to its nominal value even if the  $V_{dc}$  deviates from the nominal DC bus voltage.

### IV. COOPERATIVE DC/AC HYBRID MG CONTROL

The cooperative control consists in the integration of the Hybrid DC/AC virtual generator within the defined MG. Including the LVDC regulation based on DCVGs, the conceptual representation of the system based on virtual generators is shown in Fig. 9.

Unlike in the initial set-point presented in section II, once the proposed Hybrid DC/AC virtual generator is implemented in the NGHCs, the LVDC bus voltage behavior is coupled

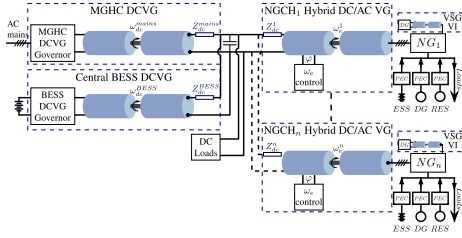


Fig. 9: MG representation with the proposed structure based on virtual generators.

to the grid frequency in the NGs. Thus, the NGHCs become sensitive to disturbances in the LVDC, and therefore, to the active power changes in other NGs, participating automatically in the LVDC regulation. This reduces the dependence on the mains, and alleviates the participation of the central BESS. During transients, the stiffness of the NGHCs will be softened and the inertial elements in the NGs (DERs operated as VSG or VI) will react to the frequency variation, injecting or absorbing active power. On the other hand, in case the BESS or the mains are not able to provide the required power during steady state, the system, including the LVDC bus, will be supported by those DERs in the NGs able to provide power during steady state. In order to allow this behavior, and increase the participation in the Hybrid DC/AC NG power sharing, either in transients or steady state, there should be DERs in the NGs that reacts to changes in frequency. This can be achieved by using VSG combined with droop controls or by using dedicated frequency compensation devices based on VI.

#### V. DGs AND ESS PARTICIPATION IN THE NGs

As mentioned before, apart from PQ mode and MPPT mode, some of the DERs within the NGs (DGs and ESS) can be operated as VI-based frequency compensators or VSGs in order to participate in the voltage magnitude and frequency regulation. This allows to provide additional inertia to the grid, and, if combined with P/f Q/V droop, decentralized cooperation during steady state. Two options are considered for voltage and frequency support in the NGs.

One of the most extended solutions for frequency compensation is to use ESSs operated as a virtual inertia. The controller in dq frame is defined by the swing equation (4), where  $i_{vi,d}^*$  is the current reference of the frequency compensator,  $K_{vi}$  the damping coefficient,  $J_{vi}$  the VI gain, and  $v_{pcc,d}$  is the voltage at the point of connection. The frequency  $\hat{\omega}_e$  is the frequency estimated at the point of common coupling.

$$i_{vi,d}^*(t) = \left( \underbrace{K_{vi} \cdot (w_e^*(t) - \hat{w}_e(t))}_{\text{Damping factor}} - \underbrace{J_{vi} \cdot \frac{d\hat{w}_e(t)}{dt}}_{\text{Virtual Inertia}} \right) \frac{\hat{w}_e(t)}{v_{pcc,d}(t)} \quad (4)$$

TABLE I: System Parameters

AC NGs and NGHCs Parameters	Values
AC Nominal Voltage ( $v_g^{k*}, \omega_g^{k*}$ )	230 V <sub>AC,rms</sub> / 50Hz
NGHCs Filter ( $L_k, C_k$ )	1mH / 80μF
NGHCs Virtual Impedance ( $L_k^k, R_k^k$ )	0.1mH / 2Ω
NGHCs AVR integral gain ( $K_{AVR}^k$ )	5
NGHCs Virtual Inertia ( $J_p^k, b_p^k$ )(case 1)	0.1kgm <sup>2</sup> / 1Nms
NGHCs Virtual Inertia ( $J_p^k, b_p^k$ )(case 2)	3kgm <sup>2</sup> / 0.01Nms
NGHCs Governor BW (case 1)	50Hz
NGHCs DC Virtual Impedance ( $L_{dc}^k, R_{dc}^k$ )	0mH / 1Ω
NGHCs freq reg $R_{\omega^k}$ ( $K_{p,\omega^k}, K_{i,\omega^k}$ )	0.01 / 0.01
NG <sub>2</sub> Frequency compensator ( $K_{vi}, J_{vi}$ )	6 / 1kgm <sup>2</sup>
LVDC Parameters	Values
DC Nominal Voltage ( $V_{dc}^*$ )	750 V
Current control BW (mains & BESS)	500Hz
DC bus Capacitor ( $C_{dc}$ )	750μF
$K_{emains}$ and $K_{dBESS}$	2.38 V·s/rad
DCVGs Virtual impedance $L_{dc}^i, R_{dc}^i$	0mH / 1Ω
mains droop gain $m_{mains}$	$2.5 \times 10^{-5}$
BESS droop gain $m_{BESS}$	$2.08 \times 10^{-4}$
mains Virtual Inertia ( $J_{mains}^i, b_{mains}^i$ )	0.005kgm <sup>2</sup> / 0.01Nms
BESS Virtual Inertia ( $J_{dc}^{BESS}, b_{dc}^{BESS}$ )	0.001kgm <sup>2</sup> / 0.015Nms
mains and BESS Governor BW	50Hz

#### VI. SIMULATION RESULTS

The proposed system has been validated through simulations in MATLAB/Simulink®. The parameters are summarized in Table I.

##### A. MG performance under the proposed control scheme

Two cases are simulated to evaluate the performance of the proposed cooperative control: 1) The first case consist on the simulation of the base set-point case describe in section II. The LVDC bus is regulated by the MGHC and BESS operated as DCVGs with a P/V DC droop as described in section II-B. The MGHC (mains) provides the majority of the inertia and steady state power sharing while the central BESS is mainly conceived as a back up for contingencies like *islanding*, presenting low inertia and reduced participation in the power sharing under normal conditions. The NGHCs are controlled as grid forming according to the VSG topology in Fig. 3, presenting a stiff governor response and a high VI. 2) In the second case, the control in the NGHCs is modified, introducing the Hybrid DC/AC virtual generator proposed in section III, shown in Fig. 8. The LVDC bus regulation remains the same as in the first case.

In both cases, the parameters in common are the same and similar conditions are established: 1) two NGs are connected to the LVDC line; 2) In the  $NG_1$  just active loads are connected to the grid. 3) a DC load ( $P_{Ldc}$ ) is directly connected to the LVDC bus. 4) In the  $NG_2$  not only active loads, but also a DER operated as a frequency compensator is present in the NG. The frequency compensator, operated based on the VI controller defined by (4), could be implemented by any DG or a local ESS with high dynamics; 5) two modes of operation are considered *grid connected* and *islanding*. Under *grid connected* the power to control the LVDC is shared by the mains and the central BESS. During *islanding*, the LVDC control relies only in the BESS. As the BESS is configure

with a reduced inertia, the DC voltage profile will be affected during transients. Moreover, due to the power limitations of the central BESS, the system stability can be compromised if an overrated operation is reached.

The simulations evaluate the 2 modes of operation under multiple active power steps in the NGs and LVDC bus. The results, comparing the two studied cases are shown in Fig. 10. It shows the DC voltage, the AC voltage in both NGs, grid frequency in each NG, the power delivered by the mains, central BESS and frequency compensator, and the load in each NG and DC bus. The figure is described as follows:

- From  $t = 0s$  to  $t = 1.2s$  the MG operates in *grid connected* mode. During this mode the  $V_{dc}$  response presents a high stiffness in both cases. For the case 1, the grid frequency is only affected by power changes in the corresponding NG, thus, the NGs does not react to the DC load. Conversely, in the second case, the frequency in both NGs is sensitive to changes in any NG and the DC bus, being slightly disturbed by the DC load connection and disconnection.
- From  $t = 1.2s$  to  $t = 3s$  the mains are disconnected and the MG changes to *islanding* mode. In case 1, the operation in the NGs is similar than in *grid connected*, however, the  $V_{dc}$  profile is notably worsen, presenting the case 2 a better LVDC profile thanks to the proposed cooperative control. For case 2, the coupling between NGs and DC bus becomes evident, in both voltage and frequency signals. Thus, the frequency compensator not only helps with the frequency regulation in  $NG_2$ , but also collaborate with the LVDC regulation and the frequency regulation in  $NG_1$  indirectly, reacting to the  $NG_1$  load and the DC load. It is clearly seen how the battery stress is reduced compared with case 1. In both cases a better frequency response is observed in the  $NG_2$ , due to the presence of the frequency compensator. Despite the  $V_{dc}$  steady state deviation due to P/V DC droop, it is worth noting how in the case 2 the frequency steady state error in both NGs is zero thanks to the frequency regulation block.
- At  $t = 3s$  the total load in the MG exceeds the central BESS maximum power. In case 1, as the NGHCs are decoupled from the  $V_{dc}$  regulation, the whole system leads to instability and collapses although there is available power in the frequency compensator of  $NG_2$ . On the other, the proposed control allows to maintain the system operation automatically, in trade of an steady state error in the  $V_{dc}$  and the NGs' frequencies, being the active power mismatch sustained by the frequency compensator of  $NG_2$ .

#### B. P/V DC droop performance

In order to evaluate the functioning of the P/V DC droop and its effects on the system performance, an additional simulation, shown in Fig. 11, has been carried out for illustrating in detail its operation under a DC load step and a sudden change in the mains and BESS droop gains during *grid connected*

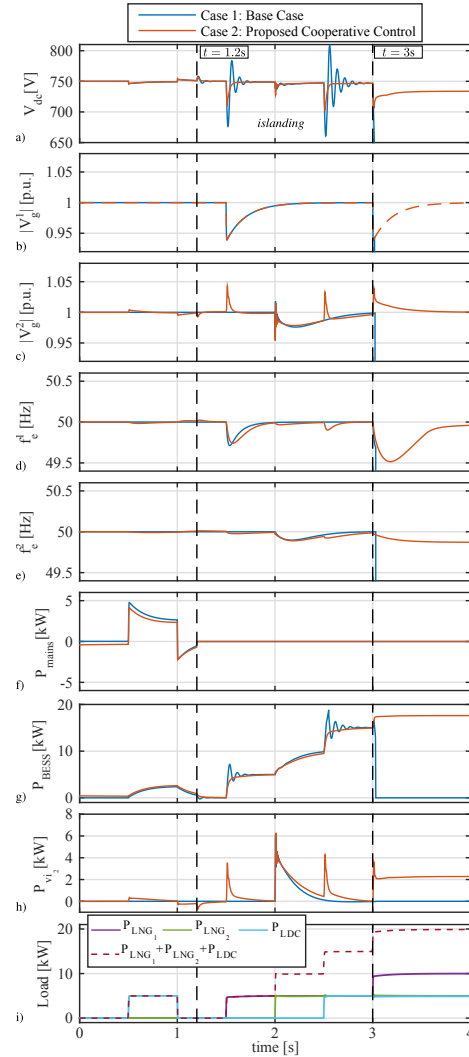


Fig. 10: Simulation results: comparison between the base case and the proposed cooperative hybrid MG control. a) LVDC bus voltage; b) and c) NGs voltage magnitude; d) and e) NGs frequency; f),g) and h) power shared by the mains, BESS and frequency compensator; i) NGs AC loads and DC load.

mode. At  $t=1s$  a DC load is connected. As a consequence the LVDC voltage drops due to the P/V droop and the mains and BESS virtual generator voltages are modified to provide a determined power sharing. The NGs frequencies are also affected, returning to its nominal value after the transient. At  $t=4s$ , the droop gains are changed, modifying the power shared by the mains and BESS as well as the virtual voltages.

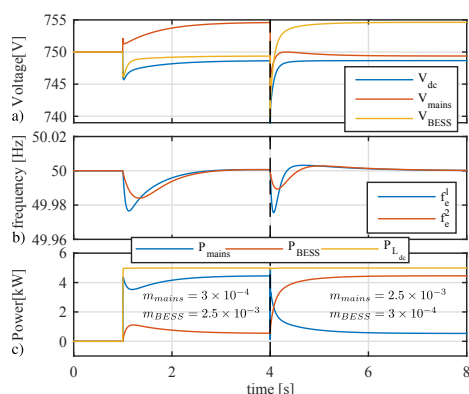


Fig. 11: Simulation results: P/V DC Droop operation. a) LVDC bus voltage and virtual mains and BESS voltages; b) NGs frequencies; c) power shared by the mains, BESS and DC load.

## VII. CONCLUSIONS

In this paper, a cooperative voltage and active power control is proposed for a hybrid AC/DC Microgrid with ESS, based on hybrid DC/AC virtual generators that allows the indirect collaboration between the regulation in the AC NGs and the LVDC bus, maintaining the grid quality in both the LVDC and the AC NGs. A control scheme based on DC virtual generators is proposed for the DC voltage regulation and power sharing between the mains and the central BESS that allows to adapt the participation of the mains and BESS in the transient and stationary power sharing for DC bus regulation and enable an automatic transition between *grid connected* and *islanding* modes. Meanwhile, the DC/AC virtual generators allow an automatic power sharing that couples the LVDC voltage and the NGs voltage and frequency, maintaining the power balance in the hybrid MG, not only reducing the stress in the central BESS and the dependence in the utility grid but also demonstrating the extended operation and improved transient response in the LVDC when the central BESS presents low inertia and power limitations. The theoretical discussion has been supported with simulations in MATLAB/Simulink.

## REFERENCES

- [1] J. M. Guerrero, "Editorial Special Issue on Power Electronics for Microgrids 2014:Part II," *IEEE Transactions on Power Electronics*, vol. 26, no. 3, pp. 659–663, March 2011.
- [2] J. Guerrero, P. C. Loh, T.-L. Lee, and M. Chandorkar, "Advanced Control Architectures for Intelligent Microgrids 2014:Part II: Power Quality, Energy Storage, and AC/DC Microgrids," *IEEE Transactions on Industrial Electronics*, vol. 60, no. 4, pp. 1263–1270, April 2013.
- [3] P. Wang, X. Liu, C. Jin, P. Loh, and F. Choo, "A hybrid AC/DC micro-grid architecture, operation and control," in *Power and Energy Society General Meeting, 2011 IEEE*, July 2011, pp. 1–8.
- [4] J. He, Y. W. Li, and F. Blaabjerg, "Flexible Microgrid Power Quality Enhancement Using Adaptive Hybrid Voltage and Current Controller," *Industrial Electronics, IEEE Transactions on*, vol. 61, no. 6, pp. 2784–2794, June 2014.
- [5] J. Zhang, D. Guo, F. Wang, Y. Zuo, and H. Zhang, "Control strategy of interlinking converter in hybrid AC/DC microgrid," in *Renewable Energy Research and Applications (ICRERA), 2013 International Conference on*, Oct 2013, pp. 97–102.
- [6] M. Ambia, A. Al-Durra, and S. Mueyeen, "Centralized power control strategy for AC-DC hybrid micro-grid system using multi-converter scheme," in *IECON 2011 - 37th Annual Conference on IEEE Industrial Electronics Society*, Nov 2011, pp. 843–848.
- [7] Y.-R. Mohamed and E. El-Saadany, "Adaptive Decentralized Droop Controller to Preserve Power Sharing Stability of Paralleled Inverters in Distributed Generation Microgrids," *Power Electronics, IEEE Transactions on*, vol. 23, no. 6, pp. 2806–2816, Nov 2008.
- [8] M. Golsorkhi and D. Lu, "A Control Method for Inverter-Based Islanded Microgrids Based on V-I Droop Characteristics," *Power Delivery, IEEE Transactions on*, vol. 30, no. 3, pp. 1196–1204, June 2015.
- [9] P. Arbolea, C. Gonzalez-Moran, and M. Coto, "A hybrid central-distributed control applied to microgrids with droop characteristic based generators," in *Power Electronics and Motion Control Conference (EPE/PEMC), 2012 15th International*, Sept 2012, pp. LS7a.5–1–LS7a.5–8.
- [10] A. Navarro-Rodriguez, P. Garcia, R. Georgious, J. Garcia, and S. Saeed, "Observer-based transient frequency drift compensation in ac microgrids," *IEEE Transactions on Smart Grid*, vol. PP, no. 99, pp. 1–1, 2017.
- [11] A. Navarro-Rodriguez, P. Garcia, R. Georgious, and J. Garcia, "A communication-less solution for transient frequency drift compensation on weak microgrids using a D-statcom with an energy storage system," in *Energy Conversion Congress and Exposition (ECCE), 2015 IEEE*, Sept 2015, pp. 6904–6911.
- [12] I. Serban and C. Marinescu, "Control Strategy of Three-Phase Battery Energy Storage Systems for Frequency Support in Microgrids and with Uninterrupted Supply of Local Loads," *Power Electronics, IEEE Transactions on*, vol. 29, no. 9, pp. 5010–5020, Sept 2014.
- [13] M. Torres L., L. Lopes, L. Moran T., and J. Espinoza C., "Self-Tuning Virtual Synchronous Machine: A Control Strategy for Energy Storage Systems to Support Dynamic Frequency Control," *Energy Conversion, IEEE Transactions on*, vol. 29, no. 4, pp. 833–840, Dec 2014.
- [14] Y. Hirase, O. Noro, K. Sugimoto, K. Sakimoto, Y. Shindo, and T. Ise, "Effects of suppressing frequency fluctuations by parallel operation of virtual synchronous generator in microgrids," in *Energy Conversion Congress and Exposition (ECCE), 2015 IEEE*, Sept 2015, pp. 3694–3701.
- [15] L. Benadero, R. Cristiano, D. J. Pagano, and E. Ponce, "Nonlinear analysis of interconnected power converters: A case study," *IEEE Journal on Emerging and Selected Topics in Circuits and Systems*, vol. 5, no. 3, pp. 326–335, Sept 2015.
- [16] T. Vandorm, B. Renders, L. Degroote, B. Meersman, and L. Vanvelde, "Active Load Control in Islanded Microgrids Based on the Grid Voltage," *Smart Grid, IEEE Transactions on*, vol. 2, no. 1, pp. 139–151, March 2011, use of Voltage-droop control.
- [17] A. Navarro-Rodriguez, P. Garcia, R. Georgious, and J. Garcia, "Adaptive active power sharing techniques for dc and ac voltage control in a hybrid dc/ac microgrid," in *2017 IEEE Energy Conversion Congress and Exposition (ECCE)*, Oct 2017, pp. 30–36.
- [18] D. Chen, Y. Xu, and A. Q. Huang, "Integration of dc microgrids as virtual synchronous machines into the ac grid," *IEEE Transactions on Industrial Electronics*, vol. 64, no. 9, pp. 7455–7466, Sept 2017.